Transactions of the ASME

Journal of Heat Transfer

Published Quarterly by The American Society of Mechanical Engineers

VOLUME 105 • NUMBER 2 • MAY 1983

HEAT TRANSFER DIVISION
Chairman, **A. E. BERGLES**
Secretary, **F. A. KULACKI**
Senior Technical Editor, **K. T. YANG**
Technical Editor, **I. CATTON**
Technical Editor, **M. EPSTEIN**
Technical Editor, **G. M. FAETH**
Technical Editor, **R. GREIF**
Technical Editor, **P. J. MARTO**
Technical Editor, **R. H. PLETCHER**
Technical Editor, **R. K. SHAH**
Technical Editor, **R. VISKANTA**

BOARD ON COMMUNICATIONS
Chairman and Vice President
MICHAEL J. RABINS

Members-at-Large
W. BEGELL
J. CALLAHAN
D. KOENIG
M. KUTZ
F. LANDIS
J. LOCKE
J. ORTLOFF
C. PHILLIPS
H. C. REEDER
K. REID

President, **SERGE GRATCH**
Executive Director
PAUL ALLMENDINGER
Treasurer,
ROBERT A. BENNETT

PUBLISHING STAFF
Mng. Dir., Publ., **J. J. FREY**
Dep. Mng. Dir., Pub.,
JOS. SANSONE
Managing Editor,
CORNELIA MONAHAN
Production Editor,
JACK RUMMEL
Editorial Prod. Asst.,
BETH DARCHI

Journal of Heat Transfer (ISSN 0022-1481) is edited and published quarterly at the offices of The American Society of Mechanical Engineers, United Engineering Center, 345 E. 47th St., New York, N. Y. 10017. ASME-TWX No. 710-581-5267, New York. Second-class postage paid at New York, N.Y., and at additional mailing offices.

CHANGES OF ADDRESS must be received at Society headquarters seven weeks before they are to be effective. Please send old label and new address.

PRICES: To members, $36.00, annually; to nonmembers, $72.00. Single copies, $24.00 each. Add $6.00 for postage to countries outside the United States and Canada.

STATEMENT from By-Laws. The Society shall not be responsible for statements or opinions advanced in papers or . . . printed in its publications (B7.1, para. 3).

COPYRIGHT © **1983** by the American Society of Mechanical Engineers. Reprints from this publication may be made on condition that full credit be given the TRANSACTIONS OF THE ASME, JOURNAL OF HEAT TRANSFER, and the author, and date of publication be stated.

INDEXED by the Engineering Index, Inc.

ANNOUNCEMENTS

TECHNICAL PAPERS

(contents continued on page 225)

Downloaded 04 Feb 2011 to 194.85.80.107. Redistribution subject to ASME license or copyright; see http://www.asme.org/terms/Terms_Use.cfm

(contents continued)

TECHNICAL NOTES

Freezing in a Vertical Tube

E. M. Sparrow
Fellow ASME

J. A. Broadbent
Department of Mechanical Engineering,
University of Minnesota,
Minneapolis, Minn. 55455

Fundamental heat transfer experiments were performed for freezing of an initially superheated or nonsuperheated liquid in a cooled vertical tube. Measurements were made which yielded information about the freezing front and the frozen mass, about the various energy components extracted from the tube, and about the decay of the initial liquid superheat. Four component energies were identified and evaluated from the experimental data, including the latent energy released by the phase change and sensible energies released from the subcooled frozen solid and the superheated liquid. Initial superheating of the liquid tended to moderately diminish the frozen mass and latent energy extraction at short freezing times but had little effect on these quantities at longer times. The extracted sensible energies associated with the superheating more than compensated for the aforementioned decrease in the latent energy. Although the latent energy is the largest contributor to the total extracted energy, the aggregate sensible energies can make a significant contribution, especially at large tube wall subcooling, large initial liquid superheating, and short freezing time. Natural convection effects in the superheated liquid were modest and were confined to short freezing times.

Introduction

In this paper, experiments are described which examine the fundamental heat transfer processes that accompany freezing of a phase-change material contained in an externally cooled vertical tube. The work was motivated by current interest in thermal energy storage devices in which a phase-change medium is encapsulated within cylindrical containers. The results obtained here may also be relevant to other applications such as the freezing of foodstuffs and biological materials and to casting processes in general.

Storage of thermal energy by liquid-solid phase change has prompted an upsurge of research on the heat transfer aspects of freezing and melting, as witnessed by two highly current survey articles [1, 2]. However, neither in these surveys nor in the general heat transfer literature were the authors able to find definitive experimental work on the heat transfer fundamentals of freezing inside a cooled vertical tube. Metallurgically oriented studies of freezing during casting are available, as are other applications-related papers, but there is little common ground between the research objectives and type of results of that literature and those of the present investigation.

In the experiments, each data run was begun with the liquified phase-change medium situated in the vertical containment tube at a uniform temperature that was either at the phase-change value or at a preselected superheat above the phase-change value. The freezing was initiated and maintained by a step-change decrease of the wall temperature of the containment tube. During the course of the run, the freezing front moved radially inward from the wall of the tube toward the axis. At any instant of time, the configuration of the phase-change medium consisted of an annulus of solidified material adjacent to the tube wall and a core of unfrozen liquid.

The difference between freezing initiated with the liquid at the phase-change temperature or at superheat was investigated in detail since the presence of superheat activates transport processes in the liquid that are otherwise dormant. One of these is natural convection, which is driven by the temperature difference between the superheated liquid and the freezing front. In studies of freezing outside of a cooled vertical tube, natural convection was found to have a profound effect in slowing and even terminating freezing [3], but its influence on internal freezing was heretofore unknown. Without superheat, heat conduction in the solidified layer is the sole heat transfer vehicle.

In addition to the degree of superheat, two other parameters were varied during the course of the experiments. One of these is the temperature imposed on the wall of the containment tube during the freezing process. The other is the duration of the freezing period.

The measurements performed during the experiments enabled the evaluation of a number of quantities of both practical and fundamental interest. Each of the components of the energy extracted from the cooled tube was evaluated from the experimental data and is presented as a function of time for each data run. For freezing initiated without liquid superheat, there are two components—the latent heat liberated by the phase change and the sensible heat liberated by the subcooling of the solid. In the case of freezing initiated with liquid superheat, there are two additional contributions, both associated with the sensible heat of the liquid. The relative magnitudes of these various energy components are compared, and a definitive conclusion is drawn about the net effect of superheating on the amount of energy that can be extracted from the phase change medium during a specified extraction period.

Direct measurements were made of the frozen mass and frozen layer thickness as a function of time and of the thermal operating conditions, and this information is presented both in dimensional and dimensionless form. These direct measurements also revealed the extent of the axial variations of the layer thickness caused by natural convection in the superheated liquid. In addition, these measurements enabled the evaluation of the end effects associated with the finite length of the containment tube. Other measurements yielded the decay of the liquid superheat as a function of time.

To supplement the experimental results, numerical solutions were carried out using a pure conduction model of the no-superheat case. The computed results for the frozen layer thickness (~ liberated latent heat) and the liberated sensible heat are compared with the corresponding experimental results.

The experiments were performed with 99-percent pure n-eicosane paraffin, with a measured melting temperature of 36.4°C.

The Experiments

Experimental Apparatus. The main components of the

Contributed by the Heat Transfer Division for publication in the JOURNAL OF HEAT TRANSFER. Manuscript received by the Heat Transfer Division May 17, 1982.

apparatus included the containment tube for the phase-change medium, a chilled-water bath which served as the thermal environment for the freezing experiments, a heated-water bath used in establishing the temperature of the liquified phase-change medium prior to a freezing run, and a vacuum system for extracting the residual liquid remaining at the end of the run. This equipment was supplemented by a chilled-water supply, by devices for heating, circulating, and controlling the temperature of the water in the respective baths, and by appropriate instrumentation.

The containment tube was a copper cylinder with an internal diameter of 5.08 cm and a 0.15-cm-thick wall, the choice of copper and of a thin wall being made to facilitate the establishment of the thermal boundary condition for the freezing experiments. The overall length of the tube, 39.4 cm, was chosen to accommodate a 5:1 length-diameter ratio for the liquified phase-change medium, with allowance made for the insulating plugs which penetrated into the bottom and top ends of the tube. These plugs were employed to minimize end effects.

At the bottom end, the insulating plug, made of closed-cell polystyrene, was cemented atop an O-ring-equipped Teflon base which provided a watertight seal. Adhesion of the solidified paraffin to the polystyrene was prevented by the presence of a thin, impermeable plastic film that was wrapped around the polystyrene prior to each data run. The insulating plug at the top end was also of polystyrene, with a self-adhering impermeable plastic coating. When the tube was charged with liquid paraffin, a small gap (~ 1.2 cm) was left between the free surface of the liquid and the lower face of the top-end plug. As will be shown later, the volume of the air gap increased as the paraffin froze and contracted.

To facilitate its vertical suspension in the respective water baths, the tube was equipped with trunions affixed to its uper end. The suspension arrangement was such that the lower 35.8 cm of the tube was immersed in the water, while the upper 3.6 cm protruded above the water surface.

The tube wall temperature was measured by eight fine-gage, chromel-constantan thermocouples deployed along the height and around the circumference. The thermocouples had been calibrated prior to their installation in the apparatus.

Attention will now be turned to the constant-temperature water baths. One of these baths was employed to establish the temperature of the liquified phase-change medium prior to the initiation of the freezing runs, either at the phase-change value or at a specified superheat. To fulfill this objective, the containment tube, already charged with liquid paraffin, was suspended in a water-filled cylindrical vessel equipped with a Lauda model B-1 heating, circulating, temperature-controlling unit. During the equilibration period, thermocouples were situated in the liquid paraffin to detect the attainment of a steady uniform temperature at the preselected value. To ensure that all the freezing runs corresponding to the same nominal initial condition actually attained that condition, the setting of the temperature controller was never touched during such a sequence of runs.

The chilled-water bath which served as the thermal environment for the freezing experiments was contained in a 53 × 41 × 38 cm (length × width × height) stainless steel tank insulated below and on all sides. The top of the tank was covered by a reinforced plexiglas plate in which apertures had been machined to facilitate installation of the containment tube and other equipment. A pair of short V-blocks situated atop the plexiglas plate served to seat the trunions of the containment tube. The bath was, in effect, an open system into which temperature-controlled chilled water was continuously introduced and withdrawn, both at the same rate, thereby maintaining a constant water level. A high degree of agitation and mixing was maintained in the water bath by circulating devices and by jet action in order to attain high convective heat transfer coefficients on the outside surface of the containment tube.

The chilled water supply was built specially for these experiments. The refrigeration unit was designed to have a very short cycling time. In addition, a large chilled-water reservoir was incorporated into the sytem to smooth any temperature fluctuations associated with cycling. Since more precise temperature control can be achieved for heating than for cooling, the chilled water was introduced into the water bath at a temperature slightly below the desired operating value. A Lauda B-1 temperature controller was employed to bring the temperature to the desired level, as detected by thermocouples.

A specially designed vacuum system was employed to remove any residual liquid paraffin remaining in the containment tube at the end of the data run and, thereby, to terminate the freezing process. A length of small diameter copper tubing, which served as the wand of the vacuum system, was inserted into the containment tube at the moment when the liquid was to be extracted.

With regard to instrumentation, the thermocouple emfs were read with a digital voltmeter with a resolving power of 1 μV(0.02°C). ASTM-certified 0.1°F or 0.1°C thermometers were used to stir and measure the temperature of the unfrozen liquid during selected freezing runs (to be discussed later). The mass of the paraffin and the containment tube were measured with an Ohaus triple-beam balance having a resolving power of 0.1 g and a capacity of 2610 g.

Experimental Procedure. The preparations for a freezing run were initiated with the containment tube empty and thoroughly clean, with the insulating plugs removed from the ends. To begin, the bottom-end plug was covered with a fresh plastic wrap which was fixed in place with rubber bands. Then, three 0.018-cm dia 61-cm long monofilament nylon

Nomenclature

c_{liq} = liquid-phase specific heat
$c_{\mathrm{liq},i}$ = value of c_{liq} at T_i
c_{sol} = solid-phase specific heat
E_{s1} = energy extracted from subcooled solid
E_{s2} = energy extracted from liquid which solidifies
E_{s3} = energy extracted from liquid which remains unfrozen
E_{tot} = total energy extracted, equations (4) and (7)
E_λ = energy liberated by feeezing
$E_{\lambda,\max}$ = energy liberated if total mass freezes
Fo = Fourier number, equation (10)
k_{sol} = solid-phase thermal conductivity
M = frozen mass
M_{tot} = total mass of phase-change material
r = radial coordinate in solid
r_w = radius of tube wall
r^* = radius of solid-liquid interface
Ste = solid-phase Stefan number, equation (11)
$\mathrm{Ste}_{\mathrm{liq},i}$ = initial liquid-phase Stefan number, equation (13)
T_b = liquid bulk temperature
T_i = initial temperature of liquid
T_m = mean temperature of frozen mass, equation (3)
T_w = tube wall temperature
$T(r)$ = temperature distribution in solid
T^* = phase-change temperature
t = time
α_{sol} = solid-phase thermal diffusivity
δ = frozen layer thickness
λ = latent heat of fusion
ρ_{sol} = solid-phase density

threads were attached to the side of the plug at uniform circumferential intervals by slipping them under the rubber bands. Later, at the end of the freezing run, these threads would facilitate removal of the solidified paraffin specimen from the containment tube. The bottom-end plug was then inserted in the containment tube and the nylon threads pulled upward through the tube and out the top, from which point they were secured against the outside of the tube by tape.

Next, the containment tube was placed on the pan of the Ohaus balance and positioned vertically on the balance pan, with its open end up. After the mass was recorded and with the tube still on the balance, 400 g of liquid paraffin was poured into the opening, whereafter the top-end insulating cap was implanted. The tube and its contents were then transferred to the equilibration bath to attain the desired liquid-phase temperature, which was achieved within about an hour and a half.

At this point, the containment tube was moved quickly (within 10 s) to the chilled-water bath, and the freezing run initiated. During the run, the tube wall and water bath temperatures were recorded at regular intervals. To terminate the run, the top-end cap was removed and the wand of the vacuum system inserted into the remaining liquid paraffin. Extraction of the liquid required from 5 to 20 s. Since, in many cases, the remaining liquid was at the fusion temperature, it was necessary to preheat both the wand and its atttached plastic hose to prevent clogging of the lines. Once the liquid paraffin had been drawn off, the containment tube was removed from the chilled water bath, carefully dried, and weighed. The mass of the frozen paraffin was determined by subtracting the initial empty weight of the containment tube from this final weight.

The next step was to remove the frozen specimen from the tube in order to measure the shape of the freezing front. This operation required a brief immersion of the tube in a hot bath in order to sever the bond between the specimen and the tube wall, after which the specimen was extracted with the aid of the nylon threads. Once removed, the specimen was sectioned transversely at selected axial stations and its internal dimensions measured with a dial-gage-equipped caliper. Additional measurements were made adjacent to the ends of the specimen in order to quantify the end effects.

Supplemental data runs were made to measure the temperature of the liquid paraffin remaining at the end of the run (relevant only to cases where the terminal temperature of the liquid was above the phase-change temperature). For these runs, the liquid was not drawn off at the termination of the run. Rather, one of the aforementioned certified thermometers, preheated to the expected temperature, was inserted into the liquid. With well-practiced vigorous stirring, a bulk temperature reading could be attained within 10 s.

Data Reduction

From the experimental data, all of the components of the energy extracted from the containment tube during a data run were determined. There are two such components for freezing initiated without liquid superheat and four components when there is liquid superheat.

If M denotes the mass frozen during a data run and E_λ is the latent heat released by the freezing process, then

$$E_\lambda = \lambda M \tag{1}$$

where λ is the latent heat of fusion. E_λ constitutes one of the components of the extracted energy—the largest.

The second component is the energy that is released as sensible heat by the subcooling of the frozen solid below the phase-change temperature. This quantity will be denoted by E_{s1}, where the subscript s denotes sensible energy. The second subscript 1 will be used to identify the sensible energy extracted from the solid (shortly, subscripts $s2$ and $s3$ will be employed to identify sensible energies released by the superheated liquid).

With regard to the method used for evaluating E_{s1}, the solid-phase specific heat, c_{sol}, was taken as a constant because there is no information available about its possible temperature dependence [4]. Then, the sensible energy liberated from the frozen mass, M, can be written as

$$E_{s1} = Mc_{\mathrm{sol}}(T^* - T_m) \tag{2}$$

where T^* is the phase-change temperature, and T_m is the mean temperature of the frozen mass, M, at the end of the data run

$$T_m = \int_{r^*}^{r_w} T(r)\,\rho_{\mathrm{sol}} 2\pi r dr \Big/ \int_{r^*}^{r_w} \rho_{\mathrm{sol}} 2\pi r dr \tag{3}$$

The range of the integration spans the frozen region—from the radius r^* of the solid-liquid interface to the radius, r_w, of the containment tube, and ρ_{sol} is the density of the solid phase.

The radial temperature distribution $T(r)$ needed for the evaluation of equation (3) was obtained by postulating a quasi-steady model and solving the energy equation $d(k_{\mathrm{sol}} r dT/dr) = 0$ subject to the boundary conditions $T = T^*$ at $r = r^*$ and $T = T_w$ (tube wall temperature) at $r = r_w$. The latter condition assumes initimate contact between the frozen paraffin and the tube wall, and this appears to have been the case because the frozen specimens could not be extracted from the tube until the bond was melted away. The thermal conductivity, k_{sol}, of the solid is a strong function of temperature, and the available data [5] were represented by a linear fit $k_{\mathrm{sol}} = C_1 + C_2 T$.

For the $T(r)$ solution corresponding to each data run, the experimental values of r^* and T_w were employed as input. For each of the resulting $T(r)$ solutions, T_m was determined from equation (3), after which the energy component E_{s1} was evaluated from equation (2).

In the case where the initial temperature, T_i, of the liquid is at the phase-change value, T^*, the total energy, E_{tot}, is the sum of E_λ and E_{s1}

$$E_{\mathrm{tot}} = E_\lambda + E_{s1}, \quad T_i = T^* \tag{4}$$

Where there is initial superheat (i.e., $T_i > T^*$), there are two additional sensible heat contributions, E_{s2} and E_{s3}, to E_{tot}.

The component E_{s2} is the sensible energy released from the liquid which is frozen during the course of the data run. Since the liquid cools from T_i to T^* before frozen and M is the mass frozen during the data run

$$E_{s2} = M \int_{T^*}^{T_i} c_{\mathrm{liq}}\, dT \tag{5}$$

The liquid-phase specific heat c_{liq} presented in [4] was fit by a linear representation and introduced into equation (5).

The final energy component, E_{s3}, is the sensible energy released from the liquid which remains unfrozen at the end of the data run. If the initial charge of paraffin has a mass M_{tot}, and M is the frozen mass, then the residual liquid is $(M_{\mathrm{tot}} - M)$. During the course of the run, this liquid cools from an initial temperature, T_i, to a final bulk temperature, T_b, so that

$$E_{s3} = (M_{\mathrm{tot}} - M) \int_{T_b}^{T_i} c_{\mathrm{liq}}\, dT \tag{6}$$

where T_b was measured directly as described earlier.

In view of the foregoing

$$E_{\mathrm{tot}} = E_\lambda + E_{s1} + E_{s2} + E_{s3}, \quad T_i > T^* \tag{7}$$

For data runs of sufficiently long duration (to be elaborated

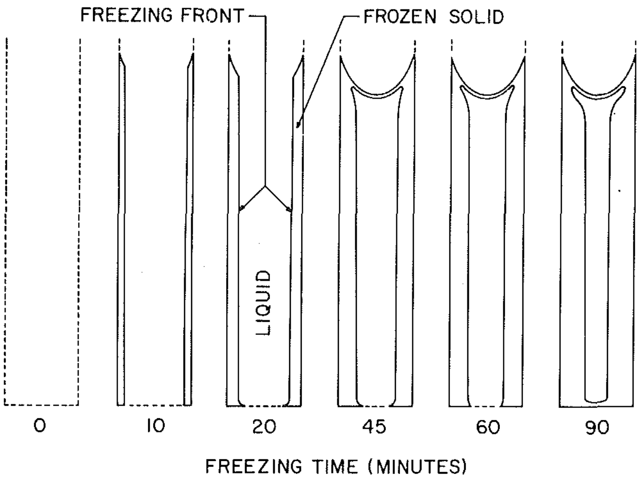

Fig. 1 Representative pattern of freezing; $(T_i - T^*) = 22.2°\mathrm{C}\ (40°\mathrm{F})$ and $(T^* - T_w) = 9.7°\mathrm{C}\ (17.5°\mathrm{F})$

later), the liquid bulk temperature, T_b, becomes equal to the phase-change temperature, T^*. In that case,

$$E_{s2} + E_{s3} = M_{\mathrm{tot}} \int_{T^*}^{T_i} c_{\mathrm{liq}} dT = \text{constant} \tag{8}$$

Thus, for run times greater than that required for T_b to drop to T^*, the sum of E_{s2} and E_{s3} is a constant, independent of time.

For a dimensionless presentation, it is convenient to normalize all energy quantitites by $E_{\lambda,\max}$, which is the latent energy that would be extracted if the entire charge of phase-change material were to be melted

$$E_{\lambda,\max} = \lambda M_{\mathrm{tot}} \tag{9}$$

The other dimensionless quantities to be used in the presentation of the results are the Fourier and Stefan numbers

$$\mathrm{Fo} = \alpha_{\mathrm{sol}} t / r_w^2 \tag{10}$$

$$\mathrm{Ste}_{\mathrm{sol}} \equiv \mathrm{Ste} = c_{\mathrm{sol}} (T^* - T_w)/\lambda \tag{11}$$

The temperature at which the properties appearing in Fo and Ste were evaluated will be discussed when the results are presented.

Results and Discussion

The presentation of results will begin with a display of the pattern of freezing. It then goes on to the basic data for the frozen mass, freezing front position, and liquid bulk temperature, with correlations sought using dimensionless variables. Finally, and most important, the results for the component and total energies are presented and discussed.

The data runs were characterized by two temperature differences:

1 The subcooling of the tube wall temperature below the phase-change temperature, $(T^* - T_w)$. Three values of $(T^* - T_w)$ were employed: 9.7. 20.0, and 30.3°C (17.5, 36.0, and 54.5°F).

2 The initial superheat of the liquified phase-change material, $(T_i - T^*) = 0$, 11.1, and 22.2°C (0, 20, and 40°F). The phase-change temperature, T^*, of n-eicosane is 36.4°C (97.5°F).

Pattern of Freezing. The direct measurements of the shapes of the frozen specimens enabled a comprehensive history of the freezing process to be synthesized. One such representative history is presented in Fig. 1, where cross-sectional views of the frozen specimens are shown at six instants of time. The freezing front, the frozen solid, and the liquid are identified in one of the views. The vertical dashed lines represent the walls of the containment tube, while the horizontal dashed lines represent the upper surface of the bottom-end insulation plug.

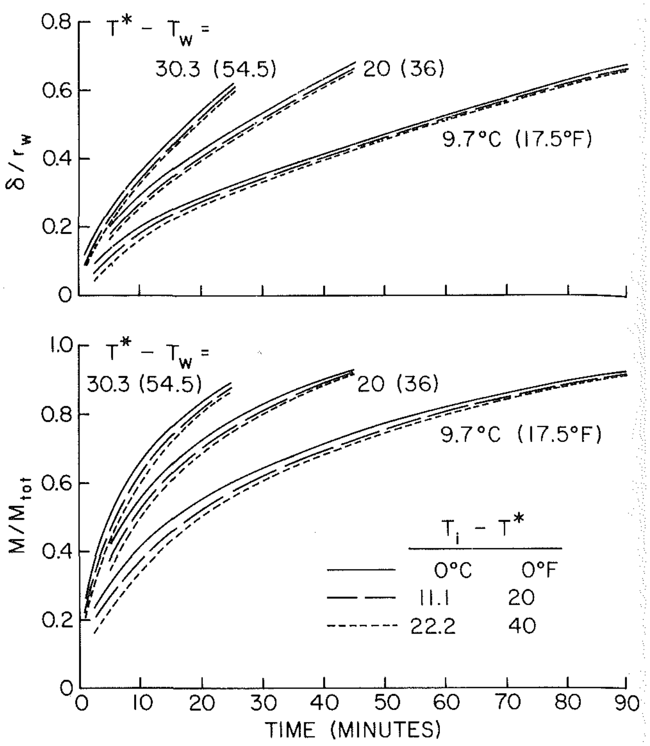

Fig. 2 Timewise variations of the frozen mass (lower graph) and the frozen layer thickness (upper graph)

The freezing pattern of Fig. 1 corresponds to the largest investigated value of $(T_i - T^*)$ and smallest value of $(T^* - T_w)$, respectively 22.2°C (40°F) and 9.7°C (17.5°F). This case is expected to show the largest effect of natural convection in the liquid, but aside from a very slight inclination of the otherwise vertical freezing-front lines, which is more distinct at early times, the freezing pattern of Fig. 1 is identical to that for the zero superheat cases (i.e., $T_i = T^*$).

As expected, the freezing front moves steadily inward with time, and the frozen layer adjacent to the wall of the containment tube grows thicker. A thin layer of frozen material is also formed along the bottom, indicating a slight, unavoidable heat leak through the insulation. Of particular interest are the events which occur at the top of the tube. Owing to the increase in density which accompanies the change of phase from liquid to solid, the liquid level drops as freezing progresses. This is reflected, for example, by the sloped regions at the top of the frozen layer in the 10- and 20-min specimens of Fig. 1.

As time passes, a skin of frozen paraffin forms atop the liquid. Meanwhile, the level of the liquid below the skin continues to drop, leaving a void beneath the skin. It was observed that when first formed, the skin is plane, but it shortly becomes concave as a result of the pressure differential between the void and ambient.

A feature of the frozen specimens that is not depicted in Fig. 1 is the presence of dendrites at the freezing front when the freezing occurs with the liquid temperature at the phase-change value, T^*. The occurrence of the dendrites signals the absence of significant natural convection motions in the liquid.

Two other features of the freezing pattern are worthy of note. The first is that natural convection did not prematurely terminate the freezing process, as in the experiments of [3], for reasons which will be elaborated shortly. Second, careful measurements of the end-effect regions at the top and bottom of the frozen specimens indicated that about 10 percent of the frozen mass was situated in those regions.

Frozen Mass, Freezing Front Position, and Liquid Temperature. A presentation will now be made of the basic data collected during the experiments. In the lower graph of Fig. 2, the frozen mass, M, (normalized by the total charge of paraffin, M_{tot}) is plotted as a function of time for all of the investigated thermal conditions. The M/M_{tot} values for a given degree of wall subcooling ($T^* - T_w$) tend to group closely together and, to preserve clarity, the actual data symbols have been omitted (individual data points will appear in all subsequent figures). For a given value of ($T^* - T_w$), there is a slight spreading of the curves with the initial superheat, ($T_i - T^*$). Of the two temperature differences, it is clear that ($T^* - T_w$) plays a much greater role in determining the frozen mass than does ($T_i - T^*$).

A similar presentation is made in the upper graph of Fig. 2 for the thickness, δ, of the frozen layer, which has been made dimensionless by the tube radius, r_w. The δ values plotted in the figure are those measured away from the end-effect regions which exist at the top and bottom of the frozen specimens. For no initial superheat, δ was found to be independent of axial position, consistent with the absence of natural convection. When $T_i > T^*$, the modest axial variations of δ were averaged out and the average δ was plotted in Fig. 2. The curves of δ/r_w follow a pattern similar to that of the M/M_{tot} curves, since δ and M are reflections of each other.

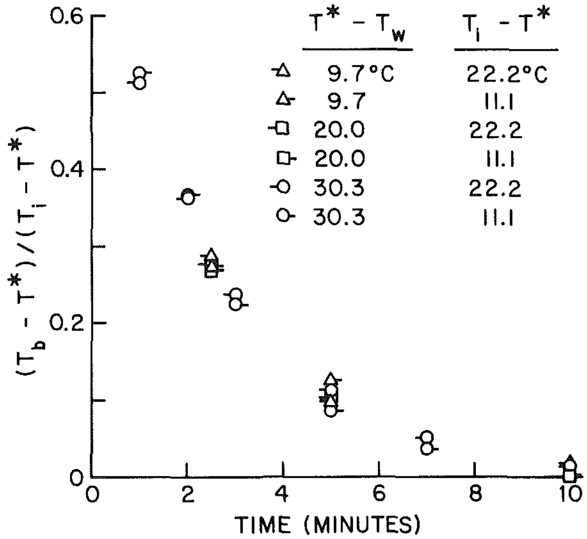

Fig. 3 Decay of the liquid superheat with time

The trend whereby the extent of the freezing at a given time increases with tube-wall subcooling is fully expected and requires little comment. What merits greater discussion is the role of the initial superheating in diminishing M and δ. As can be seen from Fig. 2, the effect of the superheating is greatest at short times and diminishes as the duration of the freezing period increases. This behavior is consistent with the fact that the superheating itself diminishes with time and goes to zero as energy passes from the liquid to the freezing interface. Once the superheating has disappeared, the sole remaining heat transport mechanism is conduction across the solidified paraffin.

The superheating-related decrease of M and δ is by no means totally due to natural convection in the liquid. The simple one-dimensional theory for the classical Neumann problem (plane freezing of a superheated, nonconvecting liquid) shows that M and δ decrease with liquid superheating, even though there is no natural convection. In the present problem, it is likely that natural convection contributes somewhat to the superheating-related decrease in M and δ. However, since the total effect of superheating is modest, the role of natural convection cannot be an important one.

Once the superheating vanishes, so does the natural convection. This behavior is altogether different from that encountered in [3]. There, the natural convection was maintained at full strength throughout the entire course of the experiment. This, in large measure, accounts for the differing roles of natural convection in the two investigations.

Definitive information about the decay of the liquid superheat with time is presented in Fig. 3. In this figure, the measured liquid bulk temperature, T_b, is embedded in a dimensionless ratio whose value is one when $T_b = T_i$ (as occurs at time = 0) and is zero when $T_b = T^*$ (vanishing superheating). In terms of this group, the data for the various cases are so overlapping that some data points had to be omitted from the figure. In general, the initial superheat was fully dissipated within 10 min after the onset of freezing. Thus, after that time, there was no further energy transfer from the liquid to the freezing front, and natural convection ceased because there was no longer a temperature difference to drive it.

The information presented in Fig. 2 for the frozen mass, M, and the frozen layer thickness, δ, was plotted as a function of the freezing time, a dimensional quantity. A generalization of this information will now be sought by employing a dimensionless time variable. For freezing controlled by heat

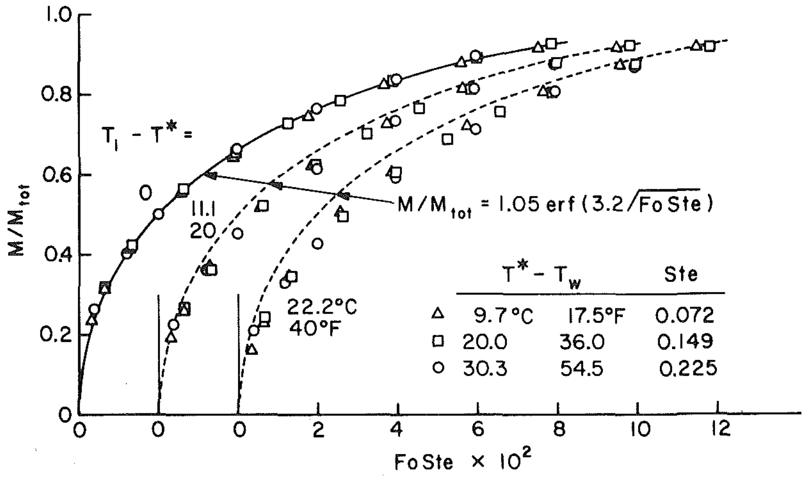

Fig. 4 Dimensionless representation of the experimental results for the frozen mass

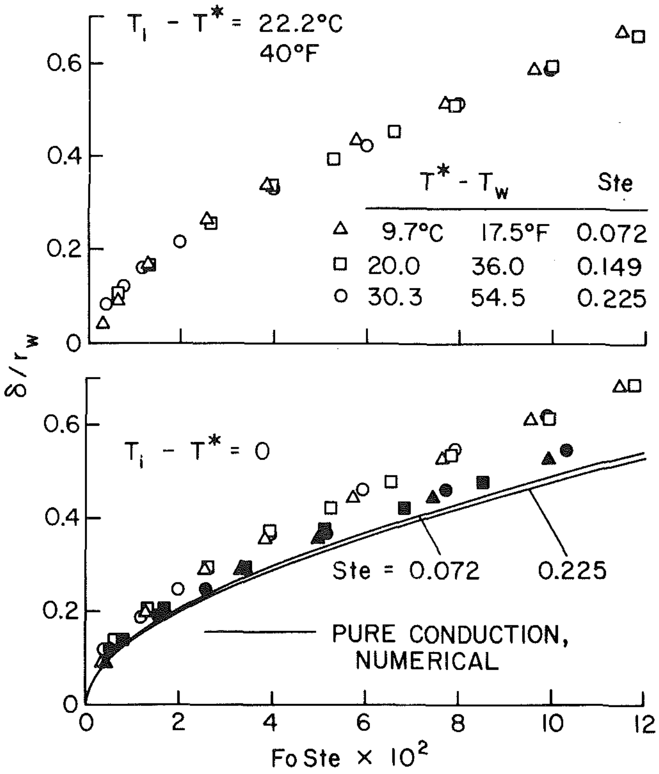

Fig. 5 Dimensionless representation of the results for the frozen layer thickness

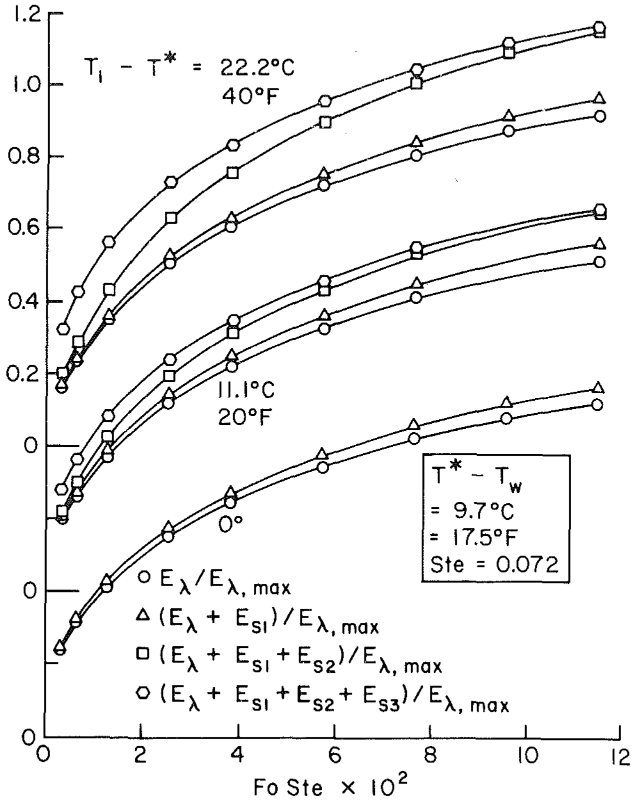

Fig. 6 Component extracted energies for a wall subcooling ($T^* - T_w$) = 9.7°C (17.5°F) and Ste = 0.072

conduction in the frozen layer, analysis has shown that the dimensionless group FoSte serves effectively as a dimensionless time. Therefore, in view of the minor importance of natural convection in the present problem, it appeared reasonable to replot the M/M_{tot} and δ/r_w data of Fig. 2 as a function of FoSte.

The thus-replotted M/M_{tot} results are presented in Fig. 4. The figure is actually a composite of three graphs which share a common ordinate but have abscissa origins which are displaced from each other. Each graph corresponds to a specific value of the initial superheat, $(T_i - T^*)$, respectively equal to 0, 11.1, and 22.2°C (0, 20, and 40°F) for the left-hand, middle, and right-hand graphs. In each graph, data are presented for the three investigated wall subcoolings, $(T^* - T_w)$ = 9.7, 20.0, and 30.3°C (17.5, 36.0 and 54.5°F). As indicated in the legend of the figure, these $(T^* - T_w)$ values can be expressed in dimensionless form via the solid-phase Stefan number Ste that was defined in equation (11), which gives Ste = 0.072, 0.149, and 0.225.

Inspection of the individual graphs of Fig. 4 shows that for each fixed initial superheating, there is virtually perfect correlation of M/M_{tot} with FoSte. The perfection of the correlation is somewhat dependent on the manner of evaluating the solid-phase thermal conductivity, k, that appears in the Fourier number. It was found that the tightest correlation was obtained with K evaluated at the phase-change temperature, T^*, and an identical finding prevails for the δ/r_w correlation to be presented shortly.[1]

The data for the no-subcooling case are remarkably well correlated by the equation

$$M/M_{tot} = 1.05\, erf(3.2\sqrt{\mathrm{FoSte}}) \qquad (12)$$

which is plotted as a solid line in the left-hand graph of Fig. 4. The equation indicates that $M/M_{tot} = 1$ (complete freezing) at a finite value of FoSte, which is as it should be for freezing in a closed container.

Equation (12) has also been plotted as a dashed line in the middle and right-hand graphs and, by this, it serves as a reference line for comparing the results of the three graphs. Such a comparison shows that initial superheating causes a modest decrease in M/M_{tot} at small and intermediate FoSte, but that there is virtually no effect at the larger FoSte.

To obtain a totally dimensionless representation in Fig. 4, it is appropriate to replace $(T_i - T^*)$ by a liquid-phase Stefan number. Since the liquid bulk temperature decreases with time and finallly becomes equal to T^*, the instantaneous liquid-phase Stefan number is a variable with a terminal value of zero. In view of this, it appears that the initial Stefan number $\mathrm{Ste}_{liq,i}$ is the most appropriate superheating parameter, where

$$\mathrm{Ste}_{liq,i} = c_{liq,i}(T_i - T^*)/\lambda \qquad (13)$$

with numerical values listed in Table 1.

A dimensionless presentation of the δ/r_w results is made in Fig. 5, where FoSte is the abscissa variable. The two graphs which comprise the figure correspond to the two extremes of the investigated range of superheats. In both graphs, the results for the various $(T^* - T_w)$ are very well correlated. From a comparison of the data appearing in the two graphs, it is seen that the δ/r_w values for $(T_i - T^*) > 0$ lie slightly below those for $T_i = T^*$.

In the lower graph, there are solid lines which represent numerical solutions based on a pure conduction model of one-dimensional inward solidification in a circular tube [6]. The data (open symbols) lie about 25 percent above the predictions. There are a number of factors which may account for the deviation. One of these is an uncertainty of as much as 30 percent in the available information for the solid-phase thermal conductivity, k_{sol}, [5] which appears in the Fo variable on the abscissa. In this connection, a reevaluation of

---

[1] The k value at T^* was obtained by extrapolating the k versus T information given in [5].

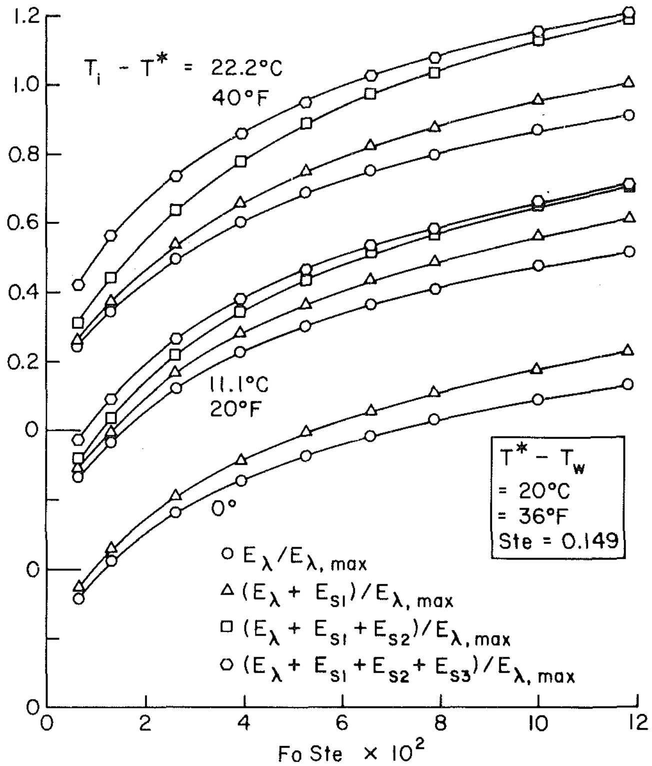

Fig. 7 Component extracted energies for a wall subcooling $(T^* - T_w)$ = 20°C (36°F) and Ste = 0.149

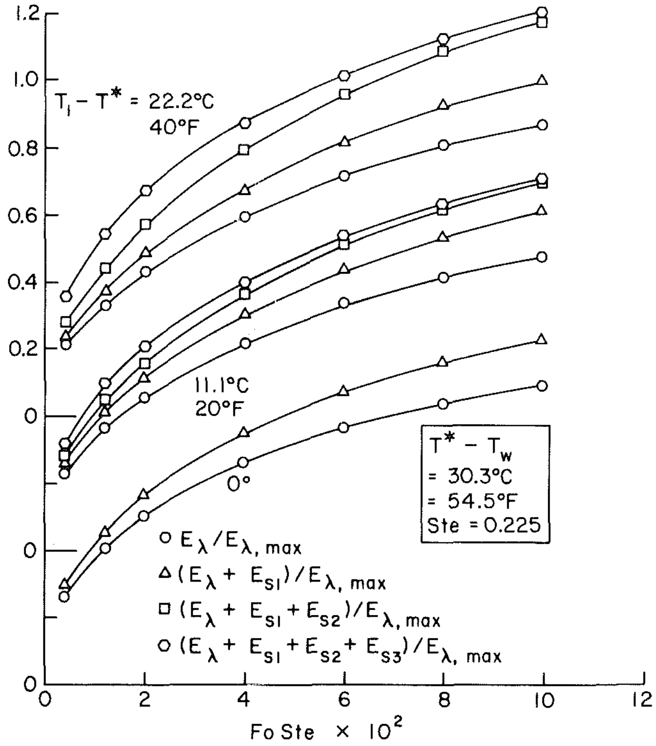

Fig. 8 Component extracted energies for a wall subcooling $(T^* - T_w)$ = 30.3°C (54.5°F) and Ste = 0.225

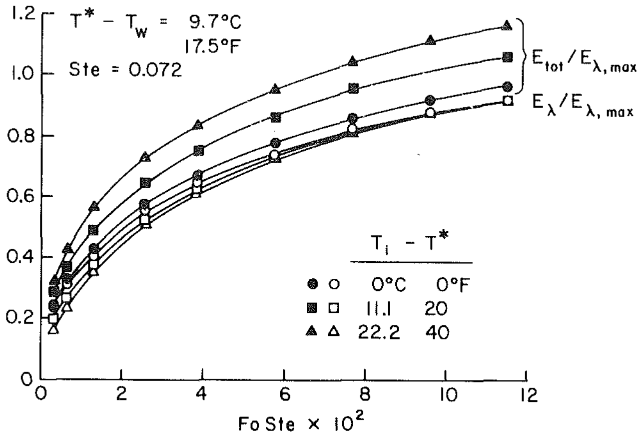

Fig. 9 Comparison of total and latent extracted energies; $(T^* - T_w)$ = 9.7°C (17.5°F) and Ste = 0.072

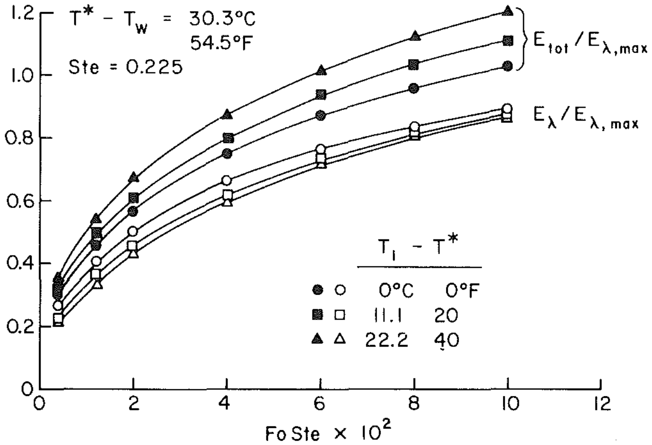

Fig. 10 Comparison of total and latent extracted energies; $(T^* - T_w)$ = 30.3°C (54.5°F) and Ste = 0.225

the data with k_{sol} increased by 30 percent (black data symbols) yields better, but not perfect, agreement with the analytical results.

In addition to the aforementioned uncertainty in k_{sol}, there are other factors which may cause deviations between the analytical and experimental results. These include: (*a*) temperature-dependent thermophysical properties, (*b*) change of density which accompanies phase change, and (*c*) the presence of dendrites at the freezing front. None of these factors is taken into account by the analytical model.

Component and Total Energies. Each of the component energies E_λ, E_{s1}, E_{s2}, and E_{s3} were evaluated from the experimental data as described earlier, and these were used to calculate E_{tot} from equations (4) and (7). This information is presented in Figs. 6, 7, and 8, respectively, for wall subcoolings $(T^* - T_w)$ = 9.7, 20, and 30.3°C (17.5, 36, and 54.5°F), i.e., for Ste = 0.072, 0.149, and 0.225. Each figure consists of three graphs that are stacked one atop the other and share a common abscissa but have displaced ordinate origins. The respective graphs, arranged from bottom to top, correspond to increasing initial superheat.

In each graph, there are several curves. The lowest curve corresponds to E_λ, the next to the sum $(E_\lambda + E_{s1})$, and, when superheat is present, the next two are for $(E_\lambda + E_{s1} + E_{s2})$ and $(E_\lambda + E_{s1} + E_{s2} + E_{s3})$. Thus, the uppermost curve in each graph also represents E_{tot}. For a dimensionless presentation, all energies are normalized by $E_{\lambda,max}$ $(= \lambda M_{tot})$ and the abscissa variable is FoSte.

Attention may first be turned to Fig. 6 (i.e., the case of the smallest tube wall subcooling). Starting with the no-superheat case (lowest graph), it is seen that the sensible energy, E_{s1}, extracted from the solid is rather small compared with the latent energy, E_λ, released by the change of phase. This finding is consistent with the small Ste value (= 0.072) for the case in question. It is also noteworthy that the magnitude of E_{s1} remains virtually unchanged in the presence of liquid superheating (middle and upper graphs).

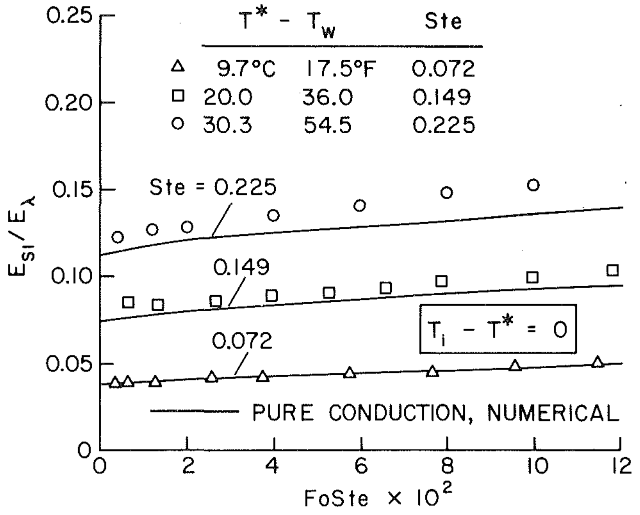

Fig. 11 Sensible energy extracted from the subcooled solid for the no-superheating case

Table 1 Values of $\mathrm{Ste}_{\mathrm{liq},i}$ for the Experiments

$(T_i - T^*)$		$\mathrm{Ste}_{\mathrm{liq},i}$
0°C	0°F	0
11.1	20	0.101
22.2	40	0.207

The energies, $(E_{s2} + E_{s3})$, extracted from the liquid become increasingly significant as the extent of the initial superheating increases, although the latent heat component remains as the dominant portion of the total energy. As noted earlier, E_{s2} is associated with the liquid which freezes and is the sensible energy released as the liquid cools from its initial superheat to the phase-change temperature. The E_{s3} component is related to the residual liquid (i.e., unfrozen liquid) and is the energy extracted as that liquid cools from T_i to T_b. At small FoSte (small times), very little liquid has frozen, so that E_{s3} is greater than E_{s2}. However, as time passes, more of the liquid is frozen, leaving less residual liquid. Correspondingly, E_{s2} increases and E_{s3} decreases. It can be seen that over a substantial range of FoSte, the sum $(E_{s2} + E_{s3})$ is a constant, as asserted by equation (8).

Figure 7 corresponds to a larger tube wall subcooling and larger Stefan number than does Fig. 6, and this is reflected in a larger value of E_{s1}. As before, the magnitude of E_{s1} is about the same whether or not there is initial superheating of the liquid. The components E_{s2} and E_{s3} which are built atop the corresponding $(E_\lambda + E_{s1})$ curves in Figs. 6 and 7 are virtually the same. That is, for a given initial superheat, $(T_i - T^*)$, E_{s2} and E_{s3} appear to be little influenced by the extent of the wall subcooling. A further comparison of Figs. 6 and 7 shows that the E_s components constitute a somewhat larger fraction of the total energy for the latter than for the former.

The aforementioned characteristics are reaffirmed by Fig. 8, which corresponds to the largest investigated tube wall subcooling and solid-phase Stefan number. This yields a still larger value of E_{s1}, which continues to be virtually independent of the extent of the initial superheat. Furthermore, the magnitudes of E_{s2} and E_{s3} corresponding to a given initial liquid superheat (given $\mathrm{Ste}_{\mathrm{liq},i}$) are hardly affected by the wall subcooling and solid-phase Stefan number.

From the standpoint of practice, the total extracted energy E_{tot}, is of direct applicability. Figures 9 and 10 have been prepared to report the E_{tot} results, respectively, for the smallest and largest of the investigated tube wall subcoolings. In addition to E_{tot}, each figure also shows the results for the extracted latent energy, E_λ, thereby facilitating a comparison between the two quantities. Both E_{tot} and E_λ are made dimensionless by $E_{\lambda,\max}(= \lambda M_{\mathrm{tot}})$ and are plotted against FoSte. In each figure, curves are presented for each of the investigated initial superheats.

Inspection of Figs. 9 and 10 indicates that while an increase in the liquid superheat brings about a moderate decrease in the extracted latent energy, the total extracted energy increases substantially. Thus, although the latent energy component constitutes the lion's share of the extracted energy, the sensible energy components can make a significant contribution. The importance of the sensible energy is accentuated at large tube wall subcooling and large initial liquid superheating and for short freezing times (i.e., small FoSte). For example, at values of FoSte = 0.02 and 0.12 in Fig. 10 and for the largest superheating, the aggregate sensible energies respectively account for 36 and 28 percent of the total energy extracted. The corresponding percentages for Fig. 9, where the tube wall subcooling is smaller, are 33 and 23.

As a final matter with regard to the sensible energy, a comparison is made between the experimental values of E_{s1} for the no-superheating case and those predicted by numerical solutions based on a one-dimensional pure conduction model [6]. These results are presented in Fig. 11 in the form E_{s1}/E_λ. For any fixed value of $(T^* - T_w)$ or Ste, this ratio is relatively independent of FoSte, so that the uncertainty in the value of k_{sol} that caused interpretational difficulties in Fig. 5 plays a lesser role here.

Both the analytical and experimental results affirm that the extracted sensible energy becomes a larger fraction of the latent energy as the wall subcooling increases (i.e., as Ste increases). In general, there is good agreement between the data and the analytical preditions.

Concluding Remarks

The work reported here has provided previously unavailable fundamental heat transfer information about freezing in a vertical tube. Measurements were made which yielded information about the time dependence of the freezing front, of the amount of frozen mass, and of the various energy components extracted from the tube. The timewise decay of the initial liquid superheat was also measured. Four component energies were evaluated from the experimental data and reported. These include the latent energy released by the liquid-to-solid phase change, the sensible energy released by the subcooling of the frozen solid, and two components of sensible energy extracted from the initially superheated liquid. Results for the total extracted energy were also presented.

Initial superheating of the liquid tends to moderately diminish the frozen mass and the associated latent energy extraction at small times but has little effect on these quantities at large times. The extracted sensible energies associated with the superheating more than compensate for the aforementioned decrease in the latent energy. Natural convection in the liquid plays a modest role only at small times and disappears when the superheat decays to zero. It is conceivable that natural convection might have played a more important role had larger initial superheat been employed.

Although the latent energy constitutes the largest contributor to the total extracted energy, the sensible energy components can make a significant contribution, especially at large tube wall subcoolings, large initial liquid superheating, and short freezing times.

The results were well correlated in dimensionless form using the Fourier-Stefan product as a primary variable. Whenever possible, the experimental results for the no-subcooling case were compared with predictions from numerical solutions based on a one-dimensional, pure conduction model of inward solidification.

Acknowledgment

This research was performed under the auspices of the U.S. Department of Energy, Office of Basic Energy Sciences.

References

1 Viskanta, R., Bathelt, A. G., and Hale, N. W., Jr., "Latent Heat-of-Fusion Energy Storage: Experiments on Heat Transfer During Solid-Liquid Phase Change," *Proceedings of the Third Miami International Conference on Alternative Energy Sources*, edited by N. J. Veziroglu, Hemisphere Publishing Corporation, Washington, D.C. (in press).

2 Viskanta, R., "Phase-Change Heat Transfer," *Solar Heat Storage: Latent Heat Materials*, edited by G. A. Lane, CRC Press, Boca Raton, Florida (in press).

3 Sparrow, E. M., Ramsey, J. W., and Kemink, R. G., "Freezing Controlled by Natural Convection," JOURNAL OF HEAT TRANSFER, Vol. 101, 1979, pp. 578–584.

4 Humphries, W. R., and Griggs, E. I., "A Design Handbook for Phase Change Thermal Control and Energy Storage Devices," NASA Technical Paper 1074, 1977.

5 Griggs, E. I., and Yarbrough, D. W., "Thermal Conductivity of Solid Unbranched Alkanes from n-Hexadecane to n-Eicosane," *Proceedings, 14th Southeastern Seminar on Thermal Sciences*, 1978, pp. 256–267.

6 Chuck, W., Personal Communication, Department of Mechanical Engineering, University of Minnesota, May, 1981.

Heat Transfer During Melting Inside a Horizontal Tube

H. Rieger
Research Assistant.

U. Projahn
Research Assistant.

M. Bareiss
Research Assistant.

H. Beer
Professor.

Institut fur Technische Thermodynamik,
Technische Hochschule Darmstadt,
6100 Darmstadt, West Germany

The melting process of a phase change material (PCM) enclosed in a horizontal, isothermal circular tube has been investigated analytically and by experiment for an interesting range of parameters. The physical process was analyzed by numerical methods, whereby the underlying mathematical model involves heat conduction as well as natural convection as the basic heat transport mechanisms. Difficulties associated with the complex and timewise changing melt region whose shape is also part of the solution, have been overcome by applying a numerical mapping technique. Computations and experiments were performed for Rayleigh numbers in the range $10^5 \leq Ra \leq 10^6$. For lower Rayleigh numbers the numerical calculations predict a streamlined design of the PCM at later times, similar to the experiment. At higher Rayleigh numbers, three-dimensional Bernard convection was observed in the bottom region of the melt layer, which was unsteady in their timewise behaviour. The appearance of several roll-cells have also been predicted by the calculations, although the mathematical model was restricted to two-dimensional flow. The experiments were performed with n-octadecane ($Pr \simeq 50$) as PCM. The test cell basically consists of a short tube filled with the PCM. The tube is closed with plexiglass disks on both ends, thus allowing the melting front to be recorded photographically with time. As a result, the interface positions as well as the overall and local heat transfer coefficients are presented as function of time. The agreement between experimental and numerical data is reasonably good.

Introduction

Phase change heat transfer is of great interest in a wide range of natural and technical processes. Therefore many papers concerning melting or freezing phenomena have been published in the recent years for various geometric arrangements. The majority of the publications report the results of experimental investigations for different geometries. The heat transfer phenomena during the phase change process (PCP) above or below a heated horizontal flat plate and at a vertical surface were studied by Hale and Viskanta [1, 2], while the influence of surface height as additional parameter has been investigated by Bareiss et al. [3]. Another important arrangement for the technical application is the PCP around a single cylinder (finned and unfinned) or arrays of horizontal cylinders. The experimental investigations for the aforementioned geometries were performed by several researchers [4, 5, 6, 7, 8] for various phase change materials (PCM) and governing parameters. The melting process in a vertical cylindrical enclosure has been studied extensively by Bareiss and Beer [9].

Due to the results of the experimental studies it has become apparent that only in the earliest stage of the PCP the heat transport is dominated by heat conduction. Photographs, shadowgraphs, and interferograms indicate clearly that natural convection plays the important role. These experimental findings lead to the conclusion that any analytical solutions assuming pure conduction as the sole heat transport mechanism [10, 11] or considering the flow as a perturbation quantity [4, 12] are unable to predict the real process satisfactorily. Therefore the only promising way to describe the PCP analytically seems to be the numerical solution of the governing set of partial differential equations. Since these equations are rather complex and the computational area changes with time (moving boundary problem) only a few studies are available in the literature.

Numerical results for the problem of melting from a vertical cylinder were presented by Sparrow et al. [13]. Due to the difficulties which arise from the moving interface, a simplified set of governing equations was used, and solved by a finite difference method. Gartling [14] uses the finite element method for the investigation of PCP concerning blockage problems in pipes and melting processes in materials with internal heat sources. In the course of the review process the works of Pannu et al. [15] and Saitoh and Hirose [16] were made available to the authors. Both studied likewise the melting process inside a horizontal cylinder by solving the governing equations numerically. The mobilization of the liquid-solid interface was performed by the application of a two-dimensional Landau transformation. In an earlier work, Saitoh and Hirose [17] studied the freezing process around a horizontal cylinder and applied the same transformation technique successfully. To overcome the troublesome moving boundary problem, Rieger, Projahn, and Beer [18] used numerically generated coordinate systems for the in-

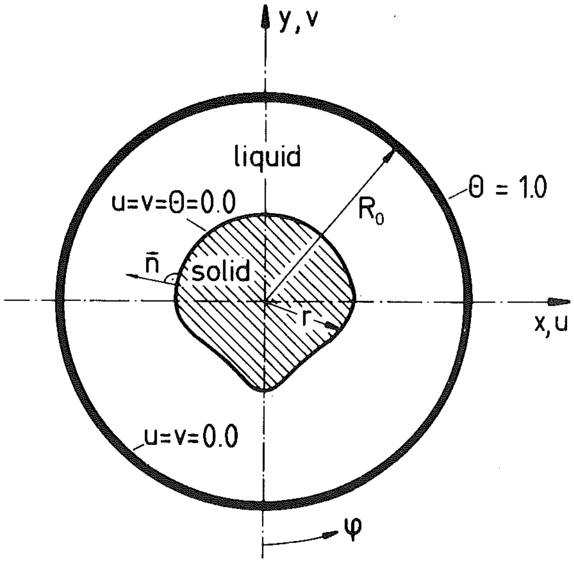

Fig. 1 Schematic representation of the physical model

Contributed by the Heat Transfer Division for publication in the JOURNAL OF HEAT TRANSFER. Manuscript received by the Heat Transfer Division March 15, 1982.

vestigation of melting processes around a horizontal cylinder. This technique seems to have a great potential for future applications because of its high flexibility.

Although the specific problem data of [15, 16] and ours are not the same, qualitatively different solutions could be observed. This fact was the motivation to solve this melting problem based on the data provided by Pannu et al. In a later section the comparison of these results will be discussed. The schematic diagram of the configuration under study is depicted in Fig. 1. It shows the horizontal tube with inner radius, R_0, and the partially melted solid, whose shape will be described by $r = r(\varphi,\tau)$. The PCM in this study is assumed to be supported at the center, so that the unmelted solid remains stationary. Another possible configuration, where the movement of the PCM on account of gravitational forces is not suppressed, was the objective of Nicholas and Bayazitoglu [19]. They analyzed the problem by considering only heat conduction in the liquid phase. The important influence of the thin liquid film which is formed at the bottom portion of the cylinder during the melting process was investigated by Bareiss and Beer [20] using assumptions quite similar to lubrication theory.

Nevertheless, the emphasis of this study lies in a direct comparison between corresponding experimental and numerical results.

Experiments

Test Apparatus. The test apparatus consists of a copper tube ① of 40 mm in length, 32 mm inside diameter and a wall thickness of 1 mm. The copper tube is closed at one end by a firmly adhered, 10-mm thick circular plexiglass disk (2a). A second plexiglass disk (2b) is held on the other end by a special adhesive, which allows the disk to be released if necessary. Thus, a horizontal cylindrical space of 32-mm dia and 40-mm length is formed which contains the PCM. Since the cell is translucent in axial direction, a visual observation and photographic registration of the melting process is possible. Through the annular gap between the copper tube and the outer cylindrical jacket ③ water acting as a heating or cooling fluid can be circulated. The water is supplied by a constant temperature thermostat through an inlet tube ④ tangentially to the annular gap. By this means high heat transfer rates and therefore constant surface temperature conditions at the wall of the copper tube can be achieved. Since the temperature drop across the copper tube wall is less than 0.02 K, the temperature of the inside surface of the wall can be assumed to be equal to that of the outside surface. For measurement of the wall temperature, T_w, thermocouples therefore could be cemented in small grooves and covered with thin copper foil on the outside surface. The volumetric expansion of the PCM during melting is compensated by an overflow pipe ⑤. Fixing of the solid PCM is done by a thin pvc-strip ⑥ fastened to the plexiglass disk (2a) and positioned axially 5 mm below the axis of the copper tube.

Phase Change Material. $C_{18}H_{38}$, n-octadecane (Pr 50, h_f = 243 kJ/kg, T_f = 301.2 K) was chosen as test material because its melting temperature is close to the ambient temperature and since paraffins are nontoxic, noncorrosive and transparent in the liquid phase.

The physical and transport properties are well established. Nevertheless some discrepancies between different literature sources exist. The data used in this study were taken from Hale et al. [21] and Vargaftik [22].

Test Procedure. Since paraffins possess a high dissolving capacity for air, the test material must be degassed carefully prior to each experiment. For this purpose the test material was subjected to a solidification-melting cycle under vacuum. The opened test cell was lengthened by an additional copper tube attached to the open end and then filled with the degassed liquid PCM. The assembly was placed vertically into an icewater bath to solidify the PCM.

After solidfication, the lengthening tube was detached, the excess of solid PCM cut off and the cross sectional area carefully planed. By this means a void-free and homogeneous solid could be obtained in the test cell. After the test cell was closed and assembled, the PCM was heated to a steady temperature 0.5 K below the melting point at the most by circulating water. During the test itself, which starts when the copper tube wall is suddenly heated to a desired temperature above the melting point, the process was registrated photographically. For this purpose photographs were taken at selected time intervals with a telelens camera.

Numerical Analysis

Govering Equations. Although the flow in the melt region may actually be three-dimensional, such a treatment would require large computer storage and long computation times. Therefore, a two-dimensional mathematical model will be considered. Further reduction of the computational effort which seems to be justified due to the experimental results is achieved by the assumption of symmetric melting.

Following additional assumptions have been made for further simplification:

Nomenclature

a = thermal diffusivity
c = specific heat
f,F = dummy variables
Fo = Fourier number, $at/R_0{}^2$
g = accleration of gravity
h_f = latent heat of fusion
J = Jacobian, $(\partial x/\partial\xi)(\partial y/\partial\eta) - (\partial x/\partial\eta)(\partial y/\partial\xi)$
$m_L{}^*$ = molten mass fraction, equation (16)
n = coordinate in normal direction
Nu = Nusselt number, equations (17*a*, 17*b*)
Pr = Prandtl number, ν/a
Ra = Rayleigh number, $g\hat{\beta}R_0{}^3(T_w - T_f)/(\nu a)$
r = distance, from center of tube to solid-liquid interface
R_0 = inner radius of tube
Ste = Stefan number, $c(T_w - T_f)/h_f$
t = time
T = temperature
u,v = dimensionless velocity components along x-,y-direction, $(u',v')/R_0$
w = velocity vector, $(u,v,0)$
x,y = dimensionless Cartesian coordinate directions in physical plane, $(x',y')/R_0$
α,β,γ = transformation factors, $(\alpha = (\partial x/\partial\eta)^2 + (\partial y/\partial\eta)^2$; $\beta = (\partial x/\partial\xi)(\partial x/\partial\eta) + (\partial y/\partial\xi)(\partial y/\partial\eta)$; $\gamma = (\partial x/\partial\xi)^2 + (\partial y/\partial\xi)^2)$
$\hat{\beta}$ = thermal expansion coefficient
θ = dimensionless temperature, $(T - T_f)/(T_w - T_f)$
ν = kinematic viscosity
ξ,η = coordinate directions in transformed plane
τ = dimensionless time, Fo•Ste
φ = angle of perimeter
ψ = stream function
ω = vorticity, $\partial v/\partial x - \partial u/\partial y$

Subscripts

b = boundary
f = fusion
i = interface
s = start
w = tube wall

Superscripts

— = mean value
′ = dimensional quantity

1 Physical properties are constant except for the density in the buoyancy term (Boussinesq approximation).

2 Density changes during melting and viscous dissipation are neglected.

3 The fluid is Newtonian and incompressible.

4 The flow is laminar and two-dimensional.

Then, the nondimensionalized conservation equations in the vorticity-stream function formulation and for Cartesian coordinates are

$$\mathrm{Ste}\,\partial\omega/\partial\tau + \nabla\cdot(\omega\mathbf{w}) = \mathrm{Pr}\,\nabla^2\omega + \mathrm{Ra}\,\mathrm{Pr}\,\partial\theta/\partial x \quad (1)$$

$$\omega = -\nabla^2\psi \quad (2)$$

$$\mathrm{Ste}\,\partial\theta/\partial\tau + \nabla\cdot(\theta\mathbf{w}) = \nabla^2\theta \quad (3)$$

Initial Conditions. Initially, at $\tau = 0$ the whole system has a temperature of $\theta = \theta_f = 0$. Because the computational area covers only the region of the liquid phase and cannot be made infinite small, it is possible to start the numerical calculations with this condition. So, for the given sufficient small initial gap it is necessary to specify a suitable time and a corresponding temperature distribution. In order to compare numerical and experimental data the starting time for the computation was chosen in such a way, that both results coincide for this very early stage. This proceeding has the advantage to eliminate the transient effects which occur at the beginning of the experiments (e.g., heating of the test cell). The analytical solution of the Stefan problem (e.g., see [23]) for the given geometry yields the temperature distribution.

Boundary Conditions. For the simplification of the physical model it is assumed that in the solid phase no heat conduction occurs; i.e., all heat transferred to the interface is utilized for melting and therefore determines the propagation speed and the shape of the interface. With regard to this additional assumption, the energy balance for the interface leads to the following dimensionless condition for the moving boundary

$$-\partial\theta/\partial n = v_n \quad (4)$$

where v_n is the dimensionless interface velocity in normal direction. The abovementioned assumption of constant density during phase change requires the kinematic no-slip condition at all solid walls, so that the boundary conditions for the complete description at $\tau > \tau_s$ are as follows

$$\theta = 1\ ;\ u = v = 0\ ;\ \text{at the wall} \quad (5a)$$

$$\theta = 0\ ;\ u = v = 0\ ;\ \text{at the interface} \quad (5b)$$

$$\partial\theta/\partial n = 0\ ;\quad u = 0\ ;\ \text{at the symmetric line} \quad (5c)$$

Transformation. To overcome the difficulties which arise due to the complex, timewise changing physical domain a numerical transformation method was employed. This mapping technique was first developed by Thompson et al. [24] and has been proven as a versatile tool for the treatment of different natural convection problems by the present authors [25, 26]. The advantage of this transformation technique is the fact that any set of the equations of interest may be solved on a rectangular and uniform spaced computational grid system which is fixed in space and time. Therefore this method is favoured for the solution of moving boundary problems like melting. The boundary-fitted curvilinear coordinates are obtained by the solution of the following system of quasi-linear elliptic partial differential equations with appropriate Dirichlet conditions along the boundaries

$$\mathcal{L}(x) = 0 \quad (6a)$$

$$\mathcal{L}(y) = 0 \quad (6b)$$

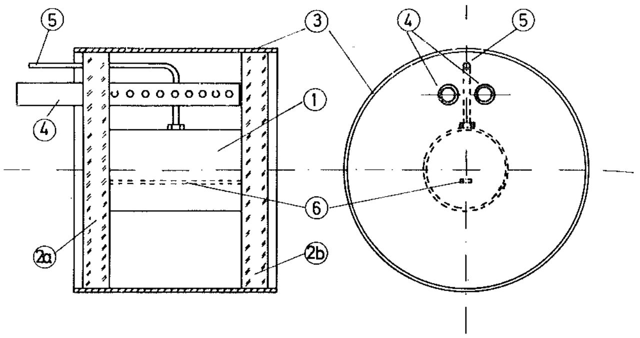

Fig. 2 **Schematic diagram of the experimental apparatus**

The operator $\mathcal{L}(f)$ represents the transformed Laplacian and is defined as

$$\mathcal{L}(f) = (\alpha\,\partial^2 f/\partial\xi^2 - 2\beta\,\partial^2 f/\partial\xi\partial\eta + \gamma\,\partial^2 f/\partial\eta^2)/J^2 + P\,\partial f/\partial\eta + Q\,\partial f/\partial\xi \quad (7)$$

The source terms P and Q contains adjustable parameters and provide some measure of control over the interior grid spacing. However, the forms of these source terms and the values of the parameters require artful selection and are problem dependent. To overcome the difficulties concerning interior grid control Thomas and Middlecoff [27] proposed the following general source terms

$$P = \phi(\xi,\eta)\,[(\partial\xi/\partial x)^2 + (\partial\xi/\partial y)^2] \quad (8a)$$

$$Q = \chi(\xi,\eta)\,[(\partial\eta/\partial x)^2 + (\partial\eta/\partial y)^2] \quad (8b)$$

The introduced parameters, ϕ and χ, are specified as limiting forms of the equations (6a, 6b) at the boundary coordinate curves $\eta = \eta_b = \text{const.}$ and $\xi = \xi_b = \text{const.}$, respectively. Assumption of local orthogonality at the boundaries yield the following expressions

$$\phi(\xi,\eta) = -(z(x,\xi) + z(y,\xi))/\gamma \quad \text{on } \eta = \eta_b \quad (9a)$$

$$\chi(\xi,\eta) = -(z(x,\eta) + z(y,\eta))/\alpha \quad \text{on } \xi = \xi_b \quad (9b)$$

$$z(F,f) = (\partial F/\partial f)(\partial^2 F/\partial f^2) \quad (9c)$$

The parameters at interior grid points are then obtained by simple linear interpolation between appropriate boundary curves. This improved procedure insures a grid point distribution with smooth and regular character. Using this transformation technique the governing equations (1-3) and the corresponding boundary conditions take the following form

$$\mathrm{Ste}\,\mathfrak{D}(\tau,\omega) + \mathfrak{N}(\psi,\omega) = \mathrm{Pr}\,\mathcal{L}(\omega) + \mathrm{Ra}\,\mathrm{Pr}\,\mathfrak{N}(y,\theta) \quad (10)$$

$$\mathcal{L}(\psi) = -\omega \quad (11)$$

$$\mathrm{Ste}\,\mathfrak{D}(\tau,\theta) + \mathfrak{N}(\psi,\theta) = \mathcal{L}(\theta) \quad (12)$$

Boundary conditions:

$\psi = 0\ ;\ \omega = 0;$

$$\alpha\,\partial\theta/\partial\xi - \beta\,\partial\theta/\partial\eta = 0 \text{ for } \xi = \xi_{\min} \quad (13a)$$

$\psi = 0\ ;\ \omega = 0;$

$$\alpha\,\partial\theta/\partial\xi - \beta\,\partial\theta/\partial\eta = 0 \text{ for } \xi = \xi_{\max} \quad (13b)$$

$\psi = 0\ ;\ \omega = -(\gamma\,\partial^2\psi/\partial\eta^2)/J^2;$

$$\theta = 0 \text{ for } \eta = \eta_{\min} \quad (13c)$$

$\psi = 0\ ;\ \omega = -(\gamma\,\partial^2\psi/\partial\eta^2)/J^2;$

$$\theta = 1 \text{ for } \eta = \eta_{\max} \quad (13d)$$

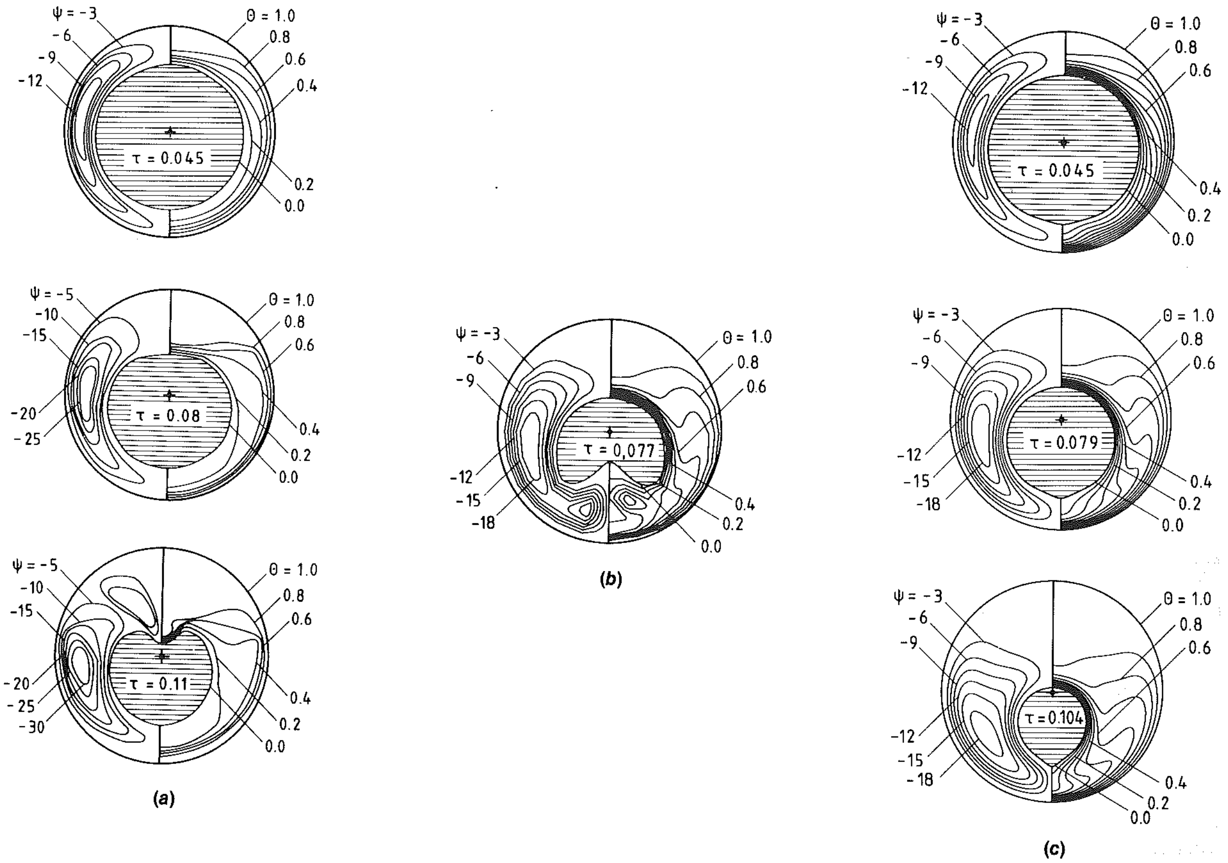

Fig. 3 Previous works in comparison for Ra = 2.10^5, Pr = 145, Ste = 0.115: (*a*) Pannu et al. [15]; (*b*) Saitoh and Hirose [16]; (*c*) Present study

The operators $\mathcal{D}(\tau, f)$ and $\mathcal{N}(f,F)$ used in equation (10–12) are defined as

$$\mathcal{D}(\tau,f) = \partial f/\partial\tau - \mathcal{N}(y,f)\ \partial x/\partial\tau + \mathcal{N}(x,f)\ \partial y/\partial\tau \qquad (14a)$$

$$\mathcal{N}(f,F) = [\partial(F\,\partial f/\partial\eta)/\partial\xi - \partial(F\,\partial/\partial\xi)/\partial\eta]/J \qquad (14b)$$

The conditions, which mobilize the boundary at the solid-liquid interface, follow from equation (4) and yield the relations for the timewise change of the boundary grid points in the physical plane

$$\partial x/\partial\tau = (\partial y/\partial\xi)(\partial\theta/\partial\eta)/J \qquad (15a)$$

$$\partial y/\partial\tau = -(\partial x/\partial\xi)(\partial\theta/\partial\eta)/J \qquad (15b)$$

To retain a properly structured physical net system during the computation—regardless of the shape of the melt zone—an implicit rezoning procedure is applied.

Numerical Procedure. To find the numerical solution of the transformed governing equations and boundary conditions these equations are discretized using only central difference approximations. The resulting finite difference analogue is then solved by a fully implicit method proposed by Stone [28]. This solution technique has been successfully applied to various heat transfer problems by the present authors [18, 25, 26], where further details of the method may be found. For one time step the calculations were performed in the following order:

1 Simultaneous solution of the vorticity and stream function equation (10, 11).

2 Simultaneous solution of the energy equation (12) and the grid generation.

If the solution satifies a certain convergence criterion the next time step is calculated otherwise return is made to 1. As a compromise between accuracy and computational effort (time, storage), a grid system containing 21 × 31 nodal point is chosen. The computations were performed on a DEC-PDP 10/70 with a computational speed of approximately 0.1 mflops. To achieve a converged solution for one time step, 4–6 iterations were necessary where one iteration took about 7 s CPU for the 21 × 31 grid. To avoid numerical instabilities, the computations were started with a time increment of $\Delta\tau = 10^{-5}$, which was raised subsequently to values of about $3 \cdot 10^{-4}$ for the heat-conduction-dominated regime.

Results and Discussions

Before going into a detailed discussion of the experimental and numerical results, a section seems to be worthwhile mentioning in which the numerical results of [15, 16] are compared with the present ones. In further sections local and average melting data are reported, accompanied by an illustrative comparison of photographs and contour plots.

Previous Works in Comparison. The fact that different numerical solutions result from the computation of a well-defined problem, although based on identical problem parameters, is extremely unsatisfying. Computations performed by Pannu et al. [15] for Ra = $2 \cdot 10^5$, Pr = 145, and Ste = 0.115 resulted in melting front contours and natural convection patterns which are quite different to those of Saitoh and Hirose [16] and ours. Figure 3 shows the transient streamlines, isotherms, and interface shapes at almost equal dimensionless times. Whereas Pannu et al. [15] predict the formation of a large eddy in the stagnant upper portion of the melting gap, a quite controversial result was presented by Saitoh and Hirose [16]. In their work the melting rate at the lower stagnation point is strongly increased due to the onset of a thermal instability. On the other hand, no indication of the development of an eddy in either the upper or the bottom portion of the melting gap could be observed in the present study for the parameters just previously mentioned. The formation of eddies were observed for higher Rayleigh numbers only, as will be discussed later. Our computations predict a melting front contour with an approximately streamlined design during the later evolution phase of the process.

This result seems to be in accordance with our experimental findings, which will be discussed in the following sections. Additional numerical experiments with a program developed for the calculations of convective flows [25, 26] in stationary grid systems are in line with our previous conclusions. No thermal instabilities were found for flows in concentric and cylindrical annuli for various gap widths and for the case of a cooled inner cylinder.

Disregarding the aforementioned discrepancies, comparisons of the results of Pannu et al. [15] and the present ones agree quite well for $\tau = 0.045$ and 0.08. The discrepancies observed for $\tau = 0.11$ might be due to the very coarse grid system (10×10) used in [15]. In the course of the solution process the physical domain becomes larger so that boundary layers, which will develop mostly in wider gaps, cannot be resolved adequately. The approach taken by Saitoh and Hirose [16] is based on an explicit method for solving the governing equations. To suppress strong numerical instabilities inherent to higher-order approximations of the convective terms, the application of a smoothing technique was necessary. The assumption of a quasi-steady melting process was utilized to uncouple rigorously the physical problem. During the solution process of the balance equations for vorticity, stream function, and energy, the grid system was kept stationary. After convergence the interface boundary was moved according to the frozen solution just obtained. The description concerning the handling of this procedure is not very clear, but some doubts are advisable if the evolution process from the fluid mechanical point of view is approximated adequately. So several effects caused by the numerical treatment interact whose consequencies on the overall solution cannot be estimated. Only severe thermal instabilities associated with a strong time dependence of the flow at the bottom portion would explain why the indicated temperature distibution (Fig. 3) could lead to the displayed melting front contour. Even at a much lower Rayleigh number similar interface shapes were found in [16] which seem to contradict our experimental findings.

In contrast to [15, 16] our computational approach is based on the solution of the full equation set at each time step. That means that the interface position is a real converged solution of the problem under study, within the limitations of a second-order finite-difference approximation to the physical problem. In addition, the flexibility of our scheme allows us to concentrate continiously the physical grid system in regions where boundary layers could be expected.

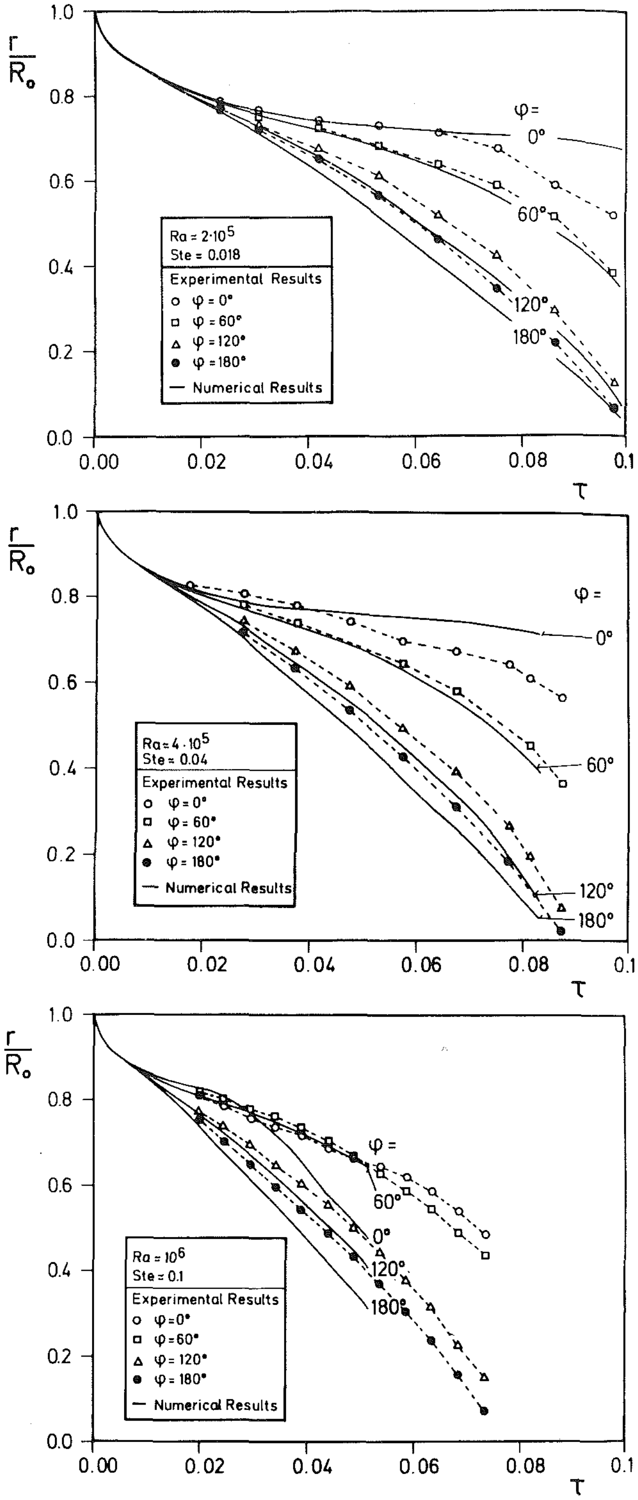

Fig. 4 Predicted and experimental local interface positions as function of dimensionless time, τ

Local Solid-Liquid Interface Positions. Solid-liquid interface positions as a function of the dimensionless time, τ, and the angle of perimeter, φ, as a parameter are presented in Fig. 4 for different Rayleigh and Stefan numbers. In each figure the regime dominated by heat conduction can be recognized by the concentric melting so that all data points coincide in this representation. The transition to a melting process influenced by natural convection begins with fanning out of the individual curves. With this definition in mind it can be seen, that with increasing Rayleigh number the conduction period becomes shorter. The motion of the molten material due to the onset of natural convection causes a faster propagation speed of the solid-liquid interface at the top of the cylinder ($\varphi = 180$ deg). Attention may now be turned to the slopes of the single curves. It is evident, that for advancing angles of perimeter the gradients and therefore the interface velocity increases. An exception are the curves of $\varphi = 0$ deg and $\varphi = 60$ deg for Ra $\simeq 10^6$. As discussed in a later section this behaviour may be explained by the occurrence of strong three-dimensional roll cells in the lower part of the melt gap. These roll cells, observed during the experiment also for the lower Rayleigh numbers may be the reason for the great deviation between computational and experimental results for $\varphi = 0$ deg.

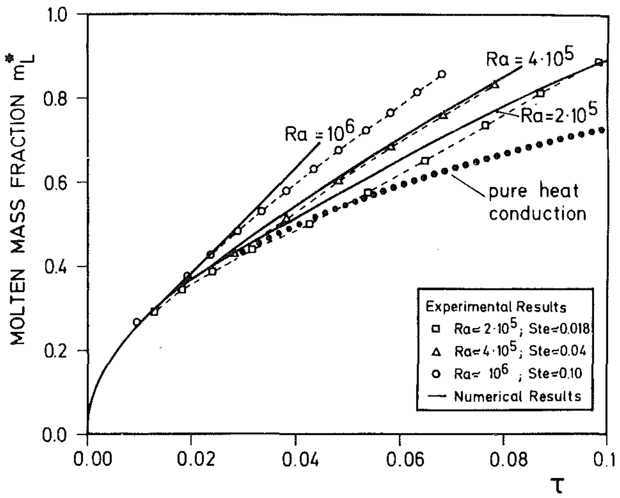

Fig. 5 Predicted and experimental molten mass fraction as function of dimensionless time, τ

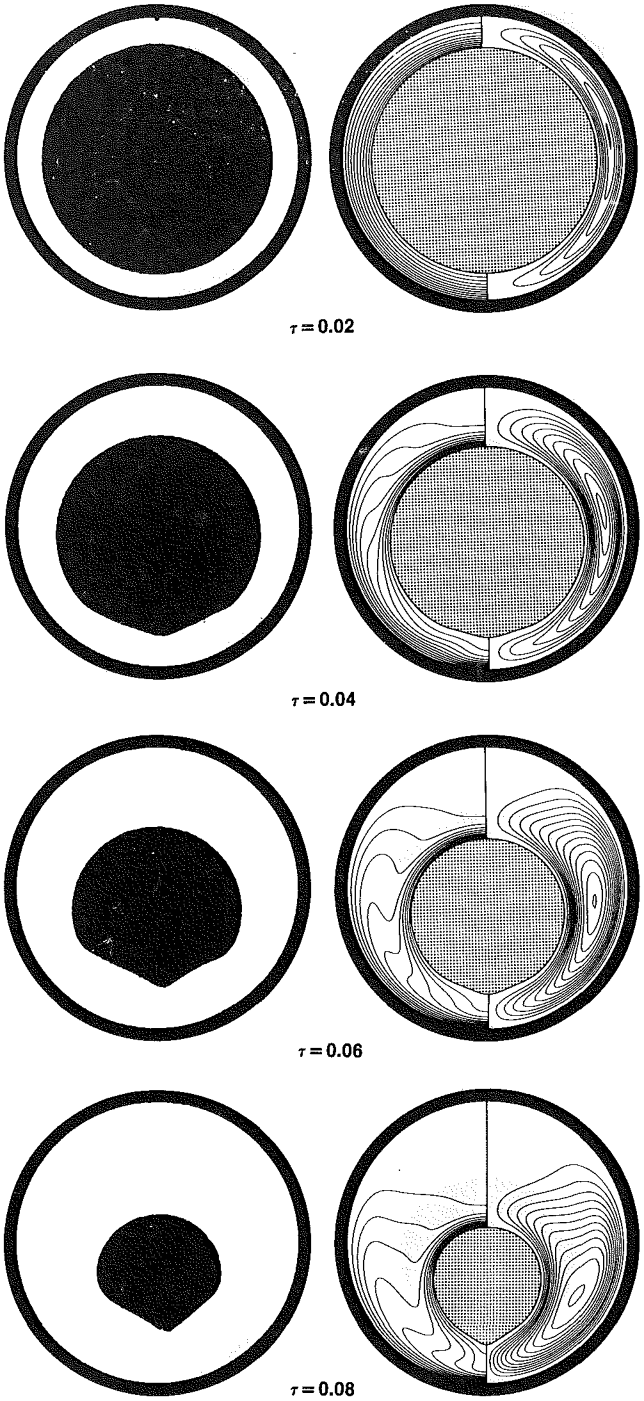

Fig. 6 Experimental (left) and numerical (right) melt front contours for Ra $\simeq$ 4.10^5 and Ste $\simeq$ 0.04 at different dimensionless times, τ. The numerical contour maps are divided into isotherms, θ, (left) and streamfunction, ψ, (right).

Although the qualitative behaviour of the curves $\varphi > 0$ deg agree quite well, it can be stated that the computer interface velocities are somewhat higher. These discrepancies may be due to small uncertainties in the physical and transport properties of the PCM, resulting in slightly incorrect experimental data in dimensionless representation. Further influence on the mentioned discrepancies may be caused by the simplifications of the mathematical model, above all neglecting the volumetric expansion of the PCM during melting. This effect seems to influence the boundary layer at the interface in such a manner that the heat transfer will be reduced. Also, the simplifying assumption of constant thermophysical properties (e.g., viscosity) may contribute to deviations between prediction and experiment.

Melting Rates. The result which represents an average melting velocity and which is available from the experimental data with sufficient accuracy is the molten mass fraction, m^*_L. Thus quantity defined as

$$m^*_L = 1 - \frac{2}{\pi R_0^2}\int_0^r \int_0^\pi r(\varphi)\, d\varphi\, dr \qquad (16)$$

is depicted in Fig. 5 versus dimensionless time, τ, for the different cases under study. From this figure it can be seen, that the increase of m^*_L with time reveals an analogous behaviour to Fig. 4. Furthermore, the results show that for the regime of developed natural convection an approximately linear timewise variation of the molten mass fraction is given. Comparing the experimental data with the computational results it is evident that the melting rate predicted by the calculations is somewhat higher. The reasons discussed in the preceding section may be responsible for these deviations. To show the influence of natural convection, the melting rate taking into account only pure heat conduction is also displayed. A comparison with the results of the present study confirm the belief that disregard of the convective motion leads to significant errors. A closer examination shows, that a difference of 10 percent is reached at $\tau \simeq 0.047$ for Ra $\simeq$ $4 \cdot 10^5$ and at $\tau = 0.023$ for Ra $\simeq 10^6$, which corresponds to a molten mass fraction of about 0.6 and 0.43, respectively.

Presentation of the Melting Process. The presentation of the melting process is done by means of photographs from the experiment and calculated results in form of contour plots for two different Rayleigh and Stefan numbers. Figure 6 shows the melting process for Ra $\simeq 4 \cdot 10^5$ and Ste $\simeq$ 0.04 at four different periods. On the left-hand side are the photographs, whereas on the right-hand side the numerical results are arranged. The sequence of transient melt contours reveal that heat transfer is greatly enhanced due to natural convection in the upper part of the annulus, leading to a fast and downward directed movement of the solid-liquid interface. Only at the very beginning can a dominating role of heat conduction be deduced from experiment and computation. After this short period, natural convection flow has an increasing influence on the physics of the system. This situation coincides subsequently with improved heat transfer in that region and accelerates the propagation of the melt front. The inverse effect can be stated in the lower part of the melt zone. The cold fluid flowing down along the solid-liquid interface inhibits heat transport due to conduction in this part. At the

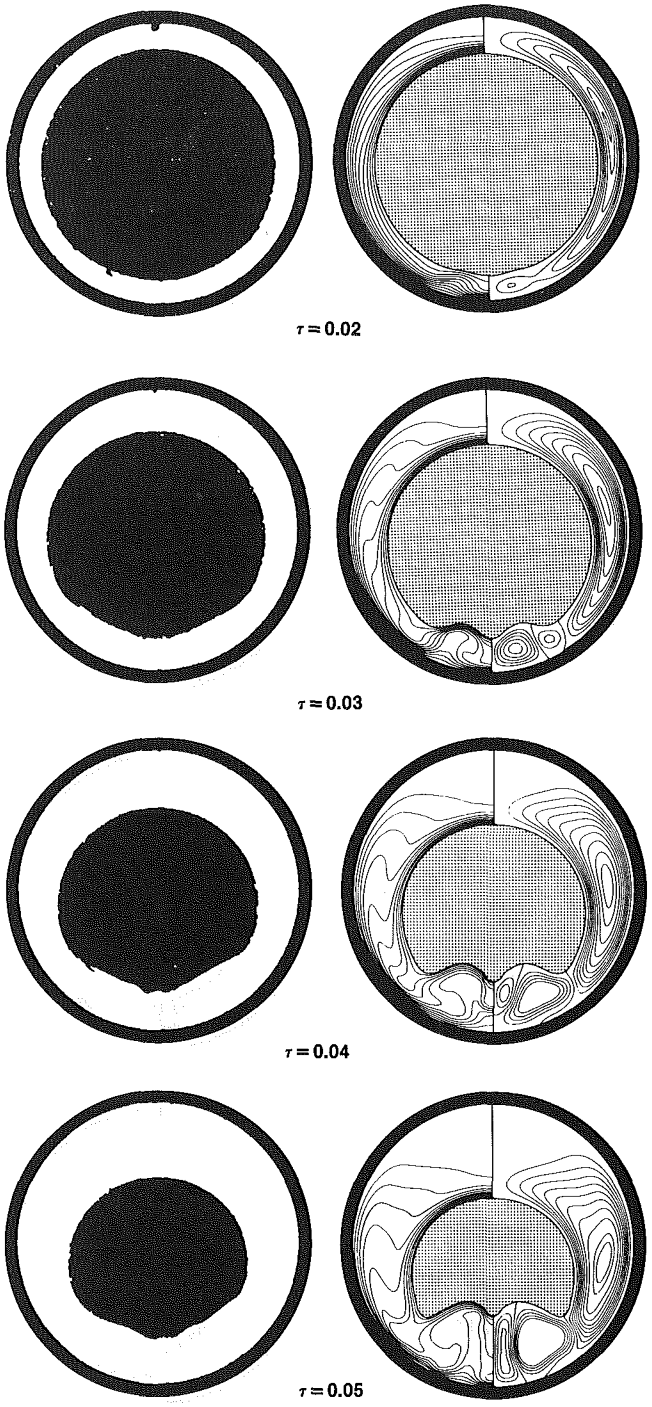

Fig. 7 Experimental (left) and numerical (right) melt front contours for Ra $\simeq 10^6$ and Ste $\simeq$ 0.1 at different dimensionless times, τ. The numerical contour maps are divided into isotherms, θ, (left) and streamfunction, ψ, (right).

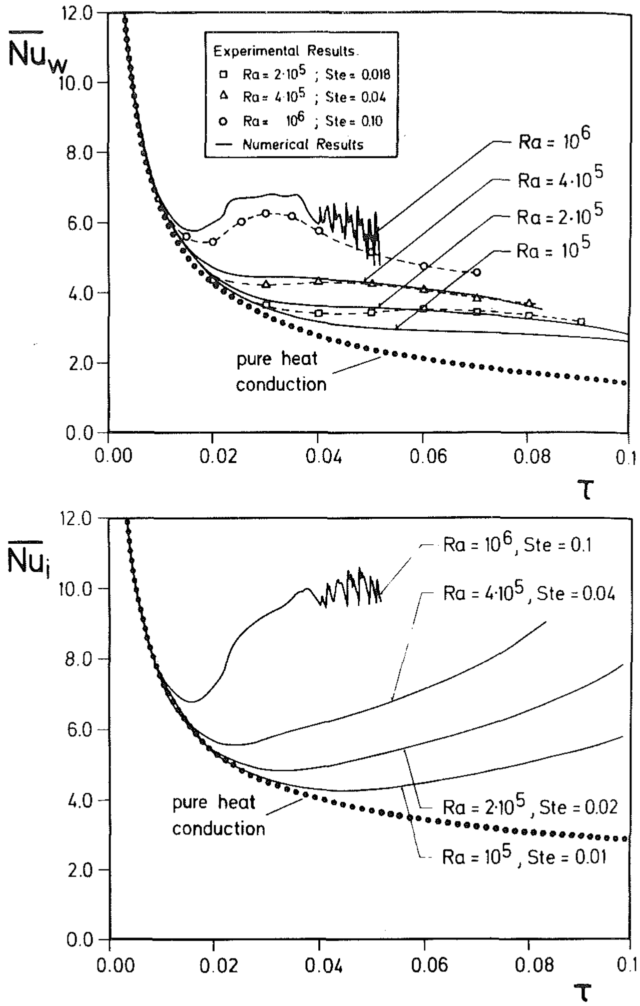

Fig. 8 Overall heat transfer coefficients at the tube wall ($\overline{\mathrm{Nu}}_w$) and the solid-liquid interface ($\overline{\mathrm{Nu}}_i$) versus dimensionless time, τ

bottom these counteracting transport mechanisms lead to an almost total stop of the melting process. In the final stages of the process (τ = 0.08) the computation predicts a streamlined design of the PCM similar to the experiment. As previously discussed, three-dimensional roll cells occur during the experimental run which may be responsible for a more accentuated shape of the melting solid.

The development of secondary roll cells is also verified by the numerical calculations for Ra $\simeq 10^6$ and Ste $\simeq$ 0.1. The formation of this flow pattern is shown in Fig. 7 and may be divided into different stages. First, at early times thermal instability at the bottom occurs. This phenomenon, which is comparable to the situation of an horizontal fluid layer heated from below, leads then in the sequel of the calculations to the development of the abovementioned roll cells. The establishment of these vortices influences the melting characteristics of the whole system. Especially the heat transfer in the lower part of the melting gap is greatly improved which results in a "moonshaped" melting contour. As indicated above, the roll cells observed in the experiment showed a three-dimensional structure and were unsteady in their timewise behaviour. The restriction of the mathematical model to two-dimensional flow may be the reason for the main differences between the experimental and calculated melt shape contours. Nevertheless, some features of the melting process, like volume and position of the PCM as well as the transition from a quasi-steady to an oscillating behaviour, are resolved reasonably.

Overall Heat Transfer Results. Attention will now be focused on the overall heat transfer coefficients $\overline{\mathrm{Nu}}$ for all cases under study. In Fig. 8 the calculated results for the heat transfer at the tube wall as well as the solid-liquid interface are plotted against the dimensionless time, τ. The overall heat transfer coefficients at the interface, $\overline{\mathrm{Nu}}_i$, and at the tube wall, $\overline{\mathrm{Nu}}_w$, are evaluated from the existing temperature distribution by the following relations

$$\overline{\mathrm{Nu}}_i = -\frac{1}{S_i(\tau)}\int(\partial\theta/\partial n)\,dS \qquad (17a)$$

$$\overline{\mathrm{Nu}}_w = -\frac{1}{2\pi R_0}\int(\partial\theta/\partial n)\,dS \qquad (17b)$$

The quantity $S_i(\tau)$ in the first equation denotes the length of the actual interface contour. Although $\overline{\mathrm{Nu}}_i$ represents the true heat transfer conditions at the moving interface, the practical evidence is questionable because of the time-dependent nominator, $S_i(\tau)$. For this reason, $\overline{\mathrm{Nu}}_w$ may be more valuable since this heat transfer coefficient reflects the proper heat input into the system and also may be obtained easily from experimental data. Nevertheless, both diagrams show high values of $\overline{\mathrm{Nu}}_i$ and $\overline{\mathrm{Nu}}_w$ at the very beginning associated with a sharp decrease which is characteristic for transient heat conduction. The end of this period of nearly one-dimensional behaviour is indicated by a spanwise spreading into individual curves. As already seen during the discussion of the local results this fanning out occurs at earlier times for high Rayleigh numbers and indicates that the melting process changes into a regime dominated by natural convection.

Attention may first be turned to the curves representing the heat flux at the tube wall. For $\mathrm{Ra} < 4 \cdot 10^5$ the sharp descent and the transition region period is followed by an only slight decrease in the timewise development. The curve for $\mathrm{Ra} \simeq 10^6$, however, passes a distinct extremum, followed by an oscillation with diminishing mean values. Worth mentioning is the fact that for very long times ($\tau \rightarrow \infty$) the liquid will take the temperature of the surrounding tube wall, and therefore the heat transfer will become zero. For comparison, also, the experimental data are depicted. They agree reasonably well with the numerical results. The discrepancy for $\mathrm{Ra} \simeq 10^6$ may be due some effects discussed previously.

The results for Nu_i show a quite different behaviour since all curves pass through a minimum and then rise with time. As before, the results for the lower Rayleigh numbers are in contrast to the highest Rayleigh numbers studied. Whereas the slopes of the former increase with advancing time the slope for $\mathrm{Ra} \simeq 10^6$ decreases sightly during the oscillation.

Special Features of the Flow Regime at Ra $\simeq 10^6$. The change in the flow characteristics for $\mathrm{Ra} \simeq 10^6$ from a quasi-steady into an unsteady phase is an interesting feature of the flow system being worthwhile for a closer examination. Regarding the lower part of the melting gap approximately as a horizontal fluid layer heated from below, it is possible to define a height, h^*, of that layer by some suitable measure. Because the layer thickness grows as the melting process advances with time, the corresponding Rayleigh number, Ra^*, increases. So basically all the flow regimes known from research on heated horizontal fluid layers must be traversed continuously. In Fig. 9, a diagram is shown, taken from Krishnamurti [29], which classifies the various flow regimes as function of Rayleigh versus Prandtl number. It is seen that for the range $\mathrm{Pr} \geq 50$ the transition to time-dependent flow occurs at $\mathrm{Ra}^* \simeq 5.5 \cdot 10^4$ followed by a change in the oscillatory behaviour at $\mathrm{Ra}^* = 1.2 \cdot 10^5$. This transition indicated by a dotted line is associated with a doubling of the oscillation frequency of the particular flow cells.

Although the mathematical model employed is restricted to planar fluid flow and the approximation of the lower part of the melt zone appears as a somewhat rough simplification, the time dependent nature of the secondary roll cells is clearly reflected by the timewise behaviour of the overall heat transfer coefficients. From Fig. 10 it can be recognized, that the periods of regular oscillations become shorter with increasing time, doubling their frequency at the end of the record. The time interval depicted in Fig. 10 corresponds with a height of the fluid layer of approximately $h^* \simeq 0.5\ \mathrm{R}_0$ which leads to $\mathrm{Ra}^* \simeq 1.25 \cdot 10^5$. This value agrees well with those found for frequency transition by Krishnamurti [29]. However some caution is indicated in the attempt to correlate fully three-dimensional phenomena by two-dimensional models. Nevertheless, the main features of such flows should be realized, apart from exact quantitative results.

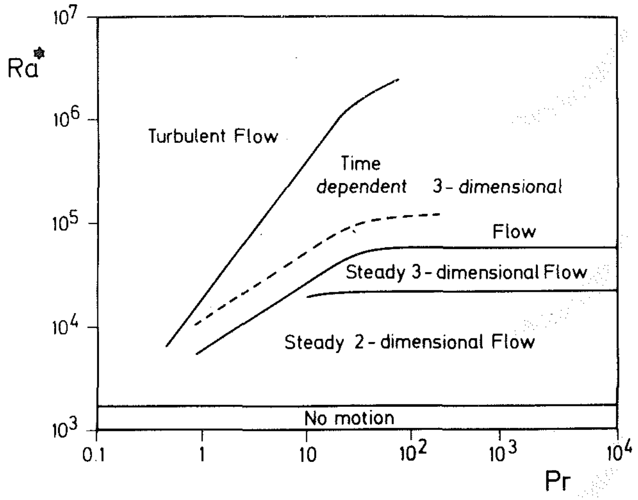

Fig. 9 Flow regimes occuring in a horizontal fluid layer heated from below [25]

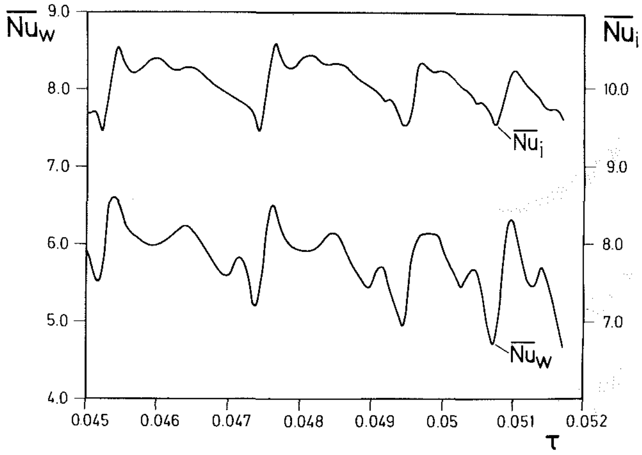

Fig. 10 Time-independent behaviour of the overall heat transfer coefficients (Ra $\simeq 10^6$; Ste $\simeq$ 0.1)

To illustrate the violent movement of the secondary vortices and the associated temperature distribution in the lower part of the melt zone a series of eight chronological arranged contour plots are presented in Fig. 11. From the single pictures development and disappearance of the secondary eddies may be recognized. Especially the contour map for $\tau = 0.05055$ should be mentioned, where four of them are present.

Conclusions

The characteristics of the melting process inside a horizontal tube have been studied theoretically and by experiments. The analytical results were obtained by means of numerical methods and have been compared to previous works [15, 16]. The method for generating boundary-fitted coordinate systems numerically has been proven to be a flexible tool for analyzing such moving boundary problems. The solution of the whole set of discretized governing equations by a fully implicit procedure leads at each time step simultaneously to the shape of the molten region as well as to the flow and temperature distributions.

As discussed in a previous section this is in contrast to the treatment of Pannu et al. [15] and Saitoh and Hirose [16]. Due to our experimental findings the predictions from [15] and [16] for $\mathrm{Ra} = 2 \cdot 10^5$, $\mathrm{Pr} = 145$, $\mathrm{Ste} = 0.115$ seem to be erroneous. The results of [15] may be explained by the very coarse grid system which did not approximate the continuous

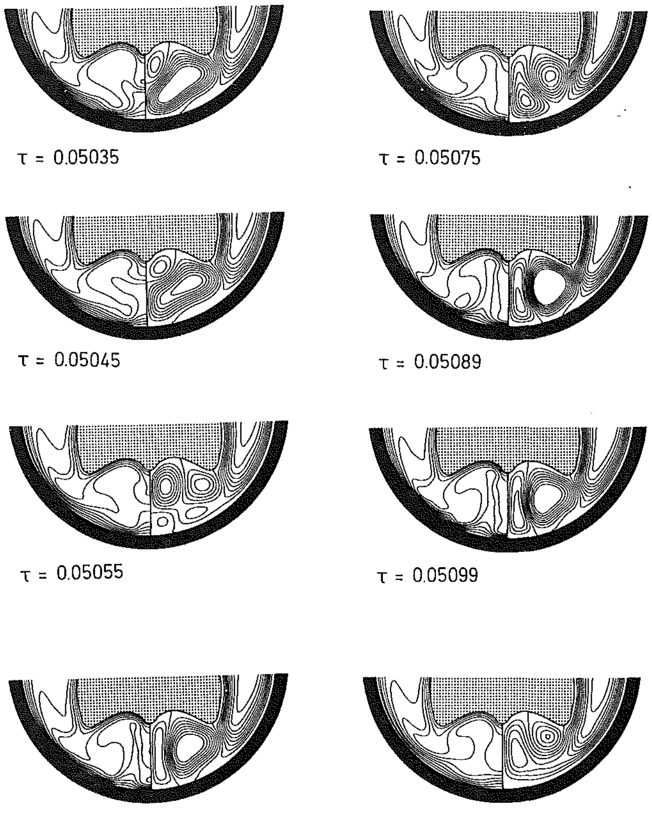

τ = 0.05035

τ = 0.05075

τ = 0.05045

τ = 0.05089

τ = 0.05055

τ = 0.05099

τ = 0.05109

τ = 0.05065

Fig. 11 Time-dependent flow in the lower part of the melt zone for Ra $\simeq 10^6$; Ste $\simeq$ 0.1. Distribution of isotherms, θ, (left) and streamfunction, ψ, (right).

physical problem in a sufficient degree during the whole evolution phase. In the procedure used by [16] the influences of the various components for stabilization of the numerical algorithm, and those for reducing simultaneously the execution times, cannot be estimated nor was this done by the corresponding authors. Therefore, the practice of [16] to compare predictions for Ra $\simeq 1.2 \cdot 10^5$ with experimental results for Ra $\simeq 3 \cdot 10^6$ seems not to be very meaningful.

From our point of view the experimental and numerical results of the problem studied should be summarized as follows:

- The period of pure heat conduction is very short and depends on the Rayleigh number.
- Almost the whole melting process is influenced by the fluid motion due to natural convection. Therefore, any analysis of processes involving phase change should consider this effect.
- At lower Rayleigh numbers, a quasi-steady melting process produces a steamlined design of the PCM in the final stages, whereas quite different melt front contours appear at higher Rayleigh numbers.
- Experimental and numerical predicted results agree well with the exception of the bottom region of the melting gap. Experimental observations showed a three-dimensional Bernard convection in this part which may be responsible for some discrepancies, mainly due to the restriction of the mathematical model to planar fluid motion.

References

1 Hale, N. W., Jr., and Viskanta, R., "Solid-Liquid Phase Change Heat Transfer and Interface Motion in Materials Cooled or Heated From Above and Below," *International Journal of Heat and Mass Transfer*, Vol. 23, 1980, pp. 283-292.

2 Hale, N. W., Jr., and Viskanta, R., "Photographic Observation of the Solid-Liquid Interface Motion During Melting of a Solid Heated from an Isothermal Vertical Wall," *Letters in Heat and Mass Transfer*, Vol. 5, 1978, pp. 329-337.

3 Bareiss, M., Betzel, T., and Beer, H., "Melting from a Vertical Wall: Influence of Different Wall Heights and Temperature Differences on Heat Transfer and Interfacial Motion," University report, Darmstadt 1980.

4 White, R. D., Bathelt, A. G., and Viskanta, R., "Study of Heat Transfer and Melting from a Cylinder Imbedded in a Phase Change Material," ASME Paper No. 77-HT-42, 1977.

5 Bathelt, A. G., Viskanta, R., and Leidenfrost, W., "Latent Heat of Fusion Energy Storage: Experiments on Heat Transfer from Cylinders During Melting," ASME JOURNAL OF HEAT TRANSFER, Vol. 101, 1979, pp. 453-458.

6 Bathelt, A. G., and Viskanta, R., "Heat Transfer at the Solid-Liquid Interface During Melting from a Horizontal Cylinder," *International Journal of Heat and Mass Transfer*, Vol. 23, 1980, pp. 1493-1503.

7 Viskanta, R., Bathelt, A. G., and Hale, N. W., "Latent Heat-of-Fusion Energy Storage: Experiments on Heat Transfer During Solid-Liquid Phase Change," *Proceedings of the 3rd International Conference on Alternative Energy Sources*, Bal Harbour, Fla., 1980.

8 Goldstein, R. J., and Ramsey, J. W., "Heat Transfer to a Melting Solid with Application to Thermal Energy Storage Systems," in *Heat Transfer Studies: A Festschrift for E.R.G. Eckert*, edited by J. P. Hartnett, Hemisphere, Washington, 1979, pp. 199-206.

9 Bareiss, M., and Beer, H., "Influence of Natural Convection on the Melting Process in a Vertical Cylindrical Enclosure," *Letters in Heat and Mass Transfer*, Vol. 7, 1980, pp. 329-338.

10 Horsthemke, A., and Marschall, E., "Speicherung von Thermischer Energie in Salz- und Metallschmelzen," *Brennstoff-Wärme-Kraft*, Vol. 28, 1976, pp. 18-22.

11 Shamsundar, N., and Sparrow, E. M., "Effect of Density Change on Multidimensional Conduction Phase Change," ASME JOURNAL OF HEAT TRANSFER, Vol. 98, 1976, pp. 550-557.

12 Yao, L. S., and Chen, F. F., "Effects of Natural Convection in the Melted Region Around a Heated Horizontal Cylinder," ASME JOURNAL OF HEAT TRANSFER, Vol. 102, 1980, pp. 667-672.

13 Sparrow, E. M., Patankar, S. V., and Ramadhyani, S., "Analysis of Melting in the Presence of Natural Convection in the Melt Region," ASME JOURNAL OF HEAT TRANSFER, Vol. 99, 1977, pp. 520-526.

14 Gartling, D. K., "Finite Element Analysis of Convective Heat Transfer Problems with Change of Phase," *Proceedings of the 1st International Conference on Numerical Methods in Laminar and Turbulent Flow*, Swansea, 1978, pp. 489-500.

15 Pannu, J., Joglekar, G., and Rice, P. A., "Natural Convection to Cylinders of Phase Change Material used for Thermal Storage," AIChE Symposium Series, 1980, pp. 47-55.

16 Saitoh, T., and Hirose, K., "High-Rayleigh Number Solutions to Problems of Latent Heat Thermal Energy Storage in a Horizontal Cylinder Capsule," ASME JOURNAL OF HEAT TRANSFER, Vol. 104, 1982, pp. 545-553.

17 Saitoh, T., and Hirose, K., "Numerical Method for the Two-Dimensional Freezing Problem Around a Horizontal Cylinder Encompassing a Density Inversion Point," *Bulletin of the JSME*, Vol. 24, 1981, pp. 147-152.

18 Rieger, H., Projahn, U., and Beer, H., "Analysis of the Heat Transport Mechanisms During Melting Around a Horizontal Circular Cylinder," *International Journal of Heat and Mass Transfer*, Vol. 25, 1982, pp. 137-147.

19 Nicholas, D., and Bayazitoglu, Y., "Thermal Storage of a Phase Change Material in a Horizontal Cylinder," *Proceedings of the 3rd International Conference on Alternative Energy Sources*, Bal Harbour, Fla., 1980.

20 Bareiss, M., and Beer, H., "Experimental and Analytical Study of the Melting Process Inside a Horizontal Tube," to be published, in the *International Journal of Heat and Mass Transfer*.

21 Hale, D. V., Hoover, M. J., and O'Neil, M. J., *Phase Change Material Handbook*, NASA-CR-61363, 1971.

22 Vargaftik, N. B., *Tables on the Thermophysical Properties of Liquids and Gases*, Hemisphere, Washington, 1975.

23 Eckert, E. R. G., and Drake, R. M., *Analysis of Heat and Mass Transfer*, McGraw-Hill, New York, 1972, pp. 222.

24 Thompson, J. F., Thames, F. C., and Mastin, C. W., "Automatic Numerical Generation of Body-Fitted Curvilinear Coordinate System for Field Containing any Number of Arbitrary Two-Dimensional Bodies," *Journal of Computational Physics*, Vol. 15, 1974, pp. 299-319.

25 Projahn, U., Rieger, H., and Beer, H., "Numerical Analysis of Laminar Natural Convection Between Concentric and Eccentric Cylinders," *Numerical Heat Transfer*, Vol. 4, 1980, pp. 131-146.

26 Rieger, H., and Projahn, U., "Laminar Natural Convection Heat Transfer in a Horizontal Gap, Bounded by an Elliptic and a Circular Cylinder," *Proceedings of the 2nd International Conference on Numerical Methods in Thermal Problems*, Venice, 1981, pp. 1036-1047.

27 Thomas, P. D., and Middlecoff, J. F., "Direct Control of the Grid Point Distribution in Meshes Generated by Elliptic Equations," *AIAA Journal*, Vol. 18, 1980, pp. 652-656.

28 Stone, H. L., "Iterative Solution of Implicit Approximations of Multidimensional Partial Differential Equations," SIAM *Journal of Numerical Analysis*, Vol. 5, 1968, pp. 530-558.

29 Krishnamurti, R., "On the Transition to Turbulent Convection, pt. 2: The Transition to Time-Dependent Flow," *Journal of Fluid Mechanics*, Vol. 42, 1970, pp. 309-320.

Shape Change of an Initially Vertical Wall Undergoing Condensation-Driven Melting[1]

K. Taghavi-Tafreshi
Student Mem.

V. K. Dhir
Mem. ASME

School of Engineering and Applied Science,
University of California,
Los Angeles, Calif. 90024

Condensation-driven melting of an initially vertical wall is studied both analytically and experimentally. It is shown that a vertical surface undergoing simultaneous melting-condensation will not stay vertical and will go through a series of transient shapes before attaining a steady-state shape. Numerical solutions are obtained both for the transient shapes of the wall and the heat transfer. The steady-state shape of the wall is found to be the one which yields a constant melting rate along the wall. The total melting rate is shown to increase during the time the shape change occurs such that the steady-state shape yields about 35 percent more melting rate than the initial vertical wall. Experiments are conducted at one atmosphere pressure by condensing saturated steam on vertical surfaces of slabs made of naphthalene, biphenyl, and stearic acid. The heat transfer and shape change data are found to compare well with the predictions.

Introduction

Simultaneous melting-condensation on vertical surfaces was first investigated by Tien and Yen [1]. In their analysis, they assumed that the condensing vapor and melting solid were the same substance. Hence, the melt and condensate layers formed a single liquid film. Limiting their analysis to high Pr liquids and using an integral technique, Tien and Yen obtained closed form solutions for the local and average heat transfer coefficients. Their results were found to compare well with the exact similarity solutions. Epstein and Cho [2] analyzed laminar film condensation on a vertical melting surface when melt and condensate were two immiscible substances. They transformed the partial differential equations for the melt and condensate using the similarity transformations technique originally employed by Sparrow and Gregg [3] and solved the equations using the integral method. The results for the heat transfer or the melting rate were presented in terms of six dimensionless parameters, $c_{pm}\Delta T_t/h_{sf}$, $c_{pc}\Delta T_t/h_{fg}$, Pr_m, Pr_c, $(\rho_m\mu_m/\rho_c\mu_c)^{1/2}$, and $k_m/k_c\,(\nu_c/\nu_m)^{1/2}$. The temperature of the interface between the melt and the condensate was, however, not evaluated. Recently Taghavi-Tafreshi and Dhir [4] have also studied condensation driven melting on a vertical wall for the case when melt and condensate are two immiscible substances. In their work, similar solutions of the governing momentum and energy equations were obtained for high Pr liquids and numerical results for melting rate, condensation rate, and interface temperatures were presented in terms of six dimensionless parameters, $c_{pm}\Delta T_t/h_{sf}$, $c_{pc}\Delta T_t/h_{fg}$, ρ_c/ρ_m, c_{pc}/c_{pm}, k_c/k_m, and μ_c/μ_m. In addition, Taghavi-Tafreshi and Dhir conducted experiments with saturated steam condensing on vertical surfaces made of naphthalene, biphenyl, and stearic acid. The experimental results of the melting rate were found to compare well with their analytical predictions.

In all of the theoretical models [1, 2, 4], it is assumed that during the time period of interest the melting surface remains vertical despite the fact that melting rate varies along the wall. The experiments reported in [4] show that, because of nonuniform melting, an initially vertical wall stays vertical only for a very short period of time. Thus the vertical wall assumption made in [1, 2, 4] is violated if large time periods of simultaneous melting-condensation are of interest. Contreras and Thorsen [5] have analyzed transient melting of a solid due to condensation of vapor. Their analysis also yielded transient shapes of the solid. However, the analysis of Contreras and Thorsen [5] has a severe weakness in that the change in the local acceleration in the direction of flow resulting from the change in the shape of the solid has been ignored. For this particular reason their analysis showed that the solid never achieved a steady-state shape.

In this paper the shape change of an initially vertical surface undergoing simultaneous melting-condensation is studied both theoretically and experimentally. The transient shapes and the effects of the shape change on the total melting rate and the heat transfer rate are investigated. Steady-state shape of the initially vertical wall undergoing simultaneous melting-

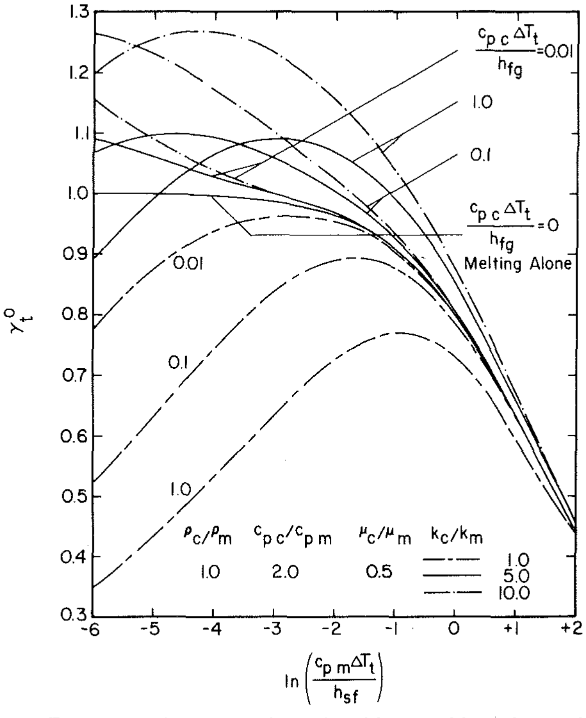

Fig. 1 Typical results for condensation-driven melting of a vertical wall [4]

---

[1] This work received partial support from NSF Grant CME 7918258.

Contributed by the Heat Transfer Division for publication in the JOURNAL OF HEAT TRANSFER. Manuscript received by the Heat Transfer Division June 19, 1982. Paper No. 81-HT-12.

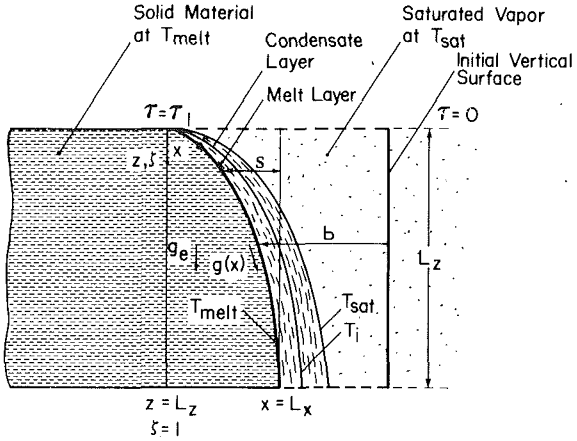

Fig. 2 Physical model for condensation on a melting surface of an arbitrary shape

condensation is also predicted. Experiments are performed by condensing saturated water vapor on initially vertical surfaces made of naphthalene, biphenyl, and stearic acid.

Analysis

Exposure of the vertical surface of a solid maintained at its melting temperature to vapor having saturated temperature higher than the melting temperature of the solid will result in condensation of the vapor and melting of the solid. Assuming that condensate and melt are immiscible and flow down the surface in the form of laminar films, Taghavi-Tafreshi and Dhir [4] have obtained results for the melting and the condensation heat transfer coefficients and for the temperature of the interface[2] between the melt and the condensate. For liquids of high Prandtl number, their expression for the overall heat transfer coefficient at the wall based on melt properties and overall temperature difference across the two layers can be written as

$$h_t^0 \equiv \frac{k_m (\partial T_m/\partial y)\,|_{y=0}}{T_{\mathrm{sat}} - T_{\mathrm{melt}}} = \gamma_t^0 \left[\frac{(\rho_m - \rho_v) g_e k_m{}^3 h_{sf}}{4 \nu_m \Delta T_t x} \right]^{1/4} \tag{1}$$

The coefficient γ_t^0 was found to be a function of the following dimensionless parameters: $c_{pm}\Delta T_t/h_{sf}$, $c_{pc}\Delta T_f/h_{fg}$, ρ_c/ρ_m, c_{pc}/c_{pm}, k_c/k_m, and μ_c/μ_m. Figure 1 shows typical results for γ_t^0 from their study. It must be pointed out that the results presented in [4] were obtained by neglecting inertia terms in the momentum equations of the melt and the condensate layers. The solutions obtained by neglecting inertia terms are within +20 percent of the exact solutions for Pr_m and $\mathrm{Pr}_c \geq 1$ and $c_{pm}\Delta T_t/h_{sf}$ and $c_{pc}\Delta T_t/h_{fg} \leq 1$. However, the differences between the two solutions [6] are much smaller for common liquids for which Pr_m and $\mathrm{Pr}_c >> 1$ and $c_{pm}\Delta T_t/h_{sf}$ and $c_{pc}\Delta T_t/h_{fg} << 1$. For example, for the melt and the condensate materials used in the present work the difference in the values of γ_t^0 obtained from the intertialess and the exact solutions is less than 0.1 percent.

Several interesting observations can be made in relation to equation (1).

(*i*) The overall heat transfer coefficient during simultaneous melting-condensation can be written in terms of melt layer properties alone in a fashion similar to that for condensation on a vertical wall. The numerical coefficient, γ_t^0, depends on both melt and condensate properties and has to be evaluated from the solution of the governing equations.

(*ii*) The numerical constant, γ_t^0, does not depend on the variation of acceleration in the direction of flow. For a surface in which the local acceleration increases with distance from the leading edge, the local heat transfer coefficient can be written as

$$h_t^0 = \gamma_t^0 \left[\frac{(\rho_m - \rho_v) g_{\mathrm{eff}} k_m{}^3 h_{sf}}{4 \nu_m \Delta T_t x} \right]^{1/4} \tag{2}$$

where g_{eff} in equation (2) is defined following the work of [7] as

$$g_{\mathrm{eff}} = \frac{[g(x)]^{4/3} x}{\int_0^x [g(x)]^{1/3} dx} \tag{3}$$

The use of equation (3) is valid only as long as at a given location the pressure gradient generated by the varying film

Nomenclature

b = local penetration of the melting surface, see Fig. 2
c_p = specific heat at constant pressure
$g(x)$ = component of gravitational acceleration in the direction of flow at location x, see Fig. 2
g_e = gravitational acceleration
g_{eff} = effective gravity defined in equation (3)
h_{fg} = latent heat of vaporization
h_{sf} = latent heat of fusion
h_t^0 = heat transfer coefficient defined in equation (1)
k = thermal conductivity
L_x = total length along the melting surface
L_z = height of the melting surface
$\dot{m}''$ = melting rate per unit area averaged over the height of the surface
Pr = Prandtl number, $\mu c_p/k$
s = horizontal distance denoting recession of the surface relative to the trailing edge, see Fig. 2
T = temperature
T_{melt} = melting temperature of the solid
T_{sat} = saturation temperature of the vapor
t = time
t_o = characteristic time defined in equation (15)
ΔT_m = temperature difference across the melt layer
ΔT_t = total temperature difference across melt and condensed layers, $T_{\mathrm{sat}} - T_{\mathrm{melt}}$
x = coordinate along the melting surface
y = coordinate normal to the melting surface
z = vertical coordinate
β = dimensionless penetration of the melting surface, b/L_z
γ_t^0 = coefficient defined in equation (1)
ζ = dimensionless vertical coordinate, z/L_z
μ = dynamic viscosity
ν = kinematic viscosity
ρ = density
τ = dimensionless time defined in equation (14)

Subscripts

c = condensate
m = melt
s = solid
ss = steady state
x = based on x-coordinate
z = based on z-coordinate

---

[2] The evaluation of the interface temperature is very important, since it will indicate if the melt will not boil or the condensate will not freeze at the interface.

thickness is much smaller than that resulting from the gravitational acceleration. The effect on γ_t^0 of neglect of inertia terms in the momentum equation is of the same order of magnitude for the variable acceleration surface as is for the vertical wall.

(*iii*) The melting rate along the vertical wall varies as $x^{-1/4}$.

The consequence of the third observation is that soon after initiation of simultaneous melting-condensation, the surface will not remain vertical because of uneven melting rate along the wall. With the change in the shape, the local acceleration will continuously vary along the surface. The acceleration will be zero at the leading edge and will be equal to the earth normal gravity at the trailing edge where the melt leaves the surface. Figure 2 shows one such surface. For the shapes in which acceleration is not constant but increases from the leading to the trailing edge, the local heat transfer coefficient or the melting rate can be calculated from equation (2) while using a proper functional form of $g(x)$ in equation (3). Next we see how the shape of the initially vertical surface will change with time and what the steady-state shape will be.

Steady-State Shape. Very rapid melting at the leading edge will cause the region near the leading edge to flatten with a resultant decrease in local acceleration in the direction of flow. Decreased acceleration will cause a reduction in the local heat transfer coefficient and in turn reduced melting rate. Such a self-limiting process will occur in time all along the wall. However, the acceleration at the trailing edge will remain unaffected since the liquid there must flow vertically downwards. Intuitively, the wall will achieve a steady-state shape, if there is one, when the melting rate is the same everywhere on the wall. Since the melting rate is directly proportional to the heat transfer coefficient, the steady-state shape will be one for which the local heat transfer coefficient is the same everywhere along the wall.

For laminar film condensation on surfaces with forward stagnation point, it has been shown by Dhir and Lienhard [7, 8] that the heat transfer coefficient is independent of the distance in the direction of flow if local acceleration increases linearly with distance from the leading edge. Local acceleration for such a surface can be written in terms of gravitational acceleration as

$$\frac{g(x)}{g_e} = \frac{x}{L_x} \tag{4}$$

The coordinate, x, in the direction of flow and coordinate, z, in the vertical direction are related by

$$\frac{dz}{dx} = \frac{g(x)}{g_e} \tag{5}$$

Integration of equation (5) while using the relation given by equation (4) and noting that $z=0$ and $x=0$ and $z=L_z$ when $x=L_x$, yields the following for such a surface

$$L_x = 2L_z \tag{6}$$

and

$$\frac{x}{L_x} = \left(\frac{z}{L_z}\right)^{1/2} \tag{7}$$

As shown in Fig. 2, the coordinate s representing the horizontal distance of the melting surface from the trailing edge is related to x- and z-coordinates as

$$\frac{ds}{dz} = \sqrt{\left(\frac{dx}{dz}\right)^2 - 1} \tag{8}$$

Use of equations (6) and (7) in (8) and integration yields a relation between the horizontal and vertical coordinates describing the surface having constant melting rate everywhere as

$$\frac{s_{ss}}{L_z} = \tan^{-1}\sqrt{\frac{L_z}{z} - 1} - \sqrt{\left(\frac{z}{L_z}\right) - \left(\frac{z}{L_z}\right)^2} \tag{9}$$

The subscript *ss* on *s* indicates the relative local penetration with respect to the trailing edge when the melt surface acquires a steady-state shape. When the gravitational acceleration given by equation (4) is used in equation (3), to evaluate g_{eff}, the heat transfer coefficient for the steady-state shape is obtained from equation (2) as

$$h_{t,ss}^0 = \gamma_t^0 \left[\frac{(\rho_m - \rho_v) g_e k_m{}^3 h_{sf}}{6\nu_m \Delta T_t L_z} \right]^{1/4} \tag{10}$$

Transient Shapes. Before accepting the above proposition that a steady-state shape exists for an initially vertical wall undergoing simultaneous melting-condensation, it is important to know if the wall would attain such a shape. Also, we would like to know what shapes the vertical wall will go through before attaining such a steady-state shape. The physical model used to analyze this is shown in Fig. 2. A relation governing the recession of the melting surface from its original position can be obtained by making an energy balance at the melting surface as

$$\frac{\partial b}{\partial t} = \frac{q}{\rho_s h_{sf}} \equiv \frac{h_t^0 \Delta T_t}{\rho_s h_{sf}} \tag{11}$$

where b is the local horizontal distance of the melt surface from its original position. The distance, b, which also represents the absolute penetration of the melt front into the solid is related to the relative penetration distance, s, used in equation (8) as

$$s = b(z,t) - b(L_z,t) \text{ or } \frac{\partial s}{\partial z} = \frac{\partial b}{\partial z} \tag{12}$$

Use of equation (2) along with equations (3), (5), (8), and (12) in (11) yields an expression for the dimensionless local horizontal position of the melt front as

$$\frac{\partial \beta}{\partial \tau} = \left[1 + \left(\frac{\partial \beta}{\partial \zeta}\right)^2\right]^{-1/6} \left[\int_0^\zeta \left[1 + \left(\frac{\partial \beta}{\partial \zeta}\right)^2\right]^{1/3} d\zeta\right]^{-1/4} \tag{13}$$

In equation (13), the dimensionless variables, β, ζ, and τ are defined as

$$\beta = b/L_z, \quad \zeta = z/L_z, \text{ and } \tau = t/t_o \tag{14}$$

where the characteristic time, t_o, is defined as

$$t_o = \frac{1}{\gamma_t^0} \left[\frac{4L_z{}^5 \rho_s{}^4 h_{sf}^3 \mu_m}{k_m{}^3 \Delta T_t{}^3 \rho_m (\rho_m - \rho_v) g_e} \right]^{1/4} \tag{15}$$

The initial and boundary conditions for equation (13) are

$$\beta = 0 \text{ at } \tau = 0 \text{ for } 0 \le \zeta \le 1 \tag{16}$$

and

$$\frac{\partial \beta}{\partial \zeta} = 0 \text{ at } \zeta = 1 \text{ for } 0 \le \tau \tag{17}$$

The boundary condition, equation (17), is obtained by utilizing the fact that at the trailing edge the melt must flow vertically downwards (note that this boundary condition is consistent with the vertical surface and with equation (9) describing the steady-state shape of the melt front).

The following procedure was used to evaluate $\beta(\zeta,t)$ from equation (13). Knowing that at $\tau=0$ the penetration distance is $\beta=0$ everywhere ($\partial\beta/\partial\tau=0$), the right-hand side of equation (13) was evaluated for values of ζ greater than zero. Thereafter, equation (13) was integrated over a very small time interval, $\Delta\tau$, using the fourth-order Runge-Kutta technique. This resulted in a set of values of $\beta(\zeta,\Delta\tau)$. The values of $\partial\beta/\partial\zeta$ were then obtained by using a central differencing scheme. Thereafter, Simpson's rule was used to

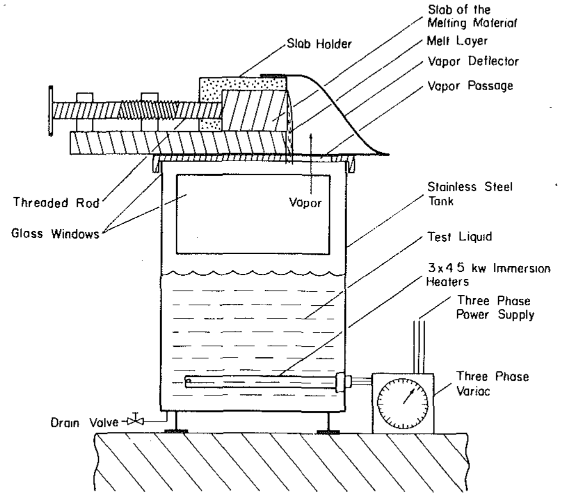

Fig. 3 Test apparatus

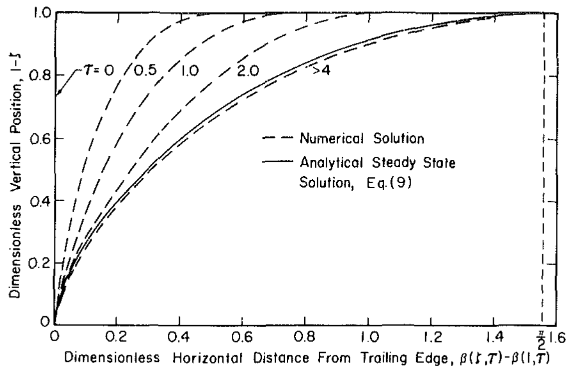

Fig. 4 Numerical solutions for the transient shapes of an initially vertical wall undergoing condensation-driven melting

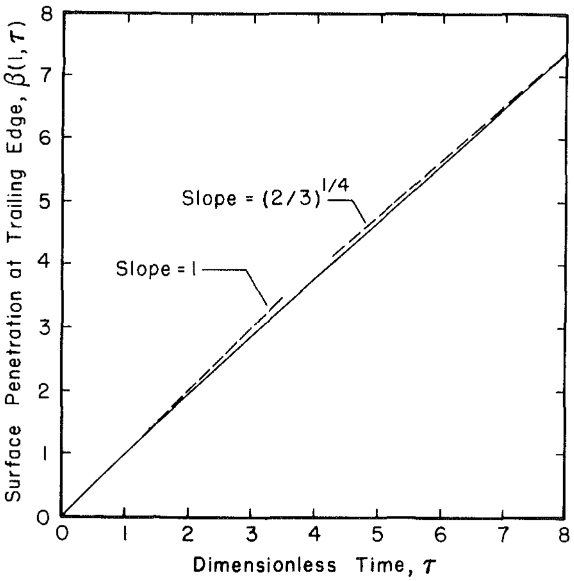

Fig. 5 Dimensionless penetration of the trailing edge as a function of dimensionless time

evaluate the integral on the right-hand side of equation (13). This in turn allowed the evaluation of the right-hand side of equation (13) at $\tau = \Delta\tau$. With the known values of the right-hand side at $\tau = 0$ and $\tau = \Delta\tau$ and the value of β at $\tau = \Delta\tau$, Adam's second-order open formula [9] was used to determine β at $\tau = 2\Delta\tau$. The above procedure was repeated to evaluate β at subsequent times. The values of β at $\tau = 0$ could not be obtained because of singularity on the right-hand side of equation (13). At a particular time the value of β at $\tau = 0$ was obtained by extrapolating the results of β near the leading edge.

Experimental Apparatus and Procedure

Condensation-driven melting experiments were conducted by condensing saturated steam on one of the vertical faces of slabs made of naphthalene, biphenyl, and stearic acid. Data for the local penetration of the melt front into the solid and the shape of the surface as a function of duration of the experiments were taken.

Experimental Apparatus. The apparatus used for performing experiments has essentially two parts—the vapor generating tank and the structure for holding the vertical surface. Figure 3 shows the apparatus which is the same as described in [4].

The vapor generating tank is made of 1.5-mm thick stainless steel sheet and has dimensions of $25 \times 38 \times 55$ cm. Glass windows are provided in two joining sides of the tank to facilitate visual observations during the experiments. A valve is placed at the bottom of the tank for draining the contents of the tank. To boil the test liquid, six cylindrical heating elements each with a rating of 4.5 kW at 220 V are attached to one of the walls of the tank. The tank is covered by an aluminum lid which has a 15-cm dia opening in it. The melting surfaces are exposed to vapor exiting from the opening.

The structure fabricated to support the slabs is made out of wood. Two side walls are rigidly fixed to a 3-cm thick wooden base. The spacing between the vertical walls is 8 cm, and is such that the test slabs just fit between these walls. A vapor deflector plate made out of aluminum sheet is placed over the opening in the lid covering the vapor generating tank. The deflector plate directs the vapor towards the melting surface and it partly covers the slab. The height of the plate is adjusted such that a small clearance exists between the deflector plate and the slab. As the melting progresses and the vertical surface starts to recede, the slab needs to be moved forward so that the melt falls off freely and the melting surface experiences minimum end effects. This is accomplished by turning a 2.5-cm dia threaded rod held between two nuts rigidly fixed to the bottom plate.

Experimental Procedure. Prior to each experiment, a slab of a given material—generally 8 cm in width, 8 cm in height, and 16 cm in length—was cast. The procedure used in casting the slab was the same as described in [4]. After casting, the slab was placed in a bath of warm water. The temperature of the slab was maintained a few degrees below the melting temperature of the solid. This was done to make sure that almost all of the energy released during condensation was utilized in melting of the solid. Meantime the heaters in the tank were switched on to boil the test liquid. The liquid in the vapor generator was kept in a boiling state for about 10 min to free the upper space in the tank and the liquid of any noncondensables. The power to the heaters was adjusted so that the vapor generation rate was usually several times the rate needed for steady-state condensation on the melting surface. However, the vapor velocity near the melting surface is calculated to be small so that effect of the inertia of the vapor on the condensation-melting process can be expected to be small. Although no precise determination of complete absence of noncondensables in the system was made, yet little change in the results was found when experiments were conducted with longer pre-experiment boiling times and higher vapor generation rates.

Table 1 Comparison of the experimental data and analytical results for condensation-driven melting of a vertical surface

Run no.	Melt/ condensate	Analytical prediction [4] γ_l^0	Analytical prediction [4] $\Delta T_m/\Delta T_l$	Surface height L_z,[m]	Real time t, [s]	Dimension-less time τ	Relative penetration of the midplane $\beta(1/2,\tau)-\beta(1,\tau)$ exp.	Relative penetration of the midplane numerical result	Relative penetration of the midplane difference %	Absolute penetration of the trailing edge $\beta(1,\tau)$ exp.	Absolute penetration of the trailing edge numerical result	Absolute penetration of the trailing edge difference %
1A	Naphthalene/ Water	0.95	0.990	0.080	115.0	0.174	--	0.032	--	0.131	0.174	−24
1B				0.080	93.6	0.142	--	0.026	--	0.138	0.142	− 2.5
2A	Biphenyl/ Water	0.89	0.991	0.083	207.4	0.440	0.060	0.078	−23	0.420	0.440	− 4.6
2B				0.076	168.0	0.398	0.055	0.052	+ 5.7	0.355	0.398	−11
2C				0.080	188.8	0.420	0.063	0.072	−12.6	0.400	0.420	− 4.7
3A	Stearic acid/ Water	0.92	0.985	0.068	178.6	0.223	0.044	0.040	+11	0.220	0.223	− 4
3B				0.076	196.8	0.207	0.040	0.037	+ 6.2	0.244	0.207	+18

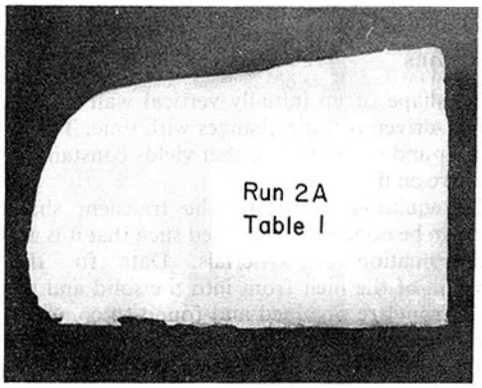

Fig. 6 Photograph showing cross section of an initially vertical surface made of biphenyl after 3.456 min ($\tau = 0.44$) of exposure to saturated steam

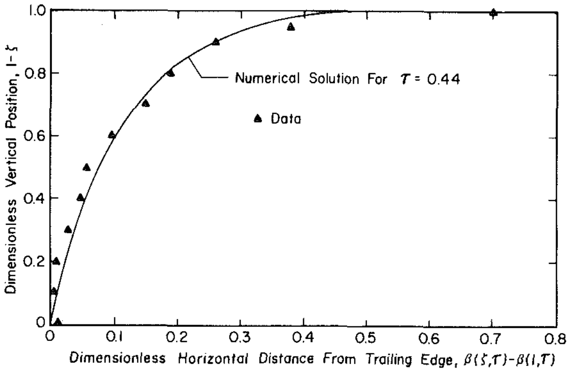

Fig. 7 Comparison of the observed and predicted surface profiles after 3.456 min ($\tau = 0.44$) of steam condensation of an initially vertical wall

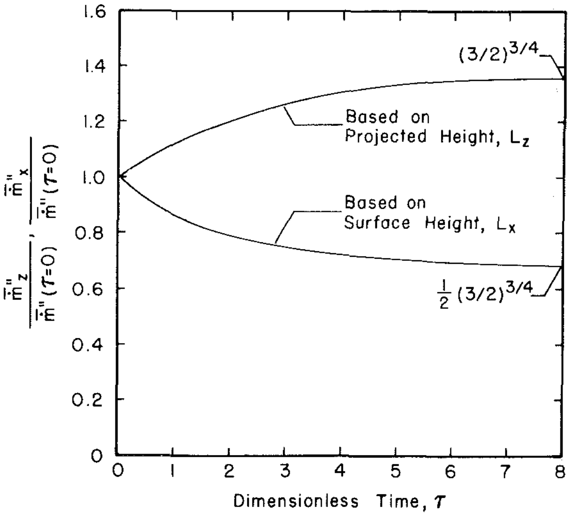

Fig. 8 Variation of the average melting rates during the time it takes the initially vertical surface to acquire a steady-state shape

Experiments were conducted by positioning the slab in the holder which was subsequently placed over the lid of the vapor generator. The vapor deflecting towards the solid led to melting of the surface. As the melting progressed and the surface receded with accompanying shape change, the threaded rod was turned fast enough to keep the trailing edge of the melting surface at the edge of the bottom support plate. The experiments were terminated when the end effects started to influence the shape of the melting surface. Thereafter, the heaters were switched off, and the slab was removed from the support structure. The size of the slab was compared with its original size to determine the penetration of the melting surface. Photographs of the slab were taken in all the experiments to obtain qualitative and quantitative information about the shape of the melting surface.

Results and Discussion

It was pointed out earlier in the section on analysis that a vertical melting surface cannot remain vertical due to the nonuniform rate of melting along the direction of flow. However, the uneven melting process is self limiting. The location with initial higher melting rate recedes faster, which results in smaller local acceleration in the direction of flow. This in turn causes a reduction in the local melting rate. Consequently, the initially vertical surface will undergo a series of transient shapes before it acquires a steady-state shape. Numerical integration of equation (13) yields the absolute penetration of the melt front into the solid as a function of dimensionless time, τ, and the dimensionless location, ζ, in the vertical direction. In Fig. 4 the results of such an integration are presented. In plotting the surface shapes (location of the melt front) relative penetration, $s/L_z = \beta(\zeta,\tau) - \beta(1,\tau)$, is used instead of the absolute penetration, $\beta(\zeta,\tau)$. This is done to facilitate the presentation of the results. In Fig. 4, the surface shape given by equation (9) for a constant melting rate everywhere is also plotted. It is noted that the numerical calculations for $\tau > 4$ compare extremely well with the analytical results proving that the steady-state shape is indeed the one for which the melting rate is the same everywhere on the surface.

Figure 5 shows the dimensionless absolute penetration of the trailing edge of the initially vertical surface as a function of dimensionless time. At small times, $d\beta/d\tau = 1$ indicates that the trailing edge behaves as part of a vertical surface. For large times, the component of gravity along the surface decreases as the surface deviates from vertical and in the limit $d\beta/d\tau$ approaches $\sqrt[4]{2/3}$. The penetration rate $d\beta/d\tau = \sqrt[4]{2/3}$

corresponds to the rate at which the trailing edge will recede when the melting surface acquires a shape in which the acceleration along the surface increases linearly from zero to earth normal gravity (steady-state shape).

Several experiments were performed by condensing saturated steam on vertical surfaces of slabs made of naphthalene, biphenyl, and stearic acid. The experiments were terminated before the end effects started to influence the shape of the melting surface. Table 1 lists the dimensionless absolute penetration of the trailing edge, $\beta(1,\tau)$, as well as the dimensionless relative penetration of the midplane, i.e., $\beta(1/2,\tau)$ - $\beta(1,\tau)$, obtained in different experiments. The observed penetration rates lie within $+18$ and -24 percent of the predicted values. The error in the measurement of relative penetration distances is expected to be ± 3 percent. However the deviation in the predicted values of β because of uncertainty in the duration of the experiment and the thermophysical properties of the melts is calculated to be ± 10 percent [6].

Figure 6 shows a photograph of cross section of an initially vertical surface of a slab of biphenyl after 3.456 min ($\tau = 0.44$) of exposure to saturated steam. Figure 7 compares this observed shape with that predicted from numerical integration of equation (13) up to $\tau = 0.44$. It is seen that the observed surface profile matches well with the numerical solution. Here it must be mentioned that the surface shapes at longer times could not be obtained experimentally because of difficulties associated with the end effects. The duration of the experiments, however, was such that the times needed for the condensate and the melt films to reach steady-state were much shorter. It has been shown in [4] that the time in which the films will reach their steady-state for the melt-condensate combinations studied in this work is less than 6 s ($\tau < 0.015$). As can be inferred from Fig. 4, hardly any change in the shape of the vertical wall will occur during this time.

During the period the shape of the surface changes, the local and total melting rates also change. The local average melting rate decreases because the newer shapes have less average effective gravity. The total melting rate, however, increases since the newer shapes provide more surface area for melting. To quantify these effects, two average melting rates per unit length and per unit height of the surface are defined as

$$\bar{\dot{m}}_x'' = \frac{\Delta T_l}{h_{sf} L_x} \int_0^{L_x} h_l^0(x)dx \tag{18}$$

$$\bar{\dot{m}}_z'' = \frac{\Delta T_l}{h_{sf} L_z} \int_0^{L_x} h_l^0(x)dx \tag{19}$$

Equation (18) gives the melting rate based on actual surface area while equation (19) represents the melting rate based on the projected area. In equations (18) and (19), h_l^0 is given by equation (2). It must be remembered that during the period the shape changes, L_z remains constant, but L_x continuously increases. Figure 8 shows the dependence of two melting rates on dimensionless time. The melting rates shown in Fig. 8 are normalized with the melting rate for the vertical wall ($\tau = 0$), where

$$\bar{\dot{m}}_x''(\tau=0) = \bar{\dot{m}}_z''(\tau=0) = \frac{4}{3} h_l^0(x = L_x = L_z) \frac{\Delta T_l}{h_{sf}} \tag{20}$$

In equation (20), h_l^0 is given by equation (1). Figure 8 shows that the average melting rate based on actual surface area decreases while the average melting rate based on the projected surface area increases. Thus, as the initially vertical surface acquires its steady-state shape the total melting rate will increase by 35.5 percent. Since the ratio, L_x/L_z, for the steady-state shape is 2, the average melting rate per unit surface area decreases by about 32.2 percent. It is seen from Fig. 8 that the melting rates attain their limiting values asymptotically. A steady-state time, $\tau_{ss} = 3.5$, can be defined based on the melting rate attaining, say, 95 percent of its asymptotic value.

Conclusions

1 The shape of an initially vertical wall undergoing condensation-driven melting changes with time. The steady-state shape is found to be the one that yields constant melting rate everywhere on the wall.

2 The equation describing the transient shapes of the surface can be nondimensionalized such that it is applicable to any combination of materials. Data for the rate of penetration of the melt front into the solid and the shape of the melt front are obtained and found to compare well with the predictions.

3 The local and the average melting rates are found to change during the time the surface goes from the initial to the steady-state shape. The total melting rate for the steady-state shape is about 35 percent more than for the vertical wall.

4 The melting rate is calculated to attain 95 percent of its asymptotic value at a dimensionless time of about 3.5.

References

1 Tien, C., and Yen, Y. C., "Condensation-Melting Heat Transfer," *Chem. Engr. Prog. Symp. Ser.*, Vol. 67, No. 113, 1971, pp. 1-9.

2 Epstein, M., and Cho, D. H., "Laminar Film Condensation on a Vertical Melting Surface," ASME JOURNAL OF HEAT TRANSFER, Vol. 98, 1976, pp. 108-113.

3 Sparrow, E. M., and Gregg, J. L., "A Boundary Layer Treatment of Laminar Film Condensation," ASME JOURNAL OF HEAT TRANSFER, Vol. 81, 1959, pp. 13-18.

4 Taghavi-Tafreshi, K., and Dhir, V. K., "Analytical and Experimental Investigation of Simultaneous Melting-Condensation on a Vertical Wall," ASME JOURNAL OF HEAT TRANSFER, Vol. 104, 1982, pp. 24-33.

5 Contreras, W., and Throsen, R. S., "Transient Melting of a Solid Heated by a Condensing Vapor—Case 1: Negligible Interface Curvature," ASME JOURNAL OF HEAT TRANSFER, Vol. 97, 1975, pp. 570-575.

6 Taghavi-Tafreshi, K., "Condensation of Saturated Vapor on Melting Surfaces," Ph.D. dissertation, UCLA, 1982.

7 Dhir, V. K., and Lienhard, J. H., "Laminar Film Condensation on Plane and Axisymmetric Bodies in Nonuniform Gravity," ASME JOURNAL OF HEAT TRANSFER, Vol. 91, 1971, pp. 97-100.

8 Dhir, V. K., and Lienhard, J. H., "Similar Solutions for Film Condensation with Variable Gravity or Body Shape," ASME JOURNAL OF HEAT TRANSFER, Vol. 95, 1973, pp. 483-486.

9 Hornbeck, R. W., *Numerical Methods*, Quantum Publishers, Inc., New York, 1975.

Effect of Transverse Misalignment on Natural Convection From a Pair of Parallel, Vertically Stacked, Horizontal Cylinders

E. M. Sparrow
Fellow ASME

D. S. Boessneck
Department of Mechanical Engineering,
University of Minnesota,
Minneapolis, Minn. 55455

Experiments were carried out to determine the effects of transverse misalignment on the natural convection heat transfer characteristics of a pair of equitemperature, parallel horizontal cylinders situated one above the other. During the course of the experiments, which were performed in air, the transverse offset was varied systematically at several fixed vertical separation distances, while the Rayleigh number ranged from 2×10^4 to 2×10^5. At small vertical separations, transverse offsetting causes an increase in the upper-cylinder Nusselt number (up to 27 percent) compared with that for the perfectly aligned case (i.e., no offset) and, furthermore, the Nusselt number is responsive to small offsets. On the other hand, at larger vertical separations, the offset-affected upper-cylinder Nusselt number is lower (by up to 20 percent) than the no-offset value but is quite insensitive to small offsets. At large transverse offsets, the upper-cylinder Nusselt number slightly exceeds that for a single cylinder, with the increase being due to a horizontal airflow induced by the acceleration of the lower cylinder's plume. For all of the cases investigated, the lower-cylinder Nusselt number was virtually identical to that for a single cylinder.

Introduction

Natural convection heat transfer from arrays of two or more parallel horizontal cylinders are encountered in numerous applications including, for example, space heating, refrigeration condensers, and oil heaters. In such arrays, there may be cylinder-to-cylinder interactions owing to the buoyant plume that is spawned by each cylinder and which may impinge on other cylinders. It has been demonstrated [1-3] that the impingement may either increase or decrease the heat transfer relative to that for a single horizontal cylinder, depending on the vertical separation distance between the cylinders of the array. In particular, enhancement of the array heat transfer can be achieved by proper positioning of the cylinders relative to each other.

In all of the quantitative studies of arrays of horizontal cylinders that appear in the published literature [1-3], the various cylinders were situated one above each other in a common vertical plane. In practice, however, transverse misalignments may occur so that the plume rising from a lower cylinder will not impinge symmetrically on the cylinder above it. The effects of such transverse misalignments are presently unknown and, in fact, it cannot be said with certainty whether the misalignment will increase or decrease the heat transfer. If it were known that misalignment increases the heat transfer at certain vertical intercylinder separation distances, then intentional misalignment could be employed as an enhancement technqiue.

The experiments described in this paper constitute a systematic study of the effect of transverse misalignment on the heat transfer characteristics of a pair of parallel horizontal cylinders situated one above the other. A schematic side view of the investigated physical situation is pictured at the left in Fig. 1. As seen there, the transverse center-to-center distance (i.e., the transverse offset) is denoted by W, while S denotes the vertical center-to-center distance. Both cylinders have the same diameter, D. The offset will be specified in terms of the W/D ratio, with $W/D = 0$ corresponding to perfect alignment.

The experiments were performed for eight distinct transverse misalignments in the range $0 \leq W/D \leq 3$. In this regard, it should be noted that while the geometrical "overlap" of the cylinders ceases to exist for $W/D > 1$, their fluid flow interactions may persist for larger W/D values. In particular, the plume which rises from the lower cylinder induces a transverse flow toward it from the ambient, and this transverse flow will wash over the upper cylinder even when W/D is considerably greater than one. Also, it is quite conceivable that the plume width might exceed the cylinder diameter, D.

The second geometrical parameter that was varied during the experiments is the dimensionless vertical separation distance, S/D. As documented in [3], S/D plays a key role in the upper-cylinder heat transfer for aligned cylinders, controlling whether the presence of the lower cylinder causes enhancement or degradation. In the present investigation, the interaction between W/D and S/D will be shown to be of great importance and, in fact, the trend of the Nusselt number variation with W/D will be different at different S/D. The experiments were performed for $2 \leq S/D \leq 9$.

For each geometrical configuration defined by W/D and S/D, the Rayleigh number, Ra, based on the cylinder-to-ambient temperature difference and on the cylinder diameter, was varied from 2×10^4 to 2×10^5. For each data run, the surface temperatures of the two cylinders were identical. The aforementioned order of magnitude range in the Rayleigh number was achieved by an order of magnitude variation in the cylinder-to-ambient temperature difference. Since the experiments were performed in air, the Prandtl number was virtually constant (~ 0.7).

The results will be presented in terms of two Nusselt number ratios, each of which conveys a different perspective.

Contributed by the Heat Transfer Division for publication in the JOURNAL OF HEAT TRANSFER. Manuscript received by the Heat Transfer Division. June 25, 1982.

One of these ratios compares the upper-cylinder Nusselt number for $W/D > 0$ to that for $W/D = 0$, at common values of S/D and Ra. This ratio provides a direct measure of the effect of the transverse offset. The second ratio compares the upper-cylinder Nusselt number to that for a single (noninteracting) cylinder operating at the same Rayleigh number. This ratio identifies the effect of the cylinder-to-cylinder interaction on the upper-cylinder heat transfer characteristics.

For completeness, mention may be made of published interferograms of natural convection about three- and four-cylinder clusters in which there is transverse offset [4, 5]. Also, in [6], experiments were reported for arrays of very fine wires oriented at various angles to the vertical. The Grashof number of those experiments was on the order of 10^{-1}, and the minimum interwire spacing was 37.5 diameters.

In [11], the overall natural convection heat transfer from bundles of horizontal tubes was measured, but without consideration of misalignment.

Experimental Apparatus and Procedure

The two cylinders that comprised the key components of the experimental apparatus were fabricated to be identical in all respects. Each cylinder consisted of a thick-walled aluminum sleeve which housed a brass, wire-wound heater core. Aluminum was chosen for the heat transfer surface because, when polished to a mirrorlike finish, it enables the radiative heat loss, which competes with the natural convection, to be maintained at a very low level. Another relevant property of aluminum is its high thermal conductivity which, coupled with the selected wall thickness (0.635 cm), yields a thermal boundary condition that closely approximates uniform wall temperature. The final outside diameter of the cylinder, after completion of the surface finishing operations (hand-lapping and polishing), was 3.787 cm, and its length-diameter ratio, $L/D = 20$, closely approximates an infinite cylinder, especially in view of the precautions used to minimize end effects (to be described shortly).

The heater core was designed to fit snugly within the bore of the aluminum sleeve, and continuous contact at the core-sleeve interface was ensured by application of copper oxide cement prior to assembly. Brass was chosen as the core-tube material because of its relatively high thermal conductivity, easy machinability, and compatibility with aluminum (i.e., nongalling sliding contact). Eight longitudinal grooves were machined into the core-tube surface to accommodate the electrical resistance wire (0.0254-cm dia chromel covered with 0.00762-cm thick Teflon insulation). The wire was wound in series in a back and forth pattern, with the bridging of the wire between longitudinal grooves being accomplished via circumferential grooves adjacent to the ends. The core tube was made slightly shorter than the external sleeve to diminish possible end losses, and its hollow center served as a conduit for the thermocouple lead wires.

Seven thermocouples embedded in the aluminum sleeve were used to measure the cylinder wall temperature. The thermocouple junctions were positioned 0.05 cm from the exposed surface of the cylinder. Three of the thermocouples were situated at midspan (midway between the ends) and were deployed around the circumference. The other four thermocouples were situated along the top of the cylinder at symmetric positions to either side of the midplane, respectively at 17.8 cm and 34.9 cm from it. All thermocouples (including those used to measure the ambient temperature) were made of small diameter (0.0127 cm) iron-constantan wire with a view to minimizing measurement errors associated with lead-wire conduction. The thermocouples had been calibrated prior to their installation.

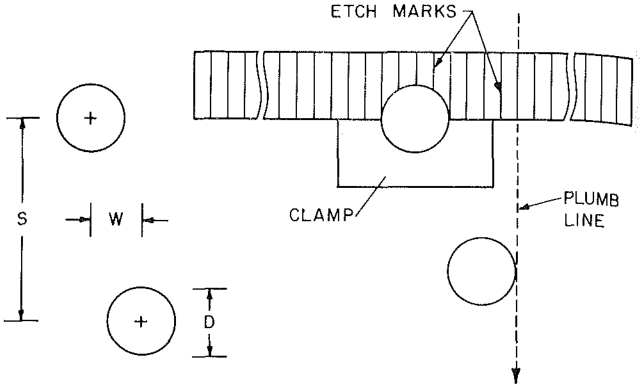

Fig. 1 Two-cylinder array with transverse misalignment (left-hand diagram); method for setting the transverse offset (right-hand diagram)

The cylinders were supported by a frame which facilitated their precise positioning and which, in particular, provided vertical and horizontal adjustment capabilities for setting the vertical separation distance, S, and the horizontal offset, W (Fig. 1, left-hand diagram). The frame was of open construction to avoid interference with the buoyancy-induced airflow about the cylinders, but it possessed strength and stability so that any cylinder positioning, once set, was maintained.

The upper cylinder was stationary with respect to the frame, and its alignment with the horizontal was adjusted by leveling the base plate of the frame. On the other hand, the horizontal and vertical positions of each end of the lower cylinder could be set independently (within bounds). This freedom enabled the lower cylinder to be leveled with the horizontal, to be aligned parallel to the upper cylinder, and to be set at any position consistent with desired values of the separation and offset distances S and W. The minimum distance between the lower cylinder and the floor of the room was 88 cm.

The design of the suport system enabled the vertical center-to-center separation distance, S, to be varied continuously over the range from one to nine diameters, with the value of S being read with an optical cathetometer having a smallest scale division of 0.005 cm (i.e., about 0.1 percent of the cylinder diameter). The transverse offset, W, could also be

Nomenclature

A = surface area of cylinder
D = diameter of cylinder
F = intercylinder angle factor
g = acceleration of gravity
h = average heat transfer coefficient
k = thermal conductivity
Nu = cylinder Nusselt number, hD/k
Nu_o = upper-cylinder Nusselt number for zero offset
Nu* = single cylinder Nusselt number
Pr = Prandtl number
Q = convective heat transfer rate
Q_{rad} = radiative heat transfer rate
Ra = Rayleigh number, $\{g\beta(T_w - T_\infty)D^3/\nu^2\}\mathrm{Pr}$
S = vertical center-to-center separation distance
T_w = cylinder wall temperature
T_∞ = ambient temperature
W = transverse center-to-center offset
β = thermal expansion coefficient
ϵ = emissivity
ν = kinematic viscosity
σ = Stefan-Boltzmann constant

varied continuously between $W/D = 0$ and 4.5, but with the adopted method for setting and quantifying the offset, it was convenient to vary W in discrete intervals, specifically, $\Delta W = \frac{1}{4}D$.

The method for setting the transverse offset will be described with the aid of the main diagram of Fig. 1. The diagram shows a plexiglas alignment fixture clamped in place on the upper cylinder. This is one of three such fixtures that were used in the offsetting procedure – two being positioned adjacent to the respective ends and the third placed at midspan. Before the clamps were secured, each fixture was carefully leveled with respect to the horizontal. As seen in the diagram, vertical etch marks at intervals of $\frac{1}{4}D$ had been machined along the face of the fixture.

With all fixtures in place and leveled, a plumb line was held along the relevant etch mark on one of the fixtures, and the lower cylinder was repositioned until the plumb line hung tangent to it. This process was repeated for the other two fixtures, and checks were made to ensure that tangencies were simultaneously attained at all three fixture positions. Once the offset had been established, the fixtures were removed.

It still remains to describe the brackets by means of which the frame supported the cylinders. These brackets were designed to minimize thermal communication between the cylinders and the frame. Each bracket was a fingerlike plexiglas rod (diameter = 0.953 cm) inserted into the bore of the cylinder at each end. Adjacent to the inserted end of the rod, an up-pointing pyramid-shaped protrusion had been fabricated. The cylinder rested on the tip of the protrusion with point contact. A slight depression in the contacting surface of the cylinder ensured that the cylinder did not "wander" with respect to the support point.

Extraneous transverse fluid flow adjacent to the ends of the cylinders was eliminated by the use of curtainlike side baffles. The baffles were made of rigid 1-cm-thick fiberglass insulation hung in a vertical plane so as to be in contact with the end faces of the aluminum sleeve[1]. Thus, the baffles also served to minimize extraneous conduction from the ends of the cylinders. At any intercylinder separation distance, the baffles extended about 10 cm above the upper cylinder and below the lower cylinder.

The ambient air temperature was sensed by a vertical array of six thermocouples attached to the frame. The thermocouple junctions were positioned so that they could not "see" the surfaces of the cylinders.

A particularly noteworthy feature of the experiments was the laboratory room in which they were performed. The walls, ceiling, and floor of the room are insulated with 46 cm of cork, and there is no ductwork or vents. It is situated in a basement, away from external walls (i.e., a room within a room). The total volume of the room is 70 m^3, and it contains various objects having a large aggregate heat capacity.The combination of the thermal isolation and large heat capacity makes for unusual thermal stability. Futhermore, thermal stratification, even after long data runs, was negligible. To avoid thermal and flow disturbances, all instrumentation and power supplies were situated outside the laboratory, and it was never entered during a data run.

With regard to instrumentation and experimental procedure, various aspects have already been mentioned, and further relevant information will now be conveyed. Electric power was fed to the cylinders by a regulated a-c supply which provided an output that was constant to within 0.1 percent or better. The heater voltage drops and current flows (measured as shunt voltages) were read to four significant figures by a multimeter which also read the thermocouple emf's to within 1 μV.

For each geometrical configuration characterized by W/D and S/D, the Rayleigh number was varied over the range from 20,000 to 200,000 by varying the wall-to-ambient temperature difference, $\Delta T = (T_w - T_\infty)$ from about 4.5°C to 57°C. The sought-for thermal boundary condition for each data run is that the ΔT's for the two cylinders are identical. Owing to the effect of the lower cylinder's plume on the upper cylinder, the attainment of precise ΔT equality was a difficult undertaking which required numerous adjustments of the input power, with appropriate equilibration periods between each setting. When the ΔT's for the two cylinders differed by less than ½ percent, equality was deemed to have been achieved. Typically, about 16 hrs were required to achieve temperature equality at a given Rayleigh number. Data reproducibility was generally in the 1 percent range.

Data Reduction

Nusselt numbers for both the upper and lower cylinders were evaluated from the experimental data, but primary attention will be focused on the upper cylinder results because the lower cylinder Nusselt numbers were found to be virtually identical to those for a single cylinder. The dimensionless groups used in the presentation of the results are the average Nusselt number, Nu, the Rayleigh number, Ra, and the geometrical parameters W/D and S/D, where Nu and Ra are defined as

$$\mathrm{Nu} = hD/k, \quad \mathrm{Ra} = \{g\beta(T_w - T_\infty)D^3/\nu^2\}\mathrm{Pr} \tag{1}$$

The thermophysical properties appearing in these equations were evaluated at the film temperature, $T_f = \frac{1}{2}(T_w + T_\infty)$, aside from β which was set equal to $1/T_\infty$. The density appearing in ν was calculated from the perfect gas law.

Attention will now be directed to the determination of the heat transfer coefficient of either cylinder. From its definition

$$h = Q/A(T_w - T_\infty) \tag{2}$$

With regard to the wall temperature, T_w, the extreme measured circumferential variation was only 0.4 percent of $(T_w - T_\infty)$, and these variations were averaged arithmetically. The extreme axial variation was 3½ percent of $(T_w - T_\infty)$, with the temperature decreasing from the midplane of the cylinder to the ends in a manner that was perfectly symmetric about the midplane. Owing to the symmetry and with x measuring the distance from midspan toward either end of the cylinder, a second-degree polynomial, $T_w(x) = a + bx + cx^2$, was passed through the data at the three axial stations where temperature data were available. This polynomial was then integrated over the length of the cylinder to give an average value for T_w, and this average was used in evaluating equation (2).

For T_∞, the virtual absence of stratification (at most, a few tenths of a percent of $(T_w - T_\infty)$) suggested that an arithmetic average of the readings of the six ambient thermocouples was sufficient.

The convective heat transfer rate, Q, was determined from the electrical power input, with due consideration of possible extraneous losses due to radiation and natural convection. For the radiation analysis, both cylinders were asumed to have the same graybody emissivity, ϵ, equal to 0.05 (highly polished aluminum). The intercylinder angle factor, F, was taken from p. 343 of [7] (configuration 7), with a multiplicative constant of ½ introduced into the right-hand side. This modification is needed because the F of [7] is based on half the cylinder circumference, while the angle factor needed here is based on the entire circumference. The laboratory room closely approximated an isothermal en-

---

[1] In actuality, thick paper rings were placed between the ends of the cylinder and the fiberglass baffles. This eliminated the possibility of the end of the cylinder being embedded in the fiberglass.

closure, so that the radiation incident per unit area on the cylinder(s) due to emission at the walls of the room is σT_∞^4.

With this information as input and noting that the two cylinders were at the same essentially uniform temperature T_w, an analysis based on a diffuse radiation model yielded

$$\frac{Q_{\rm rad}}{A} = \frac{\epsilon\{1-(1-\epsilon)F^2-\epsilon F\}\sigma(T_w^4-T_\infty^4)}{1-(1-\epsilon)^2F^2} \quad (3)$$

The values of $Q_{\rm rad}$ were found to lie in the range of 5-7 percent of the power input and were subtracted off.

Estimates of the possible extraneous heat conduction losses at the ends of the cylinder suggested that these losses were negligible (less than 1 percent of the power input). The size of these losses reflects the measures taken to minimize them – the point-contact support and the insulation curtains that contacted the ends of the cylinders. De facto support for the neglect of the conduction losses will be provided shortly by comparisons of the single cylinder results with those of the literature.

The evaluation of all quantities appearing in equation (2) has now been set forth, so that h may be determined and substituted into the Nusselt number in equation (1). All quantities needed for the Rayleigh number evaluation (equation (1)) have also been discussed.

Results and Discussion

Results for a Single Cylinder. To establish the accuracy level of the present results by comparisons with the literature, supplementary experiments were performed in which only one cylinder was employed. These experiments covered the Rayleigh number range from 2×10^4 to 2×10^5, and the corresponding Nusselt numbers were correlated by

$$\mathrm{Nu}^* = 0.592\mathrm{Ra}^{0.23} \quad (4)$$

with data scatter of 1 to 2 percent. The asterisk is used to identify the single cylinder case.

With regard to the literature, the most prominent correlations for natural convection about a single horizontal cylinder are those of McAdams [8], Churchill and Chu [9], and Morgan [10]. With respect to McAdams, it is interesting to note that the correlation which appears in the third and final edition (1954) of the McAdams monograph is the same (and is based on the same data) as that which appears in the first edition (1932). The data base for the McAdams correlation is quite limited and comes from an era where the available instrumentation was much less accurate than that of the present. In view of this, it was deemed appropriate to consider more modern correlations for comparison with the present results.

Churchill and Chu (1975) used a single algebraic equation to correlate Nusselt number data which span a Rayleigh number range of 10^{15}. Whereas such a wide-ranging correlation offers great convenience, it tends toward a moderate sacrifice of accuracy. In particular, in the Rayleigh number range of the present experiments, the Churchill-Chu correlation falls below the data on which it is based.

The most comprehensive survey of the available single-cylinder data is that of Morgan (1975). In contrast to Churchill and Chu, he chose to employ five distinct algebraic relations to respectively correlate the Nusselt numbers in various ranges of the Rayleigh number, thereby achieving greater fidelity with the data. For this reason, it is believed that the Morgan correlation is the best available representation of the literature. In the Rayleigh number range of the present data, 2×10^4 to 2×10^5, Morgan gives

$$\mathrm{Nu}^* = 0.480\mathrm{Ra}^{1/4} \quad (5)$$

A comparison of equations (4) and (5) between $\mathrm{Ra} = 2 \times 10^4$ and 2×10^5 shows a maximum deviation of 3.3 percent.

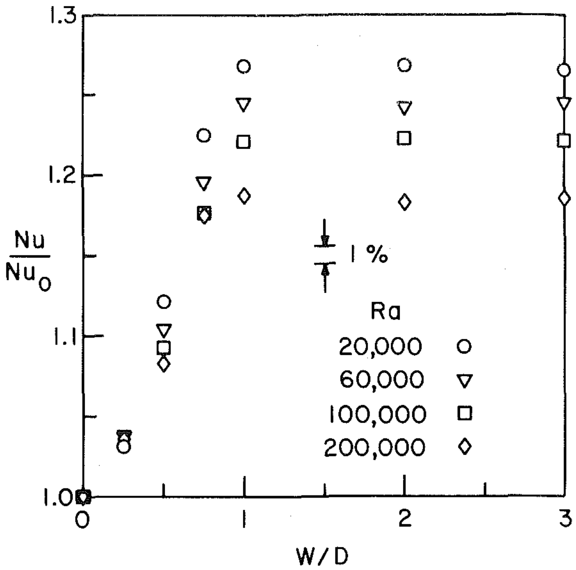

Fig. 2 Comparison of the upper-cylinder Nusselt number in the presence of transverse misalignment to that for the perfectly aligned case, $S/D = 2$

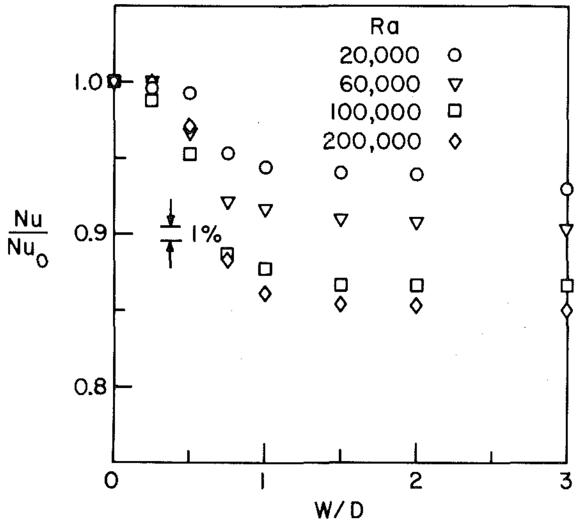

Fig. 3 Comparison of the upper-cylinder Nusselt number in the presence of transverse misalignment to that for the perfectly aligned case, $S/D = 5$

This remarkable level of agreement provides a strong affirmation of the present experimental technique and supports the contention of negligible conduction losses.

Effect of Transverse Misalignment. As noted in the Introduction, the results for the two-cylinder configuration will be presented in two distinct formats aimed at providing different perspectives. In both formats, attention will be focused on the upper-cylinder Nusselt number since, for the investigated operating conditions, the lower-cylinder Nusselt number is equal to that for the single cylinder.

The first presentation format is structured to highlight the effect of the transverse misalignment. To this end, the upper-cylinder Nusselt number, Nu, in the presence of misalignment is ratioed with the Nusselt number, Nu_o, corresponding to a perfectly aligned upper cylinder ($W/D = 0$). In the ratio, both Nu and Nu_o correspond to the same vertical center-to-center separation distance and to the same Rayleigh number. Thus, departures of $\mathrm{Nu}/\mathrm{Nu}_o$ from unity provide an immediate indication of the effect of the transverse misalignment.

The $\mathrm{Nu}/\mathrm{Nu}_o$ results are plotted as a function of the

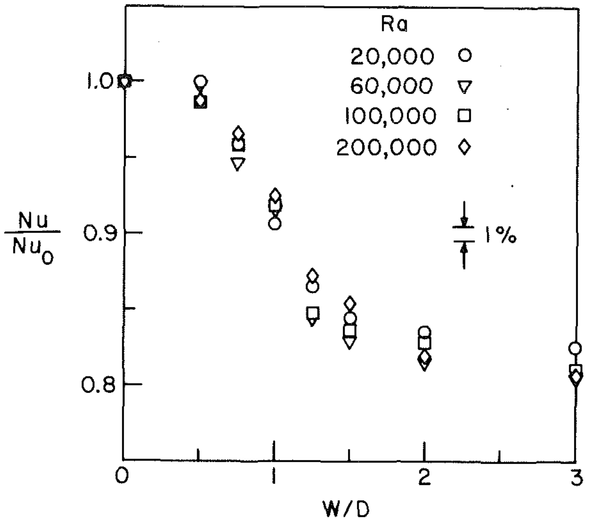

Fig. 4 Comparison of the upper-cylinder Nusselt number in the presence of transverse misalignment to that for the perfectly aligned case, $S/D = 9$

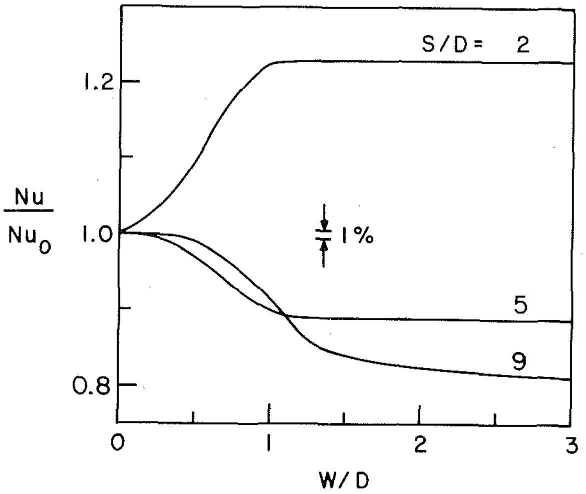

Fig. 5 Rayleigh-number-averaged Nu/Nu_0 ratios for $S/D = 2, 5$, and 9

(dimensionless) transverse offset in Figs. 2-4 over the range from $W/D = 0$ to 3. Each figure pertains to a specific vertical separation distance, S/D, respectively equal to 2, 5, and 9. In each figure, results are presented for four Rayleigh numbers, namely, $Ra = 2 \times 10^4$, 6×10^4, 10^5, and 2×10^5, as identified by the different data symbols. Furthermore, in each figure, a vertical band corresponding to a 1 percent variation in Nu/Nu_0 is identified in order to emphasize the small scatter of the data (~ 1 percent).

Examination of Fig. 2 shows that at a small vertical separation distance, such as $S/D = 2$, transverse offsetting causes an increase in the Nusselt number compared with that for the perfectly aligned case. The offsetting can give rise to a significant enhancement, the extent of which increases as the Rayleigh number decreases. At the lowest of the investigated Rayleigh numbers, enhancements as large as 27 percent are in evidence.

In contrast to the foregoing, a remarkable reversal in trend occurs as S/D increases, as can be seen from Figs. 3 and 4. At the S/D of these figures (5 and 9, respectively), transverse offsetting causes a decrease in the Nusselt number relative to that for zero offset. Overall, the decrease is greater at the largest vertical separation (17½-20 percent) than at the intermediate vertical separation (7½-15 percent).

The occurrence of offset-related enhancement at small S/D and degradation at larger S/D will now be rationalized, after which other characteristics in evidence in Figs. 2-4 will be identified and discussed. With regard to the enhancement/degradation issue, it is relevant first to examine the no-offset case and its Nusselt number, Nu_o. As will be documented shortly and as shown in the literature (e.g., [3]), Nu_o is lower than the corresponding Nusselt number for a single cylinder when S/D is small (e.g., when $S/D = 2$). That is, for small S/D, the head-on impingement of the lower cylinder's plume diminishes the upper cylinder heat transfer. When the upper cylinder is given a transverse offset, the effect of the impingement is lessened, and the heat transfer coefficient increases.

In contrast to the foregoing, the Nu_o values for $S/D = 5$ and 9 exceed those for the single cylinder, indicating that the head-on impingement of the lower cylinder's plume is beneficial for the upper cylinder heat transfer. Consequently, when the impingement is lessened or eliminated by transverse offsetting, the upper-cylinder heat transfer coefficient diminishes. It is also worthy of note that Nu_o for $S/D = 9$ is greater than that for $S/D = 5$. Consequently, when the enhancement due to head-on impingement is eliminated by the transverse offsetting, the extent of the Nusselt number decrease is greater for $S/D = 9$ than for $S/D = 5$.

The behavior of Nu_o with S/D, which forms the basis of the foregoing discussion, can be made plausible by noting that the rising plume from the lower cylinder presents the upper cylinder with a preheated, quasi-forced-convection flow. The elevated temperatures of the fluid in the impinging plume tend to diminish the upper-cylinder heat transfer, while the finite velocity of the approach flow tends to increase the heat transfer. At small vertical separation distances, the preheating is the stronger of the two effects, giving rise to a decrease in the upper-cylinder heat transfer. On the other hand, the approach-velocity effect dominates at larger separation distances, and the heat transfer is enhanced.

Returning now to Figs. 2-4, attention will be focused on the *specifics* of the Nusselt number variation with transverse offset. At the smallest vertical separation (Fig. 2), Nu is responsive even to small offsets and, in fact, most of the offset-related changes occur for $W/D \leq 0.75$. For $W/D \geq 1$, further offsetting has no effect on the Nusselt number. This behavior is reflective of the narrowness of the plume that impinges on the upper cylinder. In particular, it suggests that if the upper cylinder is positioned so that $W/D \geq 1$, it lies outside the plume of the lower cylinder.

With increasing vertical separation, the variation of the Nusselt number with W/D reflects a broadening of the impinging plume. For $S/D = 5$ and moreso for $S/D = 9$, the Nusselt number is not very responsive to small offsets. Most of the offset-related effects for $S/D = 5$ occur for $W/D \leq 1$, and the Nusselt number is independent of further offsetting when $W/D \geq 1.5$. In contrast, for $S/D = 9$, significant variations of Nu/Nu_o with W/D continue to occur for $W/D \geq 1$ and, in fact, small but noticeable variations persist to the largest of the investigated offsets, $W/D = 3$.

The Nu/Nu_o ratio is little affected by the Rayleigh number at the largest of the investigated vertical separations ($S/D = 9$), while at the other separation distances ($S/D = 2$ and 5) there is a noticeable dependence on Rayleigh number. For both of the latter S/D, the Nu/Nu_o values are arranged in a regular pattern with Rayleigh number, with larger Nu/Nu_o corresponding to lower Rayleigh numbers. The largest overall spread in Nu/Nu_o with Ra is about 0.09, and this spread is uniform for $W/D \geq 1$.

With a view toward attaining a concise comparison of the results for the various vertical separations, the Nu/Nu_o values in each of Figs. 2-4 were averaged over the Rayleigh number. The resulting Nu/Nu_o versus W/D distributions are plotted

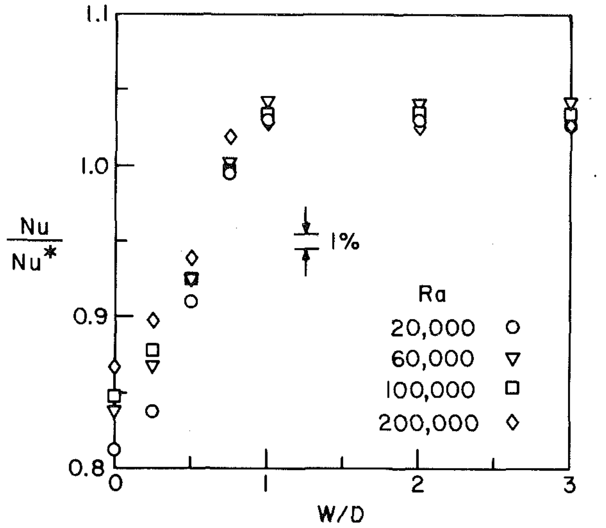

Fig. 6 Comparison of the upper-cylinder Nusselt number with that for a single cylinder, *S/D* = 2

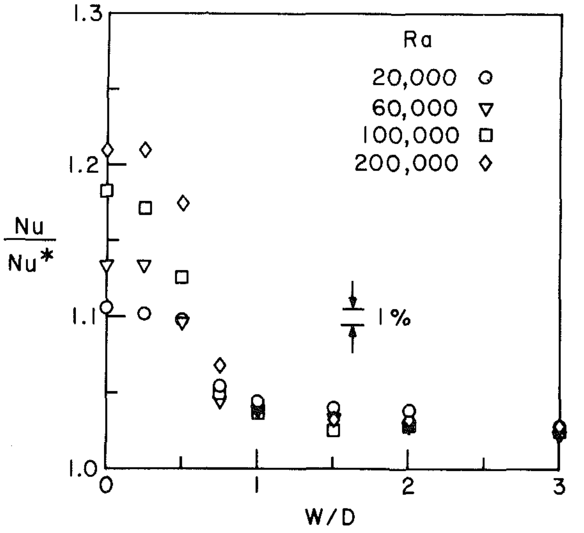

Fig. 7 Comparison of the upper-cylinder Nusselt number with that for a single cylinder, *S/D* = 5

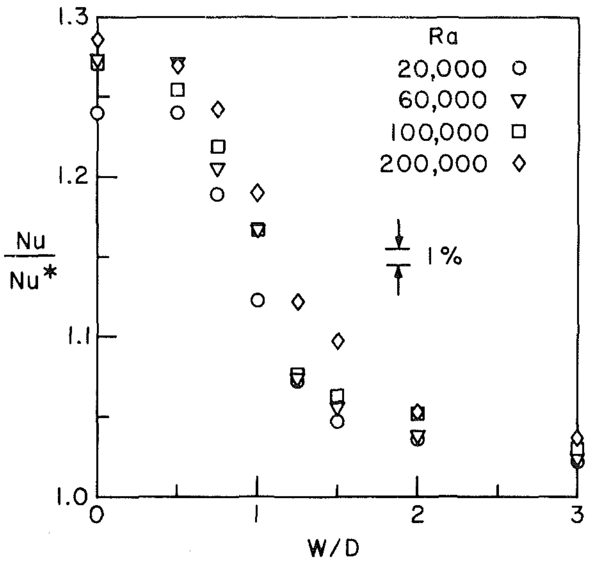

Fig. 8 Comparison of the upper-cylinder Nusselt number with that for a single cylinder, *S/D* = 9

in Fig. 5 with *S/D* as curve parameter. This figure reaffirms the importance of *S/D* in determining whether offsetting enhances or degrades the Nusselt number relative to its no-offset value. Also, the sensitivity of the Nusselt number to small offsets is seen to diminish with increasing *S/D* while, concurrently, the Nusselt number becomes more responsive to larger offsets.

Effect of Intercylinder Interactions. The upper-cylinder Nusselt numbers will now be compared with the Nusselt numbers, Nu*, for a single cylinder. For this purpose, the results will be presented in terms of the ratio Nu/Nu*, where Nu and Nu* correspond to the same Rayleigh number. Departures of Nu/Nu* from unity indicate the enhancement or degradation of the heat transfer coefficient at the upper cylinder which results from interactions with the plume that is spawned by the lower cylinder.

The Nu/Nu* results are presented in Figs. 6–8, where they are plotted as a function of the transverse offset for parametric values of the Rayleigh number. The successive figures correspond respectively to vertical separation distances *S/D* of 2, 5, and 9.

Attention is first directed to the smallest vertical separation (Fig. 6). For this case, it is seen that $Nu/Nu^* < 1$ for zero offset, thereby verifying an assertion made in the last section of the paper. The Nusselt number increases rapidly with increasing offset, with the result that $Nu \simeq Nu^*$ when $W/D = 0.75$. For larger offsets, Nu/Nu* takes on a constant value equal to 1.03 – 1.04. The fact that Nu differs from Nu* for large offsets is, at first thought, somewhat surprising. Indeed, it might be expected that the upper cylinder, when positioned well to the side of the lower cylinder's plume, would behave like a single cylinder. The rationalization of the measured behavior of Nu/Nu* for large offsets will be discussed shortly, after the results for the other *S/D* are presented.

The Nu/Nu* data for $S/D = 5$ are plotted in Fig. 7. Here, the Nusselt number for the zero-offset case is enhanced relative to that for the single cylinder. Although the overall effect of offsetting the upper cylinder is to decrease the Nusselt number, the heat transfer processes appear to be quite forgiving of small offsets such as $W/D = 0.25$. The major decrease in Nu due to offsetting occurs between $W/D = 0.25$ and 0.75. For offsets for which $W/D \geq 1.5$, $Nu/Nu^* \simeq$ constant $\simeq 1.03$. Thus, as was also true for the $S/D = 2$ case, the large-offset Nusselt numbers are slightly greater than those for the single cylinder.

For $S/D = 9$ (Fig. 8), there is appreciable enhancement of the zero-offset Nusselt numbers. Furthermore, the upper-cylinder heat transfer processes are quite forgiving of moderate offsets, as witnessed by the fact that Nu/Nu* is essentially constant over the range $0 \leq W/D \leq 0.5$. For greater offsets, Nu/Nu* decreases, with the most rapid decrease taking place in the range between $W/D = 0.5$ and 2.0, whereafter there is a slow tailing off. At $W/D = 3$, the largest offset investigated, $Nu/Nu^* \simeq 1.03$, which is consonant with the results for the other *S/D* cases.

It remains to rationalize the finding that the upper-cylinder Nusselt numbers corresponding to large transverse offsets are slightly greater than those for the single cylinder. In this regard, it is relevant to consider the pattern of fluid flow associated with a rising plume. The plume, which accelerates as it moves upward, draws additional fluid to it from the ambient, with the streamlines being essentially horizontal. Such a horizontal flow is created by the plume spawned by the lower cylinder. This flow washes over the upper cylinder when it is situated to the side of the lower cylinder's plume. Thus, under these conditions, the upper cylinder experiences what is, in effect, a horizontal forced convection flow that is super-

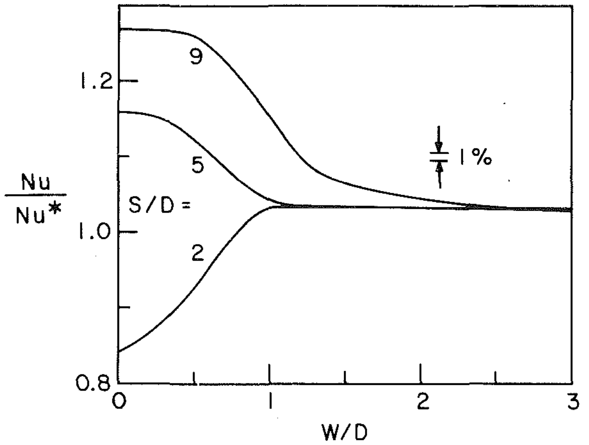

Fig. 9 Rayleigh-number-averaged Nu/Nu* ratios for $S/D = 2, 5,$ and 9

posed on its self-induced buoyant flow. The resulting mixed convection flow gives rise to a small enhancement of the heat transfer coefficient compared to that of the single cylinder.

The effect of the Rayleigh number on the Nu/Nu* results of Figs. 6-8 will now be discussed. For all cases, at those offsets where there is a significant spread of the data with Rayleigh number, Nu/Nu* increases with increasing Rayleigh number. In general, the Rayleigh number dependence is significant only in the range between $W/D = 0$ and 0.5 for $S/D = 2$ and 5, and between $W/D = 0$ and 1.5 for $S/D = 9$. For larger offsets, the data are virtually independent of Rayleigh number.

The Nu/Nu* data of Figs. 6-8 were averaged with respect to Rayleigh number and are brought together in Fig. 9 to provide a concise presentation and to highlight the effects of vertical spacing. The transition from degraded to enhanced upper-cylinder heat transfer with increasing vertical separation is clearly in evidence. Offsetting tends to moderate both the enhancement and the degradation, so that the results for the various S/D blend together to a common value, Nu/Nu* $\simeq$ 1.03 at sufficiently large offsets. Because of the broadening of the lower cylinder's plume as its length increases, the interaction of the upper cylinder with the plume extends to larger offsets as S/D increases.

Concluding Remarks

The experiments performed here constitute a systematic study of the effect of transverse misalignment on the heat transfer characteristics of a pair of equitemperature, parallel horizontal cylinders situated one above the other. The heat transfer coefficients at the lower cylinder were found to be virtually identical to those for a single cylinder, so that primary attention is focused on the upper-cylinder heat transfer results.

The upper-cylinder Nusselt numbers corresponding to a range of transverse offsets were compared with that for no offset (i.e., perfectly aligned upper and lower cylinders), with the Rayleigh number, Ra, and the vertical intercylinder separation, S, fixed for the comparison. At the smallest separation distance ($S = 2D$), transverse offsetting causes an increase in the Nusselt number (up to 27 percnet). On the other hand, at larger vertical separations ($S = 5D$ and $9D$), the offsetting decreases the Nusselt number (up to 20 percent).

The Nusselt number is responsive to small offsets when the vertical separation is small but does not respond to further offsetting when the offset exceeds the cylinder diameter. At larger separations, the heat transfer is hardly affected by small offsets but becomes more responsive to larger offsets. These characteristics reflect the broadening of the plume spawned by the lower cylinder as the plume length increases.

The ratio of the Nusselt numbers with and without offset tends to be larger at lower Rayleigh numbers than at higher Rayleigh numbers.

The upper-cylinder Nusselt numbers were also compared with those for a single cylinder. At small vertical separations, the intercylinder interactions degrade the upper-cylinder heat transfer coefficient relative to the single-cylinder value, while the interactions cause enhancement at larger separations. Offsetting tends to moderate both this enhancement and degradation. At large offsets, the upper-cylinder Nusselt number slightly exceeds that for the single cylinder (by about three percent), the increase being due to a horizontal airflow induced by the acceleration of the lower cylinder's plume.

References

1 Marsters, G. F., "Array of Heated Horizontal Cylinders in Natural Convection," *International Journal of Heat and Mass Transfer*, Vol. 15, 1972, pp. 921-933.

2 Smith, A. F. J., and Wragg, A. A., "An Electrochemical Study of Mass Transfer in Free Convection at Vertical Arrays of Horizontal Cylinders," *Journal of Applied Electrochemistry*, Vol. 4, 1974, pp. 219-228.

3 Sparrow, E. M., and Niethammer, J. E., "Effect of Vertical Separation Distance and Cylinder-to-Cylinder Temperature Imbalance on Natural Convection for a Pair of Horizontal Cylinders," ASME JOURNAL OF HEAT TRANSFER, Vol. 103, 1981, pp., 638-644.

4 Eckert, E. R. G., and Soehngen, E. E., "Studies on Heat Transfer in Laminar Free Convection With Zehnder-Mach Interferometer," AF Technical Report 5747, United States Air Force, Air Material Command, Wright-Patterson Air Force Base, Ohio, 1948.

5 Holman, J. P., *Heat Transfer*, 5th ed., McGraw-Hill, New York, 1981, p. 273.

6 Lieberman, J., and Gebhart, B., "Interactions in Natural Convection From an Array of Heated Elements, Experimental," *International Journal of Heat and Mass Transfer*, Vol. 12, 1969, pp. 1385-1396.

7 Sparrow, E. M., and Cess, R. D., *Radiation Heat Transfer*, Hemisphere Publishing Corporation, Washington, D.C., 1978.

8 McAdams, W. H., *Heat Transmission*, 3d ed., McGraw-Hill, New York, 1954.

9 Churchill, S. W., and Chu, H. H. S., "Correlating Equations for Laminar and Turbulent Free Convection From a Horizontal Cylinder," *International Journal of Heat and Mass Transfer*, Vol. 18, 1975, pp. 1049-1053.

10 Morgan, V. T., "The Overall Convective Heat Transfer from Smooth Circular Cylinders," in *Advances in Heat Transfer*, Vol. 11, Academic Press, New York, 1975, pp. 199-264.

11 Tillman, E. S., "Natural Convection Heat Transfer from Horizontal Tube Bundles," ASME paper 76-HT-36, 1976.

An Experimental Study of Plane Plumes in Cold Water

Y. Joshi

B. Gebhart
Fellow ASME

Department of Mechanical Engineering
and Applied Mechanics,
University of Pennsylvania,
Philadelphia, Pa. 19104

The peculiar density variation of water with temperature makes the Boussinesq approximations invalid in the vicinity of density extremum conditions. The buoyancy force reversals which often arise from the density extremum have been studied in many recent investigations. The formulation of an accurate density relation has resulted in a simplified analysis for many convective motions. Two such analyses have dealt with the flow generated above a heated line source in cold water, around the extremum point. We present an experimental investigation of such flow. Temperature measurements have been carried out for ambient temperatures, $t_\infty \geq t_m$, the temperature of density extremum, for pure water at atmospheric pressure. These measurements are in satisfactory agreement with the analyses. As the ambient temperature is successively increased above the density extremum temperature, the transformation of the flow behaviour from non-Boussinesq to Boussinesq is very clearly observed. Velocity measurements have been made at $t_\infty = 4°C$, the extremum temperature. For $t_\infty < t_m$, very complex flow patterns exist, due to the bidirectional buoyancy force. These patterns have been visualized. The influence of a bounding impermeable surface below the plume source has also been examined.

Introduction

Steady-state natural convection plane or line plumes have been investigated experimentally quite extensively. Most measurements, however, have been made in air, at Prandtl numbers of around 0.7. The theoretical framework for all such studies has been based on the Boussinesq approximations. A summary of laminar measurements is provided in Schorr and Gebhart [1], which also summarizes interferometric plume measurements in a silicone oil. This oil was used to ensure very high electrical resistivity, to avoid power leakage from the electrically heated wire. It also resulted in high accuracy measurements, since a large number of interferometer fringes result in liquids. The Prandtl number was about 6.7. The measurements showed a uniform 15 percent deficiency in the centerline temperature measurements, compared to boundary layer calculations. This is in agreement with earlier results in air.

More recently Fujii et al. [2] have made measurements in air, water and spindle oil. The results in air show a similar discrepancy of about 15 percent. However, for water and spindle oil, centerline temperatures were found in good agreement with calculations, for flux Grashof numbers in the range 10^3 to 10^6.

The measurements of Lyakhov [3] indicated that the measured centerline temperatures in air are increased to about 2.4 percent above calculated values by bounding the space below the line source with an impermeable plate. Lyakhov noted that this is more consistent with the laminar boundary layer approximation, which does not anticipate the induction of flow upward from below the level of the energy source.

Buoyancy induced plume flows in water abound in nature and in man made devices. Such flows are of interest in heat rejection from power plants and other industrial systems into water bodies, such as lakes and cooling ponds. They are also important in heat transfer from heated bodies in enclosures and in energy storage as sensible heat in a fluid such as water. Often the water is at low temperature, around that of the density extremum denoted later as t_m. In analyzing such buoyancy-induced flows, the Boussinesq approximation becomes invalid.

Gebhart and Mollendorf [4] developed an accurate and convenient density relationship for pure and saline water around density extrema conditions. This relationship makes the formulation of natural convection flows in cold water very convenient. In a follow-up paper [5], many circumstances were identified in which the boundary layer equations reduced to the self-similar form. Particular solutions were obtained for vertical isothermal surfaces at temperature, t_0, for various values of the parameters R and Pr, where $R = (t_m - t_\infty)/(t_0 - t_\infty)$ and Pr is the Prandtl number.

Mollendorf, Johnson, and Gebhart [6] have presented similar solutions for plane and axisymmetric plumes in cold water. The condition necessary for similarity is that the ambient medium be at the temperature of the density extremum, i.e., $R = 0$. Results were presented for a range of Prandtl numbers from 8.6 to 13.6.

Gebhart, Carey, and Mollendorf [7] developed a perturbation analysis, to extend the range of the calculations beyond the similarity limitations in [5]. Calculations were made for plane line and wall plumes and for a uniform flux surface for $R \neq 0$ but small. A perturbation parameter $R^* = (t_m - t_\infty)/(t_0 - t_\infty)_o$ was defined. Here $(t_0 - t_\infty)_o$ is the value of $(t_0 - t_\infty)$ for the similarity formulation obtained in [6]. The temperature and velocity functions were expanded in terms of this parameter. Sets of self similar equations were obtained for the zeroth order functions and first-order corrections. Solutions were obtained in Prandtl number range of 8.6 to 13.6.

The present study deals with an experimental investigation of plane plumes in cold water, at ambient temperatures, t_∞, around the density extremum temperature. A horizontal, electrically heated, teflon-coated chromel wire generated the plumes. Temperature maxima were measured across the resulting plume, at various downstream distances, x, above the source, with a .0127-cm copper-constantan thermocouple probe. The flow was visualized and flow velocities were determined from time exposure photographs of suspended particles in the water. These temperature and velocity measurements were compared to the similarity boundary layer solution for $t_\infty = t_m$, i.e., for $R = 0$. For $t_\infty > t_m, R^* \neq 0$, the comparison has been with the calculations in [7]. The influence of bounding the space below the wire with an im-

---

Contributed by the Heat Transfer Division for publication in the JOURNAL OF HEAT TRANSFER. Manuscript received by the Heat Transfer Division November 18, 1981.

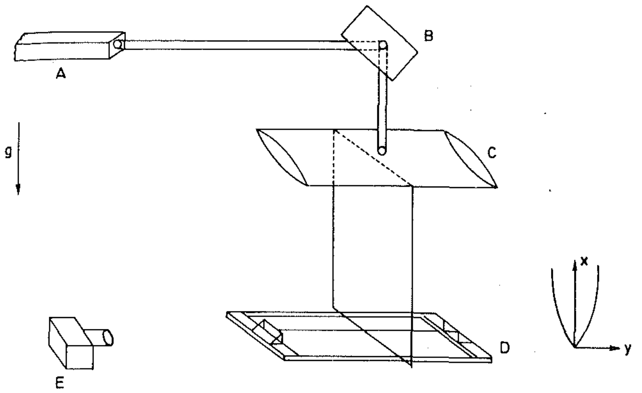

Fig. 1 Schematic sketch of the optical arrangement and the plume coordinate system: (*A*) laser source; (*B*) first surface plane mirror; (*C*) cylindrical lens; (*D*) wire holder assembly; (*E*) camera. After passing through *C* the beam emerges parallel to the *x*-*y*-plane.

permeable surface was also determined. The transition of the flow toward the Boussinesq condition, at high t_∞, has also been investigated.

Apparatus and Experimentation

The energy source used in this experiment was formed on the wire holder pictured by Lieberman [8]. The assembly had five wires. However, only one of them, the center wire, was heated in this study. The distance between the extreme wires, used as the reference length, was 5.6 cm. The stretched length of the wires across the holder was 42.0 cm. The energy source was Omega TFCY-010, teflon-insulated chromel wire of .0254-cm dia with a uniform .00762 cm coating of teflon. That is, $D=$ .0406 cm and $L/D=1034$. Chromel was chosen for its high electrical resistivity. The thin teflon coating prevented the wire from coming directly in contact with the water. This reduced the electrical power leakage directly to the water. The wire holder had been so designed that any slack in the wire due to the heating was taken up by elastic brass supports, keeping it taut.

The experiment was carried out in an insulated glass tank of dimensions 86-cm depth, 69-cm length, and 66-cm width. The insulation limited the bulk temperature rise of the 320 L of tank water to 1-2°C per day, under even the coldest test temperatures. The flow was visualized by removing part of the insulation on one of the tank walls. The tank water was deionized and demineralized to further reduce electrical leakage.

A 15 milliwatt helium-neon laser was used for visualization. The horizontal beam of light was spread into a vertical plane of light about 3-mm thick and 6-cm high, perpendicular to the axis of the wire, using a plane mirror and a cylinder lens (see Fig. 1). This method was used by Carey et al. [9] for flow visualization studies during ice melting.

Time exposure photographs of the flow were taken using a motor-driven 35-mm Nikon camera controlled by a Nikon intervalometer. The exposure was controlled to an accuracy of ±.05 s. Photographs were taken on Kodak Tri-x-Pan 400 film.

To visualize the flow, .75 g of pliolite, ground to 40 μ particle size, was added to the water. Pliolite is a solid white resin used in coatings and adhesives. It is virtually insoluble in water and has a specific gravity of 1.026. The small particles remain suspended in water for a very long time. They scatter the laser light and are thereby made visible.

Prior to each run, the ambient water temperature was reduced to the desired level, t_∞, using a circulating chiller. The water was simultaneously stirred by a motor driven stirrer to avoid nonuniformities in temperature. After removing the chiller and the stirrer, the tank was allowed to stand for 30 min to let viscous interaction damp out the circulation remaining from stirring.

The wire holder assembly had three levelling screws which were adjusted to make the wire horizontal. The electric circuit consisted of a Nobatron MR-36-30 d-c regulated power supply, connected in series to a precision .1 Ω resistor, a rheostat, and the test wire. The voltage drop across the resistor indicated circuit current. The voltage drop across the test wire was measured using a digital voltmeter.

The temperature measurements downstream, in the x-direction, were made with a 0.0127-cm copper constantan thermocouple probe. A traverse mechanism was used to move the thermocouple probe in each of the three coordinate directions, to an accuracy of .0254 cm. This assembly was rigidly connected to the tank top. The horizontal alignment of the base of the traverse mechanism was checked using a spirit level. By rotating the wireholder assembly properly in the horizontal plane, it was ensured that the movement of the probe along the axis of the wire was truly parallel to the wire.

Thermocouple output was read from a Hewlett-Packard digital voltmeter. An ice reference junction was used. To check the temperature of the ice water bath, a precise mercury thermometer was inserted inside the bath. This thermometer had the measurement range of +1°C to −1°C. The temperature of ice was always within the range 0 ± .03°C.

Results and Discussion

Temperature Measurements for $t_\infty = t_m$, i.e., $R = 0 = R^*$.

Nomenclature

c_p = specific heat of fluid
d = $(t_0 - t_\infty)$ for the similarity solution, $= Nx^{-3(q+4)}$
D = diameter of the line source including the insulation
f = nondimensional stream function, $= \psi(x,y) / \left[4\nu \left(\frac{\mathrm{Gr}_x}{4} \right)^{1/4} \right]$
g = acceleration due to gravity
Gr_x = Grashof number, $= \frac{gx^3}{\nu^2} \alpha d^q I_w$
I_p = integrated convected energy parameter $= \int_0^\infty \phi f' \, d\eta$
I_w = integrated buoyancy force parameter $= \int_0^\infty w \, d\eta$
Δl = measured length of streak
L = length of the line source
N = constant in equation (1), $= \left[\frac{Q^4}{4^3 g \alpha c_p{}^4 \mu^2 \rho^2 I_p{}^4 I_w} \right]^{1/(q+4)}$
Pr = Prandtl number of fluid
q = exponent in the density equation for cold water, 1.894816 for pure water at 1 bar
Q = half of the energy input to the line source at $x=0$, per unit length of the source
R = $\frac{(t_m - t_\infty)}{(t_0 - t_\infty)}$
R^* = $\frac{(t_m - t_\infty)}{(t_0 - t_\infty)_o}$
t = temperature
Δt = maximum temperature difference across the plume at a given x, $= (t_0 - t_\infty)$

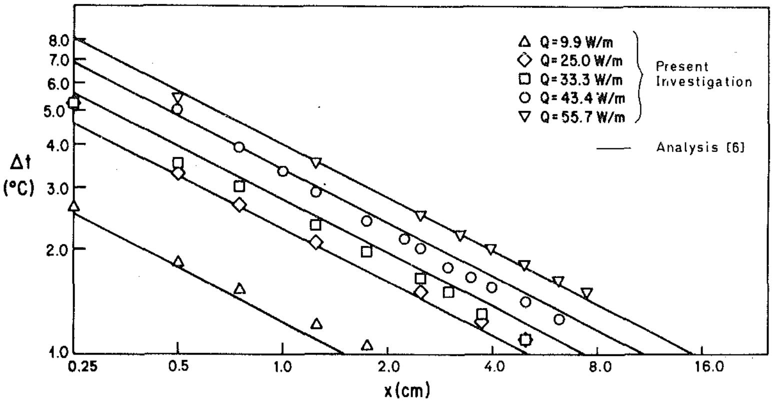

Fig. 2 Comparison of centerline temperature data variation at $t_\infty = 4.0°C$ with the similarity solution of Mollendorf et al. [6]

The local temperature maxima, $t_0(x)$, at many levels of x were measured, for $t_\infty = 4.0°C$. The data points, as $(t_0 - t_\infty)$, for five input levels, Q, are plotted in Fig. 2. The lines are the variations resulting from the similarity solution [6], which for $R=0$, yields

$$(t_0 - t_\infty) \equiv d(x) = Nx^{-3/(q+4)} \tag{1}$$

In equation (1), N is a constant which depends on the fluid properties and the strength of the line energy source, and q depends on the salinity and the pressure level of the fluid. We note that the centerline temperature decay is proportional to $x^{-3/5}$ in the similarity solution of laminar plume flows, when Boussinesq approximations are employed. $q=1$ in equation (1) corresponds to this situation. For cold pure water at 1 bar, $q=1.894816$.

All the experimental points in Fig. 2 are seen to be within 10 percent of the predicted variation using (1). The slopes n of linear least square fit lines through the data, for each Q, listed in Table 1, are very close to the theoretical value of $n = -0.5089$. The average value is $n = -0.50$.

The temperature difference, $t_0 - t_\infty$, from equation (1), is rewritten in the nondimensional form as

$$T = [(t_0 - t_\infty)/Q](4^{3/4} \mu c_p I_p) = \mathrm{Gr}_x^{-1/4} \tag{2}$$

The data is then collectively compared with the similarity solution, in Fig. 3. Again, the agreement is good.

Figure 4 is a comparison of additional data with the calculations, in terms of T, when the space below the heat source is bounded by an impermeable horizontal surface. The surface was approximately 1.4 cm below the wire. These measurements show a systematic difference from those in Fig. 3. They are consistently higher than the theory line, although they follow the predicted slope.

Table 1 The slopes of linear least square fit lines through experimental points for various Q

Q(W/m)	9.9	25.0	33.3	43.4	55.7
$-n$	.46	.50	.51	.55	.48

In comparing the data with the theoretical temperature decay, as given in (1), fluid properties have been determined at t_∞. If the properties are evaluated instead at t_0, a 3 percent difference results in calculated values of $(t_0 - t_\infty)$. This small change in the calculated lines results from off-setting effects in the expression for N in (1). N has been obtained in [6] as

$$N = \left[\frac{Q^4}{4^3 g \alpha c_p{}^4 \mu^2 \rho^2 I_p{}^4 I_w} \right]^{1/(q+4)} \tag{3}$$

A decrease in μ is compensated by an increase in I_p and I_w, due to a lower Pr at higher temperature. The variations in ρ and c_p are negligible in comparison. However, this tendency may not be taken as a general justification for using a constant property analysis. If μ and Pr vary significantly over the flow field, the constant property analysis will require correction. Carey et al. [10] examined the effects of variable viscosity on plume centerline temperatures for Boussinesq flows. It was found that, for water, the variable viscosity would tend to increase the centerline temperature, over that found by the constant property analysis. Near the source where the value of $(t_0 - t_\infty)$ is large, this correction may be quite significant.

Applied here, this tendency would result in shifting the

Nomenclature (cont.)

u = velocity component parallel to the x-direction, $= \partial\psi/\partial y$
v = velocity component parallel to the y-direction, $= -\partial\psi/\partial x$
w = buoyancy force parameter $= [|\phi - R|^q - |R|^q]$
x = coordinate in the vertical direction
y = coordinate in the horizontal direction

Greek Symbols

ρ = density
α = parameter in the density equation, 9.297173E-06(°C)$^{-q}$ for pure cold water at 1 bar
ϕ = nondimensional temperature variable, $= \dfrac{(t - t_\infty)}{(t_0 - t_\infty)}$
ψ = stream function
η = nondimensional horizontal coordinate, $= \left(\dfrac{y}{x}\right)\left(\dfrac{\mathrm{Gr}_x}{4}\right)^{1/4}$
ν = kinematic viscosity
μ = dynamic viscosity
θ = angle of inclination of the streak from the $+x$-axis
$\Delta\tau$ = exposure time of photograph
β = coefficient of thermal expansion of the fluid, $-\dfrac{1}{\rho}\left(\dfrac{\partial\rho}{\partial t}\right)_p$

Subscripts

∞ = value in the ambient
m = value at the point of density extremum
x = local value at a given x
0 = value at $y=0$
0 = value of quantity for the condition of $t_\infty = t_m$
1 = first order correction $t_\infty \neq t_m$

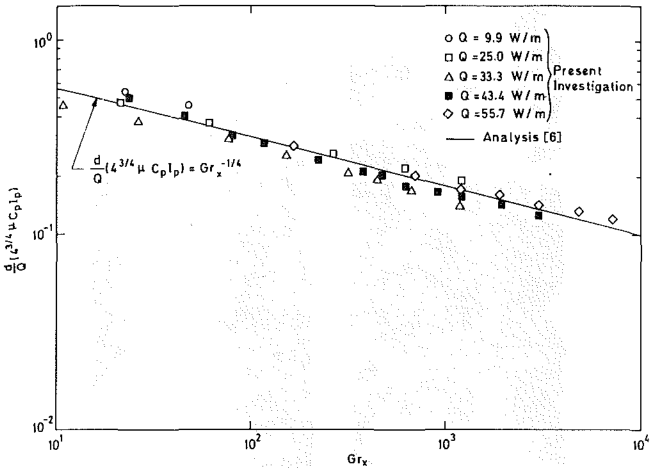

Fig. 3 Comparison of nondimensional centerline temperature measurements at $t_\infty = 4.0°C$ with similarity solution of Mollendorf et al. [6]

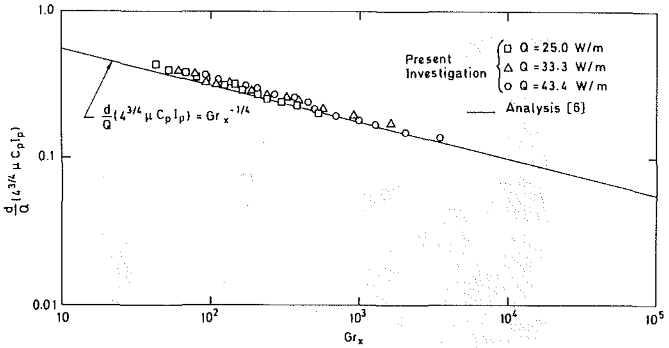

Fig. 4 Comparison of nondimensional centerline temperature measurements at $t_\infty = 4.0°C$ with the similarity solution of Mollendorf et al. [6]. The space below the heat source was bounded with an impermeable surface.

theoretical lines upward in Figs. 2, 3, and 4. The data in Figs. 2 and 3 would, as a result, fall below the modified theory, whereas measurements in Fig. 4 would probably be in closer agreement. This is in accordance with Lyakhov's [3] observations. However, a complete explanation would require an analysis of the variable property effects for the non-Boussinesq plume flows.

Another noteworthly feature in Figs. 3 and 4 is the generally good agreement over the whole range of Grashof numbers, from 10 to 10^4. The lower end of this range certainly lies outside the usual validity of boundary layer approximations. Higher Grashof number values could have been achieved at higher values of Q. However, the variable property effects would be more important, and the more rapid tank stratification would reduce the allowed time for measurements. Higher Q values also cause gases to come out of solution into bubbles on the heat source.

Hieber and Nash [11] have calculated higher-order corrections to the zeroth order boundary layer solution of the plane plume, based on the Boussinesq approximation. Although their results do not strictly apply in these experimental conditions, they are used to estimate the magnitude of corrections in $(t_0 - t_\infty)$ due to relatively small values of Gr_x. Evaluating properties at some intermediate temperature between t_∞ and the maximum value of t_0, the estimate, by Joshi [12], is a very small correction. Thus, it is not surprising that our experimental results show close agreement with the boundary layer solution [6].

Velocity Measurements at $t_\infty = t_m$, i.e., $R = 0 = R^*$. Values of the vertical component of velocity, u, at various x and y locations, were determined from enlarged time exposure photographs of the flow. The $y = 0$ position was inferred at various downstream locations, x, by bisecting the local plume thickness. Location errors of the order of 5 percent may occur, resulting in comparable errors in η in the data comparison in Fig. 5. Larger errors arise in plumes which have meandered considerably from the vertical. Therefore, photographs with very little sway from vertical were chosen for evaluation.

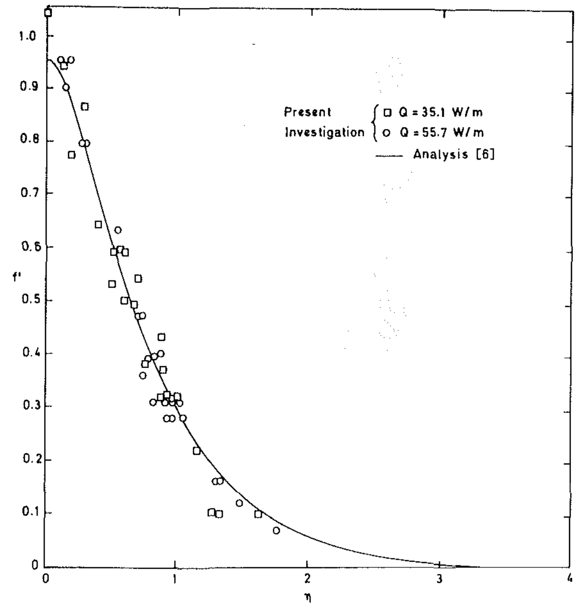

Fig. 5 Comparison of the measured velocities at $t_\infty = 4.0°C$ with the similarity solution of Mollendorf et al. [6], for $Q = 35.1$ W/m and $Q = 55.7$ W/m

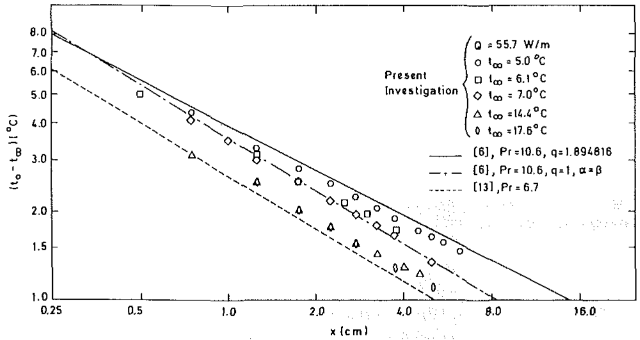

Fig. 6 Comparison of measured temperature excess maxima, $(t_0 - t_\infty)$, with available theory, at various values of $t_\infty > t_m$: – similarity solution of Mollendorf et al. [6] for $R = 0$, $q = 1.894816$ at $\mathrm{Pr} = 10.6$; – · – the same analysis with $q = 1$, $\alpha = \beta$, and $\mathrm{Pr} = 10.6$; - - - the Boussinesq plume flow solution from [13] for $\mathrm{Pr} = 6.7$. In all the theoretical curves properties have been evaluated at a temperature corresponding to the indicated Prandtl number.

The streak length component in the x-direction was measured at downstream x and y locations. The velocities were calculated from $u = (\Delta l \cos\theta)/\Delta\tau$, where $(\Delta l \cos\theta)$ is the component of the streak in the x-direction and $\Delta\tau$ the time exposure. A reasonably short exposure, 4 s, gives an accurate representation of the local flow velocities. The reference length in the photograph was the distance between the two extreme wires in the wire holder assembly, 5.6 cm. A correction in $\Delta l \cos\theta$ was made, due to the finite thickness of the streak. This correction is important for short streaks since $u \propto (\Delta l \cos\theta)$. The data for u and y were then nondimensionalized and compared with the calculations in [6], in Fig. 5, for $Q = 35.1$ W/m and 55.7 W/m. The values of u beyond $\eta \simeq 1.5$ were too small for accurate measurement.

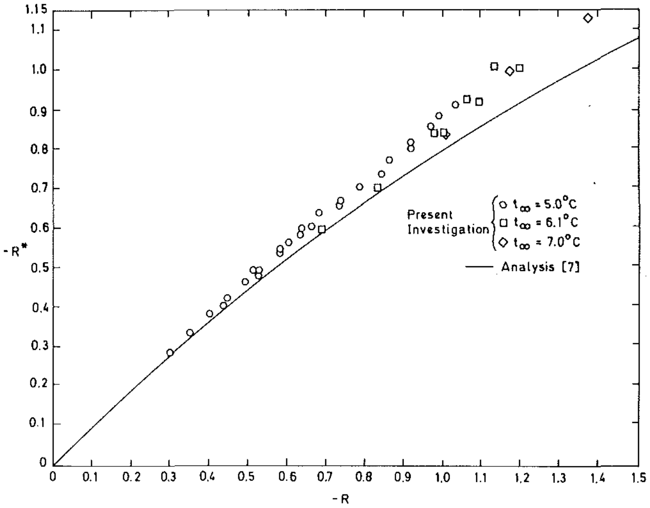

Fig. 7 Comparison of experimental results for $t_\infty > t_m$ with the perturbation solution [7]

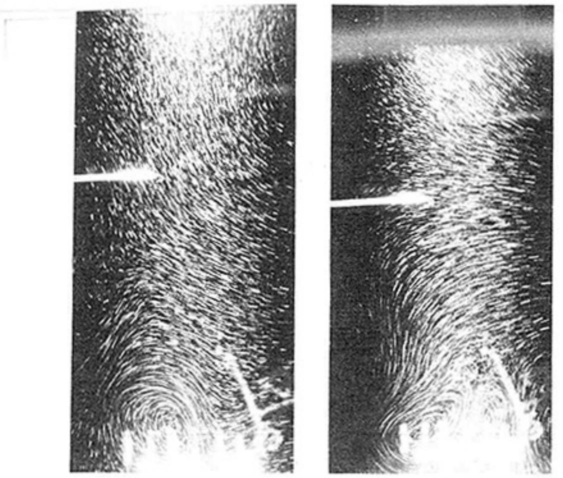

Fig. 9 Visualization of the flow at $t_\infty = 3.1$°C for two values of Q. The distance between the two extreme wire is 5.6 cm: (*a*) $Q = 25.0$ W/m and exposure time = 20 s; (*b*) $Q = 55.7$ W/m and exposure time = 20 s.

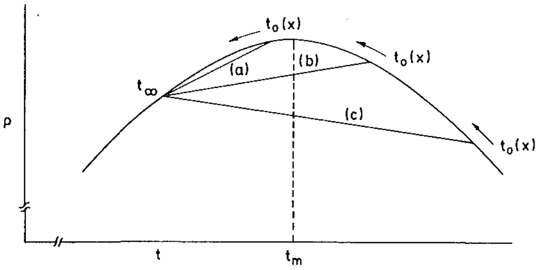

Fig. 8 Representative choices of the pair t_0 and t_∞ for $t_\infty < t_m$, for an energy source, i.e., for $t_0 > t_\infty$

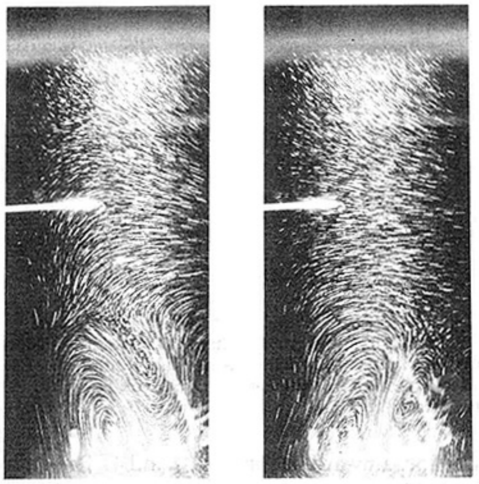

Fig. 10 Meandering pattern of the buoyant layer at $t_\infty = 3.1$°C. $Q = 55.7$ W/m and exposure time = 20 s: (*a*) the swaying buoyant layer at the extreme left position; (*b*) the swaying buoyant layer at the extreme right position.

Plume Flows for Which $t_\infty > t_m$, i.e., $R(x) < 0$ and $R^*(x) < 0$. Measured local temperature excess maxima, $(t_0 - t_\infty)$, at various x, are plotted in Fig. 6 for tests in the range of $t_\infty = 5.0$ to 17.6°C, all for $Q = 55.7$ W/m. For ambient temperatures other than t_m, a similar solution does not exist. These measurements were made to find how the flow pattern changes at increasing temperatures to the flow characteristic at higher temperatures, as the Boussinesq approximation becomes appropriate. The computed centerline temperature variations in Fig. 6 are from [6] for $R = 0$, $q = 1.894816$ and $q = 1$ at $\mathrm{Pr} = 10.6$, and from [13] for $\mathrm{Pr} = 6.7$. The computed lines are based on the properties evaluated at temperatures corresponding to indicated values of the Prandtl number. The data apply to Prandtl number range 6.8 - 10.6. As t_∞ increases from t_m, the measured values of $t_0 - t_\infty$, at any x, decrease toward the lower curve. All data lies below the upper curve, for $t_\infty = t_m$. Most of the data points for $t_\infty \leq 7.0$°C lie above the Boussinesq curve for $\mathrm{Pr} = 10.6$. The Boussinesq approximations are thus inadequate. At temperature levels, $t_\infty = 14.4$°C and 17.6°C, the data are near the Boussinesq pattern for a Prandtl number value between 6.7 and 10.6. Also, the slope of the trend of the data decreases from $-3/(q+4)$ toward -0.6 rather quickly. At $t_\infty = 7.0$°C the slope of the linear least square data fit is already $-.58$.

For R, $R^* \neq 0$ but small, the perturbation analysis in [7] yields up to the first order

$$\phi(\eta,x) = \phi_0(\eta) + (qR^*)\phi_1(\eta) \tag{4}$$

After some rearrangement (4) can be written at $\eta = 0$ as

$$R^* = \frac{R}{(1-KR)}, K = q\phi_1(0) \tag{5}$$

For pure water at 1 bar $\phi_1(0) = .250324$ for $\mathrm{Pr} = 8.6$ and $= .251802$ for $\mathrm{Pr} = 11.6$ [7]. Figure 7 compares the low-temperature data in the range $0.3 \lesssim |R^*| \lesssim 1.15$, or $0.6 \lesssim |qR^*| \lesssim 2.2$ with equation (5). The Prandtl number effect on the solid curve is not apparent on the scale of the graph in the range $\mathrm{Pr} = 8.6$-11.6. All of the experimental points in Fig. 7 are seen to fall above the calculation and the discrepancy increases with $-R$. For large $|qR^*|$ data points, it is likely that terms beyond the first order would be necessary in the analysis, for better agreement. In any case the analysis is limited by $|qR^*| << 1$. For predictions of flow and transport when $|qR^*| \equiv 0(1)$, a finite difference solution of the governing equations would be possible. In any event, the comparison in Fig. 7 indicates that the perturbation analysis prediction is quite good, even to large values of the parameter, R^*.

Flow Visualization. For $t_\infty \geq t_m$, the buoyancy force is upward in the entire flow region. Upflow is observed throughout the flow region. The observed patterns were very similar to those reported by Brodowicz and Kierkus [14] and hence are not presented here.

For $t_\infty < t_m$ the buoyancy force may change direction across the thermal transport region for locations where $t_0 > t_\infty$ is

Fig. 11 Visualization of the flow at $t_\infty = 2.3°C$. $Q = 55.7$ W/m and exposure time = 20 s

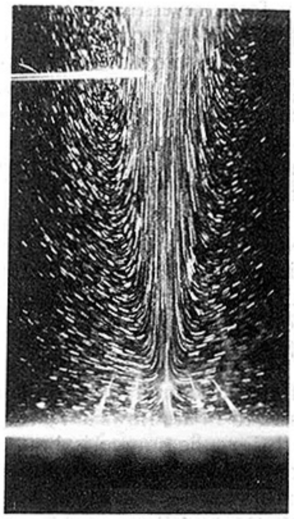

Fig. 12 Visualization of the flow with an impermeable surface below the source $t_\infty = 4.0°C$, $Q = 43.4$ W/m, and exposure time = 12 s

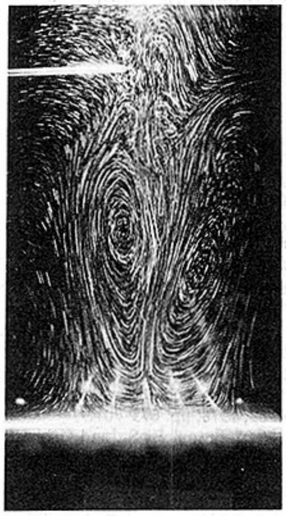

Fig. 13 Observed turbulence in the flow field, when the buoyant layer rises vertically and then splits. $t_\infty = 3.1°C$, $Q = 43.4$ W/m, and exposure time = 15 s. An impermeable surface is placed 1.4 cm below the energy source.

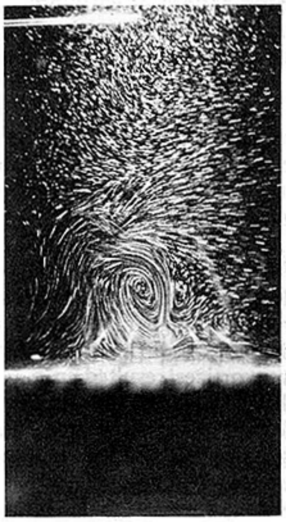

Fig. 14 Visualization of the flow with the impermeable surface below the source. $t_\infty = 2.3°C$, $Q = 55.7$ W/m, and exposure time = 15 s.

larger than t_m. This is clear from Fig. 8. Various choices of the pair $t_0 > t_\infty$, (a), (b), and (c) are shown for a heat source. When t_0 and t_∞ are both less than t_m, (a), the buoyancy force is everywhere downward. For $t_\infty < t_m$ and $t_0 > t_m$, two possibilities exist. If $(t_0 - t_m)$ is positive but small, (b), the buoyancy force is downward as in (a). However, for larger $(t_0 - t_m)$, (c), there is a buoyancy force reversal. It becomes more prominent downstream until the extremum point. The resulting flow direction is determined by the spatial distribution of the buoyancy force.

Figure 9 shows the flow field for $t_\infty = 3.1°C$ for $Q = 25.0$ and $Q = 55.7$ W/m. Regions of flow reversal are present for both Q. Some general remarks can be made about the buoyancy force variation downstream by considering (c) in Fig. 8, which is applicable here. Buoyancy force is upward very close to the source. It decreases in magnitude downstream, becomese zero locally and finally reverses sign. The reversal becomes stronger until the density extremum point and then starts disappearing. The resulting flow is, as expected, quite complicated. For $Q = 25.0$ W/m the flow reversal results in the formation of a single vortex with its center on one side of the source. Ambient fluid is seen to entrain into the vortex from the opposite side of the source. Further up from the vortex region, fluid from the top moves in the downward direction. This results in an efficient mixing process of the cold fluid from the ambient with the relatively warm fluid in the vortex region.

At the higher value of $Q = 55.7$ W/m, the flow reversal results in the formation of two vortices, one on either side of the source. The flow in the region where the upward moving fluid reverses its direction is very irregular, suggesting a turbulent flow pattern. The vortex region is entraining fluid even from far above the source. This results in a more vigorous mixing of the cold ambient fluid with the warmer fluid of the vortex region than in Fig. 9(a). The two vortices observed for $Q = 55.7$ W/m showed a meandering pattern with time, shown at the two extreme positions in Fig. 10.

In earlier investigations of Boussinesq plume flows, a regular meandering pattern has been observed (see for example [2]) with a time period of the order of five min. No satisfactory explanation for this phenomenon has been found so far. Fujii et al. [2] indicated that the meandering cannot be explained by the linear stability theory, the observed frequencies being much smaller than theory would indicate. Hieber and Nash [11] suggest the presence of a triggering mechanism in the vicinity of the wire.

With buoyancy force reversals, behavior was even more complicated. For $Q=25$ W/m the formed vortex was almost invariant with time. The buoyant layer simply bent to one side, for example, to the left, as seen in Fig. 9(*a*). It is up, above the source, and then turns down. However, when Q is increased, a regular meandering pattern is obtained as seen in Fig. 10. The structure and position of the two vortices varied in a periodic fashion with an approximate time period of 3-4 min for $Q=55.7$ W/m.

Figure 11 shows the flow at $t_\infty = 2.3$°C for $Q=55.7$ W/m. The reversal in the direction of the upward moving buoyant layer is at a relatively shorter height than in Fig. 10, because the large positive value of $(t_m - t_\infty)$ results in a downward buoyancy force, for most of the flow region.

The Effect of a Horizontal Surface Below the Energy Source. Figures 12 to 14 are flows at $t_\infty = 4$, 3.1, and 2.3°C, when the region below the source is bounded with an impermeable horizontal surface, 1.4 cm below the source. This surface prevents upflow from below.

In Fig. 12, with $Q=43.4$ W/m, a different pattern of entrainment is seen than in the absence of a bounding surface, especially near the source. The presence of the surface results in a more symmetric pattern of entrainment. Moreover, near the source, the ambient fluid is entrained almost horizontally. In the absence of a bounding surface some of the fluid is clearly seen to be entrained from below the source. A downward velocity component, however, is observed at large y in Fig. 12. It becomes quite prominent further downstream from the source. This downward component of velocity is possibly due to the first order boundary layer correction for the flow in the outer inviscid region.

At $t_\infty = 3.1$°C, flow patterns similar in appearance to those in Fig. 9 arise. For lower values of Q, the buoyant fluid layer bends to one side of the vertical. Meandering of the buoyant layer was observed for higher values of Q. Whenever the buoyant layer was vertical during the pattern of meandering, the split into two vortices resulted in a region of turbulent flow near the split zone. This is observed in Fig. 13. Figure 13 indicates that, for the same value of t_∞ and Q, the buoyant layer rises to a greater height than when the space below the source is not bounded, as in Fig. 10(*b*).

Figure 14 shows the flow at $t_\infty = 2.3$°C and $Q=55.7$ W/m. The pattern appears to be primarily turbulent in nature. The presence of the surface results in the turning of the buoyant layer and the formation of a vortex. No vortex is seen in comparable conditions, Fig. 11, where flow below the source is not impeded.

Conclusions

The conclusions which may be drawn from this study are the following:

1 For the ambient temperature $t_\infty = t_m$, the plume similarity solution agrees satisfactorily with the temperature and velocity measurements. Bounding the space below the heat source with an impermeable surface results in an increase of downstream temperature maxima somewhat above the predictions of theory, even though this configuration is more consistent with the assumptions of the boundary layer theory. These small differences are attributed to the properties variations in the plume.

2 The flow for $t_\infty > t_m$, $R<0$, resembles that at $t_\infty = 4.0$°C, in general appearance, although it departs from the $R=0$ similar solution. Temperature measurements show the gradual transition of the flow from that solution to the Boussinesq result at higher values of t_∞.

3 For $t_\infty < t_m$, $R>0$, the flow departs abruptly from boundary layer behavior, because the buoyancy force becomes bidirectional in the flow region. The visualizations indicate that any asymptotic analysis, around the solution at $R=0$ quickly becomes completely invalid for such flows. These flows would be extremely complicated to model analytically.

4 Visualization results, both with and without a bounding surface below the source, show the difference in entrainment patterns for $t_\infty = t_m$. For $t_\infty < t_m$, the presence of a surface seems to increase the region of upflow.

Acknowledgments

The authors acknowledge the support for this study under National Science Foundation Grant CME 7721641. They also acknowledge the helpful discussions with Dr. Van P. Carey about the higher order effects.

References

1 Schorr, A. W., and Gebhart, B., "An Experimental Investigation of Natural Convection Wakes Above a Line Heat Source," *International Journal of Heat and Mass Transfer*, Vol. 13, 1970, pp. 557-571.

2 Fujii, T., Morioka, I., and Uehara, H., "Buoyant Plume Above a Horizontal Line Heat Source," *International Journal of Heat and Mass Transfer*, Vol. 16, 1973, pp. 755-768.

3 Lyakhov, Y. N., "Experimental Investigation of Free Convection Above a Heated Horizontal Wire," *Journal of Applied Mechanics and Technical Physics*, Vol. 11, 1970, p. 355-359.

4 Gebhart, B., and Mollendorf, J. C., "A New Density Relation for Pure and Saline Water," *Deep-Sea Research*, Vol. 24, 1977, pp. 831-848.

5 Gebhart, B., and Mollendorf, J. C., "Buoyancy Induced Flows in a Liquid Under Conditions in which Density Extrema May Arise," *Journal of Fluid Mechanics*, Vol. 89, 1978, pp. 673-707.

6 Mollendorf, J. C., Johnson, R. S., and Gebhart, B., "Several Constant Energy Plume Flows in Pure and Saline Water at Its Density Extremum," *Journal of Fluid Mechanics*, Vol. 113, 1981, pp. 269-282.

7 Gebhart, B., Carey, V. P., and Mollendorf, J. C., "Buoyancy Induced Flow Due to Energy Sources in Cold Quiescent Pure and Saline Water," *Chemical Engineering Communications*, Vol. 3, 1979, pp. 555-575.

8 Lieberman, J., M. S. thesis, Department of Mechanical and Aerospace Engineering, Cornell University, 1969.

9 Carey, V. P., and Gebhart, B., "Visualization of the Flow Adjacent to a Vertical Ice Surface Melting in Cold Pure Water," *Journal of Fluid Mechanics*, Vol. 107, 1981, pp. 37-55.

10 Carey, V. P., and Mollendorf, J. C., "Variable Viscosity Effects in Several Natural Convection Flows," *International Journal of Heat and Mass Transfer*, Vol. 16, 1980, pp. 95-109.

11 Hieber, C. A., and Nash, E. J., "Natural Convection Above a Line Heat Source: Higher Order Effects and Stability," *International Journal of Heat and Mass Transfer*, Vol. 18, 1975, pp. 1473-1479.

12 Joshi, Y., M.S. thesis, Department of Mechanical and Aerospace Engineering, State University of New York at Buffalo, 1981, pp. 68-69.

13 Gebhart, B., *Heat Transfer*, McGraw-Hill, 2d ed., 1971, p. 350.

14 Brodowicz, K., and Kierkus, W. T., "Experimental Investigation of Laminar Free Convection in Air Above a Horizontal Wire With Constant Heat Flux," *International Journal of Heat and Mass Transfer*, Vol. 9, 1966, pp. 81-94.

The Effect of Wall Conduction on the Stability of a Fluid in a Right Circular Cylinder Heated From Below

J. C. Buell

I. Catton
Mem. ASME

Nuclear Energy Laboratory,
School of Engineering and Applied Sciences,
University of California,
Los Angeles, Calif. 90024

The onset of natural convection in a cylindrical volume of fluid bounded above and below by rigid, perfectly conducting surfaces and laterally by a wall of arbitrary thermal conductivity is examined. The critical Rayleigh number (dimensionless temperature difference) is determined as a function of aspect (radius to height) ratio and wall conductivity. The first three asymmetric modes as well as the axisymmetric mode are considered. Two sets of stream functions are employed to represent a velocity field that satisfies the no-slip boundary condition on all surfaces and conservation of mass everywhere. The Galerkin method is then used to reduce the linearized perturbation equations to an eigenvalue problem. The results for perfectly insulating and conducting walls are compared with the work of Charlson and Sani [9].

Introduction

The onset of natural convection in a completely confined fluid is of interest to researchers in many fields. Prediction of the effect of various physical parameters on the growth of crystals [1] and optimization of solar energy collection [2] are two of the applications of the theory. This paper was motivated by a desire to determine the effect of lateral wall conductivity on the stability of a cylindrical volume of fluid heated from below.

A large amount of work has been done on various aspects of the classical Benard problem (e.g., an unbounded horizontal fluid layer heated from below), a good summary of which can be found in Chandrasekhar [3]. More recently, the effect of lateral walls has been considered. At first, slip was allowed on either the lateral walls [4] or the top and bottom surfaces [5] so that an analytic solution could be obtained through separation of variables. These works approximate the case of a rigid container only for large or small aspect ratios, respectively. Later, the problem was solved with the no-slip boundary condition imposed on all surfaces [6–10]. The usual method of solution in this case is to satisfy all of the boundary conditions and then approximate the governing equations by the Rayleigh-Ritz method or its equivalent (Galerkin). Catton [8] applied this procedure to a rectangular region and found the critical Rayleigh number as a function of the two aspect ratios and two wall conductivities. Charlson and Sani [9, 10] determined the critical states in cylinders of arbitrary aspect ratio with either an insulating or conducting lateral wall.

Governing Equations

The physical system considered here consists of a rigid right cylinder filled with an initially motionless Boussinesq fluid (Fig. 1). The top and bottom surfaces are assumed to be perfectly conducting and maintained at temperatures T_C and T_H, respectively. The lateral wall is of arbitrary conductivity and is assumed to be insulated outside of the lateral walls. It follows that the initial velocity, temperature, pressure, and density distributions are given by

$$\mathbf{U}_0 = 0 \qquad T_0 = \frac{T_C + T_H}{2} - \beta z \tag{1}$$

$$\nabla P_0 = -\rho_0 g(1+\alpha\beta z)\hat{e}_z \qquad \rho = \rho_0(1+\alpha\beta z)$$

where $\beta = (T_H - T_C)/L$ is the negative initial temperature gradient.

The first three quantities are perturbed by $\mathbf{U}'$, T', and P', respectively, and substituted into the conservation equations. Products of perturbation terms are neglected and the equations are nondimensionalized by setting $\mathbf{U}' = \kappa/L\mathbf{U}$, $T' = \beta LT$, and $P' = (\rho_0\ \nu\kappa/L^2)P$. Two length scales, L and a, are used to nondimensionalize the independent variables z and r. This scaling introduces the aspect ratio $A = a/L$ into

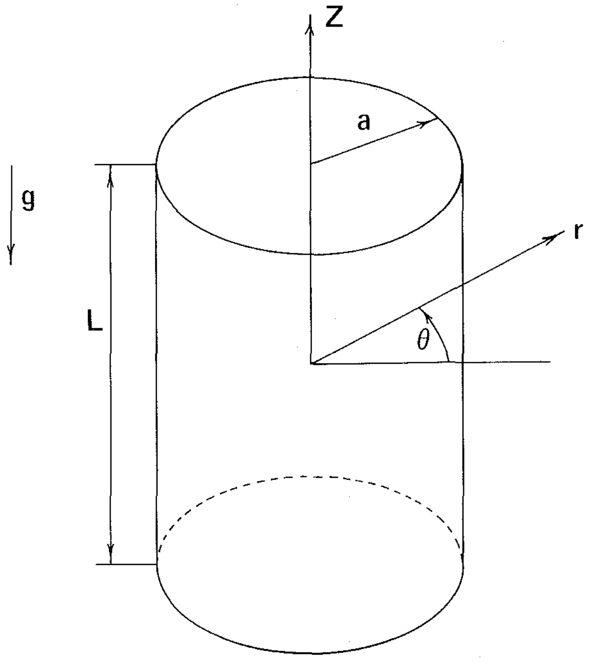

Fig. 1 The rotating cylinder and coordinate system

Contributed by the Heat Transfer Division for publication in the JOURNAL OF HEAT TRANSFER. Manuscript received by the Heat Transfer Division December 1, 1980.

the differential operators. The marginal state is thus time-independent (see [1] and [8]) with the governing equations

$$\nabla \cdot \mathbf{U} = 0 \tag{2}$$

$$\nabla^2 T + \hat{e}_z \cdot \mathbf{U} = 0 \tag{3}$$

$$\nabla^2 \mathbf{U} + \mathrm{R} T \hat{e}_z - \nabla P = 0 \tag{4}$$

The boundary conditions for velocity are

$$\mathbf{U} = 0 \text{ and } n \cdot \frac{\partial \mathbf{U}}{\partial n} = 0 \text{ (from equation 2) on all surfaces} \tag{5}$$

and for temperature

$$T = 0 \text{ at } z = \pm \frac{1}{2} \text{ (perfectly conducting)} \tag{6}$$

$$\left(\frac{\partial^2}{\partial z^2} + \frac{1}{A^2} \frac{\partial^2}{\partial \theta^2} \right) T = \frac{C}{A^2} \frac{\partial T}{\partial r} \text{ at } r = 1 \text{ (fin approximation)} \tag{7}$$

where C is the wall admittance,

$$\frac{k_f a}{k_w t_w}.$$

Equations (2-4) and boundary conditions (5-7) form an eigenvalue problem. The smallest eigenvalue with its associated eigenvector determines the critical Rayleigh number and corresponding temperature and velocity fields.

Trial Functions and Application of the Galerkin Method

From previous work [10, 12] it is known that instability will set in as one vertical roll and an unknown number of radial rolls. Therefore, the vertical velocity and temperature trial functions are chosen to be even functions in z while those for the other two velocities are odd. The approximating series for temperature is

$$T = \sum_{j=1}^{K} \sum_{m=1}^{M} H_{jm} \, T_{jm}; \quad T_{jm} = \cos\,(2m-1)\pi z \, J_n(\beta_{njm} r) \tag{8}$$

where n is the mode number (e.g., $n=0$ is the axisymmetric mode, $n=1$ is the first asymmetric mode, etc.). The β_{njm} are found by applying equation (7) to each term of (8) and evaluating at $r=1$. The resulting characteristic equation for β_{njm} is

$$\left(\frac{nC}{A^2} + (2m-1)^2 \pi^2 + \frac{n^2}{A^2} \right) J_n(\beta_{njm}) - \frac{C}{A^2} \beta_{njm} J_{n+1}(\beta_{njm}) = 0 \tag{9}$$

It is convenient to divide the rest of this section into two parts – the axisymmetric mode and asymmetric modes. For the former, only one set of stream-functions is needed to approximate the velocity field, whereas two are needed for the latter.

The Axisymmetric Mode. Following Charlson and Sani [9], the velocity is approximated by a series of solenoidal fields, where each field is derived from a streamfunction

$$\mathbf{U} \cong \sum_{j=1}^{K} \sum_{m=1}^{M} A_{jm} \mathbf{U}_{jm}; \mathbf{U}_{jm} = \mathrm{curl}\,(\psi_{jm} \hat{e}_\theta) \tag{10}$$

The boundary conditions on ψ_{jm} follow from equations (5)

$$\psi_{jm} = \frac{\partial \psi_{jm}}{\partial z} = 0, \quad z = \pm \frac{1}{2} \tag{11}$$

$$\psi_{jm} = \frac{\partial \psi_{jm}}{\partial r} = 0, \quad r = 1 \tag{12}$$

$$\psi_{jm} = 0, \quad r = 0 \tag{13}$$

Equation (13) is obtained by requiring the solution to be finite everywhere. With these conditions in mind and knowing the general shape of the mode, ψ_{jm} is chosen as follows

$$\psi_{jm} = C_m(z) \left(\frac{J_1(\alpha_j r)}{J_1(\alpha_j)} - \frac{I_1(\alpha_j r)}{I_1(\alpha_j)} \right) \tag{14}$$

The α_j's are chosen to satisfy equation (12). The result of this restriction is

Nomenclature

a = radius of cylinder
A = aspect ratio, a/L
$A_{jm}, \bar{A}, B_{jm}, \bar{B}$ = coefficients in velocity field representations
C = wall admittance, $\dfrac{k_f a}{k_w t_w}$
$\hat{e}_r, \hat{e}_\theta, \hat{e}_z$ = unit vectors
g = acceleration of gravity
$H_{jm}, \bar{H}$ = coefficients in temperature field representations
I_n = nth order Bessel function of the second kind
J_n = nth order Bessel function of the first kind
K = number of r-trial functions
k_f = thermal conductivity of fluid
k_w = thermal conductivity of wall
L = height of cylinder
M = number of z-trial functions
$\bar{\bar{M}}$ = $N \times N$ matrix
N = total number of trial functions
n = mode number
P = pressure
R = Rayleigh number, $\alpha g \beta L^4 / \nu\kappa$
r = coordinate variable, radius
t_w = thickness of cylinder wall
$\mathbf{U} = (u, v, w)$ = velocity
V = cylindrical volume
z = coordinate variable

Greek Symbols

α = coefficient of thermal expansion
α_j = roots of (17)
β = negative initial temperature gradient, $(T_H - T_c)/L$
β_{njm} = roots of (10)
δ_j = roots of (35)
ϵ = "contained in"
ζ = stream function
θ = coordinate variable
κ = thermal diffusivity
ν = kinematic viscosity
ρ_0 = initial mean density
ρ = density
ϕ = stream function
ψ = stream function
ω_j = roots of (36)
∇^2 = Laplacian, $\dfrac{1}{A^2} \dfrac{1}{r} \dfrac{\partial}{\partial r} r \dfrac{\partial}{\partial r} + \dfrac{1}{A^2 r^2} \dfrac{\partial^2}{\partial \theta^2} + \dfrac{\partial^2}{\partial z^2}$

$$I_1(\alpha_j)J_2(\alpha_j)+J_1(\alpha_j)I_2(\alpha_j)=0 \tag{15}$$

After inserting equations (8) and (10) into (3) and (4), the Galerkin method yields $2N$ equations

$$\begin{bmatrix} \bar{\bar{M}}_{11} & \bar{\bar{M}}_{12} \\ R\,\bar{\bar{M}}_{21} & \bar{\bar{M}}_{22} \end{bmatrix} \begin{bmatrix} \bar{H} \\ \bar{A} \end{bmatrix} = 0 \tag{16}$$

where

$$\bar{\bar{M}}_{11}=\int_V T_{jm}\nabla^2 T_{il}dV \quad \bar{\bar{M}}_{12}=\int_V T_{jm}\hat{e}_z\cdot\mathbf{U}_{il}dV \tag{17}$$

$$\bar{\bar{M}}_{21}=\int_V \hat{e}_z\cdot\mathbf{U}_{jm}T_{il}dV \quad \bar{\bar{M}}_{22}=\int_V \mathbf{U}_{jm}\cdot\nabla^2\mathbf{U}_{il}dV$$

Here, a double overbar denotes a $N \times N$ matrix. In order that a nontrivial solution exists for the coefficients, the determinant of the matrix must be zero.

The vector $\bar{H}$ is eliminated from (16) to reduce the problem to standard eigenvalue form

$$\left(\bar{\bar{M}}_{22}{}^{-1}\bar{\bar{M}}_{21}\bar{\bar{M}}_{11}{}^{-1}\bar{\bar{M}}_{12}-\frac{\bar{\bar{I}}}{R}\right)\bar{A}=0 \tag{18}$$

The first critical Rayleigh number and the eigenvector are found by using the power method [15]. The vector $\bar{H}$ is then found from the relation

$$\bar{H}=-\bar{\bar{M}}_{11}{}^{-1}\ \bar{\bar{M}}_{12}\bar{A} \tag{19}$$

The Asymmetric Modes. For $n \geq 1$, two two-dimensional velocity fields must be used since any one three-dimensional field derived from a stream function cannot be made to satisfy the no-slip boundary condition on all surfaces. In a manner similar to the previous section, we have

$$\mathbf{U}=\mathbf{U}^{(1)}+\mathbf{U}^{(2)} \tag{20}$$

where

$$\mathbf{U}^{(1)}\cong\sum_{j=1}^{K}\sum_{m=1}^{M}A_{jm}\mathbf{U}_{jm}{}^{(1)};\ \mathbf{U}_{jm}{}^{(1)}=\text{curl }(\phi_{jm}\hat{e}_r) \tag{21}$$

$$\mathbf{U}^{(2)}\cong\sum_{j=1}^{K}\sum_{m=1}^{M}B_{jm}\mathbf{U}_{jm}{}^{(2)};\ \mathbf{U}_{jm}{}^{(2)}=\text{curl }(\zeta_{jm}\hat{e}_z) \tag{22}$$

The boundary conditions on ϕ_{jm} and ζ_{jm} are given by

$$\phi_{jm}=\frac{\partial\phi_{jm}}{\partial z}=\zeta_{jm}=0, \quad z=\pm\frac{1}{2} \tag{23}$$

$$\phi_{jm}=\zeta_{jm}=\frac{\partial\zeta_{jm}}{\partial r}=0, \quad r=1 \tag{24}$$

$$\phi_{jm}=\partial_{jm}=0, \quad r=0 \tag{25}$$

As before, the last condition comes from the requirement that the solutions be finite. Trial functions that satisfy these conditions and approximate the desired modes are given by

$$\phi_{jm}=\sin\ n\theta\ C_m(z)J_{n+1}(\delta_j r) \tag{26}$$

$$\zeta_{jm}=\sin\ n\theta\ \sin\ 2\pi mz\left(\frac{J_n(\omega_j r)}{J_n(\omega_j)}-\frac{I_n(\omega_j r)}{I_n(\omega_j)}\right) \tag{27}$$

where δ_j and ω_j are the roots of the equations

$$J_{n+1}(\delta_j)=0 \tag{28}$$

$$J_n(\omega_j)I_{n+1}(\omega_j)+I_n(\omega_j)J_{n+1}(\omega_j)=0 \tag{29}$$

Note that for $n = 1$, equation (29) is identical to equation (15).

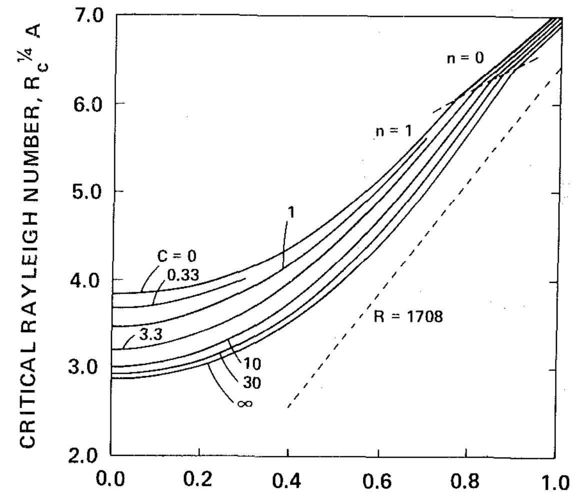

Fig. 2 The critical Rayleigh number for $0 \leq C \leq \infty$, $0 \leq A \leq 1$

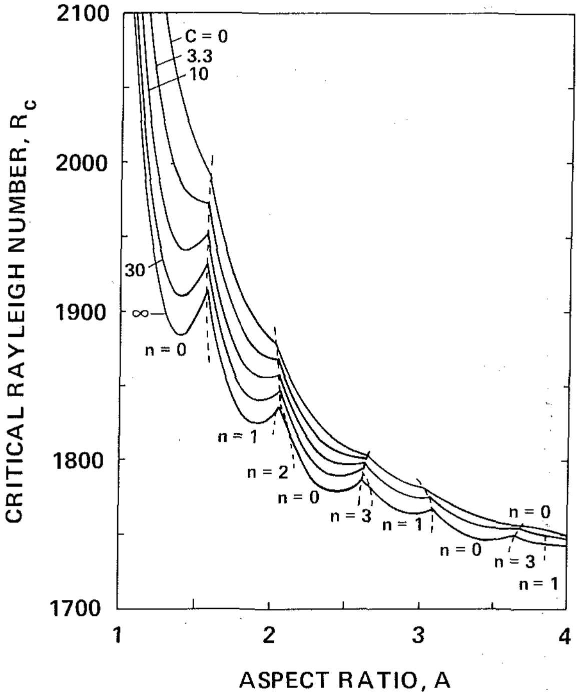

Fig. 3 The critical Rayleigh number for $0 \leq C \leq \infty$, $1 \leq A \leq 4$

The Galerkin method applied to equations (3) and (4) yields $3N$ equations.

$$\begin{bmatrix} \bar{\bar{M}}_{11} & \bar{\bar{M}}_{12} & 0 \\ R\bar{\bar{M}}_{21} & \bar{\bar{M}}_{22} & \bar{\bar{M}}_{23} \\ 0 & \bar{\bar{M}}_{32} & \bar{\bar{M}}_{33} \end{bmatrix} \begin{bmatrix} \bar{H} \\ \bar{A} \\ \bar{B} \end{bmatrix} = 0 \tag{30}$$

where

$$\bar{\bar{M}}_{11}=\int_V T_{jm}\nabla^2 T_{il}dV, \quad \bar{\bar{M}}_{12}=\int_V T_{jm}\hat{e}_z\cdot\mathbf{U}_{il}{}^{(1)}dV,$$

$$\bar{\bar{M}}_{21}=\int_V \hat{e}_z\cdot U_{jm}{}^{(1)}T_{il}dV, \quad \bar{\bar{M}}_{22}=\int_V \mathbf{U}_{jm}{}^{(1)}\cdot\nabla^2\mathbf{U}_{il}{}^{(1)}dV,$$

$$\bar{\bar{M}}_{23}=\int_V \mathbf{U}_{jm}{}^{(1)}\cdot\nabla^2\mathbf{U}_{il}{}^{(2)}dV, \quad \bar{\bar{M}}_{32}=\int_V \mathbf{U}_{jm}{}^{(2)}\cdot\nabla^2\mathbf{U}_{il}{}^{(1)}dV,$$

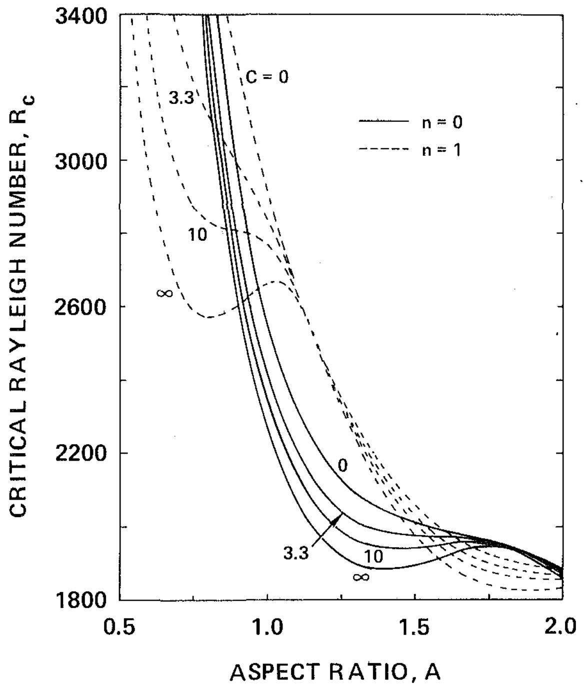

Fig. 4 Stability curves for $n = 0, 1, 0 \leq C \leq \infty, 0.5 \leq A \leq 2$

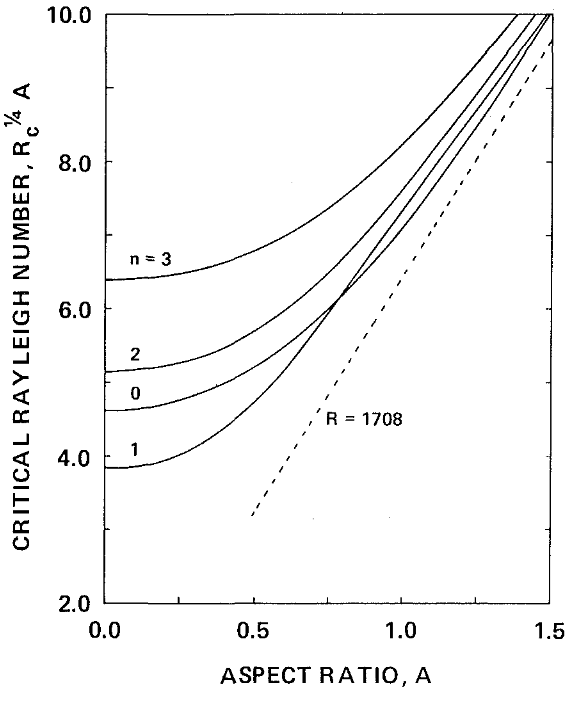

Fig. 5 Stability curves for $n = 0, 1, 2, 3, 0. \leq A \leq 1.5$, conducting walls

$$\bar{M}_{33}=\int_V \mathbf{U}_{jm}{}^{(2)}\cdot\nabla^2\mathbf{U}_{il}{}^{(2)}dV$$

The corresponding eigenvalue formulation is, after eliminating $\bar{B}$ and $\bar{H}$,

$$\left(\left(\bar{M}_{22}-\bar{M}_{23}\bar{M}_{33}{}^{-1}\bar{M}_{32}\right)^{-1}\bar{M}_{21}\bar{M}_{11}{}^{-1}\bar{M}_{12}-\frac{\bar{I}}{R}\right)\bar{A}=0 \quad (32)$$

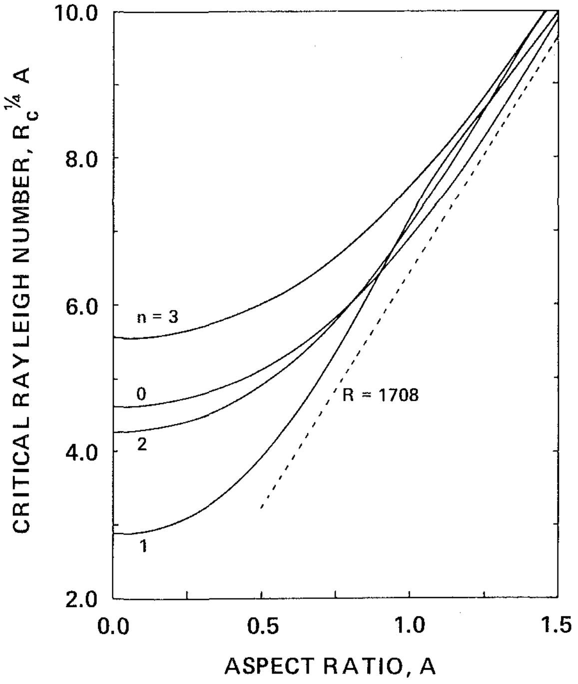

Fig. 6 Stability curves for $n = 0, 1, 2, 3, 0. \leq A \leq 1.5$, insulating walls

After the vector $\bar{A}$ is found by the power method, the rest of the Galerkin coefficients may be recovered from the relations

$$\bar{H}=-\bar{M}_{11}{}^{-1}\bar{M}_{12}\bar{A} \quad (33)$$

$$\bar{B}=-\bar{M}_{33}{}^{-1}\bar{M}_{32}\bar{A} \quad (34)$$

Numerical Results

Calculations were performed for several values of wall admittances and aspect ratios from zero to four. A sufficient number of trial functions were used so that the critical Rayleigh numbers are accurate to four significant figures. For the axisymmetric mode, 40 terms insured convergence while 60 terms were needed for the asymmetric modes. For the latter, 11 radial and up to 8 vertical terms gave the best results. Tables of the roots of equations (15), (28), and (29) are given in [16], as well as expansions of the various matrix elements.

The results are plotted on several different graphs in order to separate and clarify the various effects. Figure 2 shows the critical Rayleigh number and corresponding critical mode (i.e., axisymmetric, $n = 0$, or asymmetric, $n \geq 1$) as a function of the wall admittance for aspect ratios up to one. Figure 3 gives the same information for aspect ratios from one to four. Figure 4 demonstrates the effect of wall conductance on the critical state for each of the first two modes. Figures 5–8 give the relative importance of the first four modes for a perfectly conducting or insulating lateral wall. These figures can be compared directly with the results of Charlson and Sani [10]. It should be noted that the form of the ordinate in Figs. 2, 5, and 6 allow the critical Rayleigh number to be plotted for small aspect ratios, even though $R_c \rightarrow \infty$ as $A \rightarrow 0$.

Discussion

The effect of a cylindrical lateral wall of arbitrary conductance on the critical Rayleigh number has been determined as a function of aspect ratio. Figure 2 shows that the critical Rayleigh number is about three times higher for conducting walls ($C=0$) than for insulating walls ($C=\infty$) when the aspect ratio is small (i.e., tall cylinders). For all wall admittances, the first asymmetric mode ($n=1$) is the least stable for aspect

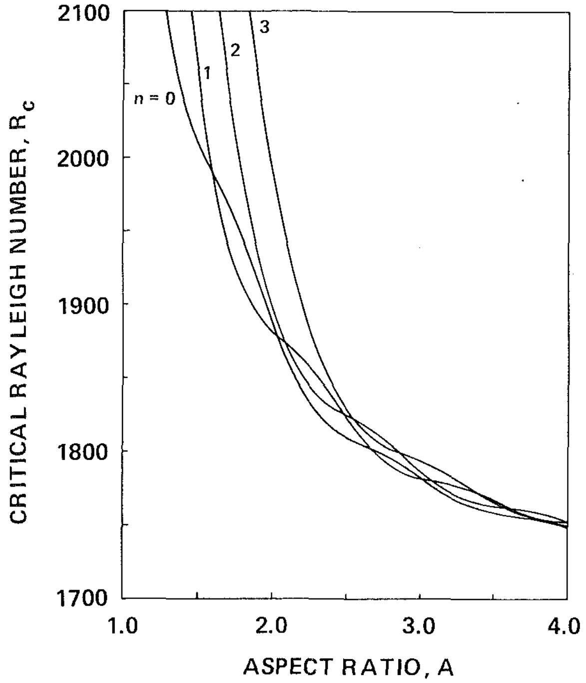

Fig. 7 Stability curves for $n = 0, 1, 2, 3, 1. \leq A \leq 4.$, conducting walls

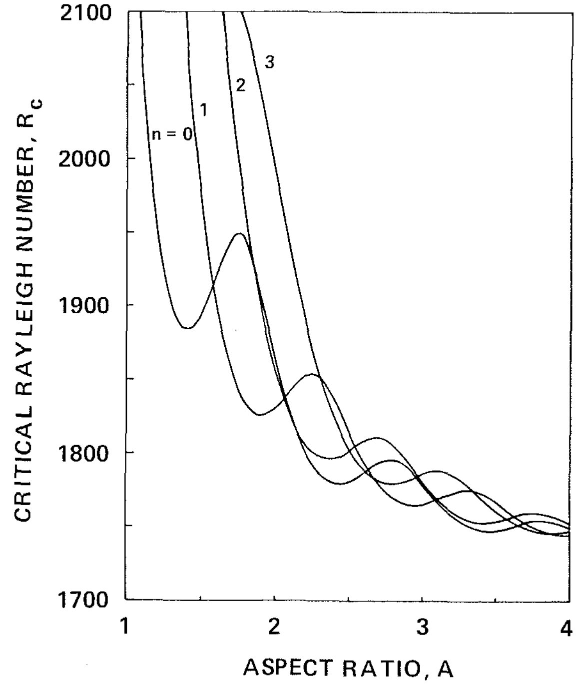

Fig. 8 Stability curves for $n = 0, 1, 2, 3, 1. \leq A \leq 4.$, insulating walls

ratios up to about 0.8 (the exact value depending on wall admittance). At aspect ratios around unity, the axisymmetric ($n=0$) mode is the least stable. At higher aspect ratios, the critical mode basically alternates between these two modes, with a few exceptions where a higher mode is the least stable.

From Figs. 2, 3, and 4, it is noted that the wall conduction affects where these "transitions" occur (this is most obvious in Fig. 2). In all cases, the effect of a higher wall conductivity ($C \rightarrow 0$) is to increase the range of aspect ratio where the axisymmetric mode is the least stable. This is reasonable in light of the differences between the axisymmetric and asymmetric modes. The dominant difference with respect to wall conductance is that the asymmetric modes have an azimuthal temperature distribution that tends to be damped out by a high wall conductance while the axisymmetric mode does not. That is, if there is an azimuthal temperature imbalance, heat will be transferred by conduction in the wall from the hot side to the cold side. The asymmetric modes are thus stabilized by a higher wall conductance more than the axisymmetric mode.

Table 1 Transition points for velocity and temperature rolls

Mode	Velocity rolls		Temperature rolls
	$C=0$	$C=\infty$	
$n=0$	1.485	1.691	1.81
	2.533	2.730	2.85
	3.575	3.754	3.88
$n=1$	.748	1.013	1.163
	2.074	2.217	2.33
	3.195	3.296	3.39

Another effect of high wall conductivity is to dampen vertical temperature fluctuations. In the case of very tall cylinders, the vertical temperature gradient in the fluid is close to that of the wall for most of the height so this effect is minimal. Similarly, it is expected that for large aspect ratios, the azimuthal effect is small while the vertical effect is dominant. A comparison of Figs. 5 and 6 verifies that both effects of wall conductance are very small for the axisymmetric mode and aspect ratios less than 0.4.

Even though a higher wall conductance always increases the stability of fluid layer, it does not always have this effect on any one mode (Fig. 4). Charlson and Sani [9] have shown that as the aspect ratio increases, rolls are added by the gradual growth of a small roll at the lateral boundary. That is, the transitions between number of temperature rolls occurs at those aspect ratios where $T = 0$ and $\partial T/\partial r = 0$ at the wall. Unlike temperature, these transition points are heavily dependent on wall conductivity, being about 0.2 units of aspect ratio lower for conducting walls than for insulating walls. This is in disagreement with Charlson and Sani [9] who found that wall conduction has little effect on the velocity roll transition points for the axisymmetric mode. The insulating wall transition points always occur within .01 units of aspect ratio of the corresponding peak in the insulating wall stability curves. The various transition points are summarized in Table 1.

Charlson and Sani [9] solved the axisymmetric problem with either a perfectly conducting or insulating lateral wall and this work agrees with theirs. In a later paper [10], they solved the asymmetric cases with the same boundary conditions but obtained critical Rayleigh numbers that are from 7 to 20 percent higher than for the present work for the first asymmetric mode and aspect ratios ranging from 0.4 to 3. The difference approaches zero for very small and very large aspect ratio cylinders. Also, the results are close for the higher asymmetric modes. All of this can be readily explained after an examination of the velocity trial functions used by Charlson and Sani.

The degree of success of any variational method is heavily dependent on the choice of trial functions. It is not enough for these functions to just satisfy the boundary conditions; they must also be complete enough to be able to approximate the dependent variables. The latter may be obvious, but it is by no means a trivial requirement, especially in cylindrical coordinates. The problem that one faces is in choosing boundary conditions along the axis of the cylinder ($r=0$) that are not too restrictive. In going from the axisymmetric to the asymmetric stability problem, Charlson and Sani added a velocity field of the form

$$\mathbf{U} = \mathrm{curl}(\psi \hat{e}_r) = \left(0, \frac{\partial \psi}{\partial z}, -\frac{1}{Ar}\frac{\partial \psi}{\partial \theta}\right) \qquad (35)$$

The second component of **U** is the only representation of the azimuthal velocity, v. In order that the vertical velocity (w) remain finite on the axis of the cylinder, ψ must approach zero linearly with r. But this means that v also equals zero on the axis which for the first asymmetric mode is definitely not true. This amounts to "restricting" v and increasing the resulting estimate of the critical Rayleigh number. Even though the azimuthal velocity is not well represented, one still expects Charlson and Sani's results to be good in both limits of aspect ratio. For very tall cylinders, the azimuthal velocity is of little importance and limiting results such as Yih's [17] are valid. At the other extreme, the region around the axis where the azimuthal velocity cannot be well approximated becomes relatively small compared to the total cylinder cross section and should not affect the overall stability calculations. The numerical calculations verify all of these conclusions.

The velocity field $\mathbf{U} = \mathrm{curl}\,(\psi \hat{e}_r)$ is also used in this paper but the important difference is that the azimuthal component is not relied upon to represent the azimuthal velocity. The second velocity field represents both the azimuthal and radial velocities satisfactorily.

There are a few more points worth noting. For aspect ratios greater than 2.5, the first four modes are close to being equally unstable. Apparently any mode is close to being the least stable after the first minimum point on its insulating-wall curve. Secondly, all of the stability curves for a given mode are smooth (e.g., Fig. 8); there are no discontinuities in slope as shown by Carlson and Sani. Finally, as the aspect ratio increases, the effect of wall conductivity on the marginal state decreases compared to the effect of the wall itself.

Summary and Conclusions

The Galerkin method was used to solve the thermal stability problem of a fluid heated from below and completely confined in a cylindrical container with rigid surfaces and an arbitrarily conducting lateral wall. Critical Rayleigh numbers were obtained for aspect ratios where the limiting solutions are not valid. The results for the axisymmetric mode with a perfectly conducting or insulating wall were the same as Charlson and Sani's while those for the asymmetric modes were up to 20 percent lower. The use of stream functions that approximate these modes better is credited with the difference. The critical Rayleigh number was determined as a function of wall conductivity for aspect ratios less than 4. The greatest effect of wall conductivity occurs at low aspect ratios, and it has a steadily diminishing effect at higher aspect ratios. Finally, transition points for velocity and temperature rolls have been determined for the first two modes.

Acknowledgments

We gratefully acknowledge useful discussions with Dr. James M. McDonough. This work was supported by the National Science Foundation Grant #P-4359-N-79.

References

1 Carruthers, J. R., "Origins of Convective Temperature Oscillations in Crystal Growth Melts," *J. Cryst. Growth*, Vol. 32, 1976, p. 13.

2 Buchberg, H., Catton, I., and Edwards, D. K., "Natural Convection in Enclosed Spaces—A Review of Application to Solar Energy Collectors," ASME JOURNAL OF HEAT TRANSFER, Vol. 98, pt. 2, 1976, pp. 182-188.

3 Chandrasekhar, S., *Hydrodynamic and Hydromagnetic Stability*, Clarendon Press, Oxford, 1961.

4 Ostrach, S., and Pneuli, D., "The Thermal Instability of Completely Confined Fluids Inside Some Particular Configurations," ASME JOURNAL OF HEAT TRANSFER, Vol. 85, No. 4, 1963, pp. 346-354.

5 Catton, I., and Edwards, D. K., "Initiation of Thermal Convection in Finite Right Circular Cylinders," *AIChE Journal*, Vol. 16, 1963, pp. 594-601.

6 Davis, S. H., "Convection in a Box," *Journal of Fluid Mechanics*, Vol. 30, pt. 3, 1967, pp. 465-478.

7 Catton, I., "The Effect of Insulating Vertical Walls on the Onset of Motion in a Fluid Heated From Below," *International Journal of Heat and Mass Transfer*, Vol. 15, 1972, pp. 665-672.

8 Catton, I., "Effect of Wall Conduction on the Stability of a Fluid in a Rectangular Region Heated From Below," ASME JOURNAL OF HEAT TRANSFER, Vol. 94, No. 4, 1972, pp. 446-452.

9 Charlson, G. S., and Sani, R. L., "Thermoconvective Instability in a Bounded Cylindrical Fluid Layer," *International Journal of Heat and Mass Transfer*, Vol. 13, 1970, pp. 1479-1496.

10 Charlson, G. S., and Sani, R. L. "On Thermoconvective Instability in a Bounded Cylindrical Fluid Layer," *International Journal of Heat and Mass Transfer*, Vol. 14, 1971, pp. 2157-2160.

11 Sherman, M., and Ostrach, S., "On the Principle of Exchange of Stabilities for the MHD Stability in Completely Confined Fluids," *Journal of Fluid Mechanics*, Vol. 24, pt. 4, 1966, pp. 661-671.

12 Koschmeider, E. L., "On Convection on a Uniformly Heated Plane," *Beitr. Phys. Atmos.*, Bd. 39, 1966, pp. 1-11.

13 Harris, D. L., and Reid, W. H., "On Orthogonal Functions Which Satisfy Four Boundary Conditions, I: Tables for Use in Fourier-Type Expansions," *Astrophys. J. Suppl. Ser.*, Vol. 13, 1958, pp. 429-447.

14 Harris, D. L., and Reid, W. H., "On Orthogonal Functions Which Satisfy Four Boundary Conditions, I: Tables for Use in Fourier-Type Expansions," *Astrophys. J. Suppl. Ser.*, Vol. 13, 1958, pp. 448-452.

15 Hornbeck, R. W., *Numerical Methods*, Quantum Publishers, Inc., New York, 1975, pp. 231-235.

16 Buell, J. C., "The Effects of Rotation and Wall Conductance on the Stability of a Fully Enclosed Fluid Heated From Below," M.S. thesis, University of California, Los Angeles, 1981.

17 Yih, C. S., "Thermal Instability of Viscous Fluids," *Quarterly of Applied Mathematics*, Vol. 17, 1959, pp. 25-42.

M. Keyhani
Department of Mechanical Engineering,
The Ohio State University,
Columbus, Ohio 43210

F. A. Kulacki
Department of Mechanical and
Aerospace Engineering,
University of Delaware,
Newark, Del. 19711
Mem. ASME

Experiments on Transient Thermal Convection With Internal Heating — Large Time Results

Experimental data and correlations are presented for the time scales of developing and decaying thermal convection with volumetric heating in a horizontal layer. The layer is bounded by rigid surfaces, with an insulated lower boundary and an isothermal upper boundary. The time for complete flow development/decay, as a result of a step change in volumetric heat generation, is simply parameterized in terms of the Fourier number for the layer, the step change in Rayleigh number, ΔRa, and the initial/final dimensionless maximum core temperature. For developing flows, $\Delta Ra > 0$, results are in good agreement with existing experiments and an approximate boundary layer theory. In decaying flows, Fourier numbers are larger than those of previously reported experiments for a motionless final state. Data for turbulent-to-turbulent transitions when $\Delta Ra < 0$ suggests that the approximate boundary layer theory underestimates the Fourier number. Experimental uncertainties on measured Fourier numbers are generally well within the limits of uncertainty allowed by the approximate theory.

Introduction

Transient thermal convection in plant layer with uniform volumetric heat sources serves as a model of more complex problems which are found in geophysical fluid dynamics, nuclear reactor safety (e.g., post-core-melt heat removal), and manufacturing processes for resin-based materials. Although thermal radiation within the layer has been analyzed as a possible energy source for the problem of transient heat removal from a nuclear reactor core melt [1], the majority of published work has dealt with either a chemical or nuclear energy source. For the latter, the full energy and momentum equations apply, and all nonlinearities are retained.

Experimental work on transient thermal convection with internal heating is somewhat limited [2-5]. These papers report both quantitative and qualitative results on both laminar and turbulent flow transitions. Theoretical work to predict temperature within the layer during the flow transition is limited to the approximate work of Cheung [6, 7], which depends on the experimental data for steady convection.

Qualitative work on the planform of developing flow ($\Delta\mathrm{Ra} = \mathrm{Ra}_F$) at low Rayleigh numbers was presented by Schwiderski and Schwab [4] and Tritton and Zarraga [5]. As long as the flow remains laminar, the planform shifts to larger wave numbers as Ra is increased. When $\mathrm{Ra}_F = 100\mathrm{Ra}_c$, turbulent flow is observed.

Quantitative work on developing and decaying flows have been reported in two similar studies [2, 3]. For developing turbulent flows in an initially motionless layer ($H_I = 0$, $\mathrm{Ra}_I = 0$), the temperature distribution exhibits a well mixed core and a well-defined thermal boundary layer at the upper surface. Flow development time is found to be nearly the same as the time required for complete decay of the flow when internal heating is stopped, i.e., $\Delta\mathrm{Ra} = -\mathrm{Ra}_I$ and $\mathrm{Ra}_F = 0$. This result was quantified by introducing a Fourier number defined in terms of the measured maximum time for the maximum (mean core) temperature to reach steady state-values, i.e., $\mathrm{Fo}_{\max} = \alpha t_{\max}/L^2$. Flow development and decay times were correlated by

$$\mathrm{Fo}_{\max,\,\mathrm{heating}} = 11.57\,(\Delta\mathrm{Ra})^{-0.213} \tag{1}$$

$$\mathrm{Fo}_{\max,\,\mathrm{cooling}} = 11.95\,(|\Delta\mathrm{Ra}|)^{-0.215} \tag{2}$$

In these equations, $\mathrm{Fo}_{\max}$ was determined as the time when the core temperature was within 2 percent of steady-state values.

Cheung's [6, 7] approximate analysis of turbulent-to-turbulent flow transitions begins with the assumption that most of the layer is well mixed at a constant temperature, T_{CO}, and that all of the thermal resistance to heat transfer is contained in a thin thermal boundary layer ($\delta/L << 1$) at the upper surface. Thus, the horizontally averaged energy equation can be integrated over the layer $0 \le z \le L$ to give

$$\frac{1}{2}\frac{d\theta_{\mathrm{CO}}}{d\mathrm{Fo}} = -\left(\frac{\theta_{\mathrm{CO}}}{\theta_{\mathrm{CO}_I}}\right)\left(\frac{\delta_I}{\delta}\right) + \frac{\mathrm{Ra}_F}{\mathrm{Ra}_I}, \tag{3}$$

where the variation of temperature and volumetric heat generation within the boundary layer has been neglected.

From steady-state heat transfer data at high Rayleigh number [3], Cheung developed the relation

$$\frac{\delta}{\delta_I} = \left(\frac{\theta_{\mathrm{CO}}}{\theta_{\mathrm{CO}_I}}\right)^{-0.293} \tag{4}$$

Under the assumption that equation (4) holds for turbulent-to-turbulent flow transitions despite any restructuring of the flow that might take place, equation (3) can be combined with equation (4) to obtain $\phi_{\mathrm{CO}}(\mathrm{Fo})$. When complete decay of flow is considered, $\mathrm{Ra}_F/\mathrm{Ra}_I = 0$, and a closed form solution is obtained which is in good agreement with experimental results [6].

The motivation for the present work arises, in part, from the lack of extensive experimental data for the time scales of the transition from one turbulent flow to another following a step change in internal heat generation. Another objective is to verify the validity of the existing data on transient flows [3] and to determine what differences may exist in the time scales of developing and decaying convection. Finally, it is desired to provide an experimental test of the analysis of Cheung [6] on developing and decaying flows.

Experimental Apparatus and Procedure

The convection chamber was constructed for earlier studies of steady convection. Details of its design are given by Emara [3]. Briefly, the fluid layer is insulated on all faces except the top. The test fluid is dilute aqueous CuSO_4. A 60 hz electrical current is passed horizontally through the fluid to provide the

---

Contributed by the Heat Transfer Division for publication in the JOURNAL OF HEAT TRANSFER. Manuscript received by the Heat Transfer Division January 13, 1982.

Table 1 Data for developing and decaying flows with a motionless initial and final state respectively

$Ra_I = 0, \theta_{CO_I} = 1$

ΔRa	θ_{CO_F}	t_{max}(h)	Fo_{max}
3.65×10^7	0.0848	3.0	0.273
5.17	0.074	–	–
6.41	0.0846	–	–
7.42	0.0814	–	–
2.34×10^8	0.0514	2.8	0.142
5.87	0.0437	2.8	0.144
1.05×10^9	0.039	2.6	0.132
1.30	0.040	1.8	0.093
2.64	0.0337	–	–
7.87	0.0306	1.5	0.078

$Ra_F = 0, \theta_{CO_F} = 1$

$\lvert\Delta Ra\rvert$	θ_{CO_I}	t_{max}(h)	Fo_{max}
2.34×10^8	0.0514	5.2	0.263
6.12	0.0463	3.6	0.184
1.1×10^9	0.0384	4.4	0.223
1.29	0.04	3.6	0.184
2.75	0.0336	3.8	0.193
6.17	0.0311	4.0	0.203
8.4	0.029	3.6	0.184

internal heat source. Temperature differences across the layer are measured with thermocouples in the upper and lower boundaries. Several thermocouples are imbedded in each of the surfaces so that a spatially averaged temperature can be measured.

The heat flux through the bottom surface is determined by a differencing thermopile using ten thermocouples. One thermocouple is placed in the bottom surface 0.128 cm from the surface for recording the temperature transient at the bottom of the fluid layer. The delay in the response of this thermocouple compared to that of the fluid at that surface is calculated by using a simple conduction model for both developing and decaying flows. For developing flow, the input voltage to the guard heater is varied during the flow transient so that the output of the thermopile is kept at zero.

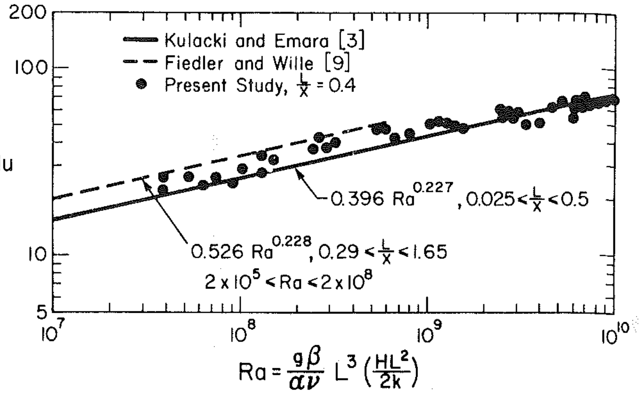

Fig. 1 Steady-state Nusselt numbers obtained from asymptotic values of the temperature difference across the layer following a step change in Rayleigh number

Any deviation from zero is corrected by manual adjustment of the voltage input to the guard heater. Therefore, the plane of zero heat flux in the bottom plate during developing flow is taken as the location of the near surface thermocouple.

Analysis of transient conduction in a slab (Plexiglas with $\alpha \approx 10^{-4}$ cm^2/s) 0.128-cm thick with an insulated bottom and time dependent input at the top surface shows that the delay between the fluid temperature and thermocouple is on the order of 100 s. However, this delay was found to have no measurable effect on the present results for developing flow and, thus, no further attempt was made to develop a correction for the measured temperature difference across the layer.

For decaying flow, the bottom plate boundary conditions cannot be maintained in the same manner as for developing flow. Once a step decrease in heat generation rate is applied to the fluid, the voltage input to the guard heater is turned off, and the temperature in the slab decays with the fluid temperature. In this case, the plane of zero heat flux in the bottom plate is taken at the guard heater location. The delay time is found to be about 300 s, which is less than 3 percent of typical decay times observed in the present experiments. The ratio of the calculated to the measured temperature input is used as a correction for the temperature response of the fluid at the

Nomenclature

A = area of heat transfer surface, m^2
c_p = specific heat, J/kg-K
Fo = Fourier number, $\alpha t/L^2$
g = constant of gravitational acceleration, m/s^2
H = volumetric energy source strength, W/m^3
h = convective heat transfer coefficient, W/m^2-K
k = thermal conductivity, W/m-K
L = Thickness of fluid layer, m
m,n = constants of correlation
Nu = Nusselt number at upper surface,

$$Nu = \frac{(P-P_L)L}{kA\Delta T} = \frac{hL}{k}$$

P = power input to the fluid layer, W
P_L = power lost from fluid layer, W
Pr = Prandtl number, $\frac{\nu}{\alpha}$
Q = heat flux at the upper surface, W/m^2
Ra = Rayleigh number,

$$\left(\frac{g\beta}{\alpha\nu}\right) L^3 \left(\frac{HL^2}{2k}\right)$$

ΔRa = step change in Rayleigh number, $Ra_F - Ra_I$
t = time, s
T = mean temperature, K
ΔT = temperature difference across fluid layer, $T_1 - T_0$
X = horizontal dimension of test cell, m
z = vertical coordinate, $0 \leq z \leq L$, m

Greek Symbols

α = thermal diffusivity,

$$\frac{k}{\rho c_p}, \text{m}^2/\text{s}$$

δ = thermal boundary layer thickness, m
ρ = density, kg/m^3
θ = dimensionless temperature,

$$\frac{2k(T - T_1)}{HL^2}$$

ν = kinematic viscosity, m^2/s
β = coefficient of thermal expansion, K^{-1}

Subscripts

c = value at critical point
CO = value at turbulent core
CO_F = final value at turbulent core
CO_I = initial value at turbulent core
F = final condition
I = initial condition
max = value to reach steady state
0 = value at lower surface of fluid layer
1 = value at upper surface of fluid layer

Table 2 Data for turbulent-to-turbulent flow transitions

Ra_I	Ra_F	ΔRa	$\left[\frac{HL^2}{2k}\right]_I$	θ_{CO_I}	$\left[\frac{HL^2}{2k}\right]_F$	θ_{CO_F}	$\frac{\Delta Ra}{\theta_{CO_I}}$	$\frac{\lvert\Delta Ra\rvert}{\theta_{CO_F}}$	t_{max} (h)	Fo_{max}
1.27×10^8	2.67×10^8	1.40×10^8	5.364	0.0574	10.92	0.0468	2.44×10^9	–	–	–
1.47	3.06	1.59	7.22	0.060	14.568	0.0495	2.65	–	2.3	0.117
2.67	5.26	2.59	10.92	0.0468	21.445	0.0409	5.53	–	1.72	0.088
3.06	7.24	4.18	14.568	0.0496	32.367	0.0445	8.43	–	1.9	0.097
5.26	1.10×10^9	5.74	21.445	0.0409	42.851	0.0383	1.40×10^{10}	–	2.0	0.103
7.24	1.49	7.66	32.368	0.0445	61.797	0.042	1.72	–	2.4	0.122
1.10×10^9	2.44	1.34×10^9	42.852	0.0384	87.076	0.0364	3.49	–	1.4	0.072
1.49	3.8	2.31	61.797	0.0421	134.10	0.0395	5.49	–	1.6	0.083
2.44	5.97	3.53	87.076	0.0364	182.387	0.0323	9.7	–	1.6	0.083
1.05	2.49	1.44	45.58	0.039	99.504	0.0325	3.7	–	1.4	0.072
5.87×10^8	2.85	2.26	21.988	0.0437	95.35	0.0348	5.17	–	1.5	0.0775
3.70×10^7	1.86×10^8	1.49×10^8	3.403	0.0848	20.64	0.0652	1.76×10^9	–	1.5	0.159
9.77×10^9	6.68×10^9	-3.09×10^8	269.5	0.0295	199.7	0.0317	–	9.75×10^{10}	3.2	0.146
6.68	2.87	-3.81	199.7	0.0317	100.8	0.034	–	1.12×10^{11}	3.0	0.155
2.87	1.23	-1.64	100.8	0.034	47.1	0.039	–	4.2×10^{10}	3.0	0.154
1.23	5.72×10^8	-6.58×10^8	47.1	0.039	23.2	0.042	–	1.57	3.2	0.164
2.53	1.1×10^9	-1.43×10^9	99.5	0.032	47.1	0.0384	–	3.72	3.0	0.153
2.84	6.12×10^8	-2.23	95.4	0.0348	22.8	0.0463	–	4.81	2.8	0.144

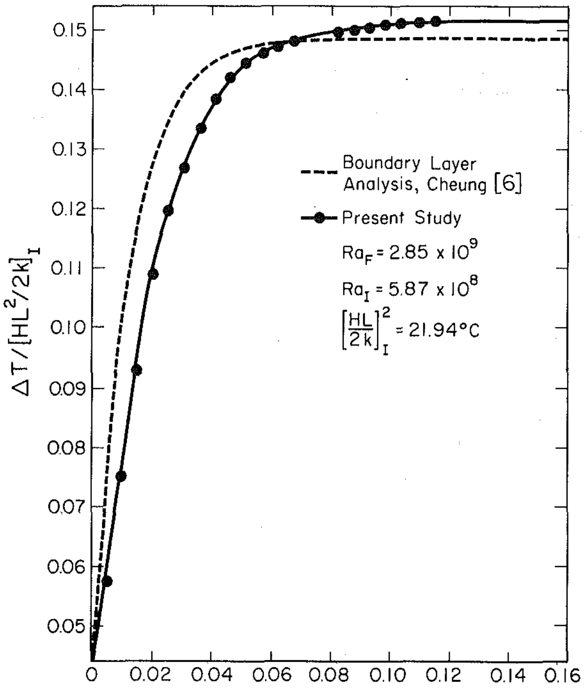

Fig. 2 Measured and predicted temperature differences for developing flow

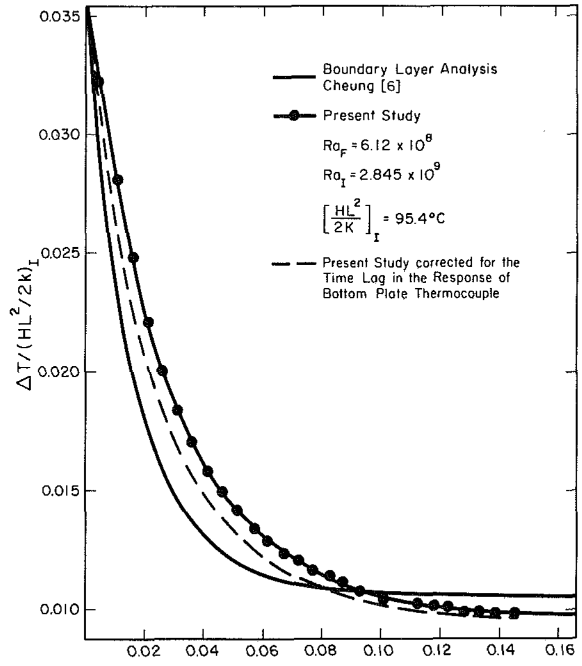

Fig. 3 Measured and predicted temperature differences for decaying flow

bottom surface. For determining maximum Fourier numbers, the time delay is subtracted from measured time.

Power to the fluid is supplied from a voltage regulator and transformer. Power consumed in the fluid is determined by measurements of current and voltage drop, both to an accuracy of 0.5 percent. A strip chart recorder is used to record temperature in the layer.

The thermophysical properties of the working fluid as a function of temperature are approximated by those of pure water. All fluid properties are evaluated at the temperature of the bottom plate.

Results

Steady-state Nusselt numbers obtained in fully developed convection are presented in Fig. 1. The layer aspect ratio, i.e., the layer depth divided by horizontal dimension, in the present work is 0.4, which is close to the upper range of aspect ratios reported by Kulacki and Emara [3] but in the lower range of aspect ratios reported by Fielder and Wille [9]. Generally, the present data are in good agreement with results of Kulacki and Emara for $10^8 \leq Ra \leq 10^{10}$.

For transient convection, there are several ways in which to present and discuss the data. For the present, we focus on the relation between the change in Ra and Fo_{max}. The measurement of Fo_{max} is, of course, made difficult by the graphical estimate of the asymptote for $\Delta T(t)$ as $t \rightarrow \infty$, but errors due to the thermocouple response lag are at a minimum for large time. The experimental data are summarized in Tables 1 and 2.

Measured and predicted temperature differences across the layer for a step increase in the Rayleigh number when $Ra_I > 0$ are presented in Fig. 2 in terms of the Fourier number. The present results for the early phase of flow development, i.e., up to approximately 20 to 30 percent of Fo_{max}, indicate temperature differences about 24 percent less than predicted by the boundary layer model. For later stages of flow development, the two results are in much better agreement. The final temperature difference is about 2 percent greater than the predictions of the boundary layer model. However,

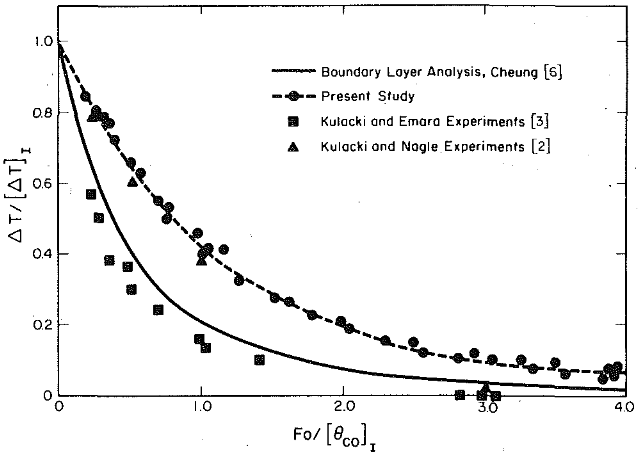

Fig. 4 Temperature difference across the layer for decaying convection, $\Delta Ra = Ra_I$

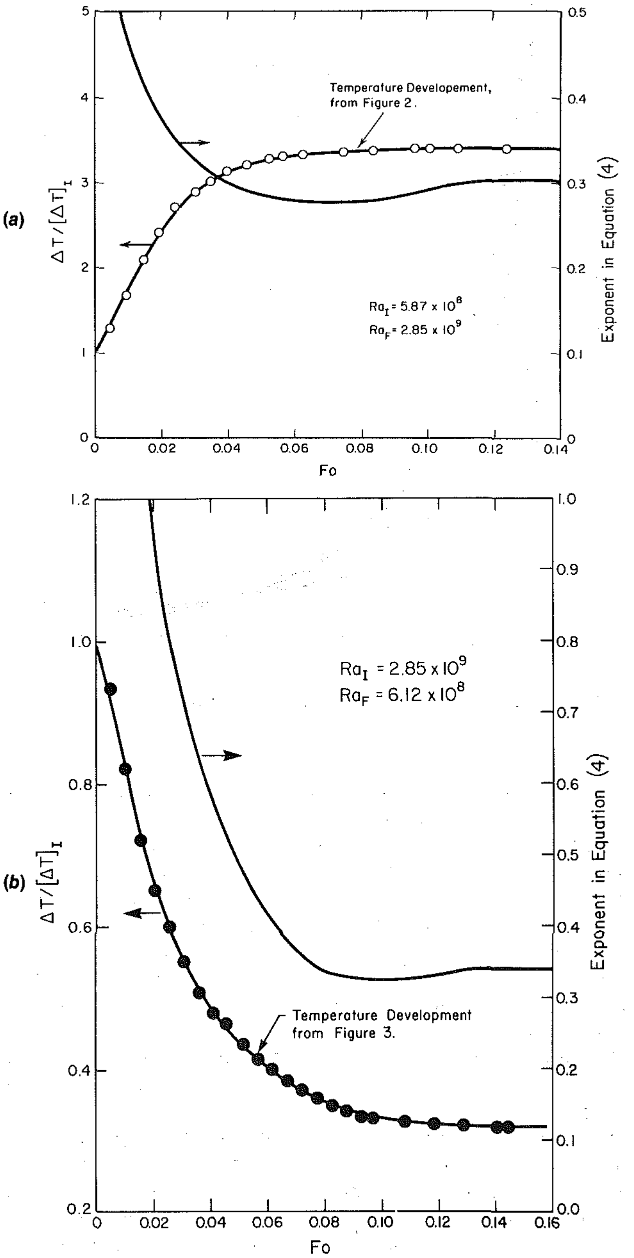

Fig. 5 Calculated time-dependent behavior of exponent of equation (4): (*a*) developing flow; (*b*) decaying flow

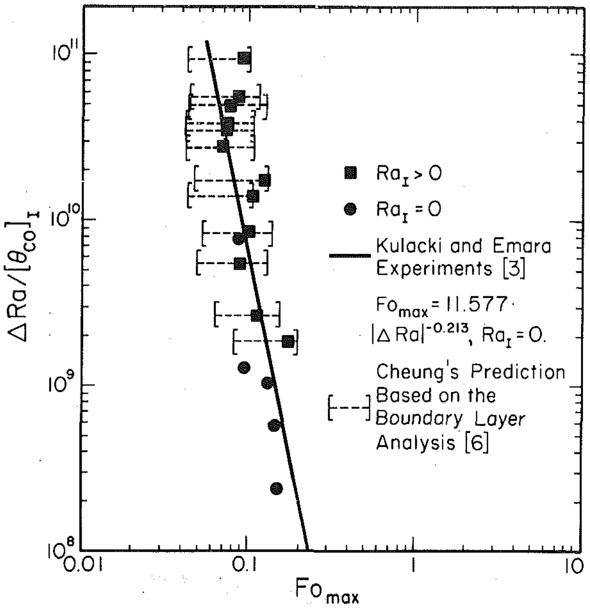

Fig. 6 Normalized step increase in Rayleigh number versus dimensionless time. Predictions of Cheung [6] give the range of Fo where the maximum temperature difference is within 2 percent of the steady-state value.

this difference leads to a much greater discrepancy in the Fourier number owing to the asymptotic approach of the temperature difference to steady state values. Experimental uncertainty in the measured temperature difference is not great enough to permit the claim of essential agreement between the two results. On the other hand, adjustment of the exponent in equation (4) as a time-dependent parameter would enable one to produce this agreement. This will be addressed shortly.

Measured and predicted temperature differences across the layer for a step decrease in Rayleigh number as a function of Fourier number are presented in Fig. 3 when $Ra_F > 0$. For the early stage of flow decay, corrected temperatures are in fairly good agreement with Chueng's analysis. The same sort of discrepancy between the time scale for complete decay occurs as in the results for developing flow.

For the case of complete flow decay, i.e., $\Delta Ra = -Ra_I$, the fractional change in temperature difference across the layer versus the Fourier number is presented in Fig. 4 with the theoretical results of Cheung [6] and earlier experimental results [2, 3]. The results of Kulacki and Emara and of Cheung indicate a much faster rate of temperature decrease than the results reported by Kulacki and Nagle and the present work. The agreement between the present results and those of Kulacki and Nagle is, perhaps, reassuring owing to the different methods of recording the temperature difference across the layer and the partial ($Ra_F \neq 0$) decay processes considered in the present work. The difference between the two curves in Fig. 4 is partly a result of the time-dependence of the exponent in equation (4).

It should be noted that the time dependence of the exponent in equation (4) can be obtained through a solution of equation (3) in conjunction with the experimental data on temperature. This has been done, and the results are presented in Figs. 5(*a*) and 5(*b*) for developing and decaying flow. From these figures, it can be seen that the exponent in equation (4) is a rapidly decreasing function of time in the early stages of both developing and decaying flow. However, the value for decaying flow assumes a larger value for a longer period of time than in developing flow. Consequently, a larger time for the completion of the decaying flow transition is the result.

The normalized step increase in the Rayleigh number, $\Delta Ra/\theta_{CO_I}$, as a function of the Fourier number, is presented

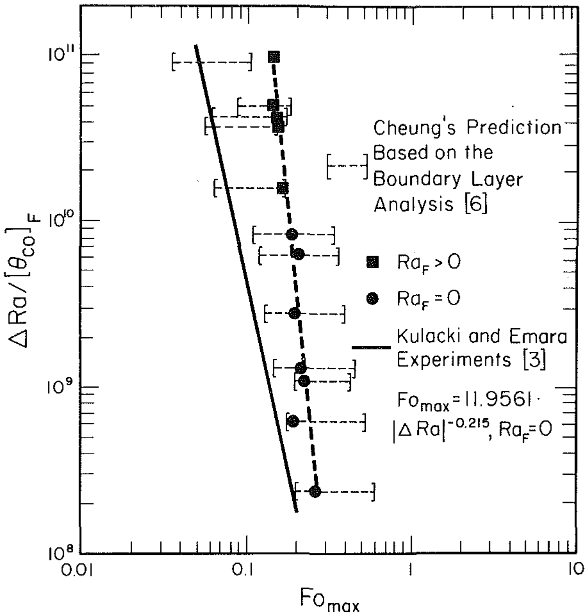

Fig. 7 Normalized step decrease in Rayleigh number versus dimensionless time. Predictions of Cheung [6] give the range of Fo where the maximum temperature difference is within 2 percent of the steady-state value.

in Fig. 6 in conjunction with the correlation of Kulacki and Emara [3], with $\theta_{CO_I} = 1$, and the predictions of Cheung [6]. The analytical results give the range of Fo where the maximum temperature difference across the layer is within 2 percent of the final steady-state value, i.e., $Fo_{98\ \mathrm{percent}} \leq Fo \leq Fo_{99.9\ \mathrm{percent}}$. The experimental results and the analysis are in satisfactory agreement for cases where $Ra_I > 0$. Also the present data indicate that for $Ra_I > 0$, a smaller time is required for the completion of the transition from one state of steady convection to another compared to that for a transition from a motionless initial state of steady convection for the same ΔRa.

The normalized step decrease in the Rayleigh number, $|\Delta Ra|/\theta_{CO_F}$, versus the Fourier is presented in Fig. 7. The correlation given by Kulacki and Emara [3], with $\theta_{CO_F} = 1$, and the predictions of Cheung [6] are also shown in Fig. 7. The boundary layer analysis again gives a range of Fourier numbers where the temperature difference across the layer is within 2 percent of the final steady-state value. The results of the present study indicate that a larger time is required for the complete decay compared to the time obtained from the correlation reported by Kulacki and Emara. (recall Fig. 4.) Cheung's predictions are in good agreement with results of the present study for complete decay, i.e., $Ra_F = 0$. When $Ra_F > 0$, the present data tend toward a flow transition somewhat longer than that resulting from the boundary layer analysis. It should be noted that, for the same step change in Ra, a longer time is required for decaying flow than that of developing flow.

Overall, the experimental data indicate that, for a given Ra_I, the larger the ΔRa, the faster the development of flow and approach to steady state. The larger Ra_I, i.e., the smaller θ_{CO_I}, for the same step *increase* in Rayleigh number, the smaller the time needed for development of flow to a new steady state. In the case of complete decay, i.e., $Ra_F = 0$, the same behavior as for developing flow is observed. But in the case of a transition from one steady state to another at a lower Ra, the behavior is somewhat different. For a given initial Rayleigh number, the greater the step decrease in Ra, a greater time is needed for the completion of the flow transition. Also, it is evident that for the same step decrease in Ra, a larger initial Rayleigh number results in faster flow transition.

An examination of the present and earlier experimental data indicate that a correlation of the form

$$Fo = \mathrm{constant.}\ (\theta_{CO_j})^m (\,|\Delta Ra|^n) \tag{5}$$

where $j = I$ for developing flow and F for decaying flow, can be used to good accuracy to describe the experimental data.

For developing flow, the data give

$$Fo_{\mathrm{max,\ heating}} = 6.844(\theta_{CO_I})^{0.097}(\Delta Ra)^{-0.195} \tag{6}$$

where

$$0.036 \leq \theta_{CO_I} \leq 0.084,\ 1.4 \times 10^8 \leq Ra \leq 3.53 \times 10^9$$

and

$$\theta_{CO_I} = 1.0,\ 2.34 \times 10^8 \leq \Delta Ra \leq 7.87 \times 10^9$$

For decaying flow, the data give

$$Fo_{\mathrm{max,\ cooling}} = 0.706(\theta_{CO_F})^{0.085}(\,|\Delta Ra|\,)^{-0.059} \tag{7}$$

where

$$0.031 \leq \theta_{CO_F} \leq 0.046,\ 6.58 \times 10^8 \leq Ra \leq 3.81 \times 10^9$$

and

$$\theta_{CO_F} = 1.0,\ 6.12 \times 10^8 \leq |\Delta Ra| \leq 8.4 \times 10^9$$

Conclusion

The major contributions of this study are a development of an expanded set of experimental data for developing and decaying flow for heat-source driven thermal convection and correlations for time scales of these transients which permit a simple parameterization for the initial and final flows. Steady-state heat transfer coefficients are also presented, and these are in good agreement with earlier measurements. However, time scales of the transition flows only partly substantiate the results of Kulacki and Emara [3].

Measured flow development time and the analysis of Cheung [6] indicate that a plot of the step change in Rayleigh numbr versus the Fourier number forms a family of curves with Ra_I, or θ_{CO_I}, for developing flow and Ra_F, or θ_{CO_F}, for decaying flow, as parameters. For developing flow with $Ra_I = 0$ ($\theta_{CO_I} = 1$), the present results are in good agreement with the experimental results of Kulacki and Emara [3] and Cheung [6]. The results obtained for the transition from one state of steady convection to another are essentially in good agreement with Cheung's analysis.

In the case of complete decay of convection, $\Delta Ra = -Ra_I$, the present results and Cheung's analysis both indicate that a time larger than that of Kulacki and Emara is required to complete the transition and that there is a much weaker dependent of Fo_{max} on $|\Delta Ra|$. Also, for transitions from one state of steady convection to another following a step decrease in power input, the present work suggests larger flow transition time than the time predicted by the boundary layer analysis. This points to a possible effect of a restricting of the flow and, hence, the relation between core temperature and boundary thickness during the transition, i.e., time dependence of the exponent in equation (4). The hypothesis that best could explain this is that the Nusselt-Rayleigh number relation becomes that of Rayleigh-Benard convection, and the flow decays with no buoyancy generation resulting from internal heat release.

Overall, we have found essential agreement between our results and the simple boundary layer model proposed by Cheung [6]. Except for the case when $\Delta Ra < 0$ with $Ra_F > 0$, the assumptions that lead to the relation given in equation (4) seem justified for large time behavior of the convection transition and its asymptotic approach to steady state. For the small time behavior, the nature of any flow restructuring that may take place needs to be examined through an analysis of the data for $\Delta T(t)$ versus t.

Error Estimates

The combined uncertainties in the thermophysical properties of the aqueous copper sulfate solution, geometrical factors and the power consumption produces an experimental uncertainty of 6 and 8 percent in the Rayleigh number. The uncertainty in the steady state Nusselt numbers is 3.5 to 3.5 percent.

In the measurement of the temperature within the layer, the uncertainty in reading the output of the strip chart recorder is 0.5 percent for both temperature and elapsed time. Measurements of temperature taken from the recorder are considered accurate to within 3.5 percent. The combined uncertainty in the uncertainty in the Fourier number was 3.5 percent. The maximum Fourier numbers are estimated to be accurate to 6 and 10 percent. While this level of experimental uncertainty is larger than for measured Nusselt and Rayleigh number, it is not considered unreasonable in view of the experimental method used.

Acknowledgment

The work was supported by the U.S. Nuclear Regulatory Commission under Contract No. NRC-04-74-149.

References

1 Anderson, E. E., "Radiative Heat Transfer in Molten UO_2 Based on the Rosseland Diffusion Method," *Nuclear Technology*, Vol. 30, 1976, pp. 65-70.

2 Kulacki, F. A., and Nagle, M. E., "Natural Convection in a Horizontal Fluid Layer with Volumetric Energy Sources," ASME JOURNAL OF HEAT TRANSFER, Vol. 97, 1975, pp. 204-211.

3 Kulacki, F. A., and Emara, A. A., "Steady and Transient Thermal Convection in a Fluid Layer with Uniform Volumetric Energy Sources," *Journal of Fluid Mechanics*, Vol. 83, 1977, pp. 375-395.

4 Schwiderski, E. W., and Schwab, J. A., "Convection Experiments with Electrolytically Heated Fluid Layers," *Journal of Fluid Mechanics*, Vol. 48, 1971, p. 703.

5 Tritton, D. J., and Zarraga, M. N., "Convection in Horizontal Layers with Heat Generation Experiments," *Journal of Fluid Mechanics*, Vol. 30, 1967, pp. 1-21.

6 Cheung, F. B., "Turbulent Natural Convection in a Horizontal Fluid with Time Dependent Volumetric Energy Sources," Paper No. 78-HT-6, AIAA-ASME Thermophysics and Heat Transfer Conference, Palo Alto, 1978.

7 Cheung, F. B., "The Boundary Layer Behavior in Transient Turbulent Thermal Convection," ASME JOURNAL OF HEAT TRANSFER, Vol. 102, 1980, pp. 373-275.

8 Emara, A. A., "On Thermal Convection with Internal Heating in Fluid Layers," Ph.D. dissertation, The Ohio State University 1977.

9 Fiedler, H., and Wille, R. Warmetransport bie frier konvektion in einer horizontalen flussegkeitsschich mit volumenheizung, Teil 1: Integraler Warmetransport, Rep. Dtsch Forschungs — Varsuchsantalt Lut — Raumfahr Inst. Rubulenzfenschung, Berlin, 1971.

10 Keyhani, M. and Kulacki, F. A., "An Experimental Study of Turbulent Thermal Convection with Time-Dependent Volumetric Energy Sources," U.S. Nuclear Regulatory Commission, NUREG/CR-1173, Dec. 1979.

W. M. M. Schinkel[1]
Research Scientist.

S. J. M. Linthorst
Research Scientist.

C. J. Hoogendoorn
Professor.

Delft University of Technology,
Delft, The Netherlands

The Stratification in Natural Convection in Vertical Enclosures

This paper presents theoretical results on natural convection in vertical air-filled enclosures with isothermal hot and cold walls. The flow is considered to be two-dimensional, laminar, and stationary. The effect of stratification of the fluid in the core region on the heat transfer and the natural convection flow is discussed. Local heat transfer relations considering this stratification are given. The Rayleigh number varied from 10^4-10^6, the aspect ratio from 1-18, and the side walls were both perfectly conducting and adiabatic.

Introduction

The problem of natural convection in vertical enclosures has been investigated over a long period of time in the literature. Excellent reviews have been given by Ostrach [1] and Catton [2].

From the experiments of Eckert and Carlson [3] and Elder [4], it is known that different flow regimes can be distinguished: the conduction, the transition, and the boundary layer regime. In the boundary layer regime the upward and downward moving fluid are separated by a stratified core region. Though the stratification in the core region is very characteristic for natural convection in vertical enclosures, relatively little attention has been paid to its properties and its effect on the convective motion.

Eckert and Carlson observed that the vertical temperature gradient at the central point of the enclosure, τ, is inversely proportional to the aspect ratio when the flow is in the boundary layer regime. They obtained a value of the proportionality constant of 0.60. Numerical computations of Grondin [5] confirmed this result. Moreover Eckert and Carlson obtained a relation for the local heat transfer in the boundary layer regime. In this relation the stratification of the core region enters as a parameter. There are no theoretical investigations known to us in which local heat transfer relations are presented.

Elder obtained analytical solutions for the component of the velocity in the vertical direction and the temperature at half the height of the enclosure. Also in this solution the stratification enters as a parameter. Elder defines the so-called stratification parameter γ: $\gamma=(\frac{1}{4}\tau \mathrm{Ra})^{\frac{1}{4}}$. For large values of γ, Elder's analytical solution becomes the same as the analytical solution of Gill [6], who obtained his solution from a boundary layer analysis. Both the solutions of Elder and Gill are approximate ones. Roux [7] compared results from numerical computations at $A = 1$ with Gill's theory. He showed that Gill's solution can describe the velocity and temperature distribution only partly.

In the present study, we re-examined natural convection in vertical enclosures with special attention to the effect of stratification in the core region. We considered the flow to be two-dimensional, laminar and stationary. The governing equations have been solved numerically using a method of finite differences. Isothermal hot and cold walls have been considered. Most of the computations are with perfectly conducting side walls (pc). For comparison additional computations with adiabatic side walls (ad) have been done. The Rayleigh number has been varied from 10^4-10^6 and the aspect ratio from 1-18. The Prandtl number of air has been used.

Formulation of the Problem

A rectangular vertical enclosure as shown in Fig. 1 is considered. The two vertical walls have a uniform temperature, T_h and T_c, respectively. T_c is assumed to be smaller than T_h. The distance between the vertical walls is D, and the height of the enclosure is H. The ratio H/D is called the aspect ratio, A. It is assumed that the problem can be considered as a two-dimensional one, i.e., the depth of the enclosure is assumed to be infinitely long. A Cartesian coordinate system as shown in Fig. 1 is used.

The governing equations are the continuity equation, the Navier-Stokes equations and the energy equation. Following the well-known Oberbeck-Boussinesq approximation [8] the dimensionless two-dimensional steady form of the governing equations can be written as

$$\frac{\partial u}{\partial x}+\frac{\partial v}{\partial y}=0 \tag{1}$$

$$\mathrm{Gr}\left(\frac{\partial uu}{\partial x}+\frac{\partial vu}{\partial y}\right)=\frac{\partial^2 u}{\partial x^2}+\frac{\partial^2 u}{\partial y^2}-\frac{\partial p}{\partial x}+\theta-\theta_o \tag{2}$$

$$\mathrm{Gr}\left(\frac{\partial uv}{\partial x}+\frac{\partial vv}{\partial y}\right)=\frac{\partial^2 v}{\partial x^2}+\frac{\partial^2 v}{\partial y^2}-\frac{\partial p}{\partial y} \tag{3}$$

$$\mathrm{Gr}\left(\frac{\partial u\theta}{\partial x}+\frac{\partial v\theta}{\partial y}\right)=\frac{1}{\mathrm{Pr}}\left(\frac{\partial^2 \theta}{\partial x^2}+\frac{\partial^2 \theta}{\partial y^2}\right) \tag{4}$$

Where D is the characteristic length, $g\beta(T_h-T_c)D^2/\nu_o$ and $\rho_o g\beta(T_h-T_c)D$ are taken as the units for velocity and pressure. The dimensionless temperature is defined by $\theta = (T-T_c)/T_h-T_c)$. The Grashof number and Prandtl number are

$$\mathrm{Gr}=g\beta(T_h-T_c)D^3/\nu_o{}^2 \tag{5}$$

$$\mathrm{Pr}=\nu_o/a_o \tag{6}$$

The fluid properties are taken at the reference temperature, $T_o = (T_h+T_c)/2$. Often the Rayleigh number has been used where Ra = Gr Pr. The boundary conditions are in dimensionless form

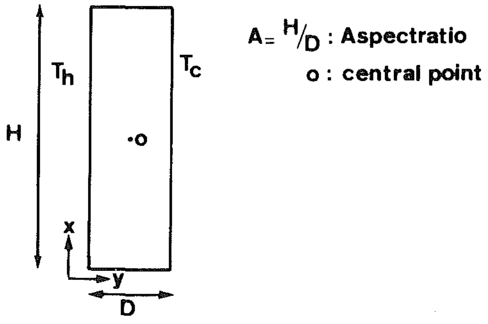

Fig. 1 A schematic view of the enclosure

---

[1] Present address: Shell/Amsterdam

Contributed by the Heat Transfer Division and presented at the 19th ASME/AIChE National Heat Transfer Conference, Orlando, Florida, July 1980. Manuscript received by the Heat Transfer Division June 23, 1981.

$u = v = 0$ at all walls

$$\theta(x,0)=1 \quad 0\leq x\leq A$$

$$\theta(x,1)=0 \quad 0\leq x\leq A$$

$$\text{pc: } \theta(0,y)=\theta(A,y)=(1-y) \quad 0\leq y\leq 1$$

$$\text{ad: } \left.\frac{\partial\theta}{\partial x}\right|_{x=0} = \left.\frac{\partial\theta}{\partial x}\right|_{x=A} = 0 \quad 0\leq y\leq 1$$

The governing equations and the boundary conditions have the centro-symmetry property. The centro-symmetry has been used to reduce the computational effort. More details are described in Schinkel [9].

The Numerical Method. The equations (1-4) are in the so-called hydrodynamical form. We used a method developed by Gosman, Pun and Spalding [10] to solve the equations (1-4). The method is based on the method of finite differences and is described in detail in [10].

The local Nusselt number has been calculated by taking the derivative of a three point $\theta-y$ parabola at the wall. The averaged Nusselt number has been found by numerical integration of the local Nusselt number along the wall.

The results obtained with the method of finite differences essentially contain errors due to the finite size of the grid. Denny and Clever [11] investigated the influence of the grid size by increasing the number of grid nodes. They used grids up to 100 × 100 nodes for the case $A = 1$. Ozoe and Churchill [12] used three different grid size and extrapolated the averaged Nusselt number to zero grid size. We developed a method to obtain the averaged Nusselt number with zero grid size which is related to the method of Ozoe and Churchill.

In our problem we expect boundary layers near the walls of the enclosure. In the boundary layers the gradients are large, while in the core region smaller gradients can be expected. In order to use an economic grid, we want to have a fine grid near the walls and a less fine grid in the core region. Therefore a nonlinear grid has been used. The nonlinear grid is defined by

$$\begin{aligned} y_{j+1} &= \tfrac{1}{2}\left(\frac{j}{k}\right)^{\alpha} y \\ y_1 &= -y_2 & \text{for } j=1,2,\ldots\ldots k \\ y_{m-j} &= 1-y_{j+1} & k=\tfrac{1}{2}(m-1) \\ y_m &= 1+y_2 & (7) \end{aligned}$$

where m is the number of grid nodes in the y-direction (m is odd) and α_y is the nonlinearity parameter. For $\alpha_y = 1$ the grid is linear. A typical value of α_y is $\alpha_y = 1.5$. The grid in the x-direction is defined accordingly. We used 21 grid nodes in the y-direction. The number of grid nodes in the x-direction increases with increasing aspect ratio. For $A = 1$, we used 21 nodes, and for $A = 18$, we used 49 nodes.

Given a certain fixed number of grid nodes, we varied the nonlinearity of the grid. Since the largest gradients are near the hot and cold wall, the nonlinearity in the y-direction has been varied only. When the non-linearity in the y-direction is increased, the distance of the second grid node, y_2, from the wall decreases. We considered $\overline{\text{Nu}}$ as function of y_2.

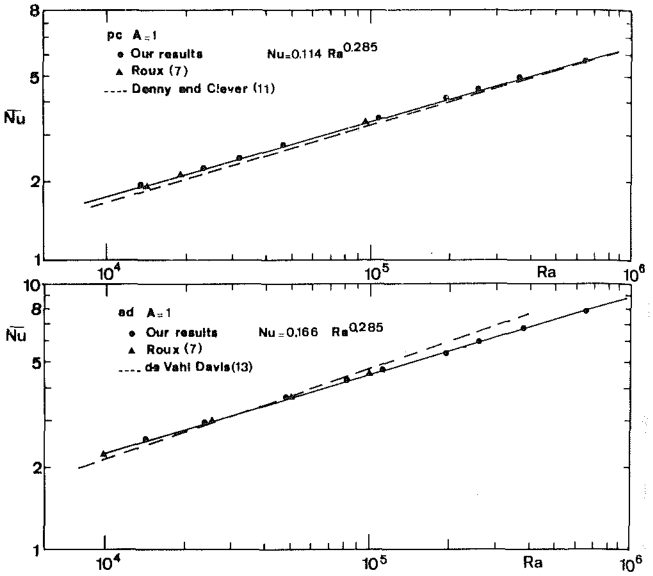

Fig. 2 The averaged heat transfer as function of Rayleigh for $A = 1$. A comparison between our results and literature.

Through four ($\overline{\text{Nu}}, y_2$) points we fitted a second-order polynomial using a least squares fit. From this second-order polynomial we computed the averaged heat transfer for $y_2 = 0$. This Nusselt number is called the averaged Nusselt number with zero grid size. The same procedure has been repeated with a larger number of grid nodes in both the y- and x-direction. It appeared that the results showed a difference less than 0.3 percent. The method of varying the nonlinearity parameter of the grid is described more detailed in Schinkel [9]. It took about 3 min CPU time to reach a converged situation and 30 s CPU time were needed to correct the results for the grid. All calculations were performed on a IBM 370/158 computer.

Results

As a test problem for the numerical method and the grid size, we considered the case $A = 1$. In Fig. 2, $\overline{\text{Nu}}$ is shown as function of Ra for the (pc) and (ad) boundary conditions.

Our results with (pc) are in excellent agreement with Denny and Clever [11] and Roux [7], who used high accurate methods. Also, in the (ad) case the agreement with Roux [7] is rather good. In Fig. 2(*b*), also, the results of De Vahl Davis [13], who used 11 × 11 grid nodes, are shown. These results show some deviation caused by the coarse grid.

Nomenclature

a_o = thermal diffusivity of air, m^2/s
A = aspect ratio: $A = H/D$,
D = distance between vertical walls, m
g = acceleration of gravity, m/s^2
Gr = Grashof number: $g\beta (T_h - T_c)D^3/\nu_o{}^2$
H = height of the enclosure, m
Nu(x) = local Nusselt number
$\overline{\text{Nu}}$ = averaged Nusselt number
p = dimensionless pressure
Pr = Prandtl number: ν_o/a_o
Ra = Rayleigh number: Gr.Pr
T_h = temperature hot wall, K
T_c = temperature cold wall, K
u = dimensionless velocity x-direction
v = dimensionless velocity y-direction
x = direction along the vertical walls
y = direction normal to the vertical walls
α_y = nonlinearity coefficient
β = coefficient of thermal expansion, K^{-1}
γ = stratification parameter: $(\tfrac{1}{4}\tau\text{Ra})^{1/4}$
θ = dimensionless temperature
ν = kinematic viscosity of air; m^2/s
ρ = density of air, kg/m^3
τ = vertical temperature gradient central point

Subscripts

o = reference temperature
max = maximum

For other aspect ratios, Table 1 shows the heat transfer relations $\overline{\text{Nu}} = a\,\text{Ra}^b$ for the case of perfectly conducting side walls ($A \geq 2$). These correlations fit our numerical results within 1 percent. We obtained the aspect ratio dependence of $\overline{\text{Nu}}$ for the case with pc side walls.

$$(\text{pc}): \overline{\text{Nu}} = 0.263\ \text{Ra}^{0.25} A^{-0.2} 8 \leq A \leq 18; 10^4 \leq \text{Ra} \leq 10^6 \qquad (8)$$

We note that the power for A is very sensitive for the aspect ratio considered. For increasing A and assuming that the flow will be laminar, a value of -0.25 can be expected. All numerical results are described more detailed in Schinkel [9].

Flow Regimes. In order to define the starting of the boundary layer regime, different criteria can be used. Eckert and Carlson [3] considered the horizontal temperature gradient at the central point $(\partial\theta/\partial y)_o$ of the enclosure. The starting of the boundary layer regime then is defined as the (Ra,A) combination where this gradient becomes zero for the first time. Gill [6] considered the shear stress at the central point $(\partial u/\partial y)_o$. He used as criterion that (Ra,A) combination where this stress becomes zero. From our calculations with (pc) side walls it appeared that

$$\left(\frac{\partial\theta}{\partial y}\right)_o = 0 \text{ for } \text{Ra} = 3.3\times10^3\times A \quad 2\leq A\leq 18 \qquad (9)$$

$$\left(\frac{\partial u}{\partial y}\right)_o = 0 \text{ for } \text{Ra} = 3.\times10^4\times A \quad 2\leq A\leq 18 \qquad (10)$$

Note that the shear stress becomes zero at a larger value of Ra/A than the horizontal temperature gradient. This follows also from the analytical solutions of Elder [4] and Gill [6] and is a typical effect of natural convection in enclosures as explained by Raithby and Hollands [14]. Grondin [5] obtained with adiabatic side walls that the horizontal temperature gradient becomes zero when Ra = $2.5 \times 10^3 \times A$.

Also, Gilly et al. [15] obtained a higher value of Rayleigh number for the starting of the boundary layer regime with perfectly conducting side walls than for adiabatic side walls. They obtained, respectively, Ra = 8500 and Ra = 7500. For adiabatic side walls and $A \geq 4$ they obtained Ra = $2.5\times10^3\times A$. The fact that the Rayleigh number for (pc)-side walls is smaller then for (ad)-side walls is caused by the heating of the fluid when it moves from the cold wall to the hot wall in the lower side wall region in the case of pc-side walls. Gill observed from the experimental results of Elder (with paraffin as the fluid) that $(\partial u/\partial y)_o$ becomes zero at Ra = $2 \times 10^4 \times A$, which is in good agreement with our results.

Table 1 Coefficients for the correlation: $\overline{\text{Nu}} = a\text{Ra}^b$ in the case of perfectly conducting side walls

A	a	b
2	0.176	0.26
3	0.193	0.25
4	0.190	0.25
6	0.180	0.25
8	0.173	0.25
11	0.162	0.25
18	0.148	0.25

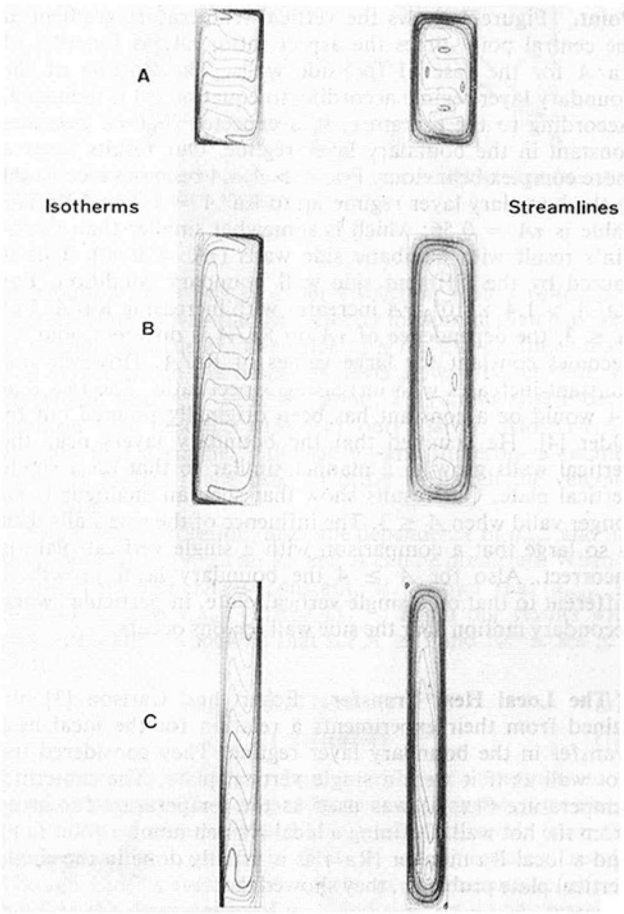

Fig. 3 Some typical examples of isotherms (left) and streamlines (right): (a) Ra = 6.6 × 10^5, A = 2, (pc); (b) Ra = 3.9 × 10^5, A = 4, (pc); (c) Ra = 2.0 × 10^5, A = 8 (ad)

Secondary Motion. The isotherms of Fig. 3 clearly show the stratification of the core region. The temperature in the vertical direction in the core region depends almost linearly on x and the temperature gradient in vertical direction is positive.

Secondary motion can be observed in Fig. 3. The secondary motion always starts in the form of a roll located near the side wall regions (Fig. 3(c)). From a careful inspection of all our computations with (pc)-side walls it appeared that this type of secondary motion occurs when Ra > $2.5 \times 10^4 \times A$ ($A \geq 2$). When secondary motion near the side wall regions is present, an increase of Ra/A causes the occurrence of secondary motion near the center of the enclosure as can be seen in Fig. 3(b). This type of secondary motion occurs at a Ra/A of about three times the critical Ra number for secondary motion near the side wall regions. A further increase of Ra/A causes tertiary motion located between the secondary motion described above (see Fig. 3(a)). The secondary motion has the same rotation as the primary motion, while the tertiary motion rotates in the opposite direction. As can be seen from the results of Linthorst and Schinkel [16], all these types of secondary motion have been observed in experiments. The secondary motion near the center of the enclosure has been obtained also in other investigations (e.g., Mallinson and De Vahl Davis [17]).

The secondary motion near the side wall region has not been mentioned in the literature known to us. It appeared that this type of secondary motion has an important effect on the stratification in the core region. This secondary motion is produced by the stratification in the side wall region. The mechanism can be described shortly as follows.

From a distance of about ¼D of the lower side wall the boundary layer near the hot wall starts to develop. The upward moving fluid is accelerated, which causes entrainment of fluid coming from the downward moving fluid layer. This leads to a positive vertical temperature gradient at y = ½. This stratification causes a decrease of the buoyancy force, but as long as the buoyancy force exceeds the viscous forces, there is an acceleration of the upward moving fluid. At a Rayleigh number at which there is no secondary motion, this process continues up to x = ½A, thus producing an almost constant positive vertical temperature gradient in the core region. However, if Ra exceeds some critical value, the initial stratification is so large that the viscous forces exceed the buoyancy force, already for $x < \frac{1}{2}A$. This causes a deceleration of upward moving fluid which gives rise to a secondary motion. The secondary motion smears the vertical temperature gradient, and therefore the buoyancy force remains constant in the region of secondary motion. But with increasing x, the viscous forces decrease. The buoyancy therefore again exceeds the viscous forces which leads to a new acceleration up to $x = \frac{1}{2}A$.

The Vertical Temperature Gradient At The Central Point. Figure 4 shows the vertical temperature gradient at the central point times the aspect ratio, τA, as function of Ra/A for the case of (pc)-side walls. The starting of the boundary layer regime according to equation (9) is indicated. According to the literature, it is expected that τA becomes constant in the boundary layer regime. Our results show a more complex behaviour. For $A > 4$, τA becomes a constant in the boundary layer regime up to Ra/A = 1.4×10^4. The value is $\tau A = 0.56$, which is somewhat smaller than Grondin's result with adiabatic side walls (τA = 0.60). This is caused by the different side wall boundary condition. For Ra/$A > 1.4 \times 10^4$, τA increases with increasing Ra/A. For A ≤ 3, the dependence of τA on Ra/A is different, and τA becomes constant for large values of Ra/A. However this constant increases with increasing aspect ratio. The fact that τA would be a constant has been originally pointed out by Elder [4]. He assumed that the boundary layers near the vertical walls grow in a manner similar to that on a single vertical plate. Our results show that such an analogue is no longer valid when $A \leq 3$. The influence of the side walls then is so large that a comparison with a single vertical plate is incorrect. Also for $A \geq 4$ the boundary layer growth is different to that on a single vertical plate, in particular when secondary motion near the side wall regions occurs.

The Local Heat Transfer. Eckert and Carlson [3] obtained from their experiments a relation for the local heat transfer in the boundary layer regime. They considered the hot wall as if it were a single vertical plate. The centerline temperature $\theta(x,\frac{1}{2})$ was used as the temperature far away from the hot wall. Defining a local Nusselt number (Nu$'(x)$) and a local Ra number (Ra$'$) as is usually done in the single vertical plate problems, they showed that

$$\mathrm{Nu}'(x) = a\mathrm{Ra}'(x)^b \qquad (11)$$

For $b = 0.3$, this relation showed reasonable agreement with their experiments.

As we described in the preceding section, an analogue based upon a single vertical plate cannot be correct, particularly for those Ra/A where secondary motion is present. However, we followed Eckert and Carlson in order to verify to what extent the vertical plate analogue holds and to investigate which modifications have to be made.

Using the same model as Eckert and Carlson, it can be shown [9] that in terms of our local Nusselt number and Ra number, equation (11) can be written as

$$\mathrm{Nu}(x) = a\mathrm{Ra}^b(1-\theta(x,\tfrac{1}{2}))^{b+1}x^{3b-1} \qquad (12)$$

The values of a and b can be obtained from the local Nusselt number at $x = \frac{1}{2}A$. In that case $\theta(x,\frac{1}{2}) = \frac{1}{2}$ and is no longer a variable. We correlated Nu ($\frac{1}{2}A$) both with Ra (A constant) and with A (Ra constant). For $A \geq 4$ and $10^5 \leq \mathrm{Ra} \leq 4 \times 10^5$, it appeared that in both cases the value for b is close to $\frac{1}{4}$. A correlation of Nu($\frac{1}{2}A$) with Ra/A showed that with $b = \frac{1}{4}$ our computations satisfy the correlation within 1 percent. Therefore we can conclude that in equation (12), $b = \frac{1}{4}$. This value has also been obtained in the single vertical plate problems when the flow is laminar and stationary.

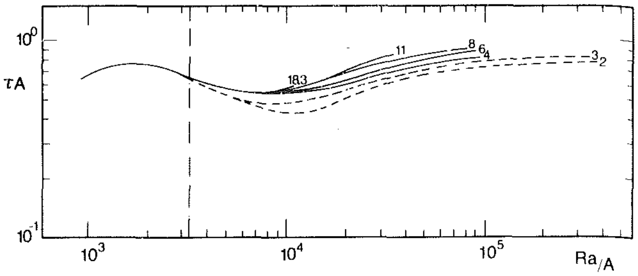

Fig. 4 τA as function of Ra/A at different aspect ratio: -.-.-., starting of the boundary layer regime

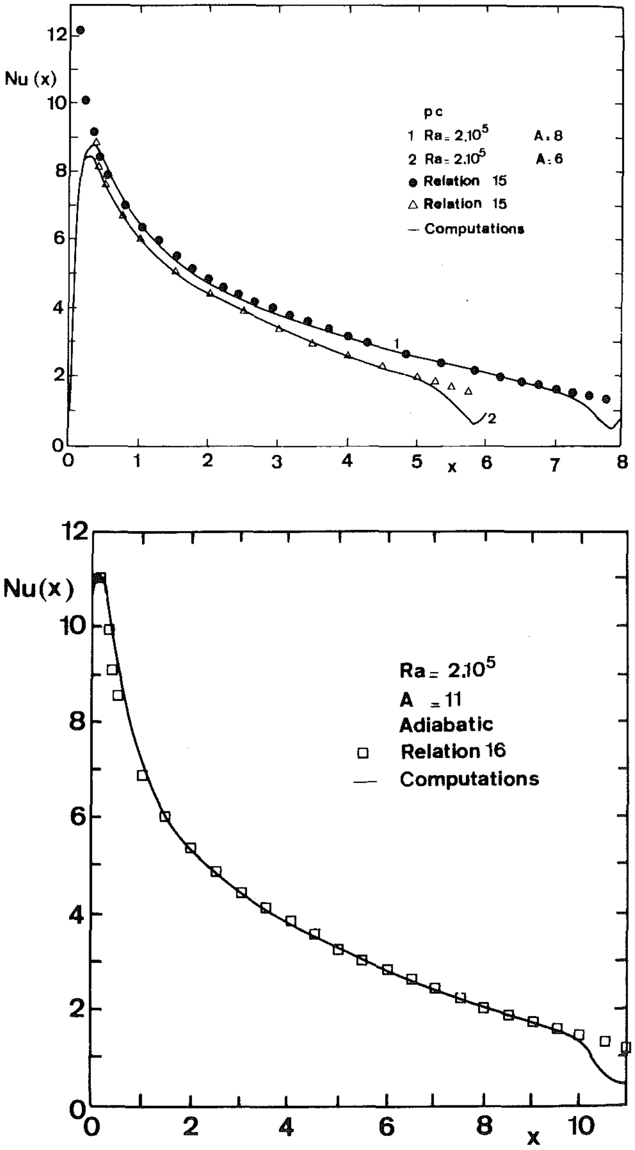

Fig. 5 The local heat transfer as function of x

With the value of b (and a) thus obtained we determined if equation (12) holds for $x \neq \frac{1}{2}A$. It appeared that the agreement is worse for $x \neq \frac{1}{2}A$. For $x < \frac{1}{2}A$, Nu(x), according to equation (12), is too large, while $x > \frac{1}{2}A$ Nu(x), according to equation (12), is too small. Since the difference with the case $x = \frac{1}{2}A$ is only the fact that $\theta(x,\frac{1}{2})$ enters as a parameter, we concluded that the centerline temperature is not a correct temperature far away from the plate. Therefore, we assumed that in equation (12) a different temperature, $\theta'(x)$, has to be used. We required that $\theta'(\tfrac{1}{2}A) = \theta(\tfrac{1}{2}A, \tfrac{1}{2}) = \tfrac{1}{2}$. Using our local heat transfer results we determined the relation between $\theta'(x)$. It appeared that $\theta(x)$ depends linearly on x

$$\theta'(x) = C + \tau' x \tag{13}$$

Moreover, we obtained that $\tau' A$ is constant

$$\text{(pc): } \tau' A = 0.40$$

$$\text{(ad): } \tau' A = 0.46 \tag{14}$$

Using these constants and the values for b and a obtained from our results at $x = \tfrac{1}{2}A$, it follows that

$$\text{(pc): } \mathrm{Nu}(x) = 0.519 \mathrm{Ra}^{1/4} x^{-1/4} (0.70 - 0.40x/A)^{1.25} \tag{15}$$

$$\text{(ad): } \mathrm{Nu}(x) = 0.526 \mathrm{Ra}^{1/4} x^{-1/4} (0.73 - 0.46x/A)^{1.25} \tag{16}$$

These relations hold for $A \geq 4$ and $10^5 \leq \mathrm{Ra} \leq 4 \times 10^5$. The agreement with our computations is excellent as can be seen from Fig. 5. Except near the side walls, deviations occur, which is obvious because the flow is different from the flow at a single vertical plate in these regions.

The fact that equations (15) and (16) are in excellent agreement with the computations is not surprising, since we used our computations in order to obtain the local heat transfer relations. The interesting results are the linear relation between $\theta'(x)$ and x and the fact that $\tau' A$ is a constant. This shows that a relation for the local heat transfer can be found by considering the hot wall as if it were a single vertical plate. In this model the fluid far away from the plate is stratified. However the stratification has to be taken smaller than the stratification in the core region. This lower stratification reflects the influence of the side walls on the convective motion. Moreover, our results show that the local heat transfer is proportional to $\mathrm{Ra}^{1/4}$ when the flow is in the boundary layer regime, laminar and stationary. The influence of the side wall boundary condition enters in a different stratification and a different proportionality constant.

Our relations for the local heat transfer are not in agreement with the relation of Eckert and Carlson. The difference might occur from inaccuracies in the measurements and from the fact that the flow might be nonstationary in the experiments.

From equations (15) and (16), it follows that for large aspect ratios $\overline{\mathrm{Nu}}$ is proportional to $(\mathrm{Ra/A})^{1/4}$. Of course, this can only be true if the flow in the boundary layer regime remains laminar and stationary. From the experiments of Schinkel [9] and Elder [18], it is known that the flow becomes nonstationary and turbulent for large A. If a single vertical plate analogue also holds for turbulent flow, it can be expected that in that case $\overline{\mathrm{Nu}}$ becomes proportional to $\mathrm{Ra}^{1/3}$ and independent of A. However numerical computations with laminar stationary governing equations should obtain that $\overline{\mathrm{Nu}} \sim ((\mathrm{Ra}/A)^{1/4}$, when A is large. Grondin [5] indeed obtained that $\overline{\mathrm{Nu}}$ is proportional to $(\mathrm{Ra}/A)^{1/4}$.

The Velocity Distribution – Comparison With Elder's Theory. In Elder's analytical solution [4] the effect of stratification of the core region is taken into account. This solution is an approximative one and holds for $x = \tfrac{1}{2}A$. The velocity in the x-direction $u(\tfrac{1}{2}A, y)$ is given as function of the stratification parameter $\gamma(\gamma = (\tfrac{1}{4}\tau \mathrm{Ra})^{1/4})$.

In Fig. 6, $u(\tfrac{1}{2}A, y)$ is shown as function of y. Because of the centrosymmetry only the results from $y = 0$ to $y = \tfrac{1}{2}$ are shown; $\mathrm{Ra} = 1.1 \times 10^5$, $A = 8$ and the side walls are (pc); γ for this case is 6.77. A comparison with Elder's solution (with this value of γ) is given (profile 1). The approximate character of Elder's solution clearly can be seen. Only near $y = \tfrac{1}{2}$ is the agreement good. In Fig. 6, we also show a velocity distribution according to Elder's solution with a value of γ chosen in such a way that the velocity maximum match as well as possible (profile 2). The value of γ for this profile is 6.35. The agreement in the boundary layer now is better, but the agreement near $y = \tfrac{1}{2}$ is less good. This shows that Elder's solution can describe $u(\tfrac{1}{2}A, y)$ only partly. Moreover it appears that a smaller value of γ – and therefore a smaller value of τ – has to be used in order to match the velocity maximum.

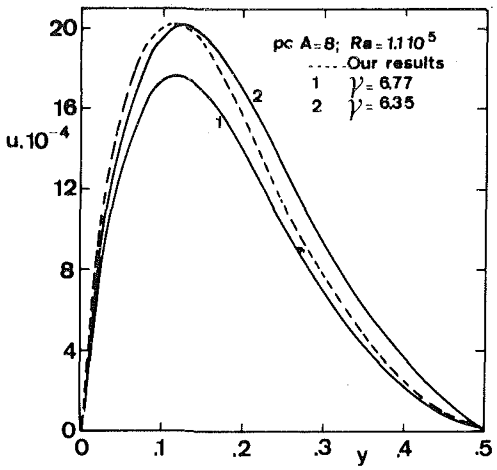

Fig. 6 The velocity in the *x*-direction at *x* = *A*/2 as function of *y*. Comparison with Elders theory.

From Elder's solution, also, the dependence of $u_{\max}$ and the location of $u_{\max}$ ($y_{\max}$) on Ra and A can be predicted. When it is assumed that τA is constant, it follows that $u_{\max} \sim (\mathrm{Ra}/A)^{-1/2}$ and $y_{\max} \sim (\mathrm{Ra}/A)^{-1/4}$. From our results with (pc) side walls it appeared that for $A \geq 3$ and $10^5 \leq \mathrm{Ra} \leq 4 \times 10^5$

$$u_{\max} = 0.277(\mathrm{Ra}/A)^{-0.49} \tag{17}$$

$$y_{\max} = 1.51(\mathrm{Ra}/A)^{-0.27} \tag{18}$$

The agreement of these relations with our computations is within 2 percent. Thus, dependence of $u_{\max}$ and $y_{\max}$ on Ra/A is in good agreement with Elder's solution (apart from the proportionality constant). This is an interesting result. Though Elder's solution is clearly an approximative one, it predicts the dependence of $u_{\max}$ and $y_{\max}$ on Ra/A correctly. One might conclude from equations (17) and (18) that τA is a constant. But as we described before, τA is not a constant. The above given dependence also has been obtained in our experiments [9].

Summary and Conclusions

In this paper we reexamined natural convection in vertical enclosures, with a special attention to the effect of stratification on the convective motion and heat transfer. It appeared that our results agree with highly accurate numerical schemes known from literature.

When the flow is in the boundary layer regime, secondary motion near the side walls occurs when $\mathrm{Ra}/A \geq 2.5 \times 10^5$ and $A \geq 2$ ((pc)-side walls). This type of secondary motion is caused by the stratification in the side wall regions. It appeared that this secondary motion has a large influence on the stratification in the center of the enclosure. τA does not become a constant as has been obtained in the literature. Secondary motion near the center of the enclosure occurs for $\mathrm{Ra}/A > 7 \times 10^4$, while at higher Ra/A tertiary motion has also been obtained. The results are in good agreement with flow visualization experiments of Linthorst and Schinkel.

From the analysis of the local heat transfer it appeared that the convective motion in the boundary layer regime can be modeled by considering the hot wall as if it were a single vertical wall with the fluid far away from the wall being stratified. However the stratification in this model has to be taken less than the stratification in the core region. Moreover, we determined that Nu(x) is proportional to $\mathrm{Ra}^{1/4}$. Also, $\overline{\mathrm{Nu}}$ is proportional to $\mathrm{Ra}^{1/4}$. The influence of the side walls and their boundary condition enters in a complex aspect ratio dependence. For large aspect ratio, $\overline{\mathrm{Nu}}$ is proportional to $A^{-1/4}$. These results are only valid for laminar flow.

The approximative character of Elder's solution has been demonstrated. However, the dependence of the maximum velocity in the boundary layer at $x = \frac{1}{2}A$ and its location agrees – apart from a proportionality constant – with the predicted dependence according to Elder's solution.

Acknowledgement

This work was supported by the Dutch Foundation for Pure Scientific Research (ZWO).

References

1 Ostrach, S., "Natural Convection in Enclosures," *Advances in Heat Transfer*, Vol. 8, 1972, pp. 161-227.

2 Catton, I., "Natural Convection in Enclosures," *Proceedings of the Sixth International Heat Transfer Conference*, Toronto, Canada, Vol. 6, Aug. 7-11, 1978, pp. 13-31.

3 Eckert, E. R. G., and Carlson, W. O., "Natural Convection in an Air-Layer Enclosed Between Two Vertical Plates With Different Temperatures," *International Journal of Heat and Mass Transfer*, Vol. 2, 1961, pp. 106-120.

4 Elder, J. W., "Laminar Free Convection in a Vertical Slot," *Journal of Fluid Mechanics*, Vol. 23, pt. 1, 1965, pp. 77-98.

5 Grondin, J. C., "Contribution à l'étude de la convection naturelle dans un capteur solaire plan," These, Institut du Mécanique des Fluides de Marseille, 1978.

6 Gill, A. E., "The Boundary-Layer Regime For Convection In A Rectangular Cavity," *Journal of Fluid Mechanics*, Vol. 26, pt. 3, 1966, pp. 515-536.

7 Roux, B., Grondin, J. C., Bontoux, P., and Gilly, B., "On A High Order Accurate Convection In A Vertical Square Cavity,' *Numerical Heat Transfer*, Vol. 1, 1978, pp. 331-349.

8 Boussinesq, J., "Theorie Analytique de Chaleur," Vol. II, p. 172.

9 Schinkel, W. M. M., "Natural Convection in Inclined Air-Filled Enclosures," Ph.D. thesis, Delft University of Technology, 1980.

10 Gosman, A. D., and Pun, W. M., "Lecture Notes for Course Entitled Calculations of Recirculating Flows," Imperial College of Science and Technology, London, 1973.

11 Denny, V. E., and Clever, R. M., "Comparisons of Galerkin and Finite Difference Methods for Solving Highly Nonlinear Thermally Driven Flows," *Journal of Computational Physics*, Vol. 16, 1974, pp. 271-284.

12 Ozoe, H., and Churchill, S. W., "Hydrodynamic Stability and Natural Convection in Ostwald de Waele and Ellis Fluids: The Development of a Numerical Solution," *AICHE Journal*, Vol. 18, 1972, pp. 1196-1207.

13 De Vahl Davis, G., "Laminar Natural Convection in an Enclosed Rectangular Cavity," *International Journal of Heat and Mass Transfer*, Vol. 11, 1968, pp. 1675-1693.

14 Raithby, G. D., and Hollands, K. G. T., "Analysis of Heat Transfer by Natural Convection Across Vertical Fluid Layers," ASME JOURNAL OF HEAT TRANSFER, Vol. 99, 1977, pp. 287-293.

15 Gilly, B., Bontoux, P., and Roux, B., "Influence Des Conditions Thermiques De Paroi Sur La Convection Naturelle Dans Une Cavite Rectangulaire Verticale, Differentiellement Chauffée," *International Journal of Heat and Mass Transfer*, Vol. 24, No. 5, 1981, pp. 829-841.

16 Linthorst, S. J. M., Schinkel, W. M. M., and Hoogendoorn, C. J., "Flow Structure With Natural Convection in Inclined Air-Filled Enclosures," ASME *Journal of Heat Transfer*, Vol. 103, No. 3, pp. 535-539.

17 Mallinson, G. D., and De Vahl Davis, G., "Three-Dimensional Natural Convection In a Box: A Numerical Study," *Journal of Fluid Mechanics*, Vol. 83, pt. 1, 1977, pp. 1-31.

18 Elder, J. W., "Turbulent Free Convection In A Vertical Slot," *Journal Fluid Mechanics*, Vol. 23, pt. 1, 1965, pp. 99-111.

K. S. Chang
Associate Professor,
Department of Aeronautical Engineering.
Assoc. Mem. ASME

Y. H. Won[1]

C. H. Cho
Graduate Student,
Department of Mechanical Engineering.

Korea Advanced Institute of
Science and Technology,
Seoul, Korea

Patterns of Natural Convection Around a Square Cylinder Placed Concentrically in a Horizontal Circular Cylinder

The Galerkin finite element method was used to analyze the natural convection heat transfer in an irregular enclosure made by two isothermal concentric horizontal cylinders: the inner square cylinder and the outer circular cylinder. Two different aspect ratios, $A/R=0.2$ and 0.4, are considered for two possible symmetric attitudes of the inner square cylinder. For the case of aspect ratio 0.4, experimental verification has also been made by obtaining field temperature measurement and streamline visualization. It is found that there is no boundary layer separation past the sharp edges of the inner cylinder in the range of Rayleigh numbers less than 10^5, although this phenomenon plays a negative role in the local and overall heat transfer. Above the upper horizontal surface of the inner square cylinder, a well-defined symmetric plume is found despite its low flow speed and temperature gradient. For the geometry of stand-on-edge position of the inner cylinder, vortex cores exist in the enclosure in quadruple for $Ra \leq 5.0 \times 10^4$ and $A/R=0.4$, and in double for other cases including $A/R=0.2$.

Introduction

Extensive studies have been made on natural convection heat transfer about relatively simple, but not necessarily easy, flow configurations for which convenient natural coordinate systems exist. They include buoyancy-driven flows about circular cylinders, spherical or elliptic bodies of revolution, flat plates, rectangular cavities and enclosures, triangles, concentric or eccentric circular annuli and spherical shells [1-23]. In the present paper, a study has been made on the laminar natural convection heat transfer from an inner isothermal horizontal square cylinder to an outer concentric circular cylinder, which was placed at a lower but constant temperature. Although the flow geometry appears unusual, this study is important in understanding how a buoyant boundary layer develops past sharp edges of the inner square cylinder and thus how the heat transfer characteristics are affected by their presence.

In the literature, natural convective flow about flat plates which are either vertical, horizontal, or inclined, has received much attention individually because of their fundamental importance. For the present problem all these basic configurations are readily produced by the surfaces of the inner square cylinder by simply rotating the whole system with respect to the direction of gravitation. In this case there is hydraulic and thermal interference between neighboring surfaces, of course, and it is this interference that makes the convective flow appear very interesting. In the practical view point, the present problem is also important since its result could be used to re-evaluate the performance of the conventional circular annuli in a comparative fashion.

The laminar forced momentum convection in a viscous fluid flow about two-dimensional rectangular bodies placed in a wind tunnel has been numerically investigated by Fromm and Harlow [24]. A small numerical perturbation introduced upstream has caused asymmetric, alternate vortex shedding behind the bluff surface of the rectangular body for Reynolds number greater than 50. For such a bluff body with sharp corners, separation occurs and subsequent trailing vortices are inevitable no matter how small the Reynolds number is. For the natural convective flow developed past a sharp-edged bluff body, however, it is not certain whether detachment of the boundary layer would occur in a considerable scale. What is known for sure at the moment is that the surface of a heated body plays the role of an energy supplier for the natural convection of the adjacent fluid medium, while the surface of a body in forced convection is an energy dissipator due to viscous friction. For the present problem, interaction among the thermally active neighboring surfaces of the inner square cylinder and existence of the enclosing outer circular cylinder produce patterns of natural convection very much different from those observable in the forced convections.

To study the possible flow patterns in the boundary layer, rising plumes and recirculatory vortex currents occuring in the process of natural convection heat transfer in the title enclosure, two most characteristic or symmetric geometries are considered among the infinitely many possible angular positions of the inner square cylinder. Aspect ratio A/R, the length of a side of the square cylinder scaled by the diameter of the circular cylinder, was allowed to have two different values, 0.2 and 0.4. In Fig. 1, we have shown a symmetric half of the several problem domains considered in the present paper: A and C stand for the stand-on-surface (SOS hereafter) position, B and D for stand-on-edge (SOE hereafter) position, A and B have $A/R=0.2$, and C and D have $A/R=0.4$. In consideration of the irregularity of the geometry, the Galerkin finite element method has been used to solve the laminar Boussinesq flow for some selected values of Rayleigh number. An experiment has also been conducted for the case of $A/R=0.4$ to obtain flow visualization and temperature measurements in the flow field.

Method of Formulation and Solution

We introduce nondimensional variables as follows,

$$x=x^*/R,\ y=y^*/R,\ u=\frac{u^*}{\mu/(R\rho_o)},\ v=\frac{v^*}{\mu/(R\rho_o)}$$

$$p=\frac{p^*}{\mu^2(R^2\rho_o)}\quad \text{and}\quad T=\frac{T^*-T_o}{T_i-T_o} \tag{1}$$

---

[1] Present Address: Daewoo Shipbuilding Industry Co.

Contributed by the Heat Transfer Division for publication in the JOURNAL OF HEAT TRANSFER. Manuscript received by the Heat Transfer Division October 27, 1981.

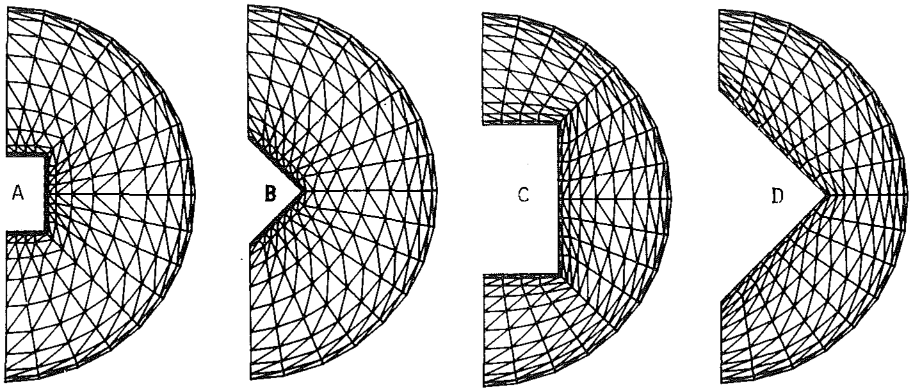

Fig. 1 Finite element mesh systems

The Boussinesq approximate equations are, when expressed in dimensionless form,

$$\frac{\partial u}{\partial x}+\frac{\partial v}{\partial y}=0 \tag{2}$$

$$u\frac{\partial u}{\partial x}+v\frac{\partial u}{\partial y}=-\frac{\partial p}{\partial x}-\mathrm{Gr}\,l_x T+\left(\frac{\partial^2 u}{\partial x^2}+\frac{\partial^2 u}{\partial y^2}\right) \tag{3}$$

$$u\frac{\partial v}{\partial x}+v\frac{\partial v}{\partial y}=-\frac{\partial p}{\partial y}-\mathrm{Gr}\,l_y T+\left(\frac{\partial^2 v}{\partial x^2}+\frac{\partial^2 v}{\partial y^2}\right) \tag{4}$$

$$u\frac{\partial T}{\partial x}+v\frac{\partial T}{\partial y}=\frac{1}{\mathrm{Pr}}\left(\frac{\partial^2 T}{\partial x^2}+\frac{\partial^2 T}{\partial y^2}\right) \tag{5}$$

The fluid properties here are treated as constant and the compressibility effect is neglected everywhere except for the buoyancy force terms, which provide the driving forces for the present flow. As boundary conditions, on the solid surface the no-slip condition is applied, and constant temperature $T=1$ and $T=0$ are taken on the inner and outer cylinders, respectively. On the vertical dividing line of symmetry, the conditions $u=0$, $\partial v/\partial x=0$, and $\partial T/\partial x=0$ are taken. The Galerkin finite element method was employed to solve the above boundary value problem using quadratic triangular elements, with linear interpolation applied for the pressure field. When the local element equations are assembled over the entire elements (see Fig. 1), one obtains a global matrix equation of the form

$$[\mathbf{C}(\mathbf{u})+\mathbf{K}]\mathbf{x}=\mathbf{F} \tag{6}$$

where,

$\mathbf{C}$ = convective matrix
$\mathbf{K}$ = diffusive matrix
$\mathbf{u}$ = velocity vector
$\mathbf{x}$ = vector of unknown nodal variables
$\mathbf{F}$ = force vector

Among the many possible ways of solving the above nonlinear matrix equation, the following two methods are considered:

(*a*) **Successive Substitution or Picard Iteration Method.** We write equation (6) as

$$[\mathbf{C}(\bar{\mathbf{u}}^{n+1})+\mathbf{K}]\mathbf{x}^{n+1}=\mathbf{F} \tag{7}$$

Hence, the vector $\bar{\mathbf{u}}^{n+1}$ is taken as $\mathbf{u}^n$, i.e., the nonlinear coefficient matrix is locally linearized by taking the values of previous iteration. This successive substitution can be slightly modified by two different manipulations such as

Nomenclature

g = gravitational acceleration
k = thermal conductivity of the enclosure fluid
l_x = cosine of the angle between x-axis and gravity force
l_y = cosine of the angle between y-axis and gravity force
n = coordinate in the direction normal to a boundary
p = scaled static pressure; see equation (1)
q = local heat flux, $-k\partial T/\partial n$
x, y = scaled Cartesian coordinates; see equation (1)
u, v = scaled velocity components in x- and y-directions, respectively; see equation (1)
A/R = aspect ratio, the length of a side of the square cylinder scaled by the diameter of the outer circular cylinder.
Gr = Graschof number, $g\beta R^3 (Ti-To)/\nu^2$
K = local heat flux for an equivalent pure-conduction problem, $-k\partial T_c/\partial n$
$\bar{K}$ = overall heat flux for an equivalent pure-conduction problem, $\int_s K ds$
$\bar{K}_{0.2}$ = the value of $\bar{K}$ for $A/R=0.2$
K_{eq} = local equivalent conductivity; see equation (14)
$\bar{K}_s$ = specific overall conductivity; see equation (15)
$\bar{K}_{eq}$ = equivalent overall conductivity; see equation (16)
Pr = Prandtl number, ν/α
R = radius of the outer circular cylinder
Ra = Rayleigh number, $g\beta R^3 \cdot (Ti-To)/\nu\alpha$
T = nondimensional field temperature; see equation (1)
T_c = nondimensional field temperature for an equivalent pure-conduction problem
Ti, To = dimensional temperature along the inner and outer cylinders, respectively
α = thermal diffusivity of the enclosure fluid
β = volumetric thermal expansion coefficient
η = fraction of enclosure gap in a constant-ϕ direction; $\eta=0$ is inner cylinder and $\eta=1$ is outer cylinder
ϕ = azimuthal angle measured from the top; $\phi=0$ coincides with the gravitational direction
μ = viscosity
ν = kinematic viscosity
ρ_0 = density taken constant at a mean temperature

Superscript

$*$ = dimensional form

Subscript

w = heat transfer evaluated on the wall

$$\bar{\mathbf{u}}^{n+1} = \frac{1}{2}(\mathbf{u}^{n} + \mathbf{u}^{n-1}) \tag{8}$$

and

$$\bar{\mathbf{u}}^{n+1} = \frac{1}{2}(\mathbf{u}^{n} + \bar{\mathbf{u}}^{n}) \tag{9}$$

It has been found that among the above three methods the last yields the best result in stability and convergence for the natural convection of the present geometry.

(*b*) **Newton-Raphson Method.**

Equation (6) is written somewhat differently this time as

$$\mathbf{x}^{n+1} = -\mathbf{J}(\mathbf{x}^{n})\mathbf{R}(\mathbf{x}^{n}) + \mathbf{x}^{n} \tag{10}$$

where

$$\mathbf{R}(\mathbf{x}) = [\mathbf{C}(\mathbf{u}) + \mathbf{K}]\mathbf{x} - \mathbf{F} \tag{11}$$

$$\mathbf{J}(\mathbf{x}) = \partial\mathbf{R}(\mathbf{x})/\partial\mathbf{x} \tag{12}$$

The above standard form of the Newton-Raphson method can be again slightly modified by incorporating the earlier scheme, equation (9), as follows,

$$\mathbf{x}^{n+1} = -[\mathbf{C}(\bar{\mathbf{u}}^{n+1}) + \mathbf{K}]\mathbf{R}(\mathbf{x}^{n}) + \mathbf{x}^{n} \tag{13}$$

where $\bar{\mathbf{u}}^{n+1}$ is again taken as $(\mathbf{u}^{n} + \bar{\mathbf{u}}^{n})/2$. This modification has also resulted in fast convergence and manifested stability with high Rayleigh numbers.

In the above methods, one must invert the so-called global stiffness matrix, which is a large, unsymmetric, sparse, and hence, poorly banded matrix. A solution algorithm for this matrix equation is usually based on bandwidth [25] or skyline storage mode [26], or more recently the frontal method [27]. The last method exhibits excellence in saving core memory and machine time for poorly banded systems of simultaneous equations, and is adopted in the present paper.

In the initial stage, the solution was started with no-flow condition in the flow domain, i.e., $u = v = 0$ for $\mathrm{Ra} < 1.0 \times 10^{3}$. For higher Rayleigh numbers the converged solution at lower Rayleigh number was reused as initial values. Convergence was achieved with a criterion, $\| T^{n} - T^{n-1} \| / \| T^{n} \| < \epsilon$, where ϵ is a prescribed small positive value. A triangular mesh system was chosen for the present problem as shown in Fig. 1. The value of ϵ taken for the convergence criterion was 0.001 and in no case did the iteration number exceeded eight for the Rayleigh numbers considered in this study.

Experimental Procedure

Two experimental models were constructed for $A/R = 0.4$: one for quantitative measurement of field temperature, and the other for flow visualization. The measurement model was made of copper tubes 2-mm thick and 25-cm long. The inner square cylinder was dimensioned 4cm × 4cm, and the concentric outer circular cylinder of 10-cm inner diameter was shrouded with an annular cooling jacket of similar design as in [19]. Here, the coolant was allowed to flow helically by a long metal strip inserted into the jacket space in a spiral form. The inner square cylinder was heated by a Nichrome resistance wire of 4 KΩ/m placed inside. Fine, dried, uniform-mesh metal powder was filled in the square cylinder around the resister wire to improve temperature uniformity in all directions. A regulated d-c power supply was used to provide a constant electrical energy source. Experiments were conducted using air at atmospheric pressure. Water was first used as a coolant, but it was found later than an air stream of room temperature was also sufficient for the various Rayleigh numbers considered in the present paper. The system normally required 3 to 4 hrs before settling to a steady state. Circumferential deviation of the nondimensional temperature from the isothermal condition was less than 0.5 percent for the outer circular cylinder and 0.1 percent for the inner square. Maximum longitudinal deviation registered less than 0.1 percent. To compare with the calculated results, the temperature was measured in the convection space, for Rayleigh numbers higher than 5.0×10^{4}, along the radial lines of azimuthal angle 0, 45, 90, 135, and 180 deg.

On the other hand, the visualization model was made using a plexiglass circular outer cylinder with air cooling on the surface. It allowed illumination light, whose beam was made straight and parallel by letting it pass through a series of lattice openings, to enter the convection space through a narrow circumferential optical slit made on the outer surface of the circular cylinder. After introducing a small quantity of cooled smoke as a tracer, a disturbance was rapidly transported by convection and diffusion to a quasi-steady state. In this transient process toward the equilibrium, flow visualization became possible and in this respect the streamlines visualized by smoke tracer were not closed, as has been also experienced by Powe et al. [28–29]. To avoid possible flow disturbance by the heating effect of the illumination light, visualization photographs were taken using an instantaneously bursting stroboscope light synchronized with the camera shutter.

Results and Discussion

In the present analysis, the numerical solution converged faster for the SOE position than the SOS for fixed Prandtl number 0.708. Success was achieved in computing the laminar convection up to Rayleigh number 5.0×10^{5} for the SOE position ($A/R = 0.4$) and up to 1.0×10^{5} for other cases. For each iteration, about 600 CPU seconds were consumed by Cyber-174 computer at KAIST Computing Center. To present the results, we define three wall conductivities as follows:

(*a*) the equivalent local conductivity

$$K_{eq} = q_{w}/K_{w} \tag{14}$$

(*b*) the specific overall conductivity

$$\bar{K}_{s} = \bar{K}/\bar{K}_{0.2} \tag{15}$$

(*c*) the equivalent overall conductivity

$$\bar{K}_{eq} = \left(\int_{s} q\, ds\right)/\bar{K} \tag{16}$$

In the preceding expressions, we have used $q = -k\partial T/\partial n$, $K = -k\partial T_{c}/\partial n$ and $\bar{K} = \int_{s} K\, ds$. Since the equivalent overall conductivity represents overall heat transfer as a multiple of pure-conduction heat flux for the same geometry, it can be used as an index showing relative importance of the convection heat transfer. To compare heat transfer between different geometries, one has to multiply the equivalant overall conductivity by the specific overall conductivity, $\bar{K}_{s}$. It then implies that the overall heat transfer is scaled by a common, pure-conduction heat flux obtained for $A/R = 0.2$, i.e., $\bar{K}_{0.2}$.

The Equivalent Overall Conductivity. The specific and equivalent overall conductivities are calculated and listed in Table 1. For a low Rayleigh number $\mathrm{Ra} = 1.0 \times 10^{3}$, the value of $\bar{K}_{eq}$ is seen to be nearly unity, implying that heat transfer is almost entirely that of pure conduction. This retarded convection is properly called pseudo-conduction by Grigull and Hauf [30]. From the values of $\bar{K}_{eq}$, it is noted that the contribution of convection to the overall heat transfer increases with higher Rayleigh numbers, which is the expected result. This increase is seen to be more pronounced for the smaller aspect ratio, $A/R = 0.2$, than for the case $A/R = 0.4$ for both SOS and SOE positions. For example, as the Rayleigh number is escalated from 1.0×10^{3} to 1.0×10^{5}, the increase in $\bar{K}_{eq}$ for

Table 1 Specific and equivalent overall conductivities (Pr = 0.7)

Attitude	A/R	$\bar{K}_s$		$\bar{K}_{eq}$
SOS	0.2	1.00	Ra = 10^3	1.003
			= 5×10^3	1.346
			= 10^4	1.644
			= 5×10^4	2.457
			= 10^5	2.846
	0.4	2.03	Ra = 10^3	1.002
			= 5×10^3	1.043
			= 10^4	1.126
			= 5×10^4	1.671
			= 10^5	1.991
SOE	0.2	1.00	Ra = 10^3	1.004
			= 5×10^3	1.346
			= 10^4	1.647
			= 5×10^4	2.482
			= 10^5	2.900
	0.4	2.03	Ra = 10^3	1.002
			= 5×10^3	1.046
			= 10^4	1.153
			= 5×10^4	1.762
			= 10^5	2.142
			= 5×10^5	3.207

$A/R = 0.4$ is on the order of 1.99 for the SOS and 2.14 for the SOE position; for $A/R = 0.2$, this increase is 2.84 for the SOS and 2.89 for SOE position. The role of convection heat transfer thus becomes important when the convection enclosure becomes more spacious. However, it should be noted that the overall heat transfer itself, which is obtained by $\bar{K}_{eq} \times \bar{K}_s \times \bar{K}_{0.2}$, is much higher for $A/R = 0.4$ than for $A/R = 0.2$, because of the doubled heat-conduction contribution or value of $\bar{K}_s$.

Comparison of $\bar{K}_{eq}$ for different attitudes but with the same aspect ratio reveals that slightly more heat is transferred for the SOE than the SOS position due to increased convection. For example, as the attitude is changed for a fixed value Ra = 1.0×10^5 from the SOS to SOE, a 1.9 percent increase in $\bar{K}_{eq}$ is seen for $A/R = 0.2$, whereas a 7.6% increase is obtained for $A/R = 0.4$. This observation indicates that the attitude effect is very small for low aspect ratios but becomes increasingly important for higher aspect ratios. There would be, then, a certain small aspect ratio ($A/R < 0.2$) for which the overall heat transfer is little affected by the attitude of the inner cylinder. In other words, in this case the inner cylinder is "small" enough so that the outer boundary cannot tell what its shape looks like, or the inner cylinder behaves as if it were a circular cylinder which has no directional dependence. The equivalent overall conductivity in Table 1 can be expressed by the correlation equations in the Rayleigh number range shown: for $A/R = 0.2$,

$$\bar{K}_{eq} = 0.1803 \text{ Ra}^{0.240} \text{ (SOS; } 10^4 \le \text{Ra} \le 10^5\text{)} \tag{17}$$

$$\bar{K}_{eq} = 0.1693 \text{ Ra}^{0.247} \text{ (SOE; } 10^4 \le \text{Ra} \le 10^5\text{)} \tag{18}$$

and for $A/R = 0.4$,

$$\bar{K}_{eq} = 0.1155 \text{ Ra}^{0.247} \text{ (SOS; } 10^4 \le \text{Ra} \le 10^5\text{)} \tag{19}$$

$$\bar{K}_{eq} = 0.0975 \text{ Ra}^{0.268} \text{ (SOE; } 10^4 \le \text{Ra} \le 5 \times 10^5\text{)} \tag{20}$$

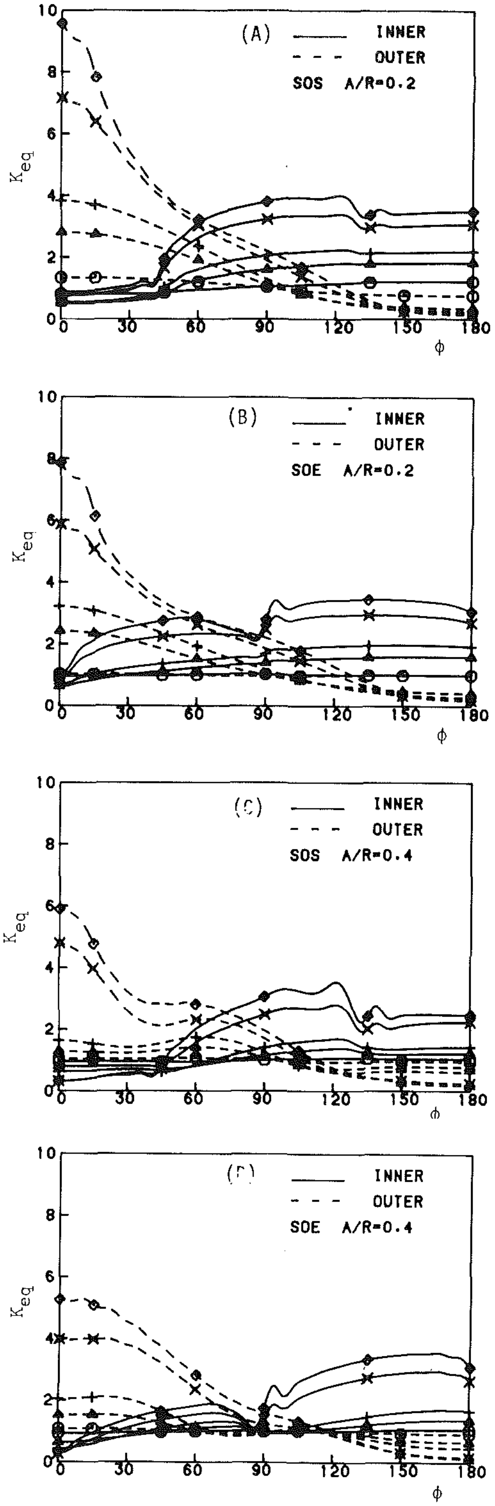

Fig. 2 Local equivalent conductivity for various Rayleigh numbers: ○ (10^3, Δ(5×10^3), + (10^4), × (5×10^4), and ◇ (10^5)

The Equivalent Local Conductivity. The equivalent local conductivity on the cylinder walls is graphically represented in Fig. 2. From this figure it can be seen that the 90 deg sharp corners have a significant effect on the convection heat transfer. In Fig. 2(*a*) and 2(*b*) for $A/R = 0.2$, the equivalent conductivity for the outer cylinder decreases more or less monotonically with the increasing azimuthal angle, ϕ, measured from the top. However, for the larger aspect ratio $A/R = 0.4$ (see Fig. 2(*c*) and 2(*d*)), the monotony is broken due to the effect of nearby sharp corners of the inner cylinder. This is manifested by the large and small depressions in the K_{eq} curves of the outer cylinder near 45 and 135 deg in Fig. 2(*c*) and near 0, 90 and 180 deg in Fig. 2(*d*). The sharp corner effect is even stronger on the inner cylinder itself. The sudden depressions and small recovery upheavals in the K_{eq} curves of the inner cylinder around each edged corner reveal this.

On the outer cylinder, maximum local heat transfer occurs at the top or $\phi = 0$ deg, and minimum at the bottom or $\phi = 180$ deg. If the enclosure were a concentric annulus, a reversed phenomenon would be expected for the inner cylinder. For the present inner square cylinder, however, the maximum heat transfer occurs off the bottom point although the minimum takes place at the usual point, $\phi = 0$ deg. The maximum heat transfer point is located for the SOS position (Fig. 2(*a*) and 2(*c*)) on the lower part of the vertical side wall, off the corner region, and for the SOE (Fig. 2(*b*) and 2(*d*)) on the lower inclined wall after the corner effect is diminished. For the SOS cases, it is noteworthy that the local heat transfer is about constant on the bottom and top horizontal surfaces of the inner cylinder, while it decreases steadily as the buoyant boundary layer flows upward along the vertical side wall. Similar steady decrease in heat transfer is observed along the ± 45 deg inclined surfaces in the case of SOE positions except in the neighborhood of the corner regions. It is noted that the reduced maximum heat transfer on the outer cylinder for the case of SOE, in comparison with the SOS, can be attributed to the effect of the nearby sharp edge at $\phi = 0$ deg.

As the Rayleigh number is decreased, the corner effect is seen also decreased by a significant amount; in the pseudo-conduction region ($\mathrm{Ra} < 4 \times 10^3$), it is almost unobserved. For high Rayleigh numbers the effect of corner is amplified dramatically.

It is clear from the above discussions that the sharp-edged corner plays a negative role in convection heat transfer although its local conduction heat transfer is a little higher than in other places, and that the attitude of the inner square cylinder is therefore important for high Rayleigh number convection.

Field Temperature and Streamlines. In Figs. 3 and 4, for fixed aspect ratio $A/R = 0.4$, the radial temperature curves obtained through calculation are plotted for two different Rayleigh numbers. Data from experimental measurement are also presented for purposes of comparison. It is observed that the overall comparison between theory and experiment is satisfactory, implying adequacy of the present finite element mesh system.

The phenomenon of temperature inversion, which means that fluid medium in the region close to the hot inner surface is cooler than that close to the colder outer surface, is found near $\phi = 90$) deg for the SOS and near $\phi = 45$ deg for the SOE position. It suggests that the convection current is most strong near the vertical side walls of the inner cylinder for the SOS, and near the upper inclined walls for the SOE. The slope of the temperature curves near the wall, or the local wall heat flux, q_w, is about constant and very small near the outer cylinder in the region between $\phi = 135$ and 180 deg for the case of SOS. The almost stagnant fluid of relatively large scale located at the bottom of the convection space is thought responsible for this. On the other hand, the temperature curves in Fig. 4 suggest that the bottom inert region is much reduced in size for the SOE position.

The aforementioned facts are well confirmed by the smoke visualization of streamlines shown in Figs. 5 and 6. The strong vortices are located near the vertical side walls for the SOS and near the upper inclined walls for the SOE. For the SOS position, the size of the inert fluid layer at the bottom is seen to be much larger than for the SOE.

Detail of Flow Patterns

We now direct our attention to the detailed flow patterns characterized by the more intuitive quantities, the isotherms and velocity vectors. They are shown in Figs. 7-10 for four different Rayleigh numbers between 5.0×10^3 and 1.0×10^5

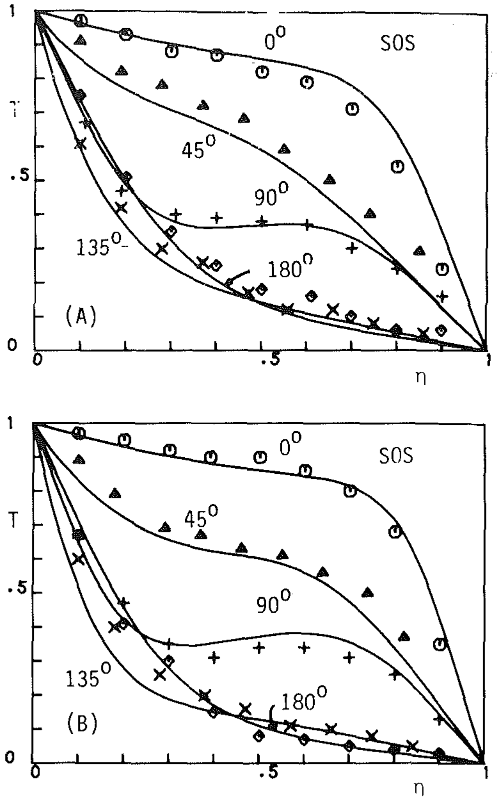

Fig. 3 Radial temperature distribution for SOS ($A/R = 0.4$): – from theory; ○ ($\phi = 0$ deg), △ (45 deg), + (90 deg), × (135 deg) and ◇ (180 deg) from experiment. Rayleigh numbers: $A = 5.0 \times 10^4$ (theory) and 5.25×10^4 (experiment), $B = 10^5$ (theory), and 1.10×10^5 (experiment)

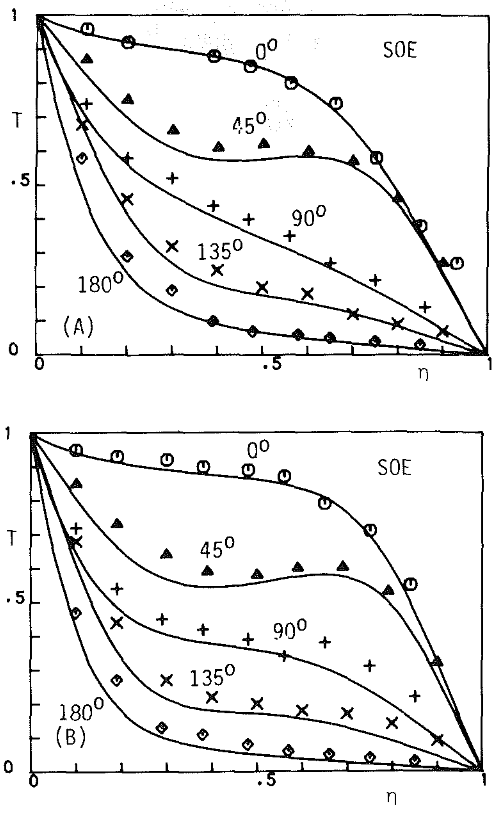

Fig. 4 Radial temperature distribution for SOE ($A/R = 0.4$): – from theory; ○ ($\phi = 0$ deg), △ (45 deg), + (90 deg), × (135 deg) and ◇ (180 deg) from experiment. Rayleigh numbers: $A = 5 \times 10^4$ (theory) and 6.01×10^4 (experiment), $B = 10^5$ (theory) and 1.15×10^5 (experiment)

and for the two different aspect ratios, 0.2 and 0.4. The isotherms in these figures suggest that convection is stronger for $A/R=0.2$ than for $A/R=0.4$. The degree of temperature inversion in the radial direction for the two Rayleigh numbers, $\mathrm{Ra}=5.0\times10^4$ and 1.0×10^5 is seen much higher for the case $A/R=0.2$. For $A/R=0.4$, the isotherms closely follow the contour for $\mathrm{Ra}=5.0\times10^3$, although there is already some convection current and the flow is nearly pseudo-conductive. As the Rayleigh number is increased, the near-conduction isothermal lines are distorted more and more by the convection current until strong temperature inversion occurs. For $A/R=0.2$, digression from conduction mode and onset of temperature inversion takes place at much lower Rayleigh numbers due to the enhanced natural convection in the more spacious room of the enclosure, as mentioned earlier. The plume above the heated inner cylinder is better developed for $A/R=0.2$ than for $A/R=0.4$ and causes higher maximum heat transfer for $A/R=0.2$ upon impingement on the outer cylinder at $\phi=0$ deg. The close local clustering of the isothermal lines with the increasing Rayleigh number is very indicative of development of the thermal boundary layers near the heated surfaces. For discussions on further flow characteristics, we now conveniently differentiate the two attitudes of the inner cylinder.

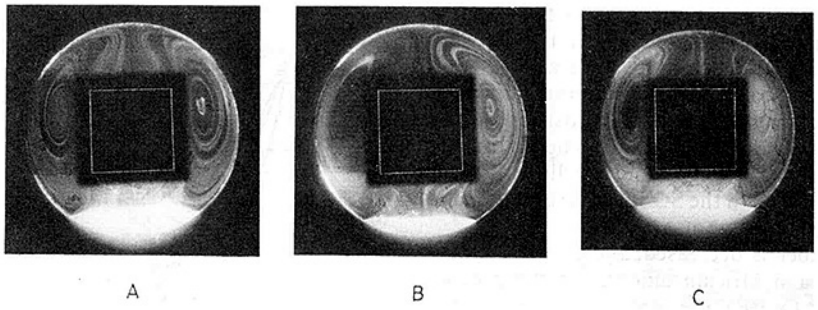

Fig. 5 Smoke streamline visualization, $P_r=0.708$. Rayleigh numbers: $A=7.15\times10^4$, $B=8.06\times10^4$, $C=1.17\times10^5$

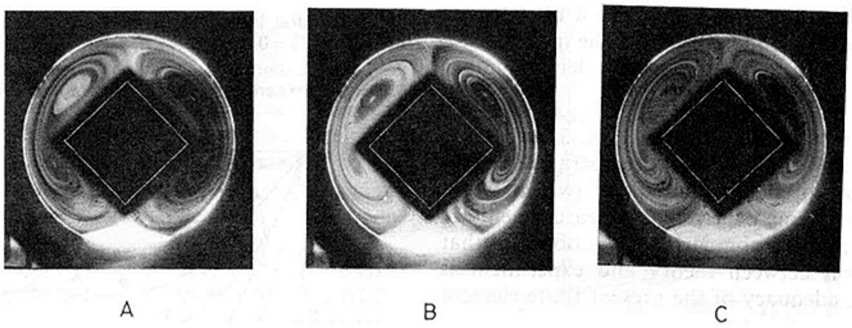

Fig. 6 Smoke streamline visualization, $P_r=0.708$. Rayleigh numbers: $A=3.95\times10^4$, $B=6.21\times10^4$, $C=1.05\times10^5$

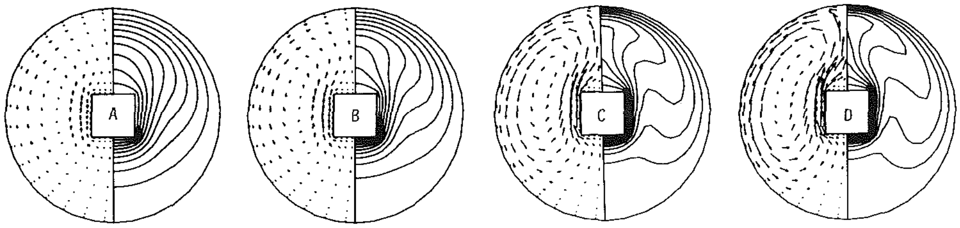

Fig. 7 Isotherms and velocity vectors for the SOS ($A/R=0.2$). Rayleigh numbers: $A=5\times10^3$, $B=10^4$, $C=5\times10^4$, and $D=10^5$

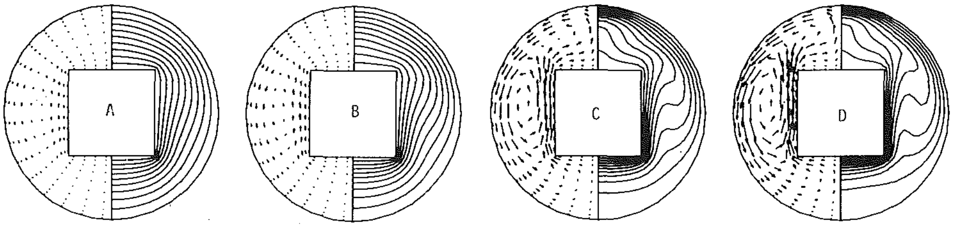

Fig. 8 Isotherms and velocity vectors for the SOS ($A/R=0.4$). Rayleigh numbers: $A=5\times10^3$, $B=10^4$, $C=5\times10^4$, and $D=10^5$

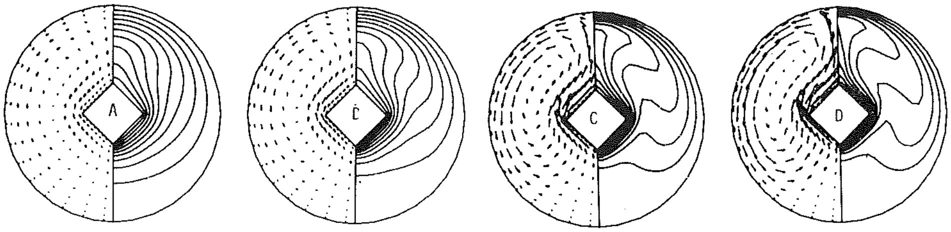

Fig. 9 Isotherms and velocity vectors for the SOE ($A/R = 0.2$). Rayleigh numbers: $A = 5 \times 10^3$, $B = 10^4$, $C = 5 \times 10^4$, and $D = 10^5$

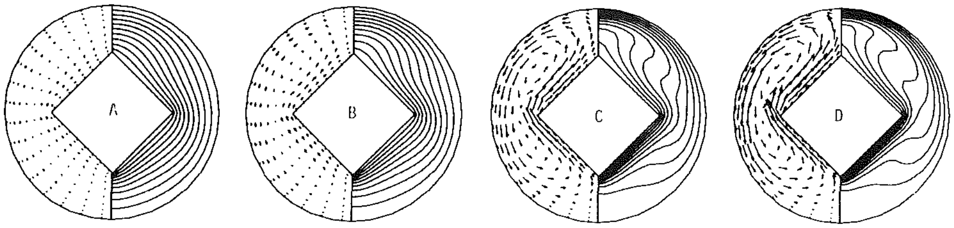

Fig. 10 Isotherms and velocity vectors for the SOE ($A/R = 0.4$). Rayleigh numbers: $A = 5 \times 10^3$, $B = 10^4$, $C = 5 \times 10^4$, and $D = 10^5$

(*a*) **The SOS Position.** The velocity vectors in Figs. 7 and 8 show that flow follows the contour of the sharp-edged inner heated square cylinder surprisingly well, although some small disturbances exist locally around the sharp corners. For high Rayleigh numbers, the thermal boundary layer is well developed along most of the surface of the inner cylinder except above the upper horizontal wall where the temperature gradient in normal direction is very small. Actually, the temperature curves for $\phi = 0$ deg in Fig. 3, which has about constant and small slope in the fraction of gap $0 \leq \eta \leq 0.65$, suggest that conduction is dominant and flow is only slowly convected right above the inner cylinder. That is, the buoyancy force is directed unfavorably away from the upper surface and the flow is consequentially retarded significantly. However, it is noteworthy that there is no evidence of flow separation, with no counter-rotating twin eddies as might be expected from the experience of forced convection. As a matter fact, flow separation is prevented because of the strong thermohydrodynamic interactions between neighboring surfaces. The heated boundary layers rising fast along the vertical walls entrain the adjacent fluid medium with lower velocity above the upper horizontal surface, which would otherwise be stagnant or separated. Since supply of fresh fluids for entrainment cannot be continued in a steady state in this region, the rising thermal boundary layer is deflected as a whole following very closely the sharp-edged inner cylinder. This theoretical prediction on the symmetric well-attached recirculating flows is confirmed experimentally by the smoke streamlines in Fig. 5. The existence of twin vortices, the dividing streamline above the inner cylinder and the attached flow patterns, are clearly demonstrated. It is observed experimentally, however, that separation could occur for the unsteady flows which might be easily introduced for the SOS position by such small disturbances as turbulent smoke injection, strong sustained illumination for observation purpose, and deviation from the exact geometrical symmetry.

(*b*) **The SOE position.** For the larger aspect ratio, $A/R = 0.4$, at lower Rayleigh numbers $\mathrm{Ra} \leq 5.0 \times 10^4$, the recirculating flow in the symmetric half of the convection space has exhibited two vortex cores within one overall large rotating current (see Fig. 10). These two subvortices are circling in the same direction, and it is concluded, therefore, that to avoid a large shear stress between the two vortices there must be a dead flow region inbetween. This dead flow occurs locally near the 90-deg edge at $\phi = 90$ deg making the heat transfer in this direction dominated by the conduction mode. This is quantitatively verified by the almost straight temperature curve along $\phi = 90$ deg in Fig. 4(*a*). In contrast to the previous SOS position, the thermal boundary layer is well defined everywhere on the inner cylinder, including the sharp-edged corners. Some slight local disturbances are seen in the velocity vectors around the sharp corner at $\phi = 90$ deg, but again there is no evidence of flow separation. For the present geometry the walls of the inner cylinder is inclined by either $+45$ deg or -45 deg, making the force component normal to the wall smaller than that for the SOS position. Such a flow pattern agrees qualitatively well with that of the natural convection obtained by the finite element method for hexagonal cylinders by Gartling [31].

The tracer streamlines in the visualization photographs of Fig. 6 verify for $A/R = 0.4$ the theoretically predicted smaller vortices within each of the larger recirculating overall twin vortices. It is remarkable that these subvortices emerge into a single one, both in the theory and experiment alike, as the Rayleigh number is increased to about 1.0×10^5, the lower-positioned subvortex being weakened and absorbed by the outer stronger vortex.

For the smaller aspect ratio $A/R = 0.2$, the above corotating subvortices do not appear due to the enhanced convection mode at the same Rayleigh number.

Concluding Remarks

The Galerkin finite element solution has produced interesting results, part of which are experimentally confirmed. The two different aspect ratios considered in the present paper have suggested profound effect of the aspect ratio on the local and overall heat transfer. For a large aspect ratio, interesting corotating subvortices are found for the SOE-position in a limited Rayleigh number range due to the constricted convection space, which is virtually partitioned by the local dead flow regions near the sharp corners. Investigation of the local and overall equivalent conductivities has revealed that sharp edges of the inner cylinder has a negative effect in heat transfer. However, it has been possible to argue that for a certain small aspect ratio, the characteristics of the angled inner cylinder disappears and the inner cylinder begins to behave as if it were a circular cylinder. It has been also shown that the strong thermohydraulic interference between adjacent walls of the inner heated cylinder causes the thermal boundary layer in a steady state to follow closely the body configuration with no premature flow separation at all in the Rayleigh number range considered.

References

1 Kao, T-T., Domoto, G. A., and Elrod, H. G., Jr., "Free Convection Along a Nonisothermal Vertical Flat Plate," ASME JOURNAL OF HEAT TRANSFER, Vol. 99, Feb. 1977, pp. 72-78.

2 Sparrow, E. M., Patankar, S. V., and Abdel-Wahed, R. M., "Development of Wall and Free Plumes Above a Heated Vertical Plate," ASME JOURNAL OF HEAT TRANSFER, Vol. 100, May 1978, pp. 184-190.

3 Mucoglu, A., and Chen, T. S., "Mixed Convection on Inclined Surfaces," ASME JOURNAL OF HEAT TRANSFER, Vol. 101, Aug. 1979, pp. 422-426.

4 Boehm, R. F., and Kamyab, D., "Established Stripwise Laminar Natural Convection on a Horizontal Surface," ASME JOURNAL OF HEAT TRANSFER, Vol. 99, May 1977, pp. 294-299.

5 Flack, R. D., Konopnicki, T. T., and Rooke, J. H., "The Measurement of Natural Convective Heat Transfer in Triangular Enclosures," ASME JOURNAL OF HEAT TRANSFER, Vol. 101, Nov. 1979, pp. 648-654.

6 Raithby G. D., Hollands, K. G. T., and Unny, T. E., "Analysis of Heat Transfer by Natural Convection Across Vertical Fluid Layers," ASME JOURNAL OF HEAT TRANSFER, Vol. 99, May 1977, pp. 287-293.

7 Choi, I. G., and Korpela, S. A., "Stability of the Conduction Regime of Natural Convection in a Tall Vertical Annulus," *Journal of Fluid Mechanics*, Vol. 99, pt. 4, 1980, pp. 725-738.

8 Bejan A., and Tien, C. L., "Laminar Natural Convection Heat Transfer in a Horizontal Cavity With Different End Temperatures," ASME JOURNAL OF HEAT TRANSFER, Vol. *100*, Nov. 1978, pp. 641-647.

9 Kee, R. J., Landram, C. S., Miles, J. C., "Natural Convection of a Heat-Generating Fluid Within Closed Vertical Cylinders and Spheres," ASME JOURNAL OF HEAT TRANSFER, Vol. 98, Feb. 1976, pp. 55-61.

10 Chu, H. H.-S., Churchil, S. W., and Patterson, C. V. S., "The Effect of Heater Size, Location, Aspect Ratio, and Boundary Conditions on Two-Dimensional, Laminar Natural Convection in Rectangular Channels," ASME JOURNAL OF HEAT TRANSFER, Vol. 98, May 1976, pp. 194-201.

11 Chan, A. M. C., and Banerjee, S., "Three-Dimensional Numerical Analysis of Transient Natural Convection in Rectangular Enclosures," ASME JOURNAL OF HEAT TRANSFER, Vol. 101, Feb. 1979, pp. 114-119.

12 Ozoe, H., Yamamoto, K., and Sayama, H., "Natural Convection Patterns in a Long Inclined Rectangular Box Heated From Below, Part II: Three-Dimensional Numerical Results," *International Journal of Heat and Mass Transfer*, Vol. 20, 1977, pp. 131-139.

13 Potter, J. M., and Riley, N., "Free Convection From a Heated Sphere at Large Grashof Number," *Journal of Fluid Mechanics*, Vol. 100, pt. 4, 1980, pp. 769-783.

14 Kuehn, T. H., and Goldstein, R. J., "Numerical Solution to the Navier-Stokes Equations for Laminar Natural Convection about a Horizontal Isothermal Circular Cylinder," *International Journal of Heat and Mass Transfer*, Vol. 23, 1980, pp. 971-979.

15 Chen, T. S., and Mucoglu, A., "Analysis of Mixed Forced and Free Convection about a Sphere," *International Journal of Heat and Mass Transfer*, Vol. 20, 1977, pp. 867-875.

16 Merkin, J. H., "Free Convection Boundary Layers on Cylinders of Elliptic Cross Section," ASME JOURNAL OF HEAT TRANSFER, Vol. 99, Aug. 1977, pp. 453-457.

17 Raithby, G. D., and Hollands, K. G. T., "Laminar and Turbulent Free Convection From Elliptic Cylinders, With a Vertical Plate and Horizontal Circular Cylinder as Special Cases," ASME JOURNAL OF HEAT TRANSFER, Vol. 48, Feb. 1976, pp. 72-80.

18 Kuehn, T. H., and Goldstein, R. J., "An Experimental and Theoretical Study of Natural Convection in the Annulus Between Horizontal Concentric Cylinder," *Journal of Fluid Mechanics*, Vol. 74, 1976, pp. 695-719.

19 Kuehn, T. H., and Goldstein, R. J., "An Experimental Study of Natural Convection Heat Transfer in Concentric and Eccentric Horizontal Cylindrical Annuli," ASME JOURNAL OF HEAT TRANSFER, Vol. 100, 1978, pp. 635-640.

20 Burns, P. J., and Tien, C. L., "Natural Convection in Porous Media Bounded By Concentric Spheres and Horizontal Cylinders," *International Journal of Heat and Mass Transfer*, Vol. 22, 1979, pp. 929-939.

21 Ozoe, H., Shibata, T., and Churchill, S. W., "Natural Convection in an Inclined Circular Cylindrical Annulus Heated and Cooled on Its End Plates," *International Journal of Heat and Mass Transfer*, Vol. 24, No. 4, 1981, pp. 727-737.

22 Zebib, A., Schubert, G., and Straus, J. M., "Infinite Prandtl Number Thermal Convection in a Spherical Shell," *Journal of Fluid Mechanics*, Vol. 97, 1980, pp. 257-277.

23 Gebhart, B., "Buoyancy Induced Fluid Motions Characteristic of Application in Technology — The 1978 Freeman Scholar Lecture," ASME *Journal of Fluids Engineering*, Vol. 101, Mar. 1979, pp. 5-28.

24 Fromm, J. E., and Harlow, F. H., "Numerical Solution of the Problem of Vortex Street Development," *The Physics of Fluids*, Vol. 6, No. 7, July 1963, pp. 975-982.

25 Segelind, L. J., *Applied Finite Element Analysis*, 1976, John-Wiley & Sons Inc.

26 Hasbani, Y., and Engelman, M., "Out-of-Core Solution of Linear Equations with Nonsymmetric Coefficient Matrix," *Computers and Fluids*, Vol. 7, 1979, pp. 13-31.

27 Iron, B. M., "A Frontal Solution Program for Finite Element Analysis," *International Journal for Numerical Methods in Engineering*," Vol. 2, 1970, pp. 5-32.

28 Powe, R. E., Carley, C. T., and Bishop, E. H., "Free Convective Flow Patterns in Cylindrical Annuli," ASME JOURNAL OF HEAT TRANSFER, Vol. 91, 1969, pp. 310-314.

29 Powe, R. E., Carley, C. T., and Carruth, S. L., "A Numerical Solution for Natural Convection in Cylindrical Annuli," ASME JOURNAL OF HEAT TRANSFER, Vol. 93, 1971, pp. 210-220.

30 Grigull, U., and Hauf, W., "Natural Convection in Horizontal Cylindrical Annuli," *Proceedings of the Third International Heat Transfer Conference*, Paper No. 60, Vol. 2, 1966, pp. 182-195.

31 Gartling, D. K., "Convective Heat Transfer Analysis by the Finite Element Method," *Computer Methods in Applied Mechanics and Engineering*, Vol. 12, 1977, pp. 365-382.

Release Rate Model for Developing Fires

E. E. Smith
Professor.

S. Satija
Graduate Student.

Department of Chemical Engineering,
The Ohio State University,
Columbus, Ohio 43210

A mathematical model for predicting the course of a developing fire in a compartment is described. The model uses release rate data obtained from laboratory-scale tests to calculate the rate of heat and smoke generation within the compartment. From these data, the model predicts rate of involvement of combustible surfaces, upper layer temperatures, and smoke concentration as a function of time. The model is described by relationships used to determine: (i) ignition and rate of vertical fire propagation, (ii) release rates based on total heat released and incident flux, and (ii) heat losses by venting and accumulation within the boundaries of the compartment. Results of predicted by the model and observed in full-scale tests of furnished compartments are compared.

Introduction

A model which predicts the course of a developing fire by tracing the progressive involvement of combustible materials in its path is described. In this paper, major interest is on a "path" described by a fire plume contacting vertical (wall) and horizontal (ceiling) surfaces that the plume may ignite. The purpose of the model is to predict how the combustible materials or products will influence the course of such a developing fire.

In order to determine the effect different combustibles have a fire's propagation, a good description of combustibility is required; one that can describe the various factors which the combustible items contribute to the progress of the fire. Experimentally determined release rate data were used to obtain the pertinent factors for a model which was designed to utilize these data.

For this release rate model, the item-related properties that are needed are: thermal properties before ignition, ignition point, rate of heat and smoke release from involved surfaces, and rate of flame propagation at right angles to the fire plume. The plume-related properties are: dimensions, temperature, and emissivity.

The present model is restricted to those situations where venting rates are not restricted by the size of opening in the compartment, and bulk air oxygen concentration is not a limiting factor. For vertical surfaces under an imposed heat flux, heat release rates do not change significantly [2] as bulk oxygen concentration varies from 21 to 14 mole percent. Release rate tests made on horizontal surfaces indicate that heat release rates change with oxygen concentration. This is due to the decrease in radiant heat feedback from the longer plume as oxygen concentration decreases.

Release Rate Data. Equipment and procedures for obtaining release rate data used in this work have been described [1]. The release rate of heat and (visible) smoke is obtained using a representative section of the combustible items found in the fire compartment, and measured as a function of time at different levels of incident flux. A set of release rate data is illustrated by Fig. 1. Information used as input to the model is interpreted from these data. The variable "time" in the release rate test was transformed to a corresponding variable that can be related to a real fire situation where the sample is exposed to a varying incident flux. For those materials whose release rate varies with time, the change in heat and smoke release rate is a function of the thickness of the char layer formed. The depth of char layer is in turn a function of the total heat released from the sample. By cross plotting release rate data as rate of release versus total heat released, the test "time" is replaced by a variable (total heat release) that can be conveniently followed during the progress of a real fire.

The definition of the sample as tested makes analysis and interpretation of experimental data relatively simple. The extent of the sample, or more precisely, the exposed "surface" of the sample is taken to include the gas phase boundary generated by the sample during the release rate tests. By this definition the incident flux to the specimen's boundary is simply the externally generated, or applied, flux. The flux to the solid surface, or to the plane of decomposition

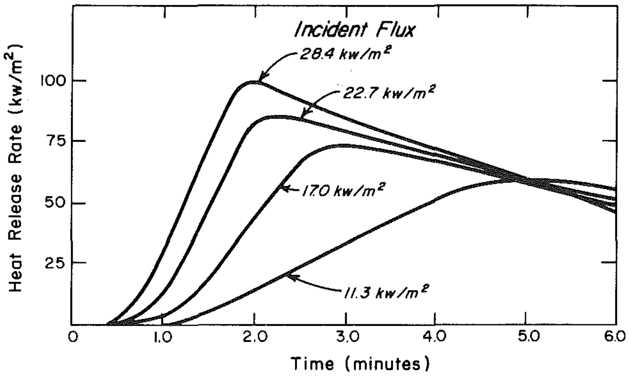

Fig. 1 Heat release of red oak

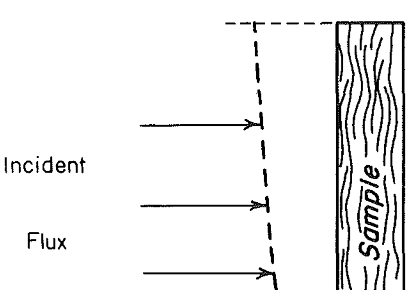

Fig. 2 Boundary of burning sample

Contributed by the Heat Transfer Division and presented at the 20th ASME/AIChE National Heat Transfer Conference, Milwaukee, Wisconsin, August 2-5, 1981. Manuscript received by the Heat Transfer Division November 4, 1981. Paper No. 81-HT-4.

in the solid in case of char-forming material, is not needed to interpret release rates. Figure 2 represents the sample. The release rate data is obtained experimentally in these terms – as a function of time and incident flux to the "boundary" of the sample as defined by Fig. 2.

In relation to modelling, there are advantages in thus defining the sample. First, release rates are determined solely as a function of applied flux and time. The model code then needs to determine only the incident flux to this boundary and keep an accounting of prior heat release to be able to effectively utilize experimental release rate data.

In an actual fire situation, the incident flux to a differential area may consist of radiant flux from a plume generated by burning fuel originating from surfaces below the differential area being considered. In either case the incident flux can be calculated if the temperature and emissivity of surroundings, and temperature, thickness, and emissivity of the plume are determinable.

The following describes how these various factors which enter into the calculation of the plume characteristics and the surroundings, together with the characteristics of the fuel source, are considered and applied in this release rate model.

Release Rate Model

The overall compartment model is based on a simple mass and energy balance *of the fire system* as illustrated by Fig. 3. The temperatures in the upper layer of the compartment are determined as a function of time by balancing heat losses and heat generated, the latter determined from release rate information on burning surfaces. The burning surfaces are predicted by the rate of surface involvement from the point of ignition.

Three major changes from an earlier release rate model [2] appear in this version:

(*i*) The criterion for fire propagation in the direction of the fire plume is determined from the flux-time history of the surfaces influenced by the plane and surroundings, not by surface temperatures or flame travel rate.[1]

(*ii*) The hot upper layer consists of two zones, one zone defined *by the continuation of the plume into the upper layer*. This effectively gives a three-zones, two-layer model.

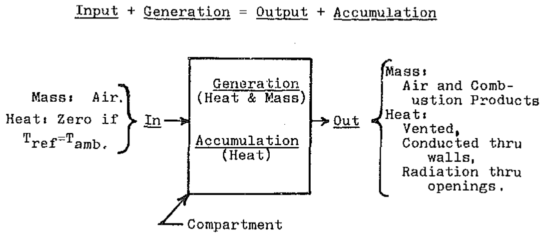

Fig. 3 Overall heat and mass balance

(*iii*) The rate of venting is equal to the "effective" entrainment into the plume in both the lower and upper thermal layers of the compartment.

Ignition-Propagation. Surface temperature is not an adequate measure of "ignition point" for many products used as wall linings, furniture, floorcoverings, etc., that make up the fuel load in real fire systems. The "point" of ignition, i.e., the criteria or conditions that describe when a product will "start to burn," (i.e., release heat if vapors are exposed to an ignition source), is based on a flux-time product (FTP) readily interpreted from release rate data [2].

The flux-time product of a material or product may be defined:

$$\mathrm{FTP} = \Sigma[\mathrm{Flux} - \mathrm{SPF})^{n}_{\Delta t}\ \Delta t]$$

where:

Flux = average incident flux over time increment, Δt
SPF = self propagating flux; that flux at which a flame will just propagate from a point of flame impingement
Δt = time span of incremented time
n = empirical constant; for many materials $n=1$; for retarded materials, n may be greater than 1.

At some level of FTP the sample will start to "burn" as indicated in Fig. 4 as the time when a significant rate of heat release occurs. The product of the excess flux (Flux – SPF) times the time to ignition is the minimum flux-time product for that heat flux. Calculation of the minumum flux-time product ($\mathrm{FTP}_{\min}$) is shown by Fig. 4, which illustrates the type of data used.

---

[1] Flame travel rate perpendicular to plume flow is still obtained from experimental flame travel rate values as a function of incident flux.

Nomenclature

A_e = area for entrainment
A_f = cross-sectional area of plume (flow area)
C_s = smoke concentration ("particles"/unit volume)
D_w = width of door (opening)
E = entrainment rate (mass/unit time)
e = entrainment coefficient
F = view factor
f_f = friction factor
$\dot{f}$ = "potential" heat of unburned combustible gases
g = acceleration due to gravity
h = heat transfer coefficient
H_v = heating value of decomposition products
ΔH = enthalpy
k = thermal conductivity
$\dot{m}$ = mass flow rate
$\dot{Q}_{ox}$ = heat released/mass oxygen consumed
$\dot{Q}_R$ = total rate of heat released to plume from wall
$\dot{Q}_s$ = total rate of heat released to plume from initiation source
r_h = rate of heat release per unit (exposed) area
$\dot{S}$ = flow rate of visible smoke ("particles"/s)
t = time
T = temperature
u = velocity
$\dot{V}$ = volumetric flow rate of plume
v_f = horizontal flame travel rate
ΔV = volume increment
x = depth (thickness) of plume
y = width of plume for center wall; for corner configuration, y = one side of corner
Z = height
ΔZ = height increment
σ = Stefan Boltzmann constant
ϵ = emissivity
ρ = density

Subscripts

a = ambient
c = convective
d = decomposition
e = entrained air
f = soffit
g = gas phase
i = in
k = increment number
l = lower layer
o = out
p = plume
r = radiative
s = surface
T = total
u = upper layer
w = wall

The minimum flux-time product has been determined for over 50 different materials and products. It has proven to be a more reliable method for describing ignition "point" than surface temperature for PVC samples, inorganic-faced laminates, FR materials, and nonthermally thick solids.

Normally, release rate curves at four or five different heat flux exposures are used to determine $(FTP)_{min}$, not just the two illustrated by Fig. 4. The $(FTP)_{min}$ values calculated at each of these flux levels consistently agree within ± 10 $(W/cm^2) \cdot s$.

Basing ignition on an incident flux rather than surface temperature also simplifies predicting the ignition point when modeling fire systems. Thermal properties of the materials are not needed; their effect has been accounted for in the experimental flux-time product determination.

Upper Layer. Upon observing compartment fire systems having combustible walls and noncombustible ceilings, it is obvious that a simple two-layer model cannot adequately predict the pattern of surface involvement for such a system. In corner configuration tests, fire spread up the walls, and its continuation along the ceiling and upper walls show that the plume continues into the upper thermal layer, producing a zone having a different temperature and velocity than the lower zone of the upper layer (Fig. 5).

In this release rate model, the plume is extended into the upper layer, with entrainment from the lower zone into the upper zone or plume. Vertical and horizontal temperature gradients in the upper layer observed in full scale tests indicate the presence of such a plume.

Venting. The pumping action of the fire in the lower layer plus the expansion of gases entrained into the plume from the lower zone was used to calculate the venting rate from the compartment. Since the application of the model is restricted to preflashover conditions, and the openings in the compartments modeled in this paper are large, the venting rates for fires examined are not restricted by size of opening.

Air entrained in the plume was calculated using the approach of J. B. Fang [3]. The air entrained in the lower layer was presumed to be vented from the upper layer. The air entrained from the lower zone into the plume (or upper zone) in the upper layer is heated and expands, producing an additional venting given by equation (12). The total mass interchanged in the upper layer is not vented; only that equivalent to the mass in the volume vented due to this expansion.

Model Code

The model's code is a bookkeeping device for fire-involved surfaces and other, nonburning surfaces in addition to making the calculations required to determine incident flux. The incident flux to a surface is from the fire plume and adjacent hot surfaces "seen" by the surface. To start, a fire initiation source, described by fire base dimensions and heat and smoke release rates as a function of time are read into the main program from Subroutine QSUB. This subroutine can be written to describe any initiation source such as a wood crib, propane burner, burning chair, waste container, etc. The initiation source may be placed in a corner, center wall, or center of the compartment. The entrainment coefficient and surface used to describe the air entrained into the lower plume will depend on location of the initiation source.

For corner and center wall fires the plume is assumed to contact the wall(s). Therefore, where combustible walls are present, the fuel contributed by the walls enters and is part of the plume from the initiating fire.

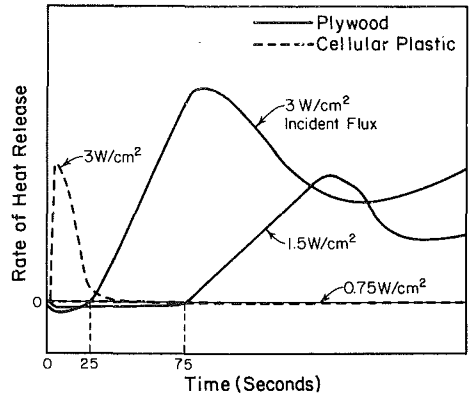

Fig. 4 Calculation of minimum flux-time product

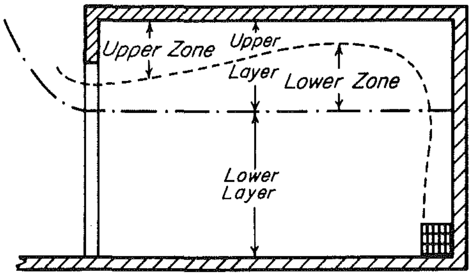

Fig. 5 Thermal zones in compartment

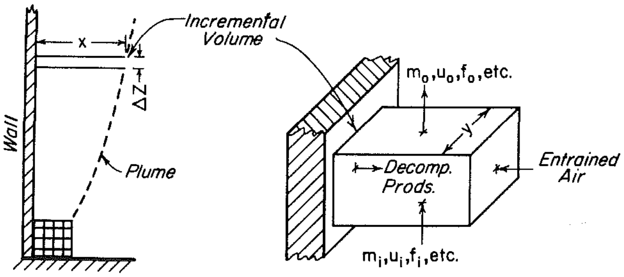

Fig. 6 Plume incremental volume

Incident flux from the plume seen at the boundary of the wall (corresponding to the boundary of the release rate test specimen) is calculated from the depth, temperature, and emissivity of the plume. In the corner configuration, average flux from the adjoining wall is calculated from temperature and emissivity of the wall, or if burning, from an effective flame temperature and emissivity of the flame. The incident flux to the boundary is the highest of the flux values seen by the wall area.

Once a surface is ignited, as indicated by the flux-time product exceeding $(FTP)_{min}$, the release rate of heat and smoke is determined from release rate data given as a function of incident flux and total heat or smoke released during prior time periods [2].

By making mass, energy, and momentum balances on an incremental volume (ΔV) of the plume, the dimensions, temperature, and pertinent gas phase compositions of the plume, along with the net energy contained in the plume at any point along its path, are determined.

The temperature of the gases vented is calculated from the temperature of the upper and lower zones in the upper layer. The smoke venting rate is assumed to be equal to the rate of smoke generation, i.e., the accumulation of smoke in the upper layer is assumed to be negligible.

Wall Plume Model

Relationships used to calculate mass, energy, and momentum changes in the plume are described below. The incremental volume of the plume across which the balances are made is illustrated in Fig. 6.

Mass Balance. Out-in = entrainment + decomposition products

$$\dot{m}_o - \dot{m}_i = \rho_o u_o A_o - \rho_i u_i A_i = e(\rho/\rho_a)^{1/2}\rho_a u(y+2x)\Delta Z + r_h y \Delta Z/H_v$$

where

$$u = (u_o + u_i)/2$$

$$\rho = (\rho_o + \rho_i)/2 \tag{1}$$

Energy Balance. (reference temperature = T_a). Out-in = heat generated − heat loss by radiation and convection,

$$\dot{m}_o c_p(T_o - T_a) - \dot{m}_i c_p(T_i - T_a) = \dot{Q}_{\text{gen}} - [\epsilon_p \sigma(T_p^4 - T_a^4 + \epsilon_p F_{pw}(T_p^4 - T_w) + h_c(T_p - T_w]y\Delta z \tag{2}$$

$$Q_{\text{gen1}} = r_h y \Delta z \quad \text{(fuel limiting)} \tag{3}$$

$$Q_{\text{gen2}} = m_{\text{ox}}\dot{Q}_{\text{ox}} \quad \text{(oxygen limiting)} \tag{4}$$

$$Q_{\text{gen3}} = \dot{m}_o c_p(T_F - T_a) + \dot{Q}_{\text{loss}} - \dot{m}_i c_p(T_i - T_a) \quad \text{(temp. limiting)} \tag{5}$$

where

Q_{loss} = (bracketed term in equation (2))

T_F = "flame temperature or maximum plume temperature

Q_{gen} = (smallest value of equations (3), (4), or (5))

Force Balance. Momentum change across increment = buoyancy force − frictional losses,

$$\dot{m}_o u_o - \dot{m}_i u_i = xyg(\rho_a - \rho)\Delta Z - f_f \rho u^2 \Delta Z/2 \tag{6}$$

Oxygen Balance.

$$(\dot{m}_{\text{ox}})_o - (\dot{m}_{\text{ox}})_i = 0.23\ \dot{m}_e - (r_h y \Delta Z + \dot{f}_i)/\dot{Q}_{\text{ox}} \tag{7}$$

Unburned Fuel Balance.

$$\dot{f}_o - \dot{f}_i = r_h y \Delta Z - \dot{Q}_{\text{gen}} \tag{8}$$

Radiant Flux from Upper Layer.

$$q/A = \epsilon_\mu \sigma F_{uk}(T_u^4 - T_a^4) \tag{9}$$

Horizontal Temperature Gradient. (Reference [6])

$$T_{pp} = [2.(2. - 0.8(\dot{Q}_r - \dot{Q}_s)/\dot{Q}_r)](T_p - T_a) + T_a \tag{10}$$

Used to determine the temperature of plume's "plateau" (T_{pp}) next to wall; a function of total energy to plume and that contributed by the vertical wall or combustible ceiling.

"Effective" Entrainment. (Reference [3])

$$\text{Lower layer:} \quad \dot{E}_1 = e(T_a/T_p)^{1/2}\rho_a u A_e \tag{11}$$

$$\text{Upper layer:} \quad \dot{E}_u = \dot{E}_1(T_p - T_u)/T_u \tag{12}$$

Incident Flux to Wall Contacting *V*.

$$h_r = \epsilon_p \rho \sigma(T_{pp}^4 - T_a^4)/(T_{pp} - T_a) \tag{13}$$

$$h_c = 1.24(T_{pp} - T_a)^{1/3} \text{(in S.I. units)} \tag{14}$$

$$(q/A) = (h_r + h_c)(T_{pp} - T_a) \tag{15}$$

If corner configuration, Flux from adjoining wall $(q/A)_2$:

$$(q/A)_2 = \epsilon_w \sigma(T_w^4 - T_a^4)F_{ww} \tag{16}$$

where

F_{ww} = 0.33, $T_w = T_s$ of adjoining wall

q/A = (the larger of $(q/A)_1$ and q/A_2)

Smoke Concentration.

$$\dot{C}_S = \dot{S}/\dot{V} \tag{17}$$

Absorptivity-Emissivity of Plume. (Reference [7, 8])

$$A = (1.0 + k_1 C_s x_p T_p)^4 - 1.0 \tag{18}$$

$$\epsilon_p = 1. - 1/[A + \text{Exp}(k_2 \dot{Q}_r x_p/\dot{m}_p T_p)] \tag{19}$$

where

k_1 = 0.184×10^{-5} m²/"particles," *K*;(1.1×10^{-5} ft²/"particles," °R)

k_2 = 0.941 kg,K/kj,m; (1.2 lb_m, °R/Btu,ft.)

Values of k_1 and k_2 were estimated from the data of Chung [8], who related the emissivity of the plume to the visible smoke concentration as calculated from release rate data and heat input to the plume.

Heat Losses to Wall. (Reference [9, 10])

For the finite difference solution of:

$$\frac{\partial T}{\partial t} = \alpha \frac{\partial^2 T}{\partial_x{}^2}$$

the wall of thickness "x" was divided into unequal incremental depths. Since the temperature gradient is greater at the heated (inside) surface, the increment at the inside surface was made thinnest and increased with distance into the wall.

In this code, the wall was divided into four slabs

$$x_w/(1.5)^5, x_w/(1.5)^4, x_w/(1.5)^3, \left(1 - \frac{x_w}{(1.5)^5} - \frac{x_w}{(1.5)^4} - \frac{x_w}{(1.5)^3}\right)$$

By heat balance at the interface between two increments

$$m_k'' cp \Delta T_{x_k} = \rho c_p x_k \Delta T_{x_k} = (q_{k-1} - q_k)\Delta t \tag{20}$$

where

$$\Delta T_{x_k} = T_{x_k}^{n+1} - T_{x_k}^n$$

$T_{x_k}^n$ = temperature in center of "k" increment at time interval "n"

Then

$$T_{x_k}^{n+1}(q_{k-1} - q_k)\Delta t/\rho c_p x_k + T_{x_k}^n \tag{21}$$

where

$$q_k = \frac{k}{x_k}(T_{x_k}^n - T_{x_{k+1}}^n)$$

At the gas-solid interface, the surface temperature is estimated by equating heat flow to and from the interface and solving for T_s

$$T_s = \frac{\frac{k}{x_i}(T_{x_i}) + hT_g}{h + k/x_i} \tag{22}$$

For stability

$$(\Delta x_k)_{\min} \geq \left(2\frac{k}{\rho c_p}\Delta t\right)^{1/2}$$

Incident Flux at Vertical Boundary of Involved Surface.

For corner configuration:

$$q/A = \epsilon_\rho \sigma F_{ww'}(T_p^4 - T_a^4) \tag{24}$$

where F_{ww} = 0.15.

Width of Wall Plume.

$$y_{t+\Delta t} = v_f \Delta t + y_t, \tag{25}$$

where

v_f = function of incident flux

Depth of Plume.

$$x = \dot{m}/\rho u y \tag{26}$$

Height of Upper Layer. (Reference [4, 5])

$$Z_u - Z_f = (\dot{m}_v/0.6D_w)^{2/3}/[g(\rho_a - \rho_o)\rho_a]^{1/3} \tag{27}$$

where

m_v = mass venting rate = $\dot{E}_T + \Sigma r_{h_j} A_j/H_v$

z_f = soffit height of door

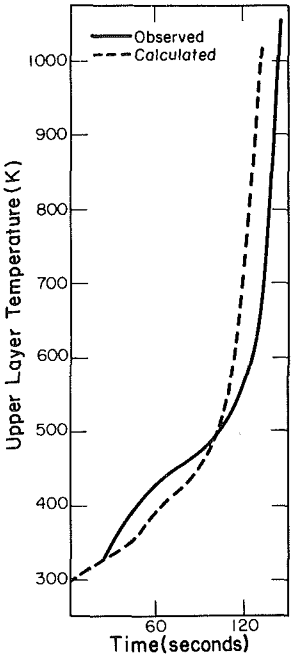

Fig. 7(*a*)
Upper layer temperature, Run A

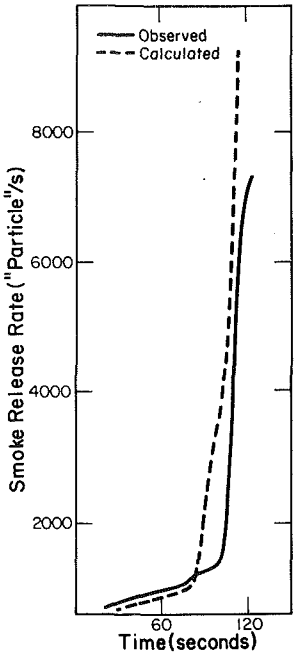

Fig. 7(*b*)
Smoke release rate, Run A

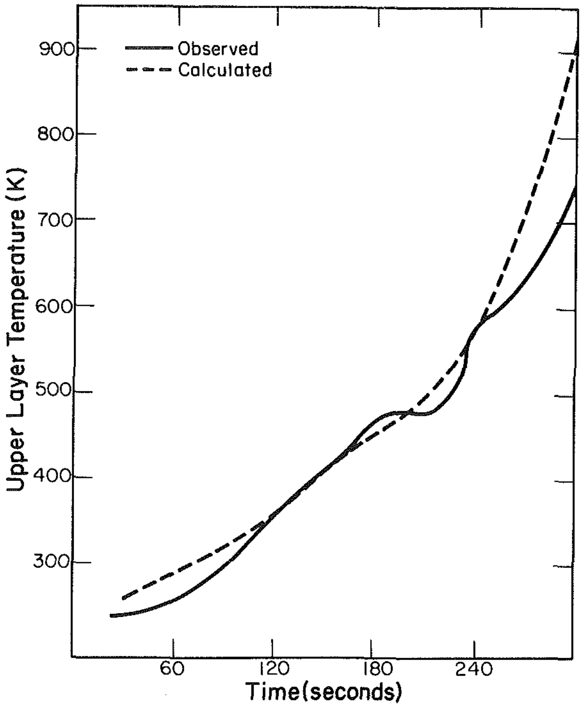

Fig. 9(*a*) Upper layer temperature, Run E

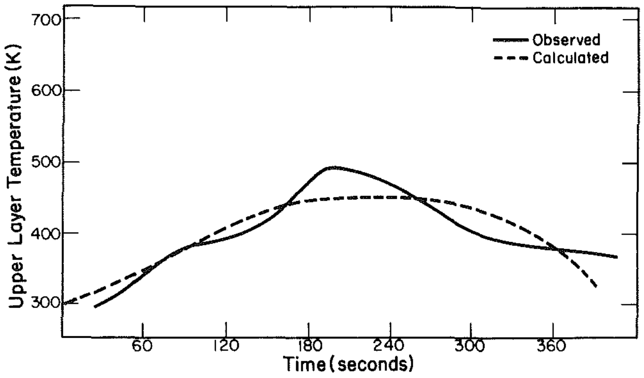

Fig. 8(*a*) Upper layer temperature, Run B

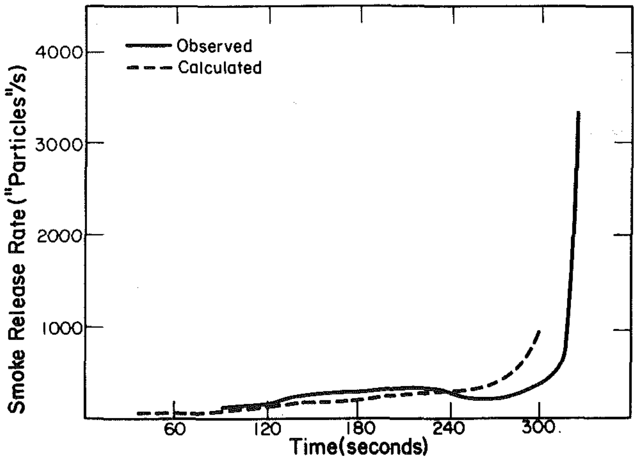

Fig. 9(*b*) Smoke release Rate, Run E

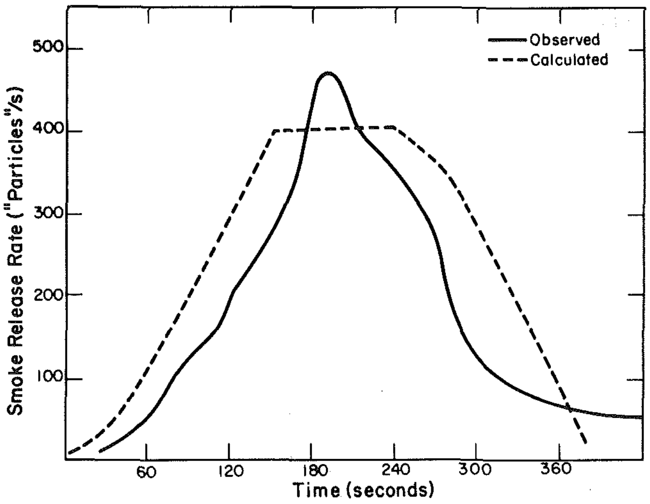

Fig. 8(*b*) Smoke release rate, Run B

Entrainment ($\dot{E}_T$) is already calculated; the height of upper layer is calculated by finding the buoyant force needed to provide flow out of opening equal to $\dot{m}_v$

Temperature of Vented Gases.

(By trail and error solution)

$$T_u = (\dot{Q}_r - \dot{Q}'_{\text{loss}})_u / \dot{m}_v C_p + T_a \tag{28}$$

where

$\dot{Q}_r$ = net heat released to upper layer
$\dot{Q}'_{\text{loss}}$ = total heat loss from lower zone, upper layer

Experimental Verification.

Experimental upgrading and verification of the model was done in several stages. The approach taken in developing the model was to use those mathematical relationships that were believed to consider all important variables and adequately predict the observed trends of the reaction being examined. The thought being that if trends are predictable, then absolute

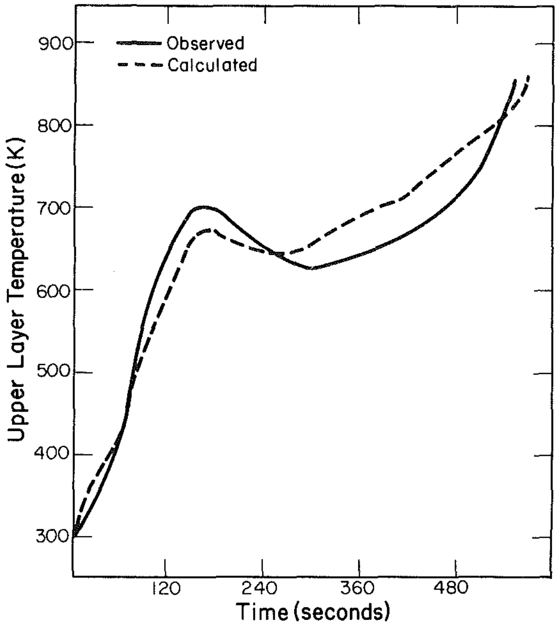

Fig. 10 Upper layer temperataure, Upjohn Test 2017

values can be obtained from one or more good data points obtained from actual fire data. In some cases, full-scale tests were designed to obtain the desired reference points. For example, actual values for the entrainment coefficients for the upper and lower plumes were determined using the 2.4 × 3.6 × 2.4-m high compartment described by Wood [11] and Satija [10]. The test facility was designed to permit accurate measurement of the rate of heat, mass, and smoke flow out its opening, a door of variable width and height.

Utilizing this capability, a line burner, 1.2-m wide, was used to generate a plume and the upper layer temperature and mass flow rate out the door was experimentally determined [10]. Entrainment coefficients were selected that gave the best match between values of venting rate and average upper layer temperature. Values selected for an open plume were 0.133 for the lower layer compared to values of 0.1 to 0.2 found by Fang [3]. For vertical plumes adjoining walls, where only half of the plume's width is open to entrainment, the entrainment coefficient was found to be 0.067. The entrainment coefficient for the upper layer, horizontal, plume was found to be 0.09.

A series of tests were made in The Ohio State University's large-scale test facility [11] using different wall and ceiling linings and ignition sources. Temperatures at 36 points in the compartment's upper half were monitored by thermocouples on three "trees," 1.8-m wide. The center tree had two sets of thermocouples, 24 g and 30 g, to check for effect of radiation on air temperature readings. Temperature deviations of less than 3 percent were found over the range of interest so no correction for radiation was made.

The upper layer temperature was taken as the temperature read by those thermocouples on the tree in the center of the compartment that were in the upper layer. The height of the upper layer was determined from a vertical string of thermocouples, 8 cm apart, hung from the ceiling. The value of "upper layer temperature" calculated by the model was the weighted average (for height) of the upper and lower zone temperatures in the center of the room.

Descriptions of materials and their orientation for several of these tests are given below. Results are described in Fig. 7–9. The Upjohn tests [12] and results of predictive modeling were recalculated using the new code. Predicted performance for Test No. 2017 compared to that observed is shown in Fig. 10.

Test Description

Run A.

Compartment: 2.1 by 3.6 by 2.1-m high; door: 0.71 by 1.9 m

Loading:

(A) Four reference[2] seats mounted as shown

(B) Wall and ceiling, lined with a PVC-ABS alloy

Ignition: both rear seats ignited (X) by pouring 200 cc of kerosene in center back of each seat and igniting each at the same time.

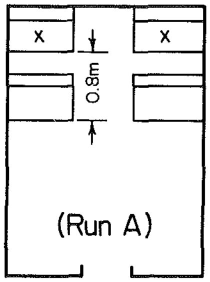

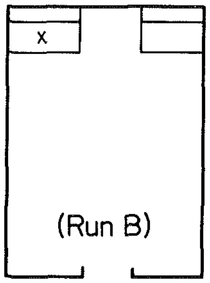

Run B.

Compartment: (Same as Run A)

Loading:

(A) Two reference seats mounted as shown

(B) Noncombustible walls and ceiling (gypsum board)

Ignition: One seat ignited (X) by pouring 200 cc kerosene in center of seat and igniting.

Run E.

Compartment: (same as Run A)

Loading:

(A) Two reference seats mounted as shown in Run B.

(B) Melamine lining on walls and ceiling.

Ignition: Left seat ignited (X) by pouring 200 cc kerosene in center of seat and igniting.

Upjohn (12) Test No. 2017. Compartment: 2.4 by 3.6 by 2.4-m high.

Loading:

(A) Two adjoining walls of exterior grade, 19-mm plywood; noncombustible ceiling.

(B) Propane burner in corner programmed to simulate a 9.1 kg wood crib.

Discussion

To evaluate the model's performance, the rate of change of upper layer temperature and heat and smoke release, as well as actual temperatures can be considered. Difference in combustibility of the materials involved are responsible for the different rate of fire development for those tests using the same initiation source. Therefore the fire's development rate should be a sensitive test for checking the objective of the model – to predict the effect materials have on a fire system.

Tests B, D, and E use the same initiation source; only the wall lining was changed. The predicted results, calculated solely from release rate data for the linings, follow the observed changes in temperature, smoke, and heat release. (See Figs. 7–10).

The time scale displacement observed in Tests A through E using the reference seat is due in part to the time required for the flame from the burning seat to contact the wall. However, the seat back shielded the wall from the flame until the back melted and burned.

---

[2] Reference seat: Seat: 408 by 813 by 51-mm thick flexible urethane slab
Back: 508 by 813 by 25-mm thick flexible urethane slab

Smoke evolution rate is a useful value since it is also a good measure of the rate of fire involvement of the PVC-ABS alloy. This material produces much smoke, so that the time at which the liner ignites, and the area involved, could be inferred from the smoke data. From this type of analysis, as well as from a semiquantitative evaluation of involved surfaces from photographs taken during the tests, it appears that the rate and pattern of fire propagation, both vertically and horizontally, are predicted by the model.

Although not shown, other tests using these materials in center wall configuration at different levels of initiating fire were made to determine if a self-propagating fire would develop. For example, using the same propane burner and plywood walls as the Upjohn Test No. 2017 in a center wall configuration, the model predicted that the fire would involve less than a 1.2-m high section of the wall with little horizontal extension beyond the plume formed by the burner. Actual charred area, which is greater than that involved by fire, was 2.1 m high by 0.76 m at the widest point.

Summary

The ability of the model to predict the progress of actual fires in systems with a wide variety of combustible materials and initiation sources is encouraging. The model's capabilities also indicate the importance of relevant release rate data to describe the fire performance characteristics of materials and products. The release rate model has been described as "simplistic," presumably in respect to its treatment of heat and fluid dynamics in the fire system. The results described above would indicate that a rigorous treatment is not necessary to predict the course of a developing fire if good release rate data are available.

The predictions for each run were made without change in the basic model. The only change to the code was the release rate information for the combustible materials, i.e., no adjustible "constants" were used to "fit the data."

In some preflashover models [13, 14, 15], rate of heat release has already been determined or is given as an exponential function with time. What these models assume is exactly what the release rate model attempts to predict. At least for the simple systems examined, the release rate model predicts the trend in a fire's development for different materials and initiation sources.

References

1 ASTM Task Group E05.21.30, "(Proposed) Test Method for Heat and Visible Smoke Release Rates for Materials and Products," American Society for Testing and Materials Annual Book of ASTM Standards, pt. 18, 1981, pp. 1493–1511.

2 Smith, E. E., "Evaluating Performance of Cellular Plastics in Fire Systems," Final Report to Products Research Committee, Grant No. RP-75-1-36 (Renewal), 1980.

3 Fang, J. B., "Analysis of the Behavior of a Freely Burning Fire in a *Quiescent Atmosphere*," NBS Report NBSIR 73-115 National Bureau of Standards, Feb. 1973.

4 Pape, R., and Waterman, T. E., "Understanding and Modeling Preflashover Compartment Fires," *Design of Building for Fire Safety*, ASTM STP 685, Amer. Soc. Testing Matls., pp. 106–138.

5 Rockett, J. A., "Fire Induced Gas Flow in an Enclosure," *Comb. Science and Tech.*, Vol. 12, 1975, pp. 165–175.

6 Yam, Sin-Hoi, "Incident Heat Flux on a Vertical Burning Surface," M.S. thesis, The Ohio State University, 1978.

7 Hottel, Sarofim, *Radiative Transfer*, McGraw-Hill, New York, 1967, pp. 243–247.

8 Chung, P. C., "The Effect of Smoke Concentration from Polystyrene and Wood on Soot Emissivity," M.S. thesis, The Ohio State University, 1980.

9 Yang, Yaw-chung, "Mathematical Model of a Developing Fire in a Compartment," M.S. thesis, The Ohio State University, 1980.

10 Stija, Sunil, "Venting Equation of a Compartment Fire Model," M.S. thesis, The Ohio State University, 1981.

11 Wood, W. D., "The Construction and Calibration of a Compartment Fire Test Facility," M.S. thesis, The Ohio State University, 1980.

12 Waszeciak, P. H., "Large Scale Experimental Evaluation of Release Rate Model for Predicting Fire Hazard Development," Final Report to Product Research Committee, Project RP-76-u-4, 1977.

13 Waterman, T. E., and Pape, R., "A Study of the Development of Room Fires," IITRI Final Report J6367 for NBS, Sept., 1976.

14 Quintiere, J., "The Growth of Fire in Building Compartments," *Fire Standards and Safety*, ASTM STP 614, Amer. Soc. for Testing and Materials, 1977, pp. 131–167.

15 Emmons, H. W., Mitler, H. E., and Trefethen, L. N., "Computer Fire Code III, Home Fire Project, TR25, Harvard University, Cambridge, Mass. 1978.

H. Khalil[1]

J. K. Shultis

T. W. Lester[2]
Mem. ASME

Department of Nuclear Engineering,
Kansas State University,
Manhattan, Kansas 66506

Stationary Thermal Ignition of Particle Suspensions

A calculational method is presented for the stationary thermal ignition of pulverized coal suspensions based on radiative energy transport in a heat generating medium. A diffusion-limited, Arrhenius model for heat generation is used in the description of the heterogeneous ignition and combustion of particles with the gases in which they are dispersed. The discrete ordinates method, which is used to solve numerically the radiative transfer equation, is combined with an iterative procedure to obtain both the temperature and radiation intensity distributions throughout the reacting system. Numerical examples are presented to show the variation in the critical behavior of a system in plane geometry with wall temperature and reflectivity, optical thickness of the system, particle size, optical parameters, anisotropy of the scattering, and the parameters of the heat generation model.

1 Introduction

The thermal theory of ignition has been the subject of numerous investigations, a comprehensive review of which is given by Gray and Lee [1]. Thermal ignition generally occurs at a critical state of a reacting system for which the heat generation by chemical reactions exceeds the rate of heat loss to the surroundings. Calculation of the critical parameters for thermal ignition of homogeneous systems is one of the classical problems of combustion theory and has been addressed by Semenov for the time-dependent case [2] and by Frank-Kamenetskii for the stationary case [3]. Both of these pioneering investigations considered the thermal ignition of reacting gases based on an Arrhenius heat generation model with conduction as the only heat transport mechanism. In reacting media containing dispersed particulates, such as pulverized coal suspensions, thermal radiation often becomes the dominant mode of heat transfer, particularly at elevated temperatures. The theories of Semenov and Frank-Kamenetskii, which are based on heat loss by conduction only, are thus not applicable.

Recently, analytical studies of the ignition and the subsequent consumption of single carbonaceous particles has been reported by Libby and Blake [4-6]. Although radiant heat loss is considered, the emphasis is on the modeling of gas phase chemistry, species diffusion, and heterogeneous reactions as a particle is immersed suddenly into a hot, oxidizing environment. By contrast, the intent of this study is to determine the influence of scattering, particle size, and global activation energy of the surface reaction of the ignition of particle suspensions.

Although the fundamental theory of ignition is unaffected by the type of energy transfer, the mathematical formulation of the criticality problem is significantly altered by substitution of radiative heat transfer for conductive heat transfer. Conductive losses are related directly to derivatives of temperature by Fourier's law, and thus the stationary energy balance yields a quasi-linear equation with temperature as the only unknown [3]. This equation is the basis of the stationary analysis by Frank-Kamenetskii. On the other hand, evaluation of radiation losses requires the calculation of the radiation intensity distribution throughout the reacting medium from the equation of radiative transfer. Moreover, this equation of transfer must be solved simultaneously with a highly nonlinear, stationary energy balance equation to compute the temperature and radiation intensity distribution in the medium.

A number of investigators have solved highly simplified or approximate versions of the equation of transfer in pulverized coal media. Essenhigh [7] and Bhaduri [8] neglected scattering and thermal emission and used Bouguer's law to compute the radiation intensity. Field et al. [9] employed the well-known flux methods to determine radiation fluxes in scattering and heat generation media. A number of authors [10, 11] have also used the directionally-integrated intensity distributions. The use of these approximate techniques can introduce serious error in calculation of the radiant energy transport in scattering media, particularly optically thin systems, which are characterized by rapid spatial variation of the radiant intensity and consequently a strong angular dependence of the intensity at each point. In this study, a powerful and accurate numerical discrete ordinates method (originally developed for solution of neutron transport problems) is used to solve the equation of transfer. The simultaneous solution of the equation of transfer with the stationary energy balance is then applied to the prediction of ignition parameters of a radiating system.

2 Theory and Model Development

2.1 The Stationary Energy Balance. By neglecting conductive and diffusive heat transfer, as well as sensible energy changes, the stationary energy balance in a reacting coal suspension can be written as

$$-Q_r(\mathbf{r})+H(\mathbf{r})=0 \tag{1}$$

where $Q_r(\underset{\sim}{r})$ is the net rate of energy loss by radiation at point $\mathbf{r}$ per unit volume, and $H(\mathbf{r})$ is the volumetric rate of heat generation from chemical reactions at point $\underset{\sim}{r}$. Equation (1) states that all the heat which is generated must be dissipated by radiant energy transfer.

2.2 The Heat Generation Term. The coal particles are assumed to be spherical, and gas phase chemical reactions are neglected. The heat generation rate H is determined exclusively by the rate of the heterogeneous reaction of the particles with the oxidizing gases (primarily O_2). The severity of neglecting both devolitization and gas phase chemical reactions is recognized. However, for some combinations of particle size, heat-up rates, and oxygen partial pressures, experimental results have been observed that are consistent with heterogeneous ignition. Howard and Essenhigh [12, 13] found experimentally that coal particles below a somewhat ill-defined size could ignite on the surface. A complete discussion

---

[1] Present Address: Department of Nuclear Engineering, Massachusetts Institute of Technology, Cambridge, Mass.

[2] Address correspondence to Professor T. W. Lester

Contributed by the Heat Transfer Division for publication in the JOURNAL OF HEAT TRANSFER. Manuscript received by the Heat Transfer Division October 28, 1981.

of the evidence and theories supporting homogeneous and heterogeneous ignition has been presented by Essenhigh [14].

A completely adequate model for the rate of heat generation during the heterogeneous ignition and combustion of carbonaceous solids has yet to be derived. The methodology of this paper is capable of using any functional form for the heat generation model. For purposes of illustration, an approximate model which is consistent with much of the available data on particle burning times (see Essenhigh [14]), is one in which the heat generation rate is limited by both the chemical kinetics at the particle surface and the rate of diffusion of oxygen to the particle surface. Assuming the heterogeneous reaction is first order, the heat generation rate is given by [9]

$$H = Ph \sum_{k=1}^{NK} \frac{S_{vk}}{K_{dk}^{-1} + K_s^{-1}} \tag{2}$$

where P is the partial pressure of oxygen, h is the energy released per unit mass of fuel consumed, NK is the number of particle size classes, and S_{vk} is the surface area of particles in the kth size class per unit volume. The quantity S_{vk} can be related to the bulk density ρ_{pk} and the diameter d_{pk} of particles in the kth size class by

$$S_{vk} = 6\rho_{pk}/(d_{pk}\rho_c) \tag{3}$$

where ρ_c is the density of coal. The quantities K_{dk} and K_s are the oxygen diffusion rate and surface reaction rate coefficients, respectively, and are given by [9]

$$K_{dk} = \frac{48 D_o T^{0.75}}{R T_o^{1.75} d_{pk}} \tag{4}$$

and

$$K_s = Z\exp(-E/RT) \tag{5}$$

where T is the temperature of the medium (the solid and gas phases are assumed to be in thermal equilibrium), D_o is the diffusivity of oxygen in air at a temperature T_o, R is the universal gas constant, Z is the pre-exponential factor (assumed independent of temperature), and E is the activation energy. The expression for the diffusional rate coefficient K_{dk} assumes that oxygen is conserved in the particle boundary layer, i.e., consumption of oxygen occurs either at the particle surface or relatively far from it.

It should be emphasized that more sophisticated models, such as those formulated by Libby and Blake [4-6] or by Matalon [15] are readily incorporated into the present formulation. Nonetheless, it is of interest to note that Libby and Blake [4] have demonstrated that under a wide range of conditions, the particle consumption is diffusion limited, and that the rate of consumption with either frozen or equilibrium chemistry in the gas phase is not appreciably different. Hence, the use of the foregoing, more simplistic model appears justified within the context of this work.

2.3 The Radiant Emission Term. The radiative energy loss term, $Q_r(\mathbf{r})$ in equation (1) represents the net radiant emission at point $\mathbf{r}$ per unit volume of the suspension and may be written

$$Q_r(\mathbf{r}) = 4\sigma_a(\mathbf{r})\,\hat{\sigma}T^4(\mathbf{r}) - \sigma_a(\mathbf{r}) \int_{4\pi} I(\mathbf{r},\mathbf{\Omega})d\Omega \tag{6}$$

where σ_a is the absorption coefficient, $\hat{\sigma}$ is the Stefan-Boltzmann constant, and $I(\mathbf{r},\mathbf{\Omega})$ is the radiation intensity integrated over all frequencies. The gaseous species have been assumed transparent to radiation, and the particles are taken as gray bodies in local thermo-dynamic equilibrium.

2.4 The Radiative Transfer Equation. Substitution for the heat generation term (from equation (2)) and the net radiant emission term (from equation (6)) into the energy balance of equation (1) yields

$$4\sigma_a(\mathbf{r})\hat{\sigma}T^4(\mathbf{r}) = \sigma_a(r)\int_{4\pi} I(\mathbf{r},\mathbf{\Omega})d\Omega + Ph \sum_{k=1}^{NK} \frac{S_{vk}}{\{K_{dk}[T(\mathbf{r})]\}^{-1} + \{K_s[T(\mathbf{r})]\}^{-1}} \tag{7}$$

Given the composition, the material properties, and the absorption coefficient of the reacting mixture, equation (7) involves two unknown functions, the radiation intensity $I(\mathbf{r},\mathbf{\Omega})$ and the temperature $T(\mathbf{r})$. An additional equation relating these unknowns is the steady-state equation of transfer,

$$[\mathbf{\Omega}\cdot\nabla + \sigma_e(\mathbf{r})]I(\mathbf{r},\mathbf{\Omega}) = \frac{\sigma_s(\mathbf{r})}{4\pi}\int_{4\pi} I(\mathbf{r},\mathbf{\Omega}')p(\mathbf{\Omega}'\rightarrow\mathbf{\Omega}) - d\Omega' + \sigma_a(\mathbf{r})\frac{\hat{\sigma}T^4(\mathbf{r})}{\pi} \tag{8}$$

where $\sigma_e(\mathbf{r})$ and $\sigma_s(\mathbf{r})$ are the extinction and scattering coefficients, respectively, and $p(\mathbf{\Omega}'\rightarrow\mathbf{\Omega})$ is the scattering phase function.

The extinction and scattering coefficients are computed from $\sigma_e = 1/4\sum_k F_{ek}\ S_{vk}$ and $\sigma_s = 1/4\sum_k F_{sk}\ S_{vk}$, respectively, where F_{ek} is the extinction efficiency, and F_{sk} is the scattering efficiency for particles in the kth size class. The extinction and scattering efficiencies are calculated from Mie theory given the particle size parameter α $(=\pi d_p/\lambda$, where λ is the radiation wavelength) and the complex refractive index of the particles, m. The wavelength at which the maximum radiation intensity occurs at combustion temperatures is roughly 2 μm, and the typical diameter of pulverized coal particles is between 10 μm and 100μm. The particle size parameter, α, thus falls in the range of 10 to 150. In this range, the extinction and scattering efficiencies are weak functions of the size parameter, and diffracted radiation is concentrated within a narrow angle about the incident direction. Treatment of the diffracted radiation as purely forward scattering allows this effect to be neglected entirely by subtracting its contribution from the extinction and scattering efficiencies. The scattering phase function is thus determined entirely by the reflected component of the scattered radiation and may be written for opaque and diffusely reflecting particles as [13]

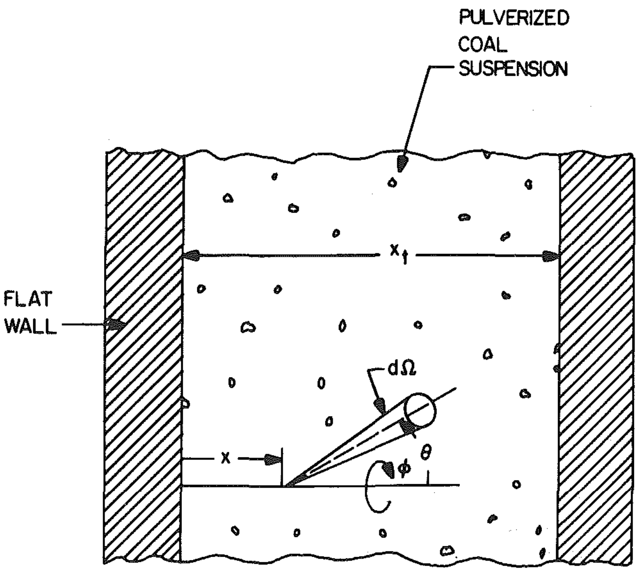

Fig. 1 Coordinate system for the description of radiative transfer in a particle suspension

$$p(\Theta) = \frac{3}{8\pi}(\sin\Theta - \Theta\cos\Theta) \tag{9}$$

where Θ is the scattering angle ($\cos\Theta = \underline{\Omega}\cdot\underline{\Omega}'$). If, on the other hand, scattering is assumed to be isotropic, the phase function is independent of the scattering angle and equals 1 for all values of Θ.

The complex refractive index of carbonaceous solids, particularly coals, is still uncertain. Field, et al. [9] cite a number of studies that indicate that the refractive index of pyrolytic graphite, soot, and coal in the wavelength region between 1 to 5 microns, has a real part of from 1.5 to 3 and a complex part of from 0.1 to 1.0. Since there is additional uncertainty as to how these quantities vary with carbon composition and flame temperature, values representative of this range have been used in the current investigation. Recently, an exhaustive study of carbon refractive index has been undertaken by Janzen [16]. His recommended value between 350 and 1,000 nm is $m = 2.0 - i$, close to that used in this study.

2.5 Simplification of the Model in Plane Geometry. For simplicity, we consider a monodisperse coal dust suspension (i.e., $NK = 1$) of thickness x_t which is homogeneous and surrounded by infinite, parallel, flat walls as shown in Fig. 1. The stationary energy balance, equation (7), becomes

$$4\sigma_a\hat{\sigma}T^4(x) = 2\pi\sigma_a\int_{-1}^{1} I(x,\mu)d\mu + \frac{PhS_v}{\{K_d[T(x)]\}^{-1} + \{K_s[T(x)]\}^{-1}} \tag{10}$$

The equation of transfer, equation (8), becomes

$$\mu\frac{\partial I(x,\mu)}{\partial x} + \sigma_e I(x,\mu) = \frac{\sigma_s}{2}\int_{-1}^{1} I(x,\mu')p(\mu' \rightarrow \mu)d\mu' + \sigma_a\frac{\hat{\sigma}T^4(x)}{\pi} \tag{11}$$

where μ is the cosine of the polar angle, θ (see Fig. 1), and where the equation has been averaged over the azimuthal angle, ϕ. The azimuthally averaged phase function is given by

$$p(\mu' \rightarrow \mu) = \frac{1}{2\pi}\int_0^{2\pi} d\phi p(\Theta) \tag{12}$$

where the angle Θ is related to the directions (μ',ϕ') and (μ,ϕ) by

$$\cos\Theta = \mu\mu' + (1-\mu^2)^{1/2}(1-\mu'^2)^{1/2}\cos(\phi - \phi') \tag{13}$$

2.6 Boundary Conditions. The simultaneous solution of the equation of transfer, equation (11), and the energy balance, equation (10), requires boundary conditions for the radiation intensity. If the walls are assumed to be diffusely reflecting and gray, the intensity incident on the medium at the boundaries can be expressed as

$$I(0,\mu) = \frac{\epsilon_{w1}\hat{\sigma}T_{w1}^4}{\pi} + 2\rho_{w1}\int_0^{-1} \mu' I(0,\mu')d\mu', \text{ for } \mu > 0 \tag{14a}$$

$$I(x_t,\mu) = \frac{\epsilon_{w2}\hat{\sigma}T_{w2}^4}{\pi} + 2\rho_{w2}\int_0^{1} \mu' I(x_t,\mu')d\mu', \text{ for } \mu < 0 \tag{14b}$$

where T_{w1}, ρ_{w1}, and ϵ_{w1} are, respectively, the temperature, the reflectivity, and the emissivity of the wall at $x = 0$; and T_{w2}, ρ_{w2}, and ϵ_{w2} are the corresponding quantities for the wall at $x = x_t$.

2.7 Dimensionless Form of the Equations. To reduce the number of parameters affecting the simultaneous solutions of equations (10) and (11) subject to boundary conditions (14*a*) and (14*b*), the equations are cast in dimensionless form. Division of each term in the energy balance by $4\sigma_a\hat{\sigma}(E/R)^4$ yields

$$\tau^4(x) = \frac{\pi}{2}\int_{-1}^{1} \tilde{I}(x,\mu)d\mu + \frac{A}{\tau(x)^{-0.75} + B\exp[1/\tau(x)]} \tag{15}$$

where

$$\tau(x) = \frac{T(x)}{(E/R)} \tag{16a}$$

$$\tilde{I}(x,\mu) = \frac{I(x,\mu)}{\hat{\sigma}(E/R)^4} \tag{16b}$$

$$A = \frac{Ph}{\hat{\sigma}(E/R)^4}\frac{C}{F_a} \tag{16c}$$

$$B = C/Z \tag{16d}$$

$$C = \frac{48D_o(E/R)^{0.75}}{RT_o^{1.75}d_p} \tag{16e}$$

and where $F_a = F_e - F_s$ is the absorption efficiency. Representative values of the activation energy (146 kJ mol^{-1}), the pre-exponential factor (0.594 kg N^{-1}s^{-1}), and the oxygen diffusivity (3.49 cm^2 s^{-1} at 1600 K) were obtained from Field et al. [9]. The remaining constants needed to compute parameters A and B were chosen so that a monodisperse suspension of 50-mm dia particles with a bulk density, ρ_p of 10^{-4} g cm^{-3} and a particle density ρ_c of 1.5 g cm^{-3} generates heat at a rate 1 W cm^{-3} at a temperature of 1750 K. The heat generation rate of 1W cm^{-3} is typical of the thermal loading in the primary heat release zones of pulverized fuel boilers (see Richter and Heap [17] and Field et al. [9]). The complex refractive index of the particles, m, was assumed to be $1.93(1 - i0.53)$, and the radiation wavelength λ was taken as 2 μm. With these values for the various constants, the dimensionless parameters A and B become 2.014×10^{-4} and 1.805×10^{-4}, respectively.

The equation of transfer is nondimensionalized by division of each term in the equation by $\sigma_e\hat{\sigma}(E/R)^4$ to obtain

$$\mu\frac{\partial\tilde{I}(\xi,\mu)}{\partial\xi} + \tilde{I}(\xi,\mu) = \frac{\omega}{2}\int_{-1}^{1} \tilde{I}(\xi,\mu')p(\mu' \rightarrow \mu)d\mu' + (1-\omega)\frac{\tau^4(\xi)}{\pi} \tag{17}$$

where $d\xi = \sigma_e dx$ is the differential optical thickness, and $\omega = \sigma_s/\sigma_e$ is the single scatter albedo.

Finally, the boundary conditions are cast in dimensionless form by division of each term in equations (14*a*) and (14*b*) by $\hat{\sigma}(E/R)^4$ to obtain

$$\tilde{I}(0,\mu) = \frac{\epsilon_{w1}\tau_{w1}^4}{\pi} + 2\rho_{w1}\int_0^{-1} \mu'\tilde{I}(0,\mu')d\mu', \mu > 0 \tag{18a}$$

$$\tilde{I}(\xi_t,\mu) = \frac{\epsilon_{w2}\tau_{w2}^4}{\pi} + 2\rho_{w2}\int_0^{1} \mu'\tilde{I}(\xi_t,\mu')d\mu', \mu < 0 \tag{18b}$$

where τ_{w1} and τ_{w2} are dimensionless wall temperatures, and ξ_t is the optical thickness of the suspension (i.e., $\xi_t = \sigma_e x_t = \frac{1}{4}F_e S_v x_t$).

2.8 Discussion of the Model. Substitution for $\tau(\xi)$ (from equation (15)) into equation (17) yields

$$\mu\frac{\partial\tilde{I}(\xi,\mu)}{\partial\xi} + \tilde{I}(\xi,\mu) = \frac{\omega}{2}\int_{-1}^{1} \tilde{I}(\xi,\mu')p(\mu' \rightarrow \mu)d\mu' + \frac{1-\omega}{2}\int_{-1}^{1} \tilde{I}(\xi,\mu')d\mu' + \tilde{H}[\tau(\xi)] \tag{19}$$

where

$$\tilde{H}[\tau(\xi)] = A\,\frac{1-\omega}{\pi}\left\{\tau(\xi)^{-0.75} + B\exp[1/\tau(\xi)]\right\}^{-1} \tag{20}$$

The dimensionless temperature, $\tau(\xi)$, is related to the dimensionless intensity, $\tilde{I}(\xi,\mu)$, by equation (15), and the term $\tilde{H}[T(\xi)]$ appearing in equation (19) is, in principle, expressible as $\tilde{H}[\tilde{I}(\xi,\mu)]$. Hence, equation (19) becomes

$$\mu\,\frac{\partial \tilde{I}(\xi,\mu)}{\partial \xi} + \tilde{I}(\xi,\mu) = \frac{\omega}{2}\int_{-1}^{1} \tilde{I}(\xi,\mu')p(\mu' \rightarrow \mu)d\mu' + \frac{1-\omega}{2}\int_{-1}^{1} \tilde{I}(\xi,\mu')d\mu' + \tilde{H}[\tilde{I}(\xi,\mu)] \tag{21}$$

in which $\tilde{H}[\tilde{I}(\xi,\mu)]$ is a highly nonlinear functional of $\tilde{I}$. Equation (21) is a nonlinear, first-order, integro-differential equation. Unfortunately, the explicit dependence of $\tilde{H}$ on the radiation intensity cannot be determined because of the transcendental relation between the temperature and the intensity in equation (15). Consequently, it is impossible to isolate analytically a critical parameter (such as Frank-Kamenetskii's δ-parameter) from equation (21).

However, the energy balance and the equation of transfer can be solved simultaneously by an iterative procedure. Since no analytical solution is known for the equation of transfer in a finite medium when scattering is present, the existence of a critical condition must be determined by numerical techniques.

The numerical method used in this investigation is described in detail in references [18] and [19], and only a brief outline is given here. An initial temperature profile $T^{(0)}(x)$ is guessed (e.g. $T(x)$ = constant), and the equation of transfer, equation (11), is solved for $I^{(0)}$ by using the method of discrete ordinates [20]. The energy balance of equation (15) is then solved to obtain a revised temperature profile $T^{(1)}(x)$. This successive solution of the radiative transfer and energy balance equations is continued until I and T converge (i.e., the change between iterations is less than some small prescribed amount). Equivalently, one may iterate between equations (20) and (21) to obtain the simultaneous solution of $\tilde{I}$ and $\tilde{H}$.

It should be noted that the simultaneous solution of equations (15) and (17) subject to the conditions (18*a*) and (18*b*) depends only on the dimensionless parameters, A and B, the single scatter albedo, ω, the scattering function, p, and the boundary conditions (i.e., the quantities ϵ_w, ρ_w, τ_w, and ξ_t). Of these dimensionless parameters, only the optical thickness of the suspension, ξ_t, depends on the particle bulk density, ρ_p, the density of coal, ρ_c, and the system size, x_t. Therefore, for a given optical thickness of the system, the computed temperature and intensity distributions are independent of the particular choices of ρ_p, ρ_c, and x_t.

It is found in this study that a steady-state temperature profile is always obtained from equations (20) and (21) for $\rho_w < 1$ (i.e., the system walls are not perfectly reflecting so that heat loss is possible). Ignition occurs when a small variation of the problem parameters causes a discontinuous increase (bifurcation) in the steady-state intensity and temperature distributions. The values of the parameters at which this discontinuous change in the steady-state solution occurs are termed the critical values. This behavior differs from Frank-Kamenetskii's thermal conduction analysis which found, under the assumption $(T(\mathbf{r}) - T_w) << T_w$, that no steady-state temperature profile existed if his δ-parameter is greater than a critical value [4]. However, a recent study [14] has shown that elimination of the assumption $(T(\mathbf{r}) - T_w) << T_w$ yields steady-state solutions for all values of δ, but that at the critical value a bifurcation in the solution occurs. This same behavior is observed for the present radiation problem.

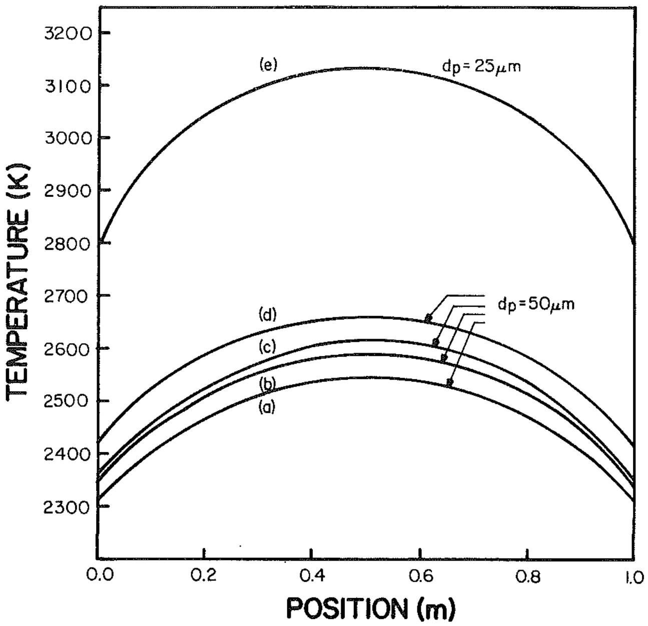

Fig. 2 Effect of particle size, the single scatter albedo, and the type of scattering on the computed temperature distribution in a 1-m thick-suspension bounded by walls at 1600 K with reflectivity of 0.2: (*a*) no scattering; (*b*) isotropic scattering, $\omega = 0.269$, $m = 1.93(1 - i0.53)$; (*c*) same as (*b*) but with anisotropic scattering; (*d*) isotropic scattering, $\omega = 0.514$, $m = 3(1 - i)$; (*e*) isotropic scattering, $\omega = 0.271$, $m = 1.93(1 - i0.53)$.

3 Numerical Results

A computer program [18] has been written to compute the radiation intensity and temperature distributions in a pulverized coal suspension and to test the effects of the problem parameters on these results. Numerical studies were also performed to determine the existence of critical ignition values of the various parameters. While these numerical studies are restricted to the simplified, but not unrealistic, model described in section 2, it is felt that the trends and variations described here are valid for more complex systems. It is only from such idealized studies that insight is gained into the combustion process and the complex nonlinear relationship among the system parameters.

While a high-order, discrete ordinates method has been used in the current study to solve the equation of transfer numerically, the differential approximation, flux methods, or a low-order discrete ordinates method could also be used. The accuracy or these more approximate methods to the present problem is presented in reference [19].

The convergence of the computed temperature and intensity distributions with respect to the number of spatial mesh points and the number of discrete ordinates was verified. The solutions were found to converge to within 1 percent of a benchmark problem (computed with very fine spatial and angular grids) if only ten mesh points per unit optical thickness and eight angular quadrature ordinates are used. The stopping criterion used in the iterative solution was that the temperature and intensity change by less than 0.1 percent between successive iterations. The independence of the solution of the initial source distributors guess was also verified, and the converged solutions were found to satisfy an energy balance in which the total heat generated by the medium per unit time equals the radiant leakage rate at the system boundaries. Finally, the temperature distribution was computed for a simple test case in which scattering is neglected ($\sigma_s = 0$), the rate of heat generation is constant ($H = 0.8368$ W cm^{-3}), and the walls are cold and nonreflecting. The result was compared with the no-scattering

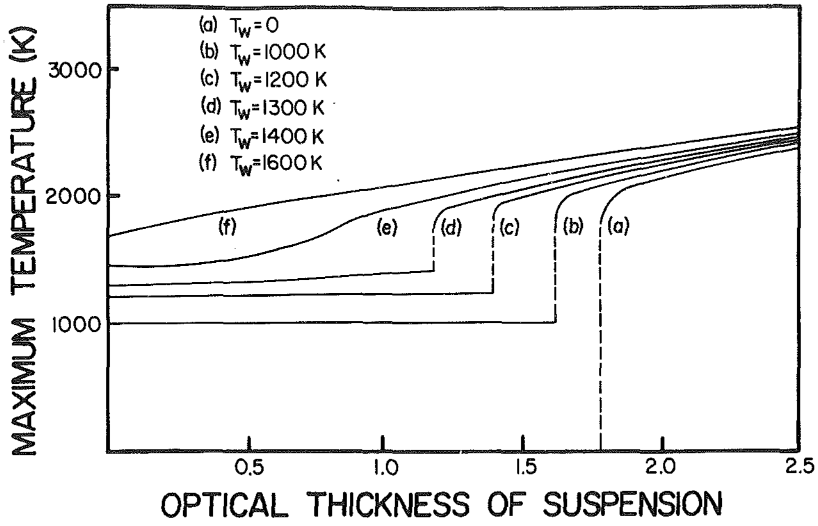

Fig. 3 Variation of the maximum temperature with the optical thickness of a medium bounded by nonreflecting walls for different values of the wall temperature. Medium scatters isotropically with $\omega = 0.269$.

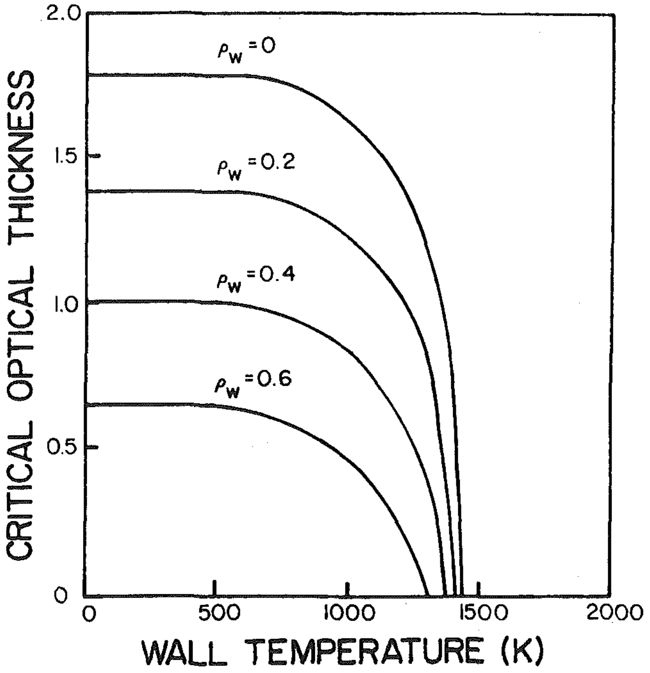

Fig. 4 The critical optical thickness as a function of wall temperature for different values of the wall reflectivity. Isotropic scattering is assumed with $\omega = 0.269$.

solution of Usiskin and Sparrow [21] (presented in Field et al. [9]) and the maximum difference in temperature was found to be less than 0.6 percent.

3.1 Effect of Particle Size and Albedo. The variation of the computed temperature distribution in a 1-m thick suspension with the single scatter albedo, the type of scattering, and the particle size is illustrated in Fig. 2. The scattering albedo ω is varied by choosing different values of the complex refractive index for the particles. It may be seen from Fig. 2 that an increase of the albedo (at constant particle diameter) causes an increase of the computed temperature at every point in the suspension, as well as a slight increase in the curvature of the temperature profile. The effect of the anisotropy of scatter is also an increase of the temperature throughout the medium. This temperature increase is explained by the predominance of backward scattering (for the anisotropic case), which decreases the radiant energy leakage at the system boundaries. Finally, the effect of halving the particle diameter is seen to be a significant rise of the computed temperature profile. Since the comparison for the two different particle sizes is based on equal particle surfaces areas per unit volume and equal refractive indices, the difference in temperature is attributed to the increase in the diffusional rate coefficient for the smaller particles.

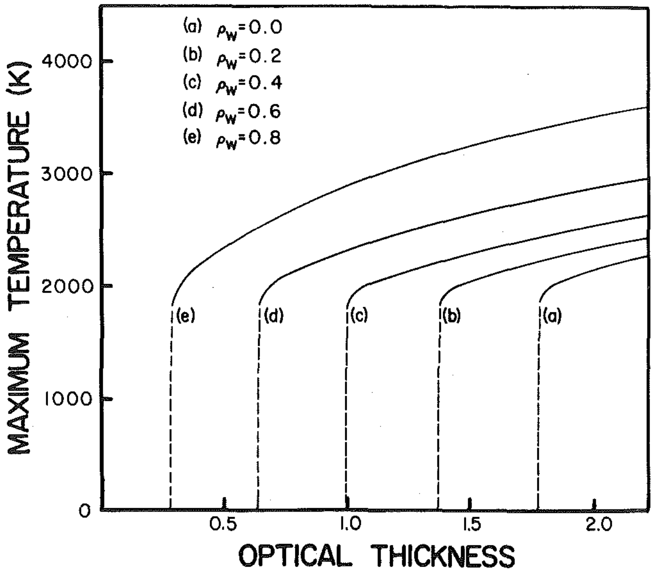

Fig. 5 Variation of the maximum particle temperature with the optical thickness of an isotropically scattering ($\omega = 0.269$) medium bounded by cold walls for different values of the wall reflectivity

3.2 Effect of Optical Thickness. The effect of the system thickness, x_t, and the particle concentration, ρ_p on the computed temperatures is examined by varying the optical thickness, ξ_t, of the medium. Rather than comparing the temperature distributions for a number of optical thicknesses, the maximum temperature of the suspension (i.e., the temperature at $\xi = \xi_t/2$) is illustrated in Fig. 3 as a function of the optical thickness with the wall temperature as a parameter (for nonreflecting walls). Curve (*a*) of Fig. 3 represents the observed variation for cold walls, and the wall temperature is increased progressively in curves (*b-d*). For the case of cold walls, the maximum particle temperature is seen to be zero for values of the system optical thickness below a critical value ξ_{cr}. As the system size passes through the critical value, the suspension ignites as the maximum temperature changes discontinuously to a large positive value. For system optical thicknesses smaller than ξ_{cr}, nonzero temperature and intensity distributions yield radiant heat losses by leakage through the walls that exceed the energy which is generated by chemical reaction.

An increase of the wall temperature to 1000 K (curve (*b*)) yields temperatures equal to the wall temperature for system optical thicknesses below a critical value (which is smaller than that observed with cold walls). Further increases of wall temperature cause both the critical thickness and the temperature discontinuity at the critical thickness to decrease. At a wall temperature of 1600 K, the bifurcation of the maximum temperature is not observed, and the suspension is seen to ignite regardless of its optical thickness.

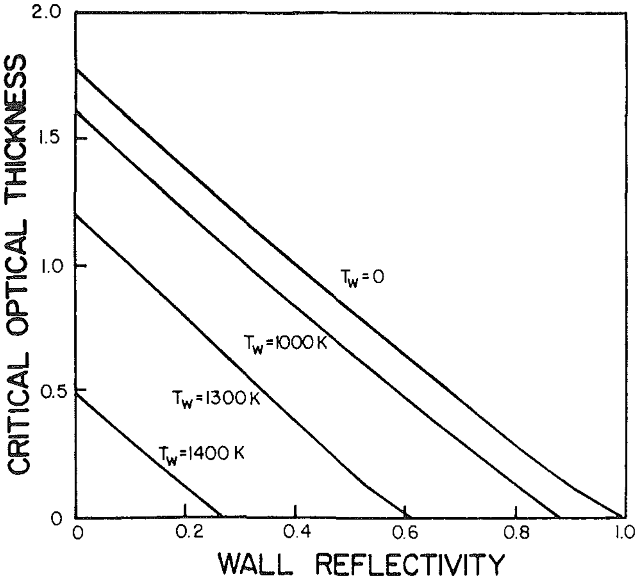

Fig. 6 The critical optical thickness as a function of wall reflectivity for different values of the wall temperature. The medium is assumed to scatter isotropically with $\omega = 0.269$.

The decrease in critical optical thickness with increasing wall temperature is illustrated in Fig. 4 for different values of the wall reflectivity. This decrease in ξ_{cr} may be explained by the fact that emission from the walls is a source of radiation to the reacting suspension. This incident radiation compensates partially for radiation leakage from the system, and allows optically thinner systems to ignite.

3.3 Effect of Wall Reflectivity. The effect of varying the wall reflectivity is illustrated in Fig. 5 for the case of cold walls. The increase of wall reflectivity is seen to have two effects: it raises the maximum temperature significantly for a given optical thickness and also decreases the critical optical thickness. The variation of the critical optical thickness with wall reflectivity is shown in Fig. 6 for several values of wall temperature. The decrease in ξ_{cr} for increasing wall reflectivity is caused by the decreased fraction of radiation incident on the walls that is lost by leakage, thereby allowing optically thinner systems to ignite.

3.4 Sensitivity to the Heat Generation Model. The effects of a variation in the activation energy and the amount of energy released for the heat generation model of equation (20) on the criticality of the system are shown in Fig. 7. A small variation of the activation energy is seen to yield a considerable change in the critical optical thickness, with ξ_{cr} decreasing for a smaller activation energy. However, for optical thicknesses greater than the critical values, the effect of the different activation energies on the maximum temperature is seen to be minimal due to the predominance of the diffusional control mechanism at high temperatures. On the other hand, an increase in the heat generation rate by a factor of three is seen to cause both a decrease in ξ_{cr} and a significant increase of the maximum temperature at any given optical thickness.

4 Summary

A coal dust suspension which generates heat by heterogeneous combustion and dissipates heat by radiation was found to ignite only if its optical thickness exceeds a critical value. This critical optical thickness was found to vary with the temperature and reflectivity of the walls bordering the suspension, and with the parameters of the heat generation model. The combination of an iterative procedure with a discrete ordinates approximation to the radiative

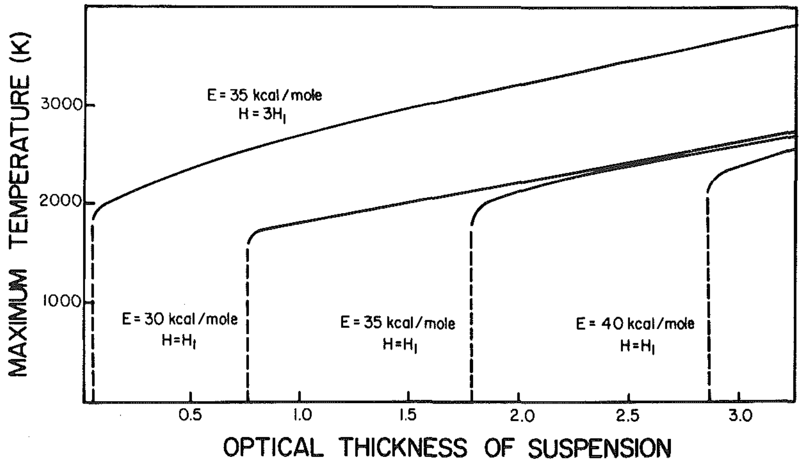

Fig. 7 Effect of activation energy and the magnitude of the heat generation rate on the variation of the maximum temperature with the optical thickness. The walls are cold and nonreflecting, scattering is isotropic, and the single scattering albedo is $\omega = 0.269$.

transfer equation allowed accurate evaluation of the temperature and radiation intensity throughout the reacting system.

It is apparent that many generalizations can be made to the simple ignition model considered here. Gas phase reactions, polydisperse particle size distributions, and conductive heat transfer can be incorporated into the present methodology without significant changes in the numerical solution algorithm. Allowance for different temperature distributions in the solid and gas phases can be accommodated by solving a separate energy balance for each phase and by adding an additional emission source term to the radiative transfer equation. Calculation of gaseous (banded) radiation and radiation from nongray particles may be performed by solving the radiative transfer equation for many frequency bands. Many of these refinements to the present study have been formulated and discussed [19], but numerical results have not yet been obtained.

Whether or not such refinements are necessary will depend on future comparisons of model predictions with experimental results. The simplified model presented in this paper for the ignition in particle suspensions dominated by radiative transfer is seen to exhibit many features one would intuitively expect. For instance, the existence of an ignition temperature for a specified particle mass loading and system size is predicted. Additionally, a minimum explosive concentration may be inferred from this model. Given the uncertainty in much of the input data, the real value of such studies is that the sensitivity of the ignition process to the model parameters can be determined.

5 Acknowledgment

Support for this work was provided by the Engineering Experiment Station of Kansas State University. One of the authors (JKS) expresses his gratitude to the Alexander von Humboldt Foundation for support provided during the preparation of this paper.

References

1 Gray, P., and Lee, P. R., "Thermal Explosion Theory," *Oxidation and Combustion Reviews*, edited by C. F. Tipper, Vol. 2, Elsevier, 1967, p. 1.

2 Kanury, A. M., *Introduction to Combustion Phenomena*, Gordon and Breech, 1977.

3 Frank-Kamenetskii, D. A., *Diffusion and Heat Transfer in Chemical Kinetics*, Plenum Press, 1969.

4 Libby, P. A., and Blake, T. R., "Theoretical Study of Burning Carbon Particles," *Combust Flame*, Vol. 36, 1979, p. 139.

5 Libby, P. A., "Ignition, Combustion, and Extinction of Carbon Particles," *Combust. Flame*, Vol. 38, 1980, p. 285.

6 Libby, P. A. and Blake, T. R., "Burning Carbon Particles in the Presence of Water Vapor," *Combust. Flame*, Vol. 41, 1981. p. 123.

7 Essenhigh, R. H., and Csaba, J., "The Thermal Radiation Theory for Plane Flame Propagation in Coal Dust Clouds," *Ninth International Symposium on Combustion*, Academic Press, New York, 1963, p. 111.

8 Bhaduri, D., and Bandyopadhyay, S., "Combustion in Coal Dust Flames," *Combust. Flame*, Vol. 17, 1971, p. 15.

9 Field, M. A., Gill, D. W., Morgan, D. B., and Hawksley, P. G. W., *Combustion of Pulverized Coal*, The British Coal Utilization Research Association, Leatherhead, Surrey, England, 1967.

10 Kranzinski, J. L., Buckius, R. O., and Krier, H., "A Model for Flame Propagation in Low Volatiles Coal Dust," ASME JOURNAL OF HEAT TRANSFER, Vol. 100, 1978, p. 105.

11 Ozerova, G. E., and Stepanov, A. M., "Effect of Radiation on Flame Propagation through a Gas Suspension of Solid Fuel Particles," *Combustion, Explosion, and Shock Waves*, Vol. 9, 1973, p. 543.

12 Howard, J. B., and Essenhigh, R. H., "The Mechanism of Ignition of Pulverized Coal," *Combust. Flame*, Vol. 9, 1965, p. 337.

13 Howard, J. B., and Essenhigh, R. H., "Combustion Mechanisms in Pulverized Coal Flames,"*Combust. Flame*, Vol. 10, 1966, p. 92.

14 Essenhigh, R. H., "Combustion and Flame Propagation in Coal System: A Review," *Sixteenth International Symposium on Combustion*, p. 353, The Combustion Institute, 1977.

15 Matalon, M., "Weak Burning and Gas Phase Ignition about a Carbon Particle in an Oxidizing Atmosphere," *Combustion Science and Technology*, Vol. 25, 1981, p. 43.

16 Janzen, J., "The Refractive Index of Colloidal Carbon," J *Colloid and Interface Sci.*, Vol. 69, 1979, p. 436.

17 Richter, W., and Heap, M. P., "The Impact of Heat Release Pattern and Fuel Properties on Heat Transfer in Boilers," ASME Paper 81-WA/HT-27.

18 Khalil, H., "Radiative Transfer in Pulverized Coal Suspensions," M.S. thesis, Kansas State University, Manhattan, Kansas, 1980.

19 Khalil, H., Shultis, J. K., and Lester, T. W., "Comparison of Three Numerical Methods for Evaluation of Radiant Energy Transfer in Scattering and Heat Generating Media," *Numerical Heat Transfer*, Vol. 5, 1982, p. 235.

20 J. J. Duderstadt, and W. R. Martin, *Transport Theory*, Wiley, New York, 1979.

21 Usiskin, C. M., and Sparrow, E. M., *International Journal of Heat and Mass Transfer*, Vol. 1, 1960, p. 28.

Transient Nonsimilarity Nonlinear Heat Diffusion Solutions

F. B. Cheung
Reactor Analysis and Safety Division,
Argonne National Laboratory,
Argonne, Ill. 60439
Mem. ASME

An approximate analytical method for treating parabolic type nonlinear heat diffusion equations is descibed in this study. The method involves transformation of the partial differential equations along with their initial and boundary conditions in terms of several pseudo-similarity variables followed by numerical solution of a system of quasi-ordinary differential equations. One obvious advantage of the approach is that the solution at a particular time can be found independently of the previous history of the temperature field. The simplicity and directness of the method are illustrated by solving the problem of combined conduction and thermal radiation in a large, heat-generating, particulate bed in contact with a solid. Comparison of the present analytical results is made with available finite difference solutions and found to be good.

1 Introduction

Most nonlinear heat diffusion problems of practical importance do not admit similarity solutions nor other forms of exact solution. Numerical or approximate techniques available at present for treating such problems often require computation of the complete time history of the temperature field. In some engineering applications, the heat diffusion solutions are obtained so as to provide necessary input initial conditions for other on-going processes and, thererefore, are needed only at certain specific times. A simple approximate method that enables us to determine the temperature field at any given instant without having to solve simultaneously for the temperature behavior at previous times is highly desired to facilitate the task of solution.

In the studies of fast reactor safety, for example, it is necessary to demonstrate the coolability of a large mass of heat-generating core debris following the dryout of sodium. One important concern is whether melting of the surrounding structure will occur before the core debris reaches the melting temperature of fuel. To address this issue, the processes of combined conduction and thermal radiation in the dry particulate bed and transient heat conduction in the structure in contact with the bed must be investigated. The primary objective is to determine the temperature distribution at the time of incipient melting of the debris bed-structure system. This information may then be employed to evaluate the mode of penetration and to initiate calculation of the rate of attack of the core debris on the structural materials [1, 2].

Many heat diffusion problems such as the one mentioned above can be described by a system of partial differential equations of the parabolic type. This sytem is mathematically similar to the familiar system of boundry layer equations [3]. It follows that with proper modifications, the approximate techniques for treating boundary layer problems may be applicable to the solution of the heat diffusion equations.

Among the various approaches in boundary layer studies, the method of local similarity appears to be the one most widely employed. One salient feature of this method is that the solution at any axial location can be found without having to perform calculations at upstream locations.[1] By suitable transformation of the boundary layer equations and deletion of the nonsimilar axial derivatives, a system of quasi-ordinary differential equations is obtained which may be readily solved by standard techniques. However, this approach cannot be justified convincingly because there is no positive way to estimate the effect of the nonsimilar terms on the final results. Hence the local similarity solutions are of uncertain accuracy. To correct this serious drawback, Sparrow and co-workers [4, 5] have developed the local nonsimilarity method, which retains all of the nonsimilar terms in the conservation equations. By neglecting only the higher order terms in the equations subsidiary to the conservation equations according to a carefully selected closure condition [6–8], a system of quasi-ordinary differential equations is obtained.[2] In so doing, the most attractive feature of the local similarity approach, i.e., the feature of streamwise-independent solutions, is preserved. The local nonsimilarity method has since been employed successfully by a number of researchers in a variety of thermal boundary layer analyses [9–14]. The numerical solution procedure is well established [13].

In this paper, a method for deriving transient nonsimilarity heat diffusion solutions is developed based on the concept of local nonsimilarity. The method is applied to the problem of nonlinear heat diffusion in a dry, heat-generating, core debris bed on top of a solid. Instantaneous temperature profiles of the bed and the solid are obtained independently of the previous temperature transients. Effects of several parameters controlling the temprature structure at the time of incipient melting of the system are described. The validity of the present analysis is tested internally and confirmed by comparison with available finite difference results. Finally, important differences in the scheme of numerical solution between the heat-diffusion transient nonsimilarity method and the boundary-layer local nonsimilarity approach are outlined and discussed.

2 The Physical Problem

We are concerned here with the situation in which a large mass of heat-generating core debris resulting from a hypothetical core-disruptive accident is on top of a solid structure. This structure could be the reactor cavity or a core-retention device. The depth of the debris bed is assumed to be much larger than the average diameter of the debris particles, and the solid structure is assumed to be very thick so that both regions may be treated as semi-infinite bodies. Initially, both the bed and the solid are considered to be at the same tem-

---

[1] This feature fits in nicely with our requirements. If the axial spatial variable is regarded as the time variable in the heat diffusion equations, the temperature profile at any instant may be determined independently of the previous history of the temperature field.

Contributed by the Heat Transfer Division for publication in the JOURNAL OF HEAT TRANSFER. Manuscript received by the Heat Transfer Division, September 21, 1982.

[2] Depending on the degrees of approximation, the local nonsimilarity system can be much larger in size than the local similarity system.

perature corresponding to the boiling point of sodium. As time proceeds, the temperature of the bed rises due to decay heating of the fuel particles whereas the temperature of the solid also rises due to heating by the bed. To describe the likely course of the accident, a criterion is needed to determine under what conditions the interface temperature would reach the melting point of the solid before the debris bed reaches the melting temperature of the fuel.

The central task is to obtain the temperature distribution of the debris bed-solid system at the time of incipient melting. Once this is known, the criterion can be established; and there is no need to determine the complete time history of the temperature field. The choice of this practically important problem to illustrate the transient nonsimilarity solution method is obvious. Another reason for selecting this problem is that finite difference numerical solutions for the same problem, needed to justify the present analytical approach, have already been obtained in [15]. Here, much wider ranges of the controlling parameters are explored so that the present solutions are more broadly applicable than those of [15].

To formulate the problem, the process of combined conduction and thermal radiation in the core debris bed is modeled by treating the bed as a continuum with its bulk properties related to the average bed voidage [16, 17]. The fuel particles are assumed to be uniformly distributed in the bed and the heat transfer area between the bed and the solid is assumed to be sufficiently large such that the heat transfer process is virtually one-dimensional. If the bed voidage, ω, is assumed to be constant, then the solid temperature, T_s, and the bed temperature, T_m, are governed respectively by [15]

$$\frac{\partial T_s}{\partial t} = \alpha_s \frac{\partial^2 T_s}{\partial x^2}, x \leq 0 \tag{1}$$

$$\frac{\partial T_m}{\partial t} = \alpha_m \frac{\partial}{\partial x}\left\{\left[1 + \frac{4}{3N}\left(\frac{T_m}{T_o}\right)^3\right]\frac{\partial T_m}{\partial x}\right\} + S, x \geq 0 \tag{2}$$

with initial and boundary conditions

$$T_m(0,x) = T_s(0,x) = T_o, \tag{3a}$$

$$T_m(t,0) = T_s(t,0) = T_i(t), \tag{3b}$$

$$k_m\left[1 + \frac{4}{3N}\left(\frac{T_i}{T_o}\right)^3\right]\left(\frac{\partial T_m}{\partial x}\right)_{x=0} = k_s\left(\frac{\partial T_s}{\partial x}\right)_{x=0}, \tag{3c}$$

$$T_m(t,\infty) = T_o + St,\ T_s(t, -\infty) = T_o, \tag{3d}$$

where x is the spatial coordinate measured upward from the debris bed-solid interface, T_i the unknown interface temperature to be determined in the course of analysis, S the decay heat generation rate, and N the modified conduction-radiation coupling parameter. The latter is defined by

$$N = 4\,k_m/3f\sigma T_o^{\,3}\,D_p \tag{4}$$

where σ is the Stefan-Boltzman constant, D_p the average particle diameter, and f is a function of the emissivity of the particles and the average bed voidage [18, 19]. Obviously, the parameter N, which depends not only on the properties of the materials of the system but also on the composition and voidage of the bed, must be determined by considering each particular accident situation. To minimize the number of independent parameters of the system, we shall assume all transport properties to be constant, including the value of N.

3 Transient Nonsimilarity Solution Method

In the limit of $S = 0$, equation (2) may admit similarity solutions, a fact which was first recognized by Yang]20]. The present problem, however, becomes trivial in this special case. With $S = 0$, there is no heating of the system and both T_m and T_s will remain unchanged. For the case in which S is a positive, nonzero quantity, similarity ceases to exist. To seek solutions by the method of transient nonsimilarity, the dependent variables, T_m and T_s, are transformed so as to yield simple, time-invariant boundary conditions. Meanwhile, the independent variables, t and x, are replaced by two pseudo-similarity variables, ξ and η, respectively, where ξ is a function only of t and η a function of both t and x. The purpose of introducing η is to weaken the dependence of the solution on ξ in the same way that a true similarity variable would eliminate the t dependence altogether. This objective is fulfilled by invoking the following transformation

$$\xi = St/T_o, \quad \eta = x/2(\alpha_m t)^{1/2}, \tag{5a}$$

$$T_m/T_o = 1 + \xi\theta_m, \quad T_s/T_o = 1 + \xi\theta_s, \quad T_i/T_o = 1 + \xi\theta_i \tag{5b}$$

With the above expressions, the initial conditions given by equation (3a) are satisfied automatically. The boundary conditions at infinities, i.e., equation (3d) now yield constant values of θ_m and θ_s. In dimensionless form, the governing system becomes

$$\theta_s + \xi\phi_s - \frac{1}{2}\eta\theta_s{}' = \frac{\alpha_s}{4\,\alpha_m}\theta_s{}'', \eta \leq 0 \tag{6}$$

$$\theta_m + \xi\phi_m - \frac{1}{2}\eta\theta_m' = 1 + \frac{\xi}{N}(1+\xi\theta_m)^2\,\theta_m'^2 + \frac{1}{4}\left[1 + \frac{4}{3N}(1+\xi\theta_m)^3\right]\theta_m'', \quad \eta \geq 0 \tag{7}$$

with boundary conditions

Nomenclature

D_p = average particle size
h_i = unkonwn functions; i = 1, 2, 3, 4 defined in equation (25), i = 5 defined in equation (32)
g_i = unknown functions; i = 1, 2 defined in equation (26), i = 3 defined in equation (33)
k_m = thermal conductivity of debris bed medium
k_s = thermal conductivity of solid
N = modified conduction-radiation coupling parameter, equation (4)
S = decay heat generation rate
t = physical time
T_i = interface temperature
T_m = bed temperature
T_{mp} = melting temperature
T_o = initial temperature
T_s = solid temperature
x = spatial coordinate measured upward from the solid surface
σ = Stefan-Boltzmann constant
α_m = thermal diffusivity of debris bed medium
α_s = thermal diffusivity of solid
θ_i = dimensionless interface temperature, equation (5b)
θ_m = dimensionless bed temperature, equation (5b)
θ_s = dimensionless solid temperature, equation (5b)
ϕ = ξ-derivative of θ, second-level equations
ψ = ξ-derivative of ϕ, third-level equations
η = pseudo-similarity variable, equation (5a)
ξ = dimensionless time, equation (5a)
ξ_c = critical value of ξ at the time of incipient melting
ω = average bed voidage

Subscripts

i = interface
m = debris bed medium
o = initial condition
s = solid

$$\eta=0:\ \theta_m=\theta_s=\theta_i,\ \left[1+\frac{4}{3N}(1+\xi\theta_i)^3\right]\theta'_m=\frac{k_s}{k_m}\,\theta'_s, \tag{8a}$$

$$\eta\rightarrow\infty:\ \theta_m=1;\ \eta\rightarrow-\infty:\ \theta_s=0 \tag{8b}$$

where the primes denote the partial derivatives with respect to η and $\phi_m=\partial\theta_m/\partial\xi$, $\phi_s=\partial\theta_s/\partial\xi$, In ξ and η coordinates, the dimensionless temperatures are bounded at all times, i.e., $0\leq\theta_s\leq\theta_i\leq\theta_m\leq 1$. Hence, it is reasonable to assume that both θ_s and θ_m depend principally on η but are weak functions of ξ.

Equations (6) to (8) may be reduced to a system of ordinary differential equations if all the terms involving ξ are neglected. This, however, is justifiable only for ξ values that are very close to zero. Clearly, retention of the ξ-terms in the conservation equations is required when ξ is not small. In this case the task of computation may still be simplified if we deleted terms involving the partial derivatives of ξ, i.e., the ϕ_s and ϕ_m terms. By treating ξ as a parameter rather than an independent variable, the resulting equations may be solved as if they were ordinary differential equations. This so-called first level of truncation[3] leads to the transient similarity solutions. The weakness of this approach is that we do not know the effect of the neglected ϕ_s and ϕ_m terms.

In the transient nonsimilarity approach, all of the terms in the transformed conservation equations are retained, with ϕ_s and ϕ_m being regarded as new dependent variables. The introduction of these two unknowns, however, calls for additional conditions to close the governing system. These are deduced by differentiating the conservation equations, (6) and (7), and the boundary conditions, (8*a*) and (8*b*), with respect to ξ. In so doing, a set of subsidiary equations, to be referred to as the second-level equations, are obtained along with their boundary conditions. The subsidiary equations contain terms involving the time derivatives of ϕ_s and ϕ_m. These terms are dropped in the second level of truncation, leading to a system of quasi-ordinary differential equations for θ_s, θ_m, ϕ_s, and ϕ_m. This procedure, which is basically the same as the one described in [5], may be employed to formulate the higher levels of truncation.

4 Similarity Solution—Small Time Behavior

For $\xi\rightarrow 0$, the terms involving ξ in equations (6) to (8) may be neglected. This results in a system of similarity equations, governing the temperature behavior at sufficiently small times

$$\theta_s{}''=\frac{4\,\alpha_m}{\alpha_s}\left[\theta_s-\frac{1}{2}\eta\,\theta_s'\right],\quad \eta\leq 0 \tag{9}$$

$$\theta''_m=4\left(1+\frac{4}{3N}\right)^{-1}\left[\theta_m-\frac{1}{2}\eta\,\theta'_m-1\right],\quad \eta\geq 0 \tag{10}$$

$$\eta=0:\ \theta_m=\theta_s=\theta_i,\ \left(1+\frac{4}{3N}\right)\theta'_m=\frac{k_s}{k_m}\,\theta'_s; \tag{11a}$$

$$\eta\rightarrow\infty:\ \theta_m=1;\ \eta\rightarrow-\infty,\ \theta_s=0 \tag{11b}$$

A closed-form solution to the above equations exists. This is

$$\theta_s=4\,\theta_i\,i^2\mathrm{erfc}\,(-\eta\sqrt{\alpha_m/\alpha_s}),\quad \eta\leq 0 \tag{12}$$

$$\theta_m=1-4(1-\theta_i)\,i^2\mathrm{erfc}(\eta/\sqrt{1+4/3N}),\quad \eta\geq 0 \tag{13}$$

$$\theta_i=(1+\gamma)^{-1},\ \text{where}\ \gamma=\frac{k_s}{k_m}\left(\frac{\alpha_m}{\alpha_s}\right)^{1/2}\left(1+\frac{4}{3N}\right)^{-1/2} \tag{14}$$

For $\xi\rightarrow 0$, the dimensionless interface temperature is completely determined by a single parameter, i.e., the parameter λ. Equation (14) gives an exact expression for the initial value of θ_i.

5 Transient Similarity Solution—First Level of Trucation

If θ_s and θ_m are truely weak functions of ξ, then the terms $\xi\phi_s$ and $\xi\phi_m$ in equations (6) to (8) may be neglected, regardless of the values of ξ. This leads to the following system of transient similarity equations

$$\theta_s{}''=\frac{4\,\alpha_m}{\alpha_s}\left[\theta_s-\frac{1}{2}\eta\,\theta_s'\right],\quad \eta\leq 0 \tag{15}$$

$$\theta''_m=4\left[1+\frac{4}{3N}(1+\xi\,\theta_m)^3\right]^{-1}\left[\theta_m-\frac{1}{2}\eta\,\theta'_m-1-\frac{1}{N}\,\xi(1+\xi\,\theta_m)^2\,\theta'^2_m\right],\quad \eta\geq 0 \tag{16}$$

$$\eta=0:\ \theta_s=\theta_m=\theta_i$$

$$\left[1+\frac{4}{3N}(1+\xi\,\theta_i)^3\right]\theta'_m=\frac{k_s}{k_m}\,\theta'_s; \tag{17a}$$

$$\eta\rightarrow\infty:\ \theta_m=1;\quad \eta\rightarrow-\infty,\quad \theta_s=0 \tag{17b}$$

In terms of the unknown interface temperature θ_i, a closed form solution may be obtained for θ_s, which has the same expression as the one given by equation (12). From this solution, we have

$$\theta'_s=\frac{4}{\sqrt{\Pi}}\left(\frac{\alpha_m}{\alpha_s}\right)^{1/2}\theta_i\quad \text{at}\ \eta=0 \tag{18}$$

The boundary conditions for θ_m at $\eta=0$ become

$$\theta_m=\theta_i\ \text{and}\ \theta'_m=\frac{4}{\sqrt{\Pi}}\left(\frac{k_s}{k_m}\right)\left(\frac{\alpha_m}{\alpha_s}\right)^{1/2}\left[1+\frac{4}{3N}(1+\xi\,\theta_i)^3\right]^{-1}\theta_i \tag{19}$$

Treating ξ as a constant parameter, equations (16) and (19) may now be integrated numerically as an initial value problem using the Runge-Kutta forward integration scheme. The correct value of θ_i at a given ξ may be obtained by requiring θ_m to approach unity as η approaches infinity. In view of equations (16) and (19), it is obvious that the dimensionless interface temperature, θ_i, is determined here by the two parameters $1/N$ and $(k_s/k_m)\,(\alpha_m/\alpha_s)^{1/2}$.

6 Transient Nonsimilarity Solutions—Second and Higher Levels of Truncation

To obtain more accurate results, it is necessary to retain without approximation all terms in the conservation equations and their boundary conditions. In the second level of truncation, equations (6) to (8) are differentiated with respect to ξ to create a set of second-level subsidary equations governing the dependent variables ϕ_s and ϕ_m. A closure condition is achieved by deleting the terms involving ξ-derivatives of ϕ_s and ϕ_m, i.e., the ψ_s and ψ_m terms, from the resultant equations. This leads to the following governing system

$$\theta_s{}''=\frac{4\,\alpha_m}{\alpha_s}\left[\theta_s-\frac{1}{2}\eta\,\theta_s'+\xi\,\phi_s\right],\ \eta\leq 0 \tag{20}$$

$$\theta''_m=4h_1\left[\theta_m-\left(h_2+\frac{1}{2}\eta\right)\theta'_m-1+\xi\,\phi_m\right],\quad \eta\geq 0 \tag{21}$$

$$\phi_s{}''=\frac{4\,\alpha_m}{\alpha_s}\left[2\,\phi_s-\frac{1}{2}\eta\,\phi_s'\right],\quad \eta\leq 0 \tag{22}$$

$$\phi''_m=4h_1\left[(2-h_3)\phi_m-\left(2h_2+\frac{1}{2}\eta\right)\phi'_m-h_4\right],\quad \eta\geq 0 \tag{23}$$

$$\eta=0:\ \theta_m=\theta_s=\theta_i,\ \phi_m=\phi_s=\phi_i,$$

---

[3] Since terms are deleted in the first-level conservation equations, the scheme is referred to as the first level of truncation.

$$g_1\,\theta_m' = \frac{k_s}{k_m}\,\theta_s'; \quad g_1\,\phi_m' + g_2\,\theta_m' = \frac{k_s}{k_m}\,\phi_s'; \qquad (24a)$$

$$\eta \to \infty:\ \theta_m = 1,\ \phi_m = 0; \quad \eta \to -\infty:\ \theta_s = \phi_s = 0; \qquad (24b)$$

where

$$h_1 = \left[1 + \frac{4}{3N}(1+\xi\,\theta_m)^3\right]^{-1}, \quad h_2 = \frac{1}{N}\xi(1+\xi\,\theta_m)^2\,\theta_m',$$

$$h_3 = \frac{1}{N}\xi(1+\xi\,\theta_m)\,[2\,\xi\,\theta_m'^2 + (1+\xi\,\theta_m)\,\theta_m''], \qquad (25)$$

$$h_4 = \frac{1}{N}[(1+\xi\,\theta_m)(1+3\,\xi\,\theta_m)\,\theta_m'^2 + (1+\xi\,\theta_m)^2\,\theta_m\,\theta_m''];$$

$$g_1 = \left[1 + \frac{4}{3N}(1+\xi\,\theta_i)^3\right], \quad g_2 = \frac{4}{N}(1+\xi\,\theta_i)^2\,(\theta_i + \xi\,\phi_i) \qquad (26)$$

Inspection of the above system indicates that the θ_s and ϕ_s equations are strongly coupled and are defined only in the negative η region, whereas the θ_m and ϕ_m equations are strongly coupled and are defined in the positive η region. Thus the above system must be solved by matching of (θ_s, ϕ_s) and (θ_m, ϕ_m) at the interface, $\eta = 0$. Obviously, the numerical scheme outlined in [13] for the boundary-layer local nonsimilarity model in which all the boundary conditions at $\eta = 0$ are known a priori cannot be applied directly to the present case. Here, an alternate solution scheme is employed in the numerical computation. To begin with, the transient similarity solution obtained in the first level of truncation is used to provide values of θ_s and θ_m in equations (25) and (26). The ϕ-equations, (22) and (23), together with their boundary conditions, equations (24a) and (24b), are integrated as ordinary differential equations using the Runge-Kutta forward integration scheme. The results so obtained are employed to determine the values of ϕ_s and ϕ_m in equations (20) and (21). These equations, together with their boundary conditions, equations (24a) and (24b), may then be itegrated as ordinary differential equations. With the new set of θ_s and θ_m, improved solutions of ϕ_s and ϕ_m can be obtained from equations (22) and (23). This procedure is repeated until satisfactory convergence is reached. Typically, four or five interations are found to be sufficient. Note that in the second level of truncation, the dimensionless interface temperature, θ_i, is controlled by the values of three independent parameters, namely, $1/N$, k_s/k_m, and α_s/α_m.

In the third level of trunation, all terms in the first-level conservation equations (i.e., the θ-equations) and the second-level subsidiary equations (i.e., the ϕ-equations) are retained. A set of third-level subsidiary equations governing ψ_s and ψ_m is generated by differentiating the second-level ϕ-equations and their boundary conditions with respect to ξ, with the terms involving $\partial\psi_s/\partial\xi$ and $\partial\psi_m/\partial\xi$ being neglected from the ψ-equations. The end result is

$$\theta_s'' = \frac{4\,\alpha_m}{\alpha_s}\left[\theta_s - \frac{1}{2}\eta\,\theta_s' + \xi\,\phi_s\right], \quad \eta \le 0 \qquad (20)$$

$$\theta_m'' = 4\,h_1\left[\theta_m - \left(h_2 + \frac{1}{2}\eta\right)\theta_m' - 1 + \xi\,\phi_m\right], \quad \eta \ge 0 \qquad (21)$$

$$\phi_s'' = \frac{4\,\alpha_m}{\alpha_s}\left[2\,\phi_s - \frac{1}{2}\eta\,\phi_s' + \xi\,\psi_s\right], \quad \eta \le 0 \qquad (27)$$

$$\phi_m' = 4\,h_1\left[(2-h_3)\,\phi_m - \left(2\,h_2 + \frac{1}{2}\eta\right)\phi_m' - h_4 + \xi\,\psi_m\right], \quad \eta \ge 0 \qquad (28)$$

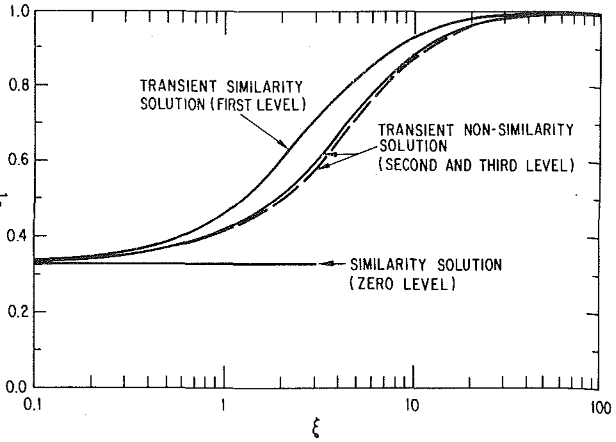

Fig. 1 Time variations of the dimensionless interface temperature

$$\psi_s'' = \frac{4\,\alpha_m}{\alpha_s}\left[3\,\psi_s - \frac{1}{2}\eta\,\psi_s'\right], \quad \eta \le 0 \qquad (29)$$

$$\psi_m'' = 4\,h_1\left[(3-h_3)\psi_m - \left(2\,h_2 + \frac{1}{2}\eta\right)\psi_m' - h_5\right], \quad \eta \ge 0 \qquad (30)$$

$$\eta = 0:\ \theta_m = \theta_s = \theta_i, \quad \phi_m = \phi_s = \phi_i, \quad \psi_m = \psi_s = \psi_i,$$

$$g_1\,\theta_m' = \frac{k_s}{k_m}\,\theta_s', \quad g_1\,\phi_m' + g_2\,\theta_m' = \frac{k_s}{k_m}\,\phi_s',$$

$$g_1\,\psi_m' + 2\,g_2\,\phi_m' + g_3\,\theta_m{}' = \frac{k_s}{k_m}\,\psi_s'; \qquad (31a)$$

$$\eta \to \infty:\ \theta_m = 1,\ \phi_m = \psi_m = 0; \ \eta \to -\infty:\ \theta_s = \phi_s = \psi_s = 0 \,(31b)$$

where h_1, h_2, h_3, h_4 are given by equation (25), g_1, g_2 by equation (26), and

$$\begin{aligned} h_5 = \frac{2}{N}[&(1+\xi\,\theta_m)^2\,(\theta_m + \xi\,\phi_m)\,\phi_m'' + \xi(1+\xi\,\theta_m)^2\,\phi_m' \\ &+ 2(1+\xi\,\theta_m)\,(1+3\,\xi\,\theta_m + 2\,\xi^2\phi_m)\,\theta_m'\,\phi_m' \\ &+ (1+\xi\,\theta_m)\,(1+3\xi\,\theta_m + \xi^2\,\phi_m)\,\theta_m''\,\phi_m \\ &+ \xi(4+6\,\xi\,\theta_m + \xi^2\,\phi_m)\,\theta_m'^2\,\phi_m \\ &+ (1+\xi\,\theta_m)\,\theta_m{}^2\,\theta_m'' + (2+3\,\xi\,\theta_m)\,\theta_m\,\theta_m'^2], \end{aligned} \qquad (32)$$

$$\begin{aligned} g_3 = \frac{4}{N}&(1+\xi\,\theta_i)\,[2(\theta_i + \xi\,\phi_i) \\ &+ (1+\xi\,\theta_i)\,(2\,\phi_i + \xi\,\psi_i)] \end{aligned} \qquad (33)$$

Once again, the dimensionless interface temperature, θ_i, is controlled by $1/N$, k_s/k_m, and α_s/α_m. The above system of coupled ordinary differential equations may be solved numerically in a manner similar to the one described before. To proceed, the transient nonsimilarity solution obtained in the second level of truncation is employed to determine the h_i and g_i values in equations (29) to (31). These equations are then integrated by the method of Runge-Kutta to get ψ_s and ψ_m. With these values of ψ_s and ψ_m, equations (27) and (28) may be integrated with their appropriate boundary conditions to obtain a new set of ϕ_s and ϕ_m. Finally, with the ϕ-solution, equation (20) and (21) may be integrated with their appropriate boundary conditions to determine the θ_s and θ_m functions. We may now start a new cycle of computation with the ψ-equations, i.e., equations (29–31). This procedure may be repeated until satisfactory convergence is reached. An obvious advantage of the present interation scheme is that, in each step, we only have to deal with two equations, i.e., the pair of equations at the same level of trunction. These two equations are coupled only through their boundary conditions

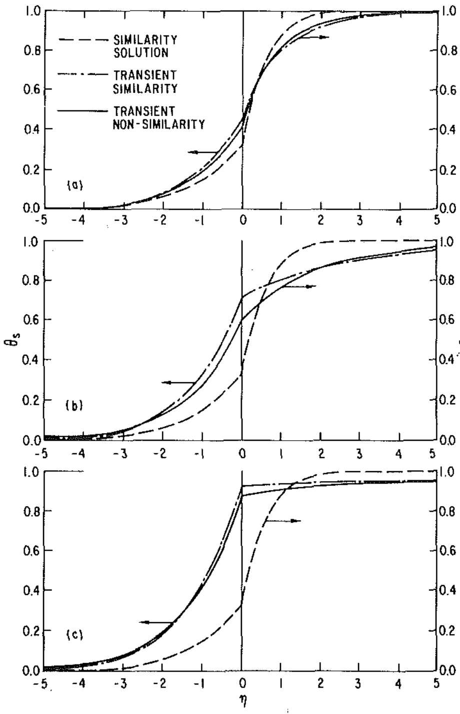

Fig. 2 Dimensionless temperature profiles at three different times: (a) $\xi = 1$, (b) $\xi = 3$, (c) $\xi = 10$

at $\eta = 0$. This iteration scheme is found to be especially useful in obtaining the third level solution which otherwise requires excessive computer time.

It should be pointed out that, although all the θ, ϕ, and ψ functions are determined in the third level of truncation, only θ_s and θ_m are of physical significance in the model. The values of θ_s and θ_m are expected to be reasonably accurate since truncation of the system of equations is now twice removed from the original θ-equations. As will be demonstrated in the next section, the third level solution differs only slightly from the second. Hence, there is no need to seek solutions at levels higher than three.

7 Results and Discussion

We have identified three independent parameters which control the time development of the interface temperature. These are the conduction-radiation coupling parameter, N, the thermal conductivity ratio, k_s/k_m, and the thermal diffusivity ratio, α_s/α_m. To illustrate the accuracy of solutions obtained at various levels of truncation, the calculated dimensionless interface temperatures are compared in Fig. 1 for the case of $N = 1$, $k_s/k_m = 10$, and $\alpha_s/\alpha_m = 10$. These values of parameters are chosen since they are typical of those encountered in nuclear reactor safety studies. At sufficiently small times, θ_i approaches a constant value predicted by the zero-level similarity solution, equation (14). For $\xi > 0.1$, similarity no longer prevails, and θ_i rises gradually in time. Based on the third-level transient nonsimilarity solution (solid curve), the second-level transient nonsimilarity solution (dashed curve) is found to slightly underestimate the interface temperature, whereas the first-level transient similarity solution is found to largely overestimate the interface temperature. Clearly, neither the similarity nor the transient similarity method is able to yield reasonably accurate results. On the other hand, the positions of the curves for various levels of truncation indicate that the transient nonsimilarity method is able to yield rapidly converging solutions. Since the largest variation of temperature always occurs at the interface (see Fig. 2), and since there is only small difference in θ_i between the second-level and the third-level solutions, there is no need to go beyond the third level of truncation. This argument will be substantiated later by comparison of the analytical results with existing finite difference numerical solutions [15].

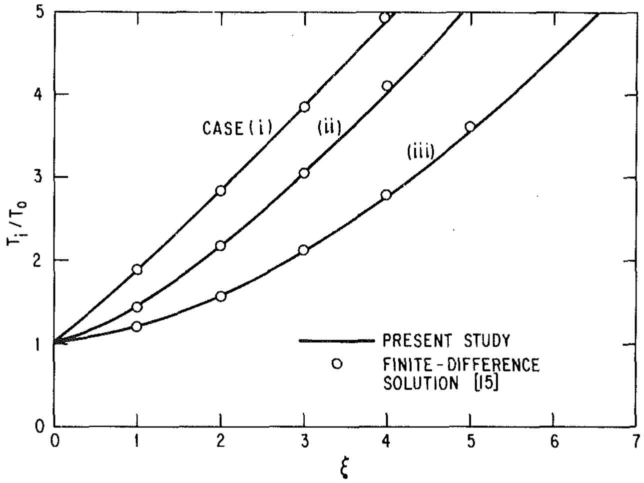

Fig. 3 Effects of k_s/k_m and α_s/α_m on the time development of the interface temperature

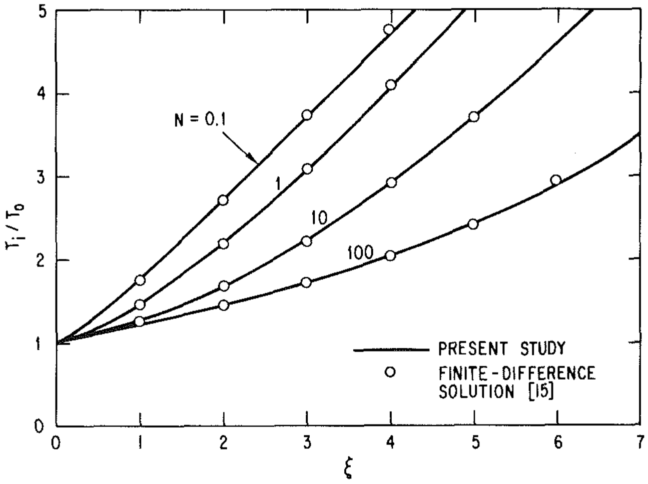

Fig. 4 Effect of N on time development of the interface temperature

The dimensionless temperature profiles at three different times are presented in Fig. 2 for the case of $N = 1$, $k_s/k_m = \alpha_s/\alpha_m = 10$. The transient nonsimilarity results in the figure are from the third level of truncation. To make the figure less busy and to prevent unnecessary confusion, the second-level solution is not included here. At $\xi = 1$ (case a), the temperature field has already deviated markedly from the small-time similarity behavior. In this stage of temperature development, the transient similarity profiles does not differ significantly from the transient nonsimilarity profile. At $\xi = 3$ (case b), however, the difference betweeen the transient similarity and the transient nonsimilarity profiles is quite pronounced.[4] Meanwhile, the similarity solution is totally invalid. At $\xi = 1$ (case c), a quasi-steady state is reached where θ_i approaches unity asymptotically. The transient similarity model is a good approximation only from this stage on. For $\xi >> 10$, both the interface temperature and the bed temperature rise linearly with time, i.e., $T_i/T_o \sim T_m/T_o \sim 1 + \xi$.

---

[4] It should be pointed out that at large values of ξ, a moderate difference in θ_s or θ_m could result in a large difference in the actual temperature, T_s or T_m (see equation 5(b)).

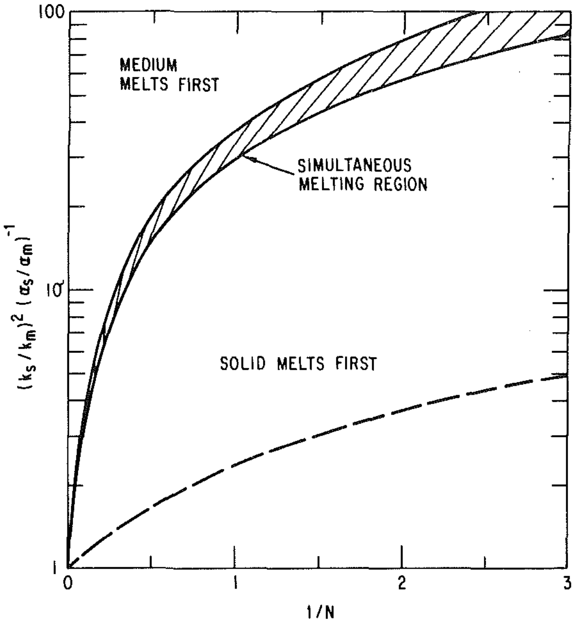

Fig. 5 Incipient melting criteria for the debris bed-solid system

Computation of the interface temperature as a function of ξ has been performed using different values of N, k_s/k_m, and α_s/α_m. Results are summarized in Figs. 3 and 4. In these figures, the solid lines represent the third-level transient nonsimilarity solution, whereas the circles represent the corresponding finite difference numerical solution [15]. The value of N was fixed at unity in Fig. 3, while in Fig. 4 both k_s/k_m and α_s/α_m were fixed at the same value of ten. Three different cases are shown in Fig. 3, namely, (*i*) $k_s/k_m = 1$, $\alpha_s/\alpha_m = 10$, (*ii*) $k_s/k_m = 10$, $\alpha_s/\alpha_m = 10$, (*iii*) $k_s/k_m = 10$, $\alpha_s/\alpha_m = 1$. Apparently, the interface temepratue ries at a higher rate for a system with a smaller value of k_s/k_m. Conversely, a system with a smaller value of α_s/α_m leads to a slower increase of the interface temperature. For given values of k_s/k_m and α_s/α_m, the rate of rise of the interface temperature may be substantially enhanced by decreasing the value of N, i.e., by promoting the effect of radiation.[5] Based upon the finite difference solution, the transient nonsimilarity method is found to yield sufficiently accurate results over the entire range of parameters explored in this study.

Physically, the speed of rise of the interface temperature signifies the potential for melting of the solid. This is because of the fact that the maximum temperature of the solid always occur at the interface and that the maximum bed temperature, occurring in the far field, always rises according to $(T_m)_{\max} \sim (1 + \xi)T_o$. Thus, by setting the maximum bed temperature equal to the melting point of fuel, the time of incipient melting of the bed can be determined, viz., $\xi_c = (T_{mp})_m/T_o - 1$. For the solid to melt at or before this critical time, we require the interface temperature to be at or above the solid melting point, viz.

$$\theta_i(\xi_c) \geq [(T_{mp})_s/T_o - 1]\xi_c^{-1} \qquad (34)$$

Criteria may thus be established to predict the conditions for which the solid would melt before the bed does. To do this, the present transient nonsimilarity approach is employed to compute the interface temperature at the instant $\xi = \xi_c$.[6] For a given value of N, the values of k_s/k_m and α_s/α_m are determined such that equation (34) is satisfied. The results for the case of $T_o = 1000$ K, $(T_{mp})_m = 3000$ K, and $(T_{mp})_s = 2000$ K, which is typical of those encountered in nuclear reactor safety studies, is shown in Fig. 5 by the solid lines. Also shown in the figure for the purpose of comparison is the dashed line representing the similarity solution, equation (14). The k_s/k_m and α_s/α_m effects are lumped together using the modified parameter $(k_s/k_m)^2\,(\alpha_s/\alpha_m)^{-1}$ as suggested by the transient similarity model. This eliminates the necessity of using three-dimensional graphical representation. Should transient similarity prevail in the temperature field, a single solid curve would appear in Fig. 5. Rather, a region is found in which simultaneous melting of the solid and the bed may occur. The width of this region increases with the value of $1/N$. This result clearly indicates that the transient similarity model is not a valid approximation at time $\xi = \xi_c$, especially for a system with strong radiation effects. Similar melting criteria may be determined for other values of T_o and T_{mp}.

8 Concluding Remarks

We have successfully employed the concept of local nonsimilarity to develop a new solution method for treating parabolic-type nonlinear heat diffusion problems. The important features of this method have been illustrated by solving the problem of heat diffusion in a large, heat-generating, particulate bed in sudden contact with a semi-inifinte solid. In addition to its simplicity and directness, the present method has several other advantages. First, the governing partial differential equations can be treated as if they were ordinary differential equations, which greatly simplifies the computation process. Second, the temperature field at the time of incipient melting of the bed may be determined independently of the previous temperature behavior of the system, which is highly desirable in engineering applications. Third, by comparing the various levels of solutions, the accuracy of the result may be checked internally. Finally, the importance of each controlling parameter of the problem may be easily assessed. Although three independent parameters (i.e., N, k_s/k_m, and α_s/α_m) have been identified in the analysis, it is only the combined parameter, λ, that is controlling in the early stage of temperature development. At later times, the system may be roughly described by the two parameters N and $(k_s/k_m)^2\,(\alpha_s/\alpha_m)^{-1}$.

As we proceed to higher levels of truncation, the number of coupled governing equations increases very quickly. Associated with this is the ever-increasing number of boundary conditions that must be satisfied by the solutions. Clearly, the success of the present method relies on the effectiveness of the numerical solution scheme. An effective multiequation solution scheme has been proposed for local nonsimilarity boundary-layer analysis [13]. Unfortunately, the procedure outlined in [13] cannot be applied to the present case. Ths is because of the fact that in the transient nonsimilarity heat-diffusion analysis, the boundary conditions at $\eta = 0$ are themselves unknown quantities which must be determined by matching of the positive-η and the negative-η solutions. Here, we have developed an alternate solution scheme. In each step of computation, only two differential equations have to be solved simultaneously regardless the level of truncation. The two equations are defined in two separate regions (i.e., the $\eta \leq 0$ and $\eta \geq 0$ regions) and are coupled only through their boundary conditions at the interface, $\eta = 0$. On the basis of comparisons internal to the method itself and with available finite difference solutions, the present scheme has been shown to yield rapidly converging

---

[5] This may be achieved by using large-diameter particles with high surface emissivities [18, 19].

[6] The advantage of this approach is now obvious; we do not have to compute the temprature profile at previous times ($\xi < \xi_c$). This saves a tremendous computer time comparing to the finite difference method [15].

and sufficiently accurate results. It is felt that with proper modification of the interfacial condition, the transient nonsimilarity method may be applied for treating phase change problem as well.

Acknowledgments

The author wishes to thank Marsha Reinke for typing the manuscript. This work was performed under the auspices of the U.S. Department of Energy.

References

1 Gluekler, E. L., and Baker, L., Jr., "Postaccident Heat Removal in LMFBRs," *Proceedings of the ASME Symp. on Thermal Hydraulic Aspects of Nuclear Reactor Safety*, Vol. 2, 1977, pp. 285-324.

2 Baker, L. Jr., Cheung, F. B., et al., "Thermal Interations of a Molten Core Debris Pool With Surrounding Structural Materials," *Proc. Int. Mtng. Fast Reactor Safety Technology*, Vol. 1, 1979, pp. 389-399.

3 Schlichting, H., *Boundary Layer Theory*, 6th ed., McGraw-Hill, New York, 1968.

4 Sparrow, E. M., Quack, H., and Boerner, C. J., "Local Nonsimilarity Boundary Layer Solutions," *AIAA Journal*, Vol. 8, 1970, pp. 1936-1942.

5 Sparrow, E. M., and Yu, H. S., "Local Nonsimilarity Thermal Boundary Layer Solutions," ASME JOURNAL OF HEAT TRANSFER, Vol. 93, 1971, pp. 328-334.

6 Coxon, M., and Parks, E. K., "Comments on Local Nonsimilarity Boundary Layer Solutions," *AIAA Journal*, Vol. 9, 1971, p. 1664.

7 Sparrow, E. M., "reply by Authors to M. Coxon and E. K. Parks," *AIAA Journal*, V l. 9, 1971, p. 1664.

8 Rogers, D. F., "Further Comments on Local Nonsimilarity Boundary Layer Solutions," *AIAA Journal*, Vol. 12, 1974, pp. 1007-1008.

9 Minkowycz, W. J., and Sparrow, E. M., "Local Nonsimilarity Solutions for Natural Convection on a Vertical Cylinder," ASME JOURNAL OF HEAT TRANSFER, Vol. 96, 1974, pp. 178-183.

10 Chen, T. S., and Montaoglu, A., "Buoyancy Effects on Forced Convection Along a Vertical Cylinder," ASME JOURNAL OF HEAT TRANSFER, Vol. 97, 1975, pp. 198-203.

11 Novotny, J. L., Bankston, J. D., and Lloyd, J. R., "Local Nonsimilarity Applied to Free Convection Boundary Layers With Radiation Interaction," *Prog. Astronaut. Aeronaut.*, Vol. 39, 1975, pp. 309-330.

12 Chen, C. C., and Eichhorn, R., "Natural Convection From a Vertical Surface to a Thermally Stratified Fluid," ASME JOURNAL OF HEAT TRANSFER, Vol. 98, 1976, pp. 446-451.

13 Minkowycz, W. J., and Sparrow, E. M., "Numerical Solution Scheme for Local Nonsimilarity Boundary Layer Analysis," *Numerical Heat Transfer*, Vol. 1, 1978, pp. 69-85.

14 Hasan, M. M., and Eichhorn, R., "Local Nonsimilarity Solution of Free Convection Flow and Heat Transfer From an Inclined Isothermal Plate," ASME JOURNAL OF HEAT TRANSFER, Vol. 101, 1979, pp. 642-647.

15 Cheung, F. B., et al., "Nonlinear Thermal Interaction Between a Heat Generating Particulate Bed and a Solid," Joint ASME/AIChE National Heat Transfer Conference, Orlando, 1980, Paper No. 80-HT-1.

16 Yagi, S., Kunii, D., and Wakao, N., "Radial Effective Thermal Conductivities in Packed Beds," *Proceedings of the International Heat Transfer Conference*, Part 4, 1961, pp. 742-749.

17 Dampt, H., and Karsten, G., "Effects of Different Types of Void Volumes on the Radial Temperature Distribution of Fuel Pins," *Nucl. Appl.*, Vol. 9, 1970, pp. 288-297.

18 Kasparek C., and Vostmeyer, D., "Warmestrahlung in Schuttungen aus Kugeln Mit Vernachlassigbarem Warmelectwiderstand," *Warme-und-Stoffubertrangung*, Vol. 9, 1976, pp. 117-124.

19 Condiff, D. W., "Radiative Heat Transfer Through a Packed Debris Beds," Argonne National Laboratory Report, ANL-RDP-84, 1979, pp. 262-265.

20 Yang, K. T., "Transient Conduction in a Semi-Infinite Solid With Variable Thermal Conductivity," *Journal of Applied Mechanics*, Vol. 25, 1958, pp. 146-147.

A. D. Snider

A. D. Kraus
Fellow ASME

College of Engineering,
University of South Florida,
Tampa, Fla. 33620

Recent Developments in the Analysis and Design of Extended Surface

Earlier papers by the authors developed a new set of parameters for characterizing heat transfer properties of single fins and fins in arrays of extended surface. The use of these parameters has facilitated the solutions to several interesting fin problems, namely: a more careful characterization of one-dimensional flow configurations, a method for accommodating continuously distributed heat sources along the fin, a perturbation approach for the approximate computation of the parameters, and new insights into the precepts of the optimal fin shape. These developments are reported in this paper.

Introduction

When fins are used to provide extended surface for the transfer of heat the interior heat flow pattern can often be fully two-dimensional. However, the resulting analytics may then become so complicated as to inhibit the design process. An approximate one-dimensional analysis would thus be advantageous to designers if it were computationally efficient, flexible, and reasonably accurate.

The authors in [1], [2], and [3] have published (one-dimensional) algorithms whose computational efficiency far exceeds that of previous methodology. Their flexibility, to date, has been hampered by two faults: their inability to incorporate continuously distributed heat sources along the face of the fins, and their incapacity to handle irregular fin geometries analytically. The present paper resolves both of these shortcomings.

In addition, the one-dimensional flow assumption is examined rigorously, producing a generalization of the condition on the transverse Biot number. Also included are a note on the conditions at the fin tip and a parametric analysis yielding guidelines for optimal design.

Background

Figure 1 displays, in general terms, the prototype of a fin. The well-known equation governing the temperature distribution in the fin, subject to several simplifying assumptions [4, 5], is [1, 6, 7, 8],

$$\frac{d}{dx}\left[kA\frac{d\theta}{dx}\right]-h\frac{dS}{dx}\theta=0 \tag{1}$$

Here, x is the coordinate measured along the fin height from its origin at the fin base ($x=0$) to the fin tip ($x=a$), k is the thermal conductivity, A is the cross-sectional area, θ is the temperature excess (fin temperature minus ambient temperature), h is the coefficient of heat transfer, and dS is the element of lateral fin surface area spanned between x and dx (taking into account the possible slope of the lateral surface). *All of the foregoing quantities may be functions of x.*

Under these circumstances the heat flow at any point in the fin is given by

$$q=-kA\frac{d\theta}{dx} \tag{2}$$

It has been shown [1, 2] that the solution to (1) is conveniently expressed using two particular solutions, $\lambda_1(x)$ and $\lambda_2(x)$, which are defined through their initial conditions

$$\begin{aligned} &\lambda_1(0)=1 && \lambda_2(0)=0 \\ &\lambda_1'(0)=0 && \lambda_2'(0)=-1/k(0)A(0) \end{aligned} \tag{3}$$

It then follows that $\theta(x)$ and $q(x)$ can be expressed in terms of their values at the fin base, $\theta_b\equiv\theta(0)$ and $q_b\equiv q(0)$, via the equations

$$\begin{aligned} \theta(x)&=\theta_b\lambda_1(x)+q_b\lambda_2(x) \\ q(x)&=-k(x)A(x)[\theta_b\lambda_1'(x)+q_b\lambda_2'(x)] \end{aligned} \tag{4}$$

and hence the fin is characterized by a *thermal transmission matrix*, Γ, relating the base and tip variables

$$\begin{bmatrix}\theta_a\\ q_a\end{bmatrix}=[\Gamma]\begin{bmatrix}\theta_b\\ q_b\end{bmatrix}$$

$$=\begin{bmatrix}\lambda_1(a) & \lambda_2(a)\\ -k(a)A(a)\lambda_1'(a) & -k(a)A(a)\lambda_2'(a)\end{bmatrix}\begin{bmatrix}\theta_b\\ q_b\end{bmatrix} \tag{5}$$

Expressions for Γ for commonly manufactured fin shapes have been developed [1, 2]. Subsequent papers [3, 8, 9] showed how the Γ's could be incorporated into a general procedure for analyzing *arrays* of fins with heat sources at the fin junctures. For future reference it is convenient to tabulate these parameters for the case of fins of fixed cross section and

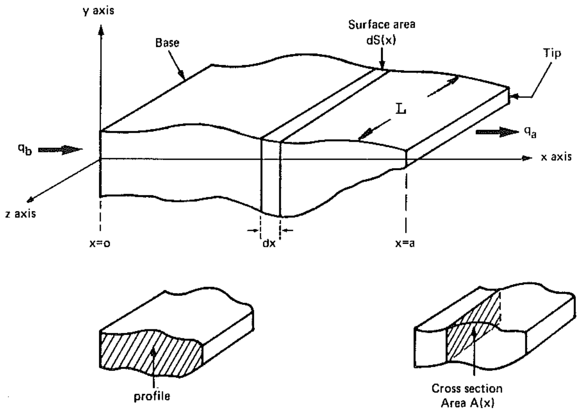

Fig. 1 A general fin

Contributed by the Heat Transfer Division for publication in the JOURNAL OF HEAT TRANSFER. Manuscript received by the Heat Transfer Division May 18, 1981.

constant h and k. Let A denote the cross-section area and P its perimeter. Then

$$\lambda_1(x) = \cosh mx, \quad \lambda_2(x) = -(\sinh mx)/Y \tag{6}$$

and

$$\Gamma = \begin{bmatrix} \cosh ma & -(\sinh ma)/Y \\ -Y \sinh ma & \cosh ma \end{bmatrix} \tag{7}$$

where

$$m = (Ph/Ak)^{1/2} \text{ and } Y = (APhk)^{1/2} \tag{8}$$

The above description must be modified for fins having zero tip width ($A(a) = 0$) because, in that event, (1) possesses a *singular point* [10]. Previous studies [1, 2] demonstrated that for some such fins only certain solutions of (1) would remain finite at the fin tip, and that this condition of finiteness restricted the value of the ratio q_b/θ_b. When this happens the fin is said to be "singular" and its thermal behavior is governed by the equation (replacing (5)).

$$q_b/\theta_b = \mu \tag{9}$$

where the *thermal transmission ratio*, μ, can be computed from the solutions λ_1, λ_2. "Regular" fins are those fins complying with (5).

It was conjectured [2] that *all* fins having zero tip width were singular but this has been recently discounted by the authors, who employed Frobenius's method [10] to show that the longitudinal fin of convex parabolic profile [6] permits a finite (nonzero) heat flow, q_a, through its tip (the zero tip width constriction is overcome by an infinite temperature gradient). As a result, this fin must be classified as *regular* and governed by (5). The mathematical details are omitted.

The One-Dimensional Flow Assumption

One of the controversial assumptions upon which equation (1) is premised is that the variation in the y-direction (Fig. 1) is negligible (there is a consensus that z-variations can be safely ignored). To estimate this effect, consider the fully general steady state two-dimensional temperature $T(x,y)$ governed by Laplace's equation [6, 7]

$$\left[\frac{\partial^2}{\partial x^2} + \frac{\partial^2}{\partial y^2}\right] T = 0 \tag{10}$$

in the fin interior, and by Newton's law of cooling [6, 7]

$$-k \frac{\partial T}{\partial n} = h(T - T_s) \tag{11}$$

on the surface. The left hand side of (11) is the heat flux just inside the fin, normal to the surface; by energy balance this equals the heat transfer flux, expressed on the right in terms of the ambient temperature, T_s. A little analytic geometry reveals that, on the upper face of the fin, ($y > 0$)

$$\frac{\partial T}{\partial n} = \left[-y' \frac{\partial T}{\partial x} + \frac{\partial T}{\partial y}\right] / (1 + y'^2)^{1/2} \tag{12}$$

where $y = y(x)$ is the profile function of the fin's surface. Thus

$$\frac{\partial T}{\partial y} = y' \frac{\partial T}{\partial x} + (1 + y'^2)^{1/2} \frac{\partial T}{\partial n}$$

$$= y' \frac{\partial T}{\partial x} - (1 + y'^2)^{1/2} \frac{h}{k} (T - T_s) \tag{13}$$

For flat fins or for fins tapering towards the tip, y' is nonpositive; moreover, the signs of $\partial T/\partial y$ and $\partial T/\partial x$ will both be opposite to that of $(T - T_s)$ for the geometry of Fig. 1. With a little thought one can see that this implies

$$\left|\frac{\partial T}{\partial y}\right| \le (1 + y'^2)^{1/2} \frac{h}{k} |T - T_s| \le (1 + y'^2)^{1/2} \frac{h}{k} |\theta_b| \tag{14}$$

(since the maximum temperature excess obviously occurs at the base.)

One can demonstrate (14) along the lower face of the fin by similar reasoning. The inequality is also valid along the base, since $\partial T/\partial y \equiv 0$ there. Thus, barring some extremely bizarre tip condition, we can say that $\partial T/\partial y$ is bounded by (14) everywhere along the surface of the fin. The maximum principle [11] then validates (14) throughout the interior of the fin as well (note that $\partial T/\partial y$ must also satisfy Laplace's equation). We conclude that *the largest variation of temperature in the y-direction is no more than*

$$|T(x,y) - T(x,0)|$$

$$\le (1 + y'^2)^{1/2} \frac{\delta}{2} \frac{h}{k} |\theta_b| = (1 + y'^2)^{1/2} \mathrm{Bi} |\theta_b| \tag{15}$$

for flat or tapered fins. Here δ is the maximum fin thickness, and Bi is the transverse Biot number.

Thus, for flat or tapered fins the flow can be taken as one-dimensional if $\mathrm{Bi} << (1 + y'^2)^{-1/2}$. This generalizes [12], which ignores the effect of the slant and quotes $\mathrm{Bi} << 1$ as the condition. Presumably two-dimensional flow *could* develop even in the presence of small Biot numbers if the fin is extremely tapered.

The other condition that has been stated, that the fin be flat or tapered, also seems to have been overlooked by other authors. A quick sketch reveals immediately that the heat flow lines from surface to base cannot possibly be horizontal if the width of the fin increases towards the tip.

Heat Sources in the Fin Face(s)

Figure 2 illustrates a situation where a fin has a continuously distributed heat source along one face. This extra heat input is described by the function $\rho(x)$ which measures heat flow per unit fin height (ρ can only depend on x, to be consistent with the one-dimensional time independent heat flow assumption). The heat balance equation (1) then becomes modified as follows

$$\frac{d}{dx}\left[kA \frac{d\theta}{dx}\right] - h \frac{dS}{dx} \theta = -\rho(x) \tag{16}$$

where positive ρ indicates heat flow to the fin.

This heat input could result, for example, from physical sources such as electric currents or external radiation. Mathematically, $\rho(x)$ could be introduced to account for nonuniformity in the surrounding temperature; a review of the derivation of (1) [1, 6, 7, 8] shows that if the ambient temperature, T_s, varies with x, then (1) becomes

$$\frac{d}{dx}\left[kA \frac{d\theta}{dx}\right] - h \frac{dS}{dx} \theta = -\frac{d}{dx}\left[kA \frac{dT_s}{dx}\right] \tag{17}$$

and the right hand behaves like a (known) distributed heat source.

The following theorem states that the situation in Fig. 2 is mathematically equivalent to the situation in Fig. 3. That is, the (known) distributed heat source can be replaced by two (also known) *discrete* heat sources, one at the fin base and one at the fin tip. This is very significant because it means that extended surface with distributed external heat loads can be analyzed by the methods in [3, 8, 9].

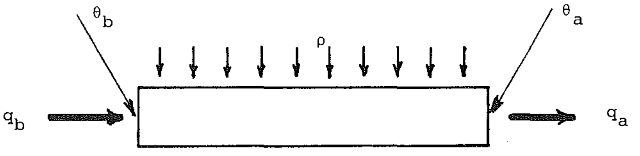

Fig. 2 Fin with distributed heat source on one face

Theorem:

Any individual fin subjected to a heat source, $\rho(x)$, distributed along its face as in Fig. 2, is mathematically equivalent to a combination of a "sourceless" fin, with the same Γ, and two discrete heat sources at the base ($Q_b{}^*$) and the tip ($Q_a{}^*$) as in Fig. 3. That is, $q_b{}^*$ and $q_a{}^*$ in Fig. 3 satisfy

$$\begin{bmatrix} \theta_a \\ q_a^* \end{bmatrix} = \Gamma \begin{bmatrix} \theta_b \\ q_b^* \end{bmatrix} \tag{18}$$

while the original flow variables, q_a and q_b, satisfy

$$\begin{aligned} q_b^* &= q_b + Q_b^* \\ q_a &= q_a^* + Q_a^* \end{aligned} \tag{19}$$

The discrete heat source strengths are given by

$$Q_b^* = \int_0^a \rho(z)\left[\lambda_1(z) - \frac{\gamma_{11}}{\gamma_{12}}\lambda_2(z)\right]dz$$

$$Q_a^* = \frac{1}{\gamma_{12}}\int_0^a \rho(z)\lambda_2(z)\,dz \tag{20}$$

where $\lambda_1(x)$ and $\lambda_2(x)$ are solutions (3) used to compute the elements γ of Γ.

The proof of this remarkable theorem is established by the *variation of parameters method* [10] and some juggling of matrix identities. At the suggestion of the referees the details have been omitted, but a short example may illustrate its usage. A three-fin cascade as displayed in Fig. 4, with a uniformly distributed external heat flux of 500 W/m impinging on the center fin, can be modeled by the discrete-source configuration of Fig. 5, with source strengths of 7.77W each. (The relevant dimensions used here are δ = .0095m, L = .305m, a = .114m, k = 173W/m°C, h = 113.5W/m^2°C). The discrete-source configuration is easily analyzed by the methods of [3, 8, 9].

Perturbation Computations for Γ

The commonly manufactured longitudinal fins have the constant cross-section profile associated with (7). It is possible to compute an approximate correction to the Γ matrix if the fin shape deviates only slightly from this form. For a longitudinal symmetric fin profile, the substitutions of the profile function $y(x)$ into (1) produces the equation

$$\frac{d}{dx}\left[y\frac{d\theta}{dx}\right] - \frac{h}{k}\,[1+[y'(x)]^2]^{1/2}\theta = 0 \tag{21}$$

The analysis here is based on first-order perturbation theory applied to (21) [13].

Let the profile function be given by

$$y(x) = \frac{\delta}{2} + \Delta y(x) = \frac{\delta}{2} + \epsilon\eta(x) \tag{22}$$

where $\eta(x)$ gives the shape of the deviation Δy and ϵ is a scale factor, presumed small. All powers of ϵ higher than the first are assumed negligible. It is also assumed that δ measures the actual width at the fin base so that $\eta(0)=0$. The perturbed solution is written as

$$\theta(x) = \theta_0(x) + \epsilon\theta_1(x) \tag{23}$$

When (22) and (23) are inserted into (21), the first order terms yield

$$\frac{d}{dx}\left[\eta(x)\frac{d\theta_0}{dx}\right] + \frac{\delta}{2}\frac{d^2\theta_1}{dx^2} - \frac{h}{k}\theta_1 = 0 \tag{24}$$

Because the unperturbed solution $\theta_0(x)$ is known, (24) is more suggestively written as

$$\frac{d^2\theta_1}{dx^2} - \frac{2h}{k\delta}\theta_1 = -\frac{2}{\delta}\frac{d}{dx}\left[\eta(x)\frac{d\theta_0}{dx}\right] \tag{25}$$

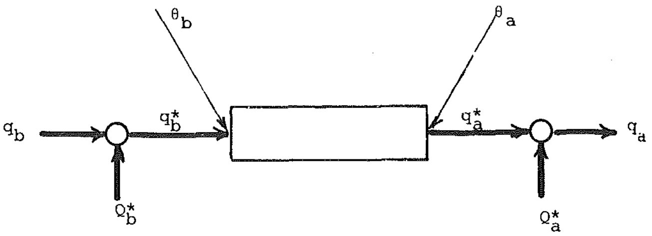

Fig. 3 Nomenclature and terminology for fin with distributed source on one face

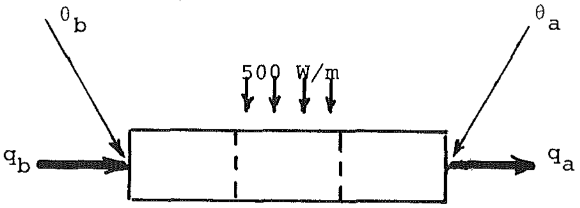

Fig. 4 Fin configuration for example

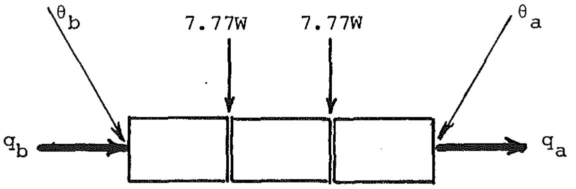

Fig. 5 Discrete-source equivalent

The associated homogeneous solutions are cosh mx and sinh mx with m as in (8), and the variation of parameters method then displays the general solution as

$$\theta_1(x) = C\sinh mx + D\cosh mx - \frac{2}{\delta}\int_0^x \frac{d}{dx}\left[\eta(z)\frac{d\theta_0(z)}{dz}\right] \cdot \frac{\sinh mz\cosh mx - \cosh mz\sinh mx}{m(\sinh^2 mz - \cosh^2 mz)}\,dz$$

which after simplification and integration by parts becomes

$$\theta_1(x) = C\sinh mx + D\cosh mx - \frac{2}{\delta}\int_0^x \eta(z)\frac{d\theta_0}{dz}\cosh(z-x)\,dz \tag{26}$$

To obtain the correction $\lambda_1(x)$, one sets $\theta_0(x) = \cosh mx$ from (7) and then chooses C and D so that the initial conditions of (3) remain intact. The result is

$$\theta_1(x) = -\frac{2m}{\delta}\int_0^x \eta(z)\sinh mz\cosh m(z-x)\,dz \tag{27}$$

Similarly, for $\lambda_2(x)$ one obtains

$$\theta_1(x) = \frac{2m}{\delta(2hk\delta)^{1/2}L}\int_0^x \eta(z)\cosh mz\cosh m(z-x)\,dz \tag{28}$$

Consequently, the perturbed solutions can be written

$$\lambda_1(x) = \cosh mx - \frac{2m}{\delta}\int_0^x \Delta y(z)\sinh mz\cosh m(z-x)\,dz \tag{29a}$$

and

$$\lambda_2(x) = \frac{-\sinh mx}{(2hk\delta)^{1/2}L} + \frac{2m}{\delta(2hk\delta)^{1/2}L}\int_0^x \Delta y(z)\cosh mz\cosh m(z-x)\,dz \tag{29b}$$

The corrected Γ matrix can then be evaluated using (29) in (5).

To test the procedure the authors treated the fin with trapezoidal profile in Fig. 6 as a perturbation of the fin with rectangular profile in the same figure. The relevant dimensions were $L = .305\text{m}$, $a = .038\text{m}$, $\delta_b = .0096\text{m}$, $\delta_a = .0080\text{m}$, $k = 173\ \text{W/m}^\circ\text{C}$, $h = 113.5\ \text{W/m}^2\ {}^\circ\text{C}$. The perturbation approach yielded

$$\Gamma = \begin{bmatrix} 1.113 & -.0852 \\ -2.726 & 1.106 \end{bmatrix}$$

incorporating corrections of up to 10 percent. The exact value [1] is

$$\Gamma = \begin{bmatrix} 1.111 & -.0846 \\ -2.734 & 1.108 \end{bmatrix}$$

and it is observed that the perturbation is quite good.

Perturbation corrections for variability of the heat transfer coefficient $h(x)$ are reported by the authors in [14].

Parametric Study

The aim of the present section is to demonstrate the roles of the various parameters—h, k and the fin dimensions—in determining the heat transfer properties of a fin. The authors pointed out at length in [2] that no one single number can characterize the efficiency of a regular fin for all situations (since Γ has *three* degrees of freedom), so two "fairly typical" sets of operating conditions will be studied.

First consider a single regular fin attached to prime surface at its base, with its tip operating adiabatically. In such a case the condition $q_a = 0$ imposes a relation on q_b and θ_b precisely analogous to that for a singular fin (9)

$$\frac{q_b}{\theta_b} = -\frac{\gamma_{21}}{\gamma_{22}} \qquad (30)$$

and this "effective thermal transmission ratio" gives a quantitative measure of how well the fin is doing its job (i.e., transferring heat!). (In fact, the classic concept of fin efficiency was defined to be proportional to this number [4].)

To see how the parameters affect this ratio, attention is focused on the commonly manufactured fins of constant cross-section (recall (7)). Then the ratio (30) takes the form

$$\mu_{\text{effective}} = \frac{q_b}{\theta_b}$$

$$= (APhk)^{1/2}\tanh\left(\frac{Ph}{Ak}\right)^{1/2} a \equiv \mu(A,P,h,k,a) \qquad (31)$$

For convenience in analyzing the role of the various parameters in (31), Fig. 7 displays the graphs of tanh x, x tanh x, and x tanh x^{-1}. From these graphs one sees that an increase in *any* of the 5 variables, A, P, h, k, or a, results in an improvement in μ. Physically, this is not surprising. However, before formulating a design policy, it is wise to consider the "payoffs."

1 As $a \to \infty$, $\mu \to (APhk)^{1/2}$. However, because of the shape of the tanh curve, μ is already within 75 percent of this limit when

$$\left(\frac{Ph}{Ak}\right)^{1/2} a = 1$$

Hence, there is little benefit in increasing the fin height a beyond the value

$$a \leq \left(\frac{Ak}{Ph}\right)^{1/2} \qquad (32)$$

Arguing on a similar basis, Lienhard [15] derives (32) with an extra factor of 2.

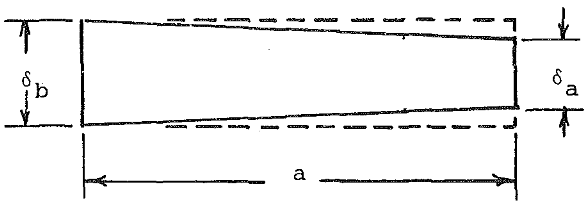

Fig. 6 Rectangular and trapezoidal fin profiles

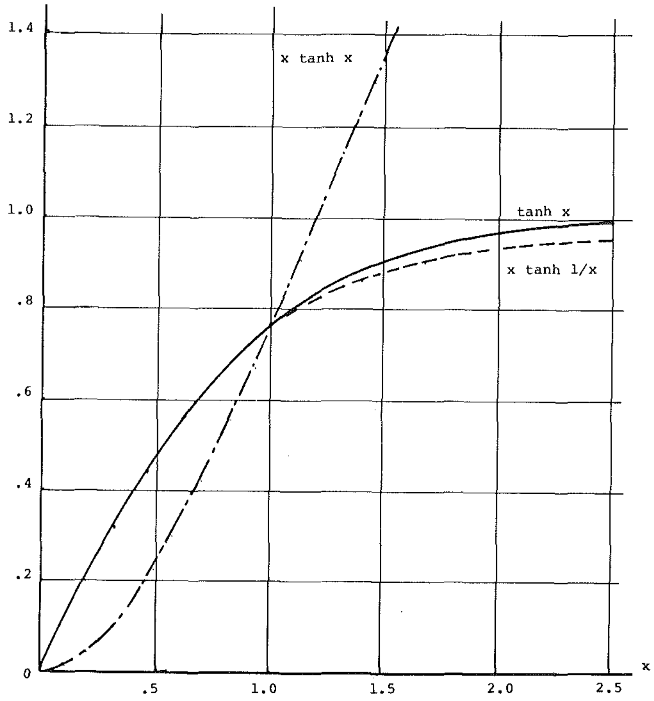

Fig. 7 Tanh x, x tanh x, and x tanh $1/x$

2 As $A \to \infty$, $\mu \to Pha$. However, again the numerics show there is little benefit in increasing A beyond

$$A \leq \frac{4a^2 Ph}{k} \qquad (33)$$

This design equation appears to be new.

3 As $k \to \infty$, $\mu \to Pha$ also; in fact, only the *combination* (kA) influences μ. So the limiting equation (33) governs the effective benefit of increasing k as well. (In passing one may note that $k = \infty$ corresponds to the classic concept of a 100 percent efficient fin.)

4 As $P \to \infty$, $\mu \to \infty$. There is *no limit* to the benefit that can be obtained by increasing P! Hence the perimeter is a more valuable control variable than the cross-section area, and when there is a trade-off, *P should be increased at the expense of A*. Fortunately, this is consistent with geometry; the "isoperimetric inequality" (which states that a circle has minimal perimeter for a given area) places a lower limit on P for a given A, but there is no upper limit.

5 As $h \to \infty$, $\mu \to \infty$. No doubt about it, increasing the heat transfer coefficient will increase the heat transfer, and without limit!!

This can be summarized in optimal design guidelines for manufacturing fins with high heat transfer. The order of priorities is as follows:

(*i*) Make h and P as large as possible

(*ii*) Make A, k, and a as large as possible without jeopardizing (*i*), but avoid overdesigning by observing the limits

$$1 \leq \frac{Ak}{Pha^2} \leq 4 \qquad (34)$$

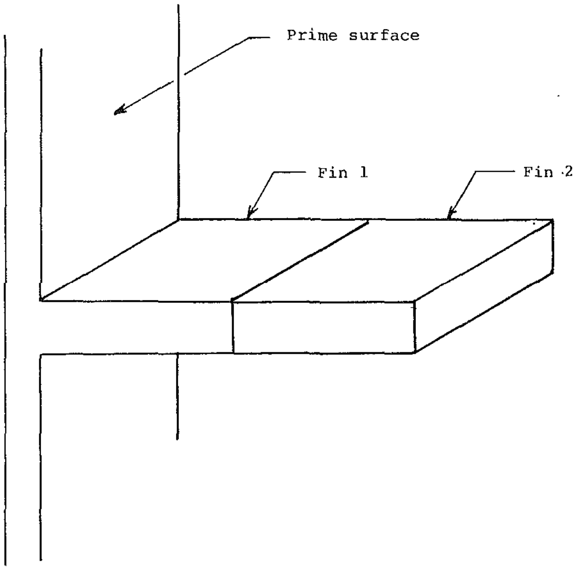

Fig. 8 Two fins in cascade

When manufacturers' constraints are present one modifies the analysis accordingly. For example, suppose this fin is to be manufactured using a given volume, V, of material. The relation $V = Aa$ can be inserted into (31), with $A = \delta L$ and $P = 2(\delta + L) \approx 2L$

$$\mu = \frac{(2hk)^{1/2} V}{a\delta^{1/2}} \tanh\left\{\left(\frac{2h}{k}\right)^{1/2} \frac{a}{\delta^{1/2}}\right\} \tag{35}$$

For fixed a, $\mu \to \infty$ as $\delta \to 0$; so choose $\delta = \delta_0$, the minimum width that can be machined.

Then with $\delta = \delta_0$, μ decreases with a—equivalently, μ increases with $L = V/\delta_0 a$—so L should be chosen as large as practicable, say L_0. This sets the fin height at $a = V/\delta_0 L_0$.

However, since the limiting value of μ as a function of L with δ_0 fixed is finite

$$\lim \mu = 2hV/\delta_0 \text{ as } L \to \infty \tag{36}$$

there is little benefit in choosing L_0 much greater than

$$L_0 \approx \frac{2V}{\delta_0}\left(\frac{2h}{k\delta_0}\right)^{1/2} \tag{37}$$

The second situation to be considered involves a fin that is used in cascade with another fin, such as fin 1 in Fig. 8. In this case the q/θ ratio at the base of fin 1 is a function of the q/θ ratio at its tip [1]

$$\frac{q_b}{\theta_b} = \frac{-\gamma_{21} + \gamma_{11} q_a/\theta_a}{\gamma_{22} - \gamma_{12} q_a/\theta_a} \tag{38}$$

If fin 2 has been designed to have a high q/θ ratio (by the previous considerations), then the q/θ ratio for the *combination* is determined by the properties of fin 1

$$\frac{q_b}{\theta_b} \to -\frac{\gamma_{11}}{\gamma_{12}} \text{ as } \frac{q_a}{\theta_a} \to \infty \tag{39}$$

In other words, the effort expended in making $-\gamma_{21}/\gamma_{22}$ (equation (30)) very large for fin 2 will be wasted unless $-\gamma_{11}/\gamma_{12}$ is comparably large for fin 1! A poor "bottom" fin in a cascade can choke off, and nullify, the heat flow to the second fin; and the measure of effectiveness for the bottom fin, equation (39), is different from the measure of effectiveness for the higher fin, equation (30).

For the common fin shapes considered herein, the ratio in equation (39) takes the form (see (7))

$$\mu_{\text{effective}} = \mu(A,P,h,k,a) = (APhk)^{1/2}\coth\left(\frac{Ph}{Ak}\right)^{1/2} a \tag{40}$$

The analogous computations now show:

(*i*) μ *decreases* with a, approaching ∞ as a goes to zero
(*ii*) μ approaches ∞ with P and h
(*iii*) μ approaches ∞ with A and k

Briefly, the bottom fin in a cascade should be short and squat; otherwise, efforts to optimize the second fin are wasted.

Conclusion

This paper has reported some recent developments by the authors in extended surface analysis and design. The technique for handling distributed heat sources and the perturbation procedure are new and practical. The parametric study mostly confirms the accepted precepts of industrial practice, but design inequality (33) seems to be new. The rigorous analysis of the transverse Biot number and the announcement of a regular fin with zero tip width are, admittedly, more of academic interest but are included because it is felt they have a place in the permanent literature.

Acknowledgment

Some of the material contained in this paper was developed under National Science Foundation Grant ENG-77-01297.

References

1 Kraus, A. D., Snider, A. D., and Doty, L. F., "An Efficient Algorithm for Evaluating Arrays of Extended Surface," ASME JOURNAL OF HEAT TRANSFER, Vol. 100, May 1978, pp. 288-293.

2 Kraus, A. D., and Snider, A. D., "New Parameterizations for Heat Transfer in Fins and Spines," ASME JOURNAL OF HEAT TRANSFER, Vol. 102, Aug. 1980, pp. 415-419.

3 Snider, A. D., and Kraus, A. D., "A General Extended Surface Analysis Method," ASME JOURNAL OF HEAT TRANSFER, Vol. 103, Nov. 1981, pp. 699-704.

4 Gardner, K. A., "Efficiency of Extended Surfaces," *Transactions ASME*, Vol. 67, 1945, pp. 621-631.

5 Murray, W. M., "Heat Dissipation Through an Annular Disk or Fin of Uniform Thickness," ASME *Journal of Applied Mechanics*, Vol. 5, 1938, pp. A78-A80.

6 Kern, D. Q., and Kraus, A. D., *Extended Surface Heat Transfer*, McGraw-Hill, New York, 1972, pp. 85-90.

7 Kreith, F., and Black, W. Z., *Basic Heat Transfer*, Harper and Row, N.Y., 1980, p. 75.

8 Snider, A. D., "New Techniques in Extended Surface Analysis," to appear in *Int. Jnl. Math. Mod.*

9 Snider, A. D., and Kraus, A. D., "A Graph Theoretical Algorithm for Evaluating Arrays of Extended Surface," *Proceedings of the 10th Annual S.E. Conf. Comb., Graph Th., Comp.*, Vol. II, 1979, pp. 873-891.

10 Hildebrand, F. B., *Advanced Calculus for Applications*, Prentice-Hall, Englewood Cliffs, N.J., 1976, pp. 24-28.

11 Weinberger, H. F., *A First Course in Partial Differential Equations*, Wiley, N.Y., 1965, pp. 55-56.

12 Irey, R. K., "Errors in the One-Dimensional Fin Solution," ASME JOURNAL OF HEAT TRANSFER, Feb. 1968, Vol. 90, p. 175.

13 Bender, C. M., and Orszag, S. A., *Advanced Mathematical Methods for Scientists and Engineers*, McGraw-Hill, New York, 1978, pp. 60-63.

14 Snider, A. D., and Kraus, A. D., "Correcting for Variations in the Heat Transfer Coefficient," *Proceedings of the 7th International Heat Transfer Conference*, Munich, 1982.

15 Lienhard, J. H., *A Heat Transfer Textbook*, Prentice-Hall, Englewood Cliffs, N.J., 1981, pp. 129-130.

Hsin-Sen Chu

Cheng-I Weng

Chao-Kuang Chen

Department of Mechanical Engineering,
National Cheng Kung University,
Tainan, Taiwan, Republic of China

Transient Response of a Composite Straight Fin

The transient response of a straight fin composed of two different materials is analyzed. The Laplace transformation and eigenfunction expansion methods are used in the analysis. The inverse Laplace transform is solved by utilizing the Fourier series technique. It is shown that the conductivity ratio plays an important role on both the heat transfer rate and the time to reach the steady state. However, the effect of diffusivity ratio is found to be insignificant on the transient response when the conductivities are constant.

1 Introduction

The extended surfaces in a heat exchanger can be constructed by coating or laminating a second material on the base material under a corrosive environment or an environment of extremely high temperature. Such an extended surface composed of two materials can be referred to as a composite fin. Barker [1] first reported an analysis on a two-dimensional composite fin. The exact solution obtained was in the form of an infinite series, but the terms beyond the first one were usually negligible. The method used in the above article is the same as that based on a general theorem developed by Tittle [2]. It was utilized to construct the orthogonal sets for solving the general boundary value problem of a composite medium. The concept of quasi-orthogonality was introduced and employed in a rigorous expansion of the boundary function into a series of a nonorthogonal eigenset that arose from the method of separation of variables. Orthogonal sets were then constructed from the nonorthogonal eigenset by the use of orthogonality factors. Since the orthogonality factors depend on the orthogonality condition for each region, the calculation in each region will require considerable efforts. Later, Feijoo et al. [3] presented the Green's function method to convert the boundary value problem of a composite solid with heat generation into a Fredholm integral equation of the second kind. The Green's function constructed by utilizing the concept of quasi-orthogonality was expanded in terms of a nonorthogonal eigenset. Recently, Huang and Chang [4] extended the Green's function method to the unsteady laminated composite problem with or without contact resistance at the interfaces.

This paper presents a more direct method to analyze the two-dimensional unsteady heat conduction in a composite of two layers. Its homogeneous boundary conditions in the transverse direction can be converted to those in the axial direction by a change of the dependant variable. Since it is not difficult to find the solution in the transformed plane, the Laplace transformation is taken with respect to the time variable first and then the eigenfunction expansion method is used for the boundary value problem. Once the solution is transformed plane is obtained, the Fourier series technique can then be used to obtain its inverse transform.

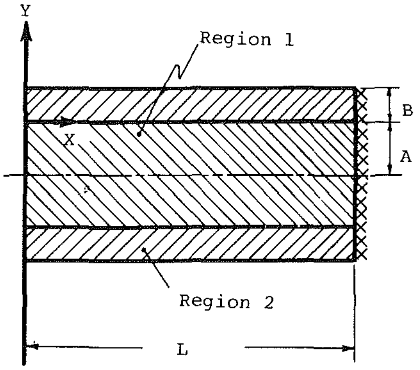

Fig. 1 Configuration of composite straight fin

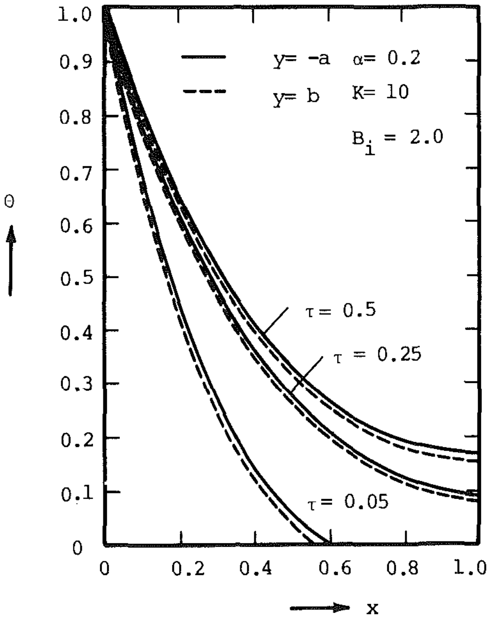

Fig. 2 Temperature profiles for $\alpha = 0.2$, $K = 10$, $B_i = 2.0$, $a = 0.045$ and $b = 0.005$

2 Analysis

Consider a rectangular straight fin, which composes a base material coated with a face material of different thermal characteristics, as shown in Fig. 1. The material of each region is isotropic and homogeneous. All the thermal properties are assumed to be constant and perfect contact is maintained at the interface. The fin tip is also taken to be insulated. Since the geometry and the boundary condition are symmetric about the centerline of the fin, only the analysis for the upper half region is necessary. In order to simplify the analysis, we choose the X-axis along the interface of the two materials. The differential equations to be solved are

$$\rho_i c_i \frac{\partial T_i}{\partial t} = \kappa_i \left(\frac{\partial^2 T_i}{\partial X^2} + \frac{\partial^2 T_i}{\partial Y^2} \right), -A<Y<B, \quad 0<X<L, \tag{1}$$

where $i = 1$, 2, which refer to the region 1 and region 2, respectively. The initial and boundary conditions are

---

Contributed by the Heat Transfer Division for publication in the JOURNAL OF HEAT TRANSFER. Manuscript received by the Heat Transfer Division August 31, 1981.

$$T_i = T_\infty, t=0 \tag{2}$$

$$T_i = T_0, X=0 \tag{3}$$

$$\frac{\partial T_i}{\partial X} = 0, X=L \tag{4}$$

$$\frac{\partial T_1}{\partial Y} = 0, Y=-A \tag{5}$$

$$\kappa_2 \frac{\partial T_2}{\partial Y} + h(T_2 - T_\infty) = 0, Y=B \tag{6}$$

and the matching conditions at the interface are

$$\left.\begin{aligned} &T_1 = T_2 && (7) \\ &\kappa_1 \frac{\partial T_1}{\partial Y} = \kappa_2 \frac{\partial T_2}{\partial Y} && (8) \end{aligned}\right\} Y=0$$

Introducing the following dimensionless quantities θ_i, x, y, a, b, τ, K, α, and B_i as defined in the Nomenclature and the dimensionless temperature Ψ_i as

$$\Psi_i = \theta_i - 1 \tag{9}$$

equations (1)-(8) become

$$\frac{\partial \Psi_1}{\partial \tau} = \frac{\partial^2 \Psi_1}{\partial x^2} + \frac{\partial^2 \Psi_1}{\partial y^2}, -a<y<0,\ 0<x<1 \tag{10}$$

$$\alpha \frac{\partial \Psi_2}{\partial \tau} = \frac{\partial^2 \Psi_2}{\partial x^2} + \frac{\partial^2 \Psi_2}{\partial y^2}, 0<y<b,\ 0<x<1$$

$$\Psi_1 = \Psi_2 = -1, \tau=0 \tag{12}$$

$$\Psi_1 = \Psi_2 = 0, x=0 \tag{13}$$

$$\frac{\partial \Psi_1}{\partial x} = 0, x=1 \tag{14}$$

$$\frac{\partial \Psi_1}{\partial y} = 0, y=-a \tag{15}$$

$$\frac{\partial \Psi_2}{\partial y} + B_i \Psi_2 = B_i, y=b \tag{16}$$

and

$$\left.\begin{aligned} &\Psi_1 = \Psi_2 && (17) \\ &K\frac{\partial \Psi_1}{\partial y} = \frac{\partial \Psi_2}{\partial y} && (18) \end{aligned}\right\} y=0$$

Equations (10-18) represent a typical initial and boundary value problem for a composite medium. We first take the Laplace transform with respect to time, and the system then becomes a boundary value problem. Owing to the homogeneous boundary conditions, equations (13) and (14), we can then expand the dimensionless temperature in an orthonormal set in the following way

$$\tilde{\Psi}_i = \sum_{n=1}^{\infty} g_{ni}(y) \frac{2}{\gamma} \sin(\gamma x) \tag{19}$$

where

$$\tilde{\Psi}_i = \int_0^\infty \Psi_i(x,y,\tau) e^{-s\tau} d\tau \tag{20}$$

$$\gamma = \left(n - \frac{1}{2}\right)\pi \tag{21}$$

It is noted that equation (19) satisfies the transformed boundary conditions of equations (13) and (14) identically. By the substitution of equations (19) and the application of appropriate boundary conditions, the solution in the transformed plane is then

$$\tilde{\Psi}_1 = \sum_{n=1}^{\infty} \left\{ A_{n_1} (\cosh(\lambda_{n_1} y) + \tanh(\lambda_{n_1} a) \sinh(\lambda_{n_1} y)) - \frac{1}{\lambda_{n1}^2} \right\} \bullet \frac{2}{\gamma} \sin(\gamma x) \tag{22}$$

$$\tilde{\Psi}_2 = \sum_{n=1}^{\infty} \left\{ A_{n_2} (\cosh(\lambda_{n_2} y) + B_{n_2} \sinh(\lambda_{n_2} y)) - \frac{\alpha}{\lambda_{n2}^2} \right\} \bullet \frac{2}{\gamma} \sin(\gamma x) \tag{23}$$

where

$$A_{n_1} = \frac{\frac{1}{\lambda_{n2}^2}\left\{ -\frac{B_i \gamma^2}{s} + \frac{\gamma^2(1-\alpha)}{\lambda_{n1}^2} (\lambda_{n_2} \sinh(\lambda_{n_2} b) + B_i \cosh(\lambda_{n_2} b)) \right\}}{\{\lambda_{n_2} \sinh(\lambda_{n_2} b) + B_i \cosh(\lambda_{n_2} b) + K\lambda_{n_1} \tanh(\lambda_{n_1} a) \cosh(\lambda_{n_2} b) + B_i \bullet K(\lambda_{n_1}/\lambda_{n_2}) \tanh(\lambda_{n_1} a) \sinh(\lambda_{n_2} b)\}} \tag{24}$$

$$A_{n_2} = A_{n_1} + \left(\frac{\alpha}{\lambda_{n2}^2} - \frac{1}{\lambda_{n1}^2} \right) \tag{25}$$

$$B_{n_2} = A_{n_1} \bullet K \bullet (\lambda_{n_1}/\lambda_{n_2}) \tanh(\lambda_{n_1} a) \tag{26}$$

and

$$\lambda_{n1}^2 = s + \gamma^2, \lambda_{n2}^2 = \alpha s + \gamma^2 \tag{27}$$

Furthermore, if the boundary condition at the base of the fin

Nomenclature

A = half-thickness of region 1
a = dimensionless half-thickness of region 1, A/L
B = half-thickness of region 2
b = dimensionless half thickness of region 2, B/L
c = heat capacity
h = heat transfer coefficient
K = conductivity ratio of the composite fin, κ_1/κ_2
L = length of the composite fin
Q = total dimensionless heat transfer at the base
T = temperature of the fin
T_∞ = ambient temperature
T_0 = step change of base temperature
T^* = half period of the periodic function defined in equation (40)
t = time
X, Y = Cartesian coordinates
x, y = dimensionless Cartesian coordinates, X/L, Y/L
α_1 = thermal diffusivity of region 1
α_2 = thermal diffusivity of region 2
α = thermal diffusivity ratio of composite fin, α_1/α_2
κ_1 = thermal conductivity of region 1
κ_2 = thermal conductivity of region 2
ψ = dimensionless temperature defined in equation (9)
ρ = density
θ = dimensionless temperature, $(T - T_\infty)/(T_0 - T_\infty)$
τ = dimensionless time, $\alpha_1 t/L$

is an arbitrary function of time, $F(t)$, the solution can be written as

$$\tilde{\Psi}_1 = \sum_{n=1}^{\infty} \Big\{ C_{n_1} (\cosh(\lambda_{n_1} y) + \tanh(X_{n_1} a)\sinh(\lambda_{n_1} y)) - \frac{S\tilde{F}(s)}{\lambda_{n1}^2} \Big\} \cdot \frac{2}{\gamma} \sin(\gamma x) \tag{28}$$

$$\tilde{\Psi}_2 = \sum_{n=1}^{\infty} \Big\{ C_{n_2} \cosh(\lambda_{n_2} y) + D_{n_2} \sinh(\lambda_{n_2} y) - \frac{\alpha s\tilde{F}(s)}{\lambda_{n2}^2} \Big\} \cdot \frac{2}{\gamma} \sin(\gamma x) \tag{29}$$

where

$$C_{n_1} = \frac{\dfrac{1}{\lambda_{n2}^2} \Big\{ -B_i \gamma^2 \tilde{F}(s) + \dfrac{(1-\alpha)\gamma^2 s\tilde{F}(s)}{\lambda_{n1}^2} (\lambda_{n_2} \sinh(\lambda_{n_2} b) + B_i \cosh(\lambda_{n_2} b)) \Big\}}{\{ \lambda_{n_2} \sinh(\lambda_{n_2} b) + B_i \cosh(\lambda_{n_2} b) + K\lambda_{n_1} \tanh(\lambda_{n_1} a)\cosh(\lambda_{n_2} b) + B_i \bullet K(\lambda_{n_1}/\lambda_{n_2})\tanh(\lambda_{n_1} a)\sinh(\lambda_{n_2} b) \}} \tag{30}$$

$$C_{n_2} = C_{n_1} + \frac{s\tilde{F}(s)\gamma^2(\alpha - 1)}{\lambda_{n2}^2 \lambda_{n2}^2} \tag{31}$$

$$D_{n_2} = C_{n_1} K(\lambda_{n_1}/\lambda_{n_2})\tanh(\lambda_{n_1} a) \tag{32}$$

If we define the quantity, $\tilde{Q}$, as

$$\tilde{Q} = -\Big\{ K \int_{-a}^{0} \frac{\partial \tilde{\Psi}_I}{\partial x} \Big|_{x=0} dy + \int_{0}^{b} \frac{\partial \tilde{\Psi}_2}{\partial x} \Big|_{x=0} dy \Big\} \tag{33}$$

or

$$\tilde{Q} = -2 \sum_{n=1}^{\infty} \Big\{ K \Big(\frac{C_{n_1}}{\lambda_{n_1}} \tanh(\lambda_n a) - \frac{a \bullet s\tilde{F}(s)}{\lambda_{n1}^2} \Big) + \frac{C_{n_2}}{\lambda_{n_2}} \sinh(\lambda_{n_2} b) + \frac{D_{n_2}}{\lambda_{n_2}} (\cosh(\lambda_{n_2} b) - 1) - \frac{b \bullet \alpha s\tilde{F}(s)}{\lambda_{n2}^2} \Big\} \tag{34}$$

then the total dimensionless heat flux at the base is given by the inverse Laplace transform of $\tilde{Q}$.

3 Method of Solution

The functions $\tilde{\Psi}_1$, $\tilde{\Psi}_2$ are very complex and it is difficult to find the inverse Laplace transform by the residue theorem. In this paper, a general method, known as the Fourier series technique [5, 6], is used to obtain the inverse transform.

When a function, $\phi(t)$, is given, the Laplace transform and its inversion formula are defined as follows, respectively

$$\tilde{\phi}(s) = \int_0^{\infty} \phi(t) e^{-st} dt \tag{35}$$

$$\phi(t) = \frac{1}{2\pi i} \int_{c-i\infty}^{c+i\infty} \tilde{\phi}(s) e^{st} ds \tag{36}$$

where the chosen positive arbitrary constant, c, should be greater than the real parts of all singularities of $\phi(s)$.

By letting $s = c + i\omega$, equations (35) and (36) are converted to those of the Fourier transform

$$\tilde{\phi}(c + i\omega) = \int_0^{\infty} \phi(t) e^{-ct} e^{-i\omega t} dt \tag{37}$$

$$\phi(t) = \frac{e^{ct}}{2\pi} \int_{-\infty}^{\infty} \tilde{\phi}(c + i\omega) e^{i\omega t} d\omega \tag{38}$$

The above integral can be approximated by

$$\phi(t) \cong \frac{e^{ct}}{2\pi} \sum_{k=-\infty}^{\infty} \tilde{\phi}(c + ik\Delta\omega) e^{ik\Delta\omega t} \Delta\omega \tag{39}$$

and letting $\Delta\omega = \pi/T^*$, we then have

$$\phi(t) \cong \frac{e^{ct}}{2T^*} \sum_{k=-\infty}^{\infty} \tilde{\phi}(c + ik\pi/T^*) e^{ik(\pi/T^*)t} \tag{40}$$

Considering the relation

$$\tilde{\phi}(c + ik\pi/T^*) e^{ik(\pi/T^*)t} + \tilde{\phi}(c - ik\pi/T^*) e^{-ik(\pi/T^*)t} = 2\mathrm{Re}\{ \tilde{\phi}(c + ik\pi/T^*) e^{ik(\pi/T^*)t} \tag{41}$$

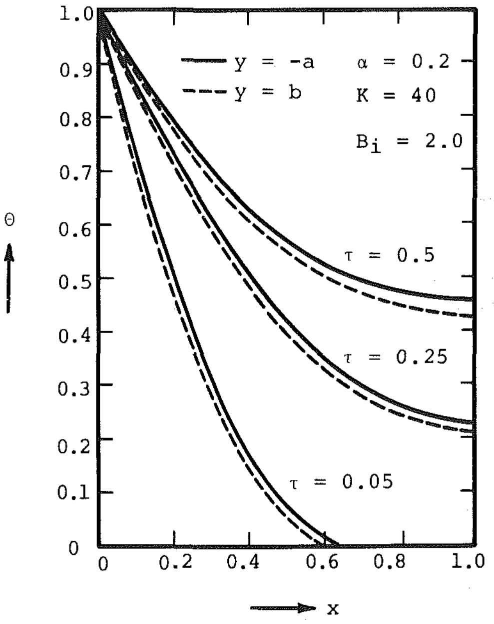

Fig. 3 **Temperature profiles for $\alpha = 0.2$, $K = 40$, $B_i = 2.0$, $a = 0.045$ and $b = 0.005$**

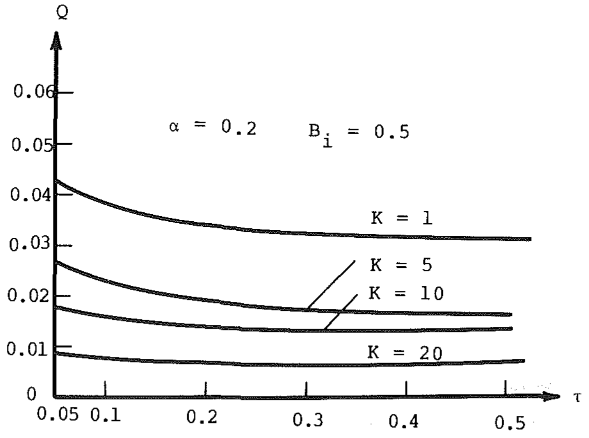

Fig. 4 **Total heat transfer from the fin for $\alpha = 0.2$, $B_i = 0.5$ when the base is subjected to a step change in temperature**

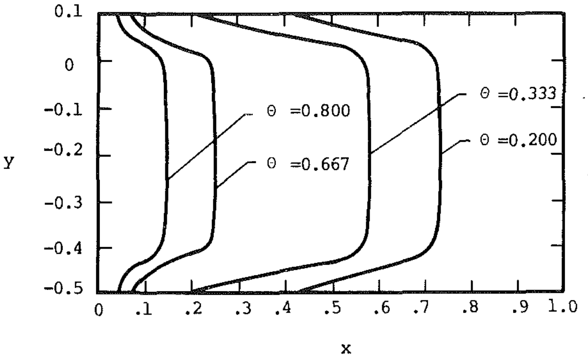

Fig. 5 Isotherms at $\alpha = 0.2$, $K = 40$, $B_i = 10$, and $a = 0.2$, $b = 0.1$

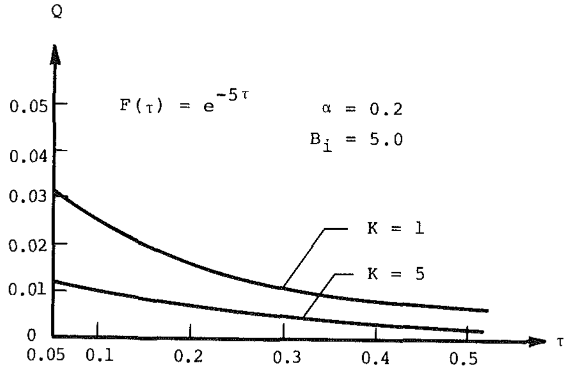

Fig. 6 Total heat transfer rates from the fin for $\alpha = 0.2$, $B_i = 5.0$ when the base is subjected to an exponential decay function of time, e^{-5t}

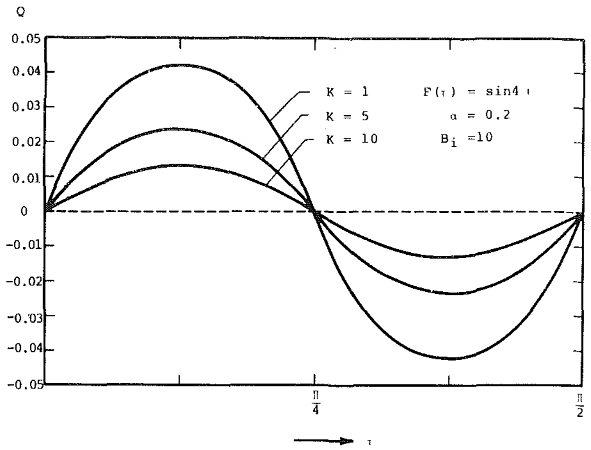

Fig. 7 Total heat transfer rates from the fin for $\alpha = 2$, $B_i = 10$ when the base is subjected to a sinusoidal function of time, sin4*t*

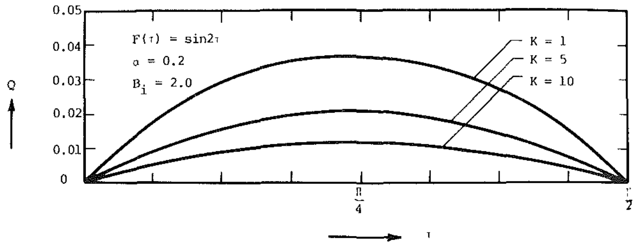

Fig. 8 Total heat transfer rates from the fin for $\alpha = 0.2$, $B_i = 2.0$ when the base is subjected to a sinusoidal function of time, sin2*t*

and truncating the infinite series by N terms, we have the following numerical inversion formula

$$\phi(t) \cong \frac{e^{ct}}{T^*}\left\{\frac{1}{2}\,\tilde{\phi}(c) + \mathrm{Re}\sum_{k=1}^{N}\tilde{\phi}(c+ik\pi/T^*)e^{ik(\pi/T^*)t}\right.,0 \le t < 2T^* \tag{42}$$

From this equation, the numerical value of $\phi(t)$ at any t in the interval $0 \le t < 2T^*$ can be obtained.

The round-off and truncation errors are magnified by the factor, e^{ct}, if the selected c is greater than the necessary figure. When the value of ct is quite large, N should be increased accordingly in order to obtain a good numerical result. Therefore, the optimal value of the constant c should be chosen when t is within the interval 0 to $2T^*$.

At $t = T^*$, (42) becomes

$$\phi(T^*) \cong \frac{e^{cT^*}}{T^*}\left\{\frac{1}{2}\,\tilde{\phi}(c) + \mathrm{Re}\sum_{k=1}^{N}\tilde{\phi}(c+ik\pi/T^*)(-1)^k\right\} \tag{43}$$

from which the numerical result at the point, T^*, can be calculated. This technique is based on the following conditions:

1 the numerical values of ϕ (T^*) are given at the points $T^* = m\Delta T^*$ (m = integer) within the interval $\Delta T^* \le T^* \le T^*_{\max}$ where ΔT^* is a time step; and

2 in this interval, cT^* is a constant to be selected, usually 4 or 5.

4 Results and Discussion

In this study, $\kappa_1 > \kappa_2$, i.e., $K > 1$, is considered since the conductivity of the coated material is generally smaller than that of the base material. In practical cases, the thickness of the fin is about 10 percent of the length, so the half dimensionless thickness of the region 1 and 2, i.e., a and b, are chosen to be 0.045 and 0.005, respectively. Figures 2 and 3 are typical dimensionless plots of temperature distribution θ versus x along the center line, and the surface with the base subjected to a step increase in temperature. It is shown that when α and B_i are fixed, the temperature difference between the center line and the surface will increase as the conductivity ratio, K, increases. This phenomena is resonable, because the large value of K means that the internal resistance to conduction heat flow in region 2 must be high, so that the heat conduction from region 1 to the surface is impeded. This causes large quantity of heat stored in the fin material so that the fin temperature will be higher. However, the temperature gradient in the x-direction is smaller, and hence the total heat transfer from the base is decreased as shown in Fig. 4; the heat transfer rate at $K = 1$ is almost four times that at $K = 20$. It is noted that the conductivity ratio also plays an important role in affecting the time to reach the steady state; the larger the conductivity ratio, the earlier the steady state can be reached.

The isothermal lines for a typical case is shown in Fig. 5; the temperature variations in each region are not significant, except that a proper change of the temperature across the interface of the two regions is necessary, and hence a two-dimensional analysis is needed.

Other cases of different base boundary conditions rather than a step change in temperature have also been calculated. Figure 6 considers the cases where the fin base is subjected to an exponential decay function in time, and Figs. 7 and 8, the sinusoidal functions of time. The heat transfer rate is seen also to be given by a sinusoidal curve. The amplitude is decreased as K increases. However, the period is unchanged. All of these results imply that, at large values of K, the influence of region 2 becomes more significant and must be taken into consideration.

5 Concluding Remarks

The transient response of a composite straight fin has been solved by using the Laplace transformation method. A more direct method is used in this paper and the concept of quasi-orthogonality can be avoid. The Fourier series technique is used to invert the Laplace transform. The computations reported herein were carried out on the Cyber CDC 172 computer of the Cheng Kung University.

References

1 Barker, J. J., "The Efficiency of Composite Fins," *Nuclear Science and Engineering*, Vol. 3, 1958, pp. 300-312.

2 Tittle, C. W., "Boundary Value Problems in Composite Media: Quasi-Orthogonal Functions," *Journal of Applied Physics*, Vol. 36, No. 4, 1965, pp. 1486-1488.

3 Feijoo, L., Davis, H. T., and Ramkrishna, D., "Heat Transfer in Composite Solids with Heat Generation," ASME JOURNAL OF HEAT TRANSFER, Vol. 101, 1979, pp. 137-143.

4 Huang, S. C., and Chang, Y. P., "Heat Conduction in Unsteady, Periodic, and Steady States in Laminated Composites," ASME JOURNAL OF HEAT TRANSFER, Vol. 102, 1980, pp. 742-748.

5 Satoshi Ichkawa, and Akira Kishima, "Applications of Fourier Series Technique to Inverse Laplace Transform," *Kyoto University Memories*, Vol. 34, pt. I, 1972, pp. 53-67.

6 Chu, H. S., Chen, C. K., and Weng, C. I., "Applications of Fourier Series Technique to Transient Heat Transfer Problem," *Chemical Engineering Communication*, Vol. 16, No. 1-6, 1982, pp. 215-227.

N. R. Keltner
Thermal Test and Analysis Division,
Sandia National Laboratories,
Albuquerque, N. M. 87185

J. V. Beck
Department of Mechanical Engineering,
Michigan State University,
East Lansing, Mich. 48824
Mem. ASME

Surface Temperature Measurement Errors

Mathematical models are developed for the response of surface mounted thermocouples on a thick wall. These models account for the significant causes of errors in both the transient and steady-state response to changes in the wall temperature. In many cases, closed form analytical expressions are given for the response. The cases for which analytical expressions are not obtainable can be easily evaluated on a programmable calculator or a small computer.

Introduction

The analysis of and correction for the errors involved when making surface temperature measurements with thermocouples attached externally is an important problem in experimental heat transfer. The errors result from the thermocouple installation altering the local surface temperature distribution and the effects of heat transfer in the thermocouple attachment and the thermcouple itself. The errors may be transient, steady-state, or both.

There are many separate causes of the errors but the most significant are:

1 Thermal constriction effects in the body to which the thermocouple is attached

2 Thermal inertia of the thermocouple [1-14]

3 Imperfect contact between the thermocouple and the surface [7, 10, 11, 15-18]

4 Heat loss from the thermocouple to the ambient [7, 11, 15-18]

5 The effective junction location being displaced from the surface [10, 11]

A number of methods and simplifying assumptions have been utilized in modeling the transient response of thermocouples. An early paper by Henning and Parker [1] used separation of variables for an idealized problem involving a connecting hemisphere of infinite conductivity and zero heat capacity. If a modification of their model suggested in an attached review is not used, the model gives large errors in the early to middle times. Others have solved less idealized models by utilizing (*a*) finite differences [4, 5, 14], (*b*) Duhamel's integral with numerical evaluation [5, 6, 11, 13], and (*c*) Duhamel's integral with Laplace transforms [7, 8, 10, 13].

A recent paper by Cassagne et al. [7] gives a thorough analysis of the transient response problem, except for the effect of junction displacement. The analytical approach is similar to the approach used herein. However, because the exact solution for uniform heat flux is used as the kernel, the solution must be evaluated numerically. The present method uses easily evaluated kernels in Duhamel's equation and in many cases analytical expressions for the response are obtainable.

The analysis is developed for the case of a thermocouple mounted on a thick wall by using the Unsteady Surface Element Method (USEM) [8, 19]. This method utilizes fundamental solutions in the two bodies (i.e., the surface or substrate and the thermocouple or wire) as kernels in Duhamel's convolution equation. The solutions may be developed using either temperature or heat flux kernels. An overall solution which considers all of the above effects will be developed first and then certain special cases will be obtained from this solution. The solutions will be in either closed form or in a form for easy numerical evaluation.

The geometry of the problem being considered is shown in Fig. 1. Two homogeneous, isotropic bodies with temperature independent thermal properties are in thermal contact over a circular region of radius, a. The interface is considered to have an imperfect contact that can be thermally modeled by a contact coefficient, h; if h goes to infinity there is perfect contact. Except for the contact area, the surface of the semi-infinite body is considered to be adiabatic.

The thermocouple is modeled as a single semi-infinite cylinder with lateral surface heat loss characterized by a heat transfer coefficient, h_c, with the ambient at the initial thermocouple temperature. If the cylinder is uninsulated, the coefficient is that due to convection and/or linearized radiation. If it is insulated, axial conduction is assumed to occur only in the wire and radial conduction only in the insulation. Following the simplications utilized by Moffat [15], Sparrow [16], and others for insulated thermocouples, the lateral resistance due to both surface losses and the insulation can be given by

$$R = \frac{1}{h_c 2\pi r} + \frac{\ln(r_o/a)}{2\pi k_i} \qquad (1)$$

where r_o is the outer radius of the insulation layer and k_i is its thermal conductivity. An overall heat transfer coefficient can be defined from equation (1) and can be used in the same manner as h_c.

In general, the temperature and heat flux at the contact vary with radial location as well as with time. In this paper the emphasis is upon providing an average heat flux or temperature across the interfaces. Two complementary assumptions are used: radially constant (*i*) heat flux, and (*ii*) temperature. For the thermocouple application the analysis given for radially constant interface heat flux is particularly appropriate for small dimensionless times. The analysis for a

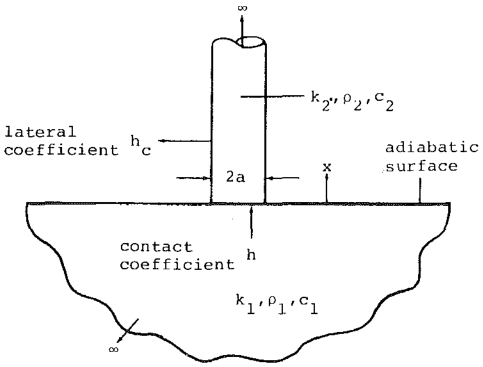

Fig. 1 Idealized geometry for a thermocouple attached externally to a solid surface

---

Contributed by the Heat Transfer Division for publication in the JOURNAL OF HEAT TRANSFER. Manuscript received by the Heat Transfer Division May 7, 1982.

radially constant interface temperature gives accurate results for middle to late times.

Heat Flux Based USE Solution

The heat flux based USE method starts with Duhamel's integral for the average interface temperature for body, j, in the form

$$T_j(0,t) = T_{ji} + \frac{\partial}{\partial t}\int_0^t q_j(\lambda)\phi_j(0,t-\lambda)d\lambda \tag{2}$$

where $q_j(t)$ is the flux *into* body, j. The kernel $\phi_j(0,t)$ is the contact area-average temperature rise in body j at $z_j = 0$ for a unit, q_j. Notice that q_1 and q_2 can be related by

$$q_1(t) = -q_2(t) = h[T_2(0,t) - T_1(0,t)] \tag{3}$$

where again area averages are implied.

Taking the Laplace transform of (2) for $j = 1$ and 2 and solving for $\bar{q}_1(s)$ using the Laplace transform of (3) gives

$$\bar{q}_1/(T_{1i} - T_{2i}) = -1/s[s(\bar{\phi}_1 + \bar{\phi}_2) + 1/h] \tag{4}$$

where the Laplace transform notation is used

$$\bar{q}_1(s) = \int_0^\infty e^{-st} q_1(t)dt \tag{5}$$

This equation can be made dimensionless by defining

$$t^* = \alpha_1 t/a^2 \tag{6a}$$

$$q^* = \frac{q_1 a}{k_1[T_{1i} - T_{2i}]} \tag{6b}$$

$$K = k_2/k_1,\ A = \alpha_2/\alpha_1 \tag{6c,d}$$

$$\phi_j^* = \phi_j k_j/a \tag{6e}$$

$$\Phi^* = \phi_1^* + \phi_2^*/K \tag{6f}$$

$$B = ha/k_1,\ s^* = a^2 s/\alpha_1 \tag{6g,h}$$

The B symbol in (6g) is used to denote a Biot type modulus based on the contact heat transfer coefficient. Using the above notation with the "*" superscripts dropped yields for equation (4)

$$\bar{q}_1 = -1/s(s\bar{\Phi} + 1/B) \tag{7}$$

For the perfect contact case, $B \rightarrow \infty$, and thus

$$\bar{q}_1 = -1/(s^2\bar{\Phi}) \tag{8}$$

The same procedure yields for the interface area-average temperatures

$$\bar{T}_1^* = \bar{\phi}_1/[s\bar{\Phi} + 1/B], \tag{9a}$$

$$\bar{T}_2^* = \bar{\phi}_2/K[s\,\bar{\Phi} + 1/B] \tag{9b}$$

where

$$\bar{T}_1^* = (\overline{T_1 - T_{1i}})/(T_{1i} - T_{2i}), \tag{10a}$$

$$\bar{T}_2^* = (\overline{T_2 - T_{2i}})/(T_{1i} - T_{2i}) \tag{10b}$$

In further use of these equations, the "" superscripts are omitted.*

The relations given by equation (7) and (9a), (9b) are termed transfer functions. Though there is specific reference to the geometry shown in Fig. 1, these relations can be employed for many other cases of two connecting geometries, both semi-infinite and finite. The task now is to invert (9b) for the Fig. 1 geometry which is distinguished from others by its particular ϕ functions.

Temperature Based USE Solution

The temperature based USE method starts with Duhamel's integral for the area-average heat flux through the disk contact

$$q_j(t) = \frac{\partial}{\partial t}\int_o^t [T_j(0,\lambda) - T_{ji}]\theta_{qj}(0,t-\lambda)d\lambda \tag{11}$$

where $\theta_{qj}(0,t)$ is the area average heat flux for a unit increase in surface temperature

$$\theta_{qj}(0,t) = \frac{1}{A}\int_A -k_j \frac{\partial\theta_j(z_j,t)}{\partial z_j}\bigg|_{z_j=0} dA \tag{12}$$

The kernel $\theta_j(z_j,t)$ is the temperature at (z_j,t) for a unit rise in surface ($r=0$ to a) temperature. Taking the Laplace transform of (3) and using (11) gives

$$\bar{q}_1 = s(\overline{T_1 - T_{1i}})\bar{\theta}_{q1} = -s(\overline{T_2 - T_{2i}})\bar{\theta}_{q2} \tag{13}$$

The Laplace transform of (3) can be rearranged to

$$\overline{T_1 - T_{1i}} = \overline{T_2 - T_{2i}} + (T_{2i} - T_{1i})/s - \bar{q}_1/h \tag{14}$$

Employing this expression in (13) produces

$$(\overline{T_2 - T_{2i}})/(T_{1i} - T_{2i}) = \bar{\theta}_{q1}/s(\bar{\theta}_{q1} + \bar{\theta}_{q2} + s\bar{\theta}_{q1}\,\bar{\theta}_{q2}/h) \tag{15}$$

Similar expressions can be derived for T_1 and q_1. Rather than giving these expressions, dimensionless forms are given below. Let

$$\theta_{qj}^* = \theta_{qj}a/k_j \tag{16a}$$

$$\theta_q^* = \theta_{q1}^* + K\theta_{q2}^* \tag{16b}$$

Nomenclature

a = thermocouple wire radius
A = thermal diffusivity ratio equation (6d)
B = contact Biot modulus equation (6)
Bi = lateral surface Biot modulus
c = specific heat
D = equation (17b)
h = contact heat transfer coefficient
h_c = lateral heat transfer coefficient
k = thermal conductivity
K = thermal conductivity ratio – equation (6c)
q = heat flux
q^* = dimensionless heat flux – equation (6b)
rerfc(x) = exp (x^2)erfc(x)
r_o = outside radius of an insulated thermocouple
s = Laplace transform parameter
t^* = dimensionless time – equation (6a)
T = temperature
T^* = dimensionless temperature
x = position along the thermocouple
x^* = dimensionless position, x/a

Greek Symbols

α = thermal diffusivity
β = $K/\sqrt{A}$
θ = temperature kernel function
θ_q = heat flux function – equation (12)
ρ = density
ϕ = heat flux kernel function – equation (2)
Φ = equation (6f)

Subscripts

1 = related to the substrate
2 = related to the thermocouple
ji = initial value of a parameter for body j

and use the dimensionless terms defined by equations (6) and (10). One then can write with the "*" being omitted

$$\bar{q}_1 = K\bar{\theta}_{q1}\bar{\theta}_{q2}/D \tag{17a}$$

$$D = \bar{\theta}_q + sK\bar{\theta}_{q1}\bar{\theta}_{q2}/B \tag{17b}$$

$$\bar{T}_1 = K\bar{\theta}_{q2}/(sD) \tag{18a}$$

$$\bar{T}_2 = \bar{\theta}_{q1}/(sD) \tag{18b}$$

Notice that for perfect contact the expressions for $\bar{q}_1$, $\bar{T}_1$, and $\bar{T}_2$ are unchanged but D becomes simply $\bar{\theta}_q$. Furthermore, $T_1 = T_2$.

Evaluation

To evaluate the sensor temperatures, the unit step response (or kernel) functions are required. For the case of a semi-infinite body with a step change in temperature over a disk region, this function has been developed in the oblate spheroidal coordinate system which is a natural coordinate system for the problem.

A "late" time asymptotic solution developed by Norminton and Blackwell [20] is used. Analyses [5, 21] have shown that this solution gives good results for dimensionless times greater than 0.1 ($\alpha t/a^2 > 0.1$, where units are used.) The heat flux based solutions are simpler to use and more accurate over the time range $0 < t < 0.3$.

Using the late time asymptotic solution, it can be shown that the average heat flux over the disk is

$$\theta_{q1} = [8(t\pi^3)^{-1/2} + 4]/\pi \tag{19}$$

which is in dimensionless form [8]. Taking the Laplace transform of (19) gives

$$\bar{\theta}_{q1} = \frac{8}{\pi^2\sqrt{s}} + \frac{4}{\pi s} \tag{20}$$

For a cylinder with lateral heat loss, that heat flux into the end for a unit step temperature change at the end is [22]

$$\theta_{q2} = \frac{\exp(-4A\mathrm{Bi}t)}{\sqrt{\pi t}} + \sqrt{4A\mathrm{Bi}}\,\mathrm{erf}(\sqrt{4A\mathrm{Bi}t}) \tag{21}$$

which has a Laplace transform of

$$\bar{\theta}_{q2} = \sqrt{s + 4A\mathrm{Bi}}/s\sqrt{A} \tag{22}$$

From equation (18*b*), the temperature at the thermocouple junction is given by

$$\bar{T}_2(0,s) = \bar{\theta}_{q1}/s(\bar{\theta}_{q1} + K\bar{\theta}_{q2} + sK\bar{\theta}_{q1}\bar{\theta}_{q2}/B) \tag{23}$$

where $\bar{\theta}_{q1}$ and $\bar{\theta}_{q2}$ are given by equations (20) and (22) and

Bi = $h_c a/2k_2$
h_c = lateral heat transfer coefficient

To account for the junction being at a location, x, inside the cylinder (see Fig. 1), the transform of the temperature at x is related to the transform of the surface temperature by

$$\bar{T}_2(x,s) = s[\bar{T}_2(0,s)^*\bar{\theta}_2(x,s)] \tag{24}$$

with

$$\bar{\theta}_2 = \exp(-x\sqrt{(s + 4A\mathrm{Bi})/A})/s \tag{25}$$

where $x^* = x/a$ and the "*" was dropped in equations (24) and (25). The quantity, θ_2, is the temperature in a semi-infinite rod with lateral heat loss when exposed to a step temperature change on its end [22, 23]. Using equations (20), (22), (23), and (25) in (24) yields

$$T_2(x,s) = \frac{F_1(s)}{F_1(s) + KF_2(s)/\sqrt{A}s + KF_1(s)F_2(s)/\sqrt{A}B} * \frac{\exp(-xF_2(s)/\sqrt{A})}{s} \tag{26}$$

where $F_1(s) = 8/\pi^2\sqrt{s} + 4/\pi s$ $F_2(s) = \sqrt{s + 4A\mathrm{Bi}}$.

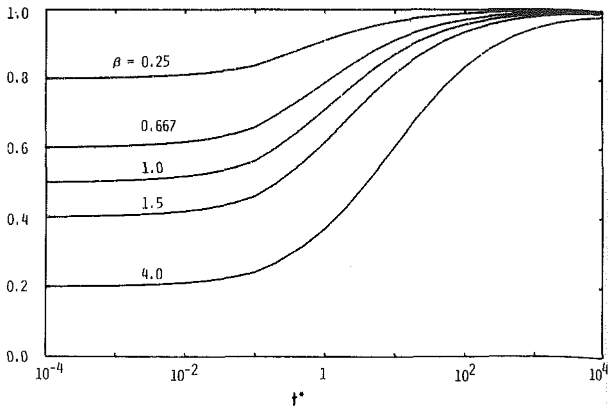

Fig. 2 Ideal intrinsic thermocouple response for a step input

In the q-based USE solution for the full thermocouple problem, ϕ_1 is the average temperature over the disk resulting from a unit step change in heat flux [24]

$$\phi_1 = 2\sqrt{t/\pi} - 2t/\pi \tag{27a}$$

$$\bar{\phi}_1 = 1/s^{3/2} - 2/\pi s^2 \tag{27b}$$

and ϕ_2 is the temperature at the end of a semi-infinite rod for a unit step change in heat flux [22].

$$\phi_2 = 2\sqrt{At/\pi} \tag{28a}$$

$$\bar{\phi}_2 = \sqrt{A}/s^{3/2} \tag{28b}$$

For a cylinder with heat loss, the step temperature change solution gives the exact Laplace transform for $\bar{\theta}_q$

$$\bar{\theta}_{q2} = \sqrt{s + 4A\mathrm{Bi}}/s\sqrt{A} \tag{29}$$

It can be shown for one-dimensional problems that $\bar{\theta}_{qi}$ and $\bar{\phi}_i$ are related by

$$\bar{\theta}_{qi} = 1/s^2\bar{\phi}_i \tag{30}$$

thus

$$\bar{\phi}_2 = \frac{\sqrt{A}}{s\sqrt{s + 4A\mathrm{Bi}}} \tag{31}$$

The expressions given by (28) are exact, but those given by (27) are valid only for small values of t or equivalently large values of s.

The effect of junction displacement can be accounted for by equations (24) and (25) in the temperature based development. Combining results gives

$$\bar{T}_2 = \frac{\bar{\phi}_2}{K[s\bar{\Phi} + 1/B]}\exp(-x\sqrt{(s + 4A\mathrm{Bi})/A} \tag{32}$$

It does not appear that the inverse Laplace transform of the full equations, equations (26) and (32), can be obtained directly. The inversion has been performed numerically using a ten-term, Gaver-Stehfest method programmed for a desktop computer and for a programmable calculator [25, 26]. Before considering the full problem, certain limiting cases (some of which have convenient closed-form solutions) will be considered. These use limiting values for three parameters; x, Bi, and B.

Case I – Ideal Intrinsic Thermocouple

The ideal intrinsic thermocouple problem has been considered by numerous authors [1, 4–8]. For this case the parameter values are: $x = 0$, $\mathrm{Bi} = 0$, and $B = \infty$. When these values are used in equation (26), the result can be inverted exactly to give the late time solution of [8]

$$T_2(0,t) = 1 - C_1\,\mathrm{rerfc}(C_2\sqrt{t}) \tag{33}$$

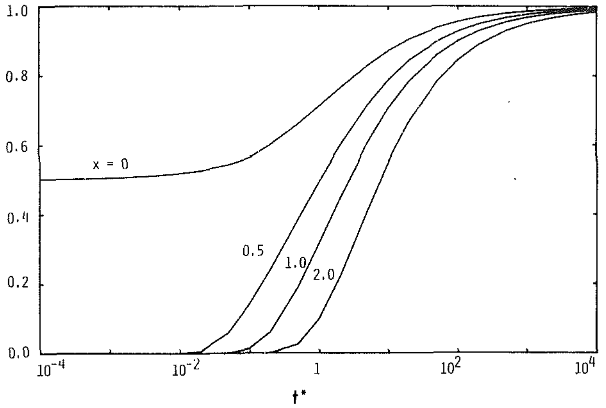

Fig. 3 Response of an ideal beaded thermocouple to a step change in substrate temperature ($K = A = 1$)

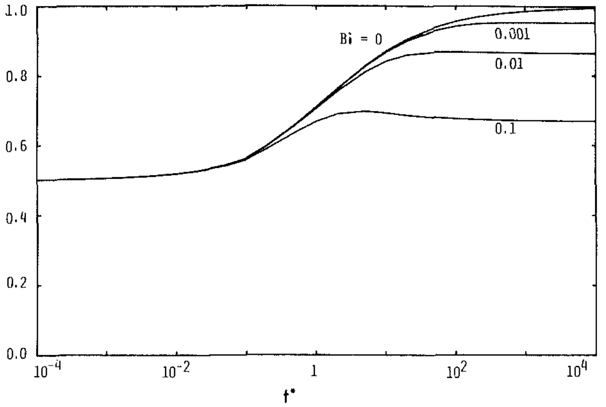

Fig. 4 Response of an intrinsic thermocouple to a step change in substrate temperature when there is lateral heat loss ($K = A = 1$)

where $C_1 = \beta/(8/\pi^2+\beta)$, $C_2 = 4/(8/\pi+\beta\pi)$, $\mathrm{rerfc}(x) = \exp(x^2)\mathrm{erfc}(x)$, and $\beta = K/\sqrt{A}$. The parameter, β, figures prominently in the analytical expressions for the thermocouple temperature. The interface temperature given by equation (33) is applicable for $t^* > 0.1$.

The early time response is obtained from the heat flux method equation (32). The solution is

$$T_2 = D_1[1+\exp(D_2^2 t)\mathrm{erf}(D_2\sqrt{t})] \tag{34}$$

where $D_1 = 1/(1+\beta)$, $D_2 = 2\beta/\pi(1+\beta)$.

The two solutions have been evaluated for a range of property values for the two bodies which cover most possible combinations of metals. It can be seen that the level of response at zero time and the transient response up to the final value are governed by a single parameter, β. These results are shown in Fig. 2 where equation (34) was used for $t \le 0.1$ and equation (33) for $t \ge 0.1$. Notice that the matching between the two solutions is excellent.

From Fig. 2 one can observe that the error (the difference between the undisturbed temperature, T_{li}, and the thermocouple temperature, $T_2(0,t)$, is always largest at zero time and goes to zero at large times. The zero time error and the dimensionless time for which a significant error exists are both directly proportional to β.

Both single-wire and two-wire intrinsic thermocouples are used in practice. For most common thermocouple pairs, there are significant thermal property differences. During a transient for the two-wire thermocouples, this results in a temperature difference between the two junctions, and the total thermoelectric circuit has three elements. Depending on the thermoelectric power of the substrate, very strange results could be produced as in [12], where a thermal pulse produced an electrical output that went negative in the early to middle times.

For the case $\beta = 4/3$, the agreement between the present model and the results of two large finite difference codes was ±3 percent [8]. In [5], an earlier version of the model was compared with data from nine experiments. The experiments involved Type K (Chromel/Alumel) thermocouples on a 304 stainless steel plate with temperature steps of 55K to 275K. The larger temperature steps produced a significant change in thermal properties. However, when the model was evaluated using the property values at a single intermediate temperature the agreement was better than ±6 percent.

Case II – Ideal Beaded Thermocouple

The ideal beaded thermocouple has no lateral surface heat loss and no contact resistance at the interface. It differs from the intrinsic thermocouple by having the effective junction displaced from the surface by the thickness of the thermocouple bead. The parameter values for this case are $x \neq 0$, $\mathrm{Bi}=0$, $B=\infty$.

The response is obtained by using equations (26) and (32) with $x \neq 0$ to account for the junction displacement. The late time response is

$$T_2(x,t) = \mathrm{erfc}\left(\frac{x}{2\sqrt{At}}\right) - C_1 \exp\left(C_2\frac{x}{\sqrt{A}} + C_2^2 t\right) * \mathrm{erfc}\left(\frac{x}{2\sqrt{At_1}} + C_2\sqrt{t}\right) \tag{35}$$

where C_1 and C_2 are defined below equation (33).

The results are shown in Fig. 3 for the case where the bodies have identical properties (i.e., $A = K = \beta = 1$), and the junction is displaced from the surface by an amount up to the wire diameter. The result of the junction being displaced from the surface is a zero response at zero time and an increase in the error for all but very late times. The delay between the step input and the first response can be obtained from the results for a semi-infinite body subjected to a step temperature change. Note that the very late time response approaches that of the ideal intrinsic thermocouple.

Case III – Intrinsic Thermocouple with Lateral Heat Loss

The case of lateral heat loss is more realistic because radiative losses and/or convective losses are always present. For this case the parameter values are: $x=0$, $\mathrm{Bi} \neq 0$, and $B=\infty$. It can be shown that the Laplace transform of the late time solution can be simplified to the form

$$\bar{T}_2(s) = \frac{\sqrt{s}+C_7}{s(\sqrt{s}+C_7+C_8\sqrt{s+C_9})} \tag{36}$$

where C_7, C_8, and C_9 are constants depending on the particular problem.

Amos [27] has shown that the inverse Laplace transform of equation (36) cannot be obtained in closed form. The inverse transform in the form of complex expression of constants, polynomials of $\sqrt{t}$, exponentials, complementary error functions, modified Bessel functions and their various products, along with two easily evaluated integrals, has been obtained. This expression can be used to look at parametric effects directly. The numerical inversion procedure is easier to evaluate and produces excellent agreement.

The numerical inversion procedure was to evaluate the response for varying values of the Biot modulus. These results are shown in Fig. 4 for Bi = 0, .001, .01, .1 and $K = A = 1$. This range of the Biot modulus covers much of that estimated to bound thermocouple applications [18]. Note that while there is little difference in the early time response, the lateral heat

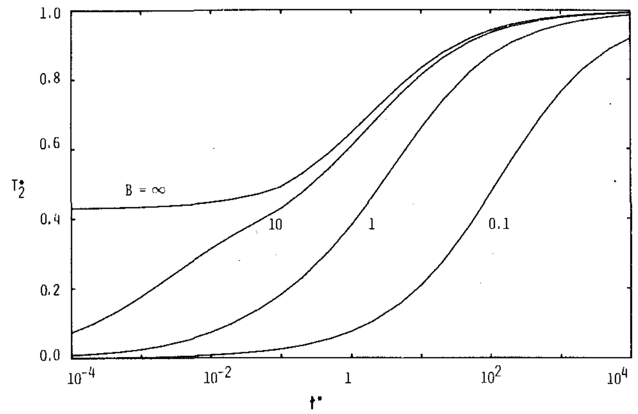

Fig. 5(a) Response of an intrinsic thermocouple to a step change in substrate temperature when there is contact resistance ($K = 1.5486$, $A = 1.3485$)

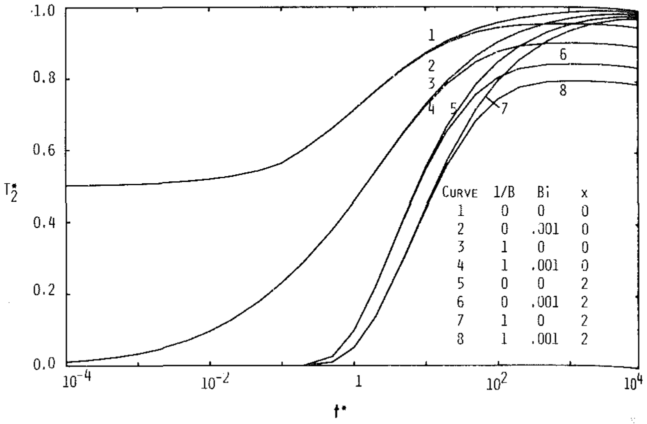

Curve	1/B	Bi	x
1	0	0	0
2	0	.001	0
3	1	0	0
4	1	.001	0
5	0	0	2
6	0	.001	2
7	1	0	2
8	1	.001	2

Fig. 6 Effects of the various parameters on the response of a thermocouple to a step change in the substrate temperature ($K = A = 1$)

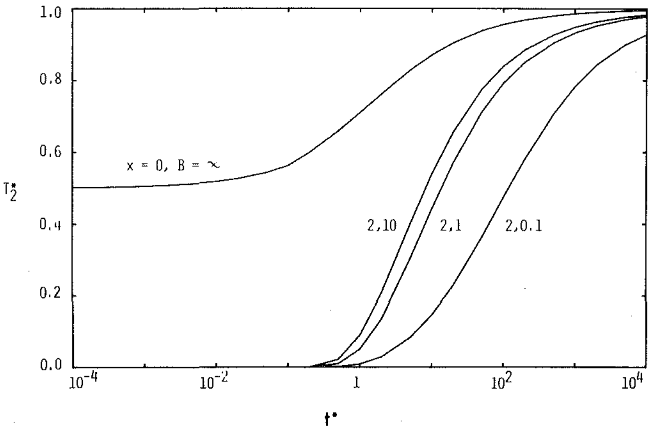

Fig. 5(b) Response of a beaded thermocouple to a step change in substrate temperature for finite contact resistance ($K = A = 1$)

loss produces a steady-state offset (i.e., there is a temperature measurement error at all times). Note that as Bi increases, the time at which the response begins to deviate from the ideal case decreases.

One surprising result observed in Fig. 4 is that the temperatures reach a maximum and then decline slightly. This drop occurs for all values of Bi, although it is very small at Bi = .001. The behavior may not be all bad in that the steady-state result is reached earlier than for the zero loss case. For example, the response is within 1 percent of its steady-state value at $t = 20$, while the Bi = 0 response is within 1 percent of its steady-state value at the much larger time of $t = 2000$.

The steady-state offset can be obtained by evaluating the full model at very large times ($t \sim 10000$). Alternatively, the steady-state portions of equations (19) and (21) can be used directly to develop the expression

$$T_2(0,\infty) = 1/(1 + \pi K\sqrt{\mathrm{Bi}}/2) \tag{37}$$

which presumes that $T_{2i} = 0$ and the ambient temperature is also zero.

Evaluating $T_2(0,\infty)$ from either the full model or equation (37) produces essentially the same results and these agree (to the accuracy of reading charts) with the results presented in [16] or [18].

Case IV – Contact Resistance at the Interface

The interface contact resistance results when the thermocouple is simply pressed against the surface or adhesively bonded with a thin bond line whose capacity can be neglected. For this case the parameter values are Bi = 0, B-finite and $x = 0$, and then x-finite. For these values, the late time solution (equation (26)) can be inverted to give

$$T_2(0,t) = \frac{B}{\beta}\left[\frac{D_1}{C_1}(1 - \mathrm{rerfc}(C_1\sqrt{t/2}) + \frac{D_2}{C_2}(1 - \mathrm{rerfc}(C_2\sqrt{t/2})\right] \tag{38}$$

where $C = (B/\beta + \pi^2 B/8 + \pi/2)$

$$C_1, C_2 = (C \pm \sqrt{C^2 - 2\pi B/\beta})/2$$

$$D_1 = (C_1 - \pi/2)/(C_1 - C_2), D_2 = (C_2 - \pi/2)/(C_2 - C_1)$$

Note the C_1, C_2, D_1, and D_2 are different than those previously defined.

Now if x is finite, then starting from equations (24) and (26) with Bi = 0 the resulting transform equation can be inverted to give

$$T_2(x,t) = \frac{B}{\beta}\left\{\frac{D_1}{C_1}\left[\mathrm{erfc}\left(\frac{x}{2\sqrt{At}}\right) - \exp\left(\frac{C_1 x}{\sqrt{2A}} + \frac{C_1^2 t}{2}\right)\mathrm{erfc}\left(\frac{x}{2\sqrt{At}} + C_1\sqrt{t/2}\right)\right] + \frac{D_2}{C_2}\left[\mathrm{erfc}\left(\frac{x}{2\sqrt{At}}\right) - \exp\left(\frac{C_2 x}{\sqrt{2A}} + \frac{C_2^2 t}{2}\right)\mathrm{erfc}\left(\frac{x}{2\sqrt{At}} + C_2\sqrt{t/2}\right)\right]\right\} \tag{39}$$

The corresponding early time solutions can be obtained, although the late time solutions are the most useful, particularly for the beaded thermocouple. Figures 5(*a*) and 5(*b*) show the effects of varying the contact resistance for $x = 0$ and $x = 2$. The effects of finite values of B are similar to the effects of the ideal beaded thermocouple (Figure 3) at late times. The early time response rises faster. Note that if B is not infinite in the $x = 0$ case that the initial measured temperature is zero. For reference, approximate values of B for a 24 gage (.02 in.) thermocouple on a mild steel plate are 0.05–0.1 for a one mil (.001 in.) epoxy bond and 0.02–0.4 for a pressed contact depending on the pressure.

Case V – Combined Case

This case includes any or all of the possible effects. Reasonable ranges for the parameter values are $0 \le x \le 2$, $0 \le \mathrm{Bi} \le 0.5$, and $.1 \le B \le \infty$. The possible combinations for this case are endless, particularly if the ranges of substrate and thermocouple properties are included. To demonstrate how the various parameters and their combinations affect the

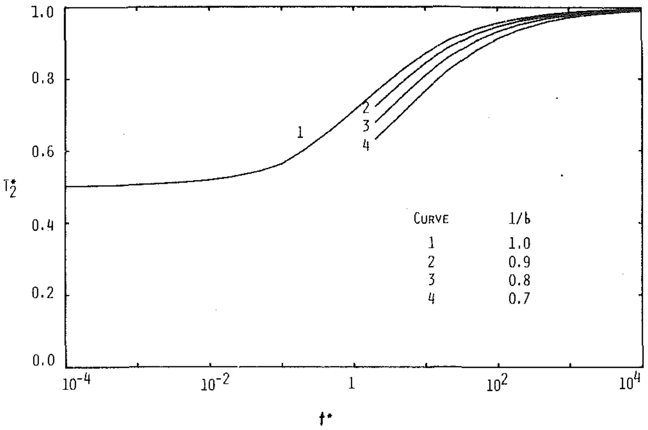

Fig. 7 Response of an intrinsic thermocouple with partial contact ($K = A = 1$)

early time response, the late time response, the time to reach steady state, and the steady state error, the full solutions were evaluated for $A = K = 1$, $x = 0$ and 2, Bi $= 0$ and .001, and $B = 1$ and ∞. The results shown in Fig. 6 indicate that having a beaded thermocouple ($x = 2$) most strongly affects the early time response, that contact resistance slows the response, and that the effect of lateral heat loss is at the late times and the steady-state error.

The case of $x = 0$ but Bi finite and $B \leq \infty$, has been developed by Cassagne et al. [7] using a method similar to the q-based USE. There appears to be excellent agreement between their work and the present model. For the case where $K = A = 1$, Bi $= .001$, $B = 1$, and $x = 0$, a comparison of the two models showed exact agreement at early times, a slight divergence in the middle time range (maximum difference of 1.7 percent at $t \sim 1$) and agreement within 0.5 percent at late times.

For large times with both imperfect contact and lateral heat loss

$$T_2(x,t) \approx \frac{T_0 \exp(-2x\sqrt{\text{Bi}})}{1 + 2K\sqrt{\text{Bi}}(1/B + \pi/4)} * \left[1 + \frac{K\sqrt{\text{Bi}}}{\pi^2\sqrt{\pi t}} \frac{1}{1 + 2K\sqrt{\text{Bi}}(1/B + \pi/4)}\right] \tag{40}$$

Notice that this expression shows a decrease of $T_2(x,t)$ with t for nonzero Bi. Also, the steady-state result is

$$T_2(x,\infty) = T_0 \exp(-2x\sqrt{\text{Bi}})/[1 + 2K\sqrt{\text{Bi}}(1/B + \pi/4)] \tag{41}$$

This expression shows that there is no steady-state error unless Bi is greater than zero; if Bi > 0, $T_2(x,\infty)$ is reduced both by the presence of Bi in the exponential and in the term in the brackets.

Case VI – Partial Contact

The previous cases have assumed that there is uniform contact over the entire end of the thermocouple. If the thermocouple is pressed against the surface (instead of being welded or bonded) the contact will be at the high points of the two surfaces or if the weld is poor it will have voids. While this will not affect the response of beaded thermocouples (except as it affects the value of the contact coefficient), it could have a serious effect on intrinsic thermocouples [4]. An alternate problem – enlargement of the junction during welding [9] – will not be considered.

For the partial contact case only the late time model will be utilized because the very early time response will be identical to that in Case I. The problem is approximated by having the contact radius be smaller than the cylinder radius. Also, it is assumed that the contact over the smaller radius disk is perfect, and there is no lateral heat loss, and the junction is at the surface.

The model uses equations (23) and (20) but replaces (22) with

$$\bar{\theta}_{q2} = \sqrt{A}/b^2 s^{3/2} + \bar{I}(1,0,b)/s \tag{42}$$

where b = cylinder radius/contact radius and $\bar{I}(1,0,b)$ is a constant [29]. The expression was obtained from the response of a semi-infinite cylinder heated by a disk source by using the relation given in equation (30); the original expression is valid for $t/b^2 > 1$. The inversion has not been performed analytically. Numerical evaluations for several contact area ratios are shown in Fig. 7. These results show that even though initial and final values are identical to the Case I results, that the partial contact significantly slows the response in the middle times.

Applications

While using the models can help to develop a feeling for the errors in temperature measurements, few experiments involve a step temperature change. A useful adjunct to the step response is the response to a temperature ramp.

The development of the step response models assumed constant thermal properties. Thus the equations are linear, and the principle of superposition can be utilized for inputs of arbitrary form. The response, $R(t)$, to a forcing function or substrate temperature change, $F(t)$, is given by

$$R(t) = \frac{\partial}{\partial t}\int_0^t F(\lambda)C(t-\lambda)d\lambda \tag{43}$$

where $C(t)$ is the unit step response (equations (26) or (32)).

For the case where $F(t) = Ht$, H = constant, $t \geq 0$, the response of an ideal intrinsic thermocouple (using equation (33)) is

$$R(t) = H\left[t - \frac{C_1}{C_2^2}[\text{rerfc}(C_2\sqrt{t}) - 1 + 2C_2\sqrt{t/\pi}]\right] \tag{44}$$

and for an ideal beaded thermocouple

$$R(t) = H\left[4ti^2\text{erfc}(C_3/\sqrt{t}) - \frac{C_1}{C_2^2}\left[(\exp(2C_2C_3 + C_2^2 t)\text{erfc}\left(\frac{C_3}{\sqrt{t}} + C_2\sqrt{t}\right) - \text{erfc}(C_3/\sqrt{t}) + 2C_2\sqrt{t}i\text{erfc}(C_3/\sqrt{t})]\right]\right. \tag{45}$$

where $C_3 = x/2\sqrt{A}$.

Note that the error in the slope or the temperature rise rate is given by

$$\text{Slope error} = \frac{dF(t)}{dt} - \frac{dR(t)}{dt} \tag{46a}$$

$$= H[1 - C(t)] \tag{46b}$$

Thus the slope error at time, t, is equal to the undisturbed rise rate multiplied by (1-unit step response at t).

A second problem is the estimation of the forcing function (i.e., the undisturbed temperature). Rearranging the Laplace transform of equation (43) gives

$$\bar{F} = \bar{R}/s\bar{C} \tag{47}$$

If the inverse Laplace transform exists, then a good estimate of $F(t)$ can be obtained. As an example consider a response function modeled by $H_1\sqrt{t} + H_2 t$ for the case of the ideal intrinsic thermocouple. The Laplace transform of $C(t)$, from equation (26) can be put in the form

$$\bar{C} = 1/s - H_4/\sqrt{s} + H_4(\sqrt{s} + H_6) \tag{48}$$

The resulting forcing function can be obtained analytically and is

$$F(t) = \left[\frac{H_1 H_4 H_6 \sqrt{\pi} - 2H_2 H_4 + 2H_2 H_4 H_6}{2H_6} \right] [1 - \mathrm{rerfc}(H_7 \sqrt{t})]$$

$$+ [H_1 + 2H_2 H_4 / \sqrt{\pi}] \sqrt{t} + H_2 t \qquad (49)$$

where $H_7 = H_6/(1 - H_4 H_6)$. Similar results can be obtained for polynomials in $\sqrt{t}$ of increasing order; however, the algebra becomes increasingly complex. The simplest approach is to numerically invert $\bar{R}(s)$.

Summary

Using the unsteady surface element method, easily evaluated models have been developed for estimating the errors in surface temperature measurements with thermocouples for a variety of conditions. The models can be adapted to a particular situation by specifying relatively few parameters. For specific limiting cases, it is shown that the results are in excellent agreement with the literature.

Acknowledgments

The research was sponsored by Sandia National Laboratories, which is operated by the Western Electric Corporation for the Department of Energy under Contract No. DE-AC04-76DP00789 and by the National Science Foundation under Grant No. CME-79-20103. The computer code used for estimating thermocouple response for Cases I-V is available from the first author. The code, approximately 100, lines, is written in HP BASIC.

References

1 Henning, C. D., and Parker, R., "Transient Response of an Intrinsic Thermocouple," JOURNAL OF HEAT TRANSFER, Vol. 39, 1967, p. 146.

2 Burnett, D. R., "Transient Measurement Errors in Heated Slabs for Thermocouples Located at an Insulated Surface," JOURNAL OF HEAT TRANSFER, Vol. 83, 1961, p. 505.

3 Larson, J. B., and Nelson, E., "Variables Affecting the Dynamic Response of Thermocouples Attached to Thin Skinned Models," JOURNAL OF HEAT TRANSFER, Vol. 41, 1969, p. 166.

4 Gat, U., et al., "The Effect of Temperature Dependent Properties on Transients Measurement with Intrinsic Thermocouple," *International Journal of Heat and Mass Transfer*, Vol. 18, 1975, p. 1337.

5 Keltner, N. R., "Intrinsic Thermocouple Response," *Proceedings of the 20th International Instrumentation Symposium*, Instrument Society of America, 1974, p. 91.

6 Keltner, N. R., and Bickle, L. W., "Intrinsic Thermocouple Measurement Errors," Paper 76-HT-65, ASME-AIChE Heat Transfer Conference, St. Louis, MO., Aug. 1976.

7 Cassagne, B., et al., "Theoretical Analysis of the Errors Due to Stray Heat Transfer During the Measurement of a Surface Temperature by Direct Contact," *International Journal of Heat and Mass Transfer*, Vol. 23, 1980, pp. 1207-1217.

8 Keltner, N. R., and Beck, J. V., "Unsteady Surface Element Method," JOURNAL OF HEAT TRANSFER, Vol. 103, 1981, pp. 759-764.

9 Maglic, K. D., and Marsicanin, B. S., "Factors Affecting the Accuracy of Transient Response of Intrinsic Thermocouples in Thermal Diffusivity Measurement," *High Temperatures-High Pressures*, Vol. 5, 1973, pp. 105-110.

10 Quandt, E. R., and Fink, E. W., "Experimental and Theoretical Analysis of the Transient Response of Surface Bonded Thermocouples," *Bettis Technical Review*, WAPD-BT-19, Reactor Technology, June, 1960, p. 31.

11 Wally, K., "The Transient Response of Beaded Thermocouples Mounted on the Surface of a Solid," *Proceedings of the 23rd International Instrumentation Symposium*, Instrument Society of America, 1977, pp. 127-132.

12 Heckman, R. C., "Intrinsic Thermocouples in Thermal Diffusivity Experiments," *Proceedings of the Seventh Symposium on Thermophysical Properties*, ASME, New York, 1977.

13 Litkouhi, B., "Surface Element Method for Transient Heat Conduction Problems," Ph.D. dissertation, Department of Mechanical Engineering, Michigan State University, E. Lansing, Michigan, 1982.

14 Shewen, E. C., "A Transient Numerical Analysis of Conduction Between Contacting Circular Cylinders and Halfspaces Applied to a Biosensor," MS thesis, University of Waterloo, Waterloo, Ontario, Canada, 1976.

15 Moffat, R. J., "Temperature Measurement in Solids," Paper 68-514, *Advances in Test Measurement*, Vol. 5, ISA, Pittsburgh, Pa., 1968.

16 Sparrow, E. M., "Error Estimates in Temperature Measurements," ch. 1, *Measurements in Heat Transfer*, 2nd ed., edited by E.R.G. Eckert and R. J. Goldstein, Hemisphere Publishing Corp. 1976.

17 Green, S. J., and Hart, T. W., "Accuracy and Response of Thermocouples for Surface and Fluid Temperature Measurements," *Temperature, Its Measurement and Control in Science and Industry*, Vol. 3, pt. 2, Reinhold, New York, p. 695.

18 Hennecke, D. K., and Sparrow, E. M., "Local Heat Sink on a Convectively Cooled Surface—Application to Temperature Measurement Error," *International Journal of Heat and Mass Transfer*, Vol. 13, 1970, pp. 287-304.

19 Beck, J. V., and Keltner, N. R., "Transient Thermal Contact of Two Semi-Infinite Bodies over a Circular Area," Paper AIAA-81-1162, AIAA 16th Thermophysics Conference, Palo Alto, Calif., June, 1981.

20 Norminton, E. J., and Blackwell, J. H., "Transient Heat Flow from Constant Temperature Spheroids and the Thin Circular Disk," *Quarterly Journal of Mechanics and Applied Mathematics*, Vol. 17, 1964, pp. 65-72.

21 Marder, B. M., and Keltner, N. R., "Heat Flow From a Disk by Separation of Variables," *Numerical Heat Transfer*, Vol. 4, 1981, pp. 485-497.

22 Luikov, A. V., *Analytical Heat Diffusion Theory*, Academic Press, New York, 1968.

23 Carslaw, H. S., and Jaeger, J. C., *Conduction of Heat in Solids*, 2nd ed., Oxford University Press, London, 1967.

24 Beck, J. V., "Average Transient Temperature Within a Body Heated by a Disk Heat Source," *Heat Transfer, Thermal Control, and Heat Pipes*, Vol. 70 of Progress in Astronautics and Aeronautics, AIAA, New York, (1980).

25 Stehfest, H., "Numerical Inversion of Laplace Transforms," *Communications of the ACM*, Vol. 13, 1970, pp. 47-49 and p. 624.

26 Woo, K., "TI-59 Inverts Laplace Transformation for Time-Domain Analysis," *Electronics*, Oct. 9, 1980, pp. 178-179.

27 Amos, D. E., On the Inverse of a Laplace Transform and its Numerical Evaluation, SAND81-2470, Sandia National Laboratories, Albuquerque, N.M., Nov. 1981.

28 Cetinkale, T. N., et al., "Thermal Conductance of Metal Surfaces in Contact." Proceedings of the *International Conference of Heat Transfer*, London, 1951, pp. 271.

29 Beck, J. V., "Transient Temperatures in a Semi-Infinite Cylinder Heated by a Disk Heat Source," *International Journal of Heat and Mass Transfer*, Vol. 24, 1981, pp. 1631-1640.

Heat Transfer From Horizontal Serrated Finned Tubes in an Air-Fluidized Bed of Uniformly Sized Particles

W. B. Krause
Resident Research Engineer,
RE/SPEC Inc.
Rapid City, S.D. 57709
Mem. ASME

A. R. Peters
Professor and Chairman,
Department of Mechanical Engineering,
University of Nebraska-Lincoln,
Lincoln, Neb. 68588
Mem. ASME

A primary objective of this work was to gather experimental convective heat transfer coefficient data for extended surfaces. The results were then compared with bare horizontal tubes in a similar flow environment. The finned tube configurations were considered an extension of the bare tube arrangements to enhance heat transfer. Heat transfer coefficients were computed from the heated tube surface temperature, the fluidized bed temperature, and the power input to the tube. Selected serrated finned tubes were used. The experimental heat transfer data were measured as a function of fluidized bed flow parameters and finned tube geometry. Several tests were performed using two different uniformly sized glass particles (.21 mm and .43 mm). Fin efficiency factors were determined and presented as a function of mass velocity and as a function of a fin length parameter. The finned tube demonstrated a better heat transfer capacity over bare tubes for similar fluidization conditions.

Introduction and Review of Previous Work

Investigations carried out by experimental/semiempirical studies of Genetti and coworkers [1–4] assumed a particle mode of heat transfer. With suitable assumptions, a boundary value problem was formulated to describe the temperature in the particle while it is near the hot tube surface. Gamma distribution functions were utilized to predict the mean particle residence times. A heat transfer model was used to predict heat transfer in a thin rectangular fin attached to the heated tube. The heat transfer rate into the fin and convection coefficieint was determined, and then a suitable correlation was found for given tube-fin configuration. Similar studies have been conducted by Ziegler et al. [5]. Genetti compared his results with a correlation by Ziegler and found good agreement. Ziegler also found that the shorter the particle contact time, the higher the predicted heat transfer coefficient.

Bartel and Genetti [3] studied bare tubes, finned tubes, and also tube bundles. They found that the rate of heat transfer from a bundle of tubes with long fins was almost independent of the spacing between tubes but with short fins the rate of heat transfer was quite sensitive to tube spacing. Heat transfer rates with all bundles increased with an increase in fluidizing air velocity, but in most cases a minimum was reached, and a further increase in air velocity resulted in a decrease in the rate of heat transfer.

Priebe and Genetti [4] studied heat transfer from horizontal serrated finned and spined tubes in an air fluidized bed. Heat flux, fin spacing, particle diameter, and mass velocity were variables for finned tubes. Spine heights, spines per turn, material and mass velocity were variables for this case. Results from their study indicated that for serrated finned tubes the heat transfer coefficient fell rapidly for fin spacings less than 10 particle diameters. For spine tubes there was little difference in the heat transfer coefficient of large or small number of spines per turn, but the increased area of a large number of spines per turn yielded higher heat transfer rates. Each tube type led to a correlation relating the particle Nusselt number to the variables studied. Deviation from the correlation was less than ±12.5 percent.

Chen and Withers [6, 7] investigated the potential for use of finned tubes to increase the heat transfer duty per unit bed volume. These investigators defined a figure of merit as $hA_{\text{finned}}/hA_{\text{bare}}$. hA_{bare} is the heat transfer coefficient times the surface area for a plain tube. The merit ratio was plotted as a function of W/d. From these results it can be observed that performance reaches a maximum over some range of W/d. Two primary cases result: increasing density of fins per unit length of tube increases performance; and fin height increase causes an improvement in performance. For the cases studied, maximum gain in heat transfer compared to plain tubes was in the range of 160 to 290 percent.

Staub and coworkers [8] studied modeling of the flow behavior along with finned tube performance in the turbulent flow regime. In their study they summarized preliminary data to validate the scaling of turbulent bed behavior from room temperature to high-temperature conditions. Wood et al. [9] also conducted measurements related to the extent of the splash zone influence on tube heat transfer coefficients in horizontal banks of both bare and finned tubes. The tests were conducted with beds of silica (0.93-mm dia) fluidized with air at atmospheric pressure and room temperature in a 0.3 m × 0.3 m cross-section.

Additional studies are discussed by Saxena et al. [10]. The primary conclusions relating to horizontal finned heat exchange tubes are:

1 Fins increase the rate of heat transfer to tubes. However, their effectiveness increases, reaches a maximum, and then decreases with decreasing spacing distance and increasing fin length.

2 An increase in tube-to-tube spacing in a bundle of short-finned tubes, which reduces the resistance to particle movement between the tubes, increases the total heat transfer coefficient.

3 Correlations developed for finned-tube heat transfer are for the most part based on the model by Ziegler et al. [5], which considers heat transfer only to the first particle layer near a heat transfer surface. This type of model is limited to

---

Contributed by the Heat Transfer Division and presented at the ASME/AIChE National Heat Transfer Conference, Orlando, Florida, July 27–30, 1980. Manuscript received by the Heat Transfer Division November 9, 1981. Paper No. 80-HT-48.

short residence times where the heat has not had sufficient time to penetrate to further particle depths.

Analytical Methods

Packet and Particle Models. Two models are used to verify experimental data. These models are based on the packet theory attributed to Mickley and Fairbanks [11] and the particle theory attributed to Ziegler et al. [5]. In the experimental considerations for the respective models, it was determined that the heat transfer coefficient in the tube vicinity depends on several factors. Because of the number of variables involved and the complexity of their influence on heat transfer, the various correlations that have been proposed are only valid within the limits of the experimental conditions on which they were based. The heat transfer rate is controlled by the residence time of the particles or packets on the heat exchange surface. Residence time may be defined as the amount of contact time the emulsion (particles and air) is in contact with the heat exchange surface.

Finned Tube Model Development. To find the temperature profile in a fin, a one-dimensional steady-state heat balance is made about a typical rectangular fin element. The details of these derivations are summarized in Kern and Kraus [12].

The first case utilized will be the Harper/Brown corrected length case. In this case the fin length is taken as

$$FLC = FL + t/2 \qquad (1)$$

For this case the heat input to each fin can be found from the Fourier heat conduction law,

$$q_{\text{fin}} = -kA\left.\frac{dT}{dx}\right|_{x=0} \qquad (2)$$

Differentiation of the temperature profile yields an expression for the heat to all fins; this expression is noted as,

$$Q_{\text{total}}\cdot\Delta T^{-1} = FN(\bar{h}\cdot P\cdot k\cdot A_{cs})^{1/2}\,\text{Tanh}(m\cdot FLC) + A_{uf}\cdot\bar{h} \qquad (3)$$

The convective heat transfer coefficient in equation (3) cannot be found explicitly; hence, it is necessary to assume an initial value for $\bar{h}$ and place this equation in an iteration scheme until convergence is reached.

Experimental Considerations

Experimental Fluidization Apparatus. The fluidization column (shown in Fig. 1) was constructed of 2.54-cm thick clear Plexiglas, with inside dimensions 33-cm wide by 30.5-cm deep and a height of 1.8 m above the distributor plate. The entrance region and upper portion of the bed were joined with an airtight seal and flange gasket. Two insulating plates (Micarta Board) were attached to opposite sides of the column to mount experimental heat exchange surfaces. Static pressure taps and bed thermocouples were installed as shown in Fig. 1 at evenly-spaced intervals. All temperatures were measured and recorded on a temperature recorder. The distributor plate utilized in the column was constructed of two sheets of perforated steel plates. To cause the required pressure drop and prevent the particles from falling into the entrance region, two layers of 140 mesh stainless steel wire cloth were sandwiched between the perforated plates.

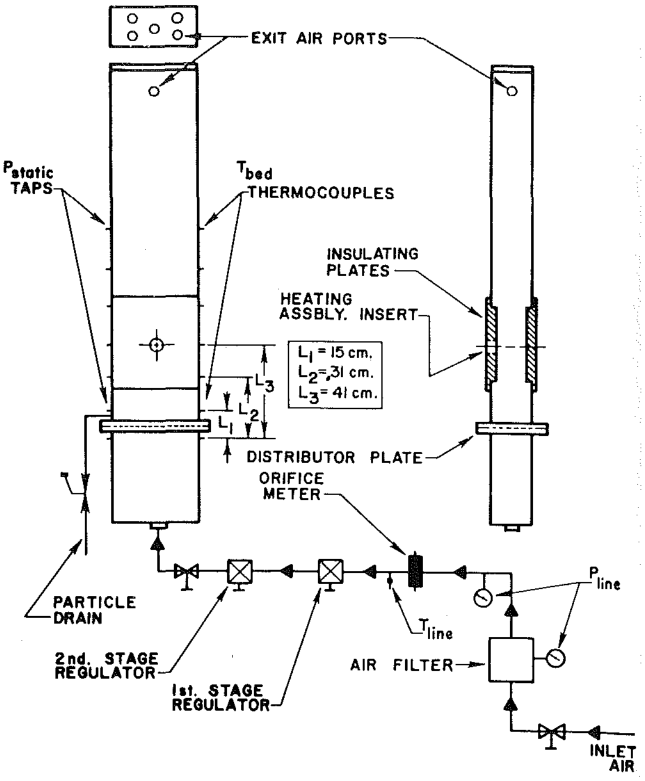

Fig. 1 Schematic diagram of fluidization apparatus and air supply system

Heat Transfer Apparatus. The bare and finned tubes were heated by a 25-cm long, 1700 W cartridge heater. Insulating mounting blocks were used at both ends to prevent heat loss. Temperatures on the tube were measured with 28 Ga. iron-constantan thermocouples silver-soldered to the tube surface.

Nomenclature

A = area, total area
A_{cs} = fin cross-section area
A_{uf} = area of unfinned portion of tube
d = particle diameter
$\bar{D}_p$ = average particle diameter
FL = fin length
FLC = corrected fin length
FN = number of fins
G = mass velocity
G_{mf} = minimum fluidization mass velocity
h = convective heat transfer coefficient
$\bar{h}$ = average "tube-side" convective heat transfer coefficient
H = $\bar{h}_{\text{fin}}/\bar{h}_{\text{bare}}$, heat transfer ratio
k = thermal conductivity of fin material
k_g = thermal conductivity of gas
k_e = thermal conductivity of emulsion
k_s = thermal conductivity of solid (glass)
m = $\left[\dfrac{\bar{h}\cdot P}{k\cdot A_{cs}}\right]^{1/2}$
$\overline{\text{Nu}}_{\text{pfin}}$ = $\bar{h}d_p/k_g$, particle Nusselt number for finned tube
P = fin perimeter
Q_{total} = total heat input to bare or finned tube
q_{fin} = fin heat transfer
t = fin thickness
T = temperature
T_{bed} = fluidized bed temperature
T_w = surface temperature
ΔT = $T_w - T_{\text{bed}}$
W = fin gap
x = distance
η = fin efficiency
Ω = $\bar{h}_{\text{fin}}A/\bar{h}_{\text{base}}A_{\text{tube}}$, heat transfer capacity function

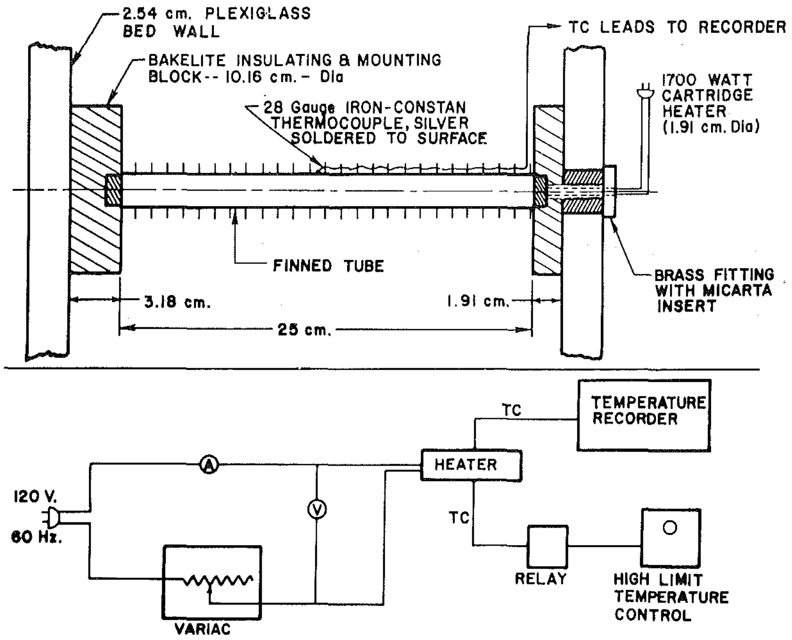

Fig. 2 Schematic diagram of finned tube configuration and heater power supply system

The details of this configuration are shown in Fig. 2 with experimental conditions summarized in Table 1.

A photograph of the representative bare and finned tube configurations is shown in Fig. 3. For both finned and bare tubes the outside surface of the cartridge heater was coated with a thin layer of copper anti-seize and heat transfer enhancing material before insertion of the heater into the tube configuration.

Experimental Procedure. The bed of particles was first fluidized at a point above minimum fluidization. When the system reached steady-state, the bed and tube temperatures were recorded. Both readings were taken on a continuous 30 s per point recording interval, and these values were averaged after running at a fixed flow rate and heat input rate. The inlet line air temperature was also recorded on a continuous basis and was utilized to find the proper air inlet conditions to the fluidized bed.

Power to the heater configurations was computed by measuring the voltage and amperage. Conduction energy losses were accounted for in the data reduction methods. A power fluctuation of ±2 percent was included in all error analyses. For all test runs the fluidization column was filled to a 60-cm static depth. All heat transfer coefficients were found by determining the tube surface temperature at either the 0 or 180 deg angular orientation, i.e.: this orientation places the measurement in a plane perpendicular to the vertical flow.

Presentation and Discussion of Results

Bare Tube Heat Transfer Results. The relative composite variation of the "tube-side" convective heat transfer coefficient (at either the 0 or 180 deg angular orientation) for bare heat exchange surfaces is shown in Fig. 4 for both large and small particles. It should be noted that the convective heat transfer coefficients found in this investigation are the average of values obtained on the "sides" of the finned or bare heat exchange tubes.

In Fig. 4, the upper and lower dashed lines represent the upper and lower error bounds as specified by the experimental measurement methods. For the small particles the composite variation of error is approximately ±7 percent, while for large particles the error variation approaches ±11 percent.

Table 1 Experimental fluidization conditions

Glass particle diameter	0.21 mm and 0.43 mm
Air fluidization mass velocity range	1–2.4 times G_{mf}
Minimum fluidization velocity, small particles	0.06 m/s
Minimum fluidization velocity, large particles	0.18 m/s
Nominal bare tube and fin-tube diameter	19.2 mm (o.d.)
Fluidized bed temperatures	38–55°C
Tube surface temperatures	66–177°C
Fin length (nominal)	4.76, 8.33, 11.11, and 17.46 mm
Fin cross-section	.76 mm × 4 mm
Fin spacing on tube	3 fins/cm (approx.)
Fin type-serrated	ESCOA Fintube Co.

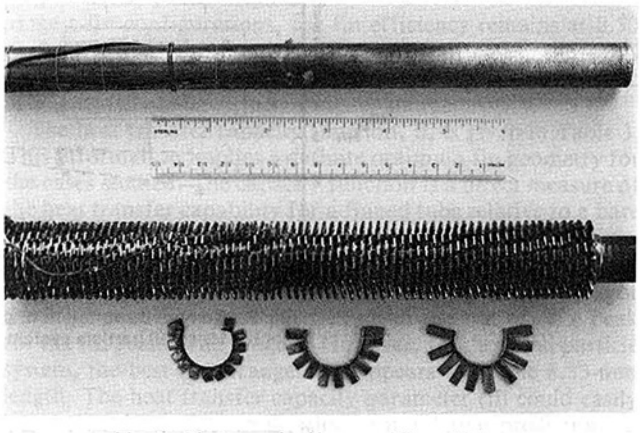

Fig. 3 Photograph of bare and finned tubes

Observation of Fig. 4 indicates the convective heat transfer coefficients increase as a function of mass velocity. For the large particles, the value of $\bar{h}$ steadily increases and appears to be reaching a peak. The increase in $\bar{h}$ with flow rate is much more rapid for the small particles. In both cases, the upper limit of flow rate was taken to be where severe slugging of the entire bed was initiated. For this reason a maximum experimental value of $\bar{h}$ was not determined. The maximum flow rate for all tests was limited to less than 2.4 times minimum fluidization flow rate. The heated bare tube data were used as a basis for comparison with the finned heat exchange tubes. The peripheral variation in temperature around the tube was very small, on the order of 1°C. This condition was present for both bare and finned tubes. Bartel and Genetti [3] confirmed this observation by determining that the largest temperature difference between any two angular points on the tube surface was less than 1°C at 100°C tube temperatures. They also used a thermocouple at the mid-length of the heated tube.

Table 2 Comparison of average bare tube convective heat transfer data for similar parameters

Investigator	$\bar{D}_p$(mm)	$G(k_g/\text{hr}-\text{m}^2)$	$\bar{h}(W/\text{m}^2-°\text{C})$
This study	0.21	732	471
This study	0.43	1709	369
Bartel et al. [1]	0.20	732	539
Bartel et al. [1]	0.47	1709	397
Vreedenberg [13]	0.20	732	426
Vreedenberg [13]	0.47	1709	256

Table 2 gives a comparison of the bare tube studies with those of Bartel et al. and also a comparison with the Vreedenberg correlation. This comparison shows that for similar flow conditions the experimental data are within ±15 percent of each other; however, the correlation underpredicts the data by about 40 percent at the extreme case.

Finned Heat Exchange Tube Results. Variation of finned tube Nusselt number with the mass velocity parameters is shown in Figs. 5 and 6. These plots show the influence of fin height and particle size on the Nusselt number based on experimental data. These results are a summary of the heat transfer data for finned tubes studied in this investigation. The best performance for the small particle system appears to be the 8.33-mm fin length at high flow rate conditions. The best performance for low flow rate conditions is obtained from the 4.76-mm fin length. It is readily apparent that a severe drop in heat transfer performance takes place with the

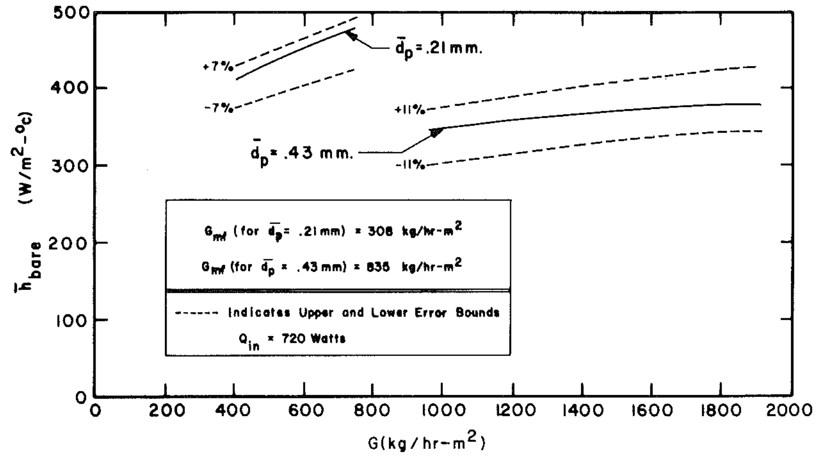

Fig. 4 Composite variation of the bare tube heat transfer coefficient for large and small particles

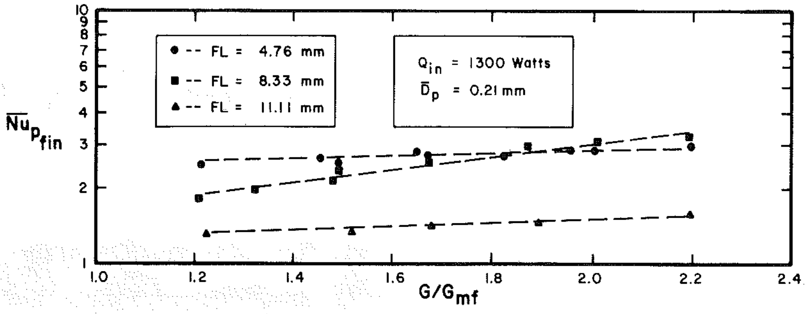

Fig. 5 Composite variation of particle Nusselt number for various fin lengths for small particle system

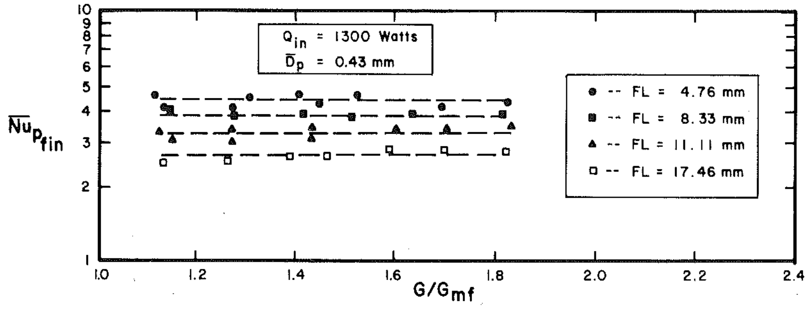

Fig. 6 Composite variation of particle Nusselt number for various fin lengths for large particle system

Table 3 Comparison of finned tube convective heat transfer coefficient with bare tube convective heat transfer coefficient for typical values of mass velocity ratio and finned tube length ratio

FL	G/G_{mf}	$\bar{D}_p = .21$ mm			$\bar{D}_p = .43$ mm		
		η	H	Ω	η	H	Ω
4.76	1.20	0.78	0.88	3.74	--	--	--
4.76	2.00	0.90	0.88	3.74	--	--	--
4.76	1.10	--	--	--	0.81	0.89	3.80
4.76	1.52	--	--	--	0.93	0.86	3.65
8.33	1.32	0.65	0.72	4.93	--	--	--
8.33	2.08	0.75	0.99	6.77	--	--	--
8.33	1.13	--	--	--	0.64	0.81	5.57
8.33	1.63	--	--	--	0.79	0.72	4.95
11.11	1.24	0.66	0.34	3.03	--	--	--
11.11	2.20	0.79	0.49	4.44	--	--	--
11.11	1.15	--	--	--	0.68	0.65	5.82
11.11	1.60	--	--	--	0.70	0.67	5.97

Table 4 Comparison of average finned single tube convective heat transfer data for similar parameters

Investigator	$\bar{D}_p$(mm)	FL(mm)	G (k_g/hr – m^2)	$\bar{h}$ (W/m^2 – °C)
This study	0.21	8.33	386	273
	0.21	8.33	547	403
	0.21	8.33	708	454
Bartel et al. [1]	0.20	9.52	*	*
	0.20	9.52	*	*
	0.20	9.52	*	*
This study	0.43	8.33	1006	273
	0.43	8.33	1260	273
	0.43	8.33	1514	273
Bartel et al. [1]	0.47	9.52	977	142
	0.47	9.52	1221	148
	0.47	9.52	1587	153
This study	0.21	11.11	386	199
	0.21	11.11	547	221
	0.21	11.11	708	227
Bartel et al. [1]	0.20	19.05	488	125
	0.20	19.05	977	136
	0.20	19.05	1221	142
	0.20	19.05	1465	148

*Testing not conducted in this range of parameters

11.11-mm fin length. The evident deviation between the 4.76 mm and 8.33 mm lengths is related to the interaction of W/d, length, and flow rate.

Large particle finned heat exchange data are presented in Fig. 6. For these data there is a uniformly decreasing heat transfer coefficient as a function of fin length. The long fins tend to have less effective heat transfer. In all cases the tube temperature for the fin configurations was considered to be the base temperature of the fin. The error bounds for the finned tube configurations may be considered essentially the same as those found for bare tubes discussed in the previous section. These bounds are on the average ±10 percent for all cases. The heat transfer coefficient for the finned tube configurations was computed by the methods given in the analytical methods section. These procedures accounted for the variation of temperature along the fins. In all cases the heat transfer coefficient computed was based on the wetted surface area of the fins plus the unfinned portion of the tube.

Comparison of Finned and Bare Heat Exchange Tubes. The fin efficiency may be defined as

$$\eta = \frac{\text{Tanh}(m \cdot FLC)}{m \cdot FLC} \qquad (4)$$

This expression applies for the insulated fin tip case and the details of this derivation are summarized by Kern and Kraus [12]. Table 3 presents the variation of fin efficiency as a function of fin length for both particle sizes studied. For the longest fin configurations, the fin efficiency remains at 0.50 to 0.70, depending on particle size. In all cases, the small particle system exhibits a general trend of higher values of fin efficiency, hence better heat transfer characteristics.

The heat transfer capacity function, Ω, is given in Table 3. This information implies a definite optimum fin geometry for the cases studied. The capacity function is a direct measure of the heat transfer capability for a finned tube relative to a bare tube under the same fluidization conditions. The heat transfer capacity can be increased by a factor of approximately six times, depending on flow conditions and fin geometry. For the large particle system this parameter did not reach a peak for the fin geometries studied. However, for the small particle system, the best fin arrangement appears to be the 8.33-mm length. The heat transfer capacity parameter (Ω) could easily be applied in design applications for relative prediction of finned tube performance over bare tube performance.

A good measure of finned tube performance is the ratio of effective convective heat transfer coefficients for fin configurations compared to heat transfer characteristics for bare tubes under similar fluidized bed flow conditions. When this ratio approaches unity, or even a fraction of unity, finned tubes will provide a higher heat transfer capacity per unit length than bare tubes. Table 3 also shows finned tube versus bare tube performance by illustrating the variation of H as a function of the fin length. Typical values of flow rate ranges are presented and compared for the different configurations. From Table 3, it may be observed that the tubes with shorter fins provide the best heat transfer when compared to bare tubes of similar geometry and identical flow conditions. The results indicate that particles penetrate into the surfaces between the fins by an interactive relationship that depends on both fin height and fin spacing (fins per length).

The finned heat exchange tubes studied in this investigation were supplied by ESCOA Fintube Company. The type of finned surface on this tubing is serrated (segmented) and to the authors' knowledge the literature includes only very limited studies of this particular tubing submerged in a fluidized bed. A previous study by Bartel et al. [1] considered this tubing. Table 4 presents a comparison of our heat transfer data compared to the Bartel et al. data. The consistent trend from this observation indicates that our heat transfer coefficients are significantly higher than those reported by Bartel et al. Both sets of data are based on the total heat transfer area on the finned tube.

Conclusions

It can be observed that there is a significant change in the heat transfer coefficient for different configurations of finned tubes. There appears to be a definite trend toward increasing heat transfer coefficients as fin height decreases. The interrelationship of fin height, fin width, fin spacing per length of tube, and finned tube material is complex and not directly shown by these results. The ability of fluidized particles to penetrate into the base region of fin tubes is influenced by both fin height and fin count. Blockage will result when fin count is increased to a degree where the spacing is less than several particle diameters.

Acknowledgment

The authors wish to thank Northern Natural Gas Company for the financial support to conduct this research. Additionally, we are grateful to ESCOA Fintube Company for supplying the finned tube material. Sincere thanks and appreciation are extended to Mrs. Bonnie Ward (UNL-M.E. Dept.) for typing the manuscript.

References

1 Bartel, W. J. et al., "Heat Transfer From a Horizontal Discontinuous Finned Tube in a Fluidized Bed," *AIChE Symposium Series*, No. 116, Vol. 67, 1971, pp. 85–89.

2 Genetti, W. E. et al., "The Effect of Tube Orientation on Heat Transfer With Bare and Finned Tubes in a Fluidized Bed," *AIChE Symposium Series*, No. 116, Vol. 67, 1971, pp. 90–96.

3 Bartel, W. J., and Genetti, W. E., "Heat Transfer From a Horizontal Bundle of Bare and Finned Tubes in an Air Fluidized Bed," *AIChE Symposium Series*, No. 128, Vol. 69, 1973, pp. 85–93.

4 Priebe, S. J., and Genetti, W. E., "Heat Transfer From a Horizontal Bundle of Extended Surface Tubes in an Air Fluidized Bed," *AIChE Symposium Series*, No. 161, Vol. 73, 1977, pp. 38–43.

5 Ziegler, E. N. et al., "Effects of Solid Thermal Properties on Heat Transfer to Gas Fluidized Beds," *Industrial and Engineering Chemistry Fundamentals*, Vol. 3, 1964, pp. 324–328.

6 Chen, J. C., and Withers, J. G., "An Experimental Study of Heat Transfer From Plain and Finned Tubes in Fluidized Beds," *AIChE Paper No. 34*, 15th National Heat Transfer Conference, San Francisco, Calif., 1975.

7 Chen, J. C., "Heat Transfer to Tubes in Fluidized Beds," *ASME Paper 76-HT-75*, presented at the Joint ASME/AIChE Heat Transfer Conference, St. Louis, Mo., 1976.

8 Staub, F. W., Kuwata, M., Ku, A. C., and Wood, R. T., "Modeling of Flow Behavior and Finned Tube Performance in the Turbulent Flow Regime," *Proceedings of the 6th International Conference Fluid Bed Combustion*, Atlanta, Ga., Vol. 3, Apr. 9–11, 1980, pp. 784–790.

9 Wood, R. T., Kuwata, M., and Staub, F. W., "Heat Transfer to Horizontal Tube Banks in the Splash Zone of a Fluidized Bed of Large Particles," *Fluidization, Proceedings of the International Fluid Conference*, Henniker, N. H., Aug. 3–8, 1980, Plenum Press, 1980, pp. 235–242.

10 Saxena, S. C., Grewal, N. S., Gabor, J. D., Zabrodsky, S. S., and Galershtein, D. M., "Heat Transfer Between a Gas Fluidized Bed and Immersed Tubes," *Advances in Heat Transfer*, edited by J. P. Hartnett and T. F. Irvine, Jr., Vol. 14, Academic Press, 1979, pp. 149–247.

11 Mickley, H. S., and Fairbanks, D. F., "Mechanism of Heat Transfer to Fluidized Beds," *A.I.Ch.E. Journal*, Vol. 1, 1955, pp. 374–380.

12 Kern, D. Q., and Kraus, A. D., *Extended Surface Heat Transfer*, McGraw-Hill, New York, 1972, pp. 85–202.

13 Vreedenberg, H. A., "Heat Transfer Between a Fluidized Bed and a Horizontal Tube," *Chemical Engineering Science*, Vol. 9, 1958, pp. 52–60.

Y. S. Yang[1]
Senior Research Engineer,
Production Research Center,
ARCO Oil and Gas Company,
Plano, Texas

J. R. Howell
E.C.H. Bantel Professor of
Professional Practice.
Mem. ASME

D. E. Klein
Associate Professor.
Mem. ASME

Mechanical Engineering Department,
University of Texas at Austin,
Austin, Texas 78712

Radiative Heat Transfer Through a Randomly Packed Bed of Spheres by the Monte Carlo Method

Radiative heat transfer through evacuated randomly packed beds of uniform-diameter spheres is considered. A Monte Carlo technique is used to simulate the energy bundle traveling through the voids of the bed. The randomly packed bed is assumed to be an absorbing-scattering medium with effective absorption and scattering coefficients. The packing pattern is modeled by a numerical simulation of rigid spheres slowly settling into a randomly packed assemblage. The Monte Carlo simulation of radiant energy transport through the packed beds generates the transmission curve as a function of bed height and sphere emissivity. The effective absorption and scattering coefficients of the randomly packed bed are evaluated by using the solution of the two-flux equations and Monte Carlo transmission results. Results show a strong dependence of the thermal radiative properties on the packing structure and the size and emissivity of constitutent spheres. Qualitative agreement is shown in comparison with other work which used regular cubic packing, and with existing experimental data.

Introduction

Radiative transfer through randomly packed beds of spheres is of importance due to its many industrial applications. Accurate prediction methods are particularly needed in high-performance cryogenic insulations [1, 2] and in the case of a loss of coolant accident for the pebble bed nuclear reactor. In general, two major transport mechanisms can occur in an evacuated randomly packed bed of spheres: conduction through the solid contact between spheres, and radiative transfer through the voids. However, these two processes can often be decoupled effectively and considered separately [3]. The main purpose of this study is to develop a methodology to examine the radiative heat transfer process through the randomly packed bed of spheres.

There are three commonly used models in the literature that describe the radiative heat transfer through packed beds. The first model common to a large number of analytical treatments is to approximate the heterogeneous random mixture of solid particles and voids by some regular geometrical arrangement of arbitrary solid and void bodies. Argo and Smith [4] and Chan and Tien [5] treated the solid and gas or void phases as alternating layers perpendicular to the direction of transfer.

The second type is based on a random walk process proposed by Rosseland [6]. It is assumed that when the mean free path of the photon in the packed beds is only a small fraction of the geometrical dimensions of the absorbing medium, the passage of a single quantum of radiant energy takes place along what may be regarded as a random path. This is a radiation diffusion process as is the diffusion of heat by gaseous conduction at ordinary pressures.

The third type of model is suggested by Van der Held [7], who considered the packed beds to be a pseudohomogeneous material, permitting description of the heat transfer processes by differential or integro-differential equations and boundary conditions. Hamaker [8] assumed that only two discrete fluxes exist inside the medium, one forward and the other backward, which leads to two coupled differential equations for radiation.

Brewster and Tien [9] have shown that dependent scattering effects must be considered when interparticle spacing is less than a few wavelengths. Thus, use of single scatter (independent scattering) properties in cases such as that studied here can introduce significant errors.

The objectives of the present study are to use a simulation of random packing of spheres to obtain information on the packed beds which affects the radiative transfer process and to perform Monte Carlo simulation of radiant energy transport through the packed beds by using the diffusion concept. The results of the transmission are used to predict the effective absorption coefficient, the scattering cross section, and the radiative conductivity.

General Considerations

The theoretical basis for this investigation is the two-flux model, which assumes only two discrete fluxes exist in the packed medium, one forward and one backward. This assumption simplifies the integro-differential equation of transfer into two coupled differential equations

$$\frac{di^+}{dx} = -(a+s)i^+ + si^- \tag{1}$$

$$-\frac{di^-}{dx} = -(a+s)i^- + si^+ \tag{2}$$

where x is the coordinate in the direction of radiative heat transfer and perpendicular to the boundary plane of the packed beds, i^+ and i^- are the radiation intensities in the positive and negative x-direction, and a and s are the effective absorption coefficient and the back-scattering coefficient. Parameters a and s have strong dependence on the geometric properties of the packing, such as the void fraction, size, and surface properties of the constituent spheres and the temperature of the system. Equations (1) and (2) can be solved readily with proper boundary conditions if the parameters a and s are known.

As shown by Chen and Churchill [10], the normalized transmitted flux defined as

$$S_n(L) = \frac{i^+(L)}{i^+(0)} = \frac{i^+(L)}{S_o} \tag{3}$$

---

[1] Formerly, Graduate Research Assistant, Mechanical Engineering Department, University of Texas at Austin, Austin, Texas 78712.

Contributed by the Heat Transfer Division for publication in the JOURNAL OF HEAT TRANSFER. Manuscript recevied by the Heat Transfer Division June 21, 1983. Paper No. 82-HT-5.

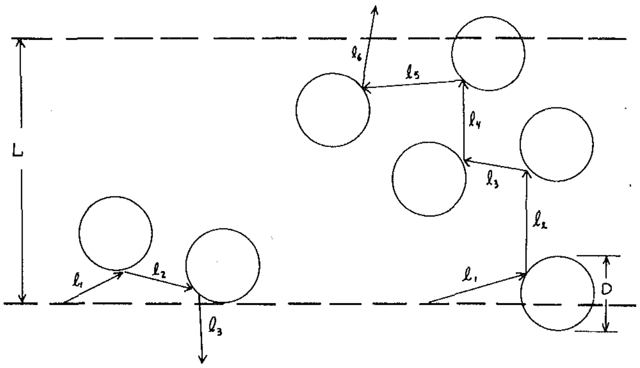

Fig. 1 Physical model of a randomly packed bed of equal-diameter spheres

can be found by solving the two-flux equations with the boundary conditions

$$i^+ = S_o \text{ at } x=0 \tag{4}$$

$$i^- = 0 \text{ at } x=L \tag{5}$$

The result is

$$S_n(L) = \frac{m}{m\cosh(mL) + a_n \sinh(mL)} \tag{6}$$

where $m^2 = a_n^2 - s^2$

$a_n = a + s$

and L is the bed height. Equations (4) and (5) represent a known input signal strength and no reflection. These boundary conditions also indicate that the boundary planes are black with emissivity equal to unity. Equation (6) is the analytical model used to fit experimental measurements or computer simulated results of S_n and L.

The functional dependence of S_n on L is affected by many factors, such as the packing structure of the bed, size and surface property of the constituent spheres, and the temperature of the system. This relationship can be obtained by either a direct measurement from an experiment or a computer simulation of the real transport process. Both of these methods encounter some difficulties. For instance, it is difficult to build a randomly packed bed of spheres, and the ordering effect due to the containing wall cannot be ignored, especially for thinner beds. The direct transmission in thin-layer samples contradicts the diffuse assumption of the two-flux model. If the bed is too thick, accurate measurement is difficult due to the weak intensity transmitted through the bed, which introduces greater deviation in the measurement data. One of the most important factors in determining the transmission curve of a packed bed may lie in the definition of the bed height. There is always a deviation of bed height within plus or minus one sphere diameter. Since the transmission ratios are plotted directly against the bed height, the bed height, L, plays an important role in the entire analysis. The scattered data reported on the value of emissivity of different materials, which must be used in the analytical predictions, also add to the uncertainty of the results.

The radiation transport through the randomly packed beds is simulated by a Monte Carlo technique using the known cumulative distribution function of the penetration distance. The radiative energy bundle is emitted from a reference plane at the higher temperature boundary of the bed. Each bundle path is traced, and all the interactions that occur in the medium before the bundle escapes from the bed are recorded.

In the analysis, the radiative properties are assumed gray and temperature-independent. The surface of the spheres is assumed specular, and the size of the bed is made large enough to make Rosseland's diffusion approximation valid. The packed beds are evacuated; i.e., there is no attenuation in the voids. The conduction mechanism is decoupled completely from the radiative process. The effects of diffraction are ignored in the present analysis. Such effects could well be important, and are a suitable area for further study.

The physical model consists of an infinite number of spheres of equal-diameter packed randomly in a slab of finite thickness as shown in Fig. 1. The randomness of the sphere packing is interpreted in the sense that the penetration distance for each energy bundle is determined from randomly packed spheres, and the center of each sphere being hit is determined randomly. Each path that a photon travels is independent of the others, and the history of the path is to be eliminated once its journey is over.

Random Packing of Spheres

Much effort has been expended on the subject of random packing of spheres in order to understand its special features and geometric properties. Knowledge of the packing structure within a randomly packed bed is essential for any rigorous analysis of the heat transfer within the bed. Among the approaches of solving the packing problem, simulation is attractive, since the construction of random assemblages of spheres is easier and the information about the packing structure needed for the heat transfer analysis is far more detailed than experimental results can offer. Moreover, the retention of the coordinates of the spheres in the randomly packed beds makes it possible to carry out later analysis for special purposes. The simulation used here is based on the work by Tory [11]. A computer code PACKUT is a modified version of the original work by Tory used to obtain information on the solid fraction distribution, as well as the extinction coefficient of the radiation in the randomly packed beds.

The simulation describes the slow sequential settling of

Nomenclature

a = absorption coefficient
a_n = $a + s$
D = sphere diameter
F = parameter for calculating radiant conductivity
I_o = incident radiation intensity
i^+ = forward radiant intensity
i^- = backward radiant intensity
K = extinction coefficient
k_r = radiant conductivity
L = bed thickness
l = penetration distance
l_m = mean penetration distance
m = $(a_n^2 - s^2)^{1/2}$
$\mathbf{n}$ = normal vector of the sphere surface
n_i = components of the normal vector
P = cumulative distribution function of the penetration distance
p = probability density function of the penetration distance
R_θ, R_γ = random numbers
S_o = initial energy bundle strength
s = scattering coefficient
u_i = directional cosines
w = size of the packing container
x,y,z = positions in Cartesian coordinate system
X,Y,Z = axes of Cartesian coordinate system
γ = cone angle
θ = circumferential angle
ϵ = radiative surface emissivity

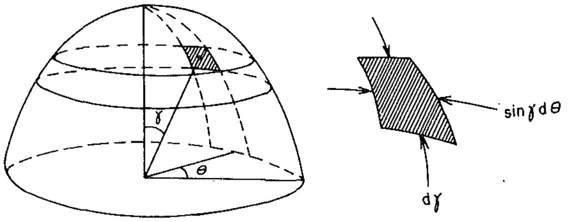

Fig. 2 Unit hemisphere used to obtain emission point and emission direction of a sphere

individual rigid spheres of equal diameter from a dilute suspension into a randomly packed assemblage. No bouncing and no bumping of precariously stable spheres to more stable positions is considered, and no consideration is made of spreading spheres apart to accommodate incoming spheres. It is assumed that each sphere in the bed must be supported by at least three others, and no sphere can overlap. Packing takes place in a semi-infinite box defined by $[x, y, z \mid 0<x<w, 0<y<w, z>0]$. The simulation can be used to describe the packing between flat walls, or between periodic vertical bounding surfaces to avoid the wall effects. The latter yields a packing which is effectively infinite in the xy-plane.

Once the initial coordinates of a sphere have been chosen, its path is completely determined. After dropping, each sphere seeks a position of minimum potential and, given the impenetrability of the spheres and floor, follows the constrained path along which the potential gradient is a maximum. With the initial position of each new sphere determined and the coordinates of spheres already in known position, the final position of each new sphere can be calculated. A sphere is stable when any roll would incresse its potential. Any sphere which touches the floor is considered to be stable. After the coordinates of all the sphere centers are stored in the computer memory, the packing properties of the bed can be computed.

The solid fraction of an array of spheres is defined as the ratio of the volume of the spheres to the total volume they occupy. Physically, it represents the density of the bed and is related to the probability that a radiant energy bundle can penetrate through the bed. There exists a range of solid fraction for a randomly packed bed of equal-diameter spheres [12]. The packing generated from this simulation represents a random loose packing and has a solid fraction of 0.58. As presently formulated, it is not possible to generate beds with other solid fractions using the simulation.

Within a randomly packed bed, spheres may have different numbers of neighbors in contact. When a radiant energy bundle is emitted from a base sphere, the immediate surrounding of the base sphere will have a great influence on the fate of the bundle. A search is done to find the clustering features of the packed beds. The contact-number frequency function is defined as the probability of the different possible contact numbers that can exist within a randomly packed bed. The simulation used in this study shows a strong peak at six contacts, and the average number of contacts is approximately six. Although it is realized that clustering in the vicinity of the base sphere does affect the radiation transport, in the following analysis, the extinction coefficient is obtained only for the most common situation when the contact number is six.

The Extinction Coefficient of Randomly Packed Beds of Equal Spheres

The radiation intensity through an evacuated randomly packed bed is attenuated by particle absorption and scattering. The change in intensity has been found experimentally to depend on the magnitude of the local intensity. If a coefficient of proportionality, K, which depends on the local properties of the medium is introduced, then the decrease is given by

$$di(l) = -K(l)\,i(l)\,dl \tag{7}$$

where i is the radiation intensity, and l is the coordinate along the direction of radiation. K is the extinction coefficient in the layer; it is a physical property of the material and has units of reciprocal length. For a gas medium, K is a function of the temperature, pressure, composition of the material, and wavelength of the incident radiation. For packed beds made up of uniform-diameter spheres of the same material, under the assumptions made in the previous section, the extinction coefficient is only a function of the packing arrangement and the size of the constituent spheres; it is independent of particle absorptivity.

A more appropriate interpretation can be achieved by reexamining equation (7) and noting that the fractional change in radiation intensity occurring over a distance, dl, is given by

$$K(l) = \frac{-\dfrac{di(l)}{i(l)}}{dl} \tag{8}$$

Hence, it is natural to interpret $K(l)$ as the probability per unit path length traveled that the radiant energy bundle will undergo a reaction with a sphere surface in the packed bed at the position l.

Equation (7) can also be solved by imposing an incident radiation intensity I_0 at $l = 0$, giving

$$i(l) = I_o \exp\left[-\int_o^l K(l^*)dl^*\right] \tag{9}$$

If we interpret this equation in the sense of probability, then

$\exp\left[-\int_o^l K(l^*)dl^*\right] \equiv$ probability that a radiant energy bundle moves a distance, dl, without any interaction

$K(l)\exp\left[-\int_o^l K(l^*)dl^*\right] \equiv$ probability that a radiant energy bundle has its first interaction in dl about l

With this interaction probability $P(l)$, we can calculate the average distance a photon travels before interacting with a sphere surface in the packed bed

$$l_m = \int_0^\infty K(l)\exp\left[-\int_o^l K(l^*)dl^*\right]dl \tag{10}$$

When $K(l)$ is constant, carrying out the integral gives

$$l_m = \int_0^\infty l\,\exp(-Kl)\,dl = \frac{1}{K} \tag{11}$$

demonstrating that the average penetration distance before absorption or scattering is the reciprocal of K when K does not vary along the path. Equation (11) provides a simple way of gaining some insight as to whether or not an absorbing-scattering medium is optically dense with regard to radiation traveling through it.

The value of K for different gas media under different physical conditions is a measurable quantity. For temperature-independent gray packed beds, the extinction coefficient is solely determined by the size of the constitutent spheres and the packing structure.

To obtain the variation of K as a function of distance from a base sphere, a Monte Carlo method is used with the known

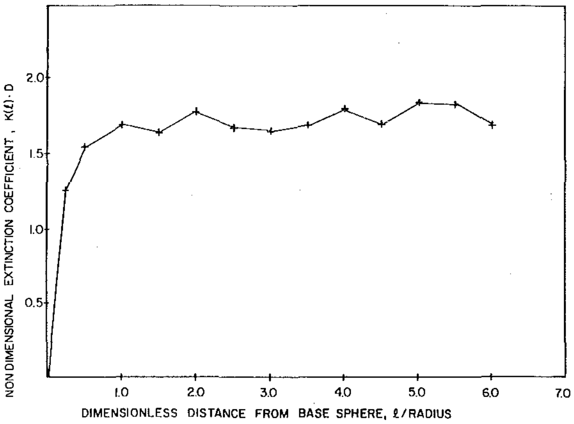

Fig. 3 Variation of extinction coefficient as a function of distance from the base sphere

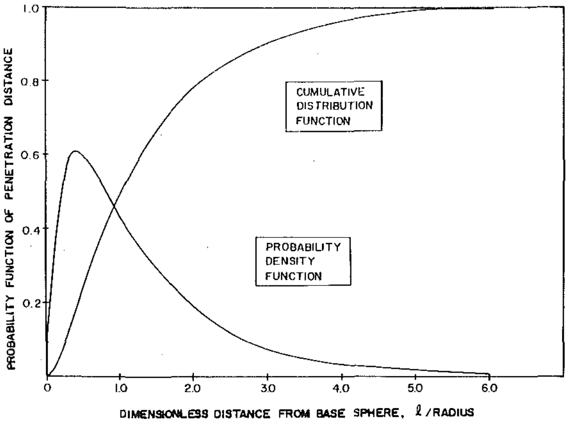

Fig. 4 Probability density function and cumulative distribution function of the penetration distance of radiant energy through a randomly packed bed of equal-diameter spheres

coordinates of all sphere centers in a randomly packed bed of spheres. A sphere with six contacts is first selected randomly as the starting base for the emission of radiant energy bundles. The emission point in the surface of the base sphere is also determined randomly by assuming that each area element or solid angle in the sphere surface has an equal probability of being selected. As shown in Fig. 2, the probability of selecting a surface point at cone angle γ, and circumferential angle θ, $p(\gamma,\theta)$, can be calculated as

$$p(\gamma,\theta)=\frac{D^2\sin\gamma\, d\gamma\, d\theta}{4\pi D^2}=\frac{\sin\gamma\, d\gamma\, d\theta}{4\pi} \tag{12}$$

Assuming no circumferential variation, the cumulative distribution function $P(\gamma)$ of $p(\gamma,\theta)$ is

$$P(\gamma)=\frac{\pi\int_0^\gamma \sin\gamma^* d\gamma^*}{4\pi}=\frac{1}{2}(1-\cos\gamma) \tag{13}$$

and $P(\gamma)$ is a number between 0 and 1. If we choose a number randomly from the range 0 to 1, then the corresponding γ angle can be calculated as

$$\gamma=\cos^{-1}(1-2R_\gamma) \tag{14}$$

Since no dependence on circumferential angle, θ, is assumed, it is fairly obvious from intuition that θ can be determined by

$$\theta=2\pi R_\theta \tag{15}$$

where R_θ is again a random number between 0 and 1.

Once the position of the emission point on a sphere surface is known, the direction of the energy bundle leaving that point can be determined following the same procedure. Again, γ and θ are determined randomly by choosing a point on the surface of the hemisphere whose base is the plane tangent to the base sphere at the emission point. Because of the constraint on the impenetrability of the sphere, the range for γ in this case is between 0 and $\pi/2$, which leds to the functional relation of $\gamma=\cos^{-1}(R_\gamma)$.

To find out whether this energy bundle emitted from that point in the direction determined above is able to penetrate a distance Δl about l, the coordinate of the midpoint of the line segment Δl is determined by

$$\begin{aligned} x&=\sin\gamma\cos\theta+x_o\\ y&=\sin\gamma\sin\theta+y_o\\ z&=\cos\gamma+z_o \end{aligned} \tag{16}$$

where (x_o, y_o, z_o) is the coordinate of the emission point. The two end points of the line segment are obtained by replacing l with $l+\Delta l/2$ and $l-\Delta l/2$. Since the coordinates of all the sphere centers are retained in the computer memory, a search can be done to check whether any of the spheres in the packed bed will intersect with the line segment identified above. The Δl chosen for this study is 1/10 of the sphere diameter. Mathematically, if any point on this line segment has a distance from the center of any sphere in the randomly packed bed of less than the sphere radius, this energy bundle is bound to be attenuated. It is assumed that the spheres are opaque, and only absorption and scattering are considered. Once the energy bundle hits the surface, there is an interaction between the bundle and the sphere surface. This process is repeated by emitting many bundles from different spheres. The fraction of the bundles that is intercepted by the spheres during travel through the distance Δl divided by Δl represents the extinction coefficient, $K(l)$, at position l. Different l are used to obtain the variation of the extinction coefficient as a function of l.

In performing the Monte Carlo calculation of $K(l)$, l up to three sphere diameters in length are examined. At each l value, 5000 energy bundles are emitted in order to obtain good statistical results. The $K(l)$ values approach a constant number in the statistical sense after l values greater than one sphere radius due to the homogeneity of the randomly packed spheres. The result of the $K(l)$ variation is shown in Fig. 3. It indicates that $K(l)\cdot D$ approaches approximately 1.75 after l greater than one sphere radius.

The product of $K(l)\cdot D$ approaching a constant reveals some interesting facts. The optical thickness of the packed beds is defined by $\int_0^l K(l^*)dl^*$, which in this case is approximately equal to $K(l)\cdot l$. If these two terms are written in nondimensional form, $(K(l)\cdot D)\cdot(l/D)$, it is clear that the optical thickness then depends directly on the extinction coefficients and the thickness of the absorbing-scattering medium. This is analogous to a gas that is of uniform composition, temperature, and pressure. $K(l)\cdot D$ equaling a constant indicates that the extinction coefficient is inversely proportional to the size of the constituent spheres in the packed bed, which implies that the effective thermal radiative properties have a strong dependence on the sphere size.

In order to calculate the radiant energy transport through the packed bed, the probability that the bundle has its first interaction in dl at different l, $p(l)dl$, must be known. With $K(l)$ at different l values known, $K(l)\exp[-\int_0^l K(l^*)dl^*]$ can be calculated by a numerical integration at each discrete point. The results are shown in Fig. 4. It shows that the most probable path length for a radiant energy bundle traveling through a randomly packed bed of equal-diameter spheres is approximately half of the sphere radius, and the probability that the bundle travels more than three sphere diameters before it hits a solid surface is nearly zero. The mean

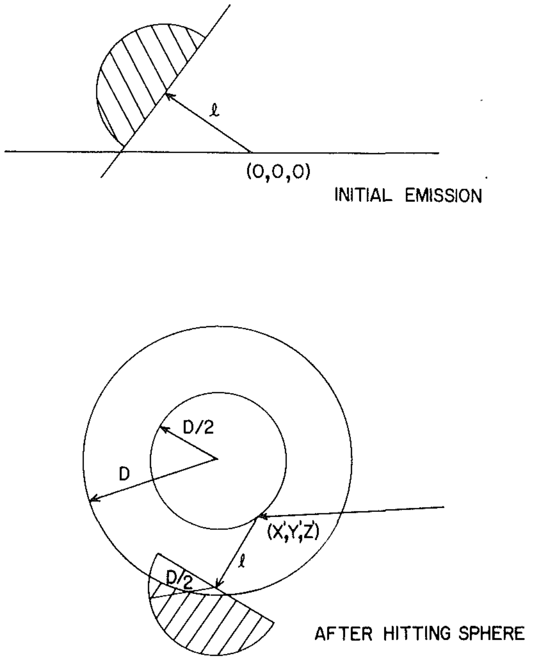

Fig. 5 Selection of sphere center coordinate after initial emission and after reflection

penetration distance of the radiation is obtained by multiplying the fraction absorbed at l by the distance l and then integrating over all path lengths from $l = 0$ to $l = \infty$ according to equation (10). The result shows that l_m of this system for the radiation is about 0.66 sphere diameters.

The cumulative distribution function of penetration distance, $P(l)$ is obtained by

$$P(l) = \int_0^l p(l^*)dl^* \tag{17}$$

The results are shown in Fig. 4. This curve is used to determine randomly the penetration distance of the radiation during each movement of the energy bundle.

Simulation of Radiant Energy Bundle Traveling Through a Randomly Packed Bed of Spheres

The main purpose of this simulation is to trace a sufficient number of radiant energy bundles to find out how much of the initial emitted energy is transmitted through the packed bed. The basic elements of the simulation consist of the determination of the penetration distance for each radiant energy bundle before it hits the solid surface, the random selection of the center coordinate of the sphere being hit, and the calculation of the reflected direction of the energy bundle by assuming that the sphere surface is specular.

In the present simulation, each radiant energy bundle is emitted from a reference origin. After emission, this energy bundle moves in a certain direction specified by the directional cosine (u_1, u_2, u_3) and penetrates a certain distance through the packed bed. This line segment with a direction can be viewed as a bound vector carrying a certain amount of energy, E_γ, in the three-dimensional space. The function relating a random number to the cone and circumferential angles for emission is given by [3]

$$\gamma = \sin^{-1}(R_\gamma^{1/2})$$

and (18)

$$\theta = 2\pi R_\theta$$

By choosing a random number between 0 and 1, the

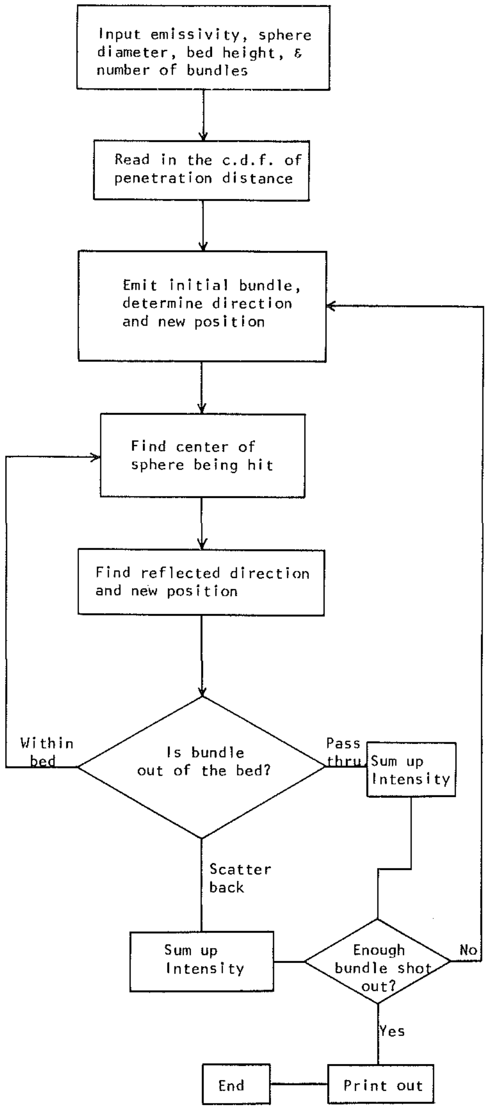

Fig. 6 Computer flow chart for radiant energy through a randomly packed bed of equal-diameter spheres

penetration distance can be obtained by mapping this random number to its corresponding function value according to Fig. 4. The end point of the radiative energy vector can now be determined. This point represents a location on the surface of the sphere that has an interaction with the incident radiation ray.

From the above given condition, an infinite number of possible choices is available for the center coordinate of the sphere being hit. To determine the center coordinate of the sphere being hit after the bundle carrying a unit of energy is first emitted, it is assumed there is no impenetrability constraint imposed on the selecting process. That is, the bounding plane of the packed bed has a wavy characteristic to eliminate the wall effect on the random packing of spheres. As shown in Fig. 5, the coordinate of the sphere center is determined by choosing randomly a point, as can be done by generating two random numbers and calculating the γ and θ angles according to the proper functional relationship, from the surface of a hemisphere whose base plane is perpendicular to the incident energy ray. The γ and θ angles are related to the random number, R_γ and R_θ, by

$$\gamma = \cos^{-1}(R_\gamma)$$

and

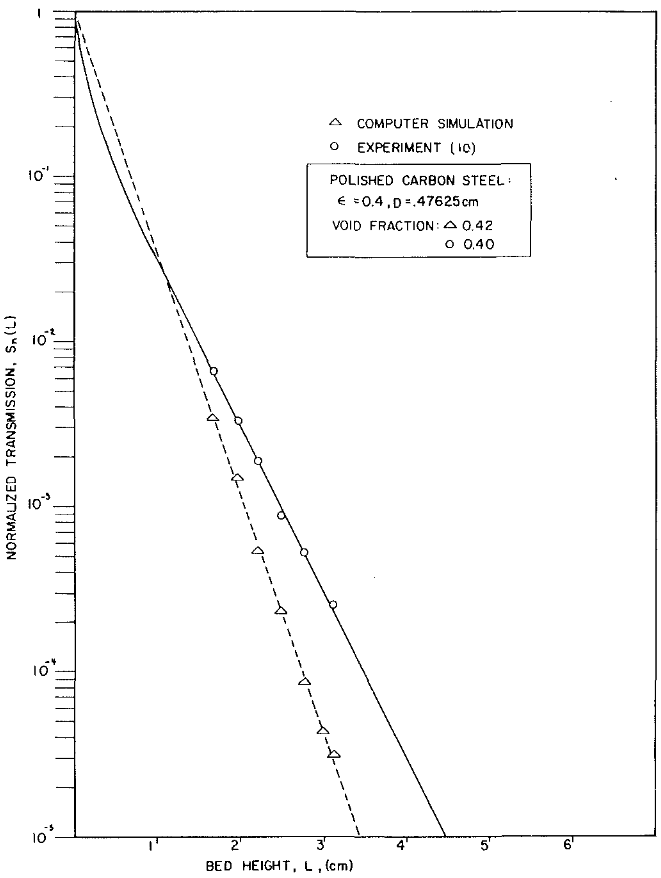

Fig. 7 Normalized transmission curves of radiant energy through a randomly packed bed of steel spheres

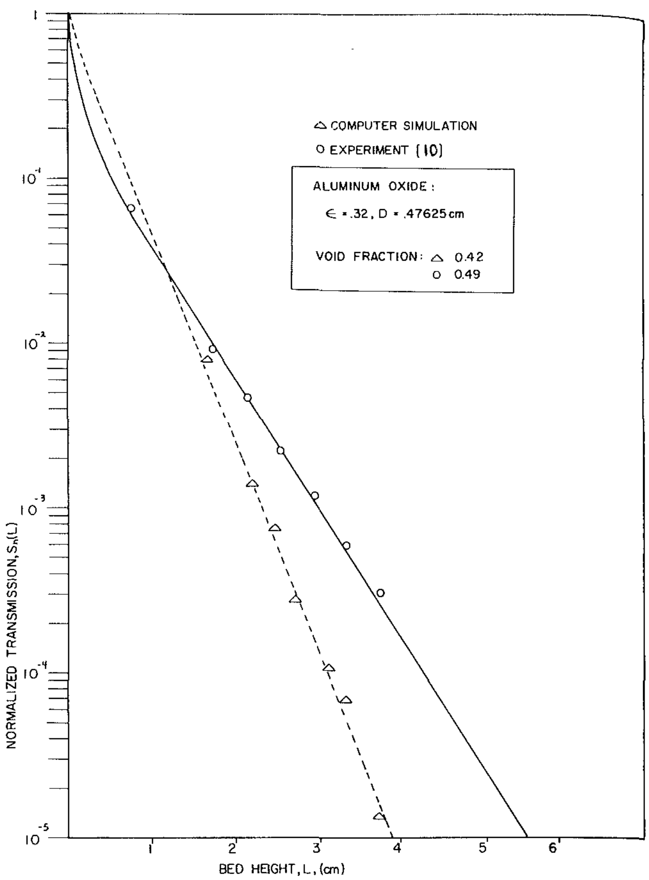

Fig. 8 Normalized transmission curves of radiant energy through a randomly packed bed of aluminum spheres

$$\theta = 2\pi R_\theta \tag{19}$$

The coordinate of the sphere center can now be calculated as

$$x' = (D/2)\sin\gamma\cos\theta$$
$$y' = (D/2)\sin\gamma\sin\theta$$
$$z' = (D/2)\cos\gamma$$

where x', y', z' are the coordinates of the sphere center at the X', Y', Z' coordinate system which uses the direction of the energy ray as the Z-axis. After a rotation and translation of the coordinate system, the sphere center coordinate according to the original coordinate system can be obtained. The transformation is needed due to the following involved reflection calculation.

After hitting a sphere surface, the energy bundle will suffer a decrease in the amount of energy it carries due to the absorption interaction. Out of the original E_γ, ϵE_γ is absorbed, and $(1-\epsilon)$ E_γ is scattered. The radiative transfer process continues with the bundle carrying less energy.

Because the surface of the sphere is assumed to be specular, the rays incident on a sphere surface are reflected according to the following fundamental laws of geometrical optics: (*a*) the angle of reflection is equal to the angle of incidence; and (*b*) the incident ray, the surface normal at the intersection point, and the reflected ray all lie in the same plane. These two laws are sufficient to determine the direction cosine u_1', u_2', u_3' of the reflected ray, given as

$$u_i = u_i - 2n_i \sum_{k=1}^{3} n_k u_k \qquad i=1,2,3 \tag{20}$$

where u_i is the direction cosine of the incident ray, and n_i is the component of the unit vector **n** at the point of intersection; **n** is given by

$$\mathbf{n} = \frac{\operatorname{grad} h_j(x',y',z')}{|\operatorname{grad} h_j(x',y',z')|} \tag{21}$$

where (x', y', z') is the initial point of the reflected vector, and h_j is a continuous function of the sphere surface.

Once the direction cosines of the reflected ray are determined, another random number is drawn to determine the path length for this bundle of energy $(1-\epsilon)E$. With this penetration length and the directional cosines u_1', u_2', u_3', the end point of the reflected ray vector can be obtained. At this point, again, interaction occurs between the energy bundle and the sphere surface whose center coordinate is yet to be determined.

In the present simulation, only one sphere reflects the ray at any moment. That sphere will impose another constraint on selecting the center coordinate of the sphere to be hit by the reflected ray due to the impenetrability of the solid sphere, which requires that two sphere centers be separated by at least a sphere diameter distance to avoid overlapping. As shown in Fig. 5, due to this extra constraint, only part of the hemisphere surface is not eligible for the selection of the sphere center. It may require several repetitions of the selecting process to obtain a satisfactory sphere center, especially when the end point of the ray vector is too close to the previously hit sphere. The process is repeated until either the ray has lost most of its energy by multiple reflections or it passes through the bounding planes.

On passing through a randomly packed bed of equal-diameter spheres, the diffuse incident flux will be absorbed and reflected repeatedly. By performing the above transport simulation, the transmittance of packed beds of different thickness can be obtained by summing all the energy passing through the bounding plane and dividing it by the total energy emitted. The flow chart of the Monte Carlo simulation program is shown in Fig. 6. Figures 7 and 8 show the result of simulation for ϵ values of 0.32 and 0.40, which represent the emissivities of aluminum oxide and polished carbon steel as reported in [10]. The diameter of the sphere is 0.476 cm. Also shown in Figs. 7 and 8 are the experimental results of [10].

The present simulation cannot exactly duplicate the experiment in [10]. The result of the transmission in this study is done in an ideally randomly packed bed of spheres. The differences in transmission results between this study and [10] stem from many factors. First, a substantial deviation exists in the emissivity data reported in the literature, which directly affects the prediction of energy transmitted through packed beds. The assumptions made in the simulation, such as the specular surface, temperature, and wavelength independence of the radiative properties may also change the transmission. The characteristics of the packed beds in the experiment are affected by the wall effect, and the deviation of the solid fraction from random packing of equal-diameter spheres makes important differences in the extinction coefficient. Different definitions of the bed height for these two approaches also contribute to the differences in the transmission curves. However, the functional dependence of the transmission on the emissivity indicates the same trend for both studies as shown in Figs. 7 and 8.

The Effective Thermal Radiative Properties of a Randomly Packed Bed of Spheres from the Transmission Simulation

Computer simulation of radiative transport through randomly packed beds supplies values of S_n as a function of l. It is also desired to obtain values of a and s by regression on equation (6). As the fractional deviation (rather than absolute deviation) is approximately equal for all data points in the simulation, the least square error requirement specified is that

$$\Phi = \sum_{j=1}^{n} \left[\frac{S_n(l_j) - S_n'(l_j)}{S_n(l_j)} \right]^2 \tag{22}$$

be minimized. In equation (22), n denotes the number of data points, $S_n(l_j)$ is the simulation value of S_n for the jth data point, and $S_n'(l_j)$ is the correlation value of S_n at l.

Since equation (6) is a nonlinear model, analytic regression is not possible, and it is necessary to resort to iterative methods. The numerical method used in this study was proposed and derived by Chen and Churchill [10]. Equation (6) is expanded into a Taylor series with higher terms truncated. Then the first derivatives of Φ, with respect to the variables a and m, are set to be zero. The resulting two equations are solved simultaneously to obtain the values of m and a_n. This iterative process repeats until m and a_n converge to as many significant figures as desired. The values of radiation parameters a and s can then be calculated from these converged values by

$$s = (a_n^2 - m^2)^{1/2} \tag{23}$$

$$a = a_n - s \tag{24}$$

The results of a and s for ϵ values of 0.32 and 0.4 are shown in Table 1. These values have a large discrepancy when compared with the values shown in [10]. But the predicted trend for the dependence of a and s on emissivity appears to agree well with that experiment. In general, the predicted absorption coefficient is much higher while the back-scattering cross section is lower. The sum of a and s for both cases, which represents the extinction coefficient of the system, centers around a constant value statistically. For D = 0.476 cm, and using the previous conclusion that $K \cdot D$ = 1.75, K can be calculated to be 3.67 cm^{-1}. This agreement verifies that the extinction coefficient in this kind of system is a function of the diameter but not of the emissivity of the constituent sphere.

Table 1 Effective absorption and back-scattering coefficients of a randomly packed bed of equal-diameter spheres

Emissivity	Absorption coefficient (cm^{-1})	Scattering coefficient (cm^{-1})	Extinction coefficient (cm^{-1})
0.32	1.325	2.477	3.80
0.40	1.847	2.073	3.92

The radiant conductivity defined by

$$k_r = -(i^+ - i^-)/(dT/dx) \tag{25}$$

can be calculated according to the following relationship derived by [10]

$$k_r = \frac{8\sigma T_o^3}{a + 2s} \tag{26}$$

where σ is the Stefan-Boltzmann constant, and T_o represents the bulk temperature of the packed bed. From Rosseland's diffusion approximation [3], the radiant conductivity can be expressed as

$$k_r = \frac{16\sigma T_o^3}{3(a+s)} \tag{27}$$

Both of these models can be rewritten as

$$k_r = 4\bar{F}\sigma D T_o^3 \tag{28}$$

where $\bar{F} = 2/(a+2s)D$ for equation (26) and $\bar{F} = 4/3(a+s)D$ for equation (27).

Equation (28) shows the radiant conductivity dependence on particle size or transmissivity, bulk bed temperature, and effective thermal radiative properties. By substituting the obtained values of a and s, the $\bar{F}$ values for the above two models, when ϵ is equal to 0.40, are 0.70 and 0.71.

Discussion and Conclusion

The transmission curves for different emissivities are obtained by a Monte Carlo simulation of radiative transport through randomly packed beds. The results of transmission are correlated in terms of a two-flux model to obtain the effective absorption coefficient and scattering cross section. The radiant conductivity can also be calculated from these quantities either by a two-flux model or by Rosseland's diffusion model.

The transmission results are compared with a similar experiment [10]. Work by Chan and Tien [5] is also compared with the results of the present study. Reference [5] studied radiative transfer through simple cubic packing by determining the scattering diagram of a unit cell, the optical properties of a series of thin microsphere layers, and the solution of the two-flux equations. No numerical results on transmission data or effective radiative properties were reported by their study; only a discussion of the qualitative variation of K, a, and s with some system parameters was presented. The fact that the extinction coefficient is inversely proportional to the sphere diameter agrees well in all three investigations and with rough extimates based on the Mie theory of single scattering [5]. The dependence of a and s on emissivity also agrees well. The difference of the transmission results between this study and the experiment was discussed in the section titled, "Simulation of Radiant Energy Bundle Traveling Through a Randomly Packed Bed of Spheres." It is also pointed out in [5] that this discrepancy may be attributed to the fact that in the experimental system, due to the finite thickness of the packed beds, a considerable portion of energy may pass through the bed without encountering the absorption and scattering process. In the present simulation, the wavy wall boundaries eliminate the nonrandomness near the wall to resemble a totally random system, which in turn reduces the transmission of radiation through the bed. The a and s are direct results of the transmission data and two-flux model. The existence of a difference between [10] and the present work is expected.

The results of the present study lead to a better understanding of the radiative heat transfer mechanism in a randomly packed bed of spheres. The Monte Carlo simulation allows a much clearer picture of the physical phenomena involved.

References

1 Tien, C. L., and Cunnington, G. R., "Cryogenic Insulation Heat Transfer," *Advances in Heat Transfer*, edited by T. F. Irvine and J. P. Harnett, Vol. 9, Academic Press, New York 1973, pp. 349-417.

2 Tien, C. L., and Cunnington, G. R., "Recent Advances in High-Performance Cryogenic Thermal Insulation," *Cryogenics*, Vol. 12, 1972, pp. 419-421.

3 Siegel, R., and Howell, J. R., *Thermal Radiation Heat Transfer*, 2d ed., McGraw Hill, New York, 1980.

4 Argo, C. K., and Smith, J. M., "Heat Transfer in Packed Beds," *Chem. Eng. Prog.*, Vol. 49, 1953, pp. 443-451.

5 Chan, C. K., and Tien, C. L., "Radiative Transfer in Packed Spheres," JOURNAL OF HEAT TRANSFER, Vol. 96, 1974, pp. 52-58.

6 Rosseland, S., *Theoretical Astrophysics*, Clarendon Press, Oxford, 1936.

7 Van der Held, E. F. M., "The Contribution of Radiation to the Conduction of Heat," *Appl. Sci. Research*, A3, 1952, pp. 237-249; A4, 1953, pp. 77-99.

8 Hamaker, H. C., "Radiation and Heat Conduction in Light Scattering Material," *Phillips Research Reports*, Vol. 2, 1953, pp. 55, 103, 112, 420.

9 Brewster, M. Q., and Tien, C. L., "Radiative Transfer in Packed/Fluidized Beds: Dependent versus Independent Scattering," ASME Paper 82-HT-4, 1982.

10 Chen, J. A., and Churchill, S. W., "Radiant Heat Transfer in Packed Beds," *A.I.Ch.E. Journal*, Vol. 9, No. 1, 1962, pp. 35-41.

11 Jodrey, W. S., and Tory, E. M., "Simulation of Random Packing of Spheres," *Simulation*, Jan. 1979, pp. 1-12.

12 Yang, Y. Sam, "Heat Transfer Through a Randomly Packed Bed of Spheres by Monte Carlo Method," Ph.D. dissertation, The University of Texas at Austin, Austin, Texas, 1981.

Two-Dimensional Radiation in Absorbing-Emitting Media Using the *P-N* Approximation[1]

A. C. Ratzel III
Sandia National Laboratories,
Albuquerque, N. M. 87185

J. R. Howell
University of Texas at Austin,
Mem. ASME

Radiative energy transfer in a gray absorbing and emitting medium is considered in a two-dimensional rectangular enclosure using the P-N differential approximation. The two-dimensional moment of intensity partial differential equations (PDE's) are combined to yield a single second-order PDE for the P-1 approximation and four coupled second-order PDE's for the P-3 approximation. P-1 approximation results are obtained from separation of variables solutions, and P-3 results are obtained numerically using successive-over-relaxation methods. The P-N approximation results are compared with numerical Hottel zone results and with results from an approximation method developed by Modest. The studies show that the P-3 approximation can be used to predict emissive power distributions and heat transfer rates in two-dimensional media with opacities of unity or greater. The P-1 approximation is identical to the diffusion solution and is thus applicable only if the medium is optically dense.

Introduction

The study of radiative heat transfer in a radiating medium has become increasingly important in such diverse fields as cryogenics, ablative protection, glass manufacture, and energy conservation. The mathematical difficulties involved in solving problems in these areas are substantial, since the basis for analyzing a radiation field in an absorbing and emitting medium is the equation of radiative transfer [1, 2], which is an integro-differential equation written in terms of the radiative intensity. By simultaneously solving coupled equations for the radiative transfer and for the conservation of energy, results for the temperature field and energy transfer are obtained. Often, these equations must be solved subject to boundary conditions which are posed as integral expressions.

An exact solution of the equation of transfer may require integrations with respect to time, position, wavelength, and solid angle. For most practical problems, these complexities are prohibitive and often the gray medium and steady-state assumptions are used to simplify the problem. In addition, there are limiting cases which can simplify the integro-differential equation of radiative transfer. The most often used approximations for the medium include (*i*) the transparent (optically thin), (*ii*) the diffusion (optically thick) and (*iii*) the cold wall (emission) approximations [2]. Because these approximations are applicable only for particular temperatures, optical thicknesses and boundary conditions, the user must be careful not to employ these methods without considering his (or her) own special problem constraints.

Although there have been several exact one-dimensional steady-state solutions presented for the radiative transfer problem, e.g., [3, 4], only limited efforts have been directed in exact multidimensional formulations [5]. Instead, approximate solution techniques have been sought. Two often used approximation methods assume that the intensity distribution is uniform over hemispherical solid angle regions, i.e., Milne-Eddington approximation [2] or that the intensity is uniform over solid angle regions (discrete ordinate method [6]). An alternative method of solution for radiative energy transfer problems incorporates the *P-N* differential approximation [7, 8, 9], in which the radiation intensity is approximated by a series of spherical harmonics. This simplification reduces the integral equation of radiative transfer to a series of differential equations by approximating the equation of transfer with a finite set of moment equations.

In this paper, the radiative heat transfer problem for a gray absorbing and emitting medium in a rectangular enclosure is considered using the *P-N* differential approximation. Governing partial differential equations for the moments of intensity are developed incorporating the *P*-1 and *P*-3 approximations for the intensity distribution. The numerical methods used to solve the governing *P-N* equations are summarized along with representative results which are compared with numerical Hottel Zone solutions [10] and with results obtained by an alternative approximation solution developed by Modest [11]. These results show that the *P*-3 differential approximation can accurately predict two-dimensional emissive power distributions and heat transfer rates for rectangular enclosures for a variety of enclosure surface radiative properties and for different opacities.

Formulation

Two-dimensional heat transfer in a rectangular enclosure where the intervening medium may absorb and emit radiation is considered. The medium: (*i*) is assumed to have a refractive index of unity, (*ii*) is assumed to be gray and to have uniform temperature independent properties and (*iii*) may have internal energy generation. Also, the medium is assumed to be in local thermodynamic equilibrium and, further, to be in a steady-state condition.

The rectangular enclosure is assumed to be infinite in the x_2-coordinate direction. The surfaces are isothermal and may diffusely emit radiative energy. The walls may be specular and/or diffuse reflectors, though the specular reflectivity is uniform for all incidence angles. For situations where adjacent walls have different emissive powers, the corner values will be assumed to be the arithmetic average of the two wall emissive powers. Figure 1 presents the geometry and gives the nondimensional coordinate axes and emissive power boundary conditions. The surface emissive powers are nondimensionalized by the emissive power of surface one, which is assumed to be the highest surface temperature in the enclosure. All other variables are defined in the nomenclature.

The medium emissive power and intensity are functions of

---

[1] This work performed at Sandia National Laboratories supported by the U.S. Department of Energy under contract number DE-AC04-76DP00789.

Contributed by the Heat Transfer Division for publication in the JOURNAL OF HEAT TRANSFER. Manuscript received by the Heat Transfer Division June 21, 1982.

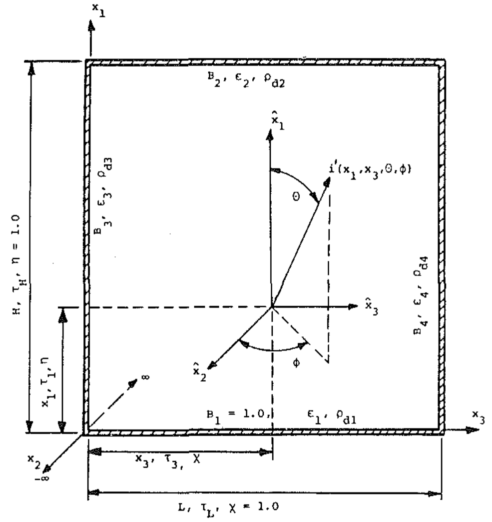

Fig. 1 Schematic of the rectangular geometry considered in the analysis

the x_1 and x_3 positions in the rectangular enclosure. The intensity distribution is also dependent on the elevation and azimuthal angles. Radiative transfer in the x_2-coordinate direction is assumed zero. In addition, it is assumed that the convective and conductive energy exchange mechanisms are unimportant and can be neglected in this analysis. The governing energy conservation relation thus reduces to

$$\frac{\partial Q_{R1}}{\partial \tau_1} + \frac{\partial Q_{R3}}{\partial \tau_3} = \frac{S}{\tau_H} \tag{1}$$

where Q_{ri} is the radiative heat transfer nondimensionalized by the emissive power of wall one. The radiative transfer is obtained by integration of the radiative intensity (multiplied by the direction cosine) over 4π steradian solid angle.

$$Q_{Ri}(\tau_1, \tau_3) = \int_{\omega = 4\pi} \hat{l}_i I'(\tau_1, \tau_3, \omega) d\omega \tag{2}$$

where

$$d\omega = \sin\theta \, d\theta \, d\phi$$

The nondimensional radiative intensity is obtained from the equation of radiative transfer, equation (3), given for an absorbing and emitting medium.

$$\hat{l}_1 \frac{\partial I'}{\partial \tau_1} + \hat{l}_3 \frac{\partial I'}{\partial \tau_3} + I' = \frac{B}{\pi} \tag{3}$$

To simplify the analysis associated with solution of coupled equations (1) and (3), the intensity distribution is represented by a series of spherical harmonics given by equation (4) [12]

$$I'(\bar{r}, \omega) = \sum_{l=0}^{\infty} \sum_{m=-l}^{l} A_l^m(\bar{r}) Y_l^m(\omega) \tag{4}$$

where $A_l^m(\bar{r})$ are position dependent coefficients and $Y_l^m(\omega)$ are normalized spherical harmonics given by equation (5)

$$Y_l^m(\omega) = \left[\frac{2l+1}{4\pi} \frac{(l-m)!}{(l+m)!} \right]^{1/2} e^{jm\phi} P_l^m(\cos\theta) \tag{5}$$

The above relation is an exact representation for the intensity distribution in the limit as l approaches infinity. The approximation occurs when the series is truncated; for these studies the first two odd spherical harmonics approximations are considered by assuming that

$$A_l^m(\bar{r}) = 0 \tag{6}$$

for $l > 1$ (P-1) and for $l > 3$ (P-3).

The intensity expression is recast in terms of the nondimensional moments of intensity (defined by equations (7)), by substituting equation (4) into equations (7), performing appropriate integrations, and

Zeroth Moment

$$I_0(\bar{r}) = \int_{\omega = 4\pi} I'(\bar{r}, \omega) d\omega \tag{7a}$$

*N*th Moment

$$I_{ij\ldots k}(\bar{r}) = \int_{\omega = 4\pi} \hat{l}_i \hat{l}_j \ldots \hat{l}_k I'(\bar{r}, \omega) d\omega$$

$$(i, j \ldots k = 1, 2, 3) \tag{7b}$$

then algebraically solving for the unknown coefficients $A_l^m(\bar{r})$

Nomenclature

a_m = absorption coefficient
A_l^m = position dependent coefficients
B = nondimensional medium emissive power = e_b/e_{b1}
B_i = nondimensional emissive power of wall $i = e_{bi}/e_{b1}$
e_{bi} = blackbody emissive power of wall i
E_i = surface radiative property factor = $(1 - \epsilon_i)/\epsilon_i$
H = height of rectangular enclosure
i' = radiative intensity distribution
I' = nondimensional radiative intensity distribution = i'/e_{b1}
I_w' = nondimensional intensity leaving enclosure surface
I_0 = nondimensional zeroth moment of intensity
I_i = nondimensional first moment of intensity ($i = 1$-3)
I_{ij} = nondimensional second moment of intensity ($i,j = 1$-3)
I_{ijk} = nondimensional third moment of intensity ($i,j,k = 1$-3)
$\hat{l}_i$ = direction cosine; $\hat{l}_1 = \cos\theta$ and $\hat{l}_3 = \sin\theta \sin\phi$
L = width of rectangular enclosure
Q''' = uniform volumetric source
$q_{i,1}$ = radiative energy incident on surface one
Q_{Ri} = nondimensional ith direction radiative heat transfer rate ($i = 1,3$)
r = aspect ratio = L/H
$\bar{r}$ = vector position in medium
R_i = surface radiative property factor = ρ_{di}/ϵ_i
S = nondimensional volumetric source = $Q''' H/e_{b1}$
x_i = position coordinate i ($i = 1$-3)
Y_l^m = normalized spherical harmonic; equation (5)

Greek Symbols

δ_{ij} = Kronecker delta
ϵ_i = diffuse emissivity of wall i
η = normalized position in x_1 coordinate direction = x_1/H
θ = elevation angle ($0 \leq \theta \leq \pi$)
ρ_i = total reflectivity of wall $i = \rho_{di} + \rho_{si}$
ρ_{di} = diffuse reflectivity of wall i
ρ_{si} = specular reflectivity of wall i
τ_i = nondimensional optical position in coordinate direction $i = ax_i$ ($i = 1$-3)
τ_H = optical depth in x_1-direction
τ_L = optical depth in x_3-direction
ϕ = azimuthal angle ($0 \leq \phi \leq 2\pi$)
χ = normalized position in x_3-coordinate direction = x_3/L
ω, ω^* = solid angle
ω_i = surface radiative property factor = $2(1 - 2E_i)/3$

in terms of the moments [8, 9, 13]. The switch from coefficients A_l^m to moments of intensity is made because the first three types of moments have physical significance. The zeroth order moment, I_0, is proportional to the radiation energy density and the first moments, I_i, are the radiative fluxes in the i-coordinate direction. The second moments, I_{ij}, divided by the speed of light comprise the radiation stress and pressure tensor, analogous to the stress tensor in fluid dynamics. The higher order moments have no specific physical significance and are generated by analogy with the first three.

For the two-dimensional geometry considered, symmetry with respect to the x_2-coordinate simplifies the P-3 approximation intensity distribution and the following conditions for moments with "2" subscripts hold [14].

$$I_2 = I_{2ij} = I_{222} = 0 \qquad (i,j=1,3) \tag{8a}$$

$$I_{2j} = \delta_{2j}(I_0 - I_1 - I_3) \tag{8b}$$

$$I_{i22} = I_i - I_{iii} - I_{ijj} \qquad (i,j=1,3 \text{ and } i \neq j) \tag{8c}$$

The P-3 approximation for the intensity distribution is thus reduced to equation (9) [14]. The P-1 approximation for the intensity is given by the first three terms of equation (9).

$$\begin{aligned} I'(\tau_1,\tau_3,\theta,\phi) = \frac{1}{4\pi}\Big[& I_0 + 3I_1\cos\theta + 3I_3\sin\theta\sin\phi + \frac{5}{4}(3I_{11} \\ & - I_0)(3\cos^2\theta - 1) + 15I_{13}\sin\phi\cos\theta\sin\theta \\ & + \frac{15}{4}(I_0 - I_{11} - 2I_{33})\cos 2\phi\sin^2\theta \\ & + \frac{7}{4}(5I_{111} - 3I_1)(5\cos^3\theta - 3\cos\theta) \\ & + \frac{21}{8}(5I_{311} - I_3)\sin\phi\sin\theta(5\cos^2\theta - 1) \\ & + \frac{105}{4}(I_1 - I_{111} - 2I_{133})\cos 2\phi\cos\theta\sin^2\theta \\ & + \frac{35}{8}(3I_3 - 4I_{333} - 3I_{311})\sin 3\phi\sin^3\theta \Big] \end{aligned} \tag{9}$$

The equation of transfer is transformed into a series of partial differential equations in terms of the moments by multiplying equation (3) by appropriate direction cosines and integrating over 4π solid angle. Equations (10) are obtained for the P-3 approximation following application of the "closure" constraints [15] and use of the x_2-coordinate symmetry conditions. The closure conditions yield expressions for the $N+1$ order moments of the P-N approximation in terms of lower order moments of intensity. Details on the simplification process to obtain equations (10) are included in [14].

$$\frac{\partial I_1}{\partial \tau_1} + \frac{\partial I_3}{\partial \tau_3} = 4B - I_0 \tag{10a}$$

$$\frac{\partial I_{11}}{\partial \tau_1} + \frac{\partial I_{13}}{\partial \tau_3} = -I_1 \tag{10b}$$

$$\frac{\partial I_{13}}{\partial \tau_1} + \frac{\partial I_{33}}{\partial \tau_3} = -I_3 \tag{10c}$$

$$\frac{\partial I_{111}}{\partial \tau_1} + \frac{\partial I_{113}}{\partial \tau_3} = -I_{11} + \frac{4}{3}B \tag{10d}$$

$$\frac{\partial I_{113}}{\partial \tau_1} + \frac{\partial I_{133}}{\partial \tau_3} = -I_{13} \tag{10e}$$

$$\frac{\partial I_{133}}{\partial \tau_1} + \frac{\partial I_{333}}{\partial \tau_3} = -I_{33} + \frac{4}{3}B \tag{10f}$$

$$\frac{6}{7}\frac{\partial I_{11}}{\partial \tau_1} - \frac{3}{35}\frac{\partial I_0}{\partial \tau_1} + \frac{3}{7}\frac{\partial I_{13}}{\partial \tau_3} = -I_{111} \tag{10g}$$

$$\frac{3}{7}\frac{\partial I_{13}}{\partial \tau_1} + \frac{6}{7}\frac{\partial I_{33}}{\partial \tau_3} - \frac{3}{35}\frac{\partial I_0}{\partial \tau_3} = -I_{333} \tag{10h}$$

$$4\frac{\partial I_0}{\partial \tau_1} - 5\frac{\partial I_{33}}{\partial \tau_1} + 5\frac{\partial I_{13}}{\partial \tau_3} = -35(I_1 - I_{111} - I_{133}) \tag{10i}$$

$$5\frac{\partial I_{13}}{\partial \tau_1} + 4\frac{\partial I_0}{\partial \tau_3} - 5\frac{\partial I_{11}}{\partial \tau_3} = -35(I_3 - I_{333} - I_{113}) \tag{10j}$$

The moment of intensity partial differential equations for the P-1 approximation are given by equations (10a-c) with the closure constraint for I_{ij} given by equation (11), where δ_{ij} is the Kronecker delta.

$$I_{ij} = \frac{1}{3}\delta_{ij}I_0 \tag{11}$$

The left-hand side of the energy conservation relation, written in terms of moments of intensity since Q_{ri} is equivalent I_i, is the same as equation (10a). Thus, the nondimensional emissive power, B, is related to the volumetric generation and zeroth moment of intensity by equation (12).

$$B(\tau_1,\tau_3) = \frac{1}{4}\left(\frac{S}{\tau_H} + I_0\right) \tag{12}$$

Solutions for the medium emissive power and for the heat transfer rates I_1 and I_3 are obtained from equations (12) and (10b) and (10c), respectively, following solution of the coupled moment of intensity partial differential equations subject to appropriate boundary conditions. The exact boundary conditions for diffusely and specularly reflecting surfaces are obtained by considering the intensity leaving the surface in some direction ω, given by equation (13)

$$I_w'(\bar{r},\omega) = f_w(\bar{r},\omega) \tag{13}$$

where

$$f_w(\bar{r},\omega) = \epsilon_i\frac{B_i}{\pi} + \rho_{si}I_w'(\bar{r},\omega^*) + \frac{\rho_{di}}{\pi}\int_{\omega^*=2\pi} I_w'(\bar{r},\omega^*)\hat{l}_j d\omega^* \tag{14}$$

and ω^* is the incident intensity direction. The diffusely reflected incident intensity is integrated over the 2π solid angle associated with incoming intensity over the hemisphere above the surface. The direction cosine multiplier in the integrand is associated with a unit vector normal to the bounding surface.

Substitution of a P-N intensity distribution into equation (13) does not result in usable boundary conditions, since the angular dependence remains in the expression. If the general Marshak conditions are applied, this angular dependency is eliminated. The exact boundary conditions are satisfied in an integral sense by utilizing the general Marshak conditions as shown in equation (15) for the P-1 ($l=1$) and P-3 ($l=1,3$) approximations [16, 17].

$$\int_{\omega=2\pi} I_w'(\bar{r},\omega)Y_l^m(\omega)d\omega = \int_{\omega=2\pi} f_w Y_l^m(\omega)d\omega \qquad (l=1,3) \tag{15}$$

The integrations are performed for the hemisphere of solid angles over the boundary surface. The normalized spherical harmonics may be posed in terms of direction cosines and in combinations of direction cosines multiplied together. Equation (16a) is valid for the P-1 approximation, while equations (16a) and (16b) hold for the P-3 approximation.

$$Y_1^m(\cos\theta) \propto \hat{l}_i \quad (i=1,3) \tag{16a}$$

$$Y_3^m(\cos\theta) \propto \hat{l}_i\hat{l}_j\hat{l}_k \quad (i,j,k=1,3) \tag{16b}$$

***P*-1 Formulation.** The *P*-1 moment partial differential equations are combined to yield equation (17) given in terms of normalized coordinates, χ and η.

$$\frac{\partial^2 I_0}{\partial\chi^2} + r^2\frac{\partial^2 I_0}{\partial\eta^2} = -3\tau_L rS \tag{17}$$

The appropriate boundary conditions are obtained by substituting $\hat{l}_1$ into equation (13) for the top and bottom surfaces and by substituting $\hat{l}_3$ for the side walls.

$$I_0(\chi,0) = \omega_1 r\frac{\partial I_0}{\partial\eta}\bigg|_{0,\chi} + 4B_1 \tag{18a}$$

$$I_0(\chi,1) = -\omega_2 r\frac{\partial I_0}{\partial\eta}\bigg|_{1,\chi} + 4B_2 \tag{18b}$$

$$I_0(0,\eta) = \omega_3\frac{\partial I_0}{\partial\chi}\bigg|_{0,\eta} + 4B_3 \tag{18c}$$

$$I_0(1,\eta) = -\omega_4\frac{\partial I_0}{\partial\chi}\bigg|_{1,\eta} + 4B_4 \tag{18d}$$

The *P*-1 approximation governing equation and boundary conditions are equivalent to the two-dimensional optically thick diffusion relations developed by Modest [11]. This is not surprising since the one-dimensional diffusion formulation was also equivalent to the *P*-1 formulation [2]. Closed form infinite series solutions for I_0 may be obtained using separation of variables techniques described in [18]. These results have been previously given by Modest [11] and are omitted from this presentation. Heat transfer results for the *P*-1 approximation are obtained directly from the I_0 results since equations (19) and (20) hold for I_1 and I_3 respectively.

$$I_1(\chi,\eta) = -\frac{1}{3}\frac{\partial I_0}{\partial\eta} \tag{19}$$

$$I_3(\chi,\eta) = -\frac{1}{3}\frac{\partial I_0}{\partial\chi} \tag{20}$$

***P*-3 Formulation.** The ten moment partial differential equations are combined algebraically to yield four second-order partial differential equations in terms of I_0, I_{11}, I_{33} and I_{13} given in equations (21) through (24) [14].

$$\frac{\partial^2 I_0}{\partial\chi^2} + 3r^2\frac{\partial^2 I_0}{\partial\eta^2} - \frac{35}{3}\tau_L^2 I_0 - 5\left[5r^2\frac{\partial^2 I_{11}}{\partial\eta^2} + \frac{\partial^2 I_{11}}{\partial\chi^2} + 4r\frac{\partial^2 I_{13}}{\partial\chi\partial\eta}\right] + 35\tau_L^2 I_{11} - \frac{20}{3}\tau_L^2(4B - I_0) = 0 \tag{21}$$

$$\frac{\partial^2 I_{11}}{\partial\chi^2} + 6r^2\frac{\partial^2 I_{11}}{\partial\eta^2} - 7\tau_L^2 I_{11} + \frac{\partial^2 I_{33}}{\partial\chi^2} + 6r\frac{\partial^2 I_{13}}{\partial\chi\partial\eta} + \frac{7}{3}\tau_L^2 I_0 - \frac{1}{5}\left[3r^2\frac{\partial^2 I_0}{\partial\eta^2} + \frac{\partial^2 I_0}{\partial\chi^2}\right] + \frac{7}{3}\tau_L^2(4B - I_0) = 0 \tag{22}$$

$$6\frac{\partial^2 I_{33}}{\partial\chi^2} + r^2\frac{\partial^2 I_{33}}{\partial\eta^2} - 7\tau_L^2 I_{33} + r^2\frac{\partial^2 I_{11}}{\partial\eta^2} + 6r\frac{\partial^2 I_{13}}{\partial\chi\partial\eta} + \frac{7}{3}\tau_L^2 I_0 - \frac{1}{5}\left[3\frac{\partial^2 I_0}{\partial\chi^2} + r^2\frac{\partial^2 I_0}{\partial\eta^2}\right] + \frac{7}{3}\tau_L^2(4B - I_0) = 0 \tag{23}$$

$$\frac{\partial^2 I_{13}}{\partial\chi^2} + r^2\frac{\partial^2 I_{13}}{\partial\eta^2} - \frac{7}{3}\tau_L^2 I_{13} + \frac{2r}{3}\frac{\partial^2}{\partial\chi\partial\eta}\left[I_{11} + I_{33} - \frac{1}{5}I_0\right] = 0 \tag{24}$$

The 16 necessary boundary conditions are obtained by substituting appropriate combinations of the direction cosines found in Table 1 into equation (15), incorporating the simplifications summarized previously in equations (16). The resulting boundary conditions are summarized in [14].

The solution of the coupled *P*-3 differential equations is accomplished numerically and the emissive power for the medium is obtained from the zeroth moment of intensity using equation (12). The radiative heat transfer in the x_1- and x_3-directions are functions of I_{11} and I_{13} (equation (10*b*)) and I_{33} and I_{13} (equation (10*c*)), respectively, and are computed using second-order accurate finite difference expressions.

Solution Method and Comparative Results

Radiative transfer results for the *P*-3 approximation were obtained by a numerical finite difference solution of the coupled equations. In the *P*-1 approximation studies, the infinite series solutions were truncated after 20 terms to assure four decimal place accuracy. All results to be shown were computed on the Cyber 170/750 computer system at the University of Texas at Austin.

The coupled equations of the *P*-3 approximation were solved using elliptic equation successive-overrelaxation (SOR) techniques described by Ames [19]. The SOR method includes a relaxation parameter which optimizes the iterative solution procedure by decreasing the number of computation passes to obtain convergence. The four elliptic equations were solved independently, with only one of the moments of intensity being unknown during each SOR computation. After a computational "pass" was completed through each of the SOR subprograms, the previous results were compared with the newly computed results before the results were updated. If the relative errors between iterations were less than the

Table 1 Direction cosine factors for the *P*-3 approximation boundary conditions

Nondimensional moment of intensity	Direction cosine factor Surface designation One (bottom)	Two (top)	Three (left)	Four (right)
I_0	$\hat{l}_1\hat{l}_1\hat{l}_1$	$\hat{l}_1\hat{l}_1\hat{l}_1$	$\hat{l}_3\hat{l}_3\hat{l}_3$	$\hat{l}_3\hat{l}_3\hat{l}_3$
I_{11}	$\hat{l}_1$	$\hat{l}_1$	$\hat{l}_1\hat{l}_3\hat{l}_3$	$\hat{l}_1\hat{l}_3\hat{l}_3$
I_{33}	$\hat{l}_3\hat{l}_1\hat{l}_1$	$\hat{l}_3\hat{l}_1\hat{l}_1$	$\hat{l}_3$	$\hat{l}_3$
I_{13}	$\hat{l}_1\hat{l}_1\hat{l}_3$	$\hat{l}_1\hat{l}_1\hat{l}_3$	$\hat{l}_3\hat{l}_3\hat{l}_1$	$\hat{l}_3\hat{l}_3\hat{l}_1$

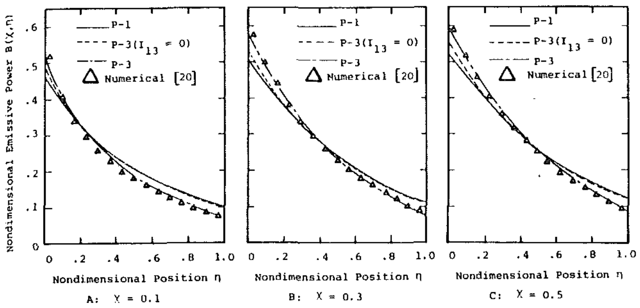

A: χ = 0.1 B: χ = 0.3 C: χ = 0.5

Fig. 2 Comparative *P-N* approximation results for the nondimensional emissive power in a square enclosure: $\tau_H = 1.0$, $r = 1.0$, $B_1 = 1.0$, $B_i = 0$ ($i = 2, 3, 4$), $\epsilon_i = 1.0$ ($i = 1\text{-}4$), $S = 0$

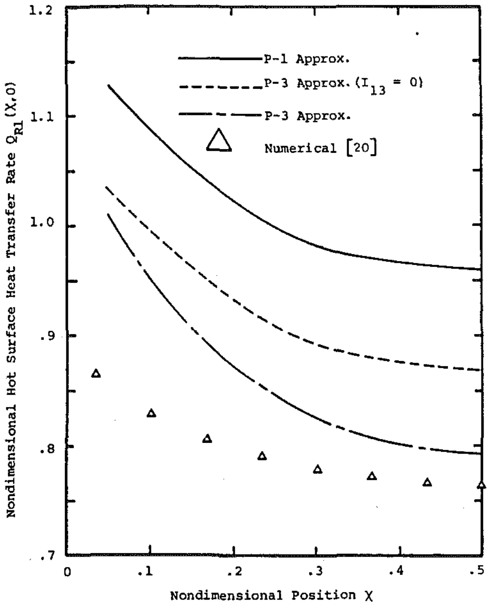

Fig. 3 Comparative *P-N* approximation results for the nondimensional hot surface heat transfer rates in a square enclosure: $\tau_H = 1.0$, $r = 1.0$, $B_1 = 1.0$, $B_i = 0$ ($i = 2, 3, 4$), $\epsilon_i = 1.0$ ($i = 1\text{-}4$), $S = 0$

prescribed maximum error criteria for all SOR computations, the solution was assumed to have converged, and the heat transfer results could be computed.

The derivative terms of the governing equations and boundary conditions were expressed in terms of second-order accurate finite difference equations. Corner values for the moments were computed assuming that the surface boundary formulations could be incorporated. Results obtained for I_0 and I_{13} for the two adjacent surfaces were "weight averaged" by the lengths of the two wall increments. Corner values for I_{11} were obtained using the top and bottom I_{11} surface boundary conditions, while I_{33} corner values were computed using the side wall boundary formulations for I_{33}.

Typical finite difference computation times for rectangular geometries with aspect ratios less than three ranged between 50 and 250 s. For aspect ratios of five, computation times approached 500 s. Solution convergence times decreased if *P*-1 results or related *P*-3 results were provided to initialize the unknown moments of intensity.

The *P-N* approximation results were compared with results obtained by Modest [11] and with numerical Hottel zone results provided by Larsen [20]. The former work incorporates the diffusion solution and improves the results for moderately thick and optically thin media by introducing a number of geometrical parameters. The governing energy and emissive power equations with the included correction factors reduce to the exact solution for the optically thin and thick limits with good accuracy for all intermediate optical thicknesses.

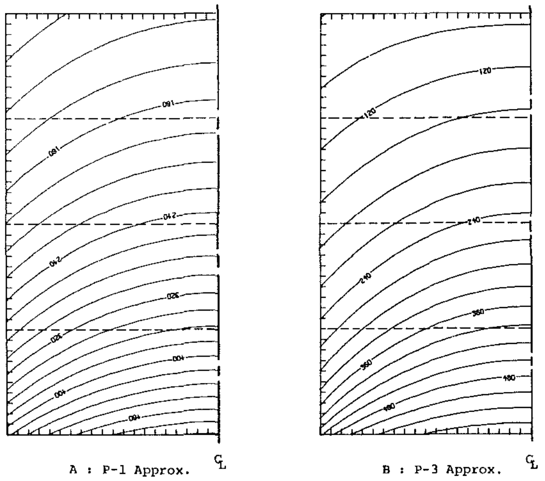

Fig. 4 Comparative *P-N* approximation results for the nondimensional emissive power distribution in a square enclosure: $\tau_H = 1.0$, $r = 1.0$, $B_1 = 1.0$, $B_i = 0$ ($i = 2, 3, 4$), $\epsilon_i = 1.0$ ($i = 1\text{-}4$), $S = 0$

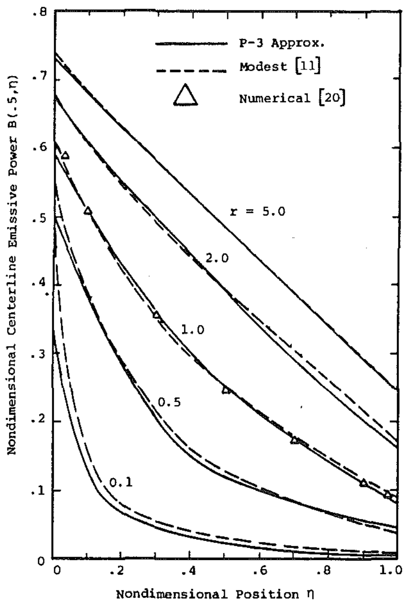

Fig. 5 Comparative nondimensional centerline emissive power distributions for different aspect ratios: $\tau_H = 1.0$, $B_1 = 1.0$, $B_i = 0$ ($i = 2, 3, 4$), $\epsilon_i = 1.0$ ($i = 1\text{-}4$), $S = 0$

The Hottel zone method is the most widely used numerical method for predicting two-dimensional emissive power and heat transfer results in rectangular enclosures. References [2] and [10] summarize the Hottel zone solution technique and should be consulted for further details. Note that 225 volume elements and 60 surface segments were used in this study to obtain the zonal results as was previously suggested by Modest [11].

Results

Blackbody Surfaces. The baseline geometry for the two-dimensional radiative transfer studies is the square enclosure with blackbody surfaces, where the optical thickness of the medium in each coordinate direction is unity. This geometry was chosen because the boundary conditions have an influence throughout the medium when the opacity is moderate. Surfaces two, three, and four have prescribed emissive powers

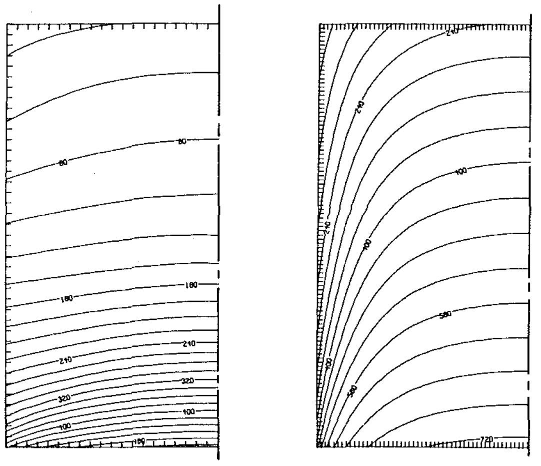

A : r = 0.5 B : r = 5.0

Fig. 6 P-3 approximation nondimensional emissive power distributions for different aspect ratios: $\tau_H = 1.0$, $B_1 = 1.0$, $B_i = 0$ ($i = 2, 3, 4$), $\epsilon_i = 1.0$ ($i = 1$-4), $S = 0$

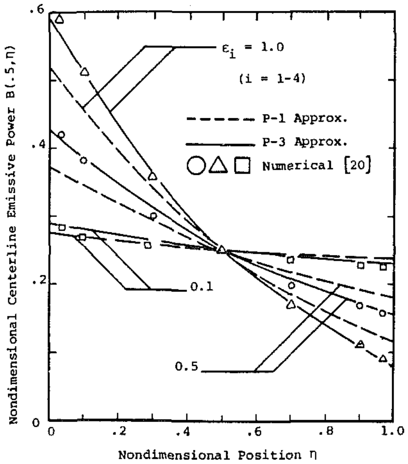

Fig. 7 Comparative nondimensional centerline emissive power distributions in a square enclosure when all walls have the same radiative properties: $\tau_H = 1.0$, $r = 1.0$, $B_1 = 1.0$, $B_i = 0$ ($i = 2, 3, 4$), $\rho_{si} = 0$ ($i = 1$-4), $S = 0$

of zero, and the emissive power of surface one is fixed at unity. The corner emissive power discontinuities have the greatest effect for the conditions defined, since the hot wall infinitesimally near the corner is emitting and absorbing and the cool side walls infinitesimally near the corner are only absorbing. For gray wall enclosures, the corner emissive power discontinuity is less critical because the cool surfaces can also reflect incident energy.

Figures 2, 3, and 4 show representative nondimensional emissive power distributions and heat transfer rates for the baseline case. Results for three differential approximations are compared in Figs. 2 and 3 with results obtained from the Hottel zonal method [20]. The first two approximation results are given for the P-1 and P-3 methods. The third differential result is a modified P-3 approximation which is obtained by solution of equations (21), (22), and (23) with I_{13} fixed at zero.

The P-3 approximation results match the zonal results for the three χ positions compared. The P-1 and modified P-3 results ($I_{13} = 0$) underestimate the emissive power near the hot surface and overestimate the emissive power near the cool (top) surface. The modified P-3 results are superior to the P-1 solution near the hot surface and are comparable to the P-1 solution for the interior region ($\eta \geq 0.2$) and near the top surface. Figure 4 shows isoemissive power distributions for

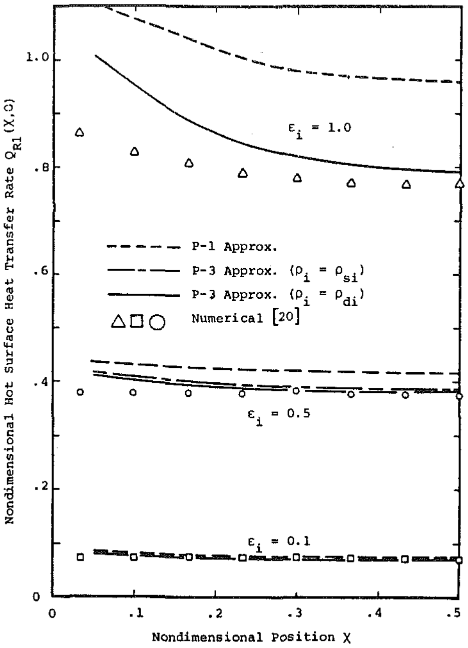

Fig. 8 Comparative nondimensional heat transfer rates for the hot surface of a square enclosure when all walls have the same radiative properties: $\tau_H = 1.0$, $r = 1.0$, $B_1 = 1.0$, $B_i = 0$ ($i = 2, 3, 4$), $\rho_i = \rho_{si}$ or ρ_{di} ($i = 1$-4), $S = 0$

the P-1 and P-3 approximations. Although the emissive power trends are similar, Fig. 2 has shown that the P-3 approximation results are more accurate.

The differential methods overestimate the hot surface heat transfer rates, as shown in Fig. 3, when compared with Hottel zone results. The error in heat transfer prediction increases near the corner where the discontinuity in emissive power occurs. The P-3 method results are superior to the P-1 and modified P-3 results, although near the corner, the nondimensional heat transfer is above one. This is physically impossible for the black wall case according to equation (29),

$$Q_{R1}(\chi,0) = 1 - \frac{q_{i,1}(\chi,\eta)}{e_{b1}} \qquad (25)$$

where $q_{i,1}$ is the radiative energy incident on wall one. The overestimation of heat transfer occurs because of numerical finite differencing inaccuracies in the heat transfer computation and because the largest inaccuracies in the moments of intensity occur near the surfaces. The latter fact is shown in Fig. 2 at the bounding surfaces and has been previously discussed in references [2] and [9]. Similar overestimations in heat transfer along the hot surface were encountered for varied aspect ratio geometries and also for square enclosures with different opacities [14], although the error decreased with increasing opacity. It is recommended, based on this work, that the P-3 surface heat transfer results only be used if the smallest optical depth is unity or greater. P-1 heat transfer results are inaccurate unless the medium is optically dense.

Centerline emissive power results from the Modest analysis are compared with the P-3 approximation method in Fig. 5 for different aspect ratio geometries. The centerline emissive power distributions for the two methods are comparable over the range of aspect ratios considered. The largest deviation occurs when the medium is optically thin in the x_3-coordinate direction. The agreement in centerline emissive power distributions improves as the opacity in the x_3-direction increases, and the two results are nearly identical to the one-dimensional radiative solution for $r = 5.0$. Additional P-3 emissive power results for aspect ratios of $r = 0.5$ and $r = 5.0$

Table 2 Nondimensional centerline emissive power distributions and hot surface heat transfer rates in a square enclosure when all walls have the same radiative properties: $\tau_H = 1.0, r = 1.0, B_1 = 1.0, B_i = 0\ (i = 2,3,4), S = 0$

Wall radiative properties			Nondimensinal centerline emissive power			Nondimensional Hot surface heat transfer centerline and (average)[a]		
Diffuse emissivity	Total reflectivity	Nondimensional position	P-1	P-3	P-3	P-1	P-3	P-3
ϵ_i	ρ_i	η		$\rho_i = \rho_{di}$	$\rho_i = \rho_{si}$		$\rho_i = \rho_{di}$	$\rho_i = \rho_{si}$
1.0	0.0	0.0	0.522	0.594	Same as for P-3 $\rho_{di} = \rho_i$	0.963 (1.013)	0.794 (.865)	Same as for P-3 $\rho_{di} = \rho_i$
		.1	.453	.510				
		.2	.392	.432				
		.4	.291	.301				
		.5	.250	.251				
		.6	.215	.208				
		.8	.159	.141				
		.9	.136	.112				
		1.0	.117	.082				
0.5	0.5	0.0	0.374	0.427	0.416	0.416 (0.424)	0.382 (0.386)	0.386 (0.390)
		.1	.344	.386	.377			
		.2	.317	.347	.340			
		.4	.270	.279	.276			
		.5	.250	.251	.250			
		.6	.232	.227	.227			
		.8	.203	.189	.190			
		.9	.192	.172	.174			
		1.0	.182	.157	.160			
0.1	0.9	0.0	0.274	0.290	0.282	0.075 (0.077)	0.075 (0.074)	0.075 (0.074)
		.1	.268	.281	.275			
		.2	.263	.273	.268			
		.4	.254	.259	.256			
		.5	.250	.252	.251			
		.6	.247	.247	.246			
		.8	.241	.238	.239			
		.9	.238	.234	.236			
		1.0	.236	.231	.233			

[a] Average nondimensional heat transfer results obtained from numerical integrations of surface heat transfer values

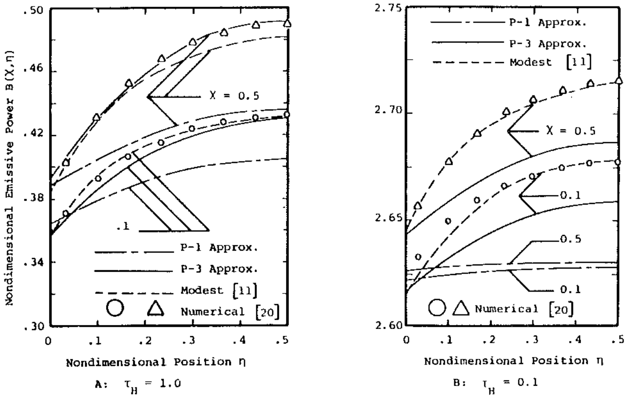

A: $\tau_H = 1.0$

B: $\tau_H = 0.1$

Fig. 9 Comparative nondimensional emissive power distributions for different optical thickness square enclosures with internal heat generation: $r = 1.0$, $B_i = 0$, $\epsilon_i = 1.0$ ($i = 1$-4), $S = 1.0$

are given in Fig. 6. The cool side walls significantly reduce the emissive powers in the interior of the medium for small aspect ratio geometries. For $r = 5.0$, the interior emissive powers are largely unaffected by the side walls and approach the one-dimensional radiative results.

Gray Surfaces. Figures 7 and 8 compare the Hottel zone and P-N differential method results for the centerline emissive power and hot surface heat transfer when the enclosure walls are all gray diffusely reflecting and diffusely emitting surfaces. A square enclosure with optical thickness $\tau_H = 1.0$ is used in these studies. The P-3 results for the centerline emissive power compare well with the Hottel numerical results. The P-1 results follow the same trends as reported for the black wall baseline case; i.e., they underestimate the emissive power near the hot surface and overestimate the emissive power near the cool (top) surface. It is interesting to note that as the wall emissivity decreases, the emissive power variation becomes less pronounced, and as the wall emissivities approach zero, the medium emissive power distribution approaches the optically thin limiting solution of $B(\chi,\eta) = 0.25$.

The differential results approach the Hottel zone results for hot surface heat transfer when the wall emissivities are reduced. The corner discontinuity effects, as seen in Fig. 8, are also reduced when the walls are gray, and the heat transfer distribution becomes nearly constant for $\epsilon_i \leq 0.5$ ($i = 1$-4). Although the P-3 method overestimates the heat transfer for $\epsilon_i > 0.5$, it is sufficiently accurate to be used instead of the Hottel method for predicting heat transfer in gray wall enclosures.

Table 2 assesses wall specularity effects on nondimensional centerline emissive power and on heat transfer from the hot surface. All wall emissivities are equal and the wall reflectivities are either entirely specular or diffuse. The P-1 results presented are for total surface reflectivities ρ_i since the boundary condition formulations do not differentiate between specularly and diffusely reflecting surfaces. Overall, the effect of specularity on the medium emissive power is limited. The medium emissive power is slightly higher near the hot surface if the walls are diffusely reflecting surfaces. This would be expected because the energy incident on the side walls from the hot wall is diffusely reflected and more of it will stay in directions near the hot wall than for the specular case. Near the top surface, the medium emissive power is increased if the walls are specular reflectors. The hot surface centerline and average heat transfer results are also nearly identical for the two types of surface reflectivity. The heat transfer is only slightly higher for the specular surfaces.

Internal Energy Generation. Uniform energy generation within a square enclosure comprised of black surfaces is considered for two values of optical thickness, $\tau_H = 0.1$ and $\tau_H = 1.0$. For an optical thickness of 5 or greater, the emissive power distributions are comparable to the two-dimensional diffusion solution, and are thus not presented. The square enclosure is studied because the results obtained for each quarter section of the medium are symmetric.

Figure 9 presents emissive power distributions (nondimensionalized by the internal generation rate) at $\chi = 0.1$ and $\chi = 0.5$ for the *P-N* approximation methods and for the Modest and Hottel zone methods. The *P*-1 results underestimate the emissive power for both optical thicknesses modeled. The inaccuracies in *P*-1 results grow with decreasing optical thickness, which would be expected since the *P*-1 solution and diffusion solution are identical. The *P*-3 approximation results are comparable to the Hottel zone results and Modest results for an optical thickness of unity. The *P*-3 results underestimate the emissive power for the optically thin medium, but follow the trends given by Modest and Hottel results. The *P*-3 results are definitely preferred over *P*-1 approximation results if $\tau_H < 1.0$ when internal energy generation is included.

Heat transfer results for the *P-N* methods along the enclosure surfaces follow similar trends. The *P*-1 approximation heat transfer results are nearly constant across the surface for optically thin media. The *P*-3 approximation results are more accurate than the *P*-1 results when compared with the Hottel or Modest results, although they typically underestimate the heat transfer near the corner and overestimate the heat transfer in the interior of the medium. For all cases considered, the integrated energy totals matched the total volumetric generation, thus maintaining conservation of energy.

Conclusions

The two-dimensional radiative heat transfer studies have shown that the *P*-3 differential approximation can accurately estimate the emissive power distributions for rectangular enclosures for a wide range of surface radiative properties and optical thicknesses. The *P*-3 method overestimates the hot surface heat transfer, especially near corners where emissive power discontinuities are present. The *P*-1 approximation method is less accurate than the *P*-3 method for all cases considered and should not be used unless the medium is optically thick. Specific observations on the *P*-3 approximation method are summarized below.

- The *P*-3 differential approximation yields accurate emissive power and heat transfer results for the radiative equilibrium case when the smallest optical thickness for the geometry is greater than 0.5. Above an optical thickness of unity, the emissive power results are comparable to the Hottel zonal method and Modest results. Though the heat transfer is overestimated, the magnitude of this error decreases with increasing opacity.
- *P*-3 heat transfer results for gray diffusely emitting surfaces and specularly or diffusely reflecting surfaces are improved over those obtained for blackbody enclosure surfaces because the corner discontinuity effects are reduced.
- The *P*-3 approximation yields accurate emissive power and heat transfer results when the medium has internal energy generation, so long as the opacity is moderate (τ_H and $\tau_L \geq 1.0$).

The overall conclusion obtained from these studies is that the *P*-3 differential approximation can be used with confidence to estimate emissive power distributions in moderate optical thickness rectangular geometries. This accomplishment is noteworthy, because radiative results for the moderate optical thickness range of unity to 5 cannot be obtained accurately using the diffusion approximation or economically using the Hottel zonal method. Moreover, changes in the surface radiative properties or inclusion of internal energy generation do not generally increase the *P*-3 method computation time. The major shortcoming of this differential method is that it overestimates the enclosure surface heat transfer characteristics. Note, however, that for "real world" situations where all surfaces would have nonzero temperatures and where there are no corner temperature discontinuities, the magnitude of this error should be reduced from the values shown here.

References

1 Kourganoff, V., *Basic Methods in Transport Problems*, Dover Publications, Inc., New York, 1963.

2 Siegel, R., and Howell, J. R., *Thermal Radiation Heat Transfer*, 2d ed., McGraw-Hill, New York, 1980.

3 Usiskin, C. M., and Sparrow, E. M., "Thermal Radiation Between Parallel Plates Separated by an Absorbing-Emitting Nonisothermal Gas," *International Journal of Heat and Mass Transfer*, Vol. 1, 1960, pp. 28-36.

4 Heaslet, M. A., and Warming, R. F., "Radiative Transport and Wall Temperature Slip in an Absorbing Planar Medium," *International Journal of Heat and Mass Transfer*, Vol. 8, No. 7, 1965, pp. 979-994.

5 Brieg, W. F., and Crosbie, A. L., "Two-Dimensional Radiative Equilibrium," *Journal of Mathematics Analysis and Applications*, Vol. 46, No. 1, 1974, pp. 104-125.

6 Greenspan, H., Kelber, C. N., and Okrent, D., ed., *Computing Methods in Reactor Physics*, Gordon & Breach Science Publishers, New York, 1968.

7 Krook, M., "On the Solutions of Equations of Transfer I," *The Astrophysical Journal*, Nov. 1955, pp. 488-497.

8 Cheng, P., "Two Dimensional Radiating Gas Flow by a Moment Method," *AIAA Journal*, Vol. 2, 1964, pp. 1662-1664.

9 Bayazitoǧlu, Y., and Higenyi, J., "Higher Order Differential Equations of Radiative Transfer: P_3 Approximation," *AIAA Journal*, Vol. 17, No. 4, 1979, pp. 424-431.

10 Hottel, H. C., and Cohen, E. S., "Radiant Heat Exchange in a Gas-Filled Enclosure: Allowance for Nonuniformity of Gas Temperature," *AIChE Journal*, Vol. 4, No. 1, 1958, pp. 3-14.

11 Modest, M. F., "Radiative Equilibrium in a Rectangular Enclosure Bounded by Gray Walls," *Journal of Quantitative Spectroscopy and Radiative Transfer*, Vol. 15, No. 6, 1975, pp. 445-461.

12 Jeans, J. H., "The Equations of Radiative Transfer of Energy," *Monthly Notices of Royal Astronomical Society*, Vol. 78, Nov. 1917, pp. 28-36.

13 Cheng, P., "Dynamics of a Radiating Gas With Application to Flow Over a Wavy Wall," *AIAA Journal*, Vol. 4, No. 2, 1966, pp. 238-245.

14 Ratzel, A. C., "P-N Differential Approximation for Solution of One- and Two-Dimensional Radiation and Conduction Energy Transfer in Gray Participating Media," Ph.D dissertation, University of Texas at Austin, Dec. 1981.

15 Traugott, S. C., "Radiative Heat Flux Potential for Non-Gray Gas," *AIAA Journal*, Vol. 4, 1966, pp. 541-542.

16 Marshak, R. E., "Note on the Spherical Harmonic Method as Applied to the Milne Problem for a Sphere," *Phys. Rev.*, Vol. 71, 1946, pp. 443-446.

17 Davison, B., *Neutron Transport Theory*, Clarendon Press, Oxford, 1958.

18 Arpaci, V. S., *Conduction Heat Transfer*, Addison-Wesley Publishing Co., Reading, Massachusetts, 1966.

19 Ames, W. F., *Numerical Methods for Partial Differential Equations*, Academic Press, New York, 1977.

20 Larsen, M., Hottel Zone Code, developed for Ph.D. research at the University of Texas at Austin, Aug. 1981.

Laminar Forced Convection Heat Transfer in Spherical Annuli

S. Ramadhyani
Assoc. Mem. ASME

M. M. Torbaty

K. N. Astill
Mem. ASME

Department of Mechanical Engineering,
Tufts University,
Medford, Mass. 02155

An analysis is presented of forced convection heat transfer in spherical annuli bounded by isothermal surfaces at different temperatures. Flow enters the annulus through a port in the outer sphere and exits through a diametrically opposite port. The conservation equations of mass, momentum, and energy are reduced to dimensionless form, and the governing parameters of the problem are identified. Solutions are obtained for several values of each of the governing parameters via a numerical finite-difference procedure. It is found that very complex flow patterns can prevail within the annulus, particularly at high Reynolds numbers. Details of the flow field are presented by means of velocity and pressure profile plots. The effect of the flow patterns on the heat transfer phenomena is discussed by examining temperature profiles and variations of the local Nusselt number along the spherical surfaces. In addition, the circumferential average Nusselt numbers at the two spherical surfaces are presented as functions of the governing parameters of the problem. These graphs of average Nusselt numbers constitute information that could be used in the design of spherical annulus heat transfer equipment.

1 Introduction

Forced convection heat transfer through spherical annuli bounded by concentric, isothermal spheres is a condition of interest to engineers on which relatively little information is available in the published literature. A practical instance in which such a flow condition occurs is when spherical containers are employed for the storage of cryogenic liquids. Since spheres offer the minimum heat transfer area for a given enclosed volume, spherical containers are ideal for this application. Heat transfer to the cryogenic fluid is minimized by surrounding the spherical container with a concentric jacket and pumping a cold, "guard-cooling" fluid through the annulus. Another interesting heat transfer situation involving the spherical annular geometry is the cooling problem associated with the temperature control of gyroscopes. This latter problem has motivated a few experimental and theoretical investigations recently [1, 2]. In addition to these two applications, spherical annulus flows are employed in the cooling of spherical fuel elements in homogeneous nuclear reactors [3].

An examination of the literature reveals only a modest amount of prior investigation of the topic. An analytical solution of the energy equation was obtained by Cobble [4] in order to furnish heat transfer predictions. The solution was based on an assumed distribution of the tangential velocity, an assumption that was later demonstrated to be invalid by Rundell et al. [5]. Bird et al. [6] presented a solution of the fluid flow problem by employing the linearized Navier-Stokes equations under the assumption of creeping flow. The complexity of the hydrodynamic problem has prohibited an analytical solution of the complete Navier-Stokes equations in this situation.

A few experimental investigations of fluid flow and heat transfer in concentric sphere annuli have been reported in the literature. Bozeman and Dalton [7] studied the fluid flow phenomena through flow visualization and demonstrated the complex flow patterns that occur in the annulus. Rundell et al. [5] measured the heat transfer rates from the inner sphere in an annulus comprising an isothermal inner and an adiabatic outer sphere. They obtained a correlation for the overall Stanton number for a range of Reynolds numbers and two radius ratios. A supplementary experimental investigation by Cox and Sahni [8] extended the range of the preceding work to lower Reynolds numbers. The sphere size combinations employed in these two studies resulted in radius ratios varying between 1.1 and 1.2. Recently, Newton [1] investigated the forced convection heat transfer between approximately isothermal spheres. The radius ratios studied ranged between 1.03 and 1.36, and the Reynolds number based on the inner sphere diameter varied between 4000 and 22,000. Correlating equations for the average Nusselt number at the inner sphere were presented.

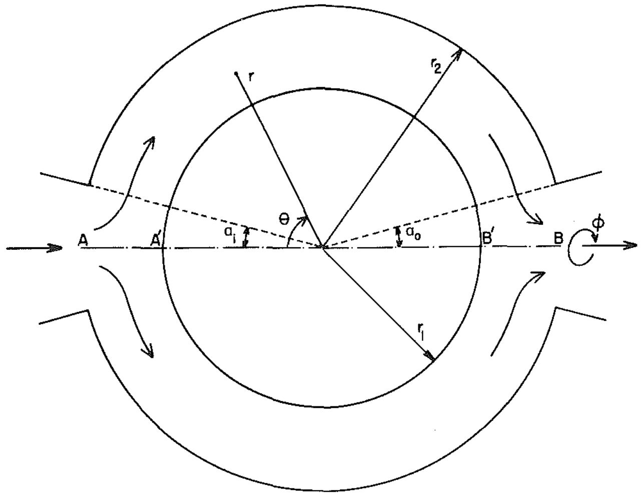

Fig. 1 Schematic depiction of the flow domain and the spherical coordinate system

The problem has also been studied numerically through finite difference calculations by Astill [2] and Tuft [3]. In Astill's computations, the governing differential equations were first simplified by deleting terms containing second derivatives in the circumferential flow direction. This simplification is part of the set of assumptions embodied in boundary layer approximations. The resulting parabolic partial differential equations were solved by performing a marching integration starting from an assumed tangential velocity distribution at the upstream boundary. These calculations provided detailed descriptions of the radial and

---

Contributed by the Heat Transfer Division for publication in the JOURNAL OF HEAT TRANSFER. Manuscript received by the Heat Transfer Division November 16, 1981.

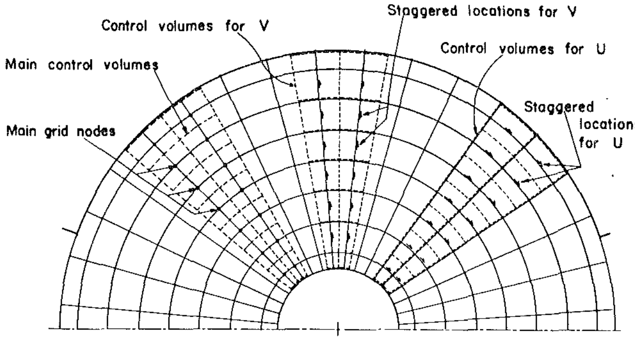

Fig. 2 Finite difference discretization of the computational domain

circumferential variations of the pertinent variables. The results are, however, limited to flow situations in which recirculation is absent. The finite difference computations of Tuft do not include the boundary layer approximations and are equally valid for flow situations with and without recirculation. However, the calculations performed in that work constitute a very limited exploration of the problem. The radius ratio was fixed at 1.2, and the effects of varying the radius ratio were not studied. Fluid properties were assumed to be those of water, and the influence of the Prandtl number was not examined. Additionally, the calculations were for a single inlet fluid temperature and a single inner sphere temperature. The thermal boundary conditions employed in that work (isothermal inner sphere, adiabatic outer sphere) are different from those employed in the present investigation.

The present study is motivated by a need for more detailed and complete information on the problem than is available from the prior work in this area. A knowledge of the values of the average Nusselt numbers at the two-sphere surfaces for various flow rates, radius ratios, etc. is important in the design of concentric-sphere heat exchange systems. This investigation is aimed at supplying such information. In addition, detailed information such as the circumferential distributions of heat transfer coefficients, and velocity and temperature distributions has also been obtained. In the present work, a study is made of the thermal and hydrodynamic phenomena occurring when a fluid is pumped into a spherical annulus through a port in the outer sphere, and flows out through a diametrically opposite port. The two spheres are assumed to be isothermal and at different temperatures. The exploration is confined to the case of pure forced convection in laminar flow. The authors recognize that at low Reynolds numbers, free convection effects might be strong enough to cause significant departures from pure forced convection. However, it was decided not to investigate the effects of buoyancy in the present work in view of the already large number of dimensionless parameters governing the problem. A study of the effects of buoyancy is a task of sufficient complexity to be reported in detail in a separate paper. Indeed, such an investigation has been completed at Tufts University and will constitute the subject of a forthcoming publication.

Since the highly complex flow field precludes an analytical solution, a finite difference solution scheme described by Patankar [9] has been adapted for this work. The large number of governing parameters makes an exhaustive study of the problem prohibitively expensive. Therefore, solutions have been obtained for judiciously selected ranges of each parameter. The results obtained from these computations include local and circumferential average Nusselt numbers, temperature, velocity, and pressure distributions, and variations of a power loss parameter that represents the pumping power required to maintain the flow.

2 Analysis and Solutions

2.1 The Governing Conservation Equations. Figure 1 is a schematic representation of the calculation domain showing the flow configuration and the spherical coordinate system employed in the solution of the problem. The domain is bounded by concentric spheres of radii, r_1 and r_2, and the flow is assumed to enter and leave the annulus through diametrically opposed circular ports, the apertures of which are denoted by α_i and α_o, respectively. It is assumed that the flow is radial and uniform over the inlet port and that it is laminar, azimuthally symmetric, incompressible, and steady, throughout the calculation domain. The figure schematically depicts the entering flow as being turned smoothly by the inner sphere and flowing in the circumferential direction as indicated by the arrows. In fact, the flow patterns that prevail in the annulus are much more complex than depicted in this figure.

The starting point of the analysis are the equations of conservation of mass, momentum, and energy, all expressed in spherical coordinates. Under the assumption of axisymmetry, all terms pertaining to the azimuthal variation of the dependent variables are omitted from the conservation equations. Additionally, all fluid properties are treated as constants, body forces (such as gravity) are assumed to be

Nomenclature

$\dot{E}_i, \dot{E}_o$ = mechanical energy fluxes at the inlet and outlet ports, equations (19), (20)
$\dot{E}_{\rm ref}$ = reference energy flux, (equation (21)
$\dot{E}_{\rm loss}$ = energy loss parameter, equation (22)
$h, \bar{h}$ = local and circumferential average heat transfer coefficients, equations (27), (24)
$\dot{m}$ = mass flow rate through the annulus
$\mathrm{Nu}_i, \mathrm{Nu}_o$ = local Nusselt numbers at inner and outer spherical surfaces, equation (28)
$\overline{\mathrm{Nu}}_i, \overline{\mathrm{Nu}}_o$ = circumferential average Nusselt numbers, equation (25), (26)
p = dimensional static pressure
P = dimensionless static pressure, equation (2)
Pr = Prandtl number
r_1, r_2 = radii of inner and outer spheres
R = dimensionless radius, equation (2)
R_o = radius ratio, r_2/r_1
Re = Reynolds number, equation (3)
T_1, T_2 = temperatures of inner and outer spheres
U = dimensionless tangential velocity
v_r, v_θ = dimensional velocities in radial and tangential directions
$\bar{v}$ = mean velocity in the equatorial plane, equation (1)
V = dimensionless radial velocity
V_i = ratio of inlet velocity to mean velocity, equation (14)
α_i, α_o = angular apertures of inlet and outlet ports
θ = tangential coordinate
Φ = dimensionless temperature, equation (2)
Φ_i = dimensionless temperature of the inflow

absent, and terms corresponding to viscous dissipation and flow work are not included in the energy equation.

To identify the governing parameters of the problem, the conservation equations are expressed in dimensionless form through the introduction of a reference velocity, $\bar{v}$, a reference length, r_1, and a reference temperature difference $(T_1 - T_2)$. $\bar{v}$ is defined as the average velocity at the equator ($\theta = 90$ deg) in the main flow direction.

$$\bar{v} = \dot{m}/[\rho\pi(r_2^2 - r_1^2)] \tag{1}$$

Dimensionless variables are then formed as follows

$$\begin{gathered} U = v_\theta/\bar{v}, V = v_r/\bar{v}, R = r/r_1 \\ P = p/\rho\bar{v}^2, \Phi = (T - T_2)/(T_1 - T_2) \end{gathered} \tag{2}$$

In addition, the following dimensionless groups, which will appear in the dimensionless form of the conservation equations, are defined

$$R_o = r_2/r_1, \mathrm{Re} = \rho\bar{v}(r_2 - r_1)/\mu, \mathrm{Pr} = \mu c_p/k \tag{3}$$

The choice of $(r_2 - r_1)$ as the characteristic length and $\bar{v}$ (the mean velocity at the maximum cross section) as the characteristic velocity must be borne in mind while examining the results to be presented later. Since the magnitudes of the Reynolds numbers at which computations were carried out will appear to be small, it may be noted that this is partly a result of the small magnitudes of $\bar{v}$ and $(r_2 - r_1)$. Other choices of characteristic length and velocity could result in appreciably larger Reynolds numbers for the same flow rate.

The dimensionless differential equations expressing conservation of mass, r and θ momentum, and of energy may then be written as

$$(1/R^2)\partial(R^2 V)/\partial R + (1/R\sin\theta)\partial(U\sin\theta)/\partial\theta = 0 \tag{4}$$

$$\begin{aligned} &V\partial V/\partial R + (U/R)\partial V/\partial\theta - U^2/R = -\partial P/\partial R \\ &+ [\nabla^2 V - 2V/R^2 - (2/R^2\sin\theta)\partial(U\sin\theta)/\partial\theta](R_o - 1)/\mathrm{Re} \end{aligned} \tag{5}$$

$$\begin{aligned} &V\partial U/\partial R + (U/R)\partial U/\partial\theta + UV/R = -(1/R)\partial P/\partial\theta \\ &+ [\nabla^2 U + (2/R^2)\partial V/\partial\theta - U/(R^2\sin^2\theta)](R_o - 1)/\mathrm{Re} \end{aligned} \tag{6}$$

$$V\partial\Phi/\partial R + (U/R)\partial\Phi/\partial\theta = \nabla^2\Phi(R_o - 1)/(\mathrm{Re\,Pr}) \tag{7}$$

Where ∇^2 is the two-dimensional Laplacian expressed in spherical coordinates as

$$\begin{aligned} \nabla^2 = &(1/R^2)\partial(R\partial/\partial R)/\partial R \\ &+ (1/R^2\sin\theta)\partial(\sin\theta\partial/\partial\theta)/\partial\theta \end{aligned} \tag{8}$$

The problem specification is completed by a description of the boundary conditions employed in the analysis. As noted previously, the situation is treated as being azimuthally symmetric; this implies that the derivatives of the temperature and the radial velocity with respect to θ are zero along the line segments AA′ and BB′ (see Fig. 1), and the tangential velocity itself vanishes there. Along the solid spherical surfaces, the conditions of no-slip and impenetrability apply. The two surfaces are isothermal and maintained at different temperatures. Over the inlet port, the fluid velocity is purely radial, and both the inlet temperature and the inlet velocity are uniform. The aforementioned conditions are all conventional and require no further discussion.

However, the appropriate boundary conditions to be applied at the outlet port is an issue that merits further amplification. It is evident that the conditions prevailing at the outlet port are strongly influenced by the flow situation upstream of the outlet port, and an *a priori* specification of the boundary conditions is not possible. On the other hand, since the fluid velocity at the outlet is expected to be predominantly in the outward radial direction, the influence of the downstream boundary values on the computed solution is expected to be minimal. Indeed, if the flow velocities are sufficiently large, the situation is completely dominated by the downstream convection of upstream values, and the outlet boundary values of U and Φ are likely to be extremely close to the values at neighboring upstream locations. The mathematical equivalent of this is to set the radial derivatives of U and Φ to zero at the outflow cross section. In the case of the radial component of velocity, this reasoning requires modification in view of the fact that the radial flow area increases with increasing radial distance. Mass conservation dictates a diminution of the radial velocity with increasing radius, and, hence, the condition of zero radial derivative would be inappropriate. However, any reasonable velocity distribution over the outlet port, that guaranteed global conservation of mass, would be acceptable. The validity of these assumptions will be discussed in section 3.1 in conjunction with the presentation of the results. Furthermore, since it is intimately linked to the finite difference computational scheme employed in the solution of the problem, the procedure adopted in specifying the radial outflow boundary velocity will be described in a subsequent section in which the finite difference solution procedure is discussed.

With the exception of the radial outflow velocity, the boundary conditions may be expressed in terms of the variables of the analysis as follows

$$\partial V/\partial\theta = U = \partial\Phi/\partial\theta = 0 \text{ along } \theta = 0, \theta = \pi \tag{9}$$

$$U = V = 0, \Phi = 1 \text{ at } R = 1 \tag{10}$$

$$U = V = \Phi = 0 \text{ at } R = R_o \text{ and } \alpha_i \leq \theta \leq \pi - \alpha_o \tag{11}$$

$$U = 0, V = V_i, \Phi = \Phi_i \text{ at } R = R_o \text{ and } 0 \leq \theta \leq \alpha_i \tag{12}$$

$$\partial U/\partial R = \partial\Phi/\partial R = 0 \text{ at } R = R_o \text{ and } \pi - \alpha_o \leq \theta \leq \pi \tag{13}$$

The quantity V_i appearing in equation (12) represents the ratio of the inlet velocity to the mean flow velocity. This ratio depends solely on the geometry, and it can be demonstrated that

$$V_i = (R_o^2 - 1)/[2R_o^2(1 - \cos\alpha_i)] \tag{14}$$

Examination of equations (4–13) reveals that the problem is influenced by a formidable array of parameters: Re, Pr, R_o, α_i, α_o, and Φ_i. In order to keep the computational effort to manageable proportions, the influence of the port apertures α_i and α_o was not studied in the present investigation; α_i and α_o were fixed at 0.2 radian. This represents ports of small aperture, and it is expected that decreasing α_i and α_o would have very little effect on the solution. Despite this reduction, only modest exploration of each of the remaining parameters was possible. Two Prandtl numbers, 5 and 0.7, and three radius ratios, 1.2, 1.5, and 2.0 were studied. The values 0, 1, and 0.5 were ascribed to Φ_i, and the Reynolds number was varied in steps from 1 to an upper limit that depended on the value of R_o.

2.2 The Finite Difference Solution Scheme. The differential equations (4) through (7) together with their associated boundary conditions comprise a system of coupled, nonlinear equations of sufficient complexity to preclude an analytical solution. The finite difference solution procedure adopted for this work has been described in considerable detail in [9], and in view of this, only a brief overview need be provided here.

The computational domain consists of a slice of the annulus that subtends an angle of one radian in the azimuthal direction. It is discretized by a set of intersecting, orthogonal control surfaces as depicted in Fig. 2. Also illustrated in Fig. 2 is the deployment of the main grid nodes at which Φ and P are computed and stored. The velocity components U and V are not, however, computed at the main grid nodes. Instead, they are computed at the "staggered" locations depicted in the figure. The use of staggered finite difference grids prevents the appearance of spurious, oscillatory solutions in the computed pressure fields. The propensity for such unphysical

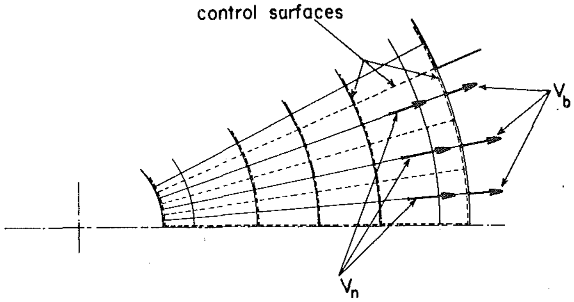

Fig. 3 Calculation of the radial velocity at the outflow boundary

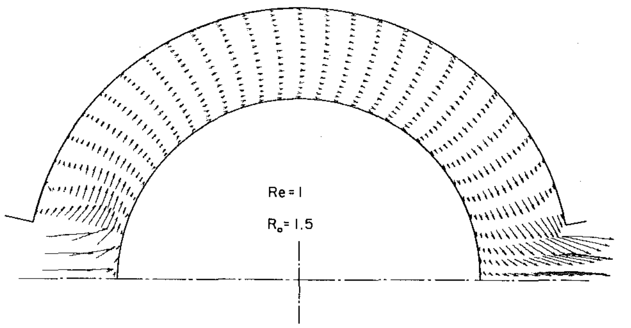

Fig. 4 Computed velocity vectors: Re = 1

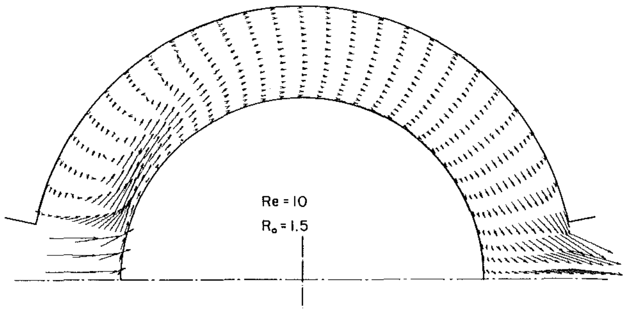

Fig. 5 Computed velocity vectors: Re = 10

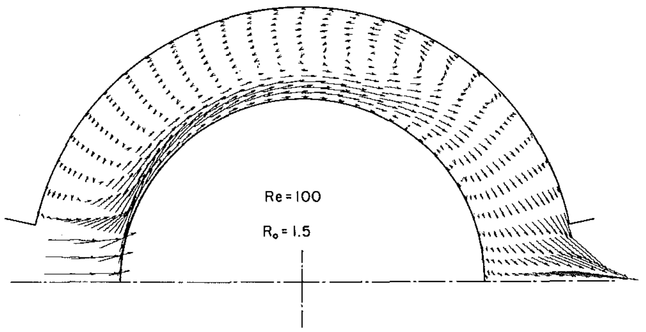

Fig. 6 Computed velocity vectors: Re = 100

solutions to manifest themselves when staggered grids are not used is well documented in the literature. As described in [9], the finite difference equations are obtained by integrating the differential equations over each of the control volumes and employing exponential profiles between nodes to approximate the integrands. Exponential profiles are chosen in preference to the simpler linear profiles (central difference approximation) in order to avoid physically unrealistic solutions at high flow rates. The choice of exponential profiles leads to the presence of computationally expensive exponential functions in the coefficients of the finite difference equations. Computational economy may, however, be preserved by approximating the exponential terms in the finite difference coefficients by simple power-law representations.

In the present problem, since the fluid flow is uninfluenced by the temperature field, it is possible, and economically desirable, to obtain the hydrodynamic solutions first and then employ them as inputs to the solution of the thermal problem. The finite difference equivalents of the hydrodynamic equations (4) through (6) were solved by employing the SIMPLER solution algorithm described in [9]. In the SIMPLER scheme, the solution process is started with guesses for the two velocity fields. Next, a finite difference analog of the Poisson equation for pressure is solved in order to extract a pressure field that is in conformity with the guessed velocity fields. The two momentum equations are then solved in sequence to obtain new velocity fields which may, however, not be in compliance with the continuity equation. Suitable corrections are then applied to the velocity fields in order to make them satisfy the continuity constraint. These corrections are calculated by the pressure correction procedure described in [9] (pp. 123–130). After these adjustments, the velocity fields exactly satsify continuity, but need not, in general, satisfy the momentum equations. Consequently, further iterations are initiated by returning to the Poisson equation for pressure, this time treating the updated velocities as initial guesses. Iterations are continued until the momentum and continuity equations are satisfied simultaneously to an acceptable level of accuracy.

The boundary condition that was applied to the radial momentum equation at the outlet port will now be described in greater detail. As mentioned earlier, the use of a zero radial derivative condition is precluded by considerations of mass conservation. A simple, but somewhat inaccurate, prescription would be to set the velocity over the outlet port as being uniform and equal to the inlet velocity. A more sophisticated prescription of the radial velocity distribution over the outlet port may be obtained as follows. It is reasonable to suppose that the velocities at the boundary nodes would be closely related to the velocities at their nearest inside neighboring nodes. Thus, with reference to Fig. 3, the radial velocity at the outflow boundary could be prescribed as

$$V_b = \gamma V_n \tag{15}$$

Where γ is a constant, yet to be determined. The subscripts b and n refer respectively to the boundary and the nearest inside neighboring locations. The constant γ is obtained by overall mass conservation. The total volumetric inflow rate at the inlet port and the volumetric outflow rate at the outlet port are, respectively, given by the expressions

$$\sum_{\text{inlet}} V_i \Delta A \text{ and } \sum_{\text{outlet}} V_b \Delta A \tag{16}$$

where ΔA represents the radial flow area of each control surface at the inlet or the outlet port, and the summations are carried out over the control surfaces spanning the ports. By continuity,

$$\sum_{\text{inlet}} V_i \Delta A = \sum_{\text{outlet}} V_b \Delta A = \sum_{\text{outlet}} \gamma V_n \Delta A \tag{17}$$

or,

$$\gamma = \Big(\sum_{\text{inlet}} V_i \Delta A \Big) \Big/ \Big(\sum_{\text{outlet}} V_n \Delta A \Big) \tag{18}$$

The determination of γ, of course, requires prior knowledge of V_n, but, since the solution is iterative, the values of V_n are chosen to be the ones from the previous iteration.

Initial computations were carried out at four different mesh sizes (21 × 11), (30 × 15), (35 × 18), and (35 × 24) in order to determine a grid distribution that would yield results of satisfactory accuracy. The numbers enclosed in parentheses denote the number of main grid points in the circumferential and the radial directions. For each grid size, one uniform and one nonuniform distribution was tried. In the case of the nonuniform distribution, the grid points were closely spaced near each spherical wall in order to fully resolve the details of the boundary layers. On the basis of these initial computations, a decision was made to employ a nonuniform 35×18 grid for all succeeding computations.

The convergence of the solutions, particularly at high Reynolds numbers, was found to be extremely slow. The reasons for slow convergence are the coupling of the momentum equations and the complex nature of the secondary flows at high Reynolds numbers. To overcome this difficulty, the initial guesses supplied to the computer program were chosen to be quite close to the final solution. This was done, for example, by supplying the converged solution for Re = 80 as the initial guess for Re = 100. For most computations it was found necessary to underrelax the momentum equations in order to obtain convergence. Despite these efforts to expedite the convergence of the iterations, central processor times of the order of 10 min were required when, for example, the converged solution at Re = 80 was employed to get a solution at Re = 100. Typically, about 100 iterations were required before an acceptable level of convergence was obtained. The computations were executed on a DEC-10 computer system.

3 Results and Discussions

Presentation and discussion of the results will be made in two parts. In the first section, the important features of the fluid flow patterns at the various radius ratios and Reynolds numbers will be highlighted. In the light of this discussion, in the subsequent section the thermal phenomena will be presented and discussed.

3.1 Fluid Flow. Figures 4 to 6 are depictions of the flow field in the form of velocity vectors drawn at chosen locations in the annulus. The magnitude of each vector corresponds to the magnitude of the dimensionless velocity at the foot of the vector. The radius ratio in all three figures is 1.5, and the Reynolds numbers vary from 1 to 100. The figures illustrate the considerable differences in the flow patterns at different Reynolds numbers. At Re = 1, the flow is mainly tangential throughout the annulus, and the velocity profiles resemble fully developed velocity profiles in pipe flow. There are no separated regions in the flow field. At Re = 10, the flow separates from the surface of the outer sphere at the edge of the inlet port and forms a toroidal recirculation region. It may also be observed that near the inlet region, the flow is deflected sharply by the inner sphere and tends to form a tangential jet. These features of the flow field may be expected to strongly influence the circumferential distributions of the heat fluxes at the two spherical surfaces. With further increase in Reynolds number, the toroidal separation bubble increases in extent and causes the main flow to be closely confined to the region adjacent to the inner sphere in the form of a wall jet. Far downstream, the jet separates from the inner sphere surface and a small recirculation bubble is formed. Similar phenomena occur at the other radius ratios as well. However, the point of separation of the wall jet on the inner sphere varies considerably with the radius ratio.

In all three figures, the acceleration of the flow in the vicinity of the outlet port is evident. Its direction may also be observed to be mainly radially outward.

In view of the fact that computations have been carried out at Reynolds numbers as low as Re = 1, the validity of specifying boundary conditions at the inlet and exit port cross sections needs to be justified. It may be felt that the inlet and exit boundary conditions need to be specified far upstream and downstream in the connecting inlet and exit pipes respectively, in order to avoid elliptic effects at the port cross sections. However, it must be borne in mind that the Reynolds number in this work is based on $\bar{v}$ (the mean velocity at the equatorial plane) as the characteristic velocity. Since the flow area in the equatorial plane is maximum, the mean flow velocity is minimum at this location. At the inlet and exit planes of the calculation domain, the flow velocities are much larger than $\bar{v}$. Thus, although computations are presented for low Reynolds numbers, the flow velocities at the inlet and exit apertures are large enough to make elliptic effects at these locations negligible; i.e., there is very little upstream propagation of the convected quantities. This has been confirmed by direct numerical experiments, which will not be described here in the interests of brevity.

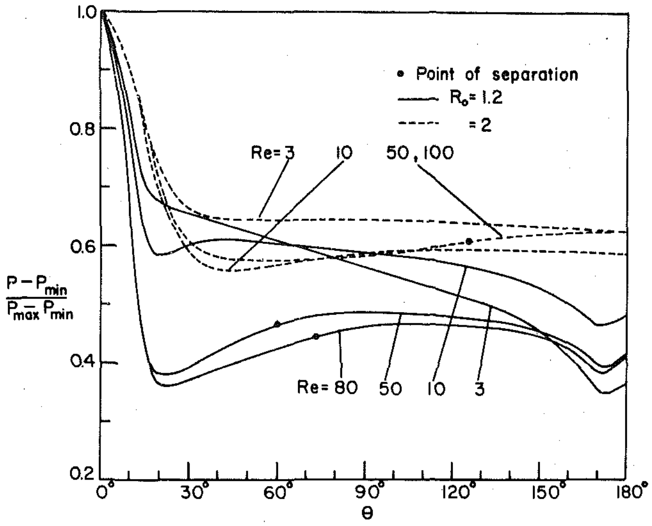

Fig. 7 Circumferential variation of pressure along the surface of the inner sphere

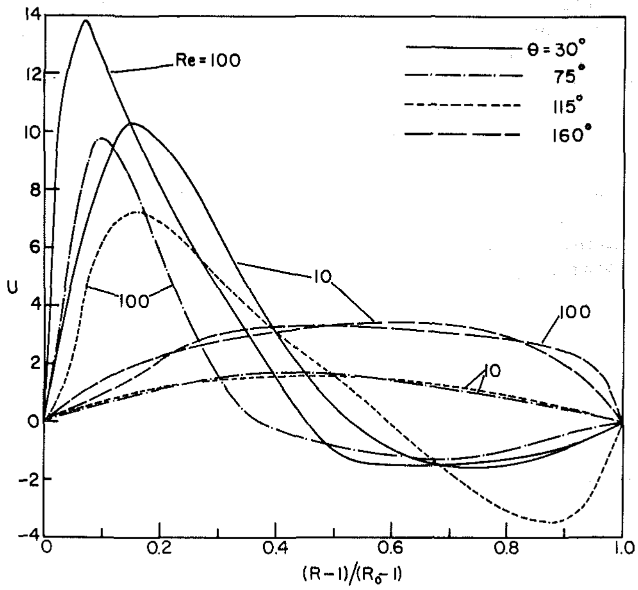

Fig. 8 Radial distribution of tangential velocity at several angular locations and Reynolds numbers: R_o = 1.5

Figure 7 depicts the circumferential variation of the nondimensional pressure along the surface of the inner sphere. Pressure distributions are shown for radius ratios of 1.2 and 2.0 and several Reynolds numbers. As may be expected, initially, the pressure drops sharply in the direction of increasing θ from the value at the forward stagnation point. Beyond the entrance region, two conflicting effects came into play. While skin friction tends to produce a steady diminution of pressure with angle, the increasing flow area tends to cause a pressure rise. The curves in Fig. 7 illustrate the various possible pressure distributions depending on the relative strengths of the two effects. In those cases in which an adverse pressure gradient exists over a portion of the circumference, the flow separates from the inner sphere at the angular locations depicted on the figure.

Further details of the flow field are presented in Fig. 8, which contains the radial distribution of the tangential velocity component at several angular locations and two Reynolds numbers. The curves are plotted for the case of $R_o = 1.5$, but similar distributions may be expected at the other two radius ratios as well. The very steep velocity gradients prevalent at high Reynolds numbers, near the inlet, are noteworthy, as are the regions of negative velocities near the outer sphere surface.

In discussions of the hydrodynamics of confined flows, it is conventional to present the friction factor, f, as a function of the geometric parameters and the Reynolds number. The friction factor is a measure of the pumping power associated with maintaining the flow in the confined passage. If the area of the flow passage is constant, and if the pressures over the inlet and outlet sections are uniform, the friction factor is conveniently defined in terms of the pressure drop between inlet and outlet. In the present problem, however, the pressure distribution over the inlet and outlet ports is nonuniform, and the friction factor cannot be defined in the conventional manner. Instead, the difference in the total mechanical energy fluxes at outlet and inlet is calculated. In terms of dimensional quantities, these energy fluxes are obtained from the following equations

$$\dot{E}_i = \int_{\text{inlet}} \left(\frac{p}{\rho} + \frac{v_r^2}{2} \right) d\dot{m} \tag{19}$$

$$\dot{E}_o = \int_{\text{outlet}} \left(\frac{p}{\rho} + \frac{v_r^2 + v_\theta^2}{2} \right) d\dot{m} \tag{20}$$

A reference energy flux $\dot{E}_{\text{ref}}$ is defined based on the inlet velocity

$$\dot{E}_{\text{ref}} = \int_{\text{inlet}} \frac{v_r^2}{2}\, d\dot{m} \tag{21}$$

The dimensionless rate of energy loss is then computed as follows

$$\dot{E}_{\text{loss}} = \frac{\dot{E}_i - \dot{E}_o}{\dot{E}_{\text{ref}}} \tag{22}$$

The variation of $\dot{E}_{\text{loss}}$ with Reynolds number for the three radius ratios investigated in this work is shown in Fig. 9. As may be observed, all three curves decrease with increasing Reynolds number and eventually level off. The asymptotic behavior of these curves is consistent with the expectation that at high Reynolds numbers, the energy loss per unit mass is proportional to the square of a characteristic velocity. As is well known, the "minor-losses" in pipe fittings and valves also vary in proportion to the square of the characteristic velocity.

3.2 Heat Transfer. Discussion of the thermal phenomena occurring in the spherical annulus will be commenced by examining the variation of the Nusselt numbers at the inner and outer spheres. The circumferential average Nusselt numbers at the two surfaces are defined by the equation

$$\overline{\text{Nu}} = \bar{h}(r_2 - r_1)/k \tag{23}$$

where $\bar{h}$ is the average heat transfer coefficient calculated as

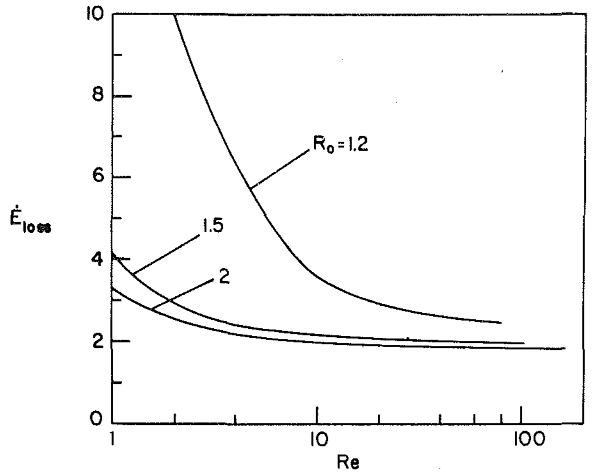

Fig. 9 Variation of the energy loss parameter with Reynolds number

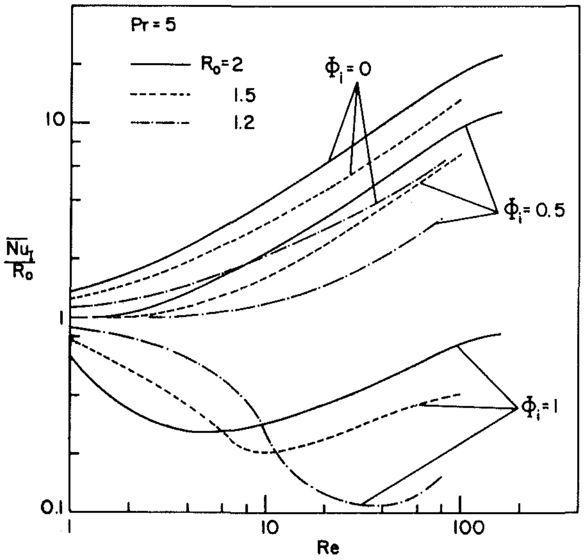

Fig. 10 Average Nusselt number at inner sphere: Pr = 5

$$\bar{h} = Q/A(T_2 - T_1) \tag{24}$$

Q is the total heat flux at the surface of either the inner or the outer sphere, and A is the corresponding surface area. By employing these equations and noting that the local heat flux per unit area is given by the expression $q = -k\, \partial T/\partial r$, the circumferential average Nusselt numbers at the two surfaces may be expressed as

$$\overline{\text{Nu}}_i = -\frac{\left[\int_0^\pi (\partial\Phi/\partial R)\sin\theta\, d\theta\right](R_2 - R_1)}{2(\Phi_1 - \Phi_2)} \tag{25}$$

with $\partial\Phi/\partial R$ evaluated at the inner sphere, and

$$\overline{\text{Nu}}_o = -\frac{\left[\int_0^\pi (\partial\Phi/\partial R)\sin\theta\, d\theta\right](R_2 - R_1)}{2(\Phi_1 - \Phi_2)} \tag{26}$$

with $\partial\Phi/\partial R$ evaluated at the outer sphere.

Attention is now directed to Figs. 10 and 11, in which the variations of $\overline{\text{Nu}}_i/R_o$ with Re have been plotted in log-log

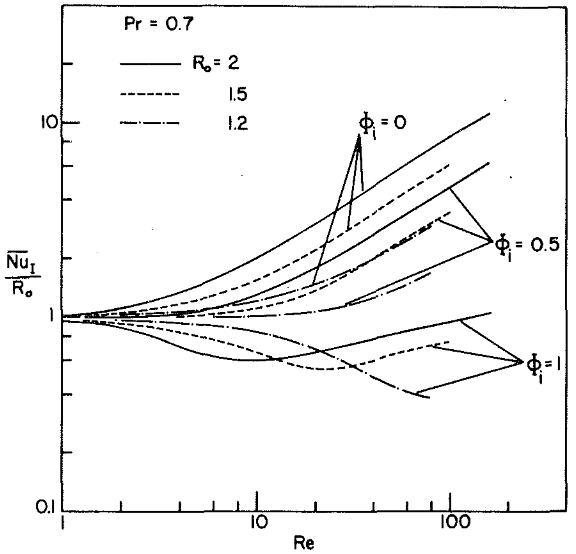

Fig. 11 Average Nusselt number at inner sphere: Pr = 0.7

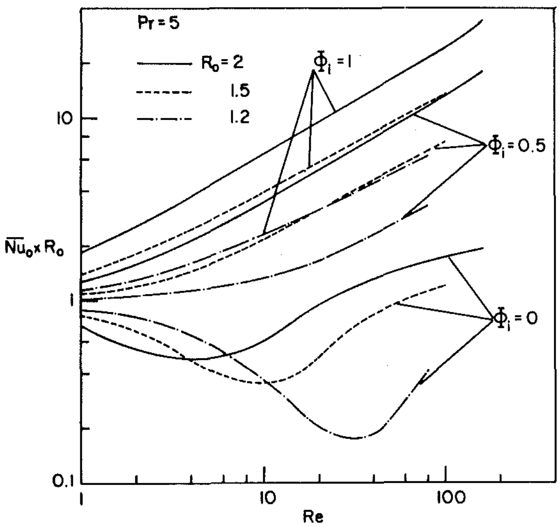

Fig. 12 Average Nusselt number at outer sphere: Pr = 5

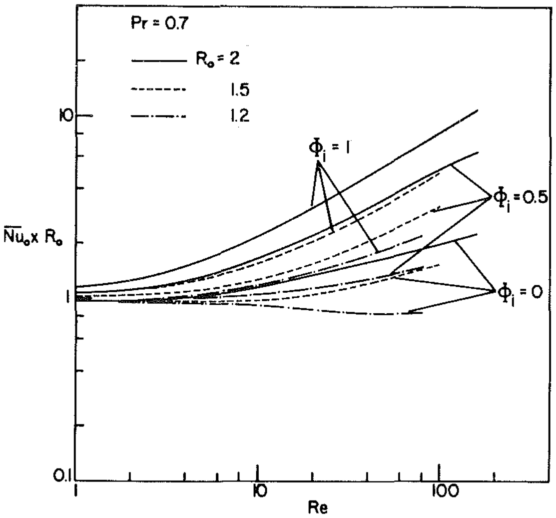

Fig. 13 Average Nusselt number at outer sphere: Pr = 0.7

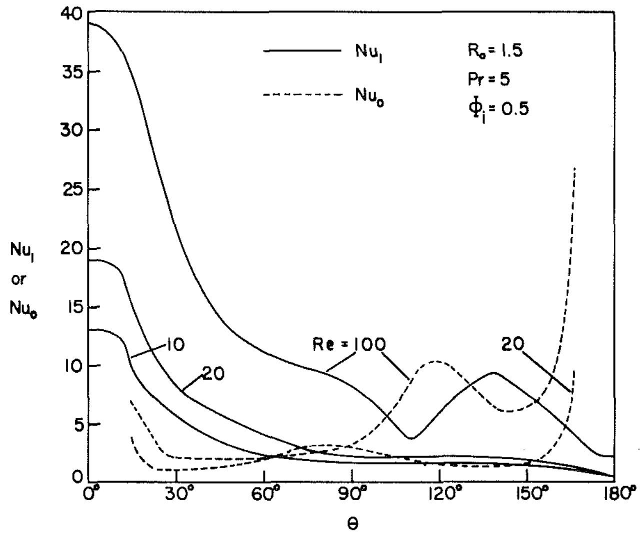

Fig. 14 Circumferential variation of local Nusselt numbers at the inner and outer sphere surfaces

coordinates. The two figures correspond to the two different Prandtl numbers investigated in this work. The parameter R_o has been employed to normalize $\overline{\mathrm{Nu}}_I$ in order to produce a value of unity in the conduction limit. Three sets of three curves are presented in each of these figures corresponding to the three values of inlet temperature, Φ_i, and the three radius ratios, R_o. As might be expected, the curves corresponding to $\Phi_i = 0$ and $\Phi_i = 0.5$ rise with increasing Re, with those for $\Phi_i = 0$ lying above the ones for $\Phi_i = 0.5$. Also, curves corresponding to greater values of R_o lie above those for smaller R_o. The augmentation of the heat transfer rate at the inner sphere surface is quite large in some of the cases shown. For instance, at Re = 100 in the annulus of radius ratio 2, for Pr = 5 and $\Phi_i = 0$, the overall heat flux at the inner sphere is enhanced by a factor of 20 over the heat flux in the limit of pure conduction. In the light of the fluid flow patterns displayed earlier, this tremendous augmentation of the heat transfer rate at high Reynolds numbers is not surprising. In sharp contrast, the curves corresponding to $\Phi_i = 1$ display an initial decrease with Re before reaching a minimum point and then rising again. Once again, the interpretation of these trends is facilitated by referring back to the figures that display the fluid flow patterns. The operating conditions corresponding to the minimum heat flux would be a desirable state to aim for in the design of cryogenic storage systems.

In Figs. 12 and 13, the variations of $\overline{\mathrm{Nu}}_o \times R_o$ with Re have been plotted in log-log coordinates. The two figures correspond to the two different Prandtl numbers investigated. As might be expected, the curves for $\Phi_i = 1$ and $\Phi_i = 0.5$ rise monotonically with Re. However, the curves for $\Phi_i = 0$ decrease initially to a minimum before rising again. These trends are akin to the ones observed in the case of $\overline{\mathrm{Nu}}_I$, and similar remarks apply to them.

A comparison of Figs. 10 and 12 reveals an interesting aspect of the role played by the flowing fluid in influencing the heat transfer phenomena. It will be recalled that the dimensionless temperatures of the inner and the outer spheres are 1 and 0, respectively. For a dimensionless fluid inlet temperature of $\Phi_i = 0$, it is observed that the Nusselt number at the surface of the inner sphere is substantially augmented over the conduction limit, particularly at intermediate and high Reynolds numbers. The outer sphere Nusselt number is, however, drastically diminished. Thus, for the value of $\Phi_i = 0$, the *outer* sphere is not an active participant in the heat

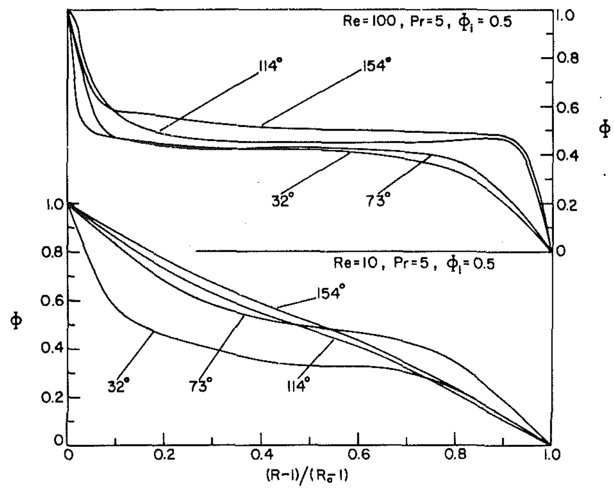

Fig. 15 Temperature variation in the radial direction at several angular locations: R_o = 1.5

transfer process. It acts as a virtually adiabatic shroud for the fluid flow, while the active thermal interaction is between the flow and the *inner* sphere.

The situation is reversed when the dimensionless fluid inlet temperature $\Phi_i = 1$. In this case, the *inner* sphere could be viewed as being virtually adiabatic, while heat exchange occurs between the flow and the *outer* sphere. For the intermediate value of $\Phi_i = 0.5$, the Nusselt numbers at the two spherical surfaces are comparable, and the rate of heat transfer from the inner sphere to the fluid is matched, approximately, by the rate of heat transfer from the fluid to the outer sphere. The thermal interactions in this case involve all three participants—the inner sphere, the outer sphere, and the fluid flow. It is evident from these observations, that the inlet temperature of the fluid plays a pivotal role in determining the relative magnitudes of the heat transfer rates at the two spherical surfaces.

The circumferential variation of the local Nusselt numbers at the two spherical surfaces will now be displayed. The local Nusselt number is defined by the equations

$$\mathrm{Nu} = h(r_2 - r_1)/k, h = q/(T_1 - T_2) \qquad (27)$$

In terms of the dimensionless variables of the analysis, the Nusselt numbers at the inner and outer spheres may be expressed as

$$\mathrm{Nu}_I = -(\partial\Phi/\partial R)_I (R_2 - R_1)/(\Phi_1 - \Phi_2) \qquad (28)$$
$$\mathrm{Nu}_o = -(\partial\Phi/\partial R)_o (R_2 - R_1)/(\Phi_1 - \Phi_2)$$

Figure 14 illustrates the circumferential variations of the local Nusselt numbers at the inner and the outer surfaces. The curves presented are for the case of $\Phi_i = 0.5$, $R_o = 1.5$, and cover a range of Reynolds numbers. The influence of the hydrodynamic phenomena on the thermal field is clearly discernable in these graphs. Attention will first be directed to the curves for Nu_I. These curves start at relatively high values of Nu_I and then decrease sharply with increasing θ. Obviously, the impingement of the entering flow on the inner sphere is responsible for the high heat transfer rates at the inner sphere surface near the entrance.

During the review of this paper, a suggestion was advanced that the Nusselt numbers at the impingement point be compared with the corresponding Nusselt numbers in classical stagnation point flow as a means of validating the numerical solutions. In this connection, it is appropriate to point out that the flow situation in classical axisymmetric stagnation point flow is somewhat different from the present one. In the classical problem, the flow velocity along the stagnation streamline *decreases* monotonically from the free stream value. In the present case, the flow velocity *increases* from the value at the inlet port owing to the diminution of flow area. Thus, if the inlet port velocity were viewed as being equivalent to the free stream velocity of the classical case, the present numerical solutions would be much higher than the classical solutions. However, there is a way of obtaining a better comparison of the two solutions. This involves establishing a correspondence between the tangential velocities near the stagnation point in the classical and the present cases. For corresponding values of tangential velocity, the classical and numerical solutions agree within 10 percent in all the cases presented in this paper. It is clear that perfect agreement between the two cases should not be expected.

Beyond the angle corresponding to the impingement region, the Nusselt numbers for Re = 10 and Re = 20 are comparatively low and do not vary appreciably with θ. However, in the case of Re = 100, the effects of flow separation and reattachment on the local Nusselt numbers are evident. The Nusselt number drops to a minimum at the point of separation from the inner sphere surface and then recovers to produce a local maximum near the point of reattachment. This behavior of the local Nusselt number curve is characteristic of flows with separation and reattachment.

The variations of the local Nusselt number at the outer sphere are depicted by the two curves corresponding to Re = 20 and Re = 100. At Re = 20, the Nusselt number values are fairly uniform with θ except for sharp peaks near the inlet and outlet ports and a local maximum near θ = 80 deg. The high heat transfer rates near the inlet and outlet ports are produced because of the large flow velocities adjacent to the sphere surface near the ports. The local maximum near θ = 80 deg is caused by the impingement of the flow that jets off tangentially from the inner sphere surface. At Re = 100, the Nusselt numbers near the inlet and outlet ports are much higher than at Re = 20. In addition, the large toroidal eddy that is centered around θ = 110 deg produces a pronounced local maximum in the heat transfer coefficient. The location of this peak corresponds well with the location of the trough and peak in the Nu_I curve.

Finally, attention is directed to Fig. 15 in which radial temperature profiles are presented at four angular locations for two Reynolds numbers. These curves are plotted for Pr = 5, $\Phi_i = 0.5$, and $R_o = 1.5$. At Re = 10, the evolution of the temperature profiles with angular location from the classic boundary layer shape to the near linear, conduction dominated shape is clearly seen. The large temperature gradient at the inner sphere surface at the angular location θ = 32 deg is noteworthy. At the other angular locations, the temperature gradients are relatively small at both spherical surfaces. In the case of Re = 100, all the temperature distributions are observed to be quite steep at both sphere surfaces and substantially flat in the middle. This heat transfer situation is evidently dominated by the convective transport processes.

4 Conclusions

In the present paper, forced convective heat transfer in laminar flow between concentric, isothermal spheres has been studied. Numerical finite difference solutions have been obtained for a range of the governing dimensionless parameters of the analysis. The circumferential average Nusselt numbers at the two spherical surfaces have been presented as functions of the Reynolds number, Prandtl number, radius ratio, and dimensionless inlet temperature.

These graphs indicate that the heat transfer rates are very strongly influenced by the Reynolds number and the dimensionless inlet temperature. Qualitatively similar effects are obtained at the two Prandtl numbers and the three radius ratios investigated in this work.

In addition to the circumferential average Nusselt numbers, the pumping power required to sustain the flow is information that is useful from the standpoint of design. A power loss parameter that is proportional to the pumping power has been presented as a function of Reynolds numbers and radius ratio. This parameter is found to decrease asymptotically with increasing Reynolds number and is highest for the lowest radius ratio.

Details of the fluid flow and heat transfer phenomena within the spherical annuli have been highlighted through velocity vector plots, graphs of local Nusselt number variations, and temperature profiles. Marked changes in the flow patterns at different Reynolds numbers and radius ratios are observed. These flow patterns in turn are demonstrated to have significant influence on the local heat transfer rates.

References

1 Newton, R. L., "An Experimental Investigation of Forced Convection Between Concentric Spheres," M.S. thesis, Department of Mechanical Engineering, Tufts University, 1977.

2 Astill, K. N., "An Analysis of Laminar Forced Convection Between Concentric Spheres," ASME JOURNAL OF HEAT TRANSFER, Vol. 98, Nov. 1976, pp. 601–608.

3 Tuft, D. B., "Numerical Analysis of Laminar Forced Convection in a Spherical Annulus," Lawrence Livermore Laboratory Report UCRL-84655, July 1981.

4 Cobble, M. H., "Spherical Shell Heat Exchanger-Dirichlet Problem," *Journal of the Franklin Institute*, Sept. 1963, pp. 197–206.

5 Rundell, H. A., Ward, E. G., and Cox, J. E., "Forced Convection in Concentric-Sphere Heat Exchangers," ASME JOURNAL OF HEAT TRANSFER, Vol. 90, Feb. 1968, pp. 125–129.

6 Bird, R. B., Stewart, W. D., and Lightfoot, E. N., *Transport Phenomena*, John Wiley and Sons, Inc., New York, 1964.

7 Bozeman, J. D., and Dalton, C., "Flow in the Entrance Region of a Concentric Sphere Heat Exchanger," ASME JOURNAL OF HEAT TRANSFER, Vol. 92, Feb. 1970, pp. 184–185.

8 Cox, J. E., and Sahni, B. K., "The Concentric Sphere Heat Exchanger," ASME JOURNAL OF HEAT TRANSFER, Vol. 93, Nov. 1971, pp. 468–469.

9 Patankar, S. V., *Numerical Heat Transfer and Fluid Flow*, McGraw-Hill, New York, 1980.

Transient Forced Convection Heat Transfer to Helium During a Step in Heat Flux

P. J. Giarratano

W. G. Steward
Mem. ASME

Thermophysical Properties Division,
National Engineering Laboratory,
National Bureau of Standards,
Boulder, Colo. 80303

Transient forced convection heat transfer coefficients for both subcritical and supercritical helium in a rectangular flow channel heated on one side were measured during the application of a step in heat flux. Zero flow data were also obtained. The heater surface which served simultaneously as a thermometer was a fast response carbon film. Operating conditions covered the following range: Pressure, 1.0×10^5 *Pa (1 bar) to* 1.0×10^6 *Pa (10 bar); Temperature, 4 K-10 K; Heat Flux, 0.1* W/cm^2*-10* W/cm^2*; Reynolds number, 0-8* $\times 10^5$*. The experimental data and a predictive correlation are presented.*

1 Introduction

A knowledge of heat transfer to helium under transient conditions is required for the design and operation of large superconducting systems. Because the heat transfer during a short heat pulse can be many times greater than the steady-state value, the use of steady-state heat transfer predictive correlations may lead to unnecessarily conservative designs. For small prototype systems this conservatism may be acceptable. However, as current densities, operating fields, stresses, etc., are pushed upward, evidence from the work of Dressner [1] and Wilson [2] indicates that some estimate of the time-dependent heat transfer is necessary to predict the superconductor performance during and following a transient heat (power) pulse.

In recent years, transient heat transfer data to static helium have been provided by several authors, e.g., Jackson [3], Tsukamoto and Kobayashi [4], Bailey [5], Iwasa and Apgar [6], Steward [7], Schmidt [8], and Brodie et al. [9].

In this report, we discuss measured transient heat transfer to helium under forced flow and zero flow conditions after a step heat input. The range of the test variables was:

(*i*) Pressure: 1.0×10^5 Pa (1 bar) to 1.0×10^6 Pa (10 bar)
(*ii*) Temperature: 4 K-10 K
(*iii*) Heat Flux: 0.1 W/cm^2-10 W/cm^2
(*iv*) Reynolds Number: $0\text{-}8 \times 10^5$

2 Description of Apparatus and Experimental Measurement

2.1 Experimental System. The basic experimental system, shown in Fig. 1, employs a small centrifugal pump, suspended from the top plate of the cryostat. Helium is circulated through the test loop, which contains a turbine flowmeter and the experimental test section. During the subcritical runs (at atmospheric pressure), the inner cell can and isolation shield are removed and the liquid helium in the outer reservoir serves as the test fluid. For the supercritical runs (at elevated pressures and temperatures) the inner cell and isolation shield are replaced so that the elevated operating condition can be attained. However, for the 4 K runs the isolation shell is removed.

2.2 Test Section. The test section heater surface, which serves simultaneously as a thermometer is a fast response (less than 1 μs) carbon film with dimensions 0.5×1 cm. The film is situated in a rectangular flow channel such that the flow is parallel to the 1-cm dimension. The depth of the flow channel, normal to the heater surface is 0.15 cm. A length of uniform channel, approximately 18 times the channel depth, precedes the test heater to insure a fully developed momentum boundary layer. In order to avoid thermal entrance effects, a preheater (L/D based on depth = 2.3) precedes the test heater and is maintained at the heat flux level of the test heater. A greater L/D would have been more desirable (e.g., 20). Due to the size limitations of the available carbon films, and in order to avoid discontinuity in the surface which would have been difficult to avoid if a second film were inserted upstream of the test film, this limited L/D was accepted. It is recognized

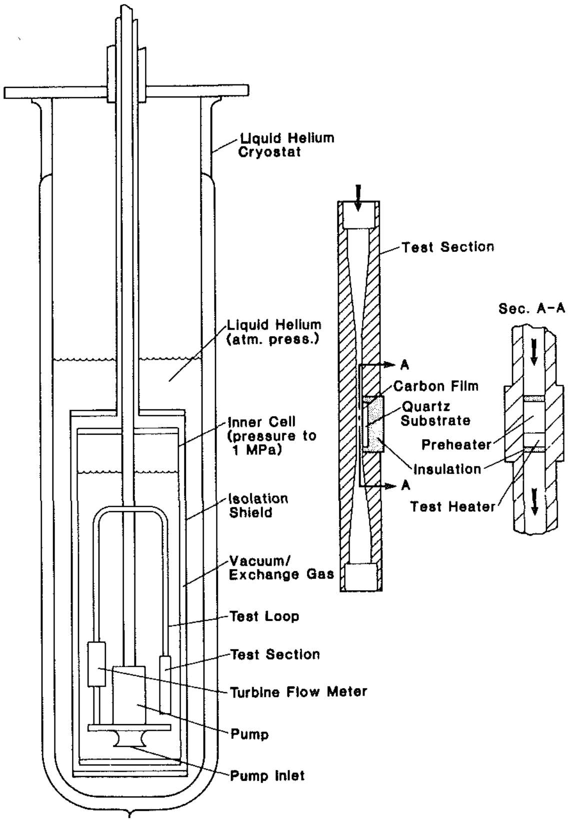

Fig. 1 Schematic of the forced convection transient helium heat transfer apparatus

---

Contributed by the Heat Transfer Division for publication in the Journal of Heat Transfer. Manuscript received by the Heat Transfer Division March 15, 1982.

that entrance effects may be more pronounced in the near-critical region.

In the early part of transient heating, where molecular conduction predominates, the ratio of heat flux going into the fluid to that going into the substrate is approximately

$$q_f/q_s \cong \left(\frac{k}{\sqrt{\alpha}}\right)_f / \left(\frac{k}{\sqrt{\alpha}}\right)_s \qquad (1)$$

where k is thermal conductivity, and α is thermal diffusivity. For helium and a quartz substrate at 4 K this ratio is approximately 16; however, at 10 K the ratio is approximately 1.0.

In the steady state the heat flux ratio before the bulk temperature in the flow channel rises significantly is

$$q_f/q_s = h_f\left(\frac{\delta_s}{k_s} + \frac{\delta_i}{k_i} + \frac{1}{h_{if}}\right) \qquad (2)$$

where h_f is the film coefficient between the carbon film and fluid, h_{if} is the film coefficient between the insulation and fluid, and δ_s and δ_i are the thickness of the substrate and insulation. Using a range $0.05 < h_f < 0.8$, and ignoring $1/h_{if}$ which is small compared to δ_i/k_i, we get

$$50 < q_f/q_s < 800$$

Therefore, in steady state the heat transfer is largely undirectional from the heated surface to the fluid, as desired, whereas in the early part of transients at the higher temperatures the flow of heat to the substrate is significant.

2.3 Experimental Procedure. The operation of the apparatus for subcritical runs consisted of the following basic procedures:

(*i*) In situ temperature calibration of carbon film at room temperature

(*ii*) Preliminary cooldown to liquid nitrogen temperature (~76 K) and in situ calibration at this temperature

(*iii*) Replacement of liquid nitrogen with liquid helium and in situ temperature calibration at liquid helium temperature

(*iv*) Data collection for a range of heat fluxes and flow rates

For the supercritical runs the procedure was the same as at atmospheric pressure except that after room temperature and liquid nitrogen temperature calibration, liquid helium was transferred to the outer cryostat and condensation of helium in the sample cell for the desired operating conditions was achieved. A helium temperature calibration point was recorded.

The preliminary cooldown was accomplished by filling the outer cryostat with liquid nitrogen and having helium exchange gas in the vacuum space surrounding the inner cell. During the cooldown, the pressure inside the cell was kept constant at 3 bar by a continuous flow of helium gas from a helium supply cylinder fitted with a pressure regulating valve. When the system reached thermal equilibrium, as evidenced by cessation of helium gas flow into the chamber and by steady carbon film resistance, the liquid nitrogen temperature calibration point, corresponding to ambient pressure, was obtained.

The liquid nitrogen was then back-transferred out of the outer cryostat and replaced with liquid helium. During the liquid helium transfer the inner cell was held at about 10 bar helium pressure and the temperature was monitored as the incoming gas cooled. When the proper density (determined from the desired operating temperature and pressure) was achieved inside the cell, the helium gas supply valve was closed. As cooling continued, the pressure dropped and liquid helium was condensed in the inner cell. The condensation was substantiated by a liquid level detector inside the chamber, and the helium temperature calibration point was determined from the vapor pressure.

An auxiliary heater (not shown in Fig. 1) located in the inner cell and an appropriate amount of exchange gas in the vacuum/exchange gas space provided control of the cell pressure and consequently the bulk temperature. Because the system was operated under constant mass conditions (approximately constant density in the inner cell), the control of desired operating pressure consequently maintained the desired operation temperature.

2.4 Experimental Measurements. The temperature of the fluid inside the test loop was measured with the test carbon film at the beginning of each run. This was taken as the bulk temperature during the entire heat pulse and was used in the calculation of the heat transfer coefficient. However, the bulk temperature was also measured at the conclusion of a pressure run. The maximum drift noted during a run was ap-

Nomenclature

h = heat transfer coefficient = $q/(T_{\mathrm{surf}} - T_b)$, W/cm^2, K
q = heat flux, W/cm^2
t = time, s
T_{surf} = surface temperature, K
T_b, T_{inf} = bulk fluid temperature, K
T_f = fluid temperature, K
T_{TC} = transposed critical temperature, K (temperature at which heat capacity, Cp, at a given pressure above the critical pressure is a maximum)
Re = Reynolds number, dimensionless
Nu = Nusselt number, dimensionless
Nu_{DB} = $0.023\,\mathrm{Re}^{0.8}\,\mathrm{Pr}^{0.4}$ – Dittus-Boelter dependence
Pr = Prandtl number, dimensionless
x = space coordinate normal to the wall, $x=0$ at the wall, cm
y = space coordinate parallel to the wall, $y=0$ at the inlet, cm
ψ = Yaskin correlation parameter = $1 + \beta\Delta T$
ΔT = $T_{\mathrm{surf}} - T_b, K$
β = thermal expansivity, $-\frac{1}{\rho}\left[\frac{\partial \rho}{\partial T}\right]_P, K^{-1} = \frac{1}{v}\left(\frac{\partial v}{\partial T}\right)_P$
γ = proportionality constant in Kapitza conductance heat flow equation dependent upon the properties of the solid carbon surface, W/cm^{2}K^4
ρ = density, g/cm^3

Subscripts

cond = conduction
f = fluid
initial = value of the subscripted parameter at the earliest measured times
K = Kapitza
pred = predicted
s = substrate
ss = steady-state condition, i.e., the value of the subscripted parameter is no longer changing with time
surf = surface
∞ = fully developed momentum and thermal boundary layer region

Table 1 Uncertainties in measurements

Parameter	Estimated uncertainties	Sources of error	Remarks
Bulk temperature, T_b	3% to 8%	(*i*) Temperature rise due to additional energy input from pump motor (*ii*) Temperature drift during the course of a pressure run due to average density in cell changing with outer cryostat liquid level changes (*iii*) Neglect of temperature rise during heating pulse (*iv*) Calibration	The percent error due to the pump is a maximum at low heat flux and high flow rate (i.e., at small temperature differences). For runs at $T_b > 4$ K, error (*i*) could be countered by reduction of auxiliary heater power.
Surface temperature, T_{surf}	1.5% T	(*i*) Calibration	
Heat flux, q	1%	(*i*) Digital recording oscilloscope accuracy (*ii*) Standard resistor accuracy	
	$\pm 10\%$ q_{nominal} was the deviation from a perfect step in heat flux.	(*i*) Deviation from perfect step in heat flux due to resistance change with temperature	
Pressure	1%	(*i*) Calibration	
Flow rate	Less than 20%	(*i*) Calibration	
Time	±0.02%	(*i*) Digital recording oscilloscope calibration (mfr's. stated accuracy)	
Heat transfer coefficient, h	5.5% to 10.5%	Combination of errors in heat flux, bulk temp., and surface temp	The percent error is a maximum at low heat flux and high flow rate.

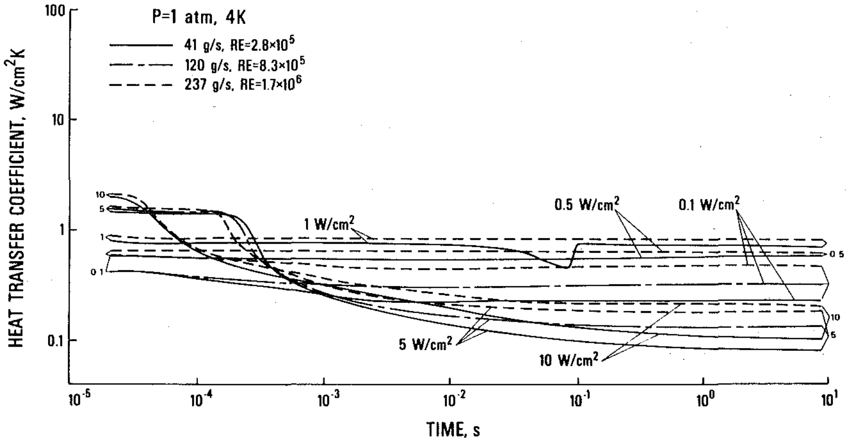

Fig. 2 Transient heat transfer to subcritical helium at 1.0 bar and 4.0 K

proximately 0.1 K, and was attributed to liquid level changes in the outer helium cryostat.

The bulk temperature rise in the test section was computed by means of a dynamic energy balance, and any points for which the bulk temperature rise was greater than 15 percent of the wall temperature rise were deleted. This occurred only in the zero flow runs. The bulk temperature also rose during some runs (as evidenced by a corresponding system pressure rise) at the high flow rate conditions due to the power dissipation from the circulating pump motor. At the elevated temperature operating conditions, this tendency toward temperature increase was approximately offset by manual reduction of power input to the inner cell auxiliary heater – thus maintaining pressure and bulk temperature approximately constant. The estimated uncertainties in the measurements are given in Table 1.

Measurements of the voltage drop across the carbon film and a standard resistor were recorded at intervals as close as 0.5 microseconds with a digital recording oscilloscope; 2048 points were recorded on each sweep of the oscilloscope on each of two channels. These data provide the carbon film heat flux and temperature rise as a function of time. A minicomputer data acquisition system processed the data and stored the results on magnetic tape for permanent record. The range of time over which data were recorded was 10 s. In order to provide sufficient resolution at short times, each heat flux run was repeated at three different sweep times of the oscilloscope – 1 millisecond, 1 s, and 10 s.

The voltage applied across the carbon film was applied as a step input with a rise time less than 2.0×10^{-5} s. However, because the resistance of the film decreased with increasing temperature, the resulting power step (heat flux) was not quite constant throughout the time interval. At high power levels, the resistance change caused a heat flux variation of up to 10 percent from the average. Thus the heat fluxes noted on the graphs and Table 2 are nominal values. A small overshoot in power level occurred at times varying from 4.5 μs to about 20μs. The largest observed magnitude of this overshoot was 40 percent of the power level at 20 μs and occurred at 4.5 μs. However the deviation in total energy input, from that which would be supplied for an ideal step input, was less than 4 percent.

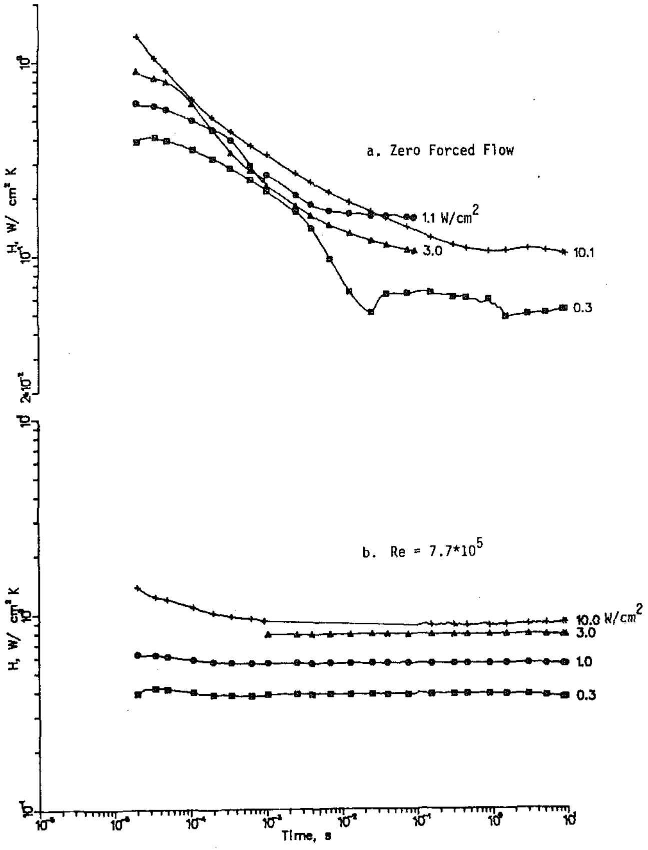

Fig. 3 Transient heat transfer to supercritical helium at 2.5 bar and 4.0 K

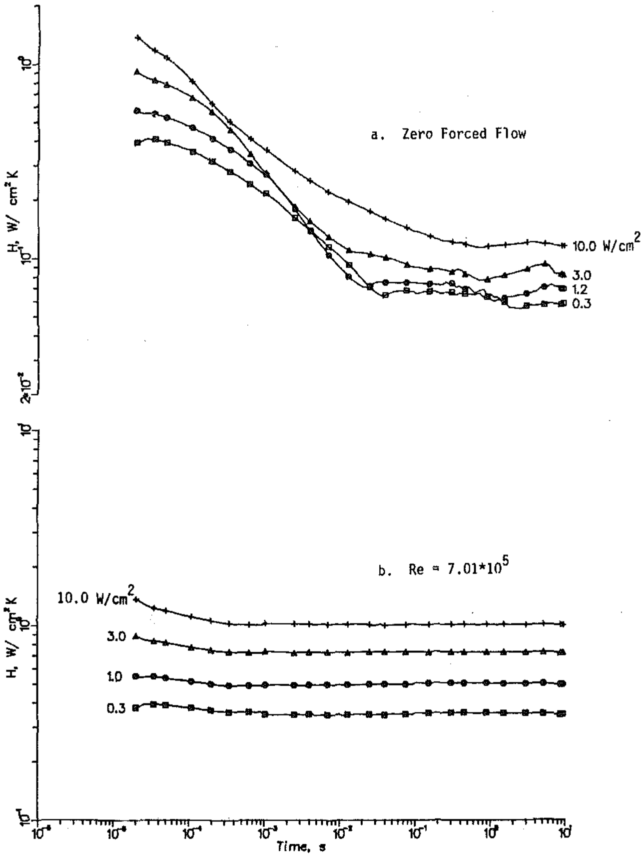

Fig. 5 Transient heat transfer to supercritical helium at 6.0 bar and 4.0 K

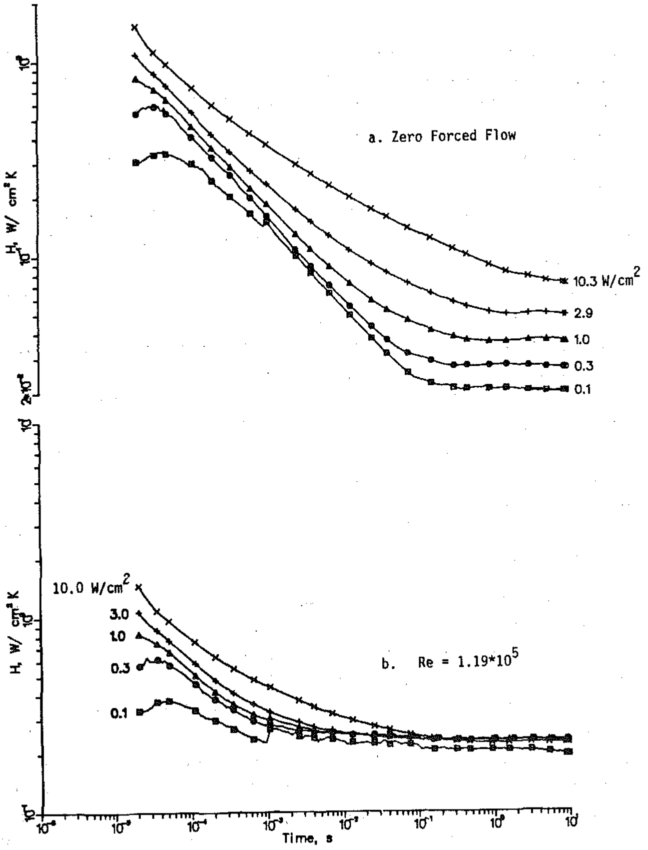

Fig. 4 Transient heat transfer to supercritical helium at 2.5 bar and 9.9 K

The flow rate, as determined from the output of the turbine meter, and pressure, measured with a bourdon tube pressure gage, were also recorded during each run.

3 Experimental Results

In Figs. 2-8, we show the results of the experimental runs where heat transfer coefficients are plotted as a function of time for the operating conditions shown on each graph. The curves shown were drawn through the experimental data points obtained during each of the three repeated separate heat flux runs (pulse widths of 1 millisecond, 1 s and 10 s). Therefore, apparent large discontinuities in some of the curves (e.g., Figs. 3(*a*) and 7(*b*)) are due to small uncontrolled changes in operating conditions occurring between runs. In Figs. 3-8, symbols for each heat flux are plotted for every tenth data point, but the curves are drawn through each of approximately 134 data points.

3.1 Supercritical Data. First we note that for a fixed temperature and pressure, the time to reach steady state, t_{ss}, increases with heat flux for each flow rate, and t_{ss} decreases with increased flow rate for a fixed heat flux. Also, it appears that, for a given pressure, t_{ss} generally increases with increasing bulk temperature and other conditions fixed. Typically, t_{ss} ranged from 1 to 10 milliseconds for the forced flow conditions and from 10 to 100 milliseconds for the zero flow conditions. t_{ss} was arbitrarily taken to be the time beyond which the heat transfer coefficient changed by less than about 3 percent. This was determined from the numerical computer printouts of the data.

The ratio of the heat transfer coefficient at the earliest measurement time of 20 μs (maximum value) to the steady-state value varied with the operating conditions. At the high

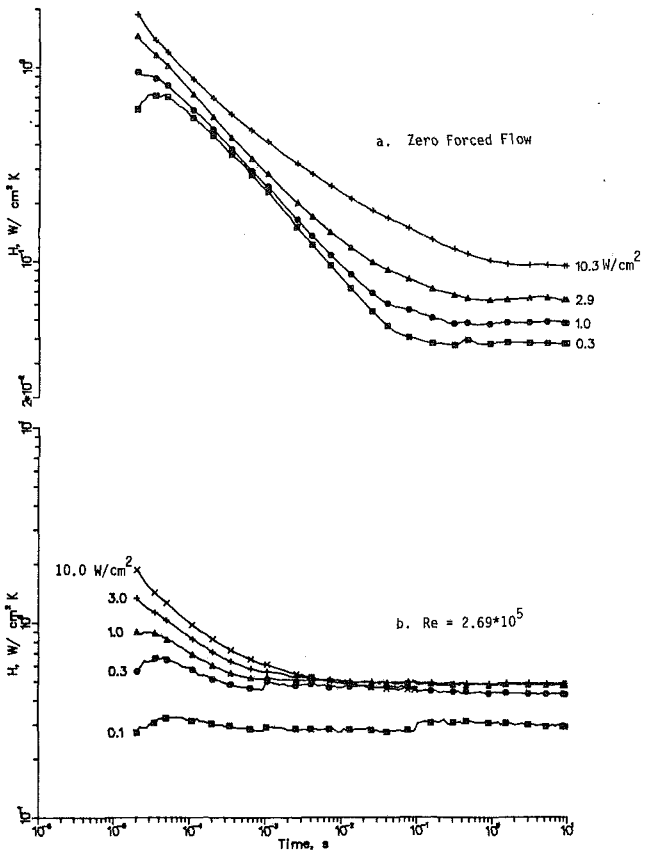

Fig. 6 Transient heat transfer to supercritical helium at 6.0 bar and 10.2 K

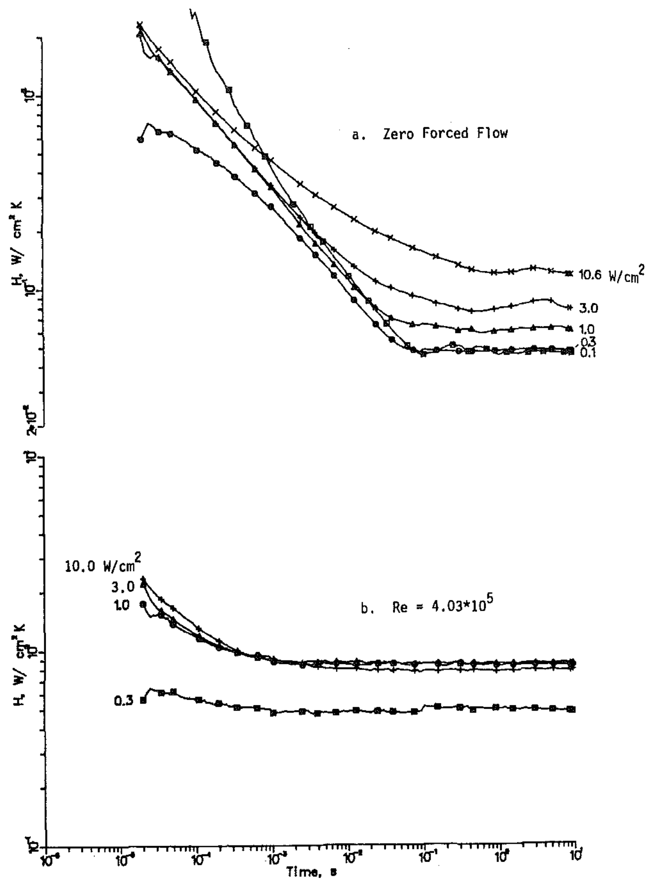

Fig. 8 Transient heat transfer to supercritical helium at 10.0 bar and 10.4 K

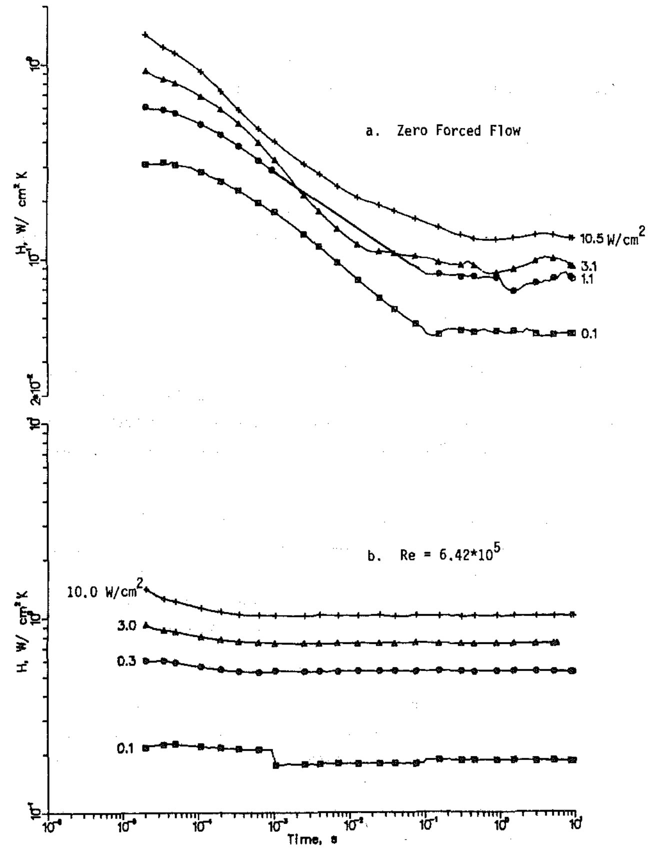

Fig. 7 Transient heat transfer to supercritical helium at 10.0 bar and 4.0 K

bulk temperature and high heat flux condition the ratio was approximately 10, whereas at the low bulk temperature, low heat flux condition the ratio was generally less than 2.

The influence of heat flux on the heat transfer coefficient is not uniform throughout the entire heat step. Initially the effect is an increase of heat transfer coefficient with increasing heat flux. However, at steady state the same is not true. For some conditions at steady state, the heat transfer coefficient exhibited maxima or minima as heat flux was increased. This result is typical of heat transfer in the near critical region where the radial variation of fluid properties may be significant and depends on the combined effect of heat flux, flow rate, and bulk temperature.

At the start of the heat step (20 μs) the effect of flow rate on the heat transfer was negligible since the thermal boundary layer was undeveloped. As time progressed and the thermal boundary layer increased, the usual heat transfer enhancement with increased flow rate is observed. The time at which flow rate influence became significant varied with operating condition.

3.2 Correlation of Supercritical Data. In an earlier study of transient heat transfer to helium during pool boiling, Steward [7] deduced from his data that Kapitza resistance (the thermal boundary resistance between a solid and liquid helium) and the pure conduction resistance of the developing thermal boundary layer, added in series, dominate the heat transfer process in the early part of the transient. This occurs before convective and boiling processes have become established. At longer times the heat transfer coefficient tends toward the steady-state value during which convection or boiling dominates.

In analyzing the data of these experiments, all of the

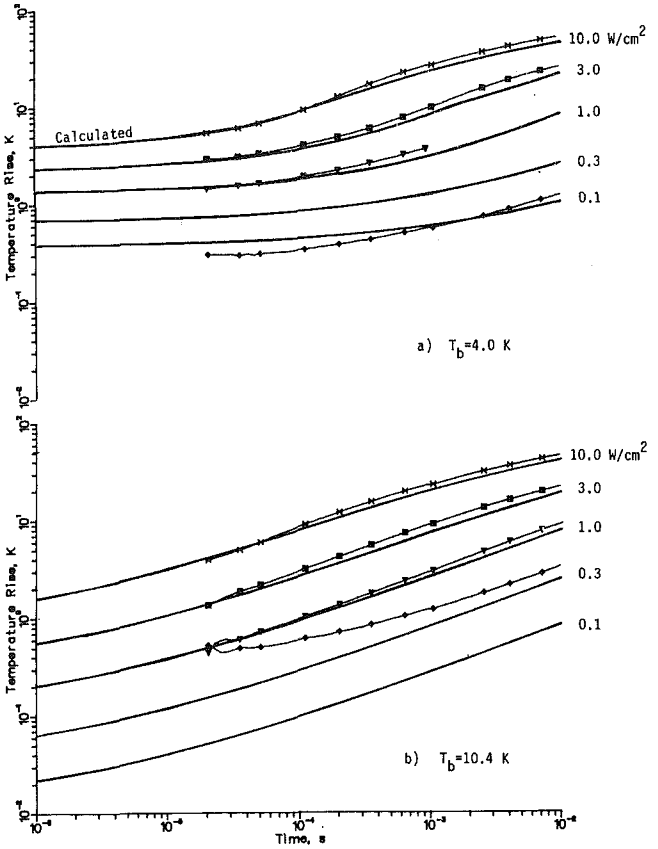

Fig. 9 Early transients for supercritical helium at 10.0 bar, zero forced flow

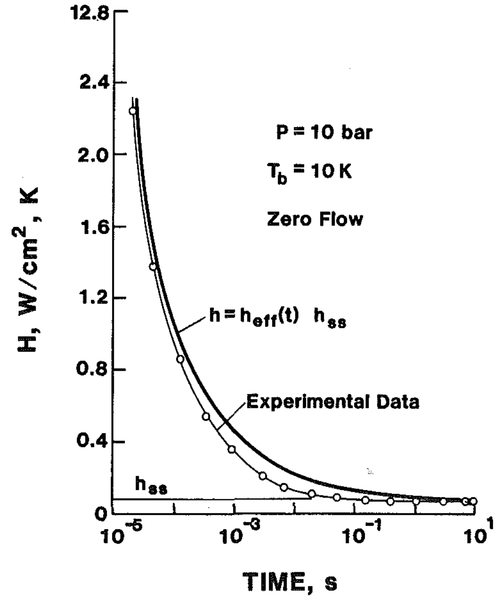

Fig. 10 Illustrative calculation of transient heat transfer coefficient by equation (8)

following factors are important at various times and conditions:

1 Spatial and temporal variation of fluid and solid properties

2 Variation in the relative importance of conduction and convection (or boiling in subcritical fluid)

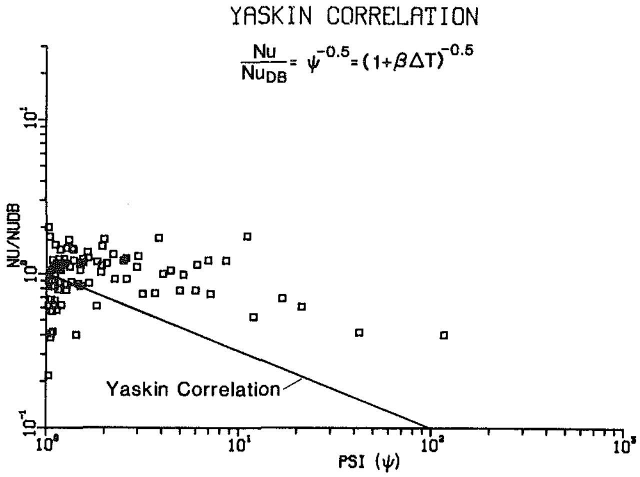

Fig. 11 Comparison of experimental steady state heat transfer coefficients with Yaskin's predictive correlation

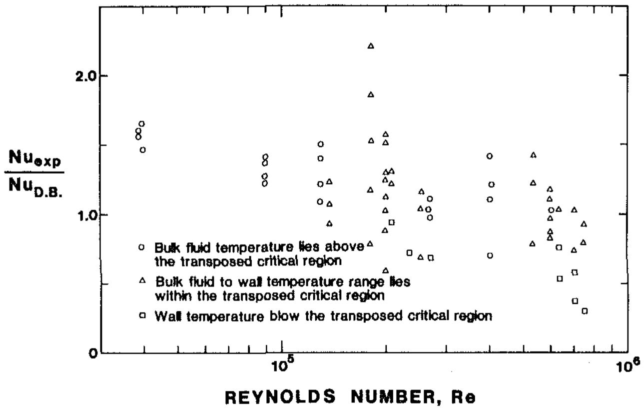

Fig. 12 Steady-state data

3 Kapitza conductance at the solid-fluid interface

4 Conduction of heat in the substrate

5 Heat convection normal to the surface due to fluid expansion

Analyses considering all of these factors will be the subjects of future reports.

The effect of gravity on the vertically oriented test section is not expected to be significant at the high Reynolds numbers of these tests. Judging from previous results [7] in transient pool boiling at various orientations one would not expect a gravity effect during the early part of the transient period in zero forced flow experiments; however, in steady state the natural convection heat transfer coefficients are higher for the vertical orientation than for other orientations. The confinement of the narrow channel and flow loop probably have some effect on zero forced flow results, but these have not been investigated here.

3.2.1 Very Early Transients. One special case, which can be treated fairly simply in an approximate way, is the very early part of transients before turbulent convection or boiling effects become significant. Then molecular conduction and Kapitza conductance are the primary heat transfer mechanisms to consider. Since the temperature disturbance penetrates a distance less than the channel depth or substrate thickness during the time period being considered, conduction solutions for infinite solid and fluid media were used. A simplified means of approximately accounting for the variable properties is given here.

The constant property solution for the transient temperature distribution is Carslaw and Jaeger [10]

$$T_f = \frac{2}{\sqrt{\pi}}\left(\frac{\sqrt{\alpha}}{k}\right)_f q_f\sqrt{t}\left[e^{-X^{*2}} - \sqrt{\pi}X^*\mathrm{erfc}X^*\right] \tag{3}$$

where

$$X^* = \frac{X}{2\sqrt{\alpha_f t}}$$

$$\frac{dT_f}{\left(\frac{\sqrt{\alpha}}{k}\right)_f} = -2q_f\sqrt{t}\,\mathrm{erfc}X^*dX^*$$

$$\int_{T_b}^{T_{f,\mathrm{surf}}} \frac{dT_f}{\left(\frac{\sqrt{\alpha}}{k}\right)_f} = 2q_f\sqrt{t}\int_0^\infty \mathrm{erfc}X^*dX^* = \frac{2}{\sqrt{\pi}}q_f\sqrt{t} \tag{4}$$

The function $(\sqrt{\alpha}/k)_f(T)$ is known from helium properties, and so the procedure amounts to solving for $T_{f,\mathrm{surf}}$ numerically from (4).

The temperature step at the surface due to Kapitza resistance was calculated by[1]

$$T_{\mathrm{surf}} = T_{f,\mathrm{surf}} + \frac{q_f}{h_K} \tag{5}$$

and from (1)

$$\frac{q_f}{q} = \frac{\left(\frac{\sqrt{\alpha}}{k}\right)_s}{\left(\frac{\sqrt{\alpha}}{k}\right)_s + \left(\frac{\sqrt{\alpha}}{k}\right)_f} \tag{6}$$

where q is the total applied heat flux.

Since q_f/q is temperature dependent, iteration is required to arrive at q_f and T_{surf}. Typical results of T_{surf} calculated from above are compared with experimental T_{surf} for zero forced flow in Fig. 9.

3.2.2 Complete Transient With Turbulent Convection. A theoretical analysis of transient heat transfer, considering the time varying roles of conduction and turbulent convection, but with constant properties, gives the fluid temperature rise at the boundary as a function of flow parameters and time in the following form

$$\frac{\Delta T_{f,\mathrm{surf}}}{\Delta T_{f,\mathrm{surf},ss}} = 1 + \sum_{n+1}^{\infty} C_n e^{-D_n t} \tag{7}$$

where C_n and D_n are functions of the Reynolds number, steady-state Nusselt number, thermal diffusivity, and geometrical factors (as well as an n). This formulation is the subject of a future paper and will not be discussed further here, except to note that preliminary analysis indicates that it does predict the kind of behavior observed in these experiments.

The case for variable fluid properties will require a numerical solution to the governing differential equations. In lieu of a theoretical treatment of the entire transient period, one can simply use an interim approximation

$$h_{\mathrm{pred}}(t) = h_{\mathrm{eff}}(t) + h_{ss} \tag{8}$$

where

$$h_{\mathrm{eff}} = \frac{q_f}{T_{\mathrm{surf}} - T_b} \tag{9}$$

and T_{surf} and q_f are obtained as discussed under 3.2.1. The steady-state heat transfer coefficient, h_{ss}, is discussed in the following section. The prediction is best at the extremes where $h_{\mathrm{eff}}(t) >> h_{ss}$ (early transients) and where $h_{ss} >> h_{\mathrm{eff}}(t)$ (steady state), but the prediction may be 25 to 40 percent high in the 10^{-3} to 10^{-1}s region. A sample calculation is shown in Fig. 10, where h_{ss} was taken to be the experimental value rather than a predicted value.

3.2.3 Steady State. The experimental steady-state heat transfer coefficients are compared in Fig. 11 with the predictive correlation of Yaskin [14]. As can be seen, the trend of the data is, in general, as predicted but the absolute agreement is rather disappointing. This result may in part be due to possible entrance effects of this data as discussed below.

In Fig. 12, the ratio of experimental Nusselt number to Nusselt number calculated by the Dittus Boelter correlation [12], for time greater than about 1 s, is plotted as a function of Reynolds number. The Dittus Boelter correlation is applicable for fully developed thermal and momentum boundary layers, i.e., beyond the entrance region. As is well known from the literature, e.g., [13], for a given axial position in a channel, y, the ratio $\mathrm{Nu}_y/\mathrm{Nu}_\infty$ decreases with increasing Reynolds number. This is true until $y \geq$ thermal entrance length where the ratio becomes 1 and is independent of Reynolds number and y. Therefore, the trend displayed in Fig. 12, Reynolds number dependence, suggests that the thermal boundary layer at the test section was not fully developed in spite of the preheater preceding the test heater. As noted by the different symbols in Fig. 12, we detect no significant difference in this result which may be attributed to thermodynamic state of the helium in the test section.

The length of the preheater was known to be marginal, (about two hydraulic diameters) and in some cases, the heat flux of the preheater may not have been sufficiently close to that of the test heater. The emphasis on transient data and the desire for very fast power rise time led to the selection of a power amplifier with limited power output. This, in turn, limited the total heater area if high heat flux was to be obtained. In any case, the deviation from predicted, fully developed heat transfer was far greater than expected. Previously reported correction factors for near-critical heat transfer, such as Giarratano [16] and Yaskin [14] have reported, are apparently overshadowed by the entrance effects of these data.

3.3 Subcritical Data. A detailed discussion of the subcritical forced convection boiling data has already been presented by Steward [15]. Therefore, a qualitative comparison with the 4 K supercritical data at 2.5 bar will be presented here (see Figs. 2 and 3(*a*)).

For low heat fluxes, less than or equal to about 1 W/cm^2, the subcritical boiling heat transfer is higher than that at the supercritical condition throughout the entire heat pulse. The peak nucleate boiling heat flux for helium occurs between 0.5 – 1 W/cm^2. Thus, for the same flow rate, the additional turbulence and stirring inherent to this boiling region accounts for the enhanced heat transfer over that at the supercritical pressure. However, at high heat flux, greater than 1 W/cm^2, and the same flow rate, the initial subcritical heat transfer coefficient is higher than the corresponding supercritical heat transfer coefficient; but then as the transition to film boiling occurs (in the subcritical case) the reverse is true, i.e., supercritical heat transfer coefficient is greater than the subcritical heat transfer. This is apparently due to improved thermal conductivity at the higher pressure. This can be seen by comparing the 10 W/cm^2 data for both pressures. The comparison of these two modes of heat

---

[1] Kapitza conductance, h_K, is discussed in the Appendix.

transfer (subcritical and supercritical) for these data is consistent with the observations of Giarratano et al. [16]. Finally, we note that for very short heat pulses at 10 W/cm^2 less than about 30 μs, the subcritical model is superior to the supercritical mode.

4 Summary

1 The time to reach steady state, following a step in heat flux, was typically less than 10 milliseconds for the forced flow conditions and less than 100 milliseconds for the zero flow condition.

2 The ratio of the heat transfer coefficient at the start of the pulse to the steady value ranged from 2 to 10, depending on the operating condition.

3 The influence of the heat flux on the heat transfer coefficient (for a fixed operating condition) was not uniform throughout the entire heat step. Initially, the effect was an increase in heat transfer with increased heat flux, but at steady-state maxima and minima in heat transfer were observed from some operating conditions.

4 An enhancement in heat transfer with increased flow rate was evident at steady state but not for short times. This suggests that heat transfer is dominated by Kapitza and pure conduction resistance (see section 3.2.1) at short times.

5 For times less than 1 millisecond or greater than 0.1 s the supercritical heat transfer data may be approximated by: $h_{\text{pred}}(t) = h_{\text{eff}}(t) + h_{ss}$ (see section 3.2.2).

6 For low heat fluxes (less than about 1 W/cm^2) the subcritical boiling heat transfer was superior to the supercritical heat transfer (2.5 bar and 4 K) throughout the heat step. However, at higher heat fluxes, the initial subcritical heat transfer coefficient was higher than the corresponding supercritical value, but then, as the transition to film boiling occurs (in the subcritical case) the reverse was true.

Acknowledgments

The authors gratefully acknowledge the contributions of Dr. V. D. Arp. His many helpful suggestions and discussions were instrumental to the completion of the study. The funding for the work was supplied by the Magnetic Fusion Energy Division, Department of Energy, Germantown, Maryland.

References

1 Dressner, L., "Propagation of Normal Zones in Composite Superconductor," *Cryogenics*, Vol. 16, No. 11, 1976, pp. 675–681.

2 Wilson, M. N., "Stabilization of Superconductors for Use in Magnets," Applied Superconductivity Conference, Palo Alto, Calif., 1976.

3 Jackson, J., "Tansient Heat Transfer and Stability of Superconducting Composites," *Cryogenics*, Vol. 9, No. 2, 1969, pp. 103–105.

4 Tsukamoto, O., and Kobayashi, S., "Transient Heat Transfer Characteristics of Liquid Helium," *J. Appl. Phys.*, Vol 46, No. 3, 1975, pp. 1359–1364.

5 Bailey, R. L., "Heat Transfer to Liquid Helium in Pulsed Heated Channels," Experiment Report RL-73-089, Department of Engineering Science, Rutherford High Energy Lab., Chilton, Didcot, Berkshire, England 1973.

6 Iwasa, Y., and Apgar, B. A., "Transient Heat Transfer to Liquid Helium From Bare and Coated Copper Surfaces in a Vertical Orientation—Part 1: Film Boiling Regime," *Cryogenics*, Vol. 18, No. 5, 1978, pp. 267–275.

7 Steward, W. G., "Transient Helium Heat Transfer Phase I—Static Coolant," *International Journal of Heat and Mass Transfer*, Vol. 21, No. 7, 1978, pp. 863–874.

8 Schmidt, C., "Transient Heat Transfer to Liquid Helium and Temperature Measurement With a Response Time in the Microsecond Region," *Appl. Phys. Lett.*, Vol. 32, No. 12, 1978, pp. 827–829.

9 Brodie, L. C., Sinha, D. N., Semura, J. S., and Sanford, C. E., Transient Heat Transfer Into Liquid Helium I," *J. Appl. Phys.*, Vol. 48, No. 7, 1977, pp. 2882–2885.

10 Carslaw, H. S., and Jaeger, J. C., *Conduction of Heat in Solids*, Oxford Press, London, 1950.

11 Snyder, N. S., "Thermal Conductance at the Interface of a Solid and Helium II (Kapitza conductance)," U.S. National Bureau of Standards, Tech Note 385, 1969.

12 Dittus, F. W., and Boelter, L. M. K., University of California, *Pubs. Engineering*, Vol. 2, 1930, p. 443.

13 Hartnett, J. P., ASME *Transactions*, Vol. 77, No. 7, 1955, p. 1211.

14 Yaskin, L. A., Jones, M. C., Yeroshenko, V. M., Giarratano, P. J., and Arp, V. D., A Correlation for Heat Transfer to Supercritical Helium in Turbulent Flow in Small Channels," *Cryogenics*, Vol. 17, No. 10, 1977, pp. 549–552.

15 Arp, V. D., Brennan, J. A., Giarratano, P. J., Parrish, W. R., Steward, W. G., Strobridge, T. R., and Voth, R. O., "Heat Transfer and Refrigeration in Support of Magnetic Fusion Energy Systems," National Bureau of Standards U.S. Interagency Report 78-877, Feb. 1978.

16 Giarratano, P. J., Hess, R. C., and Jones, M. C., "Forced Convection Heat Transfer to Subcritical Helium I," *Advances in Cryogenic Engineering*, Vol. 19, Plenum Press, New York, 1974, pp. 404–416.

APPENDIX

Determination of h_K in Equation (5)

The heat flux across a solid liquid interface due to Kapitza resistance is given by [17]

$$q = \gamma(T^4_{\text{surf}} - T^4_{f,\text{surf}}) = h_K(T_{\text{surf}} - T_{f,\text{surf}}) \tag{A1}$$

where the first equality relates the heat flux to the phonon energy density difference, and the second equality is used to define h_K.

$$h_K = \frac{\gamma(T^4_{\text{surf}} - T^4_{f,\text{surf}})}{T_{\text{surf}} - T_{f,\text{surf}}}$$

$$h_K = \gamma(T^3_{\text{surf}} + T^2_{\text{surf}} T_{f,\text{surf}} + T_{\text{surf}} T^2_{f,\text{surf}} + T^3_{f,\text{surf}})$$

and for $T_{\text{surf}} - T_{f,\text{surf}} << T_{\text{surf}}$

$$h_K \approx 4\gamma T^3_{\text{surf}} \tag{A2}$$

γ, and, therefore, h_K, was empirically determined from the experimental data as follows:

1 Assume $q_f = q$, approximately true at 4 K and 2.5 × 10^5 Pa.

2 In the early part of the transient, molecular conduction and Kapitza conductance are the primary heat transfer mechanisms.

3 Then, as derived by Steward [7], for pure transient conduction to the fluid

$$T_{f,\text{surf}} = T_b + \frac{2q\sqrt{t}}{\sqrt{\pi}\left[\frac{K_s}{\sqrt{\alpha_s}} + \frac{K_f}{\sqrt{\alpha_f}}\right]} \tag{A3}$$

Substituting (A3) in (A1)

$$\frac{1}{\gamma} = \frac{T^4_{\text{surf}} - \left[T_b + \frac{2q\sqrt{t}}{\sqrt{\pi}\left[\frac{K_s}{\sqrt{\alpha_s}} + \frac{K_f}{\sqrt{\alpha_f}}\right]}\right]^4}{q} \tag{A4}$$

For the data of this study, the average value of γ was determined to be 18.7 W/m^2•K^4 and therefore from (A2)

$$h_K \approx (4)(18.7)T^3_{\text{surf}} \tag{A5}$$

W. J. Marner
Member Technical Staff,
Instrumentation Section,
Jet Propulsion Laboratory,
California Institute of Technology,
Pasadena, Calif. 91109
Mem. ASME

A. E. Bergles
Professor and Chairman,
Department of Mechanical Engineering,
Iowa State University,
Ames, Iowa 50011
Fellow ASME

J. M. Chenoweth
Assistant Technical Director,
Heat Transfer Research, Inc.,
Alhambra, Calif. 91802
Mem. ASME

On the Presentation of Performance Data for Enhanced Tubes Used in Shell-and-Tube Heat Exchangers

As the efforts to produce more efficient heat transfer equipment continue, an increasing number of augmented surfaces are being produced commercially. Consequently, the designer faces an almost overwhelming task in comparing and evaluating the performance of various surfaces because of the many different ways in which the test data are currently presented in the literature. Thus, a uniform format for presenting pressure drop and heat transfer data for enhanced surfaces has become a necessity. This paper is concerned with one important aspect of this problem, namely, that of tubular enhanced surfaces used in shell-and-tube heat exchangers. As an initial step, the subject is limited to single-phase pressure drop and heat transfer; however, both tubeside and shellside flow are taken into consideration. A comprehensive list of commerical augmented tubes which may be considered for use in shell-and-tube exchangers is given, along with a survey of the performance data which are available in the literature. A standardized data format which uses the inside and outside envelope diameters as the basis for presenting the various geometrical, flow, and heat transfer parameters for all tubular enhanced surfaces is proposed and discussed.

Introduction

The shell-and-tube heat exchanger has been in use for many years and is the most widely used type of industrial heat transfer equipment. In order to carry out the thermal-hydraulic design of a shell-and-tube exchanger, pressure drop and heat transfer correlations (or tabulated data) must be available for both the tubeside and the shellside. Initially, only plain tubes were used in shell-and-tube exchangers. However, as increasing energy and material costs have provided significant incentives for more efficient heat exchangers, considerable emphasis has been placed on the development of various augmented, or enhanced, heat transfer surfaces. The use of enhanced surfaces allows the designer to increase the heat duty for a given exchanger, to reduce the size of the exchanger for a given heat duty, to reduce the pumping power, or to reduce the approach temperature difference.

The introduction of enhanced surfaces, and their inherently more complicated geometry, has resulted in the presentation of thermal-hydraulic data for these surfaces in many different ways. Therefore, the importance of standardization and compilation of performance data for enhanced surfaces was emphasized at the recent "Research Workshop on Energy Conservation Through Enhanced Heat Transfer" in Chicago [1]. In particular, it was pointed out that such a procedure would save the designer time, confusion, and effort in evaluating potential enhanced surfaces.

The purpose of this paper is to present a unified, straightforward procedure for the presentation of performance data for various enhanced surfaces. Since the focus here is on shell-and-tube exchangers, the major emphasis is placed on tubes which are presently available commercially. In addition to the obvious benefits of a unified presentation format, it will be shown that such a procedure can be helpful in the initial screening of enhanced tubes for a specific application. It should be noted, however, that a comprehensive treatment of Performance Evaluation Criteria is not intended as this has been done recently [2, 3]. It will also facilitate the introduction of enhanced performance data into digital computer programs which are ultimately used to design most shell-and-tube heat exchangers.

Although shell-and-tube heat exchangers are used in a broad range of applications – including those which involve condensation, boiling, and multiphase flow – only single-phase Newtonian fluids will be considered in this paper. This somewhat arbitrary restriction was imposed in order to eliminate a number of complications which can arise in multiphase flows. However, it is anticipated that the concepts outlined in this paper will provide the basis for logical extension to more complex flow situations.

The limitation to enhanced tubes used in shell-and-tube exchangers suggests two important restrictions. First, the maximum outside diameter of any tube is less than that of the tube holes in the tube sheets. This constraint is a consequence of the common procedure in the fabrication and repair of shell-and-tube heat exchangers of inserting or pulling the tubes through the tube holes in the tube sheets. Enhanced tubes typically have plain-end sections so that they can be fastened securely to the tube sheets by rolling and/or welding. Second, the layouts considered here will be limited to those specified by TEMA [Tubular Exchanger Manufacturers Association, Tarrytown, New York], i.e., equilateral triangular, rotated triangular, square, and rotated square layouts which correspond to layout angles of $\alpha = 30$, 60, 90, and 45 deg, respectively.

Commercially Available Enhanced Tubes

Current classification schemes identify more than a dozen techniques to augment or enhance convective heat transfer [4]. Of interest to shell-and-tube heat exchangers with single-phase flows are the tubes with modified surfaces or inserts. While the origins of "enhanced" tubes are rather obscure, a "corrugated" tube was in use over 60 years ago [5]. For purposes of discussion, it is convenient to identify tubes with

---

Contributed by the Heat Transfer Division and presented at the 20th ASME/AIChE National Heat Transfer Conference, Milwaukee, Wisconsin, August 2-5, 1981. Manuscript received by the Heat Transfer Division November 2, 1981.

Table 1 Representative manufacturers and sources of data for enhanced tubes

Manufacturer	Trade name or designation	Inside or outside	References for data source
	Surface roughness		
Wolverine	Korodense	I	6–8
Wolverine	S/T Turbo-chil	I	9
Wolverine	S/T Trufin*	I	10
Turbotec	Turbotec	I	11–20
Yorkshire	enhanced	I	21
Yorkshire	Integron*	I	–
Wieland	GEWA*	I	–
Hitachi	circumferential grooved	I	22
Marasei	embossed spiral	I	23
Spirance	spirally enhanced	I	24
	Extended surfaces		
Hitachi	Thermofin	I	–
Noranda	Forge Fin	I	25–33
Noranda	multipassage	I	34–35
Turbotec	Turbotec	O	20
Wolverine	Trufin	O	36–42
Wieland	GEWA	O	43
Yorkshire	Integron	O	44
Anaconda	integral low-fin	O	–
HPTI	Fine Fin	O	–
Southwest Alloy Supply	integral low-fin	O	–
Unifin	LOFIN	O	–
Dunham Bush	Inner-Fin	I	–
Weiland	EWE	I	–
American Standard	Amaclean	I	–
American Standard	Amatran	I	–
	Inserts – Swirl Flow		
Bas-Tex	turbulator	I	–
custom made	twisted-tape	I	45–52
custom made	wire inserts	I	53–55
	Inserts – Mixer		
American Standard	Amaspher	I	–
Intersurface	Generator	I	56
Kenics	Static Mixer	I	33,57–60
Koch	DY	I	33
Ross	Static Mixer	I	61

- Surface roughness
- Extended surfaces
- Inserts which create a swirl flow
- Inserts which "mix" the flow

A representative list of commercially available tubes is given in Table 1. Within each designation, the products are identified as relating to inside (*I*) or outside (*O*) enhancement and sources of heat transfer and pressure drop data are given. It is interesting to note that five countries are represented among the manufacturers.

Nomenclature

A_f = flow area
A_s = surface area
A_{shell} = flow area of empty shell
C_p = specific heat at constant pressure
D = diameter
D_b = bore diameter
F = LMTD correction factor
$F\{\ \}$ = function of { }
g = acceleration due to gravity
G = mass velocity
h = heat transfer coefficient
k = thermal conductivity
L = tube length
LMTD = logarithmic-mean-temperature difference
N_r = number of tube rows
N_t = total number of tubes
p = actual wetted perimeter
P = tube pitch
Q = heat duty
R''_w = tubewell resistance per unit area
R_{fi} = inside fouling resistance
R_{fo} = outside fouling resistance
t_w = tubewell thickness
T = absolute temperature
U_o = overall heat transfer coefficient
W = mass flow rate

Dimensionless Parameters

f = Fanning friction factor
Gr = Grashof number
Gz = Graetz number
j = Colburn j-factor
Nu = Nusselt number
Pr = Prandtl number
Re = Reynolds number
St = Stanton number

Greek Symbols

α = tube field layout angle
β = coefficient of volumetric expansion
Δp = pressure drop
μ = viscosity
ρ = density

Subscripts

b = mean bulk temperature
c = cross flow
i = inside tube
o = outside tube
p = parallel flow
w = wall

Superscript

$\tilde{}$ = envelope diameter basis

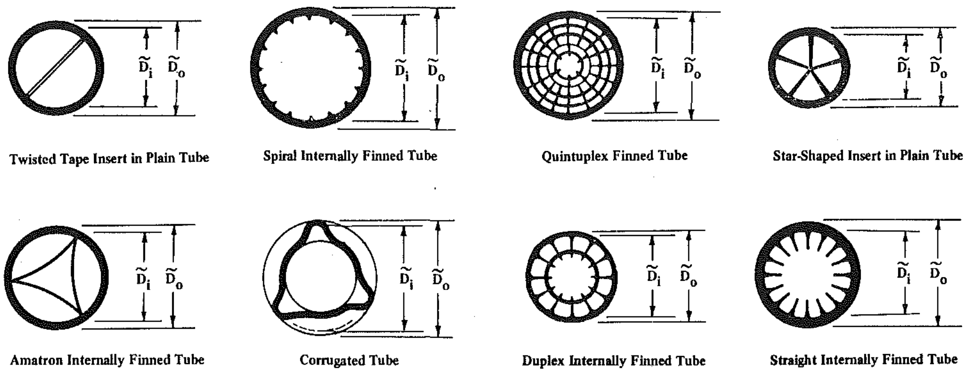

Twisted Tape Insert in Plain Tube

Spiral Internally Finned Tube

Quintuplex Finned Tube

Star-Shaped Insert in Plain Tube

Amatron Internally Finned Tube

Corrugated Tube

Duplex Internally Finned Tube

Straight Internally Finned Tube

Fig. 1 Representative commercially available tubes with internal enhancement

In addition to the commercially available tubes mentioned in Table 1, there is another type of enhancement which is of considerable interest for shell-and-tube exchangers, i.e., twisted-tape inserts. These devices are used inside tubes, frequently as a fix to exchangers which have been underdesigned. However, since they are so easy to make, most shops manufacture their own. Thus, those studies carried out with noncommercial twisted-tape inserts are also listed in Table 1. Three studies dealing with custom-made wire-coil inserts to enhance tubeside heat transfer may be of interest, and these are included in Table 1 as well.

Cross sections of eight commerically available tubes with internal enhancement are shown in Fig. 1 and two with external enhancement are shown in Fig. 2. These figures illustrate a few of the many enhanced tubes which are available commercially. It should be noted that some tubes, such as the corrugated tube shown in Fig. 2, have enhancement on both sides. In Figs. 1 and 2 each tube is identified by name and the inside and outside "smooth tube envelope" diameters are shown for each cross section. These diameters are defined as follows:

- $\tilde{D}_i$, maximum inside diameter for inside enhancement
- $\tilde{D}_o$, maximum outside diameter for outside enhancement

In this paper the superscript ˜ is used to designate quantities based on the envelope diameter, and the subscripts i and o denote inside and outside, respectively. In case there is no enhancement on one side of the tube, the envelope diameter is simply the plain tube diameter. The envelope diameter concept will be discussed more fully in the following section.

Presentation Format

For a shell-and-tube heat exchanger, the heat duty may be calculated by

$$Q = A_o U_o F \,\mathrm{LMTD} \tag{1}$$

where the overall heat transfer coefficient, U_o, based on the outside area, A_o, is given by

$$1/U_oA_o = 1/h_iA_i + R_w'' + 1/h_oA_o + R_{fi}/A_i + R_{fo}/A_o \tag{2}$$

Although the designer must have a knowledge of each term in equation 2, the inside and outside heat transfer coefficients, h_i and h_o, are of primary interest here. Unless fouling is being studied, the fouling resistances, R_{fi} and R_{fo}, given here in units of m^2K/W, are generally assumed to be negligible when obtaining performance data. The wall resistance per unit area, R_w'', is usually quite small in comparison to the convective resistances, but some attention needs to be devoted to this term. In addition to h_i and h_o, the pressure drop performance is also of considerable importance in this study.

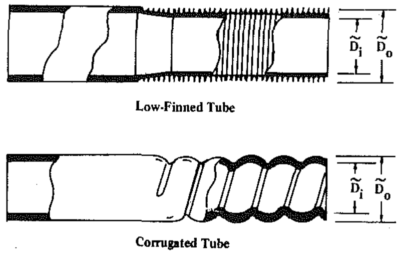

Low-Finned Tube

Corrugated Tube

Fig. 2 Representative commercially available tubes with external enhancement

The basic performance data – for the sources cited in Table 1 as well as for noncommercial tube references in the literature – are presented in many different ways. Consider Table 2, where six tubeside enhancement references have been selected to illustrate this point. In Table 2, the pressure drop data are presented in three different ways and the heat transfer data in six different ways. Both dimensional and dimensionless formats are used. The Reynolds and Nusselt numbers are calculated using five different diameters as the characteristic length. The flow area, which appears in the mass velocity and, hence, the friction factor and Reynolds number, is computed using either the actual value, or on the basis of the envelope, bore (minimum), or volumetric diameter. Finally, the surface area in Table 2, which is used as the basis for evaluating the heat transfer coefficient, is computed in five different ways. Thus, from just these limited references, it is clear that performance data for enhanced tubes are presented in many different ways in the literature. In general, the designer is faced with the unnecessary task of recasting the data from several different sources to a common form, *prior* to assessing the potential of the augmented tubes for a given application. Unfortunately, this job is frequently compounded by undefined parameters and incomplete information in the literature references.

Thus, it has been shown that standardization of the presentation format is highly desirable. While such a procedure is not absolutely essential, as long as the data treatment is complete and well defined, much confusion could be avoided and time saved if a uniform format were established and used. Although there are a number of logical choices available, the envelope diameter format is proposed here. This approach is based on simple, well-defined inside and outside characteristic diameters, $\tilde{D}_i$ and $\tilde{D}_o$, which are used to calculate all necessary parameters and dimensionless groups. In addition, this format permits a direct comparison of the performance of the augmented tube with that of the plain tube occupying the same space in the exchanger.

As a typical example, consider the corrugated tube which is

Table 2 **Format for presentation of tubeside performance data for selected enhanced tubes**

Reference	Type of enhancement	Presentation format	Diameter	Flow area	Surface area
Watkinson, Miletti, and Kubanek [30]	Internally finned tubes	f versus Re $F\{\mathrm{Nu}\}$ versus Re	Envelope and effective	Actual	Envelope and effective
Solimon and Feingold [35]	Internally finned tube Quintuplex tube	Δp versus W Q versus W	---	---	---
Carnavos [31]	Internally finned tubes	f versus Re $F\{\mathrm{Nu}\}$ versus Re	Hydraulic	Actual	Actual
Marner and Bergles [33]	Internally finned tubes Static-mixer inserts Twisted-tape inserts	f versus Re Nu versus Re Nu versus F{Gz}	Envelope	Envelope and actual	Envelope
Rozalowski and Gater [62]	Corugated tube	$F\{f\}$ versus Re $F\{\mathrm{Nu}\}$ versus F{Gz}	Bore	Bore	Bore
Dipprey and Sabersky [63]	Artificial roughness	f versus Re St versus Re	Volumetric	Volumetric	Volumetric

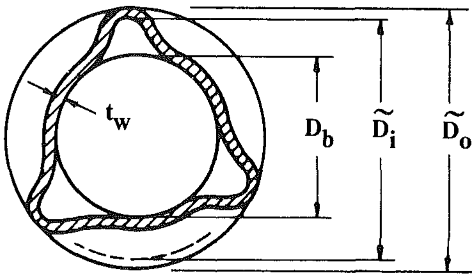

Fig. 3 Sketch of the corrugated tube showing reference diameters

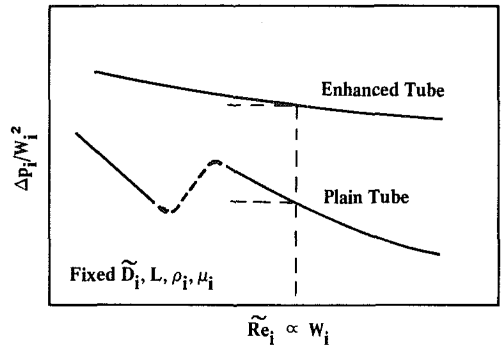

Fig. 4 Interpretation of standard friction factor log-log plot according to the envelope diameter format

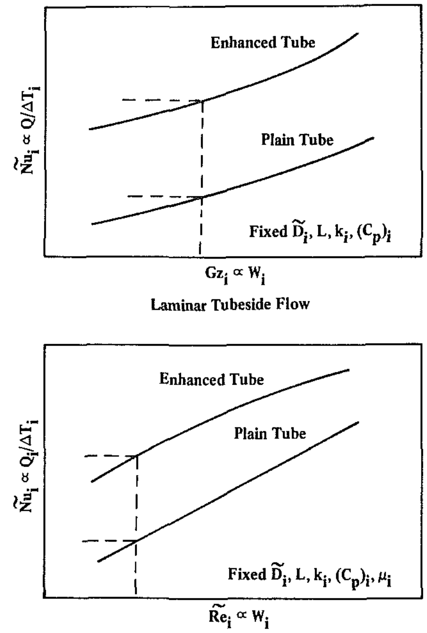

Fig. 5 Interpretation of standard Nusselt number log-log plots according to the envelope diameter format

commercially available. The cross-sectional sketch shown in Fig. 3 defines the inside envelope diameter, $\tilde{D}_i$, the outside envelope diameter, $\tilde{D}_o$, and the bore diameter, D_b. Also shown in Fig. 3 is the tube wall thickness, t_w. The actual space occupied by the corrugated tube is, of course, determined by the maximum outside diameter; however, only an internal dimension can characterize the internal thermal-hydraulics. In any event, the wall thicknesses of enhanced and smooth tubes are usually quite similar so that the true envelopes are essentially the same.

Tubeside Flow. Tubeside data for enhanced tubes are almost always obtained in single tubes. The most commonly used thermal boundary conditions are constant wall heat flux and constant wall temperature. In general, laminar flow heat transfer coefficients are highly sensitive to the thermal boundary conditions and to the thermal and hydrodynamic entry lengths. Consequently, laminar flow Nusselt numbers are characterized by the L/D_i ratio, either explicitly in the parameter $(L/D_i)/\mathrm{Re}_i\mathrm{Pr}_i$ or implicitly in the Graetz number, $\mathrm{Gz}_i = W_i(C_p)_i/k_iL$. For design purposes, it is customary to present the mean Nusselt number versus Gz_i or a function of the Graetz number, $F\{\mathrm{Gz}_i\}$. On the other hand, tubeside tubulent flow heat transfer coefficients have very short entry lengths and, except for liquid metals, are insensitive to the type of thermal boundary condition. Therefore, local heat transfer coefficients are usually measured for tubulent flow and the results presented in the form of $\mathrm{Nu}_i/\mathrm{Pr}_i^a$ versus Re_i, where a is often chosen to be 0.4 and the relationship is generally log-linear. Neither the Pr-exponent or the shape of the plain curve is critical, however, since any comparison between enhanced and plain curves will be made at constant Re and Pr. The transitional flow regime – generally taken to cover the Reynolds number range between about 2000 and 10,000 – is an ill-defined combination of laminar and turbulent flow which may be handled by prorating procedures.

The sketches shown in Figs. 4 and 5 pertaining to the im-

Table 3 Parameters for tubeside and shellside flow

Parameters	Tubeside flow	Shellside crossflow	Shellside parallel flow
Envelope diameter	$\tilde{D}_i$	$\tilde{D}_o$	$\tilde{D}_o$
Tube length	L	L	L
Total number of tubes	--	N_t	N_t
Number of tube rows	--	N_r	--
Tube pitch	--	P	P
Tubefield layout angle	--	α	α
Flow area	$\tilde{A}_{fi} = \pi \tilde{D}_i^2/4$	$(\tilde{A}_f)_{oc} = (N_t/N_r)L(P-\tilde{D}_o)$	$(\tilde{A}_f)_{op} = A_{\text{shell}} - N_t \pi \tilde{D}_o^2/4$
Mass velocity	$\tilde{G}_i = W_i/\tilde{A}_{fi}$	$\tilde{G}_{oc} = W_o/(\tilde{A}_f)_{oc}$	$\tilde{G}_{op} = W_o/(\tilde{A}_f)_{op}$
Reynolds number	$\widetilde{\mathrm{Re}}_i = \tilde{G}_i \tilde{D}_i/\mu_i$	$\widetilde{\mathrm{Re}}_{oc} = \tilde{G}_{oc}\tilde{D}_o/\mu_o$	$\widetilde{\mathrm{Re}}_{op} = \tilde{G}_{op}\tilde{D}_o/\mu_o$
Fanning friction factor	$\tilde{f}_i = \rho_i \Delta p_i (\tilde{D}_i/L)/2\mathrm{d}\tilde{G}_i^2$	$\tilde{f}_{oc} = \rho_o (\Delta p_{oc}/N_r)/2\tilde{G}_{oc}^2$	$\tilde{f}_{op} = \rho_o \Delta p_{op} (\tilde{D}_o/L)/2\tilde{G}_{op}^2$
Prandtl number	$\mathrm{Pr}_i = (C_p)_i \mu_i/k_i$	$\mathrm{Pr}_o = (C_p)_o \mu_o/k_o$	$\mathrm{Pr}_o - (C_p)_o \mu_o/k_o$
Grashof number	$\widetilde{\mathrm{Gr}}_i = \rho_i^2 g \beta_i \lvert T_{wi} - T_{bi} \rvert \tilde{D}_i^2/\mu_i^2$	$\widetilde{\mathrm{Gr}}_o = \rho_o^2 g \beta_o \lvert T_{wo} - T_{bo} \rvert \tilde{D}_o^3/\mu_o^2$	$\widetilde{\mathrm{Gr}}_o = \rho_o^2 g \beta_o \lvert T_{wo} - T_{bo} \rvert \tilde{D}_o^3/\mu_o^2$
Viscosity ratio (liquids)	μ_{bi}/μ_{wi}	$\mu_{bo} \mid \mu_{wo}$	μ_{bo}/μ_{wo}
Temperature ratio (gases)	T_{bi}/T_{wi}	$T_{bo} \mid T_{wo}$	T_{bo}/T_{wo}
Average wall temperature	T_{wi}	T_{wo}	T_{wo}
Surface area	$\tilde{A}_{si} = \pi \tilde{D} iL$	$\tilde{A}_{so} = N_t \tilde{D}_o L$	$\tilde{A}_{so} = N_t \pi \tilde{D}_o L$
Nusselt number	$\widetilde{\mathrm{Nu}}_i = \tilde{h}_i \tilde{D}_i/k_i$	--	
Colburn *j*-factor	--	$\tilde{j}_{oc} = (\tilde{h}_{oc}/(C_p)_o \tilde{G}_{oc})\mathrm{Pr}_o^{2/3}$	$\tilde{j}_{op} = (\tilde{h}_{op}/C_p)_o (\tilde{G}_{op}^2)\mathrm{Pr}_o^{2/3}$
Actual flow area	A_{fi}	$(A_f)_{oc}$	$(A_f)_{op} = (\tilde{A}_f)_{op}$
Actual wetted perimeter	p_i	--	--
Actual surface area	$A_{si} = p_i L$	$A_{so} = N_t (A_o/L)L$	$A_{so} = N_t (A_o/L)L$

portant area of internal, single-phase, forced convection flow, demonstrate the pressure drop and heat transfer considerations. Figure 4 indicates that by fixing the envelope, i.e., both $\tilde{D}_i$ and L, a vertical line on the $\tilde{f}_i$ versus $\widetilde{\mathrm{Re}}_i$ curve will give the augmented pressure drop relative to the plain tube pressure drop at the same flow rate.[1] Fluid properties and temperature-gradient effects, if any, are assumed to be the same for both tubes. It should be noted that the frictional transition from laminar to turbulent flow is typically much smoother in enhanced tubes than in plain tubes as shown in Fig. 4. Similarly, the relative $Q_i/\Delta T_i$ comparisons are given in Fig. 5. For laminar flow, ΔT_i may be the logarithmic or arithmetic mean value over the entire tube length, while for turbulent flow the usual practice is to report "fully developed" values since the developing length is much shorter than in laminar flow. Three points should be made about this presentation scheme:

1. The intercepts at constant W_i do not, with the exception of Fig. 5, give the performance of one augmented tube relative to another unless the envelope diameters are identical.
2. The envelope diameter basis may not be the best way to *correlate* data; for example, bore diameter or hydraulic diameter may be a more significant dimension.
3. While this format leads to a Performance Evaluation Criterion (No. 1 in [2] and [3]), there are many other possible criteria, depending on the problem constraints.

A complete description of the tubeside parameters for the proposed format is given in Table 3. This information is essentially self-explanatory, but a few points will be emphasized here. All parameters are based on the inside envelope diameter, $\tilde{D}_i$, unless otherwise noted. All properties are evaluated at the arithmetic mean bulk temperature between inlet and outlet, T_{bi}, unless specified otherwise. Corrections for the effect of variable properties may be then made in terms of the viscosity ratio for liquids and the absolute temperature ratio for gases. For example, it is expected that the pressure drop data will usually be taken under isothermal conditions. In general, the Grashof number will be important only for laminar flow conditions. Finally, it should be noted that the Graetz number, which is widely used in reporting laminar flow results, may be calculated as

$$\mathrm{Gz}_i = W_i (C_p)_i / k_i L = (\pi/4)\widetilde{\mathrm{Re}}_i \mathrm{Pr}_i (\tilde{D}_i/L) \quad (3)$$

Note that although both Re_i and $\tilde{D}_i$ are based on the envelope diameter, the Graetz number Gz_i is expressed only in terms of actual variables.

A very important aspect of the proposed format is that in addition to presenting all parameters in terms of $\tilde{D}_i$, it must also be possible for the individual investigator to recast these parameters in terms of any possible combination of characteristic length, heat transfer surface area, and flow area. Therefore, it is essential that each tube geometry be characterized completely. Thus, the actual inside surface area, actual inside flow area, and actual inside perimeter must also be given for each tube. Finally, a scaled drawing or a photograph of a typical cross section will, in many cases, be a valuable aid in helping to interpret the tube geometry.

Shellside Flow. In contrast to tubeside flow, which in heat exchanger terminology is unmixed, the shellside flow is much more complicated. In a baffled exchanger, the flow consists of contributions from both crossflow and parallel, or longitudinal, flow. Although these two components will be handled separately here, it should be understood that in general a stream analysis method [64, 65] must be applied to carry out a rigorous shellside thermal-hydraulic design. Such procedures almost always require the aid of a digital computer.

Low-finned tubes were among the first of the enhanced heat transfer devices to become popular in shell-and-tube heat exchangers. As might be expected, low-finned tube data have been presented in many different formats. For example, the following diameters have been used in the literature as characteristic lengths: root, fin, hydraulic, volumetric hydraulic, modified hydraulic, and plain-end diameters. Data for low-finned tubes have been reported in the literature for the following cases [36–44]:

1. Specific baffled shell-and-tube exchangers
2. Crossflow in ideal tubebanks
3. Longitudinal flow over a single tube inside a smooth annulus

Of the references cited above, only that of Obermeier and

---

[1] Frictional pressure drop only is considered here. Entrance and exit losses and pressure variation due to momentum change must be considered on an individual basis.

Schaber [43] falls in category 3, and there are apparently no data available in the literature for parallel flow over a bundle of low-finned tubes. Several sets of crossflow data have been obtained for ideal tube banks using low-finned tubes. The recent paper by Rabas, Eckels, and Sabatino [38] provides an excellent summary of the work done in this area and presents correlations for both pressure drop and heat transfer over a broad range of parameters. Their treatment uses the root diameter as the characteristic length.

Very limited data have been obtained for longitudinal flow over bundles of fuel elements in nuclear reactors. However, in the nuclear industry, data for gas-cooled reactors, which have artificially roughened fuel element rods, are generally obtained using a single tube inside a smooth circular tube. Various transformations are available which then allow one to transform these single-tube results so that they are applicable to longitudinal flow in actual tube bundles. One of the earliest, and best known, of these transformations was formulated by Hall [66] in 1962. Since then, a number of additional transformations have been developed, and these methods are summarized and discussed in detail by Dalle Donne and Meyer [67]. In view of the difficulty in obtaining longitudinal pressure drop and heat transfer data in bundles of tubes, it is suggested that greater emphasis be placed on obtaining such data using individual enhanced tubes as described above. Such an approach should be especially useful for screening potential tubes for a specific application.

In Fig. 6, pressure drop and heat transfer data for low-finned tubes, taken from Ward [39], are used to illustrate the proposed presentation format for shellside crossflow. The results are plotted in the form of $\tilde{f}_{oc}$ versus $\widetilde{\mathrm{Re}}_{oc}$ and $\tilde{j}_{oc}$ versus $\widetilde{\mathrm{Re}}_{oc}$ with all parameters calculated on the basis of the outside envelope diameter, $\tilde{D}_o$. Data are presented for plain tubes and low-finned tubes with 0.446 fins/mm and 0.768 fins/mm, all with a nominal envelope diameter of $\tilde{D}_o = 19.05$ mm, layout angle of $\alpha = 30$ deg, and pitch ratio of $P/D = 1.25$. A quick inspection of Fig. 6 indicates that of the three tube bundles, the low-finned tubes with 0.446 fins/mm clearly have the superior heat transfer versus pressure drop performance.

The proposed shellside presentation format is summarized in Table 3 and consists of both crossflow and parallel flow. In the latter case, Table 3 is applicable to either a single tube or a tube bundle. In Table 3 all properties are evaluated at the arithmetic mean bulk temperature between inlet and outlet, T_{bo}, unless otherwise specified. In all cases the outside envelope diameter, $\tilde{D}_o$, is recommended as the basis for calculating the thermal-hydraulic characteristics. As was emphasized in the case of tubeside flow, the envelope diameter may not be the best characteristic length for correlation purposes. Therefore, it is essential that sufficient information be provided to calculate any characteristic length, minimum flow area, and heat transfer surface area desired as described in Table 3.

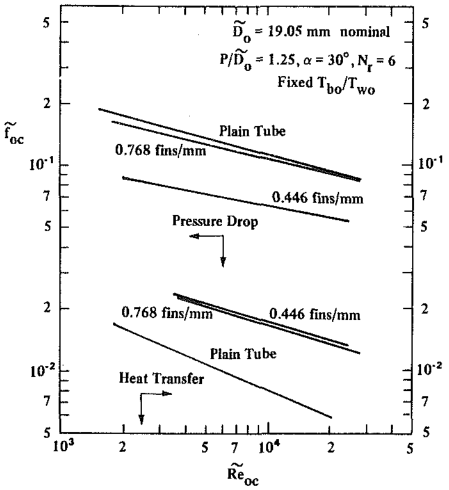

Fig. 6 Crossflow performance data from Ward [39] for low-finned tube bundles in envelope diameter format

Table 4 Tubewall parameters

Parameter	Definition of notation
Material	– –
Thermal conductivity	k_w
Actual tubewall thickness	t_w
Approximate tubewall resistance	$R''_w = t_w / A_{sw} k_w$
Inside dimensions required to completely characterize the tube	For example, for an internally finned tube with spiral fins the following parameters must be specified: • fin height • fin thickness • number of fins • fin pitch • fin efficiency • scale drawing or photograph of the fin contour
Outside dimensions required to completely characterize the tube	For example, for a low-finned tube the following parameters must be specified: • fin height • fin thickness • fins per unit length • fin efficiency • scale drawing or a photograph of the fin contour

Tubewall Parameters. Some mention must be made of the tubewall resistance, R''_w, which appears in equation 2. If either the inside or outside wall has extended surfaces (fins) attached to it, further details must be provided in order to completely define the geometry. In particular, as the heat transfer coefficient increases, the fin height increases, or the fin thermal conductivity decreases, the fin efficiency decreases and must be taken into consideration. In those situations where the fin efficiency becomes important, it is recommended that the data be corrected and presented on the basis of 100 percent fin efficiency. The most comprehensive recent treatment of fin efficiency is given by Kern and Kraus [68].

The required tube wall parameters are specified in Table 4. By treating the extended surfaces through the fin efficiency, the calculation of the tubewall resistance, R''_w, may be summarized as follows

$$R''_w = \ln(\tilde{D}_o/\tilde{D}_i)/2\pi k_w L \quad \text{(circular cross sections)} \tag{4}$$

$$R''_w = t_w / A_{sw} k_w \quad \text{(noncircular cross sections)} \tag{5}$$

where A_{sw} is the mean tubewall surface area. In general, the tubewall resistance will be quite small in comparison to the convective resistance.

Concluding Remarks

A systematic procedure for the presentation of performance data for enhanced tubes used in shell-and-tube heat exchangers has been proposed. This approach is based on the use of the inside and outside envelope diameters of the tube to evaluate all the required flow and heat transfer parameters. In addition, the procedure requires that sufficient geometric parameters be provided so that the envelope-based parameters can be recast into any form desired for purposes of comparison, correlation, and evaluation. Although the proposed procedure is based on single-phase flow, the concepts set forth in this paper should provide the basis for extension to multiphase systems.

It is recommended that tubeside pressure drop data be presented in the form of $\tilde{f}_i$ versus $\widetilde{\mathrm{Re}}_i$. Tubeside heat transfer data should be plotted as $\widetilde{\mathrm{Nu}}_i$ versus Gz_i for laminar flow and $\widetilde{\mathrm{Nu}}_i/\mathrm{Pr}_i^{0.4}$ versus $\widetilde{\mathrm{Re}}_i$ for turbulent flow. For outside enhancement it is proposed that the data be presented in the form of $\tilde{f}_o$ versus $\widetilde{\mathrm{Re}}_o$ and $\tilde{j}_o$ versus $\widetilde{\mathrm{Re}}_o$ for both crossflow and parallel flow.

The adoption of the proposed format would achieve at least four important objectives: (*i*) confusion could be avoided, (*ii*) time could be saved, (*iii*) initial screening of enhanced tubes could be carried out easily, and (*iv*) new enhanced tube data could easily be input into existing computer programs.

Finally, although performance data for a number of commercially available enhanced tubes have been reported in the literature, additional data are badly needed in several areas. In particular, data for shellside flow and heat transfer are very limited, especially for parallel flow where data are virtually nonexistent.

References

1 Junkhan, G. H., Bergles, A. E., and Webb, R. L., "Research Workshop on Energy Conservation Through Enhanced Heat Transfer," Report HTL-21, ISU-ERI-Ames-80063, COO-4649-8, Engineering Research Institute, Iowa State University, Oct. 1979.

2 Webb, R. L., "Performance Evaluation Criteria for Use of Enhanced Heat Exchanger Surfaces in Heat Exchanger Design," *International Journal of Heat and Mass Transfer*, Vol. 24, 1981, pp. 715–726.

3 Webb, R. L., and Bergles, A. E., "Performance Evaluation Criteria for Selection of Heat Transfer Surface Geometries Used in Low Reynolds Number Heat Exchangers," *Low Reynolds Number Convection in Channels and Bundles*, edited by S. Kakac, R. H. Shah, and A. E. Bergles, Hemisphere, Washington, D. C., 1982.

4 Bergles, A. E., Webb, R. L., Junkhan, G. H., and Jensen, M. K., "Bibliography on Augmentation of Convective Heat and Mass Transfer," Report HTL-19, ISU-ERI-Ames-79206, COO-4649-6, Engineering Research Institute, Iowa State University, May 1979.

5 Alberger Heater Company, Catalog No. 3, Buffalo, New York, 1921.

6 Young, E. H., Withers, J. G., and Lampert, W. B., "Heat Transfer Characteristics of Corrugated Tubes in Steam Condensing Applications," AIChE Preprint 3 for 15th National Heat Transfer Conference, San Francisco, 1975.

7 Withers, J. G., and Young, E. H., "Investigation of Steam Condensation on Vertical Rows of Horizontal Corrugated and Plain Tubes," Presented at Office of Saline Water Symposium on Enhanced Tubes for Desalination Plants, Mar. 1969.

8 Withers, J. G., "Tube-Side Heat Transfer and Pressure Drop for Tubes Having Helical Internal Ridging With Turbulent/Transitional Flow of Single-Phase Fluid, Part 1: Single Helix Ridging," *Heat Transfer Engineering*, Vol. 2, No. 1, 1980, pp. 48–58.

9 Withers, J. G., "Tube-Side Heat Transfer and Pressure Drop for Tubes Having Helical Internal Ridging With Turbulent/Transitional Flow of Single-Phase Fluid, Part 2: Multiple-Helix Ridging," *Heat Transfer Engineering*, Vol. 2, No. 2, 1980, pp. 43–50.

10 Katz, D. L., Beatty, K. O. Jr., and Foust, A. S., "Heat Transfer Through Tubes With Integral Spiral Fins," ASME Transactions, Vol. 68, 1945, pp. 665–674.

11 Blumenkrantz, A., and Taborek, J., "Heat Transfer and Pressure Drop Characteristics of Turbotec Spirally Grooved Tubes in the Turbulent Regime," Heat Transfer Research Inc., Report 2439-300-7, 1970.

12 Blumenkrantz, A. R., and Taborek, J., "Heat Transfer and Pressure Drop Performance of Turbotec Spirally-Grooved Tube in the Laminar and Transition Regime," Heat Transfer Research Inc., Report 2439-300-8, 1971.

13 Watkinson, A. P., and Martinez, O., "Scaling of Spirally Indented Heat Exchanger Tubes," ASME Journal of Heat Transfer, Vol. 97, 1975, pp. 490–492.

14 Bergles, A. E., Brown, G. S. Jr., Lee, R. A., Simonds, R. R., and Snider, G. S., "Investigation of Heat Transfer Augmentation Through Use of Internally Finned and Roughened Tubes (Final Report), Massachusetts Institute of Technology Engineering Laboratory, Report No. 70790-69, 1969.

15 Palen, J., Cham, B., and Taborek, J., "Comparison of Condensation of Steam on Plain and Turbotec Spirally Grooved Tubes in a Baffled Shell-and-Tube Condenser," Heat Transfer Research Inc., Report 2439-300-6, 1971.

16 Marto, P. J., Reilly, R. J., and Fenner, J. H., "An Experimental Comparison of Enhanced Heat Transfer Condenser Tubing," *Advances in Enhanced Heat Transfer*, ASME, New York, 1979. pp. 1–9.

17 Ciftci, H., "An Experimental Study of Filmwise Condensation on Horizontal Enhanced Condenser Tubing," M. S. thesis in Mechanical Engineering, U.S. Naval Postgraduate School, Dec. 1979.

18 Bergles, A. E., "Heat Transfer Characteristics of Turbotec Tubing," Report HTL-24, ISU-ERI-Ames-81070, Engineering Research Institute, Iowa State University, June 1980.

19 Genetti, W. E., and Everly, D., "Heat Transfer From Spiral Tubing in an Air Fluidized Bed," *71st Annual Meeting AIChE, Miami Beach, Nov. 1978.*

20 Maeda Iron Works Co. Ltd., Yoshida, Nagano-Ken, Japan, "Turbotec Spiral Tube Used in Heat Transfer—Technical Data," Apr. 1, 1975.

21 Cunningham, J., and Milne, H. K., "The Effect of Helix Angle on the Performance of Roped Tubes," *Heat Transfer 1978*, Vol. 2, Hemisphere, Washington, D.C., 1978, pp. 601–605.

22 Hitachi Mechanical Engineering Research Laboratory, Tschiura-Chi, Japan, Special Research Report 73823-4-1, Oct. 15, 1974.

23 Yoshitomi, H., Oba, K., and Arima, Y., "Heat Transfer and Pressure Drop in Tubes with Embossed Spiral," *Karyoku Genshiroyoku Hatsuden*, Vol. 27, 1976, pp. 171–182.

24 Mehta, M. H., and Rao, M. R., "Heat Transfer and Frictional Characteristics of Spirally Enhanced Tubes for Horizontal Condenser," *Advances in Enhanced Heat Transfer*, ASME, New York, 1979, pp. 11–21.

25 Bergles, A. E., Brown, G. S., Jr., and Snider, W. D., "Heat Transfer Performance of Internally Finned Tubes," ASME Paper No. 71-HT-31, 1971.

26 Carnavos, T. C., "Cooling Air in Turbulent Flow With Internally Finned Tubes," *Heat Transfer Engineering*, Vol. 1, No. 2, 1979, pp. 41–46.

27 Russell, J. R., and Carnavos, T. C., "An Experimental Study: Cooling Air in Turbulent Flow With Internally Finned Tubes," *Chemical Engineering Progress*, Vol. 73, No. 2, 1977, pp. 84–88.

28 Watkinson, A. P., Miletti, D. L., and Tarassof, P., "Turbulent Heat Transfer and Pressure Drop in Internally Finned Tubes," *AIChE Symposium Series*, Vol. 69, No. 131, 1973, pp. 94–103.

29 Watkinson, A. P., Miletti, D. L., and Kubanek, G. R., "Heat Transfer and Pressure Drop of Forge-Fin Tubes in Laminar Oil Flow," Noranda Research Center, Pointe Claire, Quebec, Internal Report No. 303, Apr. 1974.

30 Watkinson, A. P., Miletti, D. L., and Kubanek, G. R., "Heat Transfer and Pressure Drop of Internally Finned Tubes in Laminar Oil Flow," ASME Paper No. 75-HT-41, 1975.

31 Carnavos, T. C., "Heat Transfer Performance of Internally Finned Tubes in Turbulent Flow," *Advances in Enhanced Heat Transfer*, ASME, New York, 1979, pp. 61–67.

32 Webb, R. L., and Scott, M. J., "A Parametric Analysis of the Performance of Internally Finned Tubes for Heat Exchanger Application," ASME Journal of Heat Transfer, Vol. 102, 1980, pp. 38–43.

33 Marner, W. J., and Bergles, A. E., "Augmentation of Tubeside Laminar Flow Heat Transfer by Means of Twisted-Tape Inserts, Static-Mixer Inserts, and Internally Finned Tubes," *Heat Transfer 1978*, Vol. 2, Hemisphere, Washington, D.C., 1978, pp. 583–588.

34 Carnavos, T. C., "Cooling Air in Turbulent Flow with Multipassage Internally Finned Tubes," ASME Paper No. 78-WA/HT-52, 1978.

35 Soliman, H. M., and Feingold, A., "Heat Transfer, Pressure Drop, and Performance Evaluation of a Quintuplex Internally Finned Tube," ASME Paper No. 77-HT-46, 1977.

36 Briggs, D., Katz, D. L., and Young, E. H., "How to Design Finned-Tube Heat Exchangers," *Chemical Engineering Progress*, Vol. 59, No. 11, 1963, pp. 49–59.

37 Briggs, D. E., and Young, E. H., "Convection Heat Transfer and Pressure Drop of Air Flowing Across Triangular Pitch Banks of Finned Tubes," *Chemical Engineering Progress Symposium Series*, Vol. 41, No. 59, 1963, pp. 1–10.

38 Rabas, T. J., Eckels, P. W., and Sabatino, R. A., "The Effect of Fin Density on the Heat Transfer and Pressure Drop Performance of Low-Finned Tube Banks," ASME Paper No. 80-HT-97, 1980.

39 Ward, D. J., "Heat Transfer and Pressure Drop of Air in Forced Convection Across Triangular Pitch Banks of Finned Tubes," PhD dissertation, University of Michigan, 1958.

40 Williams, R. B., and Katz, D. L., "Performance of Finned Tubes in Shell-and-Tube Heat Exchangers," ASME *Transactions*, Vol. 74, 1952, pp. 1307–1320.

41 Armstrong, R. M., "Heat-Transfer and Pressure Losses in Small Commercial Shell-and-Finned Tube Heat Exchangers," ASME *Transactions*, Vol. 67, 1945, pp. 675–681.

42 Ward, D. J., and Young, E. H., "Heat Transfer and Pressure Drop of Air in Forced Convection Across Triangular Pitch Banks of Finned Tubes," *Chemical Engineering Progress Symposium Series*, Vol. 55, No. 29, 1959, pp. 37–44.

43 Obermeier, E., and Schaber, A., "Experimental Investigation of Heat Transfer From Transverse Finned Tubes With Longitudinal Flow," *Heat Transfer 1978*, Vol. 2, Hemisphere, Washington, 1978, pp. 613–618.

44 Yorkshire Imperial Metals Limited, Leeds, England, "Design Data for Shell and Tube Heat Exchangers. Integron Low-Fin Tubes."

45 Gambill, W. R., Bundy, R. D., and Wansbrough, R. W., "Heat Transfer, Burnout, and Pressure Drop for Water in Swirl Flow Tubes with Internal Twisted Tapes," *Chemical Engineering Progress Symposium Series*, Vol. 57, No. 32, 1961, pp. 127–137.

46 Gambill, W. R., and Bundy, R. D., "High-Flux Heat Transfer Characteristics of Pure Ethylene Glycol in Axial Swirl Flow," *AIChE Journal*, Vol. 9, 1963, pp. 55–59.

47 Hong, S. W., and Bergles, A. E., "Augmentation of Laminar Flow Heat Transfer in Tubes by Means of Twisted-Tape Inserts," ASME JOURNAL OF HEAT TRANSFER, Vol. 98, 1976, pp. 251-256.

48 Kidd, F. J., Jr., "Heat Transfer and Pressure Drop for Nitrogen Flowing in Tubes Containing Twisted Tapes," *AIChE Journal*, Vol. 15, 1969, pp. 551-585.

49 Klepper, O. H., "Heat Transfer Performance of Short Twisted Tapes," *AIChE Symposium Series*, Vol. 69, No. 31, 1973, pp. 87-93.

50 Lopina, R. F., and Bergles, A. E., "Heat Transfer and Pressure Drop in Generated Swirl Flow of Single-Phase Water," ASME JOURNAL OF HEAT TRANSFER, Vol. 91, 1969, pp. 434-442.

51 Smithberg, E., and Landis, F., "Friction and Forced Convection Heat Transfer Characteristics in Tubes With Twisted Swirl Generators," ASME JOURNAL OF HEAT TRANSFER, Vol. 86, 1964, pp. 39-49.

52 Zozulya, N. V., and Shkuratov., I. Y., "Effects of the Length of a Twisted-Tape Turbulence Promoter and Its Initial Twisting Pitch on Augmenting of Heat Transfer Inside a Tube," *Heat Transfer—Soviet Research*, Vol. 6, No. 6, 1974, pp. 98-100.

53 Nakoka, Z., and Watanabe, A., "Maximum Rate of Heat Transfer With Minimum Loss of Energy," *Proceedings of the 7th International Congress on Refrigeration*, Vol. 3, 1936, pp. 221-245.

54 Sams, E. W., "Heat Transfer and Pressure Drop Characteristics of Wire-Coil Type Turbulence Promoters," TID-7529, Pt. 1, Book 2, Nov. 1957, pp. 390-415.

55 Kumar, P., and Judd, R. L., "Heat Transfer with Coiled Wire Turbulence Promoters," *Canadian Journal of Chemical Engineering*, Vol. 8, 1970, pp. 378-383.

56 Bruenemann, H., and Obering, G. J., "Degree of Mixing and Pressure Drop in Static Mixers of Various Construction," *Chemie-Ingenieur-Technik*, Vol. 43, 1971, pp. 348-354.

57 Sununu, J. H., "Heat Transfer With Static Mixer Systems," Kenics Corporation Technical Report 1002, 1970.

58 Genetti, W. E., and Priebe, S. J., "Heat Transfer With a Static Mixer," AIChE Paper presented at Fourth Joint Chemical Engineering Conference, Vancouver, 1973.

59 Lin, S. T., Fan, L. T., and Azer, N. Z., "Augmentation of Single Phase Convective Heat Transfer with In-Line Static Mixers," *Proceedings of the 1978 Heat Transfer and Fluid Mechanics Institute*, Stanford University Press, 1978, pp. 117-130.

60 Morris, W. D., and Procter, R., "The Effect of Twist Ratio on Forced Convection in the Kenics Static Mixer," *Industrial and Engineering Chemistry, Process Design and Development*, Vol. 16, 1977, pp. 406-411.

61 Van der Meer, T. H., and Hoogendoorn, C. J., "Heat Transfer Coefficients for Viscous Fluids in a Static Mixer," *Chemical Engineering Science*, Vol. 33, 1978, pp. 1277-1282.

62 Rozalowski, G. R., and Gater, R. A., "Pressure Loss and Heat Transfer Characteristics for Highly Viscous Fluid Flow in Convoluted Tubing," ASME Paper No. 75-HT-40, 1975.

63 Dipprey, D. F., and Sabersky, R. H., "Heat and Momentum Transfer in Smooth and Rough Tubes at Various Prandtl Numbers," *International Journal of Heat and Mass Transfer*, Vol. 6, 1963, pp. 329-353.

64 Tinker, T., "Shell Side Characteristics of Shell and Tube Heat Exchangers: A Simplified Rating System for Commercial Heat Exchangers," ASME *Transactions*, Vol. 80, 1958, pp. 36-52.

65 Palen, J. W., and Taborek, J., "Solution of Shell Side Flow Pressure Drop and Heat Transfer by Stream Analysis Method," *Chemical Engineering Progress Symposium Series*, Vol. 65, No. 92, 1969, pp. 53-63.

66 Hall, W. B., "Heat Transfer in Channels Having Rough and Smooth Surfaces," *Journal of Mechanical Engineering Science*, Vol. 4, 1962, pp. 287-291.

67 Dalle Donne, M., and Meyer, L., "Turbulent Convective Heat Transfer from Rough Surfaces with Two-Dimensional Rectangular Ribs," *International Journal of Heat and Mass Transfer*, Vol. 20, 1977, pp. 583-620.

68 Kern, D. Q., and Kraus, A. D., *Extended Surface Heat Transfer*, McGraw-Hill, New York, 1972.

The Thermal Performance of the Wet Surface Plastic Plate Heat Exchanger Used as an Indirect Evaporative Cooler

C. F. Kettleborough
Mem. ASME

C. S. Hsieh

Texas A&M University,
College Station, Texas 77843

A mathematical model of the plate heat exchanger (PHE) cooling unit has been developed and solved using a digital computer. The equations of temperature distribution on each plate in a counterflow PHE cooling unit are derived using an energy balance analysis. The results are presented in the form of numerical values of the "overall effectiveness" of the heat exchanger. Factors affecting the effectiveness of the PHE cooling units have been investigated. The change of temperatures and humidity ratios of the air flows in the heat exchanger are also analyzed. Finally, the high performance of the PHE cooling unit is explained by introducing the concept of "enthalpy potential." This unit is of particular interest as a component in solar-assisted cooling systems.

Introduction

The plate heat exchanger (PHE) unit shown diagrammatically in Fig. 1 can be used as an air conditioning system (both heating and cooling) using thin plastic plates as heat exchange surfaces [1], as shown in Fig. 2. When used for cooling, water is sprayed into the heat exchanger, evaporation of water occurs in the secondary flow of the heat exchanger (the airflow in contact with the wetted sides of the heat exchanger plates, "refrigerant"), while the primary flow of the heat exchanger (the airflow in contact with the unwetted sides of the heat exchanger plates) is cooled without picking up any moisture. The heat exchanger unit is composed of many thin plastic plates of 0.25-mm or less thickness. The plates have small protrusions which promote turbulence in the air and at the same time provide support and spacing of adjacent plates. To avoid the complication of dividing two flows at different temperatures, the crossflow arrangement is used in practice.

Since the late 1960's, the performance and development of the PPHE[1] have been under active research in Australia. It is reported that the PPHE is an effective air cooler having competitive capital cost and significantly lower energy consumption when compared with a conventional vapor-compression system. The electrical power consumption does not exceed 1.0 W/L/s (0.5 W/cfm). Consumed water does not exceed 0.3 L/day/L/s air flow.

Data used to compare the computed results are available from experimental results by Chan [2]. Due to different flow arrangements, comparison of the numerical values is *qualitative* only.

Early work on using the wet-surfaced plate heat exchanger in air conditioning systems was reported by Watt [3]. The plate material is use then was mostly plane sheet metal.

In the late 1960s, Pescod [1] developed a system using plastic sheets as the evaporatively cooled surfaces. Typical PPHE cooling performance can be drawn on a portion of a psychrometric chart shown in Fig. 3. The performance of a simple, direct evaporative (DE) cooler (in which water is evaporated into the airstream to be conditioned) is also shown in the figure for comparison. It may be seen that for a DE cooler, a temperature drop of 10°C is possible in the air flow to be conditioned. A lower temperature of air into the conditioned space can be provided by the PPHE with a 14.4°C temperature drop. According to Pescod's report, the theoretical minimum temperature for the conditioned air is equal to the dew point of the ambient air; the theoretical minimum temperature for a simple DE cooler is equal to the wet bulb temperature of the ambient air.

The cooling performance of a PPHE is given by "the overall effectiveness" defined as

$$\epsilon_w = \frac{t_{hi} - t_{ho}}{t_{hi} - t^*_{ciw}} = \frac{\text{decrease of dry bulb (DB) temperature of the primary flow}}{\text{(primary inlet air DB temperature} - \text{secondary inlet air WB temperature)}} \tag{1}$$

The present study uses fundamental heat transfer theories to investigate the characteristics of the thermal performance of the wetted PPHE used as an indirect evaporative cooler with particular emphasis on studying the factors affecting the thermal performance. For simplicity, only the counterflow case will be considered.

The subscript, w, denotes the heat exchanger is wetted. The value of ϵ_w has been found to remain fairly constant (about 0.85) over the normal range of working conditions. Chan [2] has reported the test results for four types of PPHE; each type has two models – one of them contained plate surfaces chemically treated using colloidal silica and the other used untreated plate surfaces. Surface treatment improves the surface wettability of the plastic plates. The results showed the relationship between effectiveness (ϵ_w) and the velocity of the primary air flow (V_a) is of the form

$$\epsilon_w = \frac{1}{1 + aV_a{}^x} \tag{2}$$

---

[1] Plastic Plate Heat Exchanger

Contributed by the Heat Transfer Division and presented at the ASME Winter Annual Meeting, Washington, D.C., November 15–20, 1981. Manuscript received by the Heat Transfer Division February 22, 1981. Paper No. 81-WA/Sol-11.

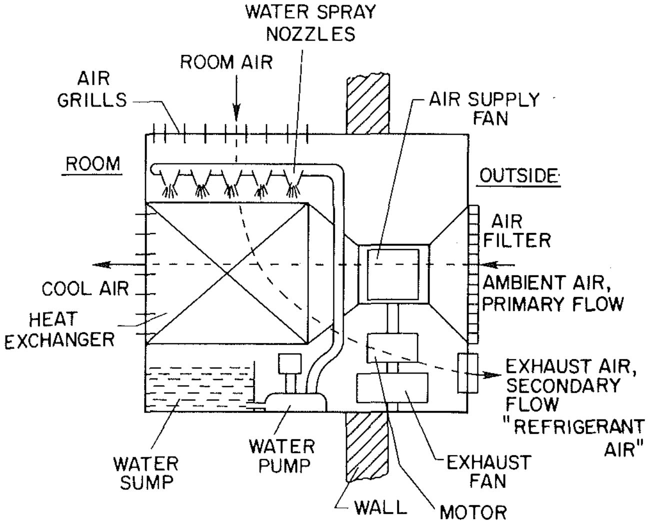

Fig. 1 A schematic diagram of an indirect evaporative cooling unit using a plate-type, crossflow heat exchanger. Although water is recirculated in practice, no water recirculation is considered in the analysis presented in this paper.

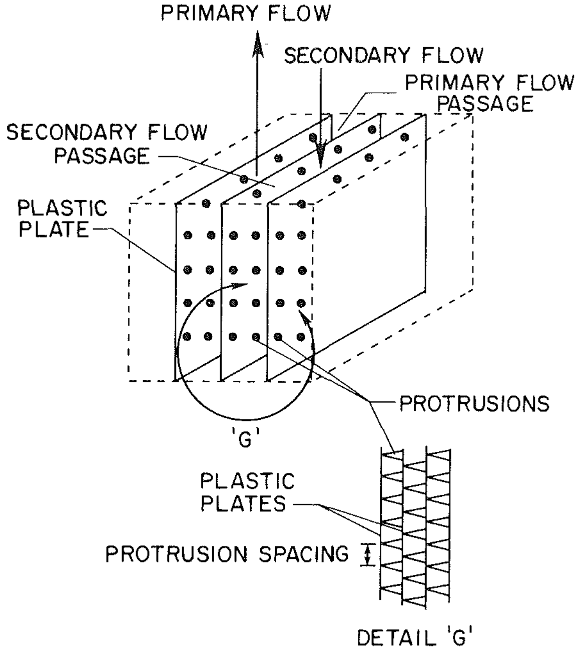

Fig. 2 Details of plastic plate heat exchanger used in the analysis

where a and x are constants. Values of a and x depend on the particular model. The effect of the surface treatment increases the effectiveness by up to 10 percent. In Chan's report, it was concluded that the plate spacings and spike densities have only slight influence on effectiveness. The most recent design of PPHE changes the direction of the refrigerant air flow through the heat exchanger from downwards to upwards [4].

The PPHE with balanced air flows is not normally used because of the need to slightly pressurize the building and reduce infiltration. The secondary air rate is usually made less than the primary rate (the secondary air is obtained from the conditioned space). Experiments have found that the cooling effectiveness is not significantly affected until the flow ratio is reduced below 0.80. In a special case of rooms having a high latent heat load, such as washrooms and kitchens, the exhaust air from the room need not be used and the cooled air from the heat exchanger may be divided, with about half entering the room and the remainder returning through wet passages of the heat exchanger. More than twice the air flow must pass through the primary passages of the heat exchanger, i.e., the flow rate will be less than 0.5. The effectiveness in this case was found to be about 12 percent lower than the system with a flow ratio of 1.00.

Factors affecting cooling performance include air flow rates, surface treatment, air flow ratio, and flow length.

Hollands [5] has carried out an analysis of evaporative cooler pads to study the process of adiabatic humidification. Kreid et al. [6] have proposed a method to correlate the data

Nomenclature

a, a', b, b' = constants
B = plate width, mm
$C_{p,a}$ = specific heat of air, J/kg °C
C_w = specific heat of water, J/kg °C
d = plate thickness, mm
dA = elemental area of plate, m^2
h = sensible heat transfer coefficient (dry) $W/m^2 {}^\circ C$
h^* = sensible heat transfer coefficient (wet) $W/m^2 {}^\circ C$
$\overset{*}{h}_m$ = mass transfer coefficient in wet passage, $kg/m^2 s$
$\overset{*}{H}_a$ = enthalpy of moist air, kJ/kg
H_d = enthalpy of water, kJ/kg
H_d' = enthalpy of water at temperature entering control volume C, kJ/kg
H_{fg} = latent heat of evaporation $(H_g - H_d)$, kJ/kg
H_g = enthalpy of saturated steam at temperature of control volume C, kJ/kg
H_s = enthalpy of water leaving the spray nozzle, kJ/kg
H_w = enthalpy of water at temperature t_w, kJ/kg
L = plate length, mm
L_e = Lewis number $= h^*/\overset{*}{h}_m C_{p,a}$, dimensionless
$\dot{M}_a$ = air mass flow rate (primary flow) in one half of the dry passage, kg/s
$\dot{M}_a^*$ = air mass flow rate (secondary flow) in one half of the wet passage, kg/s
$\dot{M}_d$ = mass flow rate of water leaving control volume C, kg/s
$\dot{M}_d'$ = mass flow rate of water entering control volume C, kg/s
$\dot{M}_e$ = mass rate of evaporation from control volume C into air stream, kg/s
$\dot{M}_s$ = mass flow rate of spray water entering control volume C, kg/s
n_s = spray water rate (times evaporation rate), dimensionless
NTU = dimensionless parameter, $hdA/(\dot{M}_a C_{p,a})$
$\dot{Q}_e$ = heat transfer rate from primary flow to the plate, W
$\dot{Q}_{s,t}$ = total sensible heat transfer to secondary flow, W
$\dot{Q}_{s,u}$ = sensible heat transfer rate from nonwetted surface, W
$\dot{Q}_{s,w}$ = sensible heat transfer rate from wetted surface, W
r = ratio, h^*/h, dimensionless
R = heat capacity rate ratio, $\dot{M}_s C_w/(\dot{M}_a C_{p,a})$, dimensionless
s = plate spacing, mm
t = temperature, °C

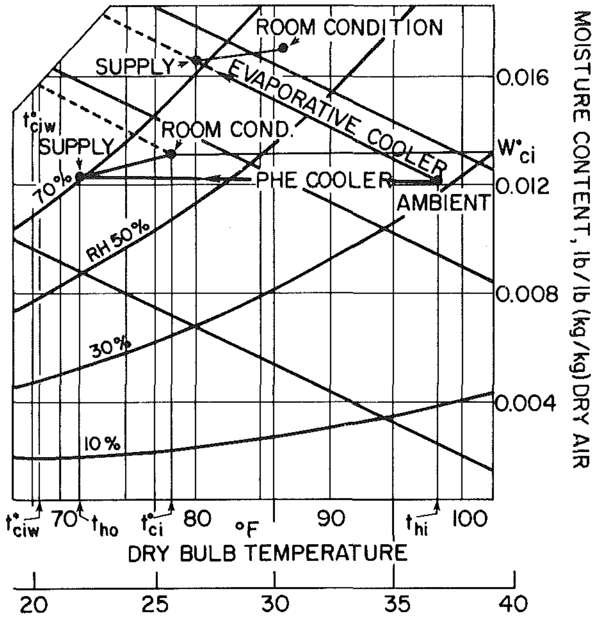

Fig. 3 Psychrometric chart showing performance of direct and indirect evaporative coolers: $t_{hi} = 98°C/36.7°C$, $t_{ho} = 72°F/22.2°C$

of wet surface heat transfer with that of dry surface operation.

More recently, McClaine-Cross and Banks [7] have analyzed this unit. They made their calculations for the whole area of the plate, leading them to use mean values for temperatures and humidity ratios based on entry and exit conditions of the heat exchanger. This caused the secondary flow properties along the flow path to follow a straight line close to the saturation line of the psychrometric chart, while at exit to atmosphere, the air states lies on the saturation line. Another assumption was that the plates were completely wet (wettability is one). Their results are 20 percent higher than the experimental results reported in [1] and [2], whereas the results of the analysis reported here are 8 percent higher than the experimental results. In both cases the analyses treated the counterflow heat exchanger, whereas the experiments were performed on crossflow heat exchanger models.

Theory

Consider a counterflow PPHE with wet surfaces. The front view of a basic heat exchanger unit is shown diagrammatically in Fig. 2.

There are small tapered protrusions, or spikes, on one side of the surfaces of each plate. The extended surface area usually is difficult to determine precisely, and, hence, the projected area of the plate will be used in the analysis.

Air flows in both passages are turbulent over the range of air velocities being used in the application (typical values are 1 to 4 m/s). For air flow in dry passages, tests performed by Pescod [8] determine the heat transfer coefficient, h, is given by

$$h = FV^b \text{W/m}^2\,°\text{C} \qquad (3)$$

Data adapted from Pescod's report show that for protrusion spacing (see Fig. 2) of 13.4 mm, F and b are 49 and 0.6, respectively. For a protrusion spacing of 6.7 mm, F and b are 54 and 0.7, respectively. For air flow in wet passages, heat transfer coefficient data is not available for this application.

Figure 4 shows the control volumes having cross-sectional area, dA, and the water which is covering the area dA at the wet side of the central plate. The heat and mass fluxes entering and leaving the control volumes, C, E (for the primary flow), and F, (for the secondary flow) are shown in Fig. 4. The following assumptions are made:

1 Air and water properties are constant.

2 The thermal resistance of the plate is negligible.

3 The wettability of the plate is uniform.

4 Temperature change of the air stream is in the direction of flow only.

5 The Lewis number is unity.

Nomenclature (cont.)

t_a = air temperature of the primary air flow, °C
t^*_a = air temperature of the secondary air flow, °C
t^*_{ci} = initial conditions at the entrance of the secondary passage where absolute humidity is w^*_{ci}, °C
t^*_{ciw} = wet bulb temperature of the secondary air flow, °C
t_g = temperature of superheated steam, °C
t_{hi} = initial temperature of the primary air flow, °C
t_{ho} = outlet temperature of the primary air flow, °C
t_p = plate temperature (element I), °C
t'_p = plate temperature (element I − 1), °C
t_s = temperature of water leaving spray nozzle, °C
t_w = water film temperature on plate, °C
$(RH)_{hi}$ = initial relative humidity of primary air stream (ambient air conditions), dimensionless
$(RH)^*_{ci}$ = initial relative humidity of secondary air (refrigerant), dimensionless
V = air velocity, m/s
V_a = velocity of primary air flow, m/s
V^*_a = velocity of secondary air flow, m/s
w^*_a = absolute humidity of air in the secondary air stream, kg/kg
w^*_{ci} = absolute humidity at the entrance of the secondary passage where the initial temperature is t^*_{ci}, kg/kg
w_d = absolute humidity of saturated air at the temperature (t_w) of the water film, kg/kg
w_{sat} = absolute humidity of saturated air, kg/kg
ΔH^*_a = elemental enthalpy change of secondary flow (equation (19)), kJ/kg
Δt_a = elemental air temperature change (equation (18)), °C
Δw^*_a = elemental absolute humidity change of secondary flow (equation (22)), kg/kg
ϵ_w = effectiveness of the PPHE, defined by equation (1), dimensionless
ϕ = flow ratio ($= \dot{M}^*_a / \dot{M}_a$), dimensionless
σ = wettability of plate ($\sigma = 0.0$: dry; $\sigma = 1.0$: completely wet), dimensionless
δ = water film thickness on plate, m
ρ = air density, kg/m^3

Superscript

$*$ = secondary flow

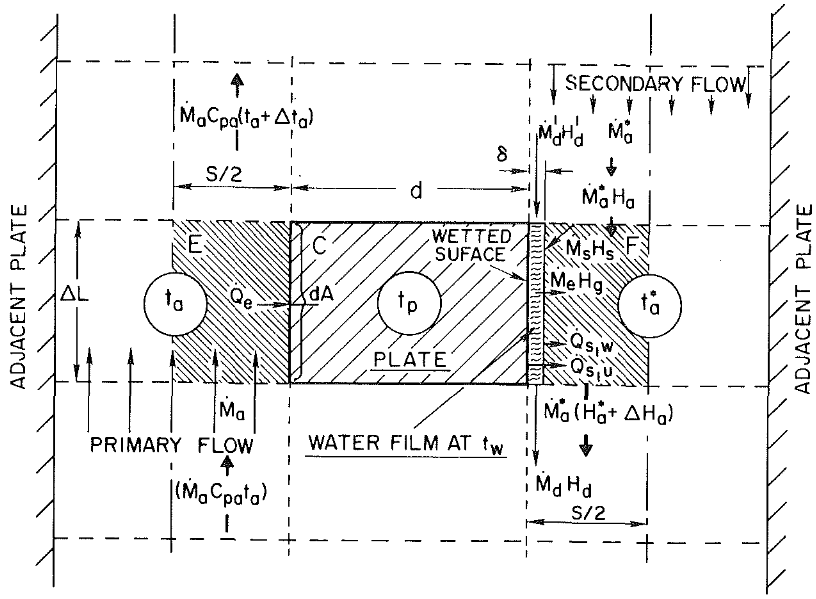

Fig. 4 Heat and mass fluxes in control volumes E (primary flow), C (plate and water film) and F (secondary flow)

Table 1 Constants *a′* and *b′* for calculation of saturated-air humidity

Temperature (°F)	(°C)	$w_{sat} \times 10^3$ (lb/lb) (kg/kg)	a'	b'
55	12.8	9.19	−0.0111	0.000369
60	15.6	11.04	−0.0151	0.000436
65	18.3	13.22	−0.0199	0.00051
70	21.1	15.77	−0.0261	0.000598
75	23.9	18.76	−0.0374	0.000713
80	26.7	22.26	−0.04302	0.000816
85	29.4	26.34	−0.05441	0.00095
90	32.2	31.09	−0.06809	0.001102
95	35.0	36.60	−0.08633	0.001294
100	37.8	43.07	−0.1067	0.001498
105	40.6	50.36	−0.1324	0.001742
110	43.3	59.27		

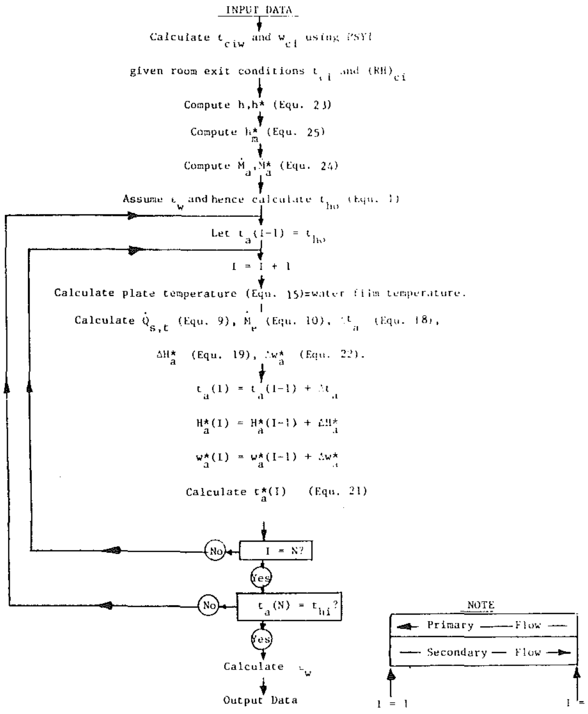

Fig. 5 Flow chart of computer program

An energy and mass balance on control volume, C, produces:

Energy balance

$$\dot{Q}_e + \dot{M}_d' H_d' + \dot{M}_s H_s = \dot{Q}_{s,w} + \dot{Q}_{s,u} + \dot{M}_e H_g + \dot{M}_d H_d \quad (4)$$

Mass balance

$$\dot{M}_s + \dot{M}_d' = \dot{M}_e + \dot{M}_d \quad (5)$$

Also

$$\dot{Q}_e = hdA\,(t_a - t_p) \quad (6)$$

$$\dot{Q}_{s,w} = h^* dA(\sigma)(t_w - t_a^*) \quad (7)$$

$$\dot{Q}_{s,u} = hdA(1-\sigma)(t_p - t_a^*) \quad (8)$$

Both heat transfer coefficients, h and h^*, are calculated based on the projected area of the plate. The area of the wetted surface is (σdA) and $(1-\sigma)\,dA$ is the nonwetted area on the wet side of the plate.

Essentially, the water on the plate is "excessive water" in the wet passage. Because the purpose of injecting water into the secondary passage is to provide sufficient evaporation, excessive water should be kept to a minimum. Even in those cases where the rate of water circulation is increased to improve the wettability of the plate, the excessive water rate should still be limited to assure low running cost of the system. Because the thickness of the water film is small, it is assumed that the temperature difference across the water film on the plate is negligible, and, hence, the local temperature of water on the plate can be taken to be the same as the local temperature of the plate. Also, assuming $h^* = h$, equations (7) and (8) can be combined to form the total sensible heat transfer

$$\dot{Q}_{s,w} + \dot{Q}_{s,u} = h^* dA\,(t_p - t_a^*) = \dot{Q}_{s,t} \quad (9)$$

Also

$$\dot{M}_e = h_m^* dA\,(w_d - w_a^*)\sigma \quad (10)$$

There are two excessive water terms in each elemental volume of the wet passage except for the one at the passage top. They are the "entering" excessive water, denoted by $\dot{M}_d'$,

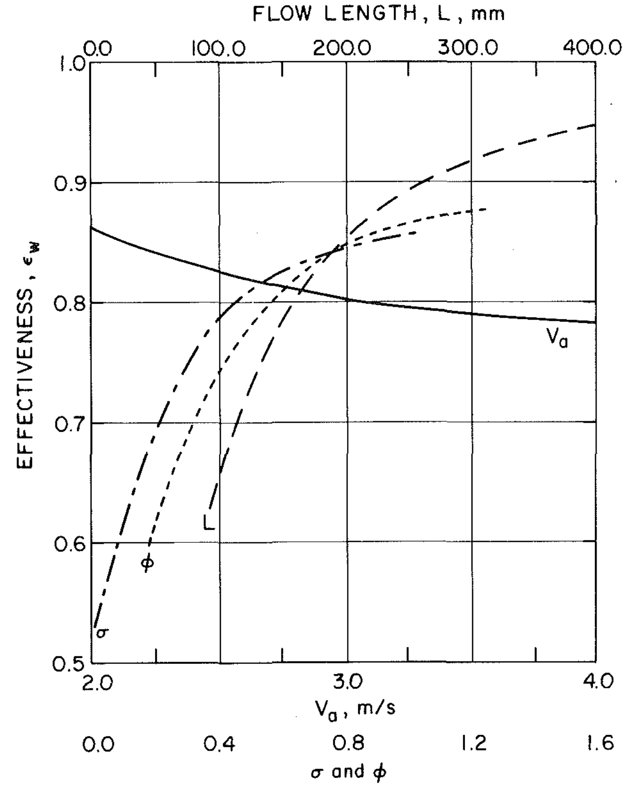

Fig. 6 The influence of various parameters on the value of the effectiveness ϵ_w, $t_{hi} = 97°F/36.1°C$, $RH_{hi} = 20$ percent, $t^*_{ci} = 79°F/26.1°C$, $RH^*_{hi} = 60$ percent:

———— effect of air flow velocity, V_a, with $\sigma = 0.6$, $\phi = 0.8$, and $L \times B = 200 \times 200 \text{ mm}^2$

-------- effect of flow rate ratio, ϕ, with $\sigma = 0.6$, $V_a = 2\text{m/s}$, and $L \times B = 200 \times 200 \text{ mm}^2$

— - — effect of wettability, σ, with $\phi = 0.8$, $V_a = 2\text{m/s}$, and $L \times B = 200 \times 200 \text{ mm}^2$

—— —— effect of flow length, L, with $\sigma = 0.8$, $\phi = 0.8$, $V_a = 2\text{m/s}$, $B = 200$ mm

and the "leaving" excessive water denoted by $\dot{M}_d$. For the top elemental volume, $\dot{M}'_d$ is zero.

H_g and H_w, the values of the enthalpy of superheated steam and water, respectively, referenced to 32°F (0°C), are given by [5]

$$H_g = \begin{cases} 1061 + 0.444\, t_g \,(°\text{F}) \text{ Btu/lb} \\ 2501.3 + 1.86\, t_g \,(°\text{C}) \text{ kJ(kg)} \end{cases} \tag{11}$$

$$H_w = \begin{cases} C_w(t_w - 32) \text{ Btu/lb} \\ C_w t_w \text{ kJ/kg} \end{cases} \tag{12}$$

Substituting equations (5) through (12) into equation (4) and rearranging, the following equation is obtained

$$t_a - t_p = r(t_p - t^*_a) + \frac{r\sigma}{L_e C_{p,a}}(H_g - H_w)(w_d - w^*_a) + \frac{R}{NTU}(t_p - t_s) + \frac{\dot{M}_d C_w}{hDA}(t_p - t'_p) \tag{13}$$

The transfer of heat from the wet plate surface to the bulk air flow in the secondary passage is made up of two components: sensible heat, and evaporative latent heat. The sensible heat transfer coefficient is affected by the following three factors: (*a*) the fluid flow mechanisms, (*b*) the air mixture properties, and (*c*) the flow geometry. It is assumed that the *sensible* heat transfer coefficient in the wet passage has approximately the same characteristics as the *sensible* heat transfer coefficient in the dry passage.

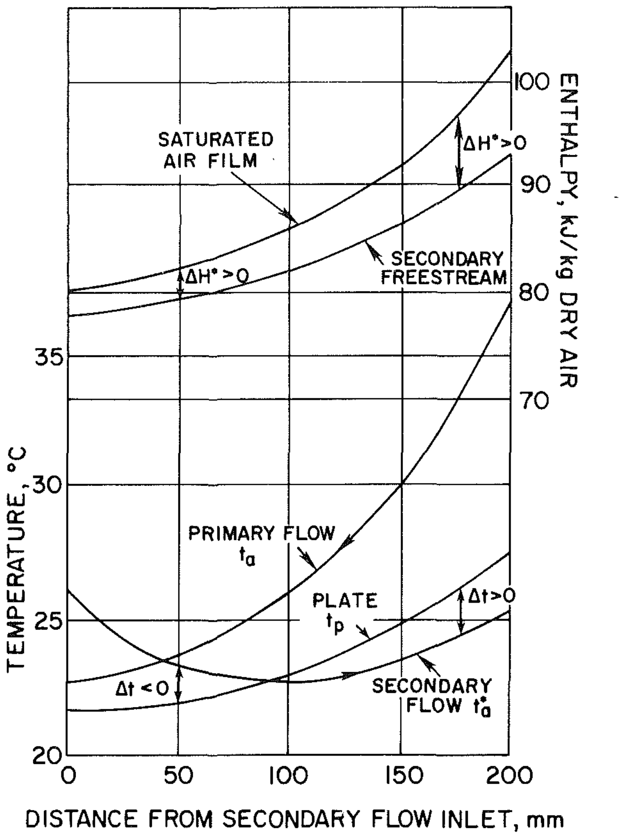

Fig. 7 Temperature distributions of the air flows and plate; enthalpy change in the secondary flow: $t_{hi} = t_a$ at inlet 97°F/36.1°C, t^*_a at inlet = 79°F/26.1°C; $RH_{hi} = 20$ percent, $RH^*_{ci} = 60$ percent, $\sigma = 0.8$, $V_a = 2$ m/s, $L \times B = 200 \times 200 \text{ mm}^2$

For a small range of temperature (5°F/2.78°C), value of the specific humidity of saturated air may be written as a linear function of temperature with general form

$$w_d = a' + b' t_p \tag{14}$$

where a' and b' are constants obtained for the proper range of temperatures. They are shown in Table 1 derived from steam tables.

Substituting equation (14) into equation (13) and solving for the plate temperature, t_p

$$t_p = \frac{t_a + r t^*_a + B(w^*_a - a') + \dfrac{R}{NTU}(t_s + C t'_p)}{(1.0 + r + Bb' + R/NTU + C)} = t_w \tag{15}$$

Equation (15)[2] gives the temperature of the plate in terms of primary flow conditions $(t_a, \dot{M}_a)$, secondary flow con-

---

[2] Constants used in equation (15):

$$B = \frac{r\sigma(H_g - H_w)}{L_e C_{p,a}}$$

$$C = \frac{\dot{M}_d C_w}{hdA}$$

$$\frac{R}{NTU} = \frac{\dot{M}_s C_w}{hdA}$$

Table 2 Values of overall effectiveness for different air flow temperature conditions: $RH_{hi} = 20$ percent, $RH^*_{ci} = 60$ percent, $\phi = 0.8$, $\sigma = 0.6$, $V_a = 2$m/s, $L \times B = 200 \times 200$ mm^2

Primary flow inlet DB temperature			Value of overall effectiveness, ϵ_w					
			Secondary flow inlet WB temperature					
		(°F)	59	62.6	66.2	69.8	73.4	77
		(°C)	15	17	19	21	23	25
(°F)	(°C)							
86	30		0.81	0.81	0.81	0.80	0.78	0.74
95	35		0.82	0.82	0.82	0.82	0.82	0.82
104	40		0.82	0.83	0.83	0.84	0.84	0.83
113	45		0.83	0.84	0.84	0.84	0.85	0.85

ditions (t_a^*, w_a^*, M_a^*), water spray conditions (t_s,$\dot{M}_s$), and the plate surface condition (σ). An energy balance for control volume E gives

$$\dot{M}_a C_{p,a} t_a = \dot{M}_a C_{p,a}(t_a + \Delta t_a) + hdA(t_a - t_p) \tag{16}$$

and for control volume F

$$\dot{M}_a^* H_a^* + \dot{Q}_{s,t} + \dot{M}_e H_g = \dot{M}_a^*(H_a^* + \Delta H_a^*) \tag{17}$$

Equations (16) and (17) can be solved for Δt_a and ΔH_a, respectively. The results are

$$\Delta t_a = -\frac{hdA}{\dot{M}_a C_{p,a}}(t_a - t_p) \tag{18}$$

$$\Delta H_a^* = \frac{\dot{Q}_{s,t}}{\dot{M}_a^*} + \frac{\dot{M}_e}{\dot{M}_a^*} H_g \tag{19}$$

The enthalpy of moist air can be written as

$$H_a^* = \begin{cases} 0.24 t_a^* + w_a^*(1601 + 0.444 t_a^*)\text{Btu/lbm} \\ 1.0 t_a^* + w_a^*(2501.3 + 1.86 t_a^*) kJ/kg \end{cases} \tag{20}$$

If H_a^* is known, then equation (20) can be used to solve for t_a^*. The result is

$$t_a^* = \frac{H_a^* - 1061 w_a^*}{0.24 + 0.444 w_a^*}\ ^\circ\text{F} \quad \text{or} \quad t_a^* = \frac{H_a^* - 2501.3 w_a^*}{(1.0 + 1.86 w_a^*)}\ ^\circ\text{C} \tag{21}$$

The change of the humidity ratio of the secondary flow is

$$\Delta w_a^* = \frac{\dot{M}_e}{\dot{M}_a^*} \tag{22}$$

The essential equations of the heat exchanger systems are composed of equations (15), (18), (19), (21), and (22). Initial conditions at the entrance of the secondary passage are t^*_{ci} and w^*_{ci}, the inlet conditions of the air. An iterative process is used to determine the physical properties of the air streams along each passage. Iteration is necessary because the initial value of the effectiveness is assumed at the beginning of the program. The increment of t_{ho} is 0.05°F, and the criteria of comparison is that the computed t_{hi} should converge within a tolerance of 0.5 percent error. The effectiveness of the heat exchanger can be computed. Properties of moist air, such as wet bulb temperature and specific humidity, are found using an existing ASHRAE subroutine [9].

One of the prototypes used in Pescod and Chan's experiments is chosen to be the system for simulation with the flow arrangement changed to counterflow. In this prototype, the plate has a protrusion spacing of 6.7 mm, the plate size is 200 mm × 200 mm, and plate spacing is 3.4 mm. Using equation (3), the heat transfer coefficients of the air flows in the dry and the wet passages are obtained [8]

$$h = h^* = 54 V_a^{0.7}\,\text{W/m}^2\,^\circ\text{C} \tag{23}$$

Numerical Procedure

A flow chart of the computer program is given in Fig. 5.

Table 3 Influence of spray water conditions on the effectiveness: $t_{hi} = 97$°F/36.1°C, $t^*_{ci} = 79$°F/26 ic, $RH_{hi} = 20$ percent, RH$^*_{ci} = 60$ percent, $\phi = 0.8$, $\sigma = 0.8$, $V_a = 2$ m/s, $L \times B = 200 \times 200$ mm^2

t_s(°C)	n_s	ϵ_w	t_s(°C)	n_s	ϵ_w	t_s(°C)	n_s	ϵ_w
22.8	5	87.0%	35	5	85.6%	65.5	5	81.8%
22.8	10	87.4%	35	10	84.0%	65.5	10	79.7%
22.8	20	87.2%	35	20	82.0%	65.5	20	73.0%
22.8	30	87.3%	35	30	81.3%	65.5	30	66.1%

The input data of the program includes the following parameters (units are as in the nomenclature):

- Dimensions of the heat exchanger (L, B, s)
- Density of the air (ρ)
- Atmospheric pressure (p_{atm})
- Latent heat of evaporation of the water (H_{fg})
- Ambient air conditions (t_{hi}, $(RH)_{hi}$)
- Refrigerant air conditions at the entrance to the passage (t^*_{ci}, $(Rh)^*{}_{ci}$)
- Spray rate ($\dot{M}_s$)
- Water temperature (t_s)
- Approach velocity (V_a)
- Flow rate ratio (ϕ)
- Wettability of the plate (σ)

The output data of the program includes the effectiveness of the heat exchanger, supply air conditions and change of fluid condition throughout the passages. Additional equations needed are:

Mass rate air flow

$$\dot{M}_a = \frac{1}{2} sBV_a\rho; \dot{M}_a^* = \frac{1}{2} sBV_a^*\rho \tag{24}$$

Mass transfer coefficient (Lewis relation)

$$h_m^* = \frac{1}{L_e C_{p,a}} h^* \tag{25}$$

The plate area is divided into a number of small elements, n_p. Computer experiments showed that an optimum value of n_p is 31.

Results and Discussion

Table 2 shows typical values of ϵ_w for the conditions stated. The condition of the entering primary air flow varies over the range 30°C (DB) to 45°C (DB). The condition of the entering secondary air flow varies over the range 15°C (DB) to 25°C (DB). The relative humidity of the entering secondary flow in this table is fixed at 60 percent, since it represents a typical value of air leaving a residential building.

Figure 6 shows the influence of various parameters on the value of ϵ_w. As the velocity of the primary air flow increases, ϵ_w decreases. As the flow rate ratio increases, ϵ_w increases. As the wettability increases, ϵ_w increases. As the flow length increases, ϵ_w increases.

Figure 7 shows the temperature changes of the plate and the air flows, and the enthalpies of the saturated air film in contact with the water film surface and the free airstream. As the *distance from the secondary flow inlet* increases from 0 to 200 mm, the plate temperature increases from 22.2 to 27°C; the primary air flow temperature increases from 23 to 36.1°C; the secondary air flow temperature firstly decreases from 26.1 to 23.0°C and then increases to 25.1°C; and the enthalpy difference increases from 4.81 to 14.30 kJ/kg.

Figure 8 shows the change of relative humidity in the secondary air flow along its flow direction. In this figure, there are three plates of different wettability ($\sigma = 0.6$, 0.4, and 0.2). For the plate with wettability of 0.2, the RH^* increases from 60 to 77 percent, then decreases to 75.5 percent.

Table 3 shows the influence of the spray-water temperature and the circulation rate on the value of ϵ_w. The spray-water temperature varies from 22.8 to 65.5°C. The circulation rate varies from 5 to 30 times the evaporation rate.

Input data for this program is as follows. The dimensions of the heat exchanger from Chan's report [2] are 227 mm (L) × 193 mm (B). The effective area of the plate is less than the total area because of methods used around the periphery to hold the unit together. It is found that the effective area of the plate is 90 percent of its total area. The heat transfer area is 0.04 m^2 (0.42 ft^2). The air density used is 1.2015 kg/m^3 (0.075 lbm/ft^3). The atmospheric pressure is assumed to be 100 kPa (29.92 in. Hg). The ambient air conditions are varied over the temperature range of 30°C (DB) to 45°C (DB). According to equation (1), the relative humidity (RH) of the ambient air will not affect the effectiveness of the heat exchanger. However, the PPHE has less application in areas where the ambient wet bulb temperature frequently exceeds 25°C, because comfort humidities can not be attained. Therefore, a RH_{hi} value of 20 percent is used in the analysis. The refrigerant air conditions are varied from 15°C (WB) to 25°C (WB), and the RH value has been fixed at 60 percent. The approach velocity is varied over the range of 2 m/s to 4 m/s. The rate of the water spray is firstly assigned a value equal to a typical value of the rate of evaporation in the passage, derived by taking two ends states of the secondary flow from the information available (see Pescod [1]) and then estimating the change in the moisture content of the air. The result is 0.018 kg/hr per 1/2 passage (0.04 lb/hr per 1/2 passage). It is found that this value is about 30 percent less than that calculated numerically. It is then adjusted to 0.025 kg/hr per 1/2 passage (0.057 lb/hr per 1/2 passage). The rate of water spray is varied by multiplying this newly determined value by a factor, n_s; the range of n_s being from 1 to 30. The wettability of the plate is assumed to be uniform thoughout, and in addition to this, it is assumed to be constant when the water spray rate is increased up to 30 times the rate of evaporation. In practice, it is found that increasing the rate up to 20 or 30 times the evaporation rate, the wettability of the plate can be improved.

Other points worth noting include: The temperature difference across the plate has been assumed to be negligible because of the small thickness of the plates. The water spray was considered to be equally distributed on the plate surfaces, this insuring that there is a constant value of $\dot{M}_s$ for every element of the plate. Actually, most of the water leaving the nozzles travels a certain distance in the free stream of the secondary circuit. Part of the water thus can be convected into the free stream in vapor form. This evaporation was neglected. It has been idealized that all the water evaporated is from the surface of the plate.

According to Threlkeld [10], Meyer has experimented with the finned-tube condenser to study the heat transfer coefficient from wet surfaces of the tubes. The results have indicated that it is slightly greater than the heat transfer coefficient of dry operation.

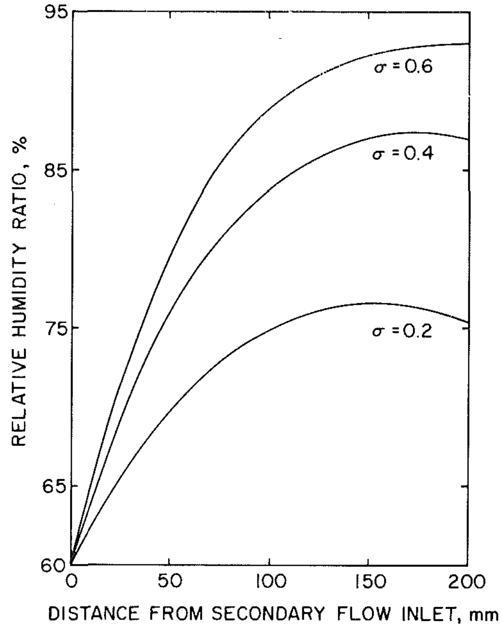

Fig. 8 Change of relative humidity of the secondary flow stream along the flow length: $t_{hi} = 97°\text{F}/36.1°\text{C}$, $t^*_{ci} = 79°\text{F}/26.1°\text{C}$, $RH_{hi} = 20$ percent, $RH^*_{ci} = 60$ percent, $\phi = 0.8$, $V_a = 2$ m/s

McQuiston [11] has published results on heat transfer coefficients in parallel plate heat exchangers. He showed that when the flow was developed over 80 percent of the channel length, the water had little effect on the heat transfer coefficient except at high Reynolds numbers. As the Reynolds number increased, the heat transfer increased. It was also found that the actual increase depended on the plate material and cleanliness. Further results are reported in [12].

In deriving equation (13), two nondimensional groups, NTU and R, have similar forms as those of NTU and R which are widely used in heat exchanger designs. But is should be noted in interpreting their physical meanings that the working fluid in the secondary passage is not solely water. The relationships between ϵ_w and R, and between ϵ_w and NTU, have been observed. From Table 3, we see an increase of n_s, causing an increase in R tends to increase ϵ_w slightly. Figure 6 shows that an increase in the flow length, which can be taken as an increase in NTU, increases ϵ_w. But as the flow length is increased up to a certain value (in this figure, 400 mm), ϵ_w reaches a maximum and remains constant as the flow length increases further. Similar relationships have been found between R and ϵ, and NTU and ϵ, for the ordinary counterflow heat exchangers.

Figure 7 shows the internal change of the fluid properties. The ambient air and plate are cooled throughout the primary passage of the heat exchanger. The secondary flow is first cooled, and then is heated. The sensible heat transfer on the dry side of the plate from the primary air flow to the plate is always in the same direction. The sensible heat transfer on the wet side of the plate is found to change directions. But the enthalpy curves on the same figure show a clear picture of the driving potential of the heat transfer in the wet passage. The enthalpy difference between the air in the saturated air film and air in the free stream is found to be always positive. It is also found that the contribution of the latent heat transfer is dominant in the wet-surface heat transfer process. Actually, 99 percent of the total heat transferred from the primary passage was converted into latent heat of the water vapor in the secondary passage. The change in direction of the sensible heat transfer is not significant. The heat transfer mechanism in the PPHE can now be described. Following the primary flow direction, the hot air stream in the dry passage continuously releases heat to the dry side of the plate, while the evaporation of water occurs on the wet side of the plate. The plate is cooled as a consequence. The circulation of water provides the wetting of the plate and hence a saturated air film is formed at the interface of the wet-plate surface and the free stream of air. The saturated air film creates an enthalpy potential for the heat flow to be transferred from the wet surface to the free stream of air. The wet surface continuously gives heat to the free stream of air until the enthalpy potential becomes zero, i.e., the enthalpy of the saturated air film is equal to that of the free-stream air. This occurs when the water film has a temperature which is equal to the wet bulb temperature of the air in the free stream. Therefore, the theoretical minimum temperature to which the plate can be cooled is the initial wet bulb temperature of the refrigerant air. Figure 2 shows the theoretical minimum temperature for the air flow being conditioned as t^*_{ciw}.

The use of the secondary air flow in the PPHE cooling unit is to provide a lower possible temperature to which the ambient air can be cooled. The appropriate air flow to be used as the refrigerant for the PPHE cooling unit thus should have a wet bulb temperature which is lower than that of the ambient primary air. From Figs. 7 and 8, the process line for the refrigerant air in the heat exchanger can be generated on the psychrometric chart. It is found that the line bends away from the saturation line at the end of the section of the refrigerant air passage.

Conclusions

An analysis has been carried out on a counterflow plastic plate heat exchanger air cooler. Computed results show qualitative agreement with experimental values of the effectiveness of the system. The concept of "enthalpy potential" has been used to explain the heat transfer process in the heat exchanger. The value of the theoretical minimum temperature to which the ambient can be cooled in the heat exchanger is verified to be the initial wet bulb temperature of the refrigerant instead of the dew point of the ambient air. To make full use of the PPHE, it is necessary that the refrigerant air should have a wet bulb temperature which is lower than the wet bulb temperature of the ambient air, and the spray water should be at a temperature which is about room temperature or lower. A low rate of water spray is preferred. If the spray rate is not larger than 5 times the evaporation rate, the water temperature can be as high as 35°C, and the same effectiveness of the heat exchanger can still be obtained. On the other hand, if water of low temperature is used, then the effectiveness will not be varied significantly while the rate of circulation water is increased from 1 to 30 times the evaporation rate. It is recommended that a detailed investigation of the crossflow PPHE air cooler be carried out.

The use of the PPHE as a component in a solar-assisted cooling system has been discussed in [13].

References

1 Pescod, D., "Unit Air Cooler Using Plastic Plate Heat Exchanger With Evaporatively Cooled Plates," *Australian Refrigeration Air Conditioning and Heating*, Vol. 22, Sept. 1968, pp. 22–26.

2 Chan, C. Y. L., "Performance Tests of Model Plate Heat Exchanger With Wetted Plates," CSIRO Division of Mechanical Engineering, Highett, Victoria, Australia, Internal Report No. 120, Mar. 1973.

3 Watt, J. R., *Evaporative Air Conditioning*, Industrial Press, New York, 1963, pp. 211–238.

4 Pescod, D., and Prudhoe, R. K., "Application of CSIRO Plate Heat Exchanger for Low Energy Cooling of Telecom Buildings," CSIRO Division of Mechanical Engineering, Highett, Victoria, Australia, Nov. 1979, pp. 1–6.

5 Hollands, K. G. T., "Analysis and Design of Evaporative Cooler Pads," *Mechanical and Chemical Engineering Transactions*, Institution of Engineers (Australia), Vol. MC6, No. 2, Nov. 1979, pp. 55–61.

6 Kreid, D. K., Johnson, B. M., and Faletti, D. W., "Approximate Analysis of Heat Transfer From the Surface of a Wet Finned Heat Exchanger," ASME Paper No. 78-HT-26, 1978.

7 McClaine-Cross, I. L., and Banks, P. J., "A General Theory of Wet Surface Heat Exchangers and its Applications to Regenerative Evaporative Cooling," ASME JOURNAL OF HEAT TRANSFER, Vol. 103. 1981, pp. 579–585.

8 Pescod, D., "Effects of Turbulence Promoters on the Performance of Plate Heat Exchangers," in *Heat Exchangers: Design and Theory Sourcebook*, edited by N. Afgan and E. U. Schlünder, McGraw-Hill, Washington, D.C., 1974, pp. 602–614.

9 Kusuda, T., *NBSLD, Computer Program for Heating and Cooling Loads in Buildings*, Center for Building Technology, National Bureau of Standards, Report No. NBSIR 74-574, Nov. 1974, pp. 150a–156a.

10 Threlkeld, J. L., *Thermal Environmental Engineering*, 2d. ed., Prentice Hall, Englewood Cliffs, New Jersey, 1970.

11 McQuiston, F. C., "Heat Mass and Momentum Transfer in a Parallel Plate Dehumidifying Exchanger," ASHRAE *Transactions*, Vol. 82, pt. 2, 1976, pp. 87–106.

12 McQuiston, F. C., "Correlation of Heat, Mass, and Momentum Transport Coefficients for Plate Fin-Tube Heat Transfer Surfaces With Staggered Tubes," ASHRAE *Transactions*, Vol. 84, pt. 1, 1978, pp. 294–309.

13 Kettleborough, C. F., "Solar-Assisted Dehumidification and Cooling with an Indirect Evaporative Cooler," ASME Paper No. 80-WA/SOL-29, 1980, pp. 1–11.

Crystalline Fouling Studies

R. B. Ritter[1]
Heat Transfer Research, Inc.,
Alhambra, Calif. 91802

In a study of fouling of heat exchangers, aqueous solutions of $CaSO_4$ and Li_2SO_4 were circulated through electrically heated tubes at controlled conditions. Measured induction periods and fouling rates of both salts were found to be primarily functions of the supersaturation of the solutions. Secondary correlating parameters were surface temperature for the Li_2SO_4 solutions and mass transfer coefficients for the $CaSO_4$ solutions.

Introduction

One of the first experimental programs at Heat Transfer Research, Inc. (HTRI) was a study of fouling as it might occur in shell-and-tube heat exchangers. Improvements in the prediction of heat transfer coefficients would be of limited value if excessive fouling resistances were to be included in the ratings to cover possible fouling. This paper reports on the tests of fouling of inverse-solubility salt solutions in the HTRI Stationary Fouling Research Unit [1]. These studies were followed by studies of cooling water fouling in the same unit and, subsequently, in Portable Fouling Research Units, [2-7] reported earlier.

Apparatus

The HTRI Stationary Fouling Research Unit is described by the flow diagram, Fig. 1. Test section tubes of brass or carbon steel 48-in. (1220-mm) long with inside diameters of 1/2, 1, and 2 in. (13, 25 and 51 mm) were operated in parallel. Each test section was heated by electrical elements as shown in Fig. 2. The cartridge heaters were embedded in machined slots with heat transfer cement to fill the voids. Copper sheets, wrapped around the heaters and cement, were strapped with hose clamps. Thermal insulation covered the assembly to keep heat losses to predictable minimums.

Thermocouples were installed in holes drilled from the outside to positions as close to the inner tube surface as possible. Seven thermocouples were installed along the length of each tube.

Power to the test sections was measured by precision wattmeters. Cutouts were used to shut off the power to a test section if a thermocouple indicated an excessively high temperature. Transmitting rotameters were used to measure the flow rate leaving each test section. Flow recorder-controllers operated control valves to hold flow rates constant.

The circulating solution was kept at constant composition by having it flow through a bed of crystals in a saturation drum. A temperature-indicating controller operated a control valve in the cooling-water line to the solution cooler to maintain a constant solution temperature at the inlet to the saturation drum. Filters were used in the line after the saturation drum to remove any fine crystals from the solution.

The pressure within the system was kept well above the bubble point by a nitrogen pad on the head drum. Distilled water was added to the system as the level in the head drum became low due to sampling, leaks at the pump seal, etc.

Calibrations

Inside diameters of the test section tubes were measured with micrometers at several points near each end of a tube before and after operation.

The thermal resistances between the tube-wall thermocouple junction and the inside surfaces of the tubes were determined by operating the unit with clean water through full ranges of flow rates and heat fluxes. Wilson plot techniques [1, 9] were then used to determine the resistances. With these data, it was possible to determine the temperature of the inside tube surface as a function of heat flux [1]. Heat balances made during these calibration runs gave data needed to predict heat losses from the test sections.

Solubilities

Laboratory determinations of solution densities and viscosities were made over the ranges of temperatures anticipated. The values were in agreement with literature data.

Solubilities, however, were not as straightforward. Calcium sulfate could deposit in either of two forms depending upon the hot surface temperature. Below 215°F (102°C) the solution is in equilibrium with gypsum, the dihydrate,

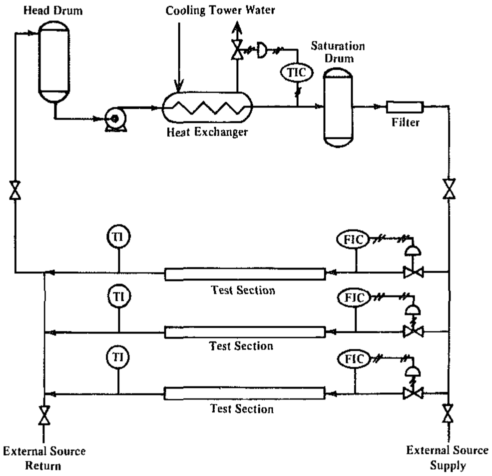

Fig. 1 Stationary fouling research unit flow diagram

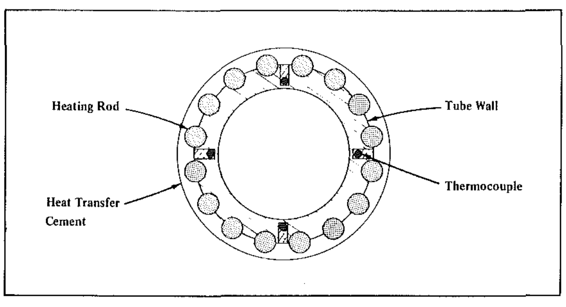

Fig. 2 Cross section of test section for the stationary fouling research unit

---

[1] Present address: Fluor Engineers Inc., Irvine, Calif. 92730

Contributed by the Heat Transfer Division and presented at the 20th ASME/AIChE National Heat Transfer Conference, Milwaukee, Wisconsin, August 2-5, 1981. Manuscript received by the Heat Transfer Division October 27, 1981.

$CaSO_4 \cdot 2H_2O$. This was the crystal form kept in the saturation drum. Above 215°F (102°C) hemihydrate crystals, $CaSO_4 \cdot \frac{1}{2}H_2O$ could deposit. Each hydrate has its own solubility curve as shown in Fig. 3.

Lithium sulfate solubility is less complicated. Only one crystalline form exists in the range of temperature studied, the monohydrate, $Li_2SO_4 \cdot H_2O$. The solubility curve for this salt is also shown in Fig. 3.

Operation

At start-up, the saturation drum was charged with crystals and the system was filled with distilled water. The liquid was circulated through the saturation drum and one of the three heated test sections to bring it to the desired saturation temperature. Upon reaching the desired concentration, a cleaned test section was opened to the stream, the desired flow rate was established, and heat was applied. Data readings were made rapidly at first to establish the clean-tube conditions. Subsequent readings were made at intervals dictated by the rate of fouling. Samples of the solution were removed periodically and checked in the laboratory for concentration.

When a test section tube fouled to the point that either the controlled flow rate could no longer be maintained or the tube wall reached the power cutoff temperature, the element was valved off, drained, and inspected. Prior to being put back into service at a new set of conditions, fouled tubes were cleaned with wet rotary brushes and thoroughly flushed with cold water to remove any traces of salt that might have acted as seed crystals.

Operating Conditions

A test series is defined as the steady-state operation of any of the three test sections from power on to power off. A total of 105 successful test series was made, with durations ranging from 20 min to 1,850 hrs. Table 1 summarizes the test program.

Tests were planned to cover fully the ranges of possible operating conditions. Table 2 gives the ranges of controlled conditions for the two salt solutions. Resulting operating parameters, either measured or calculated, are shown in Table 3.

Reynolds numbers were calculated as functions of measured flow rates, tube inside diameters, and viscosities. The viscosities were determined as functions of salt concentration based on laboratory determinations and literature data.

Circulating-solution and hot-surface concentrations were calculated as functions of the saturation-drum and hot-surface temperatures. The equations used for these calculations are represented by the curves of Fig. 3.

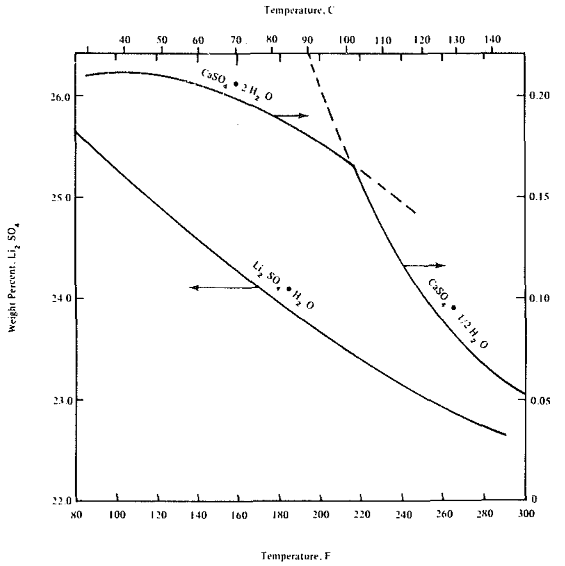

Fig. 3 Solubilities of Li_2SO_4 and $CaSO_4$ salts in water

Table 1 Test program

	$CaSO_4$	Li_2SO_4	Total
Number of test series	49	56	105
Duration of test series, hr.	1-53	0.3-1,850	–
Number of sets of data readings	503	1,804	2,307
Total test operation, hr.	906	13,000	14,000

Table 2 Ranges of controlled operating conditions

	$CaSO_4$	Li_2SO_4
In-tube solution velocity, ft/s	1-10	0.6-13
m/s	0.3-3	0.18-4
Heat flux, 10^3 Btu/ft^2 hr	20-140	6-140
kW/m^2	63-440	19-440
Saturation drum temperature, °F	107-199	99-222
°C	42-93	37-106

Heat transfer coefficients were determined from measured heat inputs and temperatures. Solution temperatures were recorded at the inlet and exit of each tube. A linear temperature rise was assumed along the length of the tube in calculating the bulk temperature at any point. The hot surface temperatures were determined from recorded wall-thermocouple temperatures and the thermal resistances between these thermocouples and the inside surface of the tube as measured in the clear-water tests.

$$q = h(T_i - T_b) = (1/r_w)(T_c - T_i) = (1/R_f)(T_i - T_s) \quad (1)$$

Mass transfer coefficients were not measured. Instead, the

Nomenclature

A = correlation constant
B = correlation constant
C_b = circulating solution concentration, weight percent
C_p = solution specific heat, J/kg °C
C_s = saturation concentration at heat surface, temperature weight percent
D_l = diffusivity, m^2/s
f = friction factor
F_r = fouling rate, m^2 °C/Ws
G = mass velocity, kg/m^{2}s
h = heat transfer coefficient, W/m^2 °C
k_l = mass transfer coefficient, kg/m^{2}s
Pr = Prandtl number
q = heat flux, W/m^2
R_f = fouling resistance, m^2 °C/W
r_w = wall resistance from T_c to T_i, m^2 °C/W
T_b = bulk solution temperature, °C
T_c = wall thermocouple temperature, °C
T_i = inside tube-surface temperature, °C
T_s = wetted surface temperature, °C
V = solution velocity, m/s

Greek

ΔC = $C_b - C_s$, weight percent
θ = induction period, hr
μ = solution viscosity, mPa s
ρ = solution density, kg/m^3
τ = shear stress, Pa

Table 3 Resulting operating parameters

	$CaSO_4$	Li_2SO_4
Reynolds number	17,000-160,000	3,400-16,000
Circulating solution concentration, C_b, wt. percent	0.173-0.211	23.4-25.3
Saturation concentration at hot surface temperature, C_s, wt. percent	0.065-0.173	22.8-25.2
Surface temperature, T_s, °F	200-285	100-280
°C	93-141	38-138
Supersaturation at surface, $\Delta C/C_s$	0.09-1.70	0.003-0.097
Heat transfer coefficient, Btu/ft^{2}hr°F	310-2,700	180-3,900
W/m^2°C	1760-15320	1020-22130
Mass transfer coefficient, lb/ft^{2}hr	16-140	10-230
kg/m^{2}s	0.022-0.19	0.014-0.32
Shear stress, lb/ft^2	0.0032-0.352	0.0016-0.752
Pa	0.15-17	0.077-36

Table 4 Ranges of results

	$CaSO_4$	Li_2SO_4
Induction periods, θ, hr	0.15-50	0.15-612
Fouling rates, F_r, ft^2 °F/Btu	0-3(10)$^{-3}$	0-1.4(10)$^{-2}$
m^2 °C/Ws	0-1.4(10)$^{-7}$	0-6.5(10)$^{-7}$

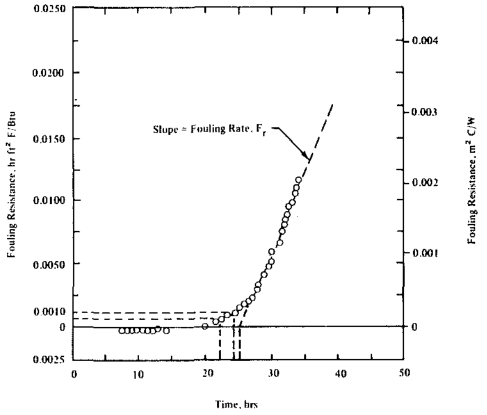

Fig. 4 Typical fouling curve

Colburn analogy for turbulent flow inside tubes was assumed in approximating the coefficient

$$\frac{k_l}{G}\left(\frac{\mu}{\rho D_l}\right)^{2/3} = \frac{h}{C_p G}(\mathrm{Pr})^{2/3} = \frac{f}{2} \tag{2}$$

Diffusivities of the salt solutions were estimated by the methods outlined by Reid and Sherwood [8]. Mass transfer coefficients were calculated on the basis of the measured heat transfer coefficients, and they were also calculated from friction factors for commercial pipe as functions of the Reynolds numbers. The k_l values based upon the measured heat transfer coefficients were considered to be more reliable and were used in correlating the data.

Shear stresses at the inside wetted surfaces were not measured. Instead, they were calculated by the equation:

$$\tau = \frac{f\rho V^2}{2} \tag{3}$$

Here again, the friction factor was calculated as a function of the Reynolds number.

Results

Not all test series resulted in fouling. Under one set of conditions no fouling was measured in eleven weeks of operation. At another set of conditions, the largest tube fouled completely in 20 min.

Similarly, not all seven thermocouples in the tube wall would show fouling at the same rate. It was not unusual to observe one end of a tube foul while the other end remained clean. This apparent inconsistency is at least partly explained by entrance effects. To eliminate such effects, only the data from two thermocouples near the exit end of each tube were considered in evaluating the results. These two thermocouples were located 9 in. (230 mm) from the exit end of the 48-in. (1220-mm) tubes. One was in the top wall and one in the bottom wall of the tube. These positions correspond to 80, 40, and 20 diameters from the inlets of the three tubes.

Unlike cooling-tower-water fouling with its typical asymptotic curves, crystalline fouling was characterized by induction periods with no fouling, followed by fouling at a constant rate. Fouling usually continued at a constant rate until it was no longer possible to maintain the flow rate, or until the tube wall temperature reached a maximum shutoff temperature of 500°F (260°C).

Interpretation of Results

Figure 4 is a typical curve of fouling resistance versus time for crystalline fouling with an induction period with little or no fouling, followed by a fixed fouling rate. Several definitions of the induction period are possible. The three considered in this study were:

(*i*) The time to reach a fouling resistance, R_f, of 0.000 5 hr ft^2 °F/Btu (0.000 09 m^2 °C/W)

(*ii*) The time to reach a fouling resistance of 0.001 hr ft^2 °F/Btu (0.000 18 m^2 °C/W)

(*iii*) The time-axis intercept of the best least-squares fit of a straight line through the data points above a fouling resistance of 0.001 hr ft^2 °F/Btu (0.000 18 m^2 °C/W)

The best data correlations resulted from the use of the second definition of the induction period—the time to reach 0.001 hr ft^2 °F/Btu (0.000 18 m^2 °C/W). The fouling rate, F_r, was taken to be the slope of the straight line resulting from a linear correlation of the data points after the induction period.

Ranges of induction periods and fouling rates observed for the two salts are given in Table 4.

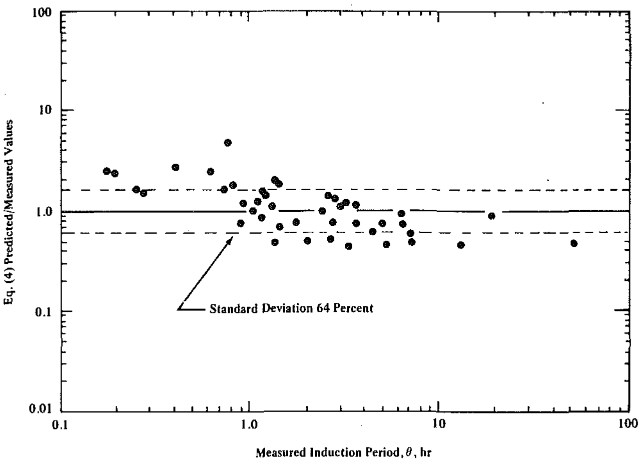

Fig. 5 Calcium sulfate induction period

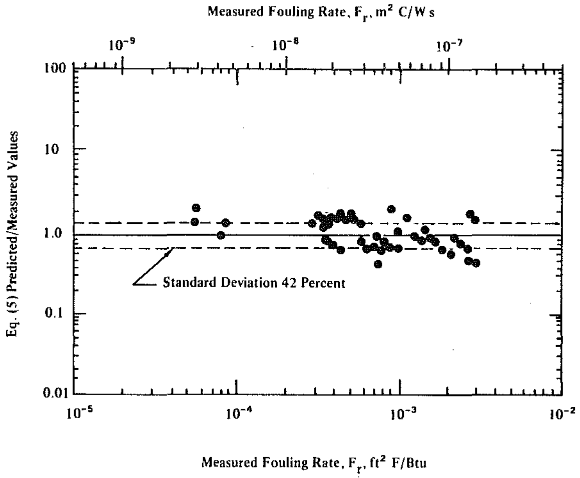

Fig. 6 Calcium sulfate fouling rate

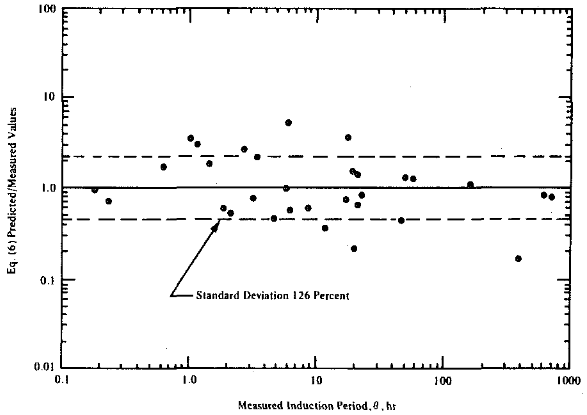

Fig. 7 Lithium sulfate induction period

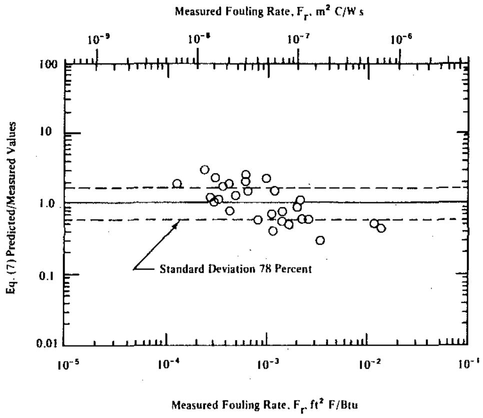

Fig. 8 Lithium sulfate fouling rates

Correlation of the Results

Six possible parameters were considered in correlating both the induction periods and the fouling rates of the two salts:

- Supersaturation, $\Delta C/C_s$
- Mass transfer coefficient
- Surface temperature
- Shear stress
- Heat flux
- Reynolds number

Many of these parameters are related. Most of them are functions of operating temperatures. Others depend upon flow rates, and some depend upon both. Because of this interdependence, it became necessary to resort to statistical methods to identify the most important parameters.

Multiple regression methods were used to evaluate the importance of each of the parameters separately and then in various combinations. Since this amounts to some 252 possible combinations of the six parameters for the four correlations, no attempt is made to report on the correlating coefficients here. Suffice it to say that these studies showed shear stress to have the least influence, except as it is related to the mass transfer coefficient. Reynolds number, too, had no influence except for the dependence of the mass transfer coefficient upon the Reynolds number. Heat flux also had no apparent effect upon the results outside of its influence on the surface temperature.

For each salt, the parameters that correlated the induction periods also correlated the fouling rates. Supersaturation was the primary correlating parameter for each salt, but the secondary parameters were not the same. In addition to supersaturation, $CaSO_4$ data were correlated by mass transfer rates, but Li_2SO_4 data were correlated by surface temperatures. This would indicate that $CaSO_4$ fouling is mass transfer controlled while Li_2SO_4 fouling is reaction-rate controlled. The difference may be attributed to the large differences in the solubilities of the two salts. As shown in Table 3, Li_2SO_4 weight percentages at the hot surfaces were some 150 to 350 times those for $CaSO_4$. This corresponds to molar concentrations of Li_2SO_4 some 230 to 540 times those for $CaSO_4$. At these higher concentrations, mass transfer may have been no obstacle for Li_2SO_4 crystallization, but a major factor in crystallization of the dilute $CaSO_4$ solutions. The Li_2SO_4 salt being at the surface in much higher concentrations apparently needed only heat, as represented by T_s, to activate the atoms to effect crystallization.

The correlating equations for calcium sulfate data are, for induction period,

$$\theta = \frac{A}{k_l(\Delta C/C_s)^2}, \text{ hr} \tag{4}$$

where

A = 0.15 for k_l as lb/ft²hr
= $2.1(10)^{-4}$ for k_l as kg/m² s

and for fouling rate

$$F_r = Bk_l(\Delta C/C_s)^2 \tag{5}$$

where

B = $3.8\,(10)^{-5}$ for k_l as lb/ft² hr, and F_r as ft² °F/Btu
= $1.9\,(10)^{-9}$ for k_l as kg/m² s and F_r as m² °C/Ws

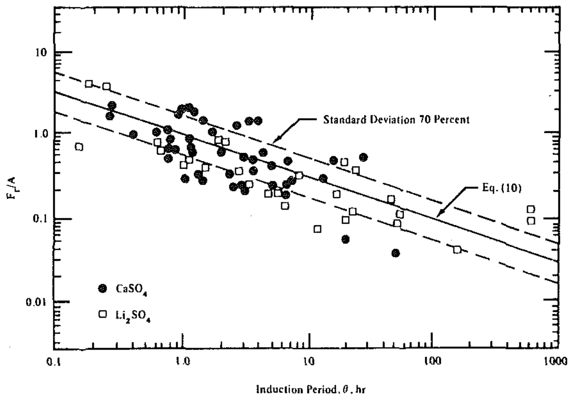

Fig. 9 $CaSO_4$ and Li_2SO_4 fouling rate versus induction periods

The correlating equations for lithium sulfate data are, for induction period

$$\theta = 6.35(10)^{-7}(\Delta C/C_s)^{-3} exp(A/T_s),\ \text{hr} \tag{6}$$

where

$$A = 3940 \text{ for } T_s \text{ as } R$$
$$= 2190 \text{ for } T_s \text{ as } K$$

and for fouling rate

$$F_r = A(\Delta C/C_s) exp(B/T_s) \tag{7}$$

where

$$A = 570,\quad B = -6540 \text{ for } T_s \text{ as } R, \text{ and } F_r \text{ as ft}^2\ ^\circ\text{F/Btu}$$
$$= 0.028, B = -3630 \text{ for } T_s \text{ as } K, \text{ and } F_r \text{ as m}^2\ ^\circ\text{C/Ws}$$

These correlations are compared to the data by error plots, Figs. 5 to 8. Figures 5 to 8 show some sloping trends of the data points indicating that somewhat better correlations might be possible if fractional powers of the parameters were used. Actually, very little improvement in the correlating coefficients results when fractional powers are used. Since the precision of fraction exponents is not warranted, only integer powers were used in the correlations, equations (4-7).

Banchero and Gordon [10] reported induction periods for a number of salts to be strong junctions of supersaturation. Logarithmic plots of θ versus $\Delta C/C_s$ for all of their salts show slopes ranging from minus 2 to minus 3. Equations (4) and (6) have slopes within the same range.

With each salt, the parameters that best correlated the induction periods also produced the best fouling-rate correlations, indicating a definite relationship between the two. Correlations of fouling rates as functions of induction periods gave, for calcium sulfate

$$F_r = 1.3\,(10)^{-3}\theta^{-0.6},\ \text{ft}^2\ ^\circ\text{F/Btu} \tag{8}$$
$$= 6.2\,(10)^{-8}\theta^{-0.6},\ \text{m}^2\ ^\circ\text{C/Ws}$$

and for lithium sulfate

$$F_r = 2.1\,(10)^{-3}\theta^{-0.4},\ \text{ft}^2\ ^\circ\text{F/Btu} \tag{9}$$
$$= 1.0\,(10)^{-7}\theta^{-0.4},\ \text{m}^2\ ^\circ\text{C/Ws}$$

Since the exponents are both close to -0.5, they may be correlated by

$$F_r/A = \theta^{-0.5} \tag{10}$$

$$\text{for } CaSO_4,\quad A = 1.5(10)^{-3} \text{ for } F_r \text{ as ft}^2\ ^\circ\text{F/Btu}$$
$$= 7.7(10)^{-8} \text{ for } F_r \text{ as m}^2\ ^\circ\text{C/Ws}$$
$$\text{for } Li_2SO_4,\quad A = 3.0(10)^{-3} \text{ for } F_r \text{ as ft}^2\ ^\circ\text{F/Btu}$$
$$= 1.5(10)^{-7} \text{ for } F_r \text{ as m}^2\ ^\circ\text{C/Ws}$$

Figure 9 shows this correlation for both salts, plotted as F_r/A versus θ.

Conclusions

The conclusions from this study are the following:

1 Crystalline fouling is characterized by an induction period with little or no fouling, followed by constant-rate fouling.

2 Induction periods and fouling rates for a given salt may be correlated by the same parameters.

3 Fouling rates of the salts tested were inversely proportional to the square roots of the induction periods.

4 Important correlating parameters were supersaturation, mass transfer coefficient, and surface temperature.

5 Calcium sulfate data were correlated by supersaturation and mass transfer coefficients.

6 Lithium sulfate data were correlated by supersaturation and surface temperature.

References

1 Fischer, P., Suitor, J. W., and Ritter, R. B., "Fouling Measurement Techniques and Apparatus," *Chemical Engineering Progress*, Vol. 71, No. 7, 1975, pp. 66–71.

2 Knudsen, J. G., and Story, M., "The Effect of Heat-Transfer Surface Temperature on the Scaling Behavior of Simulated Cooling Tower Water," *Chemical Engineering Symposium Series*, Vol. 74, No. 174, 1978, pp. 25-44.

3 Morse, R. W., and Knudsen, J. G., "Effect of Alkalinity on the Scaling of Simulated Cooling Tower Water," *Canadian Journal of Chemical Engineering*, Vol. 55, 1977, pp. 272-278.

4 Ritter, R. B., and Suitor, J. W., "Seawater Fouling of Heat Exchanger Tubes," *Proceedings of the 2nd National Conference on Complete Water Reuse*, Chicago, May 4-8, 1975, pp. 604-609.

5 Ritter, R. B., and Suitor, J. W., "Fouling Research on Copper and Its Alloys—Seawater Studies," International Copper Research Association Project 214B, New York, 1978.

6 Ritter, R. B., Suitor, J. W., and Cypher, G. A., "Thermal Fouling Rates of 90-10 Copper-Nickel and Titanium in Seawater Service," *Proceedings of the Ocean Thermal Energy Conversion Biofouling and Corrosion Symposium*, Seattle, Oct. 10-12, 1977, pp. 353-365.

7 Taborek, J., Aoki, T., Ritter, R. B., Palen, J. W., and Knudsen, J. G., "Fouling—The Major Unresolved Problem in Heat Transfer," *Chemical Engineering Progress*, Vol. 68, pt. 1 in No. 2, 1972, pp. 59-67; and pt. 2 in No. 7, 1972, pp. 69-78.

8 Reid, R. C., and Sherwood, T. K., *The Properties for Gases and Liquids*, 2d ed., McGraw-Hill, New York, 1966.

9 Wilson, E. E., "A Basis for Rational Design of Heat Transfer Apparatus," ASME *Transactions*, Vol. 37, No. 47, 1915, pp. 47-87.

10 Banchero, J. T., and Gordon, K. F., "Scale Deposition on a Heated Surface," *Advances in Chemistry Series*, No. 27, American Chemical Society, Washington, D.C., 1960, pp. 105-114.

N. Abuaf
General Electric Co.,
Schenectady, N.Y. 12301.
Mem. ASME

O. C. Jones, Jr.
Rensselaer Polytechnic Institute,
Troy, N.Y.
Fellow ASME

B. J. C. Wu
Lawrence Livermore National Laboratory,
Livermore, Calif.

Brookhaven National Laboratory,
Upton, N.Y. 11973

Critical Flashing Flows in Nozzles With Subcooled Inlet Conditions[1]

Examination of a large number of experiments dealing with flashing flows in converging and converging-diverging nozzles reveals that knowledge of the flashing inception point is the key to the prediction of critical flow rates. An extension of the static flashing inception correlation of Jones [16] and Alamgir and Lienhard [17] to flowing systems has allowed the determination of the location of flashing inception in nozzle flows with subcooled inlet conditions. It is shown that in all the experiments examined with subcooled inlet regardless of the degree of inlet subcooling, flashing inception invariably occurred very close to the throat. A correlation is given to predict flashing inception in both pipes and nozzles which matches all data available, but is lacking verification in intermediate nozzle geometries where turbulence may be important. A consequence of this behavior is that the critical mass flux may be correlated to the pressure difference between the nozzle inlet and flashing inception, through a single phase liquid discharge coefficient and an accurate prediction of the flashing inception pressure at the throat. Comparison with the available experiments indicate that the predicted mass fluxes are within 5 percent of the measurements.

Introduction

Flashing flow of initially subcooled or saturated fluid through nozzles, orifices, and other restrictions has been the subject of many studies. Such flows are of importance in such areas as liquid propellant rocket nozzles, high-temperature flows through relief valves or through partial ruptures, and in pipes. Several reviews of the literature pertaining to critical discharge of flashing flows exist including those by Hutmacher [1], Hsu [2], and Saha [3]. It has been generally found that models based on assumptions of homogeneous equilibrium underpredict the critical discharge rates. The differences have been attributed to the presence of nonequilibrium resulting in a superheated liquid state and less voids than would otherwise be predicted. No adequate model currently exists to account for these effects.

It is the purpose of this paper to present a unified theory for the calculation of critical mass flow rates through converging-diverging nozzles with subcooled inlets. It will be shown that the correlation of flashing inception leads to the determination that flashing onset occurs virtually at the throat (plane of minimum flow area) in nozzles. It will further be shown how this observation, coupled with an accurate prediction for the under-pressure at inception based on Alamgir and Lienhard [17], leads directly to an accurate computation of the critical discharge rates in nozzles.

Literature Survey

Thorough reviews of two-phase critical flows have been reported by Hsu [2], and Saha [3], emphasizing the effect of both thermal and mechanical nonequilibrium between the phases. These effects are considered to be important in short nozzles ($1 < L/D < 40$) [4] with subcooled or saturated single-phase inlet conditions.

Brown [5] and Schrock, Starkman and Brown [6] reported on a study of the flashing phenomena of subcooled water in a converging-diverging nozzle. The single-phase all water (Bernoulli) flow rate calculations overpredicted the actual measurements, while the homogeneous equilibrium results underpredicted them. A two-step model which allowed some nucleation delay was also proposed but there was no general formulation for the amount of superheat that can be allowed in the nozzle before the onset of flashing, and thus the predictions depended strongly on the bubble radii at the assumed inception point.

Powell [7] investigated the flow of subcooled water through a converging and a converging-diverging nozzle with identical inlet and throat configurations respectively. His data consisted of mass flow rates as a function of inlet and exit pressures and inlet temperatures.

Sozzi and Sutherland [8] performed vessel blowdown experiments with saturated and subcooled water, to study the variation of the critical mass flow rates with inlet fluid enthalpy and nozzle geometry. Although metastable/nonequilibrium regions were observed, no systematic way of predicting them was presented.

More recently, Collins [9] noted that mass-flux-pressure derivatives are not continuous at the saturated liquid line and thus showed that the isentropic homogeneous equilibrium model may overpredict rather than underpredict the observed mass flow rates under certain reservoir conditions.

Critical flow experiments were also reported by Simoneau [10], Simoneau and Hendricks [11], and Hendricks, Simoneau and Barrows [12] with cryogenic liquids. They measured critical mass flow rates as well as detailed pressure distributions along converging-diverging nozzles for various subcooled inlet conditions.

Experiments with subcooled water inlet conditions have also been conducted by Zimmer et al. [13] in a converging-diverging nozzle where detailed pressure distributions and void profiles were measured.

Fincke [14] and Fincke et al. [15] reported experimental and theoretical studies on critical flows in a converging-diverging nozzle having turbulence inducing grids and a length of constant area throat section. Their results consisted of pressure distributions, critical mass fluxes and turbulent intensities upstream of the nozzle throat. Their theory for the

---

[1] Work performed under the auspices of the U.S. Nuclear Regulatory Commission

Contributed by the Heat Transfer Division and presented at the ASME Century II Symposium on Poly-Phase Flow and Transport Technology, August 13–15, 1980. Manuscript received by the Heat Transfer Division February 22, 1982.

nonequilibrium critical flow is based on the heat transfer from a liquid jet.

According to accepted concepts, with subcooled inlet conditions, the liquid accelerates in the converging section, causing the local pressure to drop below the saturation pressure corresponding to either the inlet temperature (isothermal flow) or the inlet entropy (isentropic flow), resulting in a metastable superheated liquid state. At some point a limit is reached where flashing inception occurs, resulting in a two-phase mixture flowing in the balance of the test section. Although the flashing inception point was expected to play a very important role in the critical mass flow rates with subcooled inlet conditions, no general correlation of this inception criteria has yet been developed.

In what follows, an inception criterion will be described and its use will lead to an accurate computation of critical discharge rates.

Flashing Inception

Turbulence Effects. Jones [16] examined steady flow flashing in straight pipes and explained the inception superheat as a turbulence effect causing the minimum pressure to be lower than the apparent (measured) pressure. His turbulence model yielded the following prediction for flashing inception pressure undershoot below saturation

$$\Delta p^*_{Fi} = \frac{\Delta p_{Fi}}{\Delta p_{Fio}} = \mathrm{Max} \begin{cases} 0 \\ 1\text{-}27 \left[\frac{\overline{u'^2}}{U^2}\right] F_i \end{cases} \tag{1}$$

where the flashing index is defined as $F_i = \rho_f U^2/2\Delta p_{Fio}$. At that time, the inception undershoot for vanishing convective expansion, Δp_{Fio}, was unknown.

Static Decompression Effects. Alamgir and Lienhard [17] developed a semiempirical model for heterogeneous nucleation during rapid blowdown decompression of water from pipes, effectively correlating the heterogeneity factor in the nucleation work function. The resulting expression yielded the Δp_{Fio} lacking in Jones's expression as

$$\Delta p_{Fio} = p_s - p_{Fi} = 0.253 \frac{\sigma^{3/2}}{\sqrt{kT_c}} \cdot \frac{T_R^{13.73} \sqrt{1 + 14\ \Sigma'^{0.8}}}{\left[1 - \frac{v_f}{v_g}\right]} \tag{2}$$

Jones subsequently combined the two effects in the work published in [19].

Combined Convective Decompression in Nozzles.

Turbulence Effects. It is well known that in converging flows the turbulence intensity is reduced. For instance, Uberoi [18] measured axial and radial turbulence intensity for air with screen-generated inlet turbulence intensities of 0.24. (The second lateral turbulence component was assumed identical to the radial component.) If the only effect of the nozzle is to increase the stream velocity without affecting the magnitude of the turbulent fluctuations, then the turbulent intensity $\sqrt{\bar{u}'^2/U^2}$ would decrease as $(A/A_o)^2$. Uberoi's data, summarized in Table 1, show that the decrease in turbulent intensity is not as strong, varying as $(A/A_o)^n$ where $n \simeq 1.75$ for reductions up to approximately 1:4, and $n \simeq 1.4$ for larger reductions. Fincke et al. [15] also confirm the $\simeq 1.75$ power for a maximum area reduction of 1:5.9 in 75°C water. Based on this, equation (1) can be modified for converging flows as

$$\Delta p^*_{Fi} = \mathrm{Max} \begin{cases} 0 \\ 1\text{-}27 \left[\frac{\overline{u'^2}}{U_o^2}\right] \left[\frac{A}{A_o}\right]^n F_i \end{cases} \tag{3a}$$

where

$$n = \begin{cases} 1.75 & A/A_o \geq 1{:}6 \\ 1.4 & A/A_o < 1{:}6 \end{cases} \tag{3b}$$

If the turbulence intensity refers to fully developed flow in a straight pipe preceding the nozzle, the value of 0.072 used in [16] should be reasonable. Otherwise $\sqrt{\bar{u}'^2}/U_o$ must be specified "a priori," as in Fincke's data [15]. While equation (3) provides a link between straight pipe data and converging flow data, in many converging flows the turbulence effects will be small. Such is the case with the data discussed below and so these effects have been neglected.

Convective Effects. While Alamgir and Lienhard [17] developed their correlation to describe the static decompression undershoot experienced in the rapid discharge of hot fluid from long pipes, it appeared that the decompression rate Σ' utilized by these authors could just as well be set in the Eulerean frame experienced by a particle of fluid flowing in a nozzle so that Σ' could be written as

$$\Sigma' = \left.\frac{\partial p}{\partial t}\right]_z + U \left.\frac{\partial p}{\partial z}\right]_t \tag{4}$$

The first term on the right-hand side represents the static depressurization rate determined by Alamgir and Lienhard [17] while the second term represents the additional convective depressurization rate. In the case of steady flow in nozzles, only this latter term exists whereas for transient

Nomenclature

A = cross-sectional area
A_o = cross-sectional area at inlet
C_D = discharge coefficient
D = nozzle diameter
F_i = $\rho\ U^2/2\Delta p_{\mathrm{Fio}}$, inverse of cavitation index
G_T = throat mass flux
k = Boltzmann constant
L = nozzle length
$\dot{m}$ = mass flow rate
p_{Fi} = pressure at flashing inception
p_s = saturation pressure at initial temperature
T_c = critical temperature
T_R = reduced initial temperature
U = local mass-averaged velocity
$\sqrt{\bar{u}'^2}/U$ = local turbulence intensity
U_o = inlet velocity
$v_f = 1/\rho$ = specific volume of saturated liquid at initial temperature
v_g = specific volume of saturated vapor at initial temperature
z = axial coordinate
σ = surface tension
Δp_{Fio} = static flashing inception pressure undershoot
Δp^*_{Fi} = dimensionless pressure undershoot at flashing inception, $\Delta p_{Fi}/\Delta p_{Fio}$
Σ' = depressurization rate

Table 1 Comparison of turbulence intensity decrease data of Uberoi [18] with area ratio computations

A_o/A	$\dfrac{\overline{u'^2}+2\overline{v'^2}}{U^2}\times 10^4$	$\dfrac{\overline{u'^2}+2\overline{v'^2}}{\overline{u_o'^2}+2\overline{v_o'^2}}\cdot\left[\dfrac{U_o}{U}\right]^2$	$(A/A_o)^{1.75}$	$(A/A_o)^{1.4}$
1	17.2	1.0	1.000	1.000
2	5.01	0.290	0.297	0.379
4	1.89	0.109	0.088	0.144
6	1.18	0.068	0.043	0.081
8	0.83	0.048	0.026	0.054
10	0.65	0.038	0.018	0.040
12	0.52	0.030	0.013	0.031
14	0.43	0.025	0.010	0.025
16	0.36	0.021	0.008	0.021

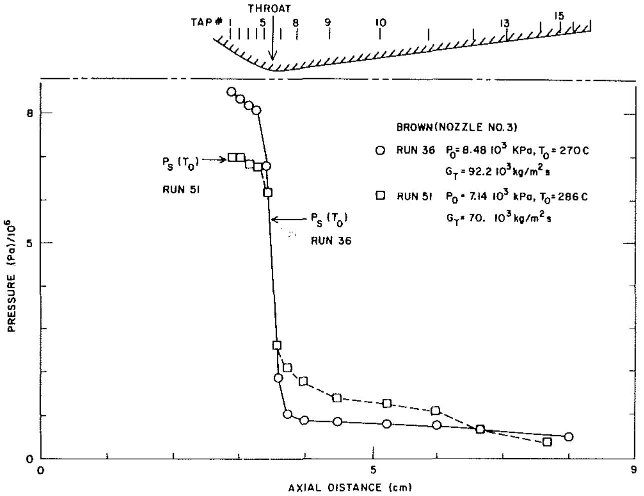

Fig. 1 Pressure distributions for two experiments (runs 36, 51) under 18.3 and 27.8°C subcooled inlet conditions (Brown [5], Schrock et al. [6])

blowdown of a reservoir through a nozzle both terms may in fact be important.

Experimental Comparisons. Although experimental accuracy left room for some slight inlet voids, Brown's data [5, 6] were reported to have both low and high subcoolings of near saturation (Run 51) and 27.8 C (Run 36) (Fig. 1). Expansions were calculated from Bernoulli's equation and mass conservation as

$$\Sigma' = \frac{dp}{dz}\cdot\frac{dz}{dt} = \frac{\dot{m}^3}{\rho^2 A^4}\cdot\frac{dA}{dz} \tag{5}$$

and were smoothed and averaged between pressure taps using a second-order polynomial. At the throat (Tap 6), since $dA/dz = 0$, the depressurization rate was calculated from the expression, $\Sigma' = dp/dz \cdot dz/dt'$, where the velocity $dz/dt = \dot{m}/\rho\ A$, and the pressure gradient, $dp/dz \cong \Delta p/\Delta z$, between taps 5 and 6. Experimental superheats (dashed lines) are compared with those required for flashing inception (solid line) in Fig. 2. Flashing is predicted to occur where the former exceeds the latter, between pressure taps 5 and 6 in both cases, tap #6 being at the minimum geometric area, whereas tap #5 is 1.2-mm upstream.

Similar loci of superheat versus expansion rates for the data of Zimmer et al. [13] are shown in Fig. 3 for 100°C inlet conditions. Expansion rates were in the range of 10^6–10^8 Pa/s compared with Brown's data having expansion rates of 10^8–10^{11} Pa/s. Even though Zimmer's data are below the minimum value of 4×10^9 Pa/s recommended by Alamgir and Lienhard [17], inception is still predicted between pressure taps 24 and 25, within 1 cm of the plane of minimum area in all cases.

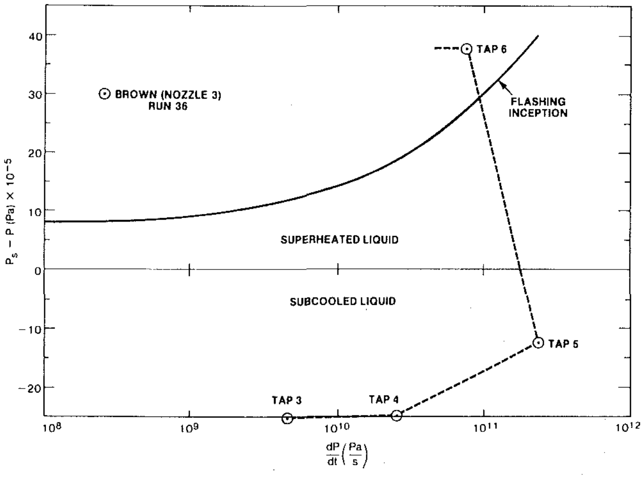

Fig. (*a*) Run 36, T_i = 270°C

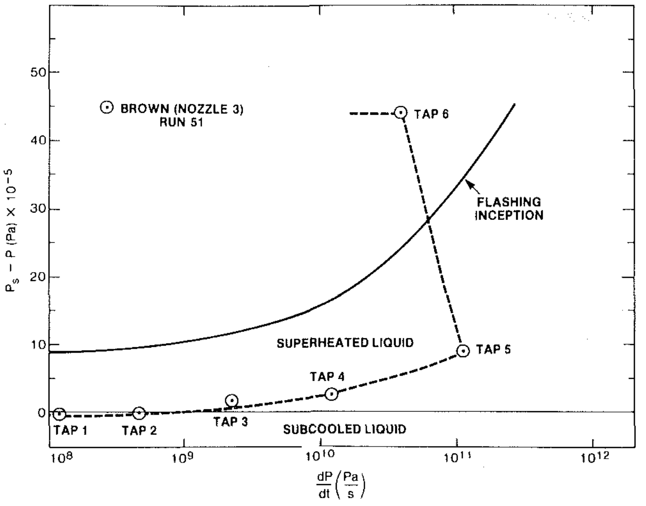

Fig. (*b*) Run 51, T_i = 286°C

Fig. 2 Comparison of the flashing inception predicted by Alamgir and Lienhard [17] (solid line) with the locus of the liquid depressurization history (circles connected by dashed line) in Brown's nozzle [5, 6]

Extension to Other Nozzles. Both Brown's data [5, 6] and Zimmer's data [13] indicate that flashing occurs within a very short distance of the plane of minimum geometric area. Based on these observations, one can perceive that the precipitous drop in the "sonic" (in the single-phase sense) velocity at the onset of flashing would limit large increases in mixture velocity due to voiding where flashing to occur any distance upstream of this location. Thus, the following hypothesis can

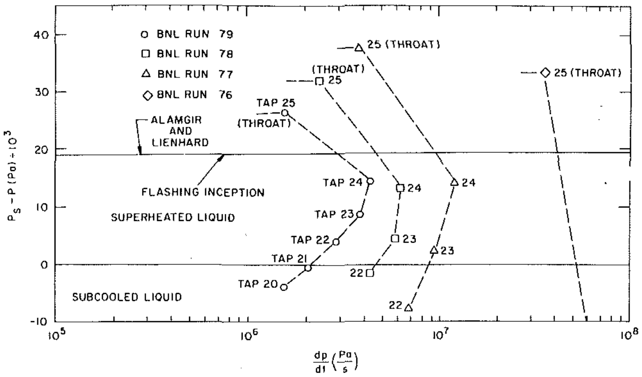

Fig. 3 Comparison of the flashing inception predicted by Alamgir and Lienhard [17] (solid line) with the locus of the depressurization history in Zimmer's nozzle (Runs 76, 77, 78, 79) [13]

be developed and extended to all nozzles used in practice for subcooled inlets.

Hypothesis: Critical two-phase discharge of initially subcooled liquids through nozzles occurs with flashing inception predicted by equations (2-4) occurring essentially at the plane of minimum flow area.

Before arguing the merit of this hypothesis and presenting a stability criterion, a very simple test may be applied to this hypothesis. If flashing inception occurs close to the plane of minimum flow area, flow upstream would be single-phase liquid. The nozzle discharge coefficients determined using the measured flow rates and throat and inlet pressures would then agree with single-phase values.

Data of Brown [5, 6], Sozzi [8], Zimmer [13], and Simoneau [11], the latter for liquid nitrogen, are shown in Fig. 4. In all cases the resultant discharge coefficients are scattered near a value of 0.94 ± 0.04,[2] quite close to expected single-phase values. It is felt that this is a reasonable confirmation of the hypothesis.

Stability of Flashing Location. Even though significant controversy exists at this time between the relationship between choked flow and "sonic" velocity in two-phase flows, these terms shall be used herein in the single-phase sense. It is well known that, on an equilibrium basis, a discontinuity in sonic velocity is predicted at the flashing front which may be close to two orders in magnitude. If the two-phase mixture velocity is limited to a "Mach number" of unity at the throat, little voids could be formed upstream of the throat without choking occurring. Thus, for all practical purposes, even in very benign situations of a very slight convergence, except at very low flows entering quite near saturation, the flashing front must exist, in the case of subcooled inlet, virtually at the plane of minimum area.

Since the sonic velocity (c) for pure vapor may be in the vicinity of 350 m/s, a minimum will generally occur in the c-α curve. If flow approaching a converging (accelerating) region undergoes flashing inception, it appears that the rate of void generation due to friction upstream of the accelerating region and due to the acceleration downstream of the start of this region must always be less than that required to reach sonic conditions upstream of the throat. If this does not occur, then upstream choking would occur which if the flow reduces sufficiently to cause the flashing inception point to move into the region of acceleration, will cause it to immediately move to the throat. Thus, a stability criteria may be qualitatively stated as follows:

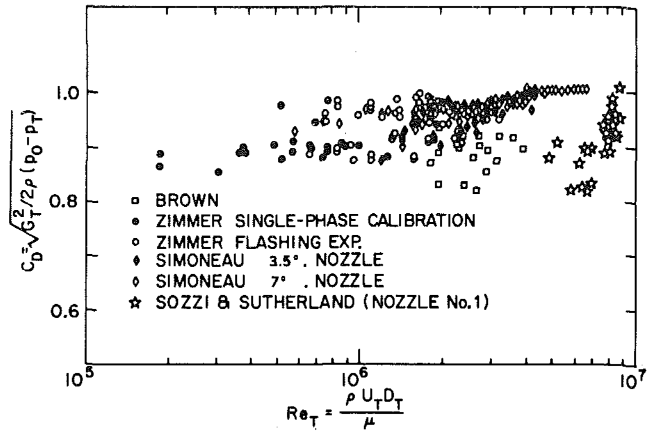

Fig. 4 Variation of the discharge coefficient with the Reynolds number for data in a converging-diverging nozzle with subcooled liquid inlet conditions. Brown [5], Schrock et al. [6], $C_D = 0.91 \pm 0.04$; Sozzi and Sutherland [8], $C_D = 0.92 \pm 0.06$; Zimmer et al. [13], $C_D = 0.93 \pm 0.04$; Simoneau and Hendricks [11], $C_D = 0.97 \pm 0.02$

Stability Criteria. Flashing inception in nozzles and other geometries with restrictions causing accelerations will always occur virtually at the throat (plane of minimum flow area). Flashing inception will remain stable at this location unless the conditions change to cause the inception point to move either upstream of the accelerating zone, or downstream out of the decelerating zone to a new single-phase region of negative pressure gradient.

Critical Mass Flows

The two pieces of information necessary to predict the critical mass flow rates in nozzles with subcooled inlet conditions include:

(*a*) The "Stability Criteria" which fixes the flashing inception to occur at the throat (minimum flow area)

(*b*) The pressure at the flashing inception which is predicted by equations 2-4

The proposed method thus consists in considering single-phase flow up to the throat and providing an expression for predicting the throat pressure. For the case where the liquid density is relatively constant, the critical mass flux at the throat is given by

$$G_c = C_D \sqrt{2\,\rho\,(p_o - p_s + \Delta p_{Fi})} \qquad (6)$$

where Δp_{Fi} is given by equations (2-4). The expansion rate, Σ', for nozzles may be calculated from equation (4)

$$\Sigma' = \frac{G_c^3}{\rho^2} \cdot \frac{d(\ln A)}{dz} + \Sigma_o' \qquad (7)$$

where frictional losses have been neglected and where Σ'_o is the transient component and is equal to zero for steady flows. Since Δp_{Fi} has also a functional dependance on G_c, equation (6) becomes transcendental but may be solved by an iteration method.

The method outlined above was applied to Powell's data [7] covering a wide range of inlet pressures (2800-17,000 kPa) and inlet temperatures (203-288°C). The measured critical mass fluxes are compared with the calculated values in Figs. 5 and 6. The latter lie within 5 percent of the reported data. The calculational method also correctly predicts the trends observed of decreasing critical mass flux at a given inlet pressure with increasing inlet temperature.

The deviations observed between the predictions and Powell's data [7] may be due to:

(*a*) The value of the discharge coefficient of 0.9 used in the calculations in the absence of single-phase calibration data

(*b*) The quoted 10 percent accuracy of the Alamgir-Lienhard correlation

---

[2] The slightly larger standard deviation in Sozzi and Sutherland's data (Nozzle No. 1) could be due to the possibility that inlet voids existed for some of the experiments reported here. Their stagnation qualities were deduced from fluid density in the vessel, ρ, obtained through hydrostatics, and the stagnation pressure, p_o. All the data presented by Sozzi [8] with Nozzle No. 1, with a negative inlet quality implying subcooled inlet conditions were included in the results presented in Fig. 4.

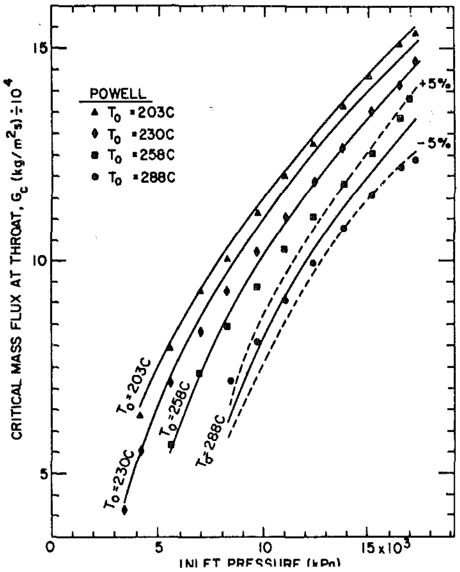

Fig. 5 Comparison of critical throat mass fluxes measured by Powell [7] with those calculated by the present method for different nozzle inlet pressure and temperatures

(*c*) The experimental uncertainty in Powell's data [7] concerning the mass flow rates, pressures and temperatures

In spite of all these points, the present method predicts the critical mass flow rates quite accurately as a function of nozzle inlet conditions (p_o, T_o) and nozzle geometry.

Conclusions and Recommendations

Flashing Inception.

1 Flashing inception for water in nozzles with subcooled single-phase inlet conditions is well predicted by the Alamgir-Lienhard [17] correlation (equation (2)), where the depressurization rate is expressed in Lagrangean terms (equation (4)).

2 A stability criterion has been proposed and verified by existing data that flashing inception in nozzles will occur virtually at the throat if the pressure there is reduced to that at which flashing inception occurs. If flashing inception does not occur at the throat, then it will not occur in the nozzle at all.

3 A relationship connecting the flashing inception criteria in pipes [16, 17] with that in nozzles as developed in the present paper has been proposed (equation (3)) which agrees with the available data.

4 Data are needed on flashing inception in nozzles in order to better define the geometric effects on the turbulent pressure fluctuations.

Critical Flows.

1 Critical discharge of flashing flows from nozzles with subcooled inlet conditions occurs without flashing up to the throat and may thus be described through the single-phase discharge coefficient (equation (6)); the throat pressure required for the flow calculations is specified through the pressure at which flashing inception occurs (equations (2-4)).

2 Where data exist with measurements of throat pressure, agreement with this theory has been obtained where discharge coefficients of 0.94 were found within 4 percent. For the data of Powell [7], where throat pressures were not available, a discharge coefficient of 0.90 correlated the data within 5 percent. The range of data tested includes pressures from 27 to 170 bars, temperatures between 100 and 300°C, and critical mass flows up to 150,000 kg/m^2 s.

3 To apply the criteria developed herein, both single-phase flow (discharge) coefficients in terms of the minimum area for a given geometry, as well as the effective expansion rates at the flashing inception point must be determined.

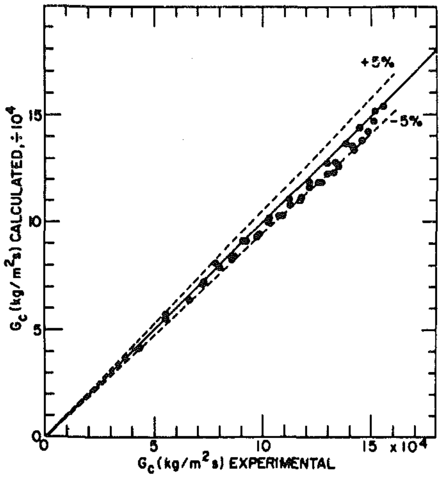

Fig. 6 Comparison of calculated with measured critical throat mass fluxes [7] for various nozzle inlet conditions

Acknowledgements

The authors would like to thank Dr. N. Tutu for helping with the turbulence intensity calculations in nozzles.

References

1 Hutmacher, E. S., Nesmith, B. J., and Brukiewa, J. B., "Study of Safety Relief Valve Operation Under ATWS Conditions," En. Technology Engineering Center, ETEC-TDR-78-19, Jan. 1979.

2 Hsu, Y. Y., "Review of Critical Flow, Propagation of Pressure Pulse and Sonic Velocity," NASA TND-6814, 1972.

3 Saha, P., "Review of Two-Phase Steam-Water Critical Flow Models with Emphasis on Thermal Nonequilibrium," NUREG/CR 0417, BNL-NUREG-50907, 1978.

4 Seynhaeve, J. M., "Critical Flow Through Orifices," Paper presented at the European Two-Phase Group Meeting, Grenoble, 1977.

5 Brown, R. A., "Flashing Expansion of Water Through a Converging-Diverging Nozzle," M.S. thesis, University of California, Berkeley, USAEC Report UCRL-6665-T, 1961.

6 Schrock, V. E., Starkman, E. S., and Brown, R. A., "Flashing Flow of Initially Subcooled Water in Convergent-Divergent Nozzles," ASME JOURNAL OF HEAT TRANSFER, Vol. 99, 1977, pp. 263-268; Erratum, JOURNAL OF HEAT TRANSFER, Vol. 99, 1977, p. 647.

7 Powell, A. W., "Flow of Subcooled Water Through Nozzles," *Westinghouse Electric Corporation*, WAPD-PT-(V)-90, Apr. 1961.

8 Sozzi, G. L., and Sutherland, W. A., "Critical Flow of Saturated and Subcooled Water at High Pressure," General Electric Company Report NEDO-13418, 1975.

9 Collins, R. L., "Choked Expansion of Subcooled Water and the Isentropic Homogeneous Equilibrium Model," ASME JOURNAL OF HEAT TRANSFER, Vol. 100, 1978, pp. 275-280.

10 Simoneau, R. J., "Pressure Distributions in a Converging-Diverging Nozzle During Two-Phase Choked Flow of Subcooled Nitrogen," *Nonequilibrium Two-Phase Flows*, ASME, New York, 1975, pp. 37-45.

11 Simoneau, R. J., and Hendricks, R. C., "Two-Phase Choked Flow of Cryogenic Fluids in Converging-Diverging Nozzles," NASA Technical Paper 1484, July 1979.

12 Hendricks, R. C., Simoneau, R. J., and Barrows, R. F., "Two-Phase Choked Flow of Subcooled Oxygen and Nitrogen," NASA-TN-D-8169, 1976.

13 Zimmer, G. A., Wu, B. J. C., Leonhard, W. L., Abuaf, N., and Jones, O. C. Jr., "Pressure and Void Distributions in a Converging-Diverging Nozzle with Nonequilibrium Water Vapor Generation," BNL-NUREG-26003, 1979.

14 Fincke, J. R., "The Correlation of Nonequilibrium Effects with Choked Nozzle Flow with Subcooled Upstream Conditions," Conference Paper, ANS Small Break Specialist Meeting, California, pp. 4-1, 4-30, 1981.

15 Fincke, J. R., Collins, D. R., and Wilson, M. L., "The Effects of Grid Turbulence on Nonequilibrium Choked Nozzle Flow," NUREG/CR-1997, EGG-2088, Apr. 1981.

16 Jones, O. C. Jr., "Flashing Inception in Flowing Liquids," *Nonequilibrium Two-Phase Flows*, edited by J. C. Chen and S. G. Bankoff, ASME, New York, 1979, pp. 29-34.

17 Alamgir, M. D., and Lienhard, J. H., Personal Communication, 1979; "Correlation of Pressure Undershoot During Hot-Water Depressurization," ASME JOURNAL OF HEAT TRANSFER, Vol. 103, 1981, pp. 52-55.

18 Uberoi, M. S., "Effect of Wind Tunnel Contraction on Free-Stream Turbulence," *J. of Aeron. Sciences*, Vol. 23, No. 8, 1956, pp. 754-764.

19 Jones, O. C. Jr., "Flashing Inception in Flowing Liquids," ASME JOURNAL OF HEAT TRANSFER, 1980, pp. 439-444.

M. Renksizbulut[1]

M. C. Yuen
Professor and Chairman.
Mem. ASME

Department of Mechanical and
Nuclear Engineering,
Northwestern University,
Evanston, Ill. 60201

Experimental Study of Droplet Evaporation in a High-Temperature Air Stream

Heat transfer rates to simulated and freely suspended liquid droplets were measured in an atmospheric hot air tunnel. The experiments were limited to water, methanol, and heptane droplets in a Reynolds number range of 25 to 2000, and a mass transfer number range of 0.07 to 2.79. The present experimental data together with data by others can best be correlated by $Nu_f(1+B_f)^{.7}=2+0.57\ Re_M^{1/2}\ Pr_f^{1/3}$, *where properties are evaluated at film conditions except for the density in the Reynolds number which is the free-stream density. Thus the data shows that at higher temperatures, evaporation reduces heat transfer rates directly by a factor of* $(1+B_f)^{.7}$. *Indirectly, evaporation affects heat transfer rates through the changes in both the composition and temperature of the surrounding gaseous medium.*

1 Introduction

The importance of the study of heat and mass transfer of evaporating liquid droplets needs no introduction. The knowledge acquired is essential to the understanding and the prediction of the performance of a liquid spray. Much work has been done in the past. The majority of the work is, however, concentrated in low temperature environments. For heat and mass transfer of droplets in a low-temperature environment, the most recent review is found in a book by Clift, Grace, and Weber [1].

In a high-temperature environment, due to evaporation, the liquid remains at the wet-bulb temperature which is usually considerably lower than the free stream temperature. Under this circumstance, the driving potential for evaporation is the temperature gradient. In quasi-steady evaporation, the evaporation rate is the heat transfer rate divided by the heat of evaporation. Thus, heat and mass transfer are energetically synonymous. We shall follow the literature to consider only the heat transfer rate.

From the previous work of Eisenklam, Arunachalam, and Weston [2], Yuen and Chen [3], Harpole [4] and others, a clear picture of the effect of evaporation on heat and mass transfer emerges. Physically, the mass flux from evaporation dynamically affects the flow field surrounding the droplet. Energetically, evaporation causes large temperature gradients and changes the chemical composition; both directly affect the fluid properties adjacent to the droplets. Together, these effects can significantly alter the heat and mass transfer processes. The effect of mass flux is usually taken into account by the use of the mass transfer number, B. The variable properties effect can be taken into account by either the reference state method or the use of a correction factor.

Due to experimental difficulty, heat transfer data of evaporating droplets at high temperatures are rather scarce and individual investigators tend to correlate their own data.

In the reference state method, the reference temperature and mass fraction are defined as

$$T_r=T_d+r(T_s-T_d) \tag{1}$$

$$X_r=X_d+r(X_s-X_d) \tag{2}$$

where the value, r, varies from 0 to 1, depending on the particular reference state. For example, $r=0.5$ refers to the widely used film condition which is often denoted by the subscript f in the heat transfer literature. The mass transfer number, B, is defined as

$$B_r=\bar{B}_r(1+Q_R/Q_c) \tag{3}$$

where $\bar{B}_r$ is equal to $C_{pr}(T_s-T_d)/L_d$.

Early measurements of heat transfer rates were performed by Spalding [5] on various hydrocarbons in air with Reynolds numbers in the range from 800 to 4000 and B from 0.6 to 5. The correlation was found to be

$$\mathrm{Nu}\,B_f^{2/5}=.53\,\mathrm{Re}^{1/2}\,\mathrm{Pr} \tag{4}$$

where the thermophysical properties are those of air at 20°C except for B_f.

Downing [6] carried out extensive measurements on suspended droplets of water, acetone, benzene and n-hexane in laminar air jets where temperatures ranged from 27°C to 340°C, Re ranged from 24 to 325 and the mass transfer number ranged from 0 to 2. The correlation of data is

$$\mathrm{Nu}\,G=[1-0.4(1-T_s)][2+0.6\,\mathrm{Re}^{1/2}\mathrm{Pr}^{1/3}] \tag{5}$$

where $G=\{[1-0.4(1-B^{-1}ln(1+B))]B^{-1}ln(1+B)\}^{-1}$. The properties are evaluated at a reference state of $r=0.6$.

Evaporation of water and other hydrocarbon droplets in high-temperature (up to 1000°C) air streams was reported in [2]. The Reynolds numbers varied from .01 to 15 and the mass transfer numbers from 0 to 3. The correlation is

$$\mathrm{Nu}_f(1+B_f)=2+1.6\,\mathrm{Re}_f^{1/2} \tag{6}$$

where the properties are evaluated using the film conditions ($r=1/2$).

Narasimhan and Gauvin [7] investigated the evaporation of water from porous Celite spheres in superheated steam at temperatures from 500 K to 1000 K. The correlation is shown to be

$$\mathrm{Nu}_f(1+B_f)^{2/3}=.68\,\mathrm{Re}_s^{1/2} \tag{7}$$

More recently, evaporation rates of water and methanol droplets were measured in a vertical air tunnel with temperatures up to 1000°C as shown in [3]. The Re varied from 200 to 2000 and B from 0 to 0.5. The correlation was shown to be

$$\mathrm{Nu}_f[1+B_f]=2+0.60\,\mathrm{Re}_M^{1/2}\mathrm{Pr}_f^{1/3} \tag{8}$$

where Re_M is defined as $\rho_s u_s d/\mu_f$.

Theoretically, the problem of flow past an evaporating sphere at finite Reynolds numbers where both the effects of blowing and variable properties are considered is yet to be solved. Recently, Harpole [4] obtained the solution for evaporation at an axisymmetric stagnation point where both

---

[1] Present address: Westinghouse Canada, Inc., Hamilton, Ontario, Canada L8N 3K2.

Contributed by the Heat Transfer Division for publication in the JOURNAL OF HEAT TRANSFER. Manuscript received by the Heat Transfer Division February 2, 1982.

the blowing and variable properties were taken into account. He then claimed that these effects for a sphere and a stagnation point are the same. Therefore, the solution for a sphere with evaporation is the solution for a sphere of constant property without evaporation multiplied by the ratio of the stagnation point solution with and without evaporation. In his solution for the stagnation point flow, the variable property effects are presented by correction factor method in contrast to the common usage of the reference state method. He claims that his solution agrees well with available experimental data.

It is quite apparent from the above discussion that the existing correlations pertinent to large temperature and concentration gradients exhibit considerable differences in their treatment of evaporation and variable property effects. The present study is therefore an extension of our earlier work at Northwestern University [3] to a wider range of mass transfer numbers and Reynolds numbers, and an attempt for a general correlation to incorporate all the existing available data.

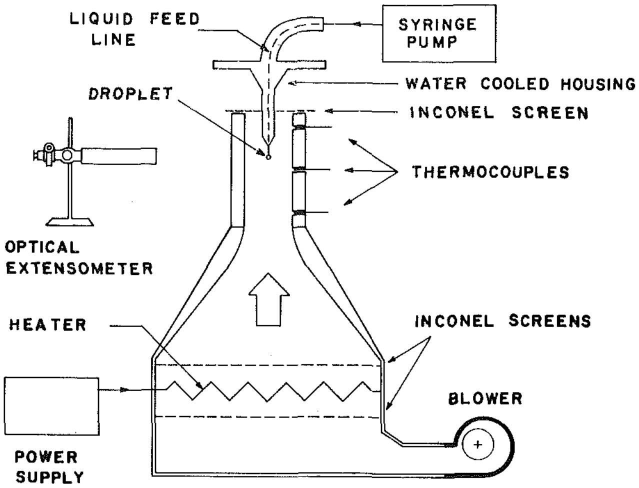

Fig. 1 Schematic of the experimental set-up

2 Experiment

The present experiment is a continuation of [3] which is described in detail in [8] and will not be repeated here. Instead we shall only give a brief summary.

The experimental set-up is shown schematically in Fig. 1. The vertical wind tunnel has a contraction ratio of 13 to 1 and is capable of providing air velocities up to 20 m/s and temperatures up to 1000°C in the test-section. The heating elements are powered by d-c welders and consist of Inconel 601 strips which are arranged to act as flow straightener as well.

The test section is 36-cm long and has a $76 \times 76\text{-mm}^2$ cross-sectional flow area. Two of the side walls are made up of Vycor glass for observations and the other two are brick. Free stream and wall temperatures can be measured at three stations by using 50 μm platinum – 13 percent rhodium traversing thermocouples and air velocities can be determined by using a Pitot tube. In turbulence measurements carried out at room temperature with a hot wire anemometer, it was found that, in the velocity range of the present measurements, the free-stream flow remained uniform with a turbulence intensity less than one-third of 1 percent within the $50 \times 50\text{-mm}^2$ core area of the test section.

The liquid feed line from the syringe pump to the droplet suspension tube is protected from the high-temperature air stream by a water-cooled housing and an elbow. The syringe pump is a high precision positive displacement injector which through a combination of different syringe sizes, a variable speed d-c motor and a gear box can supply flow rates in the range from 1.32×10^{-5} to 0.64 cm^3/s. The optical extensometer used for droplet size measurements provides 20X magnification at a working distance of 40 cm with 2.5-μm resolution.

Three methods are used to simulate the droplets depending on flow rate and the kind of liquid. The first method is to use a porous bronze sphere of 6.35-mm dia, with a thin liquid layer coating the surface of the sphere as in [3]. This is used in the Reynolds number range of 200 to 2000. The second method is to use a perforated brass sphere of 1.58-mm dia. This is used in the Reynolds number range of 50 to 500. The third method is to have a free liquid droplet suspending at the end of a capillary tube of 250-μm dia. This method is applicable to water droplets below Reynolds number of 200.

In the measurement of evaporation rate, the steady-state approach is used. Steady state is reached when the drop size remains constant (free droplet) or the liquid layer on the drop surface (porous or perforated sphere) remains uniform for a sufficient period of time. In this case the rate of liquid supply to the droplet must be equal to the evaporation rate.

In a typical experiment, the velocity and the temperature of the air stream in the test section were first brought into the range of preselected values by adjusting the power inputs to the wind tunnel blower and heater. Because of the large thermal inertia of the system, this process took over 3 hrs to complete when the wind tunnel was originally at room

Nomenclature

a = $(M_a/M_v)^n$
A = parameter used in equation (11)
B = $\bar{B}(1+Q_R/Q_c)$, mass transfer number
$\bar{B}$, = $C_p(T_s-T_d)/L_d$, mass transfer number without radiation heat transfer
C_p = heat capacity
d = diameter of droplet
E = parameter used in equation (14)
h = heat-transfer coefficient, enthalpy
k = thermal conductivity
L = latent heat of vaporization per unit mass
M = molecular weight
$\dot{m}$ = mass flux
n = constant
Nu = hd/k, Nusselt number
p = parameter used in equation (11)
Pr = $C_p\mu/k$, Prandtl number
Q = heat transfer
Re = $\rho ud/\mu$, Reynolds number
Re_M = $\rho_s u_s d/\mu_f$
T = temperature
ΔT = (T_s-T_d), temperature difference
u = velocity
X = mass fraction
Z = defined in equation (11)

Greek Symbols

α = $\ln[(\rho k)_s/(\rho k)_d]/\ln(T_d/T_s)$
ϵ = emissivity
σ = Stephan-Boltzmann constant
ρ = density
μ = viscosity coefficient

Subscripts

a = air
c = convection
d = droplet surface
e = tube entrance
f = film reference state
l = liquid
R = radiation
r = reference state
s = free stream
t = tube
v = vapor
w = wall

temperature, and about 30 min between successive observations. Next, the water-cooled suspension probe was lowered into the test section until the droplet was approximately 8 cm from the exit plane. Subsequently, the test-liquid supply rate was monitored by changing the speed of the syringe pump while the droplet diameter was measured repetitively (with the optical extensometer), size variations being corrected through adjustments on the pump. Eventually, the desired steady state was reached when the droplet size remained fixed, and thus the rate of liquid supply by the pump was equal to the rate of evaporation. As a rule, a record of the observation was made only when steady-state evaporation persisted for at least 2 min. Thermocouple, pressure transducer, and pump readings were then registered completing the process.

For interpretation of the experimental data, the steady-state energy equation is applied to the control volume as shown in Fig. 2.

$$Q_c + Q_R = \dot{m}L_d + \dot{m}[h_l(T_d) - h_l(T_e)] - (Q_t + Q_l) \qquad (9)$$

where Q_c and Q_R are the convective and radiative heat flux to the drop, $\dot{m}$ is the mass flux, L_d is the latent heat, h_l is the enthalpy of the liquid, T_d is the drop surface temperature, T_e is the liquid temperature at the end of the tube, Q_t and Q_l are the heat loss or gain from the tube and liquid in the tube. An order of magnitude analysis has shown that the last term in equation (9) is negligible [8].

The values of wet-bulb temperature (T_s) as a function of free-stream temperatures are listed in Table 1. These wet-bulb temperatures are taken from Yuen and Chen [9]. In the case of the porous sphere, T_e was measured and was found to have a maximum deviation of 4°C from T_d. For smaller droplets (perforated sphere and suspended droplets), it was assumed that T_e was equal to T_d. The effect of natural convection in this case has been estimated in reference [8] to be negligible. Thus, Q_c in equation (9) represents only heat transfer from forced convection.

Wall temperatures in the test section were maintained essentially uniform by placing an Inconel screen at the channel exit. For isothermal walls at a temperature, T_w, surrounding the droplet, the thermal radiation can be computed from

$$Q_R = \pi d^2 \, \sigma \epsilon [T_w^4 - T_d^4] \qquad (10)$$

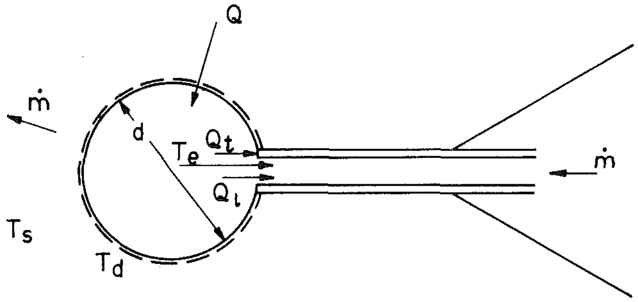

Fig. 2 Schematic diagram of an evaporating droplet

where σ is the Stephan-Boltzmann constant and the emissivity, ϵ, of the liquid is assumed to be 0.95 and equal to absorptivity. A more accurate formulation of the radiation problem using shape factors and appropriate emissivities (e.g., $\epsilon = 0.85$ for Vycor and 0.65 for refractory brick walls) for the surfaces involved is given in detail in [8]. The result shows that equation (10) can predict Q_R to within 4 percent. The physical reason is that in an enclosure, the net result of interreflections is to make the wall radiosity more nearly that of a black body. For most of the present experimental data, Q_R is much less than 1/3 of Q_c.

3 Results and Discussion

Heat transfer rates of water, methanol, and n-heptane droplets at atmospheric pressure were measured with air stream temperatures up to 800°C. A total of 288 data points were recorded covering the range of variables summarized in Table 2. Other pertinent information for each of the data points can be found in [8].

Following [3], it was found that the data can be correlated in the following form

$$Z^p \equiv [\mathrm{Nu}(1+B)^p - 2]\mathrm{Pr}^{-1/3} = A\,\mathrm{Re}^{1/2} \qquad (11)$$

For Re→0 and negligible evaporation ($B \rightarrow 0$), equation (11) approaches the theoretical limit of Nu = 2, provided that free convection can be neglected. Furthermore, for small temperature differences between the droplet and the free stream ($B \rightarrow 0$), equation (11) agrees with the correlation of Ranz and Marshall [10] if A equals 0.6. In the present study, the Prandtl number varied between 0.7 and 1. Hence, the difference between $\mathrm{Pr}^{1/3}$ and $\mathrm{Pr}^{0.38}$ as proposed by [4] has negligible effect on the overall correlation. What remains to be determined in equation (11) is the proper reference state to evaluate the thermodynamic and transport properties in the dimensionless numbers and the exponent p.

Table 1 Wet-bulb temperatures and mass transfer numbers as a function of free-stream temperatures.

T_s(°C)	T_d(°C)	$\bar{B}_f$
	Water	
100	33	0.028
200	50	0.067
400	71	0.061
600	84	0.267
800	90	0.415
	Methanol	
100	26	0.067
200	45	0.16
400	55	0.42
600	60	0.74
	n-Heptane	
100	36	.20
200	55	.56
400	75	1.75
600	90	3.62

Table 2 Experimental range of variables

Test liquid	Water	Methanol	n-Heptane	All data
Data size	120	81	87	288
T_s, (°C)	204-786	193-485	238-450	193-786
ΔT, (°C)	154-696	149-427	178-371	149-696
u_s, (m/s)	0.8-5.1	0.9-9.0	1.4-8.6	0.8-9.0
d, (mm)	0.9-2.12	1.62-6.35	1.64-6.35	0.92-6.35
Re_M	24-201	58-1788	78-1974	24-1974
B_f	0.07-0.46	0.16-0.64	0.9-2.79	0.07-2.79
$(Q_R/Q_C)_{\max}$	0.173	0.221	0.340	0.340

According to [3], the best correlation of experimental data following equation (11) is

$$Z_f^{1.0} = [\mathrm{Nu}_f(1+B_f)-2]\mathrm{Pr}_f^{-1/3} = 0.60\,\mathrm{Re}_M^{1/2} \qquad (12)$$

where the exponent p is 1, A is 0.60 and $\mathrm{Re}_M = \rho_s U_s d/\mu_f$. The subscript f denotes the film condition as defined in equations (1) and (2) with $r = 1/2$.

The present experimental data are shown in Fig. 3 together with equation (12). Figure 3 shows that the water and methanol data agree well with equation (12); the heptane data, however, are consistently higher. The correlation of equation (12) was based on water and methanol data in [3], where the maximum B number was about 0.5. Therefore the correlation was not sensitive to the exponent p.

One of the primary purposes of the present experimental investigation is to extend the range of Re and B in order to further test the validity of equation (12). It now appears that equation (12) does not correlate well with data where the B number is higher than one. The new experimental results show that the best correlation of the data is

$$Z_f^{0.70} \equiv [\mathrm{Nu}_f(1+B_f)^{0.70}-2]\mathrm{Pr}_f^{-1/3} = 0.57\,\mathrm{Re}_M^{1/2} \qquad (13)$$

The uncertainties associated with $A = 0.57$ and $p = 0.70$ are ± 0.032 and ± 0.062, respectively. The latter standard deviation is based on data points with $B_f > 0.15$. Equation (13) together with the experimental data are plotted in Fig. 4.

The use of two different reference states for the Reynolds' number ($\mathrm{Re}_M = \rho_s u_s d/\mu_f$) is perhaps inconvenient but

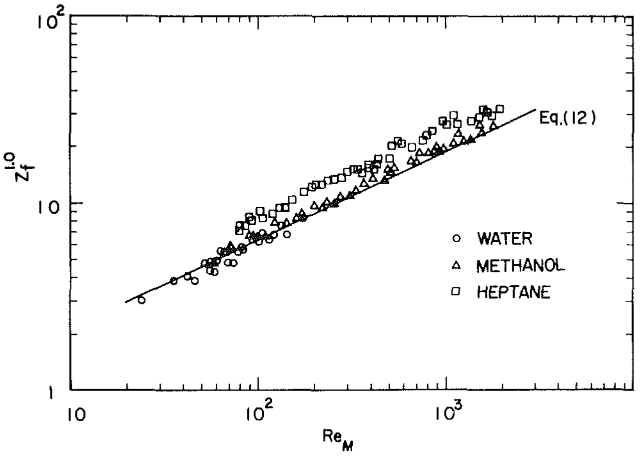

Fig. 3 Correlation of present heat transfer rates of evaporating liquid droplets in air according to [3]

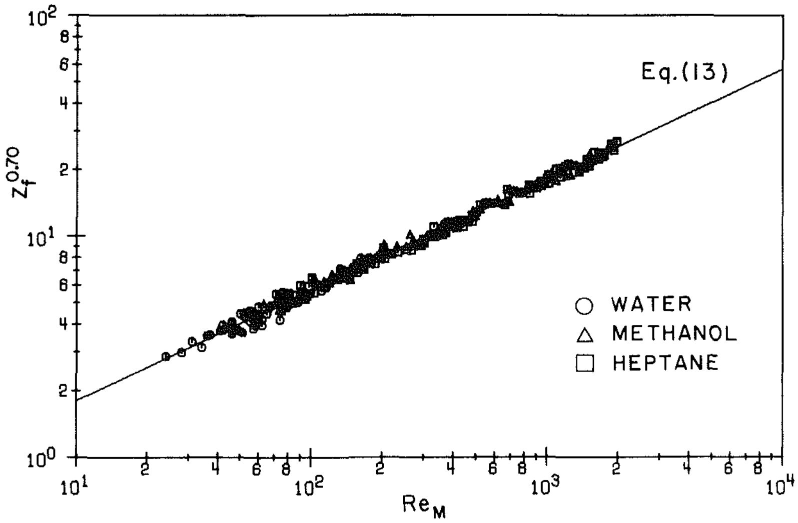

Fig. 4 Improved correlation of present heat transfer rates of evaporating liquid droplets in air

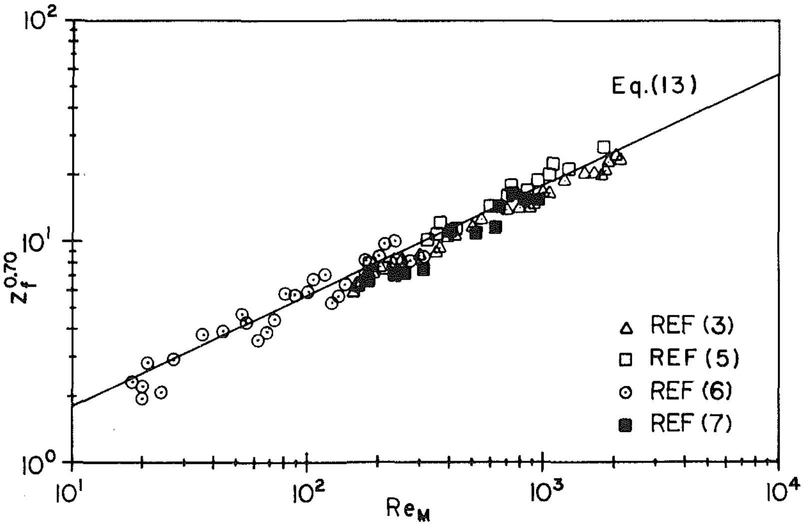

Fig. 5 Comparison of present correlation with other experimental data

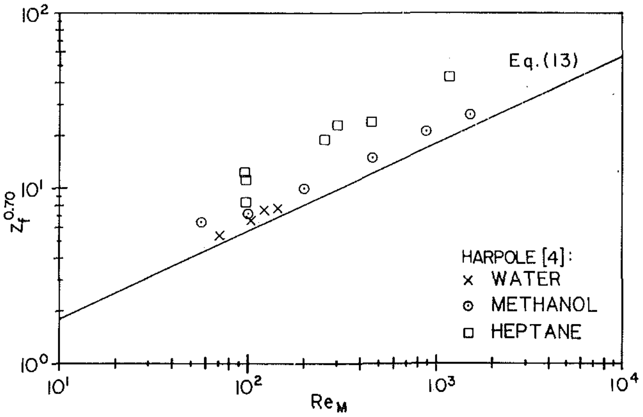

Fig. 6 Comparison of present correlation with Harpole's correlation [4]

physically justifiable if the Reynolds number is interpreted as a ratio of inertia to viscous forces. As shown in [3, 9] the inertia force is proportional to $\rho_s u_s^2$, and the viscous force is proportional to $\mu_r u_s / d$, where the viscosity should be evaluated using a reference state close to the body. In this case the film condition ($r = 0.5$ in equations (1) and (2)) is appropriate.

In Fig. 5, the data of [3] are shown and the comparison with equation (13) appears to be satisfactory. The reason is that for relatively small values of B (less than 0.5) as in [3], the difference between $(1+B)^{0.7}$ and $(1+B)$ is only a few percent which is well within the experimental error. For further comparison, the data of [5, 6, 7] are also plotted in Fig. 5. They seem to agree satisfactorily with the new correlation of equation (13).

Harpole [4] has claimed that his calculation agrees well with the data of [3]. He used a multiplicative correction factor to take into account the effect of variable properties. Since the data of [3] agrees with equation (13) which includes a liquid of high molecular weight, it is useful to see if the calculation of Harpole agrees with equation (13). Equation (31) of [4] can be expressed as

$$\mathrm{Nu}_s[1+aB_s]^{.7} = E[1.56 + .626\mathrm{Pr}_s^{.38}\mathrm{Re}_s^{1/2}] \tag{14}$$

where

$$E = [1 + (0.327\alpha - .0844)(1 - T_d/T_s)]$$

and

$$\alpha = ln[\rho k)_s / (\rho k)_d]/ln(T_d/T_s),$$

$$a = (M_a/M_v)^n$$

A detailed calculation shows that α varies from about 0.16 at low temperatures to about .22 at high temperatures. Thus, E is very close to 1. Therefore, any variable property effect due to both temperature and composition changes is represented by "a" which is the ratio of the molecular weights of air and liquid vapor to the power n.

In equation (14), Re_s is the free-stream Reynolds number which for the same free-stream condition is larger than Re_M in equation (13). For the same rate of convective heat transfer, Nu_f is much larger than Nu_s because k_s/k_f is larger than 1. Thus dividing equation (14) by equation (13) we have

$$\frac{\mathrm{Nu}_s}{\mathrm{Nu}_f}\left(\frac{\mathrm{Re}_M}{\mathrm{Re}_s}\right)^{1/2} \approx \left[\frac{1+\bar{B}_f}{1+aB_s}\right]^{.7} \tag{15}$$

Since the left-hand side of equation (15) is always less than 1, that means $aB_s > \bar{B}_f$. Again, a detailed calculation shows that $B_s < \bar{B}_f$ and therefore "a" has to be larger than 1. This is certainly not true when the molecular weight of the liquid is much larger than that of air as in the case of heptane.

Although in [4] the author mentioned that "a" is equal to M_a/M_v raised to a certain power, but in effect, in the case of water droplets, the author used $a = 1.6$ which is the ratio of the molecular weights to the first power. Data obtained from equation (14) after assuming $a = M_a/M_v$ are compared with equation (13) in Fig. 6. The predictions of equation (14) do not correlate with equation (13) as shown in Fig. 6. In particular, the heptane results disagree significantly with the new experimental correlation. The data of water and methanol agree better with equation (13). Part of the discrepancy is due to the predicted wet-bulb temperatures of water droplets which are systematically lower than the experimental values as listed in Table 1. However this cannot completely account for the disagreement. Apparently both the temperature and composition variation change the properties in a more complicated fashion than that indicated by the simple correction factor "a" (ratio of the molecular weights).

4 Conclusion

The present investigation shows that Nusselt numbers for single component droplets evaporating in high-temperature air streams can be accurately predicted by equation (13). In a low-temperature environment, equation (13) reduces to essentially the standard heat transfer equation of Ranz and Marshall [10]. At a high-temperature environment, the present correlation shows that evaporation reduces heat transfer rates directly by a factor of $(1+B_f)^{.70}$. Indirectly evaporation affects heat transfer rates through changes in both the temperature and composition of the surrounding gaseous medium. This effect is accounted for by evaluating the thermophysical properties at the film conditions provided that the definition of Reynolds number is based on the free stream mass flux $\rho_s u_s$.

Acknowledgement

This work was supported by the National Science Foundation.

References

1 Clift, R., Grace, T. R., and Weber, M. E., *Bubbles, Drops and Particles*, Academic Press, New York, 1978.

2 Eisenklam, P., Arunachalam, S. A., and Weston, J. A., "Evaporation Rates and Drag Resistance of Burning Drops," *Eleventh International Symposium on Combustion* 1967, pp. 715-727.

3 Yuen, M. C., and Chen, L. W., "Heat Transfer Measurements of Evaporating Liquid Droplets," *International Journal of Heat and Mass Transfer*, Vol. 21, 1978, pp. 537-542.

4 Harpole, G. M., "Droplet Evaporation in High Temperature Environments," ASME JOURNAL OF HEAT TRANSFER, Vol. 103, 1981, pp. 86-91.

5 Spalding, D. B., "Experiments on the Burning and Extinction of Liquid Fuel Spheres," *Fuel*, Vol. 32, 1953, pp. 169-185.

6 Downing, C. G., "The Evaporation of Drops of Pure Liquids at Elevated Temperatures, Rates of Evaporation and Wet-Bulb Temperatures," *AIChE Journal*, Vol. 12, 1966, pp. 760-766.

7 Narashimhan, C., and Gauvin, W. H., "Heat and Mass Transfer to Spheres in High Temperature Surroundings," *Can. J. Chem. Eng.*, Vol. 45, 1967, pp. 181-188.

8 Renksizbulut, M., "Energetics and Dynamics of Droplet Evaporation in High Temperature Intermediate Reynolds Number Flows," Ph.D. dissertation, Northwestern University, 1981.

9 Yuen, M. C., and Chen, L. W., "On Drag of Evaporating Liquid Droplets," *Combustion Science and Technology*, Vol. 14, 1976, pp. 147-154.

10 Ranz, W. E., and Marshall, W. R., "Evaporation from Drops: I, II," *Chemical Eng. Progress*, Vol. 48, 1952, pp. 141-146, pp. 173-180.

Numerical Study of Droplet Evaporation in a High-Temperature Stream

M. Renksizbulut[1]

M. C. Yuen
Professor and Chairman.
Mem. ASME

Department of Mechanical and
Nuclear Engineering,
Northwestern University,
Evanston, Ill. 60201

Numerical solutions for high-temperature air flowing past water and methanol droplets and solid spheres, and superheated steam flowing past water droplets were obtained in the Reynolds number range of 10 to 100. The coupled momentum, energy, and specie continuity equations of variable thermophysical properties were solved using finite difference techniques. The numerical results of heat transfer and total drag agree well with existing experimental data. Mass transfer decreases friction drag significantly but at the same time increases pressure drag by almost an equal amount. The net effect is that the standard drag curve for solid spheres can be used for evaporating droplets provided the density is the free stream density and the viscosity of the vapor mixture is evaluated at an appropriate reference temperature and concentration. Both the mass efflux and variable properties decrease heat transfer rates to the droplets.

1 Introduction

This paper describes an attempt to study theoretically a high-temperature gas flow past an evaporating liquid droplet. As such it is in sequel to our experimental measurements of heat and mass transfer from liquid droplets in a high temperature air stream [1].

Flow past a sphere in the intermediate Reynolds number range of 10 to 100 is of interest in many fields of engineering. For a uniform free stream, the flow field is axisymmetrical and steady. However, in this Reynolds number range, the Navier-Stokes equations cannot be simplified and numerical methods have to be used. The variable-property case is difficult enough that only a few attempts have been made to study the problem.

In his pioneering work, Jenson [2] solved the Navier-Stokes equations for a constant-property flow past a sphere in the stream function/vorticity formulation for Reynolds numbers between 5 and 40. The finite-difference equations were correct to second order in grid spacing. Since ψ and ω vary most rapidly near the droplet, variable grid spacing is desirable with finer mesh near the sphere and coarser mesh far away. Jenson accomplished this with the coordinate transformation $r=e^{\xi}$ which has been adopted in almost all subsequent studies.

Much work has been done to extend and improve on the work by Jenson. These include studies by Hamielec, Hoffman, and Ross [3], Rimon and Cheng [4], LeClair, Hamielec, and Pruppacher [5], Woo and Hamielec [6], and Rivkind, Ryskin, and Fishbein [7]. Similar efforts by Dennis and Walker [8], and Dennis, Walker, and Hudson [9], using a series truncation method, were also successful in solving the problem of flow past a sphere, including heat transfer, up to a Reynolds number of 40. The results obtained by different investigators show reasonably good agreement with one another and also with related experimental correlations for heat transfer and drag.

The study of the variable-property problem in the past was limited to the low Reynolds number flows ($\mathrm{Re} < < 1$) using the method of matched asymptotic expansions. This included the work of Chang [10], Kassoy, Adamson, and Messiter [11], and Fendell, Coats, and Smith [12]. More recently, Sayegh and Gauvin [13] numerically solved the coupled momentum and energy equations for variable-property heat transfer to a solid sphere in high-temperature surroundings. Their results are for $\mathrm{Pr} = .67$, Re between 0.1 and 50, and $T_d^*/T_s^* = .25$, .5, .75 and 1. The constant-property solutions ($T_d^*/T_s^* = 1$) are in good agreement with the literature, but their variable property solutions show negative pressure drag coefficients for $\mathrm{Re} \geq 20$ with $T_d^*/T_s^* = .25$. Harpole [14] investigated both variable-property and blowing effects from evaporation on axisymmetric stagnation point flows. He assumed that the ratio of solutions with and without evaporation is the same for the stagnation point flow and flow past a sphere.

The present study is focussed on flow past a single component liquid droplet in a high-temperature environment at intermediate Reynolds numbers. A finite difference scheme is used to solve the coupled momentum, energy, and species equations. The numerical results are compared with the drag data of Yuen and Chen [15] and heat transfer data of Renksizbulut and Yuen [1].

For a high-temperature gas flow past a liquid droplet, the effect of evaporation is twofold. Firstly, the mass efflux changes the flow field which directly affects the drag and heat transfer. Secondly, evaporation keeps the droplet at the wet-bulb temperature which is generally much lower than the free stream temperature. At the same time the evaporating specie changes the gas composition near the droplet. The drag data of reference [15] indicates that the net effect of evaporation can be taken into account by the change in the thermophysical properties. On the other hand, the data of [1] indicates that both mass efflux and variable property effects reduce heat transfer. The present numerical study is undertaken to

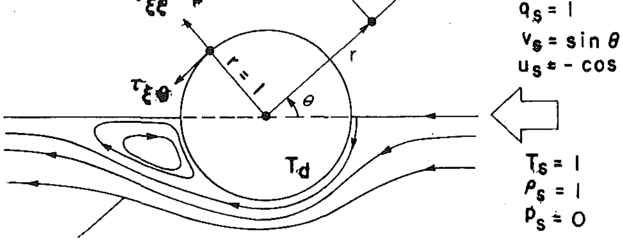

Fig. 1 Schematic of flow past an evaporating droplet

---

[1] Present address: Westinghouse Canada, Inc., Hamilton, Ontario, Canada L8N 3K2

Contributed by the Heat Transfer Division for publication in the JOURNAL OF HEAT TRANSFER. Manuscript received by the Heat Transfer Division February 5, 1982.

develop a better understanding of the physics of the problem and to give a successful numerical scheme to calculate variable-property heat transfer and drag of evaporating droplets.

2 Mathematical Formulation

A schematic of the flow past an evaporating droplet is shown in Fig. 1. The equations describing the flow include the conservation equations of mass, momentum, energy, and specie for both the gas and liquid phases. Additional equations are the equation of state and other thermodynamic and transport relationships. In order to make the problem tractable, the following assumptions are made:

1 The gas phase is assumed to be a binary mixture of ideal gases of equal molecular weights and equal and constant specific heats. Only Fick's law of diffusion and Fourier heat conduction are considered.

2 It is assumed that the gas-phase processes are quasi-steady. This is justified by the fact that the gas-phase heat and mass transport rates are of the order of 10^{-4}-10^{-5} m^2/s which are much larger than the surface regression rates of 10^{-7}-10^{-8} m^2/s. The numerical calculations of Hubbard, Denny, and Mills [16] have substantiated this assumption.

3 Liquid phase motion and core heating are neglected. The droplet temperature remains uniformly at the wet-bulb temperature and the vapor pressure of the evaporating specie is the equilibrium vapor pressure corresponding to the wet-bulb temperature. Liquid phase motion is induced by the gas phase motion. At atmospheric pressure, the liquid phase motion is of the order of one-hundredth of the gas phase motion. This value is further reduced by the presence of interfacial surface contaminants. In fact, for all the drag measurements of water droplets in air, the drag coefficients are the same as that of solid spheres. Law and Sirignano [17] have shown that at atmospheric pressure, core heating is a small fraction of the energy budget after the initial 10-20 percent of the lifetime of a droplet. For a single component liquid, temperature distribution and liquid phase motion do not affect heat transfer as long as core heating is negligible. Thus, unsteadiness and coupling between liquid and gas phase processes due to liquid motion and core heating can be neglected for a single component liquid at low or moderate pressures. This, however, is not true for high-pressure evaporation or for multicomponent liquid as shown by Prakash and Sirignano [18, 19].

4 Effects of gravity, chemical reaction, viscous dissipation, compressibility, turbulence, and thermal radiation are neglected.

5 The flow field is axisymmetric. For constant-property flow, this symmetry starts to deteriorate at the onset of wake instability ($\mathrm{Re}_s \simeq 130$).

The governing equations are nondimensionalized with respect to the free stream quantities and the radius of the sphere as indicated in the nomenclature. With the coordinate transformation, $r = -\xi^{-1}$, and by introducing the stream function and vorticity as

$$\rho u \sin\theta = \xi^2 \frac{\partial \psi}{\partial \theta},$$

$$\rho v \sin\theta = \xi^3 \frac{\partial \psi}{\partial \xi},$$

$$\omega = \xi^3 \frac{\partial}{\partial \xi}\left(\frac{v}{\xi}\right) + \xi \frac{\partial u}{\partial \theta} \tag{1}$$

it is possible (see [20]) to express the governing equations in the following unified format

$$a_\phi \xi^2 \left[\frac{\partial}{\partial \xi}\left(\phi \frac{\partial \psi}{\partial \theta}\right) - \frac{\partial}{\partial \theta}\left(\phi \frac{\partial \psi}{\partial \xi}\right)\right] - \xi^2 \frac{\partial}{\partial \xi}\left[b_\phi \sin\theta \frac{\partial}{\partial \xi}(c_\phi \phi)\right]$$

$$- \frac{\partial}{\partial \theta}\left[b_\phi \sin\theta \frac{\partial}{\partial \theta}(c_\phi \phi)\right] + d_\phi \xi^{-2} \sin\theta = 0 \tag{2}$$

where $\phi(\xi,\theta)$ is used as a generalized variable to represent T, Y, ψ, or $\Omega = -\omega\xi/\sin\theta$, and the equation of state is given by $\rho T = 1$. The first term in equation (2) is the convection term, the second and third terms are diffusion terms, and the last one is the source term. The corresponding coefficient functions a_ϕ, b_ϕ, c_ϕ, and d_ϕ are given in Appendix A.

The boundary conditions are

$$\xi = -1: \quad T = T_d,\ Y = Y_d,$$

$$\frac{\partial \psi}{\partial \theta} = \frac{2k\sin\theta}{\mathrm{Re}_s \mathrm{Pr}_s L_d}\left(\frac{\partial T}{\partial \xi}\right),$$

$$\Omega = \frac{1}{\rho \sin^2\theta}\left\{2\frac{\partial \psi}{\partial \xi} - \frac{\partial^2 \psi}{\partial \xi^2} - \frac{\partial^2 \psi}{\partial \theta^2} + \left(\frac{\partial \psi}{\partial \theta}\right)\cot\theta\right\} \tag{3}$$

Nomenclature

a^* = radius of sphere
B = mass transfer number, $c_p^*(T_s^* - T_d^*)/L^*$
C_D = total drag coefficient, $F_D^*/(\pi a^{*2} \rho_s^* q_s^{*2}/2)$
C_F = friction drag coefficient, $F_F^*/(\pi a^{*2} \rho_s^* q_s^{*2}/2)$
C_P = pressure drag coefficient, $F_P^*/(\pi a^{*2} \rho_s^* q_s^{*2}/2)$
C_T = thrust coefficient, $F_T^*/(\pi a^{*2} \rho_s^* q_s^{*2}/2)$
c_p^* = heat capacity
D = mass diffusivity, (D^*/D_s^*)
d^* = diameter of sphere
F^* = force
h^* = heat transfer coefficient
k = thermal conductivity, (k^*/k_s^*)
L = heat of vaporization, $L^*/(c_p^* T_s^*)$
$\dot{m}$ = mass transfer rate, $\dot{m}^*/(a^{*2} \rho_s^* q_s^*)$
Nu = Nusselt number, $(h^* d^*/k^*)$
p = pressure, $(p^* - p_s^*)/(\rho_s^* q_s^{*2}/2)$
Pr = Prandtl number, $(c_p^* \mu^*/k^*)$
q^* = velocity
r = radial coordinate, (r^*/a^*)
Re = Reynolds number, $(\rho^* q^* d^*/\mu^*)$
Re_s = $\rho_s^* q_s^* d^*/\mu_s^*$
Re_M = $\rho_s^* q_s^* d^*/\mu_f^*$
Re_t = $\rho_s^* q_s^* d^*/\mu_t^*$
T = temperature, (T^*/T_s^*)
u = velocity in r-direction, (u^*/q_s^*)
v = velocity in θ-direction, (v^*/q_s^*)
Y = mass fraction of evaporating specie
Z = $[\mathrm{Nu}(1+B)^{0.7} - 2]\mathrm{Pr}^{-1/3}$
δ = boundary layer thickness, (δ^*/d^*)
θ = angular coordinate
μ = viscosity coefficient, (μ^*/μ_s^*)
ξ = modified radial coordinate, $(-r^{-1})$
ρ = density, (ρ^*/ρ_s^*)
$\underset{\sim}{\tau}$ = stress tensor, $\underset{\sim}{\tau}^*/(\mu_s^* q_s^*/a^*)$
ψ = stream function, $\psi^*/(\rho_s^* q_s^* a^{*2})$
Ω = modified vorticity, $\omega/(r\sin\theta)$
ω = vorticity, $\omega^*/(q_s^* a^*)$
ϕ = generalized variable, T, Y, ψ or Ω

Superscript

* = dimensional quality
$\bar{\ }$ = averaged quantity

Subscript

d = droplet surface
f = film condition
o = stagnation point
s = free-stream condition
t = one-third reference state

Table 1 Summary of problems studied numerically

Case	Description	Re_s	Pr_s	T_s^*(K)	T_d^*(K)	Y_s	Y_d	B
1	Water-steam	10, 20, 40, 70, 100	.986	600	373	1.0	1.0	.204
2	Water-steam		1.01	800	373	1.0	1.0	.407
3	Water-steam		1.02	1000	373	1.0	1.0	.783
4	Methanol-air		.869	800	331	0.0	.766	.462
5	Water-air		.869	800	353	0.0	.355	.213
6	Solid sph.-air		.700	$T_d - T_s \rightarrow 0$		0	0	0
7	Solid sph.-air		.680	600	340	0	0	0
8	Solid sph.-air		.689	800	353	0	0	0

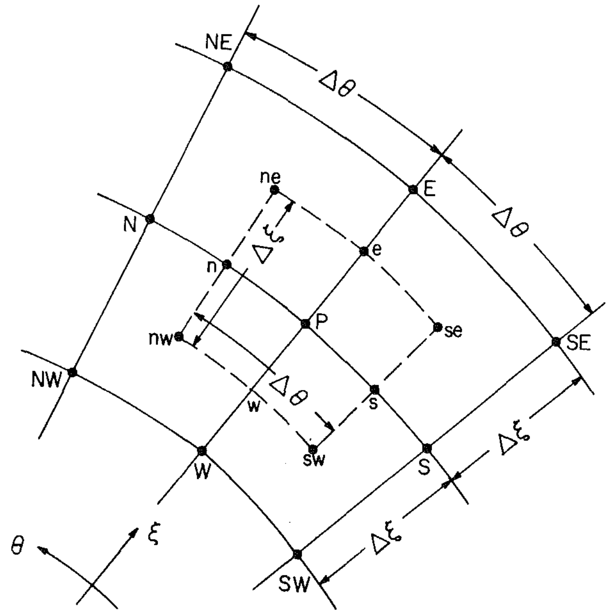

Fig. 2 The finite-difference grid

$\xi \rightarrow 0$: $T \rightarrow 1$, $Y \rightarrow 0$, $\Omega \rightarrow 0$,

$$\psi \rightarrow -\frac{\sin^2\theta}{2\xi^2} + \frac{\dot{m}}{4\pi}(1-\cos\theta) \tag{4}$$

The heat transfer to the sphere can be expressed as the local and averaged Nusselt numbers

$$\mathrm{Nu}_d = \frac{2k_d}{(1-T_d)}\left(\frac{\partial T}{\partial \xi}\right)_d \tag{5}$$

$$\overline{\mathrm{Nu}} = \frac{1}{2}\int_0^\pi \mathrm{Nu}_d \sin\theta d\theta \tag{6}$$

The drag forces acting on the sphere can be expressed in terms of the drag coefficients

$$C_F = \frac{8}{\mathrm{Re}_s}\int_0^\pi (\tau_{\xi\theta,d}\sin\theta - \tau_{\xi\xi,d}\cos\theta)\sin\theta d\theta \tag{7}$$

where

$$\tau_{\xi\theta,d} = \left[-\mu\Omega\sin\theta + \frac{2\mu}{\rho\sin\theta}\left(2\frac{\partial\psi}{\partial\xi} - \frac{\partial^2\psi}{\partial\xi^2}\right)\right]_d$$

$$\tau_{\xi\xi,d} = \left[-\frac{4\mu}{\rho\sin\theta}\left(\frac{\partial\psi}{\partial\theta}\right)\left(1+\frac{1}{3\rho}\frac{\partial\rho}{\partial\xi}\right)\right]_d$$

$$C_P = \int_0^\pi p_d \sin(2\theta)d\theta \tag{8}$$

$$C_T = \int_0^\pi 2\rho_d u_d^2 \sin(2\theta)d\theta \tag{9}$$

$$C_D = C_F + C_P + C_T \tag{10}$$

In order to determine the pressure distribution on the droplet surface, first the radial momentum equation is integrated along the leading axis ($\theta = 0$) to obtain the stagnation pressure (p_0). Next, the surface pressure (p_d) is calculated by integrating the tangential momentum equation from the stagnation point along the droplet surface. The equations for the stagnation pressure and the surface pressure are

$$p_0 = 1 - (\rho u^2)_0 - \frac{16}{3\mathrm{Re}_s}\left(\frac{\mu u}{\rho}\frac{\partial\rho}{\partial\xi}\right)_0 - \int_{-1}^{0}\left(u^2\frac{\partial\rho}{\partial\xi}\right)_{\theta=0}d\xi$$
$$+ \frac{8}{\mathrm{Re}_s}\int_{-1}^{0}\left[-\frac{\mu}{\xi}\frac{\partial\omega}{\partial\theta} - \frac{\partial\mu}{\partial\xi}\left(\frac{\partial u}{\partial\xi} + \frac{u}{\rho}\frac{\partial\rho}{\partial\xi}\right)\right]_{\theta=0}\xi^2 d\xi \tag{11}$$

$$p_d = p_0 + \int_0^\theta\left[\frac{2}{\sin^2\theta}\frac{\partial\psi}{\partial\theta}\xi^2\frac{\partial}{\partial\xi}\xi^2\frac{\partial\psi}{\partial\xi} + \frac{4}{\mathrm{Re}_s}\left\{\mu\left(\omega + \xi^2\frac{\partial\omega}{\partial\xi}\right)\right.\right.$$
$$-\xi^2\frac{\partial\mu}{\partial\xi}\left(\omega + \frac{2}{\rho\sin\theta}\xi^2\frac{\partial}{\partial\xi}\xi^2\frac{\partial\psi}{\partial\xi}\right) - \frac{4\mu}{3}\frac{\partial}{\partial\theta}\left(\frac{\xi^2}{\rho^2\sin\theta}\right.$$
$$\left.\left.\left.\frac{\partial\psi}{\partial\theta}\frac{\partial\rho}{\partial\xi}\right)\right\}\right]_{\xi=-1}d\theta \tag{12}$$

Further details can be found in [21].

3 Numerical Method

The generalized governing equations as represented by equation (2) are solved using a finite difference method, the main features of which follow [20]. In Fig. 2, a typical element of the finite difference grid is shown. The central node is P and the four surrounding nodes which are equally spaced are identified with E, W, N and S. Equation (2) is discretized using second-order central differences. The exception is in the convective term where the "upstream" differencing principle is introduced. The result is a successive substitution formula

$$\phi_\mathrm{P} = C_\mathrm{E}\phi_\mathrm{E} + C_\mathrm{W}\phi_\mathrm{W} + C_\mathrm{N}\phi_\mathrm{N} + C_\mathrm{S}\phi_\mathrm{S} + D_\mathrm{P} \tag{13}$$

where C_E, C_W, C_N, C_S and D_P are defined in Appendix B.

For numerical analysis, the conditions along the axis have to be specified, they are

$$\theta = 0: \qquad \psi = \frac{\partial T}{\partial\theta} = \frac{\partial Y}{\partial\theta} = 0,\ \Omega = -\xi\frac{\partial\omega}{\partial\theta} \tag{14}$$

$$\theta = \pi: \qquad \frac{\partial T}{\partial\theta} = \frac{\partial Y}{\partial\theta} = 0,\ \Omega = \xi\frac{\partial\omega}{\partial\theta},$$

$$\psi = \frac{\dot{m}}{2\pi} = \int_0^\pi\left[\frac{2k\sin\theta}{\mathrm{Re}_s\mathrm{Pr}_s L_d}\left(\frac{\partial T}{\partial\xi}\right)\right]_d d\theta \tag{15}$$

The numerical task is to solve simultaneously $4N$ nonlinear algebraic equations as given by equation (13) where N is the total number of grid points in the flow field. These equations will be solved using successive overrelaxation coupled with the Gauss-Seidel method. The iterative process is as follows:

1 Initially, all ϕ and the boundary conditions are specified.

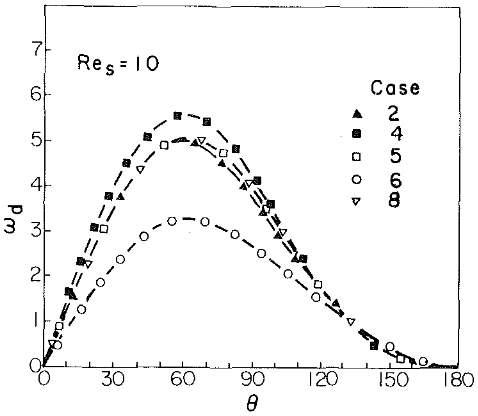

Fig. 3 Surface vorticity distributions for $Re_s = 10$. Case numbers are listed in Table 1.

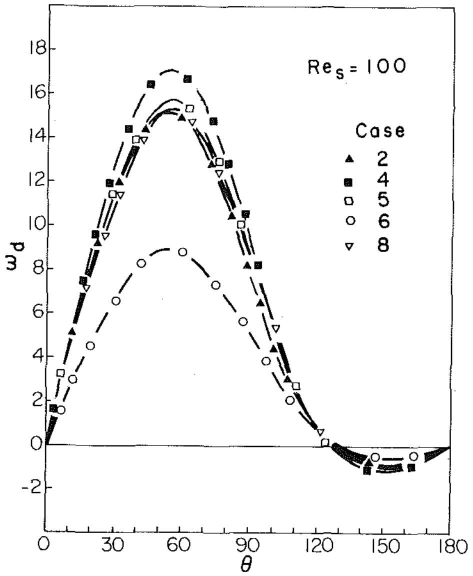

Fig. 4 Surface vorticity distributions for $Re_s = 100$. Case numbers are listed in Table 1.

2 Each cycle of iteration consists of four subcycles corresponding to solving equation (13), and hence equation (2), for Ω, ψ, T, and Y in the order stated.

3 Overrelaxation parameters in the range between 1 and 1.5 are used to increase the rate of convergence of the iterative scheme.

4 Convergence is assumed in the Kth iteration when

$$[1-\phi_P{}^{(K-1)}/\phi_P^{(K)}]_{\max} \sim 10^{-4}$$

Iterative schemes such as the present one do not always converge to a stable and physically meaningful solution. No convergence criterion exists for the nonlinear algebraic system (equation (13)) under consideration. However, well-known convergence conditions for linear systems can be used as guide-lines, and compliance with such criteria may be considered as a minimum requirement for stability.

A detailed study by Varga [22] shows that the linearized algebraic version of equation (13) (i.e., constant C_E, C_W, C_N, C_S, and D_P) satisfy the convergence criteria with the upwind differencing scheme. Although the present numerical scheme satisfies the linearized convergence criteria, the numerical scheme may still diverge if C's and D_P exhibit large variations from one iteration to the next. Such a problem is likely to arise in the early stages of the computation process particularly if the initial guesses are poor. Divergence problems were not encountered in the present work.

While the upwind-difference scheme assures convergence for convection dominated flow, under certain conditions, it is responsible for large truncation errors to generate a false diffusion effect which tends to reinforce real diffusion. If this occurs, the grid spacing may have to be reduced to the extent that it renders the computation uneconomical. Further investigation as given in reference [21] indicates that the consequences of false diffusion is most serious in the flow where the molecular diffusion is important relative to forced convection and also where the streamline is not parallel to one of the grid lines. With the present grid spacing of $\Delta\xi = .025$ and $\Delta\theta = 3$ deg, the only region where false diffusion effect is important is the wake region. Thus the exact location of the flow separation point or the exact size of the recirculation zone cannot be determined with the same accuracy as the rest of the flow variables. However, the integrated results such as drag and heat transfer coefficients are not much affected because it is only at higher Reynolds numbers that the contribution to momentum and heat transfer from the wake region becomes significant. For example Frössling's [23] experimental results on the evaporation of naphthalene spheres in air show that at Reynolds numbers below 550, heat transfer rates to the wake region of the spheres are less than 12 percent of the overall transfer rates.

Some attempts were made to adopt the exponential differencing scheme to suppress the false diffusion effect. This method was first proposed by Allen and Southwell [24] and a recent analysis is given by Chow and Tien [25]. The present study shows that for the variable-property problems under consideration, this technique is not superior to the present method. This is partly due to the longer computation times associated with exponential functions. More importantly perhaps is that the assumption of conservation of directional flux is violated in the variable property case by the presence of the source term, D_p, in equation (13).

4 Results and Discussion

Numerical solutions for air flowing past solid spheres, water, and methanol droplets, and steam flowing past water droplets were obtained up to a Reynolds number of 100. The range of the numerical solutions are summarized in Table 1. All computations were carried out using the grid spacings of $\Delta\xi = .025$ and $\Delta\theta = 3$ deg. Solutions obtained with smaller radial grid spacing ($\Delta\xi = 0.0165$) showed negligible improvement at the expense of much longer computation times. The free stream boundary conditions were applied at $r = 40$. Convergence is assumed when the maximum fractional change in the calculated variables, ϕ_P, after K iterations (typically $K \sim 350$ steps) was of order 10^{-4} for all independent variables.

The transport coefficients of air and steam were approximated by $\mu = T^{.67}$, $k = T^{.81}$ and $\mu = kT$, respectively. For water and methanol droplets evaporating in air, it was assumed that $\rho D = T$, and the mixture viscosity and thermal conductivity were computed using Wilke's rule [26] subject to the equal molecular weight assumption. In all cases, the fluid density varied with temperature as $\rho = 1/T$. The constant specific heat assumption leads to $B = (1 - T_d)/L_d$. The isothermal condition is $T_d = 1$. For solid spheres, B is equal to zero in all cases.

(*a*) The Flow Field. The surface vorticity, ω_d, distributions for $Re_s = 10$ and 100 are given in Figs. 3 and 4. Both figures show that the surface vorticity values increase with decreasing T_d for the solid sphere. This can be seen from the fact that $\omega_d \sim 1/\delta$ where δ is the dimensionless thickness of the viscous layer. Generally, $1/\delta \sim (\rho\ Re_s/\mu)^{1/2}$, and, therefore, the properties that influence ω_d are ρ/μ. As T_d decreases, i.e., the surface gets colder, the surface ρ increases and μ decreases resulting in an increase in ω_d. This also holds

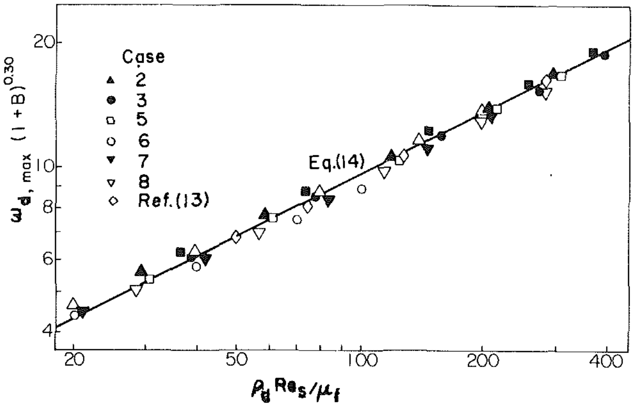

Fig. 5 Maximum vorticity correlation. Case numbers are listed in Table 1 except as noted.

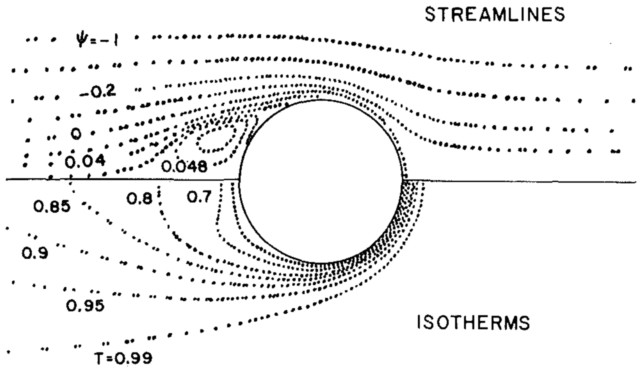

Fig. 6 Stream function and isotherms of methanol droplets in air for $T_s = 800$ K, $T_d = 0.414$, and $\mathrm{Re}_s = 100$

true for evaporating droplets. Mass efflux from the evaporating droplet directly increases δ and reduces ω_d. However, the viscosity coefficient of mixtures of air and vapor are generally lower than that of air at the same temperature resulting in a larger increase in ω_d. For the same T_d, these two effects tend to cancel each other and the resulting surface vorticity levels for the solid sphere and evaporating sphere are about the same.

Figures 3 and 4 further show that the location of $\omega_{d,\max}$ is at about $\theta = 60$ deg relatively independent of Reynolds number, fluid properties, and evaporation rate. The correlation of $\omega_{d,\max}$ as a function of Reynolds and B numbers is shown in Fig. 5. The numerical results correlate well with the following equation

$$\omega_{d,\max}(1+B)^{0.30} = 0.97(\rho_d \mathrm{Re}_s/\mu_f)^{0.50} \tag{16}$$

where the subscript f refers to the film condition defined by $r = 1/2$ in the following equations

$$T_r^* = T_d^* + r(T_s^* - T_d^*), \quad Y_r = Y_d + r(Y_s - Y_d) \tag{17}$$

The surface vorticity distributions given by [3] for $\mathrm{Re}_s = 100$ with constant fluid properties and prescribed asymmetric blowing ($B \simeq 4$) show a 40 percent reduction in $\omega_{d,\max}$. For the same B number, equation (16) predicts a 38 percent reduction in $\omega_{d,\max}$ due to mass transfer alone. This good agreement suggests that the accuracy of the blowing correction term $(1+B)^{0.3}$ *is not limited to the relatively low* B *numbers encountered in the present work.* With regard to variable-property effects, a limited number of data points available from [13] for solid spheres show excellent agreement with the present results as can be seen in Fig. 5.

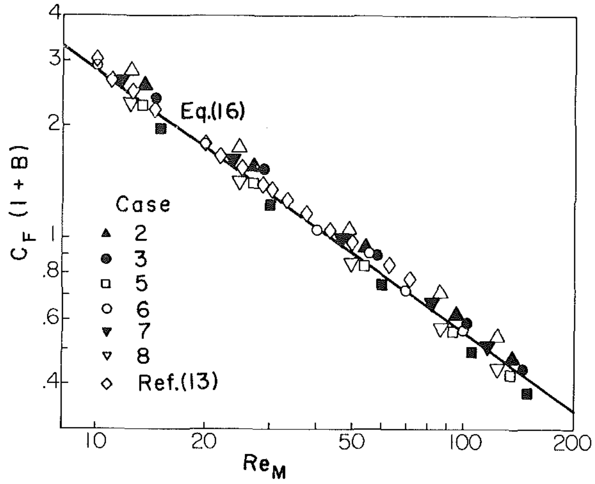

Fig. 7 Friction drag correlation. Case numbers are listed in Table 1 except as noted.

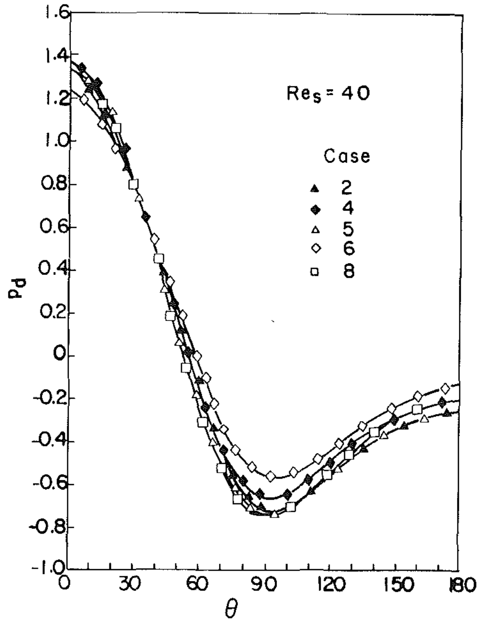

Fig. 8 Surface pressure distribution for $\mathrm{Re}_s = 40$. Case numbers are listed in Table 1.

In Fig. 6, the upper half shows the stream lines and the lower half shows the isotherms for a methanol sphere in a free stream air of 800 K and a Reynolds number of 100. As shown in the figure, several stream lines originate from the sphere due to evaporation. The wake behind the sphere is no longer a closed wake as there is some leakage near the axis ($\theta = \pi$). The isotherms show steep gradients at the front stagnation point, indicating that heat transfer rate is much higher at the front half of the sphere.

(*b*) **Drag.** The friction drag coefficients as a function of mass transfer numbers and Reynolds numbers are shown in Fig. 7. The numerical data of C_F correlates well with the equation

$$C_F(1+B) = 14.5\,\mathrm{Re}_M^{-.71} \tag{18}$$

where Re_M is defined as $\rho_s^* q_s^* d^*/\mu_f^*$. Equation (18) shows that mass transfer plays a significant role in reducing friction drag. In the case of a flat plate, the reduction in the friction drag coefficient by evaporation was shown by Emmons [27] to be $(1+B)^{.75}$ for B below 4. Further reduction in C_F occurs due to lower fluid viscosity ($\mu < 1$) within the cold boundary layer

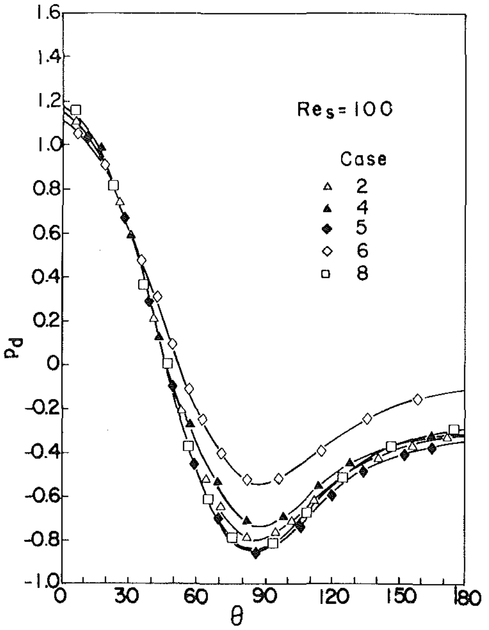

Fig. 9 Surface pressure distribution for $Re_s = 100$. Case numbers are listed in Table 1.

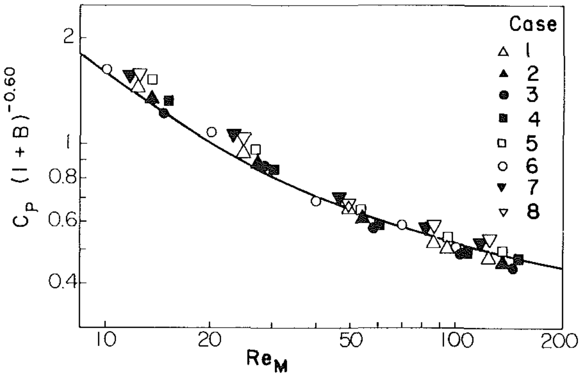

Fig. 10 Pressure drag correlation. Case numbers are listed in Table 1.

which is reflected through the Reynolds number definition, Re_M. Friction drag coefficients obtained from reference [13] for solid spheres ($B=0$) are also shown in Fig. 7 as a function of Re_M. The agreement with equation (18) is good.

Figures 8 and 9 show surface pressure distributions for $Re_s = 40$ and 100. These figures indicate that the surface pressure generally decreases with decreasing T_d, except for a small region near the stagnation point. From the surface pressure distribution, the pressure drag coefficient (C_p) can be computed using equation (8). The results are shown in Fig. 10 as a function of Reynolds and mass transfer numbers. Figure 10 indicates that for the same free stream conditions, C_p depends on both B and μ_f^* for evaporating droplets, but it depends only on μ_f^* for solid spheres. For evaporating droplets, the effect of mass efflux is to increase C_p by a factor of $(1+B)^{0.6}$ for the same Re_M. The mixture viscosity coefficient of an evaporating droplet is lower than that of pure air at the same temperature. Therefore, for the same free stream conditions and droplet temperature, Re_M of an evaporating droplet is larger than Re_M of a solid sphere. It follows that the ordinate of Fig. 10 of an evaporating droplet is smaller than that of a solid sphere. However, this does not necessarily mean that C_p of an evaporating droplet is smaller. For $T_d < 1$, B is greater than zero for an evaporating droplet. Depending on the magnitude of B, C_p of an evaporating droplet can even be larger. Detailed calculations as shown in [21] indicate that

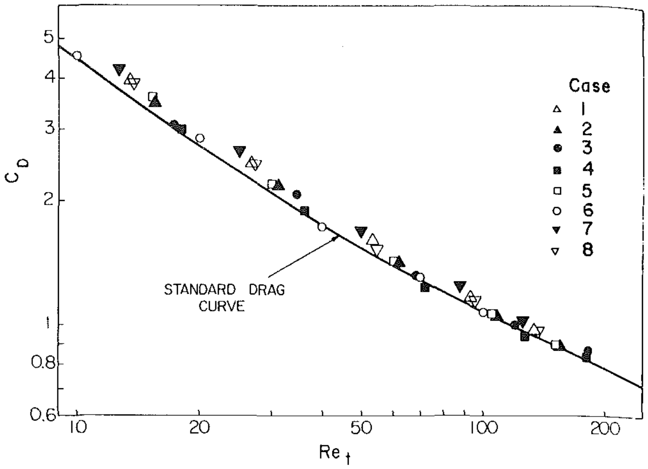

Fig. 11 Total drag correlation. Case numbers are listed in Table 1.

C_p of an evaporating droplet is actually larger than a corresponding solid sphere at the same free stream conditions and T_d.

In addition to pressure and shear forces, an evaporating droplet experiences a net thrust due to asymmetric blowing at its surface. The computed thrust coefficients, C_T, show that the values are at least two orders of magnitude smaller than the corresponding C_F and C_P values and are therefore neglected.

Figure 11 shows that the computed total drag coefficient C_D values correlate well with the standard drag curve without the need for a B number correction provided that the Reynolds number is defined as $Re_t = \rho_s^* q_s^* d^* / \mu_t^*$ where μ_t^* is the mixture viscosity based on the one-third reference state ($r = 1/3$ in equation (17)). Since this type of correlation was originally suggested in [15] based on their experimental data as well as those of Eisenklam, Arunchalam, Weston [28], it means that the present numerical results are in good agreement with experimental data. In the Reynolds number range of 10 to 260, it is also possible to correlate the results as

$$C_D(1+B)^{0.20} = \frac{24}{Re_M}[1 + .2\, Re_M^{0.63}] \tag{19}$$

This correlation agrees satisfactorily with experimental data as shown in Fig. 12.

(c) Heat Transfer. The surface distributions of the local Nusselt numbers, Nu_d, are shown in Figs. 13 and 14 for $Re_s = 10$ and 100. As expected, much higher heat transfer rates are observed over the leading half of the sphere particularly near the front stagnation point. It is also observed that both the blowing and variable-property effects decrease Nu with decreasing T_d. The numerical results of [13] indicate similar reductions in local transfer rates which are entirely due to variable fluid properties.

At a given Reynolds number, the local temperature gradient on the droplet surface becomes steeper as T_d is reduced either by increasing the free-stream temperature or by lowering the surface temperature. Normally, this would lead to a higher heat transfer rate. However, due to the cold boundary effect, such reduction in T_d is accompanied by a large reduction in the local thermal conductivity of the gas. The present results as well as those of [13] indicate that the effect of decrease in thermoconductivity of the gas outweighs the effect of increase in temperature gradient such that the local heat transfer rate decreases.

In the case of an evaporating droplet, the vapor leaving the surface opposes the flow of hot gas toward the surface resulting in a thicker thermal boundary layer. Furthermore, pure steam and, mixtures of water and methanol vapors with

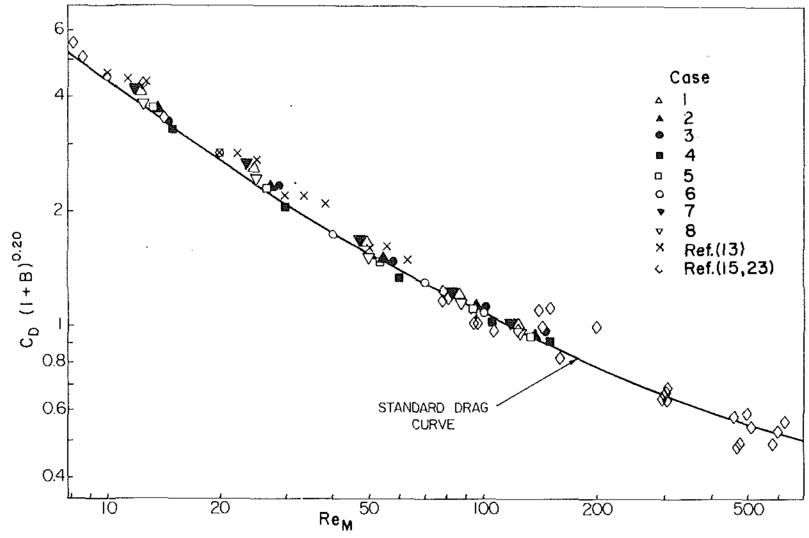

Fig. 12 Total drag correlation. Case numbers are listed in Table 1 except as noted.

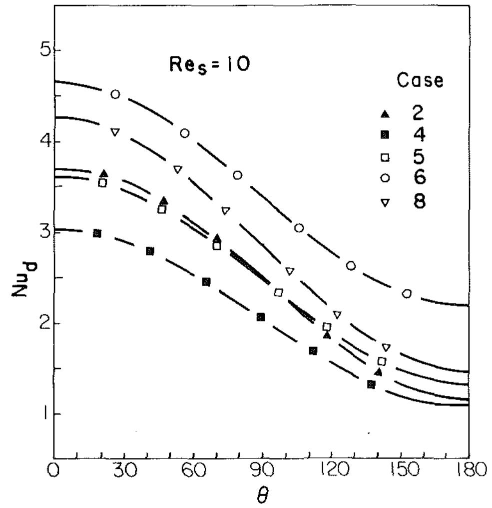

Fig. 13 Surface Nusselt number distributions for $\mathrm{Re}_S = 10$. Case numbers are listed in Table 1.

air have lower thermal conductivities than pure air at the same temperature; therefore, the cold boundary effect on thermal conductivity is even more pronounced. Hence, both blowing and variable property effects reinforce one another in reducing heat transfer rates to droplets.

The present numerically calculated stagnation point Nusselt numbers, Nu_o, are shown in Fig. 15 as a function of Reynolds, Prandtl and B numbers. It is seen that the results correlate quite well with the equation

$$Z_{o,f} = [\mathrm{Nu}_{o,f}(1+B)^{0.70} - 2]\mathrm{Pr}_f^{-1/3} = 0.90\mathrm{Re}_M^{0.57} \tag{20}$$

in the Re_M range from 10 to 150. Thus, equation (20) indicates that mass transfer reduces stagnation-point heat transfer by a factor of $(1+B)^{0.70}$. Also shown in Fig. 15 are the numerical results of [13] and [14] for solid spheres in air, and water droplets in superheated steam, respectively. The three sets of results agree well with each other.

The most recent experimental correlation of heat transfer for evaporating droplets in air, as shown in [1], is

$$Z_f = [\overline{\mathrm{Nu}}_f(1+B)^{0.70} - 2]\mathrm{Pr}_f^{-1/3} = 0.57\,\mathrm{Re}_M^{1/2} \tag{21}$$

In Fig. 16, the present numerical results are compared with equation (21). The numerical data of [13] for solid spheres are also included in the same figure. The agreement is satisfactory (within about 15 percent), considering the fact that there is

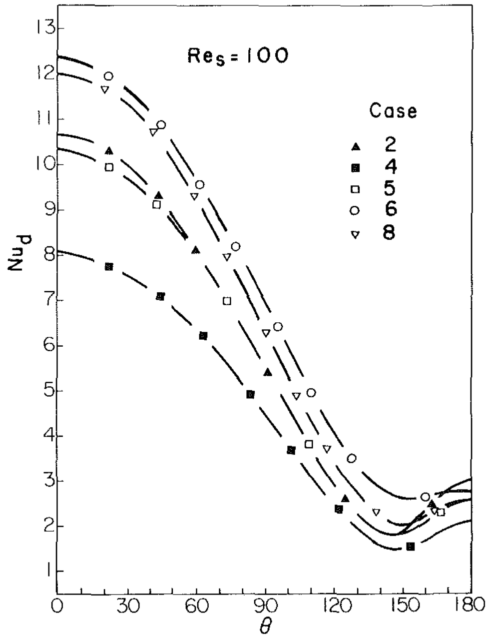

Fig. 14 Surface Nusselt number distribution for $\mathrm{Re}_S = 100$. Case numbers are listed in Table 1.

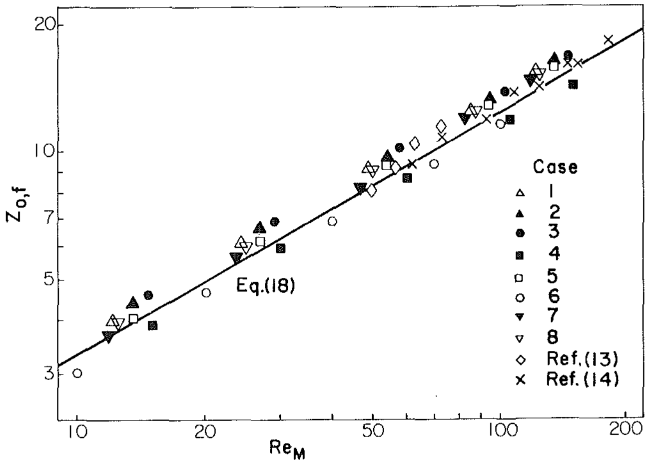

Fig. 15 Numerical stagnation-point heat transfer data. Case numbers are listed in Table 1 except as noted.

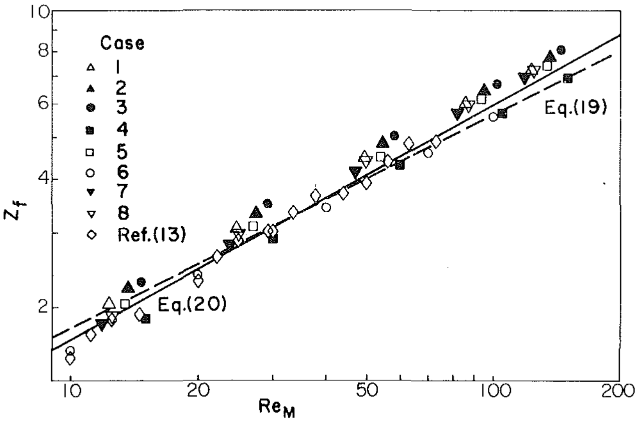

Fig. 16 Numerical heat transfer data. Case numbers are listed in Table 1 except as noted.

considerable scattering among the numerical data. It appears that a better fit to the data in the Re_M range from 10 to 150 is

$$Z_f = 0.48\ \mathrm{Re}_M^{0.55} \tag{22}$$

Presently it is not clear whether the 15 percent discrepancy is the result of some of the simplifying assumptions or perhaps numerical inaccuracy or perhaps both.

Conclusion

Numerical solutions for variable-property flows past solid and liquid droplets were obtained in the Reynolds number range of 10 to 100 with free-stream temperatures up to 1000 K. The numerical values of heat transfer and drag agree well with the existing experimental data. The results detail the effects of mass efflux and variable properties on drag and heat transfer. Mass efflux directly reduces friction drag by a factor of $(1+B)$, but increases pressure drag by a factor of $(1+B)^6$. The net effect on total drag is that the standard drag curve can be used for both evaporating and solid droplets provided the characteristic density is the free-stream density and the characteristic viscosity is evaluated using the 1/3 rule ($r=1/3$ in equation (15)). Both the mass efflux and variable properties decrease heat transfer to the droplet. The numerically calculated average Nusselt numbers agree with experimental data to within 15 percent.

Acknowledgment

This research was supported by NSF and Northwestern University.

References

1 Renksizbulut, M., and Yuen, M. C., "Experimental Study of Droplet Evaporation in a High Temperature Air Stream," ASME Journal of Heat Transfer, Vol. 105, No. 2, May 1983, pp. 384-388.

2 Jenson, V. G., "Viscous Flow Round a Sphere at Low Reynolds Numbers, (<40)," *Proc. Royal Soc.*, Vol. 249A, 1959, pp. 346-366.

3 Hamielec, A. E., Hoffman, T. W., and Ross, L. L., "Numerical Solution of the Navier-Stokes Equation for Flow Past Spheres, Part 1: Viscous Flow Around Spheres With and Without Radial Mass Efflux," *AIChE Journal*, Vol. 13, 1967, pp. 212-224.

4 Rimon, J., and Cheng, S. I., "Numerical Solution of a Uniform Flow Over a Sphere at Intermediate Reynolds Numbers," *Phys. Fluids*, Vol. 12, 1969, pp. 949-959.

5 Le Clair, B. P., Hamielec, A. E., and Pruppacher, H. R., "A Numerical Study of the Drag on a Sphere at Low and Intermediate Reynolds Numbers," *J. Atmos. Sci.*, Vol. 27, 1970, pp. 308-315.

6 Woo, S. E., and Hamielec, A. E., "A Numerical Method of Determining the Rate of Evaporation of Small Water Drops Falling at Terminal Velocity in Air," *J. Atmos. Sci.*, Vol. 28, 1971, pp. 1448-1454.

7 Rivkind, V., Ryskin, G. M., and Fishbein, G. A., "Flow Around a Spherical Drop at Intermediate Reynolds Numbers," *Appl. Math. Mech.*, Vol. 40, 1976, pp. 687-691.

8 Dennis, S. C. R., and Walker, J. D. A., "Calculation of the Steady Flow Past a Sphere at Low and Moderate Reynolds Numbers," *Journal of Fluid Mechanics*, 1971, Vol. 48, pp. 771-789.

9 Dennis, S. C. R., Walker, J. D. A., and Hudson, J. D., "Heat Transfer From a Sphere at Low Reynolds Numbers," *Journal of Fluid Mechanics*, Vol. 60, 1973, pp. 273-283.

10 Chang, I.-D., "Slow Motion of a Sphere in a Compressible Viscous Fluid," *J. Appl. Math. Phys.*, Vol. 16, 1965, pp. 449-469.

11 Kassoy, D. R., Adamson, T. C. Jr., and Messiter, A. F., "Compressible Low Reynolds Number Flow Around a Sphere," *Phys. Fluids*, Vol. 9, 1966, pp. 671-681.

12 Fendell, F. E., Coats, D. E., and Smith, E. B., "Compressible Slow Viscous Flow Past a Vaporizing Droplet," *AIAA Journal*, Vol. 6, 1968, pp. 1953-1960.

13 Sayegh, N. N., and Gauvin, W. H., "Numerical Analysis of Variable Property Heat Transfer to a Single Sphere in High Temperature Surroundings," *AIChE Journal*, Vol. 25, 1979, pp. 522-534.

14 Harpole, G. M., "Droplet Evaporation in High Temperature Environments," ASME Journal of Heat Transfer, Vol. 103, 1981, pp. 86-91.

15 Yuen, M. C., and Chen, L. W., "On Drag of Evaporating Liquid Droplets," *Combustion Sci. Tech.*, Vol. 14, 1976, pp. 147-154.

16 Hubbard, G. L., Denny, V. E., and Mills, A. F., "Droplet Evaporation: Effects of Transients and Variable Properties," *International Journal of Heat and Mass Transfer*, Vol. 18, 1975, pp. 1003-1008.

17 Law, C. K., and Sirignano, W. A., "Unsteady Droplet Combustion with Droplet Heating—II: Conduction Limit," *Combustion and Flame*, Vol. 28, 1977, pp. 175-186.

18 Prakash, S., and Sirignano, W. A., "Liquid Fuel Droplet Heating With Internal Circulation," *International Journal of Heat and Mass Transfer*, Vol. 21, 1978, pp. 885-895.

19 Prakash, S., and Sirignano, W. A., "Theory of Convective Droplet Vaporization With Unsteady Heat Transfer in the Circulating Liquid Phase," *International Journal of Heat and Mass Transfer*, Vol. 23, 1980, pp. 253-268.

20 Gosman, A. D., Pun, W. M., Runchal, A. K., Spalding, D. B., and Wolfshtein, M., *Heat and Mass Transfer in Recirculating Flows*, Academic Press, London, 1969.

21 Renksizbulut, M., "Energetics and Dynamics of Droplet Evaporation in High-Temperature Intermediate Reynolds Number Flows," Ph.D. dissertation, Northwestern University, Evanston, Ill., 1981.

22 Varga, R. S., *Matrix Iterative Analysis*, Prentice-Hall International, London, 1962.

23 Frössling, N., "Uber die Verdungtung Fallenden Tropfen," *Gerlands Beitr. Geophys.*, Vol. 52, 1938, pp. 170-216.

24 Allen, D. N. G., and Southwell, R. V., "Relaxation Methods Applied to Determine the Motion, in Two Dimensions, of a Viscous Fluid Past a Fixed Cylinder," *Quart. J. Mech. Appl. Math.*, Vol. 8, 1955, pp. 129-145.

25 Chow, L. C., and Tien, C. L., "An Examination of Four Differencing Schemes for Some Elliptic-Type Convection Equations," *Num. Heat Transfer*, Vol. 1, 1978, pp. 87-100.

26 Wilke, C. R., "A Viscosity Equation for Gas Mixtures," *J. Chem. Phys.*, Vol. 18, 1950, pp. 517-519.

27 Emmons, H. W., "The Film Combustion of Liquid Fuel," *ZAMM*, Vol. 36, 1956, pp. 60-71.

28 Eisenklam, P., Arunachalam, S. A., and Weston, J. A., "Evaporation Rates and Drag Resistance of Burning Drops," *Eleventh International Symposium on Combustion*, 1967, pp. 715-728.

APPENDIX A

Coefficient Functions Associated With Equation (2)

ϕ	a_ϕ	b_ϕ	c_ϕ	d_ϕ
Ω	$.5\,\mathrm{Re}_s \xi^{-2} \sin^2\theta$	$\xi^{-2}\sin^2\theta$	μ	$d_\Omega{}^\dagger$
ψ	0	$\xi^2/(\rho \sin^2\theta)$	1	$-\Omega$
T	$.5\,\mathrm{Re}_s \mathrm{Pr}_s$	k/c_p	1	0
Y	$.5\,\mathrm{Re}_s \mathrm{Sc}_s$	ρD	1	0

$^\dagger d_\Omega = 2\xi^2 \sin\theta\,((\mathrm{Re}_s P/4) - S)$,

$$P = \frac{\partial\rho}{\partial\xi}\left(u\frac{\partial u}{\partial\theta} + v\frac{\partial v}{\partial\theta}\right) - \frac{\partial\rho}{\partial\theta}\left(u\frac{\partial u}{\partial\xi} + v\frac{\partial v}{\partial\xi}\right)$$

$$S = \left[\xi\frac{\partial\mu}{\partial\xi}\left(v\cot^2\theta - 2\xi\frac{\partial v}{\partial\xi} - \frac{\partial v}{\partial\theta}\cot\theta - \frac{\partial^2 v}{\partial\theta^2} - \frac{\partial u}{\partial\theta}\right.\right.$$

$$\left. + \xi\frac{\partial^2 u}{\partial\xi\partial\theta} - \frac{\Omega\sin\theta}{\xi^2}\right) + \frac{\partial\mu}{\partial\theta}\left(u - \xi\frac{\partial u}{\partial\xi} - \xi^2\frac{\partial^2 u}{\partial\xi^2}\right.$$

$$+v\cot\theta+\xi\frac{\partial v}{\partial \xi}\cot\theta+\xi\frac{\partial^2 v}{\partial\xi\partial\theta}\bigg)-\xi^2\frac{\partial^2\mu}{\partial\xi^2}\left(\frac{\Omega\sin\theta}{\xi^2}\right.$$

$$\left.+\xi\frac{\partial v}{\partial\xi}\right)+\xi\frac{\partial^2\mu}{\partial\theta^2}\frac{\partial v}{\partial\xi}-\xi\frac{\partial^2\mu}{\partial\xi\partial\theta}\left(u+\frac{\partial v}{\partial\theta}+\xi\frac{\partial u}{\partial\xi}\right)\bigg]$$

APPENDIX B

Coefficient Functions Associated With Equation (13)

$$C_i=(A_i+B_ic_{\phi,i})/G; i=\mathrm{E, W, N, S}$$

$$D_P=-\Delta\xi\Delta\theta d_{\phi,P}\sin\theta_P/(G\xi_P^2),$$

$$G=A_\mathrm{E}+A_\mathrm{W}+A_\mathrm{N}+A_\mathrm{S}+c_{\phi,P}(B_\mathrm{E}+B_\mathrm{W}+B_\mathrm{N}+B_\mathrm{S}),$$

$$A_\mathrm{E}=\frac{1}{8}a_{\phi,P}\xi_P^2[(\psi_\mathrm{SE}+\psi_\mathrm{S}-\psi_\mathrm{NE}-\psi_\mathrm{N}) + |\psi_\mathrm{SE}+\psi_\mathrm{S}-\psi_\mathrm{NE}-\psi_\mathrm{N}|],$$

$$A_\mathrm{W}=\frac{1}{8}a_{\phi,P}\xi_P^2[(\psi_\mathrm{NW}+\psi_\mathrm{N}-\psi_\mathrm{SW}-\psi_\mathrm{S}) + |\psi_\mathrm{NW}+\psi_\mathrm{N}-\psi_\mathrm{SW}-\psi_\mathrm{S}|],$$

$$A_\mathrm{N}=\frac{1}{8}a_{\phi,P}\xi_P^2[(\psi_\mathrm{NE}+\psi_\mathrm{E}-\psi_\mathrm{NW}-\psi_\mathrm{W}) + |\psi_\mathrm{NE}+\psi_\mathrm{E}-\psi_\mathrm{NW}-\psi_\mathrm{W}|],$$

$$A_\mathrm{S}=\frac{1}{8}a_{\phi,P}\xi_P^2[(\psi_\mathrm{SW}+\psi_\mathrm{W}-\psi_\mathrm{SE}-\psi_\mathrm{E}) + |\psi_\mathrm{SW}+\psi_\mathrm{W}-\psi_\mathrm{SE}-\psi_\mathrm{E}|],$$

$$B_\mathrm{E}=\frac{1}{2}\xi_P^2\sin\theta_P\left(\frac{\Delta\theta}{\Delta\xi}\right)(b_{\phi,\mathrm{E}}+b_{\phi,P}),$$

$$B_\mathrm{W}=\frac{1}{2}\xi_P^2\sin\theta_P\left(\frac{\Delta\theta}{\Delta\xi}\right)(b_{\phi,\mathrm{W}}+b_{\phi,P}),$$

$$B_\mathrm{N}=\frac{1}{4}\left(\frac{\Delta\xi}{\Delta\theta}\right)(b_{\phi,N}+b_{\phi,P})(\sin\theta_\mathrm{N}+\sin\theta_P),$$

$$B_\mathrm{S}=\frac{1}{4}\left(\frac{\Delta\xi}{\Delta\theta}\right)(b_{\phi,S}+b_{\phi,P})(\sin\theta_\mathrm{S}+\sin\theta_P)$$

Journal of Heat Transfer

Technical Notes

This section contains shorter technical papers. These shorter papers will be subjected to the same review process as that for full papers.

Effect of the Fluid Media Viscosities on the Downward Heat Transfer in a Miscible, Melting System[1]

R. Farhadieh[2]

Nomenclature

Cp = specific heat
dz/dt = downward melting rate
g = gravitational constant
h = heat transfer coefficient
k = thermal conductivity
l = length scale, equation 1
Nu = Nusselt number, hl/k_m
Pr = Prandtl number, μ/kCp
Ra = Rayleigh number, $g\Delta\rho l^3/\rho_m \nu_m \kappa_m$
T = temperature

Greek symbols

$\Delta T = T_l - T_m$
$\Delta T_s = T_m - T_i$
κ = thermal diffusivity
λ_f = latent heat of solid
$\lambda_c = \lambda_f + Cp + \Delta T_s$
μ = viscosity
ρ = density
$\rho^* = \rho_l/\rho_m$

Subscript

i = initial temperature of solid
l = liquid phase or liquid pool temperature
m = melt phase or melting point temperature of solid
s = solid

Introduction

The downward melting of a horizontal solid surface by a hot liquid pool falls into miscible and immiscible categories. In the immiscible melting system removal of the melt layer occurs through upside-down pendent drops that are pinched-off from the melt layer and collected on the top of the liquid pool [1]. On the other hand, in the miscible melting system, which is of interest in here, when and if a gravitationally unstable fluid system (liquid pool and the melt) is encountered, mixing of the liquid pool and the melt becomes inevitable, thus affecting the heat transfer characteristic of the liquid pool [2]. In the gravitationally unstable fluid system configuration, the liquid pool density is greater than that of the melt. Such is the state of the molten core debris coming in contact with the ceramic materials or concrete underlying the reactor building in the study of postulated melt-down accident [3]. The molten phase of these materials is miscible with the molten core debris. Owing to the complex nature of the problem an in-depth experimental study of this problem with different material pairs and geometries was undertaken. The effect of the liquid pool and melt viscosities on the downward heat transfer and the development of an empirical correlation for the heat transfer are the purpose of this study.

In the melting system under study the density difference between the liquid pool and the melt is the convective driving force. Onset of convection is marked by density-driven currents in the form of melt fingers penetrating into the initially stable overlying liquid pool. The observed flow regime is named laminar. Beyond a critical density ratio of the liquid to the melt, ρ^*, the currents breakup the thermally stable layer, thus resulting in thermal and material mixing of the layer; this is referred to as "convective mixing" [2]. Increase in the convective mixing strength which is brought about by increase in ρ^* enhances the downward melting heat transfer in stages as different density ratio bands are encountered. Transition, turbulent, and upper turbulent are the hydrodynamic flow regimes, encountered at the different density ratio bands.

Downward heat transfer in a similar melting system was investigated by Catton et al. [4], who utilized C_6H_6 as the solid substrate and CCl_4 and CH_2I_2 as the liquid pool. The material pairs yielded a ρ^* as high as 3.4. The viscosities of CCl_4 and the melted solid were in the order of 10^{-2} cp and 10^{-3} cp, respectively; no data is available on the viscosity of CH_2I_2. Assuming that the Rayleigh-Taylor instability breaks up the melt layer into small jets, which were the source of melt removal, and balancing the jet momentum versus the bouyancy force, Catton et al. derived a semi-empirical expression for the downward heat transfer. In their expression, only the melt viscosity was required. The small data scatter observed in the correlation of Catton et al. is attributed to the small viscosity of the upper fluid (KI/Poly 1500 of [2] and CCl_4/C_6H_6 of their experiment). Moreover, the data encompasses the turbulent regime.

Experimental Apparatus and Technique

Materials meeting requirements on miscibility and a relatively large variation in ρ^* were: aqueous solution of potassium iodide, KI, and zinc bromide, $ZnBr_2$, as the liquid pool; ice, and three different water soluble waxes [polyethylene glycol (Poly) 1500, 600, 400] as the solid

---

[1] Work performed under the auspices of the U.S. Department of Energy.

[2] Reactor Analysis and Safety Division, Argonne National Laboratory, Argonne, Ill. 60439. Mem. ASME

Contributed by the Heat Transfer Divison for publication in the JOURNAL OF HEAT TRANSFER. Manuscript received by the Heat Transfer Division March 31, 1982.

Table 1 Thermophysical properties of solids

Solid phase	Melt pt. T_mK	Density ρ_m(kg/m^3)	Thermal conductivity K_m(W/m – K)	Heat capacity C_{pm}(J/kg – K) × 10^{-3}	Latent heat λ_f(J/kg) × 10^{-5}	Viscosity μ_m (CP)
Ice	273	1000	0.552	4.18	3.34	1.78
Poly 1500	318	1095	0.2509	2.09	1.63	80
Poly 600	294	1125	0.2509	2.47	1.463	140
Poly 400	278	1125	0.2509	2.048	1.505	250

Table 2 Physical properties and experimental parameters for the tested material pairs

Solid phase	Liquid phase	Liquid-melt temperature difference ΔT(K)	Range of ρ^*	Range of liquid viscosity μ_l (cp)	Range of Prandtl number ratio $\mathrm{Pr}_l/\mathrm{Pr}_m$	$\frac{\lambda_c \rho_m}{\Delta T}$ (J/m^3 – K) × 10^{-7}
Ice	KI	60	1.55-1.05	0.89-0.96	0.28-0.47	0.696
Poly 1500	KI	20	1.55-1.05	0.89-0.96	0.0042-0.0098	1.121
Poly 600	KI	24	1.51-1.02	0.89-0.96	0.002-0.005	1.147
Ice	$ZnBr_2$	60	2.31-1.03	53-3	29.8-1.68	0.696
Poly 1500	$ZnBr_2$	20	2.28-1.12	53-3.5	0.59-0.0035	1.121
Poly 600	$ZnBr_2$	11	2.22-1.35	53-4.5	0.29-0.025	2.505
Poly 400	$ZnBr_2$	27	2.22-1.07	53-3	0.20-0.011	0.832

substrate (see Table 1 for properties of the melt). It should be noted that the molten phase viscosities of Poly 1500, 600, and 400 were non-Newtonian. The melt characteristic of solids remained constant in each set of experiments. Experiments reported here covered a density ratio range of $1.1 < \rho^* \leq 2.22$. The Prandtl numbers for the overlying liquid pool and the melt were in the range of $2.8 < \mathrm{Pr}_l < 400$ and $13.5 < \mathrm{Pr}_m < 2000$, respectively. The viscosity of zinc bromide solution was concentration-dependent (see Table 2). The viscosity of aqueous $ZnBr_2$ solution was measured at different concentration. Accuracy of the measured data was within 5 percent. The viscosity data for KI solution at different concentration is given in the handbook of chemistry.

The test section utilized in this experimental study consisted of an upright, de-silvered, evacuated glass Dewar, having a height and internal diameter of 380 and 76 mm, respectively. A 65-mm-deep cast of the solid was prepared inside the Dewar making sure that the surface exposed to the liquid pool was initially flat. The liquid pool overlying the solid was heated by a planar electrical heater grid, suspended about 35 mm above and parallel to the initial position of the interface. The distance between heater grid and the initial position of the interface had negligible effect on the melting rate [2]. The liquid temperature at the heater grid was thermostatically controlled to a constant ΔT above the melting point of the solid (see Table 2), thus insuring a quasi-steady experiment. A liquid pool of relatively large volume was chosen to minimize density changes owing to melting and dissolution. This was further ensured by terminating the experiment when the penetration depth of 20 to 25 mm was reached. Mutual dissolution of the melted volume and the liquid pool resulted in 2 percent variation in the initial density of the liquid pool. The test section was back-lighted to photograph the melt front advancement at regular time intervals. Measurements obtained from the photographs were utilized in calculating the melting rates.

Discussion and Concluding Remarks

The plot of melting rate, dz/dt, versus ρ^* for material pairs tested shows a great deal of data scatter (Fig. 1). This scattering is not due to either the difference in λ_f of the different solids or their non-Newtonian nature, rather it can be related to the effect of the liquid pool viscosity on the melting rate; for example, compare ice/$ZnBr_2$ and ice/KI system where the same solid is utilized for λ_f, and ice/KI and Poly 1500/KI system where the same liquid pool is utilized for non-Newtonian nature of the melt.

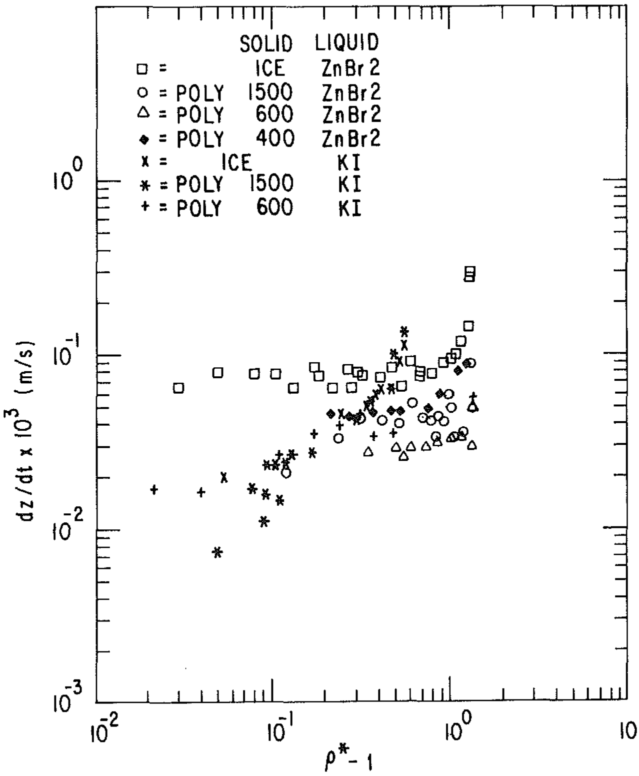

Fig. 1 Downward melting rate versus density ratio, ρ^*

The product of dx/dt and μ_l at each ρ^* simply rearranges the data along the turbulent and upper turbulent hydrodynamic flow regimes, as depicted in Fig. 2. The value of μ_l is chosen at the pool operating temperature in the turbulent regime data for $ZnBr_2$ and KI as the upper liquid pools fall along two separate curves. For the same ρ^*, a greater melting rate is measured when the more viscous $ZnBr_2$ is the upper liquid pool. Melt removal by the less viscous KI is considerably less. In this regime the combined effect of the liquid pool viscosity and the density ratio, ρ^*, contributes to the melt-removal energy. Beyond a critical ρ^* (transition from turbulent to upper turbulent flow regime) all the data fall on a straight line. In this regime the viscosity of the upper solution is the major contributing factor to the melt removal energy; the effect of the density ratio is small.

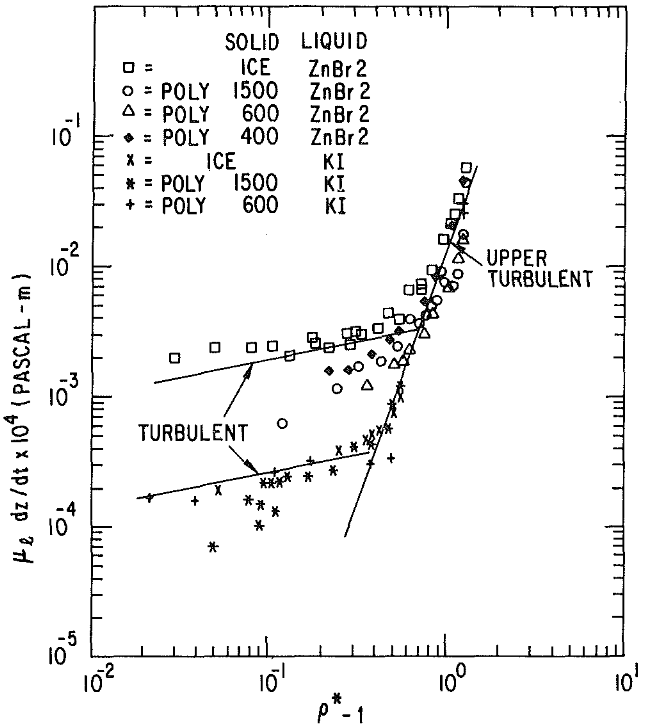

Fig. 2 Product of liquid pool viscosity and the downward melting rate versus ρ^*

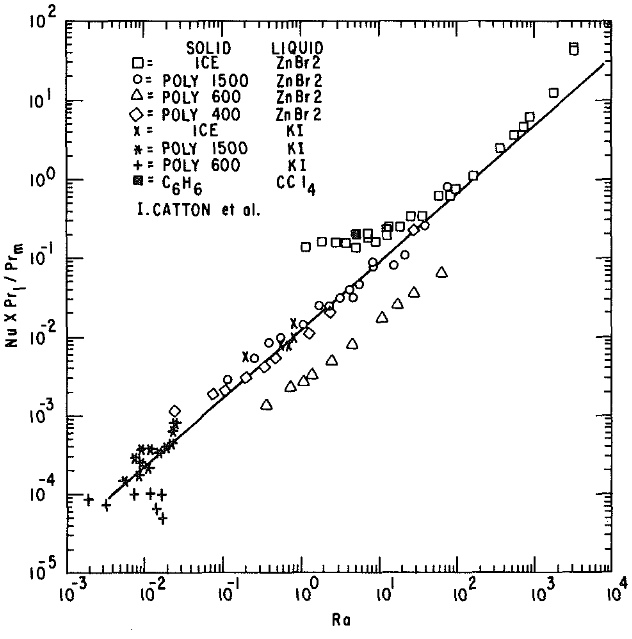

Fig. 3 The downward melting heat transfer versus the Rayleigh number

Heat transfer for the type of natural convection observed in the melting system under study can be described by Nusselt-Rayleigh number relationship. Experiments with KI and Poly 1500 as the test material pairs, conducted in test sections of different cross-sectional area (square [2] and circular) as well as those reported by Catton et al. [4] indicated there was no dependency between downward heat transfer and geometry (size and shape of the test cell). Accordingly, in the definition of the Nusselt number, Nu = hl/k_m, and the Rayleigh number, Ra = $g\Delta\rho l^3/\rho_m \nu_m \kappa_m$, the length scale, l, is defined as

$$l=[(\mu_l/\rho_l)^2/g]^{1/3} \tag{1}$$

The values of ν_m and κ_m are selected at the melting point temperature. The expression for h (heat transfer coefficient), developed in [2], incorporates the heat of fusion of the solid. The nondimensional heat transfer coefficient is given by

$$\mathrm{Nu} \triangleq \frac{hl}{k_m} = \frac{\rho_s (C_{ps}\Delta T_s + \lambda_f)\,\dfrac{dz}{dt}\,l}{k_m \Delta T} \tag{2}$$

In deriving equation (2), the solid was assumed to be an insulator and all the heat was expended for melting. Equation (1) contains only the physical properties of the test materials. The thermal and momentum boundary layer dominance of the melt layer and the liquid pool are incorporated in the heat transfer expression through the Prandtl number ratios of the two fluid media. Figure 3 shows the plot of the correlated Nu $\mathrm{Pr}_l/\mathrm{Pr}_m$ versus Ra number. The best fit curve through majority of the data points is given by the expression

$$\mathrm{Nu}\,\frac{\mathrm{Pr}_l}{\mathrm{Pr}_m} = (1.239\times 10^{-2})\mathrm{Ra}^{(0.877)} \tag{3}$$

The correlation given by equation (3) best describes the upper turbulent flow regime where the liquid pool viscosity dominates. This includes the range of Ra > 10^0 for ice/ZnBr_2 system as well as Ra > 10^{-2} for Poly 1500/KI system. The curve encompassing Δ's (Poly 600/ZnBr_2 system) has a similar trend as correlated data given by equation (3). Nevertheless, the value of Δ's are low which is attributed to the experimental value of the parameter $\rho_m \lambda_c/\Delta T$ (see Table 2). The value of the parameter for Δ's is about 2.5, considerably larger than that for other sets. Data scatter about the correlated curve, equation (3), could have been reduced significantly if the parameter $\rho_m\lambda_c/\Delta T$ were kept constant in all the experiments. In the range Ra < 10^0 for ice/ZnBr_2 and Ra < 2×10^{-2} for Poly 1500/KI system where the flow regime is characterized to be turbulent [2], the Rayleigh-Taylor instability mechanism for two superimposed viscous fluid layer can best describe the process. In this regime the combined effects of liquid pool viscosity and the density ratio, ρ^*, dominates. The correlation for the regime is not presented here pending further investigation.

A single data point from [4] on $\mathrm{CCl}_4/\mathrm{C}_6\mathrm{H}_6$ system is also given in Fig. 3. This point agrees well with the ZnBr_2/Ice system in the turbulent flow regime where the combined effects of viscosity and density ratio dominate. Data points for $\mathrm{CH}_2\mathrm{I}_2/\mathrm{C}_6\mathrm{H}_6$ system could not be included, owing to the lack of thermophysical properties of $\mathrm{CH}_2\mathrm{I}_2$. The correlation of Catton et al. [4] was also tested with the viscous data of this study which resulted in large scatter.

References

1 Farhadieh, R., and Epstein, M., "Downward Penetration of a Hot Liquid Pool into the Horizontal Surface of Solid," ASME JOURNAL OF HEAT TRANSFER, Vol. 104, 1982, pp. 199–201.

2 Farhadieh, R., and Baker, L., Jr., "Heat Transfer Phenomenology of a Hydrodynamically Unstable Melting System," ASME JOURNAL OF HEAT TRANSFER, Vol. 100, 1978, pp. 305–310.

3 Gluekler, E. L., and Baker, L., Jr., "Post-Accident Heat Removal in LMFBR's," Symposium on the Thermal and Hydraulic Aspects of Nuclear Reactor Safety," Vol. 2, *Liquid Metal Fast Breeder Reactors*, ASME Press, New York, 1977, pp. 285–324.

4 Catton, I., Brinsfield, W. A., and Ghiaasiaan, M., "Heat Transfer From a Heated Pool to a Melting Miscible Substrate," ASME Paper No. 81-WA/HT-31.

Exact Solution for Freezing in Cylindrically Symmetric, Porous, Moist Media

M. A. Boles[1] and M. N. Özişik[2]

Nomenclature

K_{12} = thermal conductivity ratio, $\dfrac{k_1}{k_2}$

L = dimensionless latent heat, $\dfrac{lu_0}{c_2 T_0}$

Q = dimensionless strength of the line sink, $\dfrac{q}{k_1 T_0}$

R = dimensionless radial coordinate, $\dfrac{r}{r_0}$

$S(\tau)$ = the dimensionless location of freeze-front, $\dfrac{s(t)}{r_0}$

$U(R,\tau)$ = nondimensional moisture concentration for the region $r > S(t), \dfrac{u_0 - u(r,t)}{u_0}$

α = diffusivity

α_{ij} = diffusivity, $\dfrac{\alpha_i}{\alpha_j}$

Δ = nondimensional thermal gradient coefficient, $\dfrac{T_0 \delta}{u_0}$

$\theta_i(R,\tau)$ = nondimensional temperature for the regions $i = 1$ and $i = 2$, $\dfrac{T_i(r,t)}{T_0}$

θ_v = nondimensional freeze-front temperature, $\dfrac{T_v}{T_0}$

τ = nondimensional time, $\dfrac{\alpha_2 t}{{r_0}^2}$

Subscripts

1,2,m = refers to solid, liquid, and moisture, respectively.

Introduction

Experimental investigations [1, 2] of freezing in a porous medium, such as a wet soil, have shown that the freezing is accompanied by moisture migration towards the freezing front. The migration of moisture effects the temperature distribution in the medium and the location of the freezing front. Freezing in a wet porous medium has numerous engineering applications. For example, during the extraction of energy from the earth using a heat-pump, earth-coupled thermal system, the cooling pipe buried in the earth can be regarded as a line heat sink in an infinite medium. As the energy is extracted from the moist porous soil, the moisture is redistributed, lowered in temperature, and becomes frozen. It is of interest to know the temperature distribution and the location of the freezing front. Also, in the measurements of thermal conductivity in moist porous media, the knowledge of the moisture distribution upon freezing is important.

The standard formulation of phase-change problem without allowing for the movement of moisture within the medium is not applicable for the analysis of this type of freezing problems. More complicated phase-change problems allowing for the movement of moisture have been studied in connection with evaporation [3] and freezing [4] only for a semi-infinite medium. The studies of freezing due to a line heat sink in an infinite medium with cylindrical symmetry are also limited [5, 6] and do not allow for moisture movement.

In the present study exact solutions are developed for the temperature and moisture distribution and the location of the freezing front caused by cooling with a line heat sink in an infinite medium with cylindrical symmetry.

Formulation of the Problem

Consider a line heat sink of strength, q, (W/m) positioned at the origin of the radial coordinate, $r = 0$, in a moist, porous, infinite medium. Initially the medium is at a uniform temperature, T_o, and contains moisture of uniform distribution, u_o. At time $t = 0$, the heat sink is activated. The freezing process begins and the freezing front propagates in the radial direction. Let $r = s(t)$ be the position of the freeze front at any time, t. The dimensionless temperature distribution $\theta_1(R,\tau)$ in the freezing zone, $0 < R < S(\tau)$, where there is no moisture is governed by the equation

$$\frac{\partial \theta_1(R,\tau)}{\partial \tau} = \alpha_{12} \frac{1}{R} \frac{\partial}{\partial R}\left(R \frac{\partial \theta_1}{\partial R}\right), \text{ in } 0<R<S(\tau), \tau>0 \qquad (1)$$

In the unfrozen region $S(\tau) < R < \infty$, the dimensionless temperature distribution $\theta_2(R,\tau)$ and the moisture distribution $U(R,\tau)$ are governed by the following system obtained as a special case from the Luikov's system of equations (87) and (88) of [7]

$$\frac{\partial \theta_2(R,\tau)}{\partial \tau} = \frac{1}{R} \frac{\partial}{\partial R}\left(R \frac{\partial \theta_2}{\partial R}\right), \text{ in } S(\tau)<R<\infty, \tau>0 \qquad (2)$$

$$\frac{\partial U(R,\tau)}{\partial \tau} = \alpha_{m2} \frac{1}{R} \frac{\partial}{\partial R}\left(R \frac{\partial U}{\partial R}\right) - \alpha_{m2} \Delta \frac{1}{R} \frac{\partial}{\partial R}\left(R \frac{\partial \theta_2}{\partial R}\right),$$
$$\text{in } S(\tau)<R<\infty, \tau>0 \qquad (3)$$

It is to be noted that in the Luikov system [7] the zones 1 and 2 refer, respectively, to evaporation and moisture zones, whereas in the present system they refer to solid and liquid zones, respectively. The boundary and initial conditions become

$$\underset{R\to 0}{\mathcal{L}im}\left(2\pi R \frac{\partial \theta_1}{\partial R}\right) = Q \qquad (4)$$

$$\theta_1(S,\tau) = \theta_2(S,\tau) = \theta_v \qquad (5)$$

$$K_{12} \frac{\partial \theta_1(S,\tau)}{\partial R} - \frac{\partial \theta_2(S,\tau)}{\partial R} = L[1 - U(S,\tau)] \frac{dS}{d\tau} \qquad (6)$$

$$\frac{\partial U(S,\tau)}{\partial R} - \Delta \frac{\partial \theta_2(S,\tau)}{\partial R} = 0 \qquad (7)$$

$$\theta_2(R,0) = 1 \qquad (8a)$$

$$U(R,0) = 0 \qquad (8b)$$

$$\theta_2(\infty,\tau) = 1 \qquad (9a)$$

$$U(\infty,\tau) = 0 \qquad (9b)$$

---

[1] Mechanical and Aerospace Engineering Department, North Carolina State University, Raleigh, N. C. 27650, Mem. ASME

[2] Mechanical and Aerospace Engineering Department, North Carolina State University, Mem. ASME

Contributed by the Heat Transfer Division for publication in the JOURNAL OF HEAT TRANSFER. Manuscript received by the Heat Transfer Division May 13, 1982.

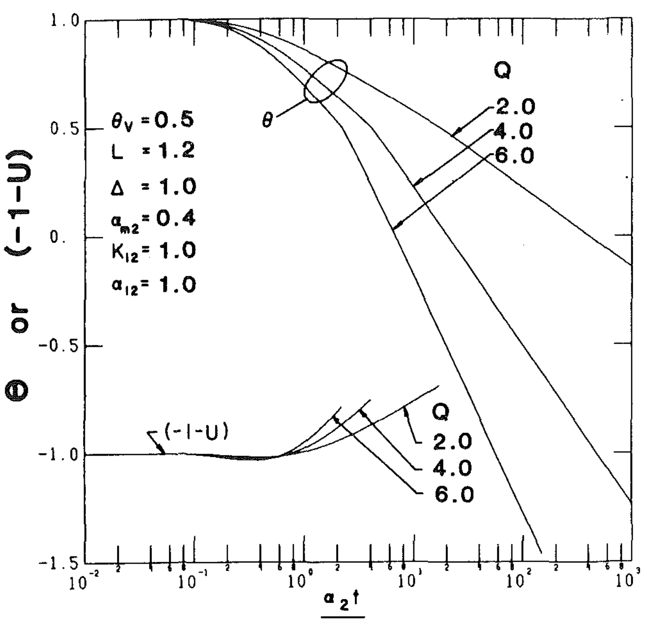

Fig. 1 Effect of nondimensional line heat strength, *Q*, on temperature, *θ*, and moisture, *U*

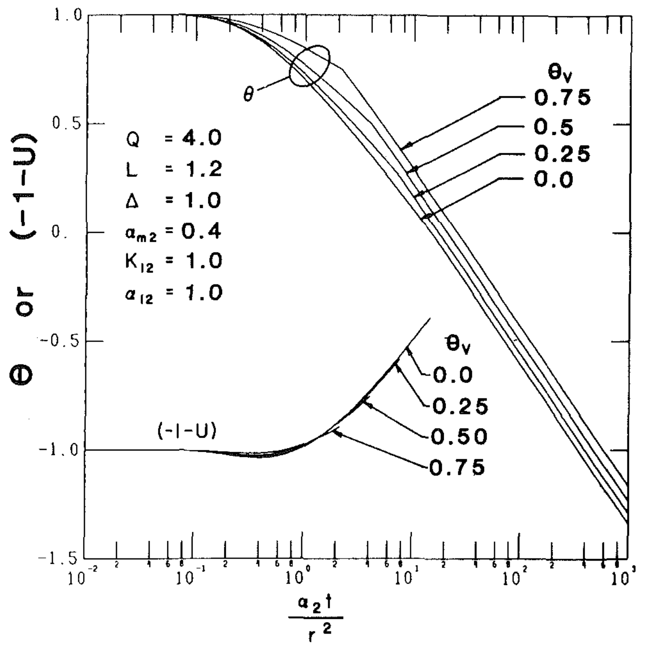

Fig. 2 Effect of nondimensional freeze-front temperature, θ_v, on temperature, *θ*, and moisture, *U*

Solution of the Problem

Equations (2) and (3) can be decoupled by defining a new variable $Z(R,\tau)$ as [8]

$$Z(R,\tau)=\theta_2(R,\tau)+CU(R,\tau) \tag{10a}$$

where

$$C=\frac{1-\alpha_{m2}}{\alpha_{m2}\Delta} \tag{10b}$$

After some manipulation the equation for $Z(R,\tau)$ is determined as

$$\frac{\partial Z(R,\tau)}{\partial \tau}=\alpha_{m2}\frac{1}{R}\frac{\partial}{\partial R}\left(R\frac{\partial Z}{\partial R}\right), \text{ in } S(\tau)<R<\infty, \tau>0 \tag{11}$$

Now the problem has been reduced to the solution of three

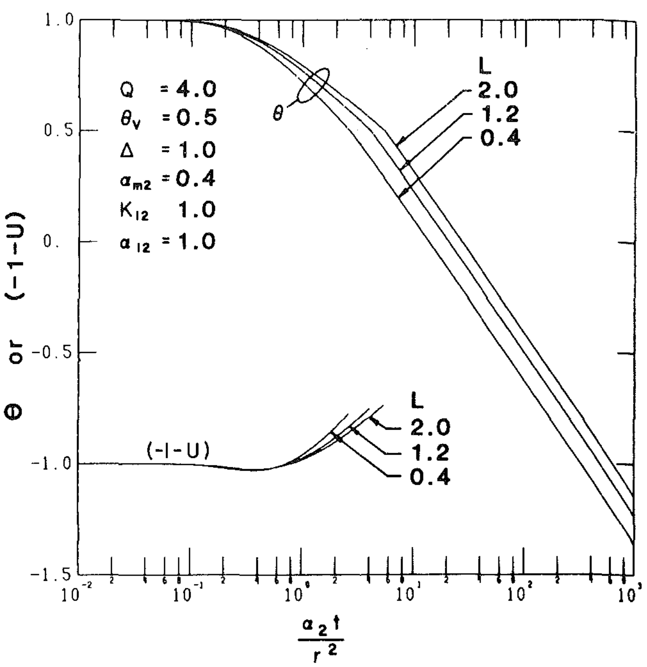

Fig. 3 Effect of nondimensional latent heat, *L*, on temperature, *θ*, and moisture, *U*

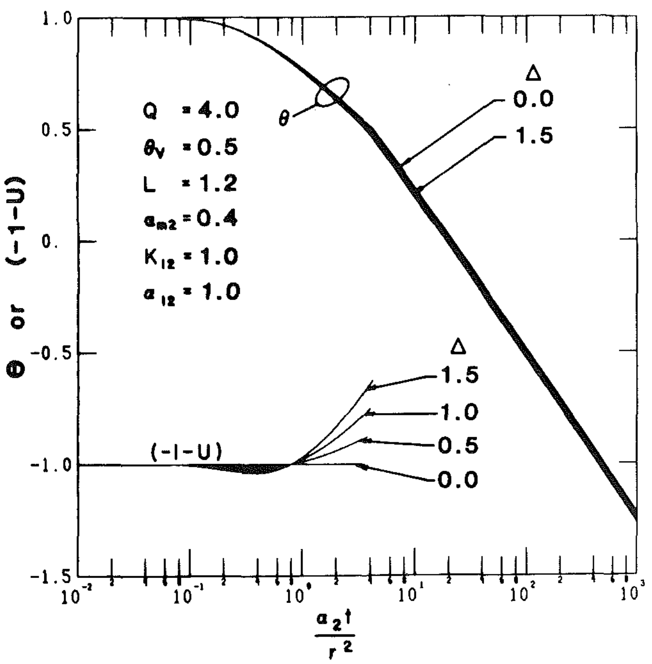

Fig. 4 Effect of nondimensional thermal gradient coefficient, Δ, on temperature, *θ*, and moisture, *U*

diffusion type homogeneous equations, (1), (2), and (11), subject to the boundary and initial conditions given above. These solutions are determined as

$$\theta_1(R,\tau)=\theta_v+\frac{Q}{4\pi}\left[Ei\left(-\frac{R^2}{4\alpha_{12}\tau}\right)-Ei(-\lambda^2)\right], \text{ in } 0<R<S(\tau) \tag{12}$$

$$\theta_2(R,\tau)=1+(\theta_v-1)\frac{Ei\left(-\frac{R^2}{4\tau}\right)}{Ei(-\lambda^2\alpha_{12})}, \text{ in } R>S(\tau) \tag{13}$$

and

$$U(R,\tau)=\frac{\alpha_{m2}\Delta}{1-\alpha_{m2}}\,\frac{\theta_v-1}{Ei(-\lambda^2\alpha_{12})}\left[\frac{1}{\alpha_{m2}}e^{\frac{1-\alpha_{m2}}{\alpha_{m1}}\lambda^2}\right.$$
$$\left.\cdot Ei\left(-\frac{R^2}{4\alpha_{m2}\tau}\right)-Ei\left(-\frac{R^2}{4\tau}\right)\right], R>S(\tau) \qquad (14)$$

where

$$\lambda=\frac{S(\tau)}{2(\alpha_{12}\tau)^{1/2}} \qquad (15)$$

Finally, the transcendental equation for the determination of λ is obtained by introducing the solutions given by equations (12), (13), (14) together with the definition (15) into the interface energy balance equation (6). We find

$$K_{12}\frac{Q}{4\pi}e^{-\lambda^2}-\frac{\theta_v-1}{Ei(-\lambda^2\alpha_{12})}e^{-\lambda^2\alpha_{12}}=\lambda^2\alpha_{12}L\left\{1\right.$$
$$\left.-\frac{\Delta}{1-\alpha_{m2}}(\theta_v-1)\left[\frac{e^{\frac{1-\alpha_{m2}}{\alpha_{m1}}\lambda^2}}{Ei(-\lambda^2\alpha_{12})}Ei(-\lambda^2\alpha_{1m})-\alpha_{m2}\right]\right\} \qquad (16)$$

Results and Discussion

Once the constant λ is computed from the solution of the transcendental equation (16) for a given set of system parameters, the location of the freeze-front $S(\tau)$ at any time τ is determined according to equation (15), the temperature distribution $\theta_1(R,\tau)$ in the freeze-zone is calculated from equation (12), and the temperature distribution $\theta_2(R,\tau)$ and the moisture distribution $U(R,\tau)$ outside the freeze-zone are calculated from equations (13) and (14), respectively.

Sample calculations are performed to illustrate the effects of various system parameters on the temperature and moisture distribution in the region. These results are presented in Figs. 1-4 by plotting the temperature and the moisture content as a function of the dimensionless parameter $\tau/R^2 \equiv \alpha_2 t/r^2$. The physical significance of such figures can be interpreted in two different ways:

1 For a fixed value of time, the curves represent the variation of temperature or moisture as a function of the radial position, r, in the medium. Then, on these figures the origin $r = 0$ corresponds to a location $\alpha_2 t/r^2 \rightarrow \infty$, and the right-hand side of the curves correspond to the frozen zone. The curves for the moisture content show that the moisture is highest at the freeze-front; moving away from the freeze-front with increasing r, there exists a region where moisture content falls below the initial value, followed by the zone where the initial value of the moisture content remains unchanged.

2 For a fixed value of the radial position, r, the curves represent the variation of temperature or moisture with time. Then, $\alpha_2 t/r^2 \rightarrow 0$ corresponds to the beginning of the cooling process. As time increases, the temperature at a given location continuously decreases; on the other hand, the moisture content falls below the initial value for a short period, then begins to increase continuously until the freezing front reaches to that location.

Having discussed the general behavior of the variation of temperature and moisture as a function of time and position in the region, we now focus our attention to the effects of various system parameters.

Figure 1 illustrates the effects of the nondimensional line heat strength, Q, on temperature and moisture. As the sink strength is increased, the freeze-front moves deeper into the medium at a given time; or the freeze-front arrives much quicker at a given location. Increasing Q, lowers the values of temperature and moisture.

Figure 2 illustrates the effects of the nondimensional freeze-front temperature, θ_v, on the temperature and moisture distribution in the medium. Decreasing θ_v, increases the maximum moisture content and moves the freeze-front towards the origin, $r = 0$.

Figure 3 illustrates the effects of nondimensional latent heat, L, on the temperature and moisture distribution. Lowering L forces the freeze-front further away from the origin, $r = 0$. The minimum and maximum moisture contents do not seem to depend on L.

Figure 4 shows the effects of the nondimensional thermal gradient coefficient, Δ, on the temperature and moisture distribution. The maximum moisture content is strongly dependent upon Δ; increasing Δ increases the maximum moisture content. The temperature level and the freeze-front location, however, are very little affected by Δ.

Acknowledgment

This work was supported in part by the National Science Foundation through the Grant MEA-8110 705.

References

1 Aguirre-Puente, J., and Philippe, A., "Quelques recherches effectuées en France sur le probléme de la congélation des sols," *Rev. Gên. Thermique*, Vol. 96, 1969, pp. 1123-1141.

2 Aguirre-Puente, J., Dupas, A., and Philippe, A., "Quelques résultats concernant le gonflement au gel et leur application au classement des sols selon leur degré de gélivité," *Bull. liason Labo. P. et Ch.*, Vol. 68, 1973, pp. 23-29.

3 Mikhailov, M. D., "Exact Solution of Temperature and Moisture Distributions in a Porous Half-Space With Moving Evaporation Front," *International Journal of Heat and Mass Transfer*, Vol. 18, 1975, pp. 797-804.

4 Mikhailov, M. D., "Exact Solution for Freezing of Humid Porous Half-Space," *International Journal of Heat and Mass Transfer*, Vol. 19, 1976, pp. 651-655.

5 Patterson, S., "Propagation of a Boundary of Fusion," *Proceedings of the Glasgow Mathematics Association*, Vol. 1, 1952, pp. 42-47.

6 Özişik, M. N., and Uzzel, J. C., "Exact Solution for Freezing in Cylindrical Symmetry With Extended Freezing Temperature," JOURNAL OF HEAT TRANSFER, Vol. 101, 1979, pp. 331-334.

7 Luikov, A. V., "Systems of Differential Equations of Heat and Mass Transfer in Capillary-Porous Bodies (Review)," *International Journal of Heat and Mass Transfer*, Vol. 18, 1975, pp. 1-14.

8 Mikhailov, M. D., "General Solution of the Diffusion Equations Coupled at the Boundary," *International Journal of Heat and Mass Transfer*, Vol. 16, 1973, pp. 2155-2164.

9 Lebeolev, N. N., *Special Functions and Their Applications*, Prentice-Hall, Inc., Englewood Cliffs, N.J., 1965.

Natural Convection From Needles With Variable Wall Heat Flux

J. L. S. Chen[1]

Nomenclature

a = dimensionless needle size
b = needle shape parameter, $2(m-1)/5$
f = dimensionless stream function
g = gravitational acceleration
Gr = modified Grashof number, $g\beta q_o L^4/(k\nu^2)$
h = convection heat transfer coefficient

---

[1] Associate Professor, Department of Mechanical Engineering, University of Pittsburgh, Pittsburgh, Pa. 15261, Mem. ASME

Contributed by the Heat Transfer Division for publication in the JOURNAL OF HEAT TRANSFER. Manuscript received by the Heat Transfer Division July 23, 1982.

$$U(R,\tau)=\frac{\alpha_{m2}\Delta}{1-\alpha_{m2}}\,\frac{\theta_v-1}{Ei(-\lambda^2\alpha_{12})}\left[\frac{1}{\alpha_{m2}}e^{\frac{1-\alpha_{m2}}{\alpha_{m1}}\lambda^2}\right.$$

$$\left.\bullet Ei\left(-\frac{R^2}{4\alpha_{m2}\tau}\right)-Ei\left(-\frac{R^2}{4\tau}\right)\right],R>S(\tau) \tag{14}$$

where

$$\lambda=\frac{S(\tau)}{2(\alpha_{12}\tau)^{1/2}} \tag{15}$$

Finally, the transcendental equation for the determination of λ is obtained by introducing the solutions given by equations (12), (13), (14) together with the definition (15) into the interface energy balance equation (6). We find

$$K_{12}\frac{Q}{4\pi}e^{-\lambda^2}-\frac{\theta_v-1}{Ei(-\lambda^2\alpha_{12})}e^{-\lambda^2\alpha_{12}}=\lambda^2\alpha_{12}L\left\{1\right.$$

$$\left.-\frac{\Delta}{1-\alpha_{m2}}(\theta_v-1)\left[\frac{e^{\frac{1-\alpha_{m2}}{\alpha_{m1}}\lambda^2}}{Ei(-\lambda^2\alpha_{12})}Ei(-\lambda^2\alpha_{1m})-\alpha_{m2}\right]\right\} \tag{16}$$

Results and Discussion

Once the constant λ is computed from the solution of the transcendental equation (16) for a given set of system parameters, the location of the freeze-front $S(\tau)$ at any time τ is determined according to equation (15), the temperature distribution $\theta_1(R,\tau)$ in the freeze-zone is calculated from equation (12), and the temperature distribution $\theta_2(R,\tau)$ and the moisture distribution $U(R,\tau)$ outside the freeze-zone are calculated from equations (13) and (14), respectively.

Sample calculations are performed to illustrate the effects of various system parameters on the temperature and moisture distribution in the region. These results are presented in Figs. 1-4 by plotting the temperature and the moisture content as a function of the dimensionless parameter $\tau/R^2 \equiv \alpha_2 t/r^2$. The physical significance of such figures can be interpreted in two different ways:

1 For a fixed value of time, the curves represent the variation of temperature or moisture as a function of the radial position, r, in the medium. Then, on these figures the origin $r = 0$ corresponds to a location $\alpha_2 t/r^2 \rightarrow \infty$, and the right-hand side of the curves correspond to the frozen zone. The curves for the moisture content show that the moisture is highest at the freeze-front; moving away from the freeze-front with increasing r, there exists a region where moisture content falls below the initial value, followed by the zone where the initial value of the moisture content remains unchanged.

2 For a fixed value of the radial position, r, the curves represent the variation of temperature or moisture with time. Then, $\alpha_2 t/r^2 \rightarrow 0$ corresponds to the beginning of the cooling process. As time increases, the temperature at a given location continuously decreases; on the other hand, the moisture content falls below the initial value for a short period, then begins to increase continuously until the freezing front reaches to that location.

Having discussed the general behavior of the variation of temperature and moisture as a function of time and position in the region, we now focus our attention to the effects of various system parameters.

Figure 1 illustrates the effects of the nondimensional line heat strength, Q, on temperature and moisture. As the sink strength is increased, the freeze-front moves deeper into the medium at a given time; or the freeze-front arrives much quicker at a given location. Increasing Q, lowers the values of temperature and moisture.

Figure 2 illustrates the effects of the nondimensional freeze-front temperature, θ_v, on the temperature and moisture distribution in the medium. Decreasing θ_v, increases the maximum moisture content and moves the freeze-front towards the origin, $r = 0$.

Figure 3 illustrates the effects of nondimensional latent heat, L, on the temperature and moisture distribution. Lowering L forces the freeze-front further away from the origin, $r = 0$. The minimum and maximum moisture contents do not seem to depend on L.

Figure 4 shows the effects of the nondimensional thermal gradient coefficient, Δ, on the temperature and moisture distribution. The maximum moisture content is strongly dependent upon Δ; increasing Δ increases the maximum moisture content. The temperature level and the freeze-front location, however, are very little affected by Δ.

Acknowledgment

This work was supported in part by the National Science Foundation through the Grant MEA-8110 705.

References

1 Aguirre-Puente, J., and Philippe, A., "Quelques recherches effectuées en France sur le probléme de la congélation des sols," *Rev. Gén. Thermique*, Vol. 96, 1969, pp. 1123-1141.

2 Aguirre-Puente, J., Dupas, A., and Philippe, A., "Quelques résultats concernant le gonflement au gel et leur application au classement des sols selon leur degré de gélivité," *Bull. liason Labo. P. et Ch.*, Vol. 68, 1973, pp. 23-29.

3 Mikhailov, M. D., "Exact Solution of Temperature and Moisture Distributions in a Porous Half-Space With Moving Evaporation Front," *International Journal of Heat and Mass Transfer*, Vol. 18, 1975, pp. 797-804.

4 Mikhailov, M. D., "Exact Solution for Freezing of Humid Porous Half-Space," *International Journal of Heat and Mass Transfer*, Vol. 19, 1976, pp. 651-655.

5 Patterson, S., "Propagation of a Boundary of Fusion," *Proceedings of the Glasgow Mathematics Association*, Vol. 1, 1952, pp. 42-47.

6 Özişik, M. N., and Uzzel, J. C., "Exact Solution for Freezing in Cylindrical Symmetry With Extended Freezing Temperature," JOURNAL OF HEAT TRANSFER, Vol. 101, 1979, pp. 331-334.

7 Luikov, A. V., "Systems of Differential Equations of Heat and Mass Transfer in Capillary-Porous Bodies (Review)," *International Journal of Heat and Mass Transfer*, Vol. 18, 1975, pp. 1-14.

8 Mikhailov, M. D., "General Solution of the Diffusion Equations Coupled at the Boundary," *International Journal of Heat and Mass Transfer*, Vol. 16, 1973, pp. 2155-2164.

9 Lebeolev, N. N., *Special Functions and Their Applications*, Prentice-Hall, Inc., Englewood Cliffs, N.J., 1965.

Natural Convection From Needles With Variable Wall Heat Flux

J. L. S. Chen[1]

Nomenclature

a = dimensionless needle size
b = needle shape parameter, $2(m-1)/5$
f = dimensionless stream function
g = gravitational acceleration
Gr = modified Grashof number, $g\beta q_o L^4/(k\nu^2)$
h = convection heat transfer coefficient

---

[1] Associate Professor, Department of Mechanical Engineering, University of Pittsburgh, Pittsburgh, Pa. 15261, Mem. ASME

Contributed by the Heat Transfer Division for publication in the JOURNAL OF HEAT TRANSFER. Manuscript received by the Heat Transfer Division July 23, 1982.

k = fluid thermal conductivity
L = needle length
m = exponent of power-law wall heat flux variation
Nu = local Nusselt number
Pr = Prandtl number, ν/α
q = heat flux
r = radial coordinate
T = temperature
u = axial velocity
v = radial velocity
z = similarity variable defined by equation (6)
α = fluid thermal diffusivity
β = coefficient of thermal expansion
θ = dimensionless temperature defined by equation (8)
ν = kinematic viscosity
Ψ = stream function

Subscripts

w = needle surface
o = reference quantity
∞ = ambient fluid

Superscript

$'$ = differentiation with respect to z

Introduction

Recently, Chen [1] investigated the free convection from a vertical needle with variable wall temperature and found that there was significant influence of its shape, size, and wall temperature variation upon the flow and heat transfer. It is noted that the results obtained therein may not, in general, be applied to the present problem of needles with variable surface heat flux, unlike the case where the results for a uniform heat flux flat plate (or cylinder) can be closely correlated with those for a uniform wall temperature plate (or cylinder) [2, 3]. Furthermore, in view of the fact that this type of variable heat flux surface condition is commonly encountered in engineering practice, it merits separate attention.

The objective of this paper is to analyze the laminar natural convection from slender needles with axial power-law wall heat flux variation. Similarity velocity and temperature profiles as well as transfer results are presented for three different needles (in shape) with two sizes in fluids having Pr ranging from 0.02 to 100. To the author's knowledge, there appears no results for the variable heat flux needles reported in the literature except for the special case of uniform heat flux.

Analysis

A vertical needle surrounded by a quiescent bulk fluid at a constant temperature, T_∞, is subject to the power-law surface heat flux, $q_w = q_0 \, (x/L)^m$, along the axis. Under the assumption of a thin needle, the effect of its transverse curvature is of importance, but the pressure gradient along the body may be neglected [1, 4]. The boundary-layer equations for the steady-state, incompressible, laminar axisymmetric flow are

$$\frac{\partial(ru)}{\partial x} + \frac{\partial(rv)}{\partial r} = 0 \qquad (1)$$

$$u\frac{\partial u}{\partial x} + v\frac{\partial u}{\partial r} = \frac{\nu}{r}\frac{\partial}{\partial r}\left(r\frac{\partial u}{\partial r}\right) + g\beta(T-T_\infty) \qquad (2)$$

$$u\frac{\partial T}{\partial x} + v\frac{\partial T}{\partial r} = \frac{\alpha}{r}\frac{\partial}{\partial r}\left(r\frac{\partial T}{\partial r}\right) \qquad (3)$$

with the boundary conditions

$$r = r(x): \quad u = v = 0; -k\frac{\partial T}{\partial r} = q_w(x)$$

$$r \rightarrow \infty: \quad u = 0; T = T_\infty \qquad (4)$$

The axisymmetric stream function is introduced as

$$\psi = \nu x f(z) \qquad (5)$$

with the similarity variable

$$z = \mathrm{Gr}^{2/5}\left(\frac{x}{L}\right)^b \left(\frac{r}{L}\right)^2 \qquad (6)$$

where $b = 2(m-1)/5$. By setting $z = a =$ constant in (6), a description is given of the size and shape of the needle body. For a thin needle, the value of a will in general be numerically small. At $z = a$, the shape prescribed by (6) is dependent on the exponent b. For example, surfaces are cylindrical wires for $b = 0$, paraboloids for $b = -1$, and cones for $b = -2$. Since the body shape parameter, b, is coupled with the wall flux index, m, the wall flux variation is thus restricted by a given needle in order to have similarity solution – a penalty one often has to pay in seeking for such solutions.

Continuity equation (1) is identically satisfied when the velocity components are expressed as

$$u = 2\frac{\nu}{L}\,\mathrm{Gr}^{2/5}\left(\frac{x}{L}\right)^{b+1} f'$$

$$v = -\frac{\nu}{L}\mathrm{Gr}^{1/5}\left(\frac{x}{L}\right)^{b/2} z^{-1/2}(f + bzf') \qquad (7)$$

Further, introducing the dimensionless temperature

$$\theta = \mathrm{Gr}^{1/5}\left(\frac{x}{L}\right)^{b/2} (T - T_\infty)/(q_w L/k) \qquad (8)$$

and substituting (6), (7), and (8) into (2) and (3), one has

$$8zf''' + 4(2+f)f'' - \frac{4}{5}(2m+3)(f')^2 + \theta = 0 \qquad (9)$$

$$z\theta'' + \left(1 + \frac{1}{2}\mathrm{Pr}f\right)\theta' - \frac{1}{10}(4m+1)\mathrm{Pr}f'\theta = 0 \qquad (10)$$

with the boundary conditions

$$f(a) = f'(a) = f'(\infty) = 0$$

$$\theta'(a) = -\frac{1}{2}a^{-1/2}, \theta(\infty) = 0 \qquad (11)$$

Note that, by setting $m = 0$ herein, (9) to (11) reduce to the case of uniform wall flux needle studied by Narain and Uberoi [5].

The local Nusselt number is found to be

$$\mathrm{Nu} = \frac{q_w x}{k(T_w - T_\infty)} = \mathrm{Gr}^{1/5}\left(\frac{x}{L}\right)^{(4+m)/5}\theta(a)^{-1} \qquad (12)$$

Results and Discussion

The transformed equation (9–11) were solved numerically using the technique for treating the asymptotic boundary condition developed by Nachtsheim and Swigert [6]. Table 1 gives the values of $f''(a)$ and $\theta(a)$ for three needle shapes associated with the wall flux distributions for $m = -1.0$, 0, and 1.0, and for two sizes, $a = 0.01$ and 0.1, of needle in fluids having $\mathrm{Pr} = 0.02$, 0.1, 0.733, 10, and 100. By setting $z = a$ in (6), it can be readily shown that the results for the three cases reported herein represent:

Table 1 Values of $f''(a)$ and $\theta(a)$

		$f''(a)$		$\theta(a)$	
Pr	m	$a=0.01$	$a=0.1$	$a=0.01$	$a=0.1$
0.02	−1.0	7.9394	2.9230	0.5017	1.3759
	0	5.4456	1.8590	0.4626	1.1596
	1.0	4.4437	1.4645	0.4473	1.0741
0.1	−1.0	7.0545	2.4619	0.4844	1.2659
	0	4.4115	1.4239	0.4121	0.9557
	1.0	3.5275	1.1259	0.3907	0.8798
0.733	−1.0	4.8317	1.5089	0.4293	0.9984
	0	2.8448	0.8772	0.3429	0.7290
	1.0	2.2558	0.6972	0.3215	0.6649
10	−1.0	2.0621	0.6341	0.3409	0.7126
	0	1.2252	0.3770	0.2688	0.5144
	1.0	0.9779	0.3013	0.2501	0.4647
100	−1.0	0.8626	0.2722	0.2815	0.5380
	0	0.5091	0.1604	0.2177	0.3798
	1.0	0.4074	0.1284	0.2009	0.3390

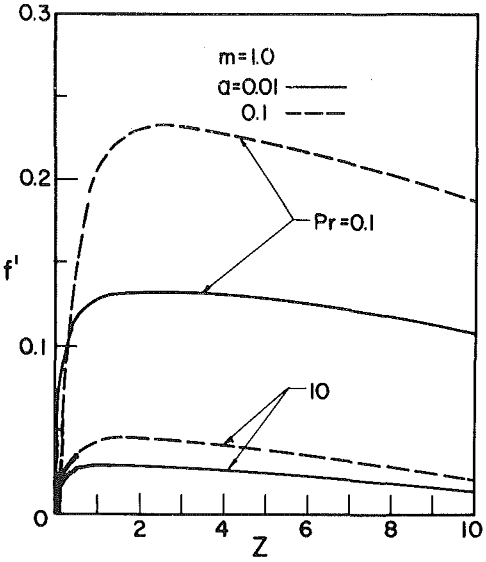

Fig. 1 Velocity profiles for m = 1.0

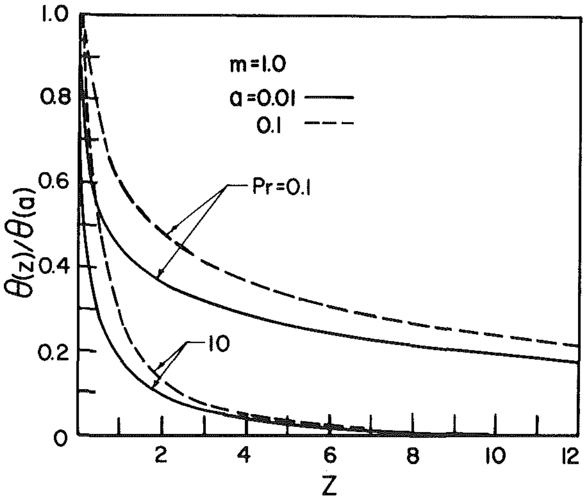

Fig. 2 Temperature profiles for m = 1.0

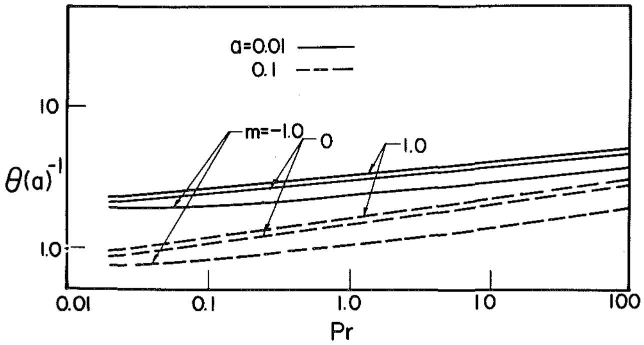

Fig. 3 Surface heat transfer results

(i) $m=1.0$: a cylindrical wire with linear wall flux distribution

(ii) $m=0$: a blunt-nosed needle with uniform wall flux

(iii) $m=-1.0$: a relatively sharped-nosed needle with wall flux varying as x^{-1}

It can be seen from the table that, in addition to the Pr, the needle size and shape coupled with wall flux variation all have quite significant effects on the surface friction and thermal characteristics. The influence of needle size and Pr on the dimensionless axial velocity and dimensionless temperature profiles are illustrated in the respective Figs. 1 and 2 for cylindrical wires with linear wall flux ($m=1.0$). At a given Pr, the decrease of wire size promotes heat transfer rate. To maintain the linear wall flux condition, however, the convective velocity decreases. On the other hand, for a given size, the increase of Pr results in reduced temperature difference between the wire surface and the ambient fluid, and hence the convective velocity. Also, the velocity and thermal boundary layers decrease with increasing Pr, as is expected.

The surface heat transfer parameter $1/\theta$ (a) are plotted versus Pr in Fig. 3 for two needle sizes, $a=0.01$ and 0.1. A reduction of needle size produces higher surface heat transfer rate. These curves also show the increase of surface heat transfer rate with increasing Pr. These trends are similar to those in free convection from vertical plates or cylinders, which we are familiar with. The combined effect of needle shape and wall flux distribution, reflected by various values of m, is such that for a given needle size the cylindrical wire with a linear wall flux ($m=1.0$) yields the highest surface heat transfer among the three cases considered.

The results in Fig. 3 show that the local Nusselt number is approximately proportional to the tenth root of the Pr for $a=0.01$ and the seventh root for $a=0.1$. Thus, the local Nusselt number may be correlated as

$$\mathrm{Nu}=A_1\mathrm{Gr}^{1/5}\left(\frac{x}{L}\right)^{(4+m)/5}\mathrm{Pr}^{1/10}\quad \text{for } a=0.01$$

$$\mathrm{Nu}=A_2\mathrm{Gr}^{1/5}\left(\frac{x}{L}\right)^{(4+m)/5}\mathrm{Pr}^{1/7}\quad \text{for } a=0.1 \tag{13}$$

with A_1 = 3.2, 3.04, 2.3, and A_2 = 1.6, 1.43, 1.0 for $m=1.0$, 0, −1.0, respectively. These correlations are found to differ at most by 5 percent from the analytical solutions given by (12) for all the cases considered, except for $m=-1.0$ and Pr $\leq$ 0.1, for which the under estimate amounts to 8 to 19 percent.

Similar to the case of a flat plate or a thick cylinder, the modified Grashof number appears as the fifth root. However, unlike the fourth-root-Pr law associated with those cases, the exponent of Pr varies with needle size. This clearly confirms the strong effect of the transverse curvature of the needle on heat transfer. In the study of free convection from vertical cylinders with uniform wall heat flux, Nagendra et al. [3] reported a similar trend. Their experimentally varified correlation shows that the exponent of Pr decreases from 0.4 for long cylinders to 0.048 for thin cylindrical wires, while for short cylinders the familiar value of 0.2 holds true.

Conclusions

1 Free convection from thin needles with power-law surface heat flux leads to similarity solutions when the needle shape parameter, b, and the wall-flux index, m, have the relation $b=2(m-1)/5$.

2 Needle size has strong effects on both flow and thermal characteristics. Thinner needles produce higher skin-friction and surface heat transfer rate.

3 Correlation of data for the local Nusselt number shows that the Prandtl number appears as the seventh root for $a=0.1$ and as the tenth root when the needle size is reduced with $a=0.01$. This trend is qualitatively in agreement with that reported in [3] for the case of long cylinders and wires having uniform surface heat flux.

References

1 Chen, J. L. S., "Natural Convection From Needles With Variable Wall Temperature," ASME Paper No. 80-HT-72, 1980.

2 Sparrow, E. M., and Gregg, J. L., "Laminar Free Convection From a Vertical Plate With Uniform Surface Heat Flux," ASME *Transactions*, Vol. 78, 1959, pp. 435–440.

3 Negendra, H. R., Tirunarayanan, M. A., and Ramachandran, A., "Laminar Free Convection From Vertical Cylinders With Uniform Heat Flux," ASME JOURNAL OF HEAT TRANSFER, Vol. 92, 1970, pp. 191–194.

4 Lee, L. L., "Boundary Layer Over a Thin Needle," *Physics of Fluids*, Vol. 10, No. 4, 1967, pp. 820–822.

5 Narain, J. P., and Uberoi, M. S., "Laminar Free Convection From Thin Vertical Needles," *Physics of Fluids*, Vol. 15, No. 5, May, 1972, pp. 928–929.

6 Nechtsheim, P. R., and Swigert, P., "Satisfaction Asymptotic Boundary Conditions in Numerical Solution of Nonlinear Equations of Boundary-Layer Type," NASA TN D-3004, Oct. 1965.

Nusselt Number Distribution in Vertical and Inclined Air Layers

S. M. ElSherbiny[1], K. G. T. Hollands[2], and G. D. Raithby[2]

Nomenclature

A = vertical aspect ratio, $A = H/L$
A_H = horizontal aspect ratio, $A_H = W/L$
g = gravitational acceleration
h = average heat transfer coefficient between isothermal plates
H = plate height
k = thermal conductivity of air
L = plate spacing
Nu = average Nusselt number, $\mathrm{Nu} = hL/k$
Nu_1 = average Nu on lower third of heated plate
Nu_2 = average Nu on middle third of heated plate
Nu_3 = average Nu on upper third of heated plate
Pr = Prandtl number of air, $\mathrm{Pr} = \nu/\kappa$
Ra = Rayleigh number, $\mathrm{Ra} = L^3\beta g\Delta T/\nu\kappa$
T_c = temperature of cold plate
T_h = temperature of hot plate
W = plate width
β = volumetric thermal expansion coefficient of air
ΔT = temperature difference, $\Delta T = T_h - T_c$
κ = thermal diffusivity of air
ν = kinematic viscosity of air
ϕ = angle of tilt from horizontal

Introduction

Several recent studies [1–8] have reported on the heat transfer by natural convection across air layers. The air layers in the present experimental study (Fig. 1) was bounded on the sides by two flat isothermal plates, and around the edges by a highly conductive sheet which took up a linear temperature profile between the plate temperatures. Measurements were obtained for horizontal aspect ratios in the range $A_H \gtrsim 15$, for vertical aspect ratios in the range $5 \leq A \leq 80$, and for tilt angles in the range 0 deg $\leq \phi \leq$ 90 deg. The average heat transfer measurements have been reported previously [6]. This Note presents a few of the "local" measurements obtained from the three separate areas of the hot plate shown in Fig. 1; a more complete set of measurements may be found in the thesis of ElSherbiny [8].

Previous local measurements [1, 3, 4] have covered the conduction regime and the laminar boundary layer regime. In the conduction regime, Eckert and Carlson [1] and Randall et al. [4] established that the local Nusselt number decreases with distance along the plate from a maximum at the "starting corner" (the lower corner of the hot plate or the top corner of the cold plate) to unity over the middle portion. It then decreases again, to a minimum at the "departure corners" (the top corner of the hot plate or the bottom of the cold plate). A small, but significant, departure of the average Nu from unity was observed at small A [4]. Tilting the layer from the vertical results in a flattening of the Nusselt number distribution [3]. In the laminar boundary layer regime, Randall et al. [4] found that the flow can be of two types: in the transition type, which is observed at low Ra and low A, the local Nu decreases steadily from one corner to the other; in the fully developed type, which is observed at higher Ra and higher A, the local Nu is uniform over the central part of each plate, and the average Nu equals the local value of the center. The last result explains the good agreement between

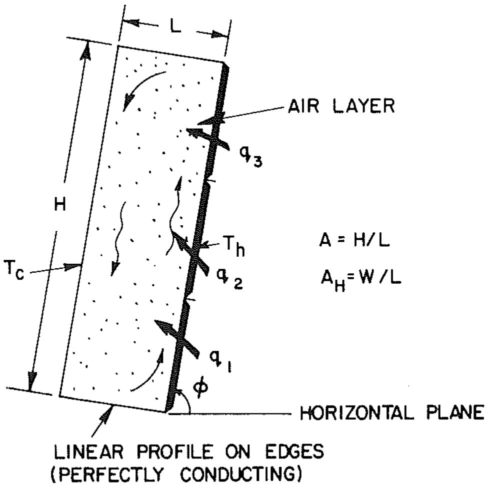

Fig. 1 A sketch of the layer

---

[1] Department of Mechanical Engineering, University of Waterloo, Waterloo, Ontario, Canada, N2L 3G1

[2] Department of Mechanical Engineering, University of Waterloo, Mem. ASME

Contributed by the Heat Transfer Division for publication in the JOURNAL OF HEAT TRANSFER. Manuscript received by the Heat Transfer Division April 16, 1982.

Conclusions

1 Free convection from thin needles with power-law surface heat flux leads to similarity solutions when the needle shape parameter, b, and the wall-flux index, m, have the relation $b=2(m-1)/5$.

2 Needle size has strong effects on both flow and thermal characteristics. Thinner needles produce higher skin-friction and surface heat transfer rate.

3 Correlation of data for the local Nusselt number shows that the Prandtl number appears as the seventh root for $a=0.1$ and as the tenth root when the needle size is reduced with $a=0.01$. This trend is qualitatively in agreement with that reported in [3] for the case of long cylinders and wires having uniform surface heat flux.

References

1 Chen, J. L. S., "Natural Convection From Needles With Variable Wall Temperature," ASME Paper No. 80-HT-72, 1980.

2 Sparrow, E. M., and Gregg, J. L., "Laminar Free Convection From a Vertical Plate With Uniform Surface Heat Flux," ASME *Transactions*, Vol. 78, 1959, pp. 435–440.

3 Negendra, H. R., Tirunarayanan, M. A., and Ramachandran, A., "Laminar Free Convection From Vertical Cylinders With Uniform Heat Flux," ASME Journal of Heat Transfer, Vol. 92, 1970, pp. 191–194.

4 Lee, L. L., "Boundary Layer Over a Thin Needle," *Physics of Fluids*, Vol. 10, No. 4, 1967, pp. 820–822.

5 Narain, J. P., and Uberoi, M. S., "Laminar Free Convection From Thin Vertical Needles," *Physics of Fluids*, Vol. 15, No. 5, May, 1972, pp. 928–929.

6 Nechtsheim, P. R., and Swigert, P., "Satisfaction Asymptotic Boundary Conditions in Numerical Solution of Nonlinear Equations of Boundary-Layer Type," NASA TN D-3004, Oct. 1965.

Nusselt Number Distribution in Vertical and Inclined Air Layers

S. M. ElSherbiny[1], K. G. T. Hollands[2], and G. D. Raithby[2]

Nomenclature

A = vertical aspect ratio, $A = H/L$
A_H = horizontal aspect ratio, $A_H = W/L$
g = gravitational acceleration
h = average heat transfer coefficient between isothermal plates
H = plate height
k = thermal conductivity of air
L = plate spacing
Nu = average Nusselt number, Nu = hL/k
Nu_1 = average Nu on lower third of heated plate
Nu_2 = average Nu on middle third of heated plate
Nu_3 = average Nu on upper third of heated plate
Pr = Prandtl number of air, Pr = ν/κ
Ra = Rayleigh number, Ra = $L^3\beta g\Delta T/\nu\kappa$
T_c = temperature of cold plate
T_h = temperature of hot plate
W = plate width
β = volumetric thermal expansion coefficient of air
ΔT = temperature difference, $\Delta T = T_h - T_c$
κ = thermal diffusivity of air
ν = kinematic viscosity of air
ϕ = angle of tilt from horizontal

Introduction

Several recent studies [1–8] have reported on the heat transfer by natural convection across air layers. The air layers in the present experimental study (Fig. 1) was bounded on the sides by two flat isothermal plates, and around the edges by a highly conductive sheet which took up a linear temperature profile between the plate temperatures. Measurements were obtained for horizontal aspect ratios in the range $A_H \gtrsim 15$, for vertical aspect ratios in the range $5 \leq A \leq 80$, and for tilt angles in the range 0 deg $\leq \phi \leq 90$ deg. The average heat transfer measurements have been reported previously [6]. This Note presents a few of the "local" measurements obtained from the three separate areas of the hot plate shown in Fig. 1; a more complete set of measurements may be found in the thesis of ElSherbiny [8].

Previous local measurements [1, 3, 4] have covered the conduction regime and the laminar boundary layer regime. In the conduction regime, Eckert and Carlson [1] and Randall et al. [4] established that the local Nusselt number decreases with distance along the plate from a maximum at the "starting corner" (the lower corner of the hot plate or the top corner of the cold plate) to unity over the middle portion. It then decreases again, to a minimum at the "departure corners" (the top corner of the hot plate or the bottom of the cold plate). A small, but significant, departure of the average Nu from unity was observed at small A [4]. Tilting the layer from the vertical results in a flattening of the Nusselt number distribution [3]. In the laminar boundary layer regime, Randall et al. [4] found that the flow can be of two types: in the transition type, which is observed at low Ra and low A, the local Nu decreases steadily from one corner to the other; in the fully developed type, which is observed at higher Ra and higher A, the local Nu is uniform over the central part of each plate, and the average Nu equals the local value of the center. The last result explains the good agreement between

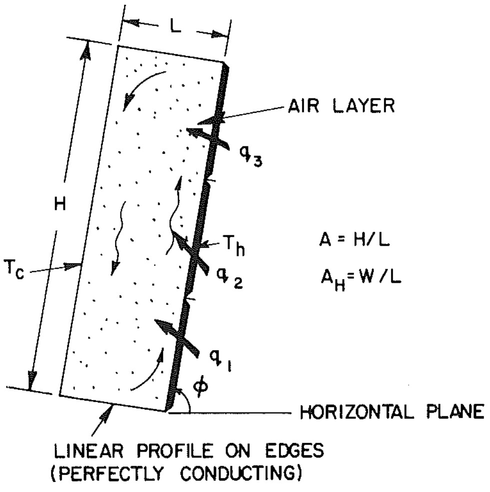

Fig. 1 A sketch of the layer

---

[1] Department of Mechanical Engineering, University of Waterloo, Waterloo, Ontario, Canada, N2L 3G1

[2] Department of Mechanical Engineering, University of Waterloo, Mem. ASME

Contributed by the Heat Transfer Division for publication in the Journal of Heat Transfer. Manuscript received by the Heat Transfer Division April 16, 1982.

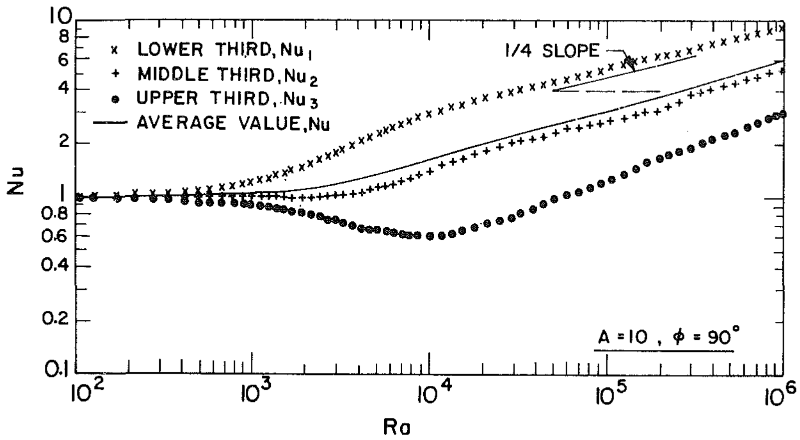

Fig. 2 Average values of Nu on heater plates: $A = 10$, $\phi = 90$ deg

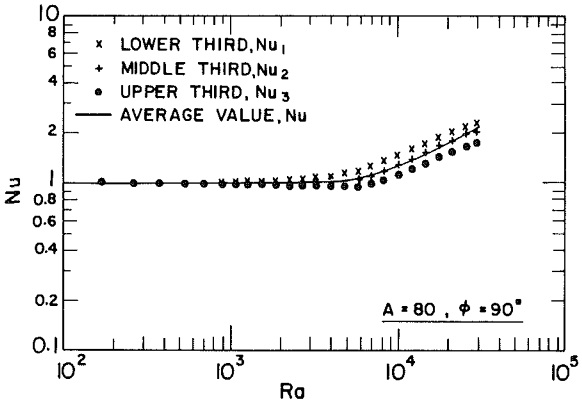

Fig. 3 Average values of Nu on heater plates: $A = 80$, $\phi = 90$ deg

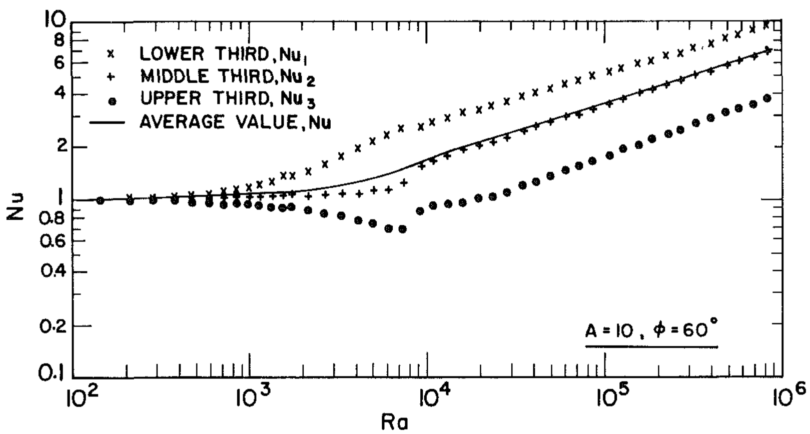

Fig. 4 Average values of Nu on heater plates: $A = 10$, $\phi = 60$ deg

the Nu measurements over the central region by Hollands et al. [2] and those averaged over the entire plate [6] for $A \geq 20$ and $\phi < 60$ deg. Previous measurements of the local heat transfer covered a smaller range of Ra, ϕ, and A than the present study; in particular the measurements of Randall et al. were restricted to $9 \leq A \leq 36$, 40 deg $\leq \phi \leq 90$ deg, and $4 \times 10^3 \leq \mathrm{Ra} \leq 3 \times 10^5$.

Experiment

The present "local" heat transfer measurements represent average values over 200×200 mm areas centered along a line midway between the vertical edges of the air layer, as shown in Fig. 1. The extent of the heated and cooled plates exposed to the air was $W = 635$ mm, and $H = 635$ mm. The aspect ratio was altered by changing the plate spacing, L. The method of measuring the heat fluxes q_1, q_2, and q_3, of varying the Rayleigh number, and all other details of the experiment are described elsewhere [2, 6, 8].

Results and Discussion

Figure 2 shows the average Nusselt number on the upper, middle, and lower third of the hot plate for a low aspect ratio ($A = 10$) in the vertical orientation ($\phi = 90$ deg). In the early conduction regime (very low Ra), all three values of the Nusselt number (Nu_1, Nu_2, Nu_3) were equal to unity. When

Ra was increased, the average Nusselt number, Nu, on the lower third of the hot plate rose above unity and approached a line of about 1/4 slope in the laminar regime at $Ra > 10^4$. The average Nusselt number on the middle third of the hot plate, Nu_2, also increased above unity when Ra was increased and approached the same 1/4 slope for $Ra > 10^4$, but fell below Nu_1. The value of Nu_3 dropped below unity with increasing Ra, reached a minimum of about 0.6 at $Ra = 10^4$, and thereafter increased along a line of 1/4 slope. The average Nusselt number, Nu, plotted in Fig. 2 as a solid line, is seen to be consistently higher than Nu_2 in the laminar boundary layer regime, by up to 12 percent. Thus, for $A = 10$ and $\phi = 90$ deg, measurements over the central region can underestimate the average Nusselt number by as much as 12 percent. This is consistent with the findings of Randall et al. [4].

To show the effect of aspect ratio on the measurements of Nu_1, Nu_2, Nu_3, the data from a higher aspect ratio ($A = 80$) are plotted in Fig. 3 for the same vertical orientation. Again $Nu_1 > Nu_2 > Nu_3$, but the differences among the three values are smaller than for the case of $A = 10$; the value of Nu_3 in this case decreased slightly below unity (to 0.96). In this instance the average Nusselt number over the whole air layer is well expressed by the measurements at the central part of the air layer, indicated in the figure by the solid line.

Figure 4 shows the effect of the angle of tilt on the distribution of Nusselt number along the hot plate where measurements were taken for $A = 10$ and $\phi = 60$ deg (heated from below). The same general behavior for Nu_1, Nu_2, and Nu_3, as in the case for $\phi = 90$ deg, was obtained for $\phi = 60$ deg, but Nu_2 was a better approximation of the average Nusselt number, Nu, than was observed for $\phi = 90$ deg. In the range $2000 < Ra < 10^4$, where the transition from conduction to laminar boundary layer regimes occurred, the value of Nu_2 is appreciably lower than Nu, as explained by Randall et al. [4]. For larger A or smaller ϕ, or both, the agreement between Nu_2 and Nu improves. The measurements support the assumption by Hollands et al. [2] that the heat transfer over the central region of the hot plate is representative of the average heat transfer from the entire plate for $A \geq 20$ and $\phi \leq 60$.

Acknowledgment

This study has been supported by operating grants from the Natural Science and Engineering Research Council and the Department of Mechanical Engineering, University of Waterloo. This support is gratefully acknowledged.

References

1 Eckert, E. R. G., and Carlson, W. O., "Natural Convection in an Air Layer Enclosed between Two Vertical Plates with Different Temperatures," *International Journal of Heat and Mass Transfer*, Vol. 2, 1961, pp. 106–120.

2 Hollands, K. G. T., Unny, T. E., Raithby, G. D., and Konicek, L., "Free Convection Heat Transfer Across Inclined Air Layers," ASME JOURNAL OF HEAT TRANSFER, Vol. 98, 1976, pp. 189–193.

3 Schinkel, W. M. M., and Hoogendoorn, C. J., "An Interferometric Study of the Local Heat Transfer by Natural Convection in Inclined Air-Filled Enclosures," *Proceedings of the Sixth International Heat Transfer Conference*, Toronto, 1978, pp. 287–292.

4 Randall, K. R., Mitchell, J. W., and El-Wakil, M. M., "Natural Convection Heat Transfer Characteristics of Flat Plate Enclosures," ASME JOURNAL OF HEAT TRANSFER, Vol. 101, 1979, pp. 120–125.

5 Catton, I., Ayyaswamy, P. S., and Clever, R. M., "Natural Convection Flow in a Finite, Rectangular Slot, Arbitrarily Oriented With Respect to the Gravity Vector," *International Journal of Heat and Mass Transfer*, Vol. 17, 1974, pp. 173–184.

6 ElSherbiny, S. M., Raithby, G. D., and Hollands, K. G. T., "Heat Transfer by Natural Convection Across Vertical and Inclined Air Layers," ASME JOURNAL OF HEAT TRANSFER, Vol. 104, 1982, pp. 96–102.

7 ElSherbiny, S. M., Hollands, K. G. T., and Raithby, G. D., "Effect of Thermal Boundary Conditions on Natural Convection in Vertical and Inclined Air Layers," ASME JOURNAL OF HEAT TRANSFER, Vol. 104, 1982, pp. 515–520.

8 ElSherbiny, S. M., "Heat Transfer by Natural Convection Across Vertical and Inclined Air Layers," Ph.D. thesis, University of Waterloo, Canada, 1980.

The Effect of a Surface Coating on the Constriction Resistance of a Spot on an Infinite Half-Plane[1]

J. R. Dryden[2]

Nomenclature

$A(\xi)$ = defined in equation (7)
a = contact spot radius
$B(\xi)$ = defined in equation (7)
$2b$ = distance between contact spots
$C(\xi)$ = defined in equation (8)
$f(r)$ = function of the radial coordinate, defined in equations (6) and (10)
$\bar{f}(\xi)$ = Hankel transform of $f(r)$
$J_0(\ )$, $J_1(\ )$ = Bessel functions of the first kind of order zero and one
k = thermal conductivity
k_1, k_2 = thermal conductivities of materials 1 and 2
Q = total axial heat flux; (flux/area) integrated over area
r = radial coordinate
R = constriction resistance of a spot on an infinite plane
t = thickness of coating material 1
$T_1(r,x)$, $T_2(r,x)$ = temperatures in materials 1 and 2
$\bar{T}_1(\xi,x)$, $\bar{T}_2(\xi,x)$ = Hankel transforms of temperatures T_1 and T_2
$\hat{T}$ = average temperature of the contact spot, defined in equation (15)
x = axial coordinate
α_j = $\alpha_j = 2j(t/a)$
θ = $\lambda_1/\lambda_2 = (k_1 - k_2)/(k_1 + k_2)$
λ_1 = $(1 - k_2/k_1)/2$
λ_2 = $(1 + k_2/k_1)/2$
ρ = dimensionless constriction resistance, $\rho = R(4ak_{21})$

Introduction

The effect of surface coatings on the thermal constriction resistance must be known to analyze the heat flux across, for example, an oxidized interface. Recently, several papers [1–3] have considered the constriction resistance for a cylinder of finite radius, b, with a coated end, where an axial heat flux is specified for a contact spot of radius, a. This cylinder represents an average solid-solid contact where a is the average contact spot radius and $2b$ is the average distance between contacting spots. The constriction resistance is obtained in the form of an infinite series which is slowly convergent when a/b is small. For example, if $a/b = 0.001$, about 5000 terms are required for convergence to three significant figures.

When the ratio a/b is very small, the thermal constriction of each spot is unaffected by neighbouring spots. It is then appropriate to consider the effect of a surface coating upon

---

[1] Issued as AECL-7467

[2] Atomic Energy of Canada Limited, Whiteshell Nuclear Research Establishment, Pinawa, Manitoba, Canada ROE 1L0

Contributed by the Heat Transfer Division for publication in the JOURNAL OF HEAT TRANSFER. Manuscript received by the Heat Transfer Division January 12, 1982.

Ra was increased, the average Nusselt number, Nu, on the lower third of the hot plate rose above unity and approached a line of about 1/4 slope in the laminar regime at $\mathrm{Ra} > 10^4$. The average Nusselt number on the middle third of the hot plate, Nu_2, also increased above unity when Ra was increased and approached the same 1/4 slope for $\mathrm{Ra} > 10^4$, but fell below Nu_1. The value of Nu_3 dropped below unity with increasing Ra, reached a minimum of about 0.6 at $\mathrm{Ra} = 10^4$, and thereafter increased along a line of 1/4 slope. The average Nusselt number, Nu, plotted in Fig. 2 as a solid line, is seen to be consistently higher than Nu_2 in the laminar boundary layer regime, by up to 12 percent. Thus, for $A = 10$ and $\phi = 90$ deg, measurements over the central region can underestimate the average Nusselt number by as much as 12 percent. This is consistent with the findings of Randall et al. [4].

To show the effect of aspect ratio on the measurements of Nu_1, Nu_2, Nu_3, the data from a higher aspect ratio ($A = 80$) are plotted in Fig. 3 for the same vertical orientation. Again $\mathrm{Nu}_1 > \mathrm{Nu}_2 > \mathrm{Nu}_3$, but the differences among the three values are smaller than for the case of $A = 10$; the value of Nu_3 in this case decreased slightly below unity (to 0.96). In this instance the average Nusselt number over the whole air layer is well expressed by the measurements at the central part of the air layer, indicated in the figure by the solid line.

Figure 4 shows the effect of the angle of tilt on the distribution of Nusselt number along the hot plate where measurements were taken for $A = 10$ and $\phi = 60$ deg (heated from below). The same general behavior for Nu_1, Nu_2, and Nu_3, as in the case for $\phi = 90$ deg, was obtained for $\phi = 60$ deg, but Nu_2 was a better approximation of the average Nusselt number, Nu, than was observed for $\phi = 90$ deg. In the range $2000 < \mathrm{Ra} < 10^4$, where the transition from conduction to laminar boundary layer regimes occurred, the value of Nu_2 is appreciably lower than Nu, as explained by Randall et al. [4]. For larger A or smaller ϕ, or both, the agreement between Nu_2 and Nu improves. The measurements support the assumption by Hollands et al. [2] that the heat transfer over the central region of the hot plate is representative of the average heat transfer from the entire plate for $A \geq 20$ and $\phi \leq 60$.

Acknowledgment

This study has been supported by operating grants from the Natural Science and Engineering Research Council and the Department of Mechanical Engineering, University of Waterloo. This support is gratefully acknowledged.

References

1 Eckert, E. R. G., and Carlson, W. O., "Natural Convection in an Air Layer Enclosed between Two Vertical Plates with Different Temperatures," *International Journal of Heat and Mass Transfer*, Vol. 2, 1961, pp. 106-120.

2 Hollands, K. G. T., Unny, T. E., Raithby, G. D., and Konicek, L., "Free Convection Heat Transfer Across Inclined Air Layers," ASME JOURNAL OF HEAT TRANSFER, Vol. 98, 1976, pp. 189-193.

3 Schinkel, W. M. M., and Hoogendoorn, C. J., "An Interferometric Study of the Local Heat Transfer by Natural Convection in Inclined Air-Filled Enclosures," *Proceedings of the Sixth International Heat Transfer Conference*, Toronto, 1978, pp. 287-292.

4 Randall, K. R., Mitchell, J. W., and El-Wakil, M. M., "Natural Convection Heat Transfer Characteristics of Flat Plate Enclosures," ASME JOURNAL OF HEAT TRANSFER, Vol. 101, 1979, pp. 120-125.

5 Catton, I., Ayyaswamy, P. S., and Clever, R. M., "Natural Convection Flow in a Finite, Rectangular Slot, Arbitrarily Oriented With Respect to the Gravity Vector," *International Journal of Heat and Mass Transfer*, Vol. 17, 1974, pp. 173-184.

6 ElSherbiny, S. M., Raithby, G. D., and Hollands, K. G. T., "Heat Transfer by Natural Convection Across Vertical and Inclined Air Layers," ASME JOURNAL OF HEAT TRANSFER, Vol. 104, 1982, pp. 96-102.

7 ElSherbiny, S. M., Hollands, K. G. T., and Raithby, G. D., "Effect of Thermal Boundary Conditions on Natural Convection in Vertical and Inclined Air Layers," ASME JOURNAL OF HEAT TRANSFER, Vol. 104, 1982, pp. 515-520.

8 ElSherbiny, S. M., "Heat Transfer by Natural Convection Across Vertical and Inclined Air Layers," Ph.D. thesis, University of Waterloo, Canada, 1980.

The Effect of a Surface Coating on the Constriction Resistance of a Spot on an Infinite Half-Plane[1]

J. R. Dryden[2]

Nomenclature

$A(\xi)$ = defined in equation (7)
a = contact spot radius
$B(\xi)$ = defined in equation (7)
$2b$ = distance between contact spots
$C(\xi)$ = defined in equation (8)
$f(r)$ = function of the radial coordinate, defined in equations (6) and (10)
$\bar{f}(\xi)$ = Hankel transform of $f(r)$
$J_0(\ )$, $J_1(\ )$ = Bessel functions of the first kind of order zero and one
k = thermal conductivity
k_1, k_2 = thermal conductivities of materials 1 and 2
Q = total axial heat flux; (flux/area) integrated over area
r = radial coordinate
R = constriction resistance of a spot on an infinite plane
t = thickness of coating material 1
$T_1(r,x)$, $T_2(r,x)$ = temperatures in materials 1 and 2
$\bar{T}_1(\xi,x)$, $\bar{T}_2(\xi,x)$ = Hankel transforms of temperatures T_1 and T_2
$\hat{T}$ = average temperature of the contact spot, defined in equation (15)
x = axial coordinate
α_j = $\alpha_j = 2j(t/a)$
θ = $\lambda_1/\lambda_2 = (k_1 - k_2)/(k_1 + k_2)$
λ_1 = $(1 - k_2/k_1)/2$
λ_2 = $(1 + k_2/k_1)/2$
ρ = dimensionless constriction resistance, $\rho = R(4ak_{21})$

Introduction

The effect of surface coatings on the thermal constriction resistance must be known to analyze the heat flux across, for example, an oxidized interface. Recently, several papers [1-3] have considered the constriction resistance for a cylinder of finite radius, b, with a coated end, where an axial heat flux is specified for a contact spot of radius, a. This cylinder represents an average solid-solid contact where a is the average contact spot radius and $2b$ is the average distance between contacting spots. The constriction resistance is obtained in the form of an infinite series which is slowly convergent when a/b is small. For example, if $a/b = 0.001$, about 5000 terms are required for convergence to three significant figures.

When the ratio a/b is very small, the thermal constriction of each spot is unaffected by neighbouring spots. It is then appropriate to consider the effect of a surface coating upon

---

[1] Issued as AECL-7467

[2] Atomic Energy of Canada Limited, Whiteshell Nuclear Research Establishment, Pinawa, Manitoba, Canada ROE 1L0

Contributed by the Heat Transfer Division for publication in the JOURNAL OF HEAT TRANSFER. Manuscript received by the Heat Transfer Division January 12, 1982.

the constriction resistance of a spot on an infinite half-plane. For a spot on an uncoated half-plane, the constriction resistance, is $1/4ak$, (see [4]). This note considers the change in R due to a coating with a thermal conductivity different from that of the base material.

Analysis

Figure 1 shows a spot of radius a on an infinite half-plane with a surface coating of material 1 having thickness, t. The temperatures T_1 and T_2 must satisfy the Laplace equation in regions 1 and 2, respectively

$$\nabla^2 T_1 = 0 \qquad r>0, 0<x<t \tag{1}$$

$$\nabla^2 T_2 = 0 \qquad r>0, x>t \tag{2}$$

and for axisymmetric heat flow the Laplacian is

$$\nabla^2 \frac{\partial^2}{\partial r^2} + \frac{1}{r}\frac{\partial}{\partial r} + \frac{\partial^2}{\partial x^2} \tag{3}$$

Both temperature and heat flux continuity are required at the interface between materials 1 and 2, viz.,

$$T_1 = T_2 \qquad r>0, x=t \tag{4}$$

$$k_1 \frac{\partial T_1}{\partial x} = k_2 \frac{\partial T_2}{\partial x} \qquad r>0, x=t \tag{5}$$

The boundary condition at the surface ($x = 0$) is

$$\frac{\partial T_1}{\partial x} = f(r) \qquad a>r>0, \quad x=0 \tag{6}$$

$$= 0 \qquad r>a$$

It is assumed that as $(r^2 + x^2)^{1/2} \rightarrow \infty$, T_1 and $T_2 \rightarrow 0$.

If a Hankel transform [5] of order zero is applied to both sides of equations (1) and (2), then the transformed variables will have the form

$$\bar{T}_1(\xi, x) = A(\xi)e^{\xi x} + B(\xi)e^{-\xi x} \tag{7}$$

$$\bar{T}_2(\xi, x) = C(\xi)e^{-\xi x} \tag{8}$$

The coefficient $C(\xi)$ can be found by using equations (4), (5), and (6) and is given by

$$C(\xi) = \frac{\bar{f}(\xi)}{(\lambda_1 \exp(-2\xi t) - \lambda_2)} \tag{9}$$

In particular, if

$$f(r) = \frac{-Q}{2k_1 \pi a (a^2 - r^2)^{1/2}} \tag{10}$$

then

$$C(\xi) = \frac{Q}{2k_1 \pi a} \frac{\sin(\xi a)}{\xi^2} \frac{1}{\lambda_2 - \lambda_1 \exp(-2\xi t)} \tag{11}$$

The coefficients $A(\xi)$ and $B(\xi)$ can be expressed in terms of $C(\xi)$, which leads to the following expression for $\bar{T}_1(\xi, x)$

$$\bar{T}_1(\xi, x) = (\lambda_1 e^{\xi(x-2t)} + \lambda_2 e^{-\xi x}) C(\xi) \tag{12}$$

and then

$$T_1(r, x) = \int_{\xi=0}^{\infty} \xi \bar{T}_1(\xi, x) J_0(\xi r) d\xi \tag{13}$$

The expression for $f(r)$ in equation (10) is the flux which causes an isothermal contact spot if there is no coating or if the coating is very thick.

Constriction Resistance

The constriction resistance, R, of a spot on a half-plane is given by

$$R = \frac{\Delta T}{Q} = \frac{\hat{T}}{Q} \tag{14}$$

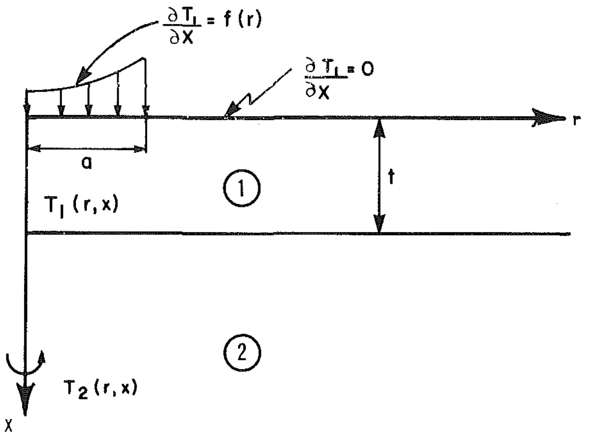

Fig. 1 Contact spot of radius, a, on an infinite half-plane with surface coating of thickness, t

where ΔT is the temperature change due to the thermal constriction, and Q is the total flux passing through the spot. Since both T_1 and T_2 approach zero at a sufficiently large distance from the contact spot, ΔT will be equal to the average temperature $\hat{T}$ of the contact spot.

$$\hat{T} = \frac{1}{\pi a^2} \int_{r=0}^{a} T_1(r, 0) 2\pi r \, dr \tag{15}$$

The resulting expression for R, found by using equations (11), (12), (13), (14), and (15), is

$$R = \frac{1}{\pi k_1 a} \int_{\xi}^{\infty} \left[\frac{\lambda_2 \exp(\xi t/a) + \lambda_1 \exp(-\xi t/a)}{\lambda_2 \exp(\xi t/a) - \lambda_1 \exp(-\xi t/a)} \cdot \frac{J_1(\xi) \sin \xi}{\xi^2} \right] d\xi \tag{16}$$

This expression relates R to t, a, k_1, and k_2. This integral can be evaluated numerically; however, an analytical expression is possible and leads to some simple limiting cases for either very thick or very thin coatings.

To evaluate the integral in equation (16) the denominator of the first term in square brackets is expanded by using the binomial theorem. The constriction resistance can then be re-expressed as

$$R = \frac{1}{4k_1 a} + \frac{2}{\pi k_1 a} \sum_{j=1}^{\infty} \theta^j I(\alpha_j) \tag{17}$$

where

$$I(\alpha_j) = \int_{\xi=0}^{\infty} \exp(-\alpha_j \xi) \left[\frac{\sin \xi \, J_1(\xi)}{\xi^2} \right] d\xi \tag{18}$$

The integral in equation (18) can be evaluated by differentiating $I(\alpha_j)$ with respect to α_j and then integrating (see [6]). The resulting expression for $I(\alpha_j)$ is

$$I(\alpha_j) = -\alpha_j + \left(D - \frac{1}{2D}\right)\sqrt{1 - \frac{1}{D^2}} + \frac{1}{2}\sin^{-1}\left(\frac{1}{D}\right) \tag{19}$$

where

$$D = \frac{\alpha_j}{2} + \left(\frac{\alpha_j 2}{4} + 1\right)^{1/2}$$

Thin Coatings. If t/a is small, then the expression for $I(\alpha_j)$ in equation (19) reduces to

$$I(\alpha_j) \simeq -\alpha_j + \pi/4 \tag{20}$$

Using this expression for $I(\alpha_j)$ in equation (17) (and after replacing the series with its closed form summation),

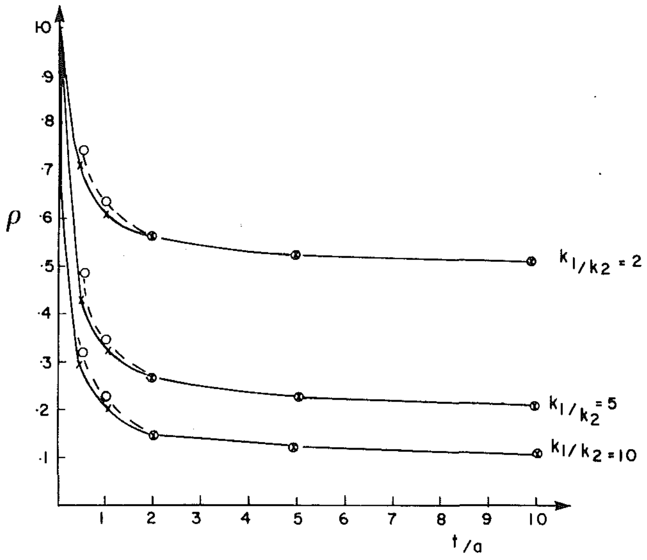

Fig. 2 Variation of the dimensionless constriction resistance with t/a for different values of $k_1/k_2 > 1$: x, derived from equation (17) using (19); o, asymptotic solution, equation (26)

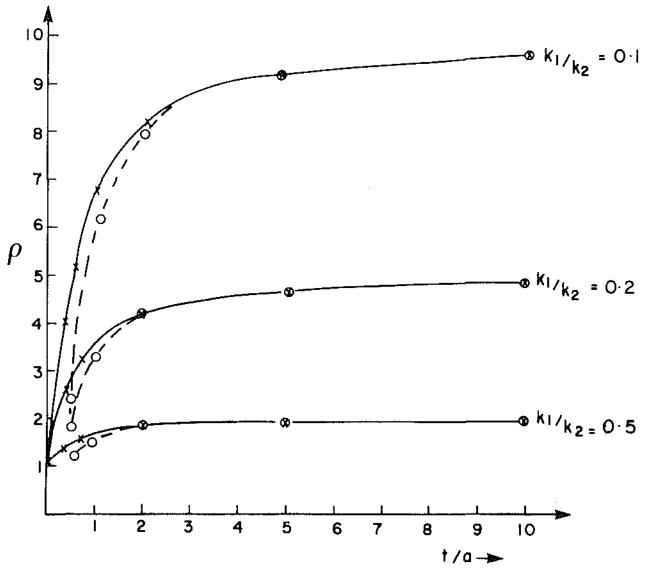

Fig. 3 Variation of the dimensionless constriction resistance with t/a for different values of $k_1/k_2 < 1$: x, derived from equation (17) using (19); o, asymptotic solution, equation (26)

$$R \simeq \frac{1}{4k_2 a} + \frac{1}{\pi k_1 a}\left(\frac{t}{a}\right)\left[1-\left(\frac{k_1}{k_2}\right)^2\right] \qquad (21)$$

Equation (21) gives the constriction resistance as a perturbation from the case where there is no coating. In equation (21), the first term on the right-hand side represents the constriction resistance for a spot of radius a on a half-plane with no surface coating. The second term represents the effect of the coating upon the constriction resistance. The ratio k_1/k_2 determines whether this term causes a positive or negative change in the constrictive resistance. Note that for a given spot size, a, the constriction resistance, R, depends linearly upon the coating thickness, t.

Thick Coatings. Equation (21) gives values of R as a perturbation from the case where there is no coating. For sufficiently large values of t/a, it is more sensible, from a physical viewpoint, to give R as a deviation from the case where $t/a = \infty$.

When t/a becomes large, the expression for $I(\alpha_j)$ in equation (19) can be simplified. For values of α_j greater than 2, $D \simeq (\alpha_j + 1/\alpha_j)$ and $I(\alpha_j)$ reduces to

$$I(\alpha_j) \simeq \frac{1}{2\alpha_j} \qquad (22)$$

where the higher order terms have been omitted. Using this expression for $I(\alpha_j)$ in equation (17) (and after replacing the series with its closed form summation)

$$R \simeq \frac{1}{4k_1 a} - \frac{1}{2\pi k_1 a}\left(\frac{a}{t}\right) ln\left(\frac{2}{1+k_1/k_2}\right) \qquad (23)$$

Equation (23) gives the constriction resistance which is valid for a thick coating. The first term on the right-hand side represents the constriction resistance for a spot of radius a on a half-plane of thermal conductivity k_1. The second term represents the effect of the substrate material with thermal conductivity k_2. There is a logarithmic dependence on the ratio k_1/k_2.

Results and Discussion

A dimensionless constriction resistance $\rho (= 4a\,k_2\,R)$ can be defined. In Figs. 2 and 3, the various curves represent ρ for different values of k_1/k_2 as the coating thickness t is increased. In Fig. 2, $k_1/k_2 > 1$ and in Fig. 3, $k_1/k_2 < 1$. In both figures, when t/a is small, from equation (21)

$$\rho = 1 + \left(\frac{4}{\pi}\right)\left(\frac{t}{a}\right)\left[\frac{k_2}{k_1} - \frac{k_1}{k_2}\right] \qquad (24)$$

and the slope at $t/a = 0$ is

$$\left[\frac{d\rho}{d(t/a)}\right]_{t/a=0} = \frac{4}{\pi}\left[\frac{k_2}{k_1} - \frac{k_1}{k_2}\right] \qquad (25)$$

Note that in Figs. 2 and 3, for say $k_1/k_2 = 10$ and $k_1/k_2 = 0.1$, the rate of change of ρ are numerically equal, but of opposite sign.

When $t/a > 2$, the constriction resistance exhibits thick film behaviour. From equation (23)

$$\rho = \frac{k_2}{k_1} - \frac{2}{\pi}\,\frac{k_2}{k_1}\left(\frac{a}{t}\right) ln\left(\frac{2}{1+k_1/k_2}\right) \qquad (26)$$

Values of ρ calculated from equation (26) are indicated in Figs. 2 and 3 for several values of $t/a > 2$.

Conclusions

The effect of a surface coating on the constriction resistance of a spot on an infinite half-plane has been analyzed. For very thin coatings, the change in constriction resistance depends linearly on coating thickness. As the coating thickness increases, the constriction resistance continues to change but at a decreasing rate. For coating thicknesses greater than twice the contact spot size, the constriction resistance depends hyperbolically on thickness.

References

1 Kharitonov, V. V., Kokorev, L. S., and Tyurin, Yu. A., "Effect of Thermal Conductivity of Surface Layer on Contact Thermal Resistance," *Sov. At. Energy*, Vol. 36, 1974, pp. 385–387.

2 Yip, F. C., "The Effect of Oxide Films on Thermal Contact Resistance," AIAA/ASME Thermophysics and Heat Transfer Conf., Boston, Mass., Paper No. 74-693, July 1974.

3 Yovanovich, M. M., Tien, C. H., and Schneider, G. E., "General Solution of Constriction Resistance within a Compound Disk," 17th Aerospace Sciences Meeting, New Orleans, Jan. 1979.

4 Carslaw, H. S., and Jaeger, J. C., *Conduction of Heat in Solids*, Oxford University Press, Toronto, 1959, p. 216.

5 Sneddon, I. N., *The Use of Integral Transforms*, McGraw-Hill, Toronto, 1972, pp. 325–326.

6 Gradshteyn, I. S., and Ryzhik, I. B., *Table of Integrals, Series and Products*, Academic Press, Toronto, 1980, p. 763.

The Optimum Dimensions of Convective Pin Fins

P. Razelos[1]

Nomenclature

b = pin base radius
B = Biot number, hb/k
C_1, C_2 = constants
D = $(dt/dx)_{x=u}$
h = heat transfer coefficient
k = thermal conductivity
L = length of the pin
q = heat dissipated by the pin
r = coordinate
S = lateral surface of the pin
T = temperature in excess of the ambient
t = dimensionless temperature
u = $(L/b)\sqrt{2B}$ aspect number
V = volume of the pin
x = $r(2h/kb)^{1/2}$ = dimensionless coordinate
y = z/b = dimensionless radius
z = pin radius
$*$ = indicates optimum values

1 Introduction

Pin fins or spines are extended surfaces usually with circular cross sections that vary in a specified manner along the length. Although their effectiveness for several profiles has been determined [1, 2], their optimum dimensions, i.e., "the dimensions of the base radius, b, and the length, L, that minimize its volume for a given heat dissipation" have not been fully analyzed. Only recently Sonn and Bar-Cohen [3] determined the optimum dimensions of a constant thickness pin that maximize the heat dissipation for a given pin volume. A general analysis of the optimum pin problem following the method introduced by the author in [4] is presented in this technical note. The results are expressed in a dimensionless form such that certain properties of the optimized fin can be immediately derived and a meaningful comparison with other optimum fins can be made.

2 Analysis and Results

Consider the pin depicted schematically in Fig. 1 with a profile, $z=f(r)$, and a base temperature, T_b, in excess of the ambient fluid temperature. Assuming one-dimensional conduction, thermal constant parameters and negligible surface curvature, the dimensionless temperature $t=T/T_b$ satisfies the following equation and boundary conditions [2]

$$d/dx(y^2dt/dx=yt \tag{1}$$

$t(u)=1, u=(L/b)\sqrt{2B}$
which is the aspect number, and (2)

$$(dt/dy)_{x=0}=0, y(0)\neq 0 \tag{3a}$$

$$t(0),\ \text{finite}\ y(0)=0 \tag{3b}$$

where $x=r(2h/kb)^{1/2}, y=z/b=f(r/L)=f(x/u)$ and $B=hb/k$, the Biot number. Clearly, the dimensionless temperature is only a function of x and u. The heat dissipated by the fin is equal to

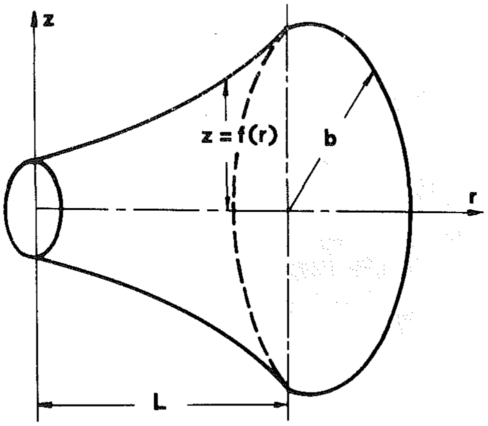

Fig. 1 Schematic pin diagram

$$q=k\pi b^2(dT/dr)_{r=L}=T_b k\pi b(2B)^{1/2}(dt/dx)_{x=u} \tag{4}$$

The derivative $(dt/dx)_{x=u}$, which for brevity is denoted here by D, is only a function of u. We now define a dimensionless heat dissipation, Q, as

$$Q\equiv(hq)/2^{1/2}\pi k^2 T_b=(B^{3/2})D \tag{5}$$

The optimization problem then is, for a given Q, to determine the values of b and L (or B and u) that minimize the volume, V, of a given profile pin

$$V=\int_0^L \pi z^2 dr=\pi L b^2\int_0^1 y^2 d\xi=C_1\pi L b^2 \tag{6}$$

where $\xi=r/L=x/u$ and $C_1=\int_0^1 y^2 d\xi$, a constant determined from the given pin profile. Using the aspect number, u, to eliminate L from (6), we can also define a dimensionless volume, U, as

$$U\equiv(2^{1/2})(h^3 V)/(C_1\pi k^3)=uB^{5/2} \tag{7}$$

Therefore, the values of u and B that for a given Q minimize U can be determined from the roots of the equation

$$\left(\frac{\partial Q}{\partial B}\right)\left(\frac{\partial U}{\partial u}\right)-\left(\frac{\partial Q}{\partial u}\right)\left(\frac{\partial U}{\partial B}\right)=0 \tag{8}$$

Since the values of u and B that maximize Q for a given U are also determined from equation (8), the two problems are equivalent. Moreover, one may readily show by taking the second derivatives that U (or Q) determined from equation (8) is minimum (maximum). Introducing further the expressions (5) and (7) into equation (8) and carrying out the algebra, we obtain the transcendental equation

$$3D-5u(\partial D/\partial u)=0 \tag{9}$$

from which the optimum value u^* is determined. Therefore, if for a given profile the function $D(u)$ is known, i.e., the temperature distribution is known, the optimum values of u^* and B^* can be determined from equations (9) and (5) or (7).

In order to acquire a better understanding of the influence of the material properties upon the optimum results, we can use expressions (5), (7) and the definition of u to rearrange our results in the form of dimensionless quantities that are expressed in terms of the number u^* and D^*. These quantities, given below, are defined according to whether the heat dissipation, the volume, or the length of the pin is given. The latter is useful in many practical problems where there are space limitations.

(*a*) When heat dissipation, q, given

---

[1] School of Engineering, University of Patras, Greece. Mem ASME

Contributed by the Heat Transfer Division for publication in the JOURNAL OF HEAT TRANSFER. Manuscript received by the Heat Transfer Division February, 8, 1982.

$$b^* \equiv b_{op}(hk)^{1/3}/(q/T_b)^{2/3}$$
$$= 1/(2^{1/2}\pi D^*)^{2/3} = 0.3700/(D^*)^{2/3} \qquad (10a)$$

$$L^* \equiv L_{op}h^{2/3}/(kq/T_b)^{1/3} = [1/(4\pi)^{1/3}]$$
$$u^*/(D^*)^{1/3} = 0{,}4301u^*/(D^*)^{1/3} \qquad (10b)$$

$$V^* \equiv V_{op}(h^4k)^{1/3}/(q/T_b)^{5/3} = [1/(4\pi)^{2/3}]$$
$$C_1u^*/(D^*)^{5/3} = 0.1850C_1u^*/(D^*)^{5/3} \qquad (10c)$$

(*b*) When the volume, V, is given

$$b_v^* \equiv b_{op}k^{1/5}/(hV^2)^{1/5} = (2/\pi^2)^{1/5}$$
$$/(C_1u^*)^{2/5} = 0.7267/(C_1u^*)^{2/5} \qquad (11a)$$

$$L_v^* \equiv L_{op}(h/kV^2)^{2/5} = (u^*)^{4/5}/(4\pi C_1)^{1/5}$$
$$= 0.6028(u^{*4}/C_1)^{1/5} \qquad (11b)$$

$$Q_v^* \equiv (q_{op}/T_b)/h^4kV^3)^{1/5} = (16\pi^2)^{1/5}D^*/$$
$$(C_1u^*)^{3/5} = 2.7522D^*/(C_1u^*)^{3/5} \qquad (11c)$$

(*c*) When length of the pin, L, is given

$$b_L^* \equiv b^*/L^{*2} = (kb_{op})/hL^2) = 2/(u^*)^2 \qquad (12a)$$

$$V_L^* \equiv V^*/L^{*5} = V_{op}k^2/h^2L^5 = 4\pi C_1/(u^*)^4 \qquad (12b)$$

$$Q_L^* \equiv (q_{op}k)/(h^2T_bL^3) = 4\pi D^*/(\mu^*)^3 \qquad (12c)$$

It is now clear from the above equations that even if their right-hand sides are not exactly known we can make certain conclusions (that are discussed later) about the thermal performance of the optimized pins. Moreover, in the design of the extended surfaces, the effectiveness and the removal number defined below are also important quantities. The effectiveness indicates how well the material of the pin is utilized while the removal number gives the degree of the usefulness of the pin.

$$E = q/hST_b \qquad (13)$$

$$N_r = q/\pi b^2hT_b \qquad (14)$$

where S the convective pin surface is equal to

$$S = 2\int_0^L \pi z dr = 2\pi bL\int_0^1 y(\xi)d\xi = C_2\pi bL \qquad (15)$$

Substituting the expression of q from (4) into equations (13) and (14), we obtain

$$E^* = D^*/C_2u^* \qquad (16)$$

$$N_rB^{1/2} = 2^{1/2}D^* \qquad (17)$$

Since in practice N_r should exceed a certain number that is determined from economic considerations, equation (17) imposes certain limitations on $B(b)$. However, b is not a given parameter of the problem; therefore, we rearrange (17) to include q, V, or L that are specified by the problem. Using expressions (5) and (7), we obtain the relationships

$$N_{rq}^* = N_r^3(hq)/(k^2T_b) = 4\pi(D^*)^4 \qquad (18a)$$

$$N_{rV}^* = N_r^5(h^3V)/k^3 = 4\pi C_1u^*(D^*)^5 \qquad (18b)$$

$$N_{rL}^* = N_r(hL)/k = u^*D^* \qquad (18c)$$

For the pin profiles $y = \xi^n$, $n = 0, 1/2, 1$, and 2, the expressions for the effectiveness are given in [1]; thus, with the aid of equation (16) (without the *) the derivative $D(u)$ is determined for each profile. Using these relationships for $D(u)$, that are shown in Table 1, we have used the transcendental equation (9) to obtain u^* and consequently all the other optimum quantities. These results are also summarized in Table 1. Note that some of our constants for the profile with $n = 0$ differ from those reported in [3] because a volume $V_p = (4/\pi)V$ was used instead of V.

Discussion and Conclusions

We now employ the foregoing analysis to examine the influence of thermal conductivity and the profile of the optimized pin upon its thermal performance. From the expressions (10) we can conclude that for a given heat dissipation, the base radius and the volume of the pin are proportional to the one-third the power of the thermal conductivity, while the length is proportional to that quantity. We can also observe that the optimum volume is proportional to the five-thirds the power of the dissipated heat. In contrast, the optimum longitudinal and radial fins [4, 5, 6] have base thicknesses and volumes inversely proportional to the thermal conductivity, length (which depends only on the profile), and the optimum volume (proportional to the third power of the dissipated heat). For example, comparing three typical materials – copper, aluminum, and iron – the ratio of the optimum volumes to that of the highest thermal conductivity (copper) in longitudinal fins [6] is 1:1.835:7.400 while in optimum pins this ratio becomes 1:1.224:1.945. Moreover, in longitudinal and radial fins, and eightfold increase in volume is required for doubling the heat dissipation, while in pins this can be achieved with approximately a threefold increase of the volume. One may readily arrive at other similar conclusions

Table 1 Optimum parameters of pin fins

Profile	Const. thickness	Parabolic	Triangular	Parabolic
n	0	1/2	1	2
C_1	1	1/2	1/3	1/5
C_2	1	2/3	1/2	1/3
D	tanh u	$\dfrac{I_1(4u/3)}{I_0(4u/3)}$	$\dfrac{I_2(2u)}{I_1(2u)}$	$\dfrac{2u/3}{1+1+(4u^2/9)^{1/2}}$
D^*	0.7256	0.6123	0.5526	0.5000
u^*	0.9193	1.1749	1.4320	2.0000
E^*	0.7893	0.7817	0.7718	0.7500
b^*	0.4582	0.5131	0.5494	0.5873
L^*	0.4400	0.5951	0.7505	1.0838
V^*	0.2903	0.2462	0.2373	0.2349
b_v^*	0.7516	0.8990	0.9768	1.0484
L_v^*	0.6448	0.7877	1.0008	1.4481
Q_v^*	2.1004	2.3188	2.3703	2.3846
b_L^*	2.3665	1.4489	0.7065	0.5000
V_L^*	17.5947	3.2974	0.9961	0.1571
Q_L^*	11.7364	4.7443	2.3648	0.7854
N_{rq}	3.4834	1.7663	1.1718	0.7854
N_{rv}^*	2.3236	1.2707	0.9273	0.7854
N_{rL}	0.6670	0.7194	0.7913	1.0000

by inspection of the definitions (11) and (12); note, for example, that in pins with restricted length (12), the high thermal conductivity material has a favorable effect upon the heat dissipation and volume where the above ratios may now become 1:3.367: :54.760. The interesting point here is that the influence of the material upon the optimum dimensions of the pin depends on the problem's specifications.

Let us now turn our attention to the effect that the various profiles have on the pin's thermal performance. In general, the choice of an extended surface profile depends on many factors, such as strength and fragility, cost of fabrication, etc. The results presented in Table 1 are helpful in making preliminary estimates. From the tabulated results, we can see that when the heat dissipation or the volume is specified and as the power of n increases, the pins become thicker at the base, and longer, with small volumes or for fixed volume dissipated more heat. Comparing the two extreme cases $n=0$ with $n=2$, we see that the constant thickness pin requires 24 percent more volume, or dissipates 88 percent of the heat, than the one with parabolic profile. Also, in both cases the triangular profile pin approximates very closely the one with the parabolic profile, and since the former is easier to fabricate, it appears to be the preferable one. In pins with restricted length, as n increases the base radius volume and heat dissipation decreases. However, the heat dissipation per unit volume, $Q_L{}^*/V_L^* = (q/T_b)/(hL/k)$, increases from 0.6670 to 5.00 when $n=0$ and 2, respectively. Therefore, in this case, the use of parabolic profile spines, despite their fragility, should be given serious consideration.

Finally, for the pins to be economically justified, N_r must be much larger than one; thus, the expressions (18) impose certain restrictions on the quantities that specify the problem q, V, or L. In addition, from the tabulated results, we observe that the product $2^{1/2} \cdot D^*$ is of the order of one; thus, by virtue of (10), we conclude that B is of the order of $1/N_r{}^2 < < 1$, while from the aspect number, $u = (L/b)\sqrt{2B}$, and (17), we see that L/b is of the order of $N_r > 1$. Therefore, the assumption of one-dimensional conduction upon which we have based our analysis seem to be well justified.

References

1 Gardner, K. A., "Efficiency of Extended Surface, "*Trans.* ASME, Vol. 67, Nov. 1945 pp. 621-631.

2 Kern, D. Q., and Kraus, A. D., *Extended Surface Heat Transfer*, McGraw-Hill, 1972, pp. 113-114.

3 Sonn, A., and Bar-Cohen, A., "Optimum Cylindrical Pin Fin," ASME JOURNAL OF HEAT TRANSFER, Vol. 103, 1980, pp. 814-815.

4 Razelos, P., "The Optimization of Longitudinal Convective Fins With Internal Heat Generation," *Nuclear Engineering and Design* Vol. 54, Oct. 1979, pp. 289-299.

5 Razelos, P., and Imre, K., "The Optimum Dimensions of Circular Fins with Variable Thermal Parameters," ASME JOURNAL OF HEAT TRANSFER, Vol. 102, 1980, pp. 420-425.

6 Jakob, M., *Heat Transfer*, Vol. 1, John Wiley and Sons, 1949, pp. 228-229.

Laser Generated Smoke for Fluid Flow Visualization

N. M. Farukhi[1]

1 Introduction

In many thermohydraulic experiments, visualization of the flow field is an essential part of the experimental procedure. In gaseous systems, flow visualization may be accomplished by either injecting smoke into the system or by generating smoke within the system. Of the many techniques reported in the literature [1, 2] the most common method for generating smoke is by vaporizing paraffin oil either inside small-diameter electrically heated tubes, or off the surface of small diameter electrically heated nichrome wires (smoke wire techniques). The former method is generally employed for system injection while the latter is for in situ generation. However, both techniques have drawbacks and would disqualify them for use in some experiments. In the first place, injecting smoke into a system could distort the flow field. Secondly, controlling the injection rate to avoid saturation of the flow field with smoke can be extremely difficult. Moreover, injecting into a pressurized system is a very complex task, and finally, placement of nichrome wires for in situ smoke generation and/or coating them with paraffin oil, after each test, may be totally impractical.

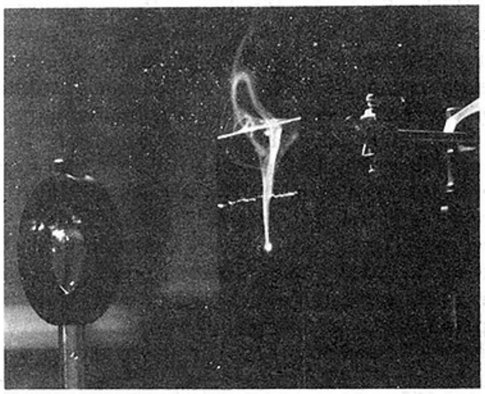

Fig. 1 Smoke generation off a flat vertical plate into an environment with crosswinds

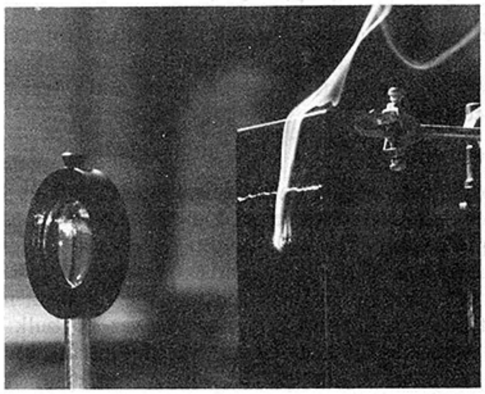

Fig. 2 Smoke generation off a flat vertical plate into a calm environment

Some of the aforementioned drawbacks were encountered by the author during a recent flow visualization experiment when smoke from a commercial paraffin oil smoke generator was injected into the test apparatus. Since flow visualization was an essential part of the experiment, a technique for generating smoke nonintrusively was developed. This technique, which involves the sublimation of a chemical using a laser beam, was verified by conducting a simple test and it will be described in context of this verification test.

2 Smoke Generation Technique

The smoke generation technique was developed for in situ nonintrusive applications and was verified with a simple experiment where the target was a stationary flat vertical plate. The test was conducted in the following manner.

The chemical compound that was sublimated was formed by mixing finely ground ammonium chloride with Sudan

---

[1] Senior Engineer, Westinghouse Research and Development Center, Pittsburgh, Pa. 15235. Mem ASME

Contributed by the Heat Transfer Division for publication in the JOURNAL OF HEAT TRANSFER. Manuscript received by the Heat Transfer Division July 9, 1982.

by inspection of the definitions (11) and (12); note, for example, that in pins with restricted length (12), the high thermal conductivity material has a favorable effect upon the heat dissipation and volume where the above ratios may now become 1:3.367: :54.760. The interesting point here is that the influence of the material upon the optimum dimensions of the pin depends on the problem's specifications.

Let us now turn our attention to the effect that the various profiles have on the pin's thermal performance. In general, the choice of an extended surface profile depends on many factors, such as strength and fragility, cost of fabrication, etc. The results presented in Table 1 are helpful in making preliminary estimates. From the tabulated results, we can see that when the heat dissipation or the volume is specified and as the power of n increases, the pins become thicker at the base, and longer, with small volumes or for fixed volume dissipated more heat. Comparing the two extreme cases $n=0$ with $n=2$, we see that the constant thickness pin requires 24 percent more volume, or dissipates 88 percent of the heat, than the one with parabolic profile. Also, in both cases the triangular profile pin approximates very closely the one with the parabolic profile, and since the former is easier to fabricate, it appears to be the preferable one. In pins with restricted length, as n increases the base radius volume and heat dissipation decreases. However, the heat dissipation per unit volume, $Q_L{}^*/V_L^* = (q/T_b)/(hL/k)$, increases from 0.6670 to 5.00 when $n=0$ and 2, respectively. Therefore, in this case, the use of parabolic profile spines, despite their fragility, should be given serious consideration.

Finally, for the pins to be economically justified, N_r must be much larger than one; thus, the expressions (18) impose certain restrictions on the quantities that specify the problem q, V, or L. In addition, from the tabulated results, we observe that the product $2^{1/2}\,.\,D^*$ is of the order of one; thus, by virtue of (10), we conclude that B is of the order of $1/N_r{}^2 < < 1$, while from the aspect number, $u = (L/b)\sqrt{2B}$, and (17), we see that L/b is of the order of $N_r > 1$. Therefore, the assumption of one-dimensional conduction upon which we have based our analysis seem to be well justified.

References

1 Gardner, K. A., "Efficiency of Extended Surface, "*Trans.* ASME, Vol. 67, Nov. 1945 pp. 621-631.

2 Kern, D. Q., and Kraus, A. D., *Extended Surface Heat Transfer*, McGraw-Hill, 1972, pp. 113-114.

3 Sonn, A., and Bar-Cohen, A., "Optimum Cylindrical Pin Fin," ASME JOURNAL OF HEAT TRANSFER, Vol. 103, 1980, pp. 814-815.

4 Razelos, P., "The Optimization of Longitudinal Convective Fins With Internal Heat Generation," *Nuclear Engineering and Design* Vol. 54, Oct. 1979, pp. 289-299.

5 Razelos, P., and Imre, K., "The Optimum Dimensions of Circular Fins with Variable Thermal Parameters," ASME JOURNAL OF HEAT TRANSFER, Vol. 102, 1980, pp. 420-425.

6 Jakob, M., *Heat Transfer*, Vol. 1, John Wiley and Sons, 1949, pp. 228-229.

Laser Generated Smoke for Fluid Flow Visualization

N. M. Farukhi[1]

1 Introduction

In many thermohydraulic experiments, visualization of the flow field is an essential part of the experimental procedure. In gaseous systems, flow visualization may be accomplished by either injecting smoke into the system or by generating smoke within the system. Of the many techniques reported in the literature [1, 2] the most common method for generating smoke is by vaporizing paraffin oil either inside small-diameter electrically heated tubes, or off the surface of small diameter electrically heated nichrome wires (smoke wire techniques). The former method is generally employed for system injection while the latter is for in situ generation. However, both techniques have drawbacks and would disqualify them for use in some experiments. In the first place, injecting smoke into a system could distort the flow field. Secondly, controlling the injection rate to avoid saturation of the flow field with smoke can be extremely difficult. Moreover, injecting into a pressurized system is a very complex task, and finally, placement of nichrome wires for in situ smoke generation and/or coating them with paraffin oil, after each test, may be totally impractical.

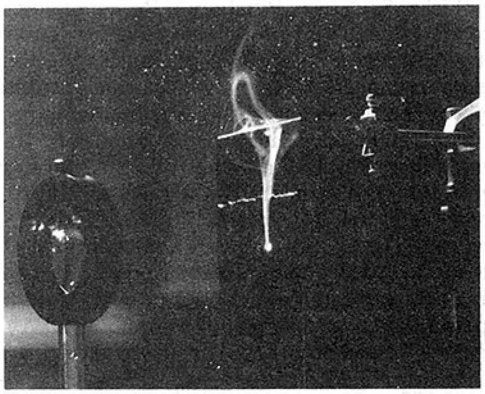

Fig. 1 Smoke generation off a flat vertical plate into an environment with crosswinds

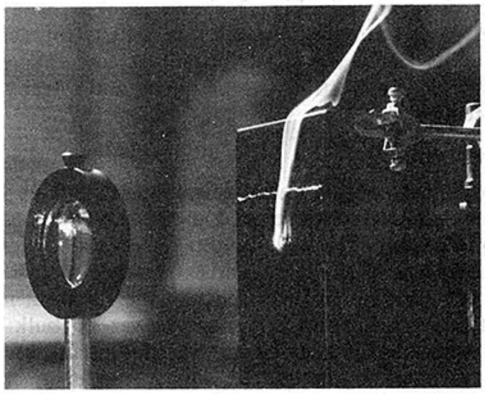

Fig. 2 Smoke generation off a flat vertical plate into a calm environment

Some of the aforementioned drawbacks were encountered by the author during a recent flow visualization experiment when smoke from a commercial paraffin oil smoke generator was injected into the test apparatus. Since flow visualization was an essential part of the experiment, a technique for generating smoke nonintrusively was developed. This technique, which involves the sublimation of a chemical using a laser beam, was verified by conducting a simple test and it will be described in context of this verification test.

2 Smoke Generation Technique

The smoke generation technique was developed for in situ nonintrusive applications and was verified with a simple experiment where the target was a stationary flat vertical plate. The test was conducted in the following manner.

The chemical compound that was sublimated was formed by mixing finely ground ammonium chloride with Sudan

---

[1] Senior Engineer, Westinghouse Research and Development Center, Pittsburgh, Pa. 15235. Mem ASME

Contributed by the Heat Transfer Division for publication in the JOURNAL OF HEAT TRANSFER. Manuscript received by the Heat Transfer Division July 9, 1982.

Black B (Fisher Scientific, Pittsburgh, Pa.), a biological stain, to make the mixture uniformly black in color. The stain was added to ammonium chloride to minimize reflection of the laser beam, or conversely, to maximize beam absorption. The mixture was then blended with Westinghouse epoxy varnish B-276 (Westinghouse Electric Corporation, Insulation Division, Manor, Pa.) to form a paste (with an air drying time of several hours). The mixture was then applied to the flat aluminum plate. A 5-W Spectra Physics Model 164 argon laser was used (because of its ready availability) to sublimate the mixture. In order to minimize laser power, a lens was used to focus the laser beam from 1.6 mm down to 1.0 mm. The actual power used to generate smoke was about 2 W.

Smoke was generated off the surface by directing the laser beam onto the surface at low power (where it barely lases), positioning the lens for proper focusing of the beam and then increasing the power till dense smoke was generated. Figure 1 is a photograph of smoke rising off the vertical plate into some crosswind while Fig. 2 shows smoke rising off the vertical plate into a relatively calm environment. The photographs and the description of the experimental procedure clearly illustrate the simplicity and effectiveness of the procedure.

3 Conclusion

A novel nonintrusive smoke generation technique for fluid flow visualization was developed and successfully tested. The technique is not only simple to apply, but is also inexpensive (assuming a laser is available) and extremely effective.

The technique's significance lies in the fact that it can be used effectively to study boundary layer or bulk flow in devices where space restrictions will not permit the use of smoke wire techniques and/or where smoke injection will disturb the flow field. A typical example where this technique would be useful is in the study of convection patterns off tightly packaged electronic components. (For a totally enclosed system a small hole to permit the laser beam to enter the system could be used).

Acknowledgments

The author thanks Drs. W. T. Lindsay and J. D. B. Smith for giving helpful information on sublimating chemicals and epoxies respectively.

References

1 *Flow Visualization*, edited by T. Asanuma, McGraw-Hill, New York, 1979.

2 Yu, J. P., Sparrow, E. M., and Eckert, E. R. G., "A Smoke Generator for Use in Fluid Flow Visualization," *International Journal of Heat and Mass Transfer*, Vol. 15, 1972, pp. 557–558.

Thermal Radiation, Convection, and Conduction in Porous Media Contained in Vertical Enclosures

T. W. Tong[1], R. C. Birkebak[2], and I. E. Enoch[3]

Nomenclature

a_n = coefficients, see equation (7)

A = aspect ratio, L/d

b = back-scattered fraction factor

C_p = specific heat of the fluid

d = width of the enclosure

e_b = blackbody emissive power

g = gravitational acceleration

k = thermal conductivity of the porous medium and the fluid at stagnant flow

L = height of the enclosure

M = number of intervals in the $\bar{x}$-direction

N = conduction-radiation parameter, $k\sigma_e(T_h - T_c)/(4\sigma T_h{}^4)$; number of intervals in the $\bar{y}$-direction

Nu = Nusselt number

q = radiant heat flux

Q = dimensionless radiant heat flux, $q/(4\sigma T_h{}^4)$

Ra_o = modified Rayleigh number, $\rho g\beta(T_h - T_c)\kappa d/(\bar{\mu}_c\alpha)$

T = temperature

$\bar{u}$ = horizontal velocity

u = dimensionless horizontal velocity, $\bar{u}d/\alpha$

$\bar{v}$ = vertical velocity

v = dimensionless vertical velocity, $\bar{v}d/\alpha$

$\bar{x}$ = horizontal coordinate

$\bar{y}$ = vertical coordinate

α = thermal diffusivity

β = thermal expansion coefficient

ϵ = surface emissivity

θ = dimensionless temperature, $(T - T_c)/(T_h - T_c)$

κ = permeability

$\bar{\mu}$ = viscosity

μ = dimensionless viscosity, see equation (7)

ρ = density of fluid

σ = Stefan-Boltzmann constant

$\sigma_a, \sigma_s, \sigma_e$ = absorption, scattering and extinction coefficients, respectively

τ_x, τ_y = optical depths in the $\bar{x}$- and $\bar{y}$-directions, respectively, $\sigma_e\bar{x}$ and $\sigma_e\bar{y}$

τ_{ox}, τ_{oy} = optical thicknesses in the $\bar{x}$- and $\bar{y}$-directions, respectively, $\sigma_e d$ and $\sigma_e L$

ϕ = dimensionless temperature, T/T_c

ψ = dimensionless stream function

ω = single scattering albedo, σ_s/σ_e

Subscript

c = cold wall

---

[1] Assistant Professor, Department of Mechanical Engineering, University of Kentucky, Lexington, Ky. 40506, Assoc. Mem. ASME

[2] Professor, Department of Mechanical Engineering, University of Kentucky, Mem. ASME

[3] Graduate Research Assistant, Department of Mechanical Engineering, University of Kentucky

Contributed by the Heat Transfer Division for publication in the JOURNAL OF HEAT TRANSFER. Manuscript received by the Heat Transfer Division March 30, 1982.

[4] In Whitaker's analysis [8], he has assumed the solid phase to be opaque. If one extends his derivation for a solid phase that is non-opaque, one would obtain equation (1).

Black B (Fisher Scientific, Pittsburgh, Pa.), a biological stain, to make the mixture uniformly black in color. The stain was added to ammonium chloride to minimize reflection of the laser beam, or conversely, to maximize beam absorption. The mixture was then blended with Westinghouse epoxy varnish B-276 (Westinghouse Electric Corporation, Insulation Division, Manor, Pa.) to form a paste (with an air drying time of several hours). The mixture was then applied to the flat aluminum plate. A 5-W Spectra Physics Model 164 argon laser was used (because of its ready availability) to sublimate the mixture. In order to minimize laser power, a lens was used to focus the laser beam from 1.6 mm down to 1.0 mm. The actual power used to generate smoke was about 2 W.

Smoke was generated off the surface by directing the laser beam onto the surface at low power (where it barely lases), positioning the lens for proper focusing of the beam and then increasing the power till dense smoke was generated. Figure 1 is a photograph of smoke rising off the vertical plate into some crosswind while Fig. 2 shows smoke rising off the vertical plate into a relatively calm environment. The photographs and the description of the experimental procedure clearly illustrate the simplicity and effectiveness of the procedure.

3 Conclusion

A novel nonintrusive smoke generation technique for fluid flow visualization was developed and successfully tested. The technique is not only simple to apply, but is also inexpensive (assuming a laser is available) and extremely effective.

The technique's significance lies in the fact that it can be used effectively to study boundary layer or bulk flow in devices where space restrictions will not permit the use of smoke wire techniques and/or where smoke injection will disturb the flow field. A typical example where this technique would be useful is in the study of convection patterns off tightly packaged electronic components. (For a totally enclosed system a small hole to permit the laser beam to enter the system could be used).

Acknowledgments

The author thanks Drs. W. T. Lindsay and J. D. B. Smith for giving helpful information on sublimating chemicals and epoxies respectively.

References

1 *Flow Visualization*, edited by T. Asanuma, McGraw-Hill, New York, 1979.

2 Yu, J. P., Sparrow, E. M., and Eckert, E. R. G., "A Smoke Generator for Use in Fluid Flow Visualization," *International Journal of Heat and Mass Transfer*, Vol. 15, 1972, pp. 557–558.

Thermal Radiation, Convection, and Conduction in Porous Media Contained in Vertical Enclosures

T. W. Tong[1], R. C. Birkebak[2], and I. E. Enoch[3]

Nomenclature

a_n = coefficients, see equation (7)
A = aspect ratio, L/d
b = back-scattered fraction factor
C_p = specific heat of the fluid
d = width of the enclosure
e_b = blackbody emissive power
g = gravitational acceleration
k = thermal conductivity of the porous medium and the fluid at stagnant flow
L = height of the enclosure
M = number of intervals in the $\bar{x}$-direction
N = conduction-radiation parameter, $k\sigma_e(T_h - T_c)/(4\sigma T_h{}^4)$; number of intervals in the $\bar{y}$-direction
Nu = Nusselt number
q = radiant heat flux
Q = dimensionless radiant heat flux, $q/(4\sigma T_h{}^4)$
Ra_o = modified Rayleigh number, $\rho g\beta(T_h - T_c)\kappa d/(\bar{\mu}_c\alpha)$
T = temperature
$\bar{u}$ = horizontal velocity
u = dimensionless horizontal velocity, $\bar{u}d/\alpha$
$\bar{v}$ = vertical velocity
v = dimensionless vertical velocity, $\bar{v}d/\alpha$
$\bar{x}$ = horizontal coordinate
$\bar{y}$ = vertical coordinate
α = thermal diffusivity
β = thermal expansion coefficient
ϵ = surface emissivity
θ = dimensionless temperature, $(T - T_c)/(T_h - T_c)$
κ = permeability
$\bar{\mu}$ = viscosity
μ = dimensionless viscosity, see equation (7)
ρ = density of fluid
σ = Stefan-Boltzmann constant
$\sigma_a, \sigma_s, \sigma_e$ = absorption, scattering and extinction coefficients, respectively
τ_x, τ_y = optical depths in the $\bar{x}$- and $\bar{y}$-directions, respectively, $\sigma_e\bar{x}$ and $\sigma_e\bar{y}$
τ_{ox}, τ_{oy} = optical thicknesses in the $\bar{x}$- and $\bar{y}$-directions, respectively, $\sigma_e d$ and $\sigma_e L$
ϕ = dimensionless temperature, T/T_c
ψ = dimensionless stream function
ω = single scattering albedo, σ_s/σ_e

Subscript

c = cold wall

---

[1] Assistant Professor, Department of Mechanical Engineering, University of Kentucky, Lexington, Ky. 40506, Assoc. Mem. ASME

[2] Professor, Department of Mechanical Engineering, University of Kentucky, Mem. ASME

[3] Graduate Research Assistant, Department of Mechanical Engineering, University of Kentucky

Contributed by the Heat Transfer Division for publication in the JOURNAL OF HEAT TRANSFER. Manuscript received by the Heat Transfer Division March 30, 1982.

[4] In Whitaker's analysis [8], he has assumed the solid phase to be opaque. If one extends his derivation for a solid phase that is non-opaque, one would obtain equation (1).

h = hot wall
m = mean

Superscript

r = net
$+$ = positive $\bar{x}$-direction
$-$ = negative $\bar{x}$-direction

Introduction

Earlier publications on heat transfer in vertical rectangular enclosures containing a porous medium have considered convection and conduction only and have neglected the effect of thermal radiation [1-5]. It has been found, however, that even under some of the most unexpected situations such as in fur [6] and building insulations [7], radiation heat transfer could account for a non-negligible amount of the total heat transfer. It is the objective of this work to study the role of thermal radiation in the overall heat transfer problem.

Mathematical Formulation

The geometry of the system under investigation is a two-dimensional vertical rectangular enclosure. The top and bottom surfaces are insulated, and the left and right walls are isothermal. The enclosure is considered to be tall enough so that one-dimensional radiation exchange can be assumed to take place between the two vertical surfaces. It is further assumed that the fluid is nonparticipative in the radiative transfer process whereas the solid matrix emits, absorbs, and scatters thermal radiation. If only convection and conduction are considered, the continuity, momentum (Darcy's law) and energy equations have been well established [1, 2]. When radiation is also included in the analysis, the forms of the continuity and Darcy's equations remain the same, and they will not be repeated here. A derivation similar to that presented by Whitaker [8] for a two-phase porous medium can show that the energy equation takes the form[4]

$$\rho C_p\left(\bar{u}\frac{\partial T}{\partial \bar{x}}+\bar{v}\frac{\partial T}{\partial \bar{y}}\right)=k\left(\frac{\partial^2 T}{\partial \bar{x}^2}+\frac{\partial^2 T}{\partial \bar{y}^2}\right)-\frac{dq^r}{d\bar{x}} \qquad (1)$$

where $\bar{u}$, $\bar{v}$, T, and q^r are all volumetric averaged quantities. The two-flux model will be employed to govern the radiative transport process. It is

$$\frac{dq^+}{d\bar{x}}=-2\sigma_a q^+ -2\sigma_s b q^+ +2\sigma_a e_b +2\sigma_s b q^- \qquad (2a)$$

$$-\frac{dq^-}{d\bar{x}}=-2\sigma_a q^- -2\sigma_s b q^- +2\sigma_a e_b +2\sigma_s b q^+ \qquad (2b)$$

Equation (2) is a simplified form of the equation of transfer that governs the intensity traversing a participating medium. The equation of transfer is derived from a macroscopic consideration of the interaction between the radiation field and a unit volume characterized by its volumetric averaged radiation properties [9]. Implicit in the equation of transfer, and hence the two-flux model, is that the dependent variables are volumetric-averaged quantities as well. Therefore the present formulation is consistent in the sense that both equations (1) and (2) are in terms of volumetric-averaged variables. Typical values of σ_a, σ_s, and b for fiberglass insulations can be found in the literature [7]. The coupling between equations (1) and (2) is provided by

$$q^r=q^+-q^- \qquad (3)$$

We invoke the Boussinesq approximation and rewrite the continuity [1, 2], Darcy's law [1, 2] and equations (1) and (2) in the following dimensionless form in terms of the stream function

$$\frac{\partial^2\psi}{\partial\tau_x^2}+\frac{\partial^2\psi}{\partial\tau_y^2}=\left\{-\frac{\mathrm{Ra}_o}{\tau_{ox}}\frac{\partial\theta}{\partial\tau_x}+\left[\frac{\partial\psi}{\partial\tau_y}\frac{\partial\theta}{\partial\tau_y}+\frac{\partial\psi}{\partial\tau_x}\frac{\partial\theta}{\partial\tau_x}\right]x\,\frac{\sum_{n=1}^{\infty}na_n\theta^{n-1}}{\left(1+\sum_{n=1}^{\infty}a_n\theta^n\right)^2}\right\}\left(1+\sum_{n=1}^{\infty}a_n\theta^n\right) \qquad (4)$$

$$\frac{\partial\psi}{\partial\tau_y}\frac{\partial\theta}{\partial\tau_x}-\frac{\partial\psi}{\partial\tau_x}\frac{\partial\theta}{\partial\tau_y}=\frac{\partial^2\theta}{\partial\tau_x^2}+\frac{\partial^2\theta}{\partial\tau_y^2}-\frac{1}{N}\frac{dQ^r}{d\tau_x} \qquad (5)$$

$$\frac{dQ^+}{d\tau_x}=-2(1-\omega+\omega b)Q^+ +\frac{(1-\omega)}{2}\phi^4+2\omega bQ^- \qquad (6a)$$

$$-\frac{dQ^-}{d\tau_x}=-2(1-\omega+\omega b)Q^- +\frac{(1-\omega)}{2}\phi^4+2\omega bQ^+ \qquad (6b)$$

In arriving at equation (4), a temperature-dependent viscosity of the following form has been assumed

$$\mu=\frac{\bar{\mu}}{\bar{\mu}_c}=\left(1+\sum_{n=1}^{\infty}a_n\theta^n\right)^{-1} \qquad (7)$$

Thus, the analysis will also allow us to examine the relative effects of thermal radiation and a variable viscosity. The boundary conditions for the present problem are

$$\tau_x=0:\ \theta=1,\ \psi=0,\ Q^+=\epsilon_h/4+(1-\epsilon_h)Q^- \qquad (8)$$

$$\tau_x=\tau_{ox}:\ \theta=0,\ \psi=0,\ Q^-=\epsilon_c\phi_c{}^4/4+(1-\epsilon_c)Q^+ \qquad (9)$$

$$\tau_y=0:\ \frac{\partial\theta}{\partial y}=0,\ \psi=0 \qquad (10)$$

$$\tau_y=\tau_{oy}=A\tau_{ox}:\ \frac{\partial\theta}{\partial y}=0,\ \psi=0 \qquad (11)$$

The vertical walls have been assumed to be diffusely emitting and reflecting in writing the radiation boundary conditions as appeared in equations (8) and (9).

Method of Solution

The detailed procedure of the solution method has been presented in the ASME Paper No. 82-HT-50 under the same title of the present work. Basically, analytical expressions for Q^+ and Q^- were obtained by solving equations (6a) and (6b) with the method of variation of parameters. The expressions were in terms of an arbitrary temperature distribution, ϕ. Hence, once ϕ (or equivalently θ) was specified, Q^+ and Q^- could be computed. The net radiant heat flux, Q^r, in turn could be determined from a relation obtained by re-expressing equation (3) in dimensionless form. With Q^r available, equations (4) and (5) could be solved numerically.

The enclosure was divided to a $M \times N$ grid, and equations (4) and (5) were discretized using a central-difference scheme. At the boundaries, one-sided three-point difference was employed so that the order of numerical error was kept compatible with the central-difference equations. The procedure involved assuming initial values for θ and ψ, determining Q^r, and computing new θ and ψ. The procedure was repeated until convergence (variation less than 0.01 percent) for both θ and ψ has been achieved at all grid points. Notice that θ in equations (4) and (5) and ϕ in equation (6) are related by

$$\phi=\theta(1-\phi_c)+\phi_c \qquad (12)$$

Since θ is a two-dimensional function of τ_x and τ_y, ϕ should also depend on both τ_x and τ_y. But to be consistent with the

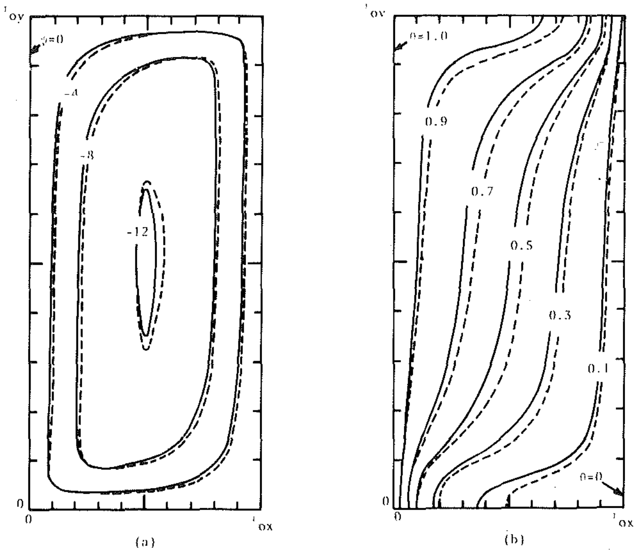

Fig. 1 The flow field and temperature distribution for constant viscosity: (a) streamlines; (b) isotherms, (——— convection and conduction for $Ra_o = 100$, $A = 10$, $\tau_{ox} = 5$; ···· radiation, convection, and conduction for $Ra_o = 100$, $A = 10$, $\tau_{ox} = 5$, $N = 0.5$, $b = \omega = 0.5$, $\epsilon_h = \epsilon_c = 1$ and $\phi_c = 0.5$)

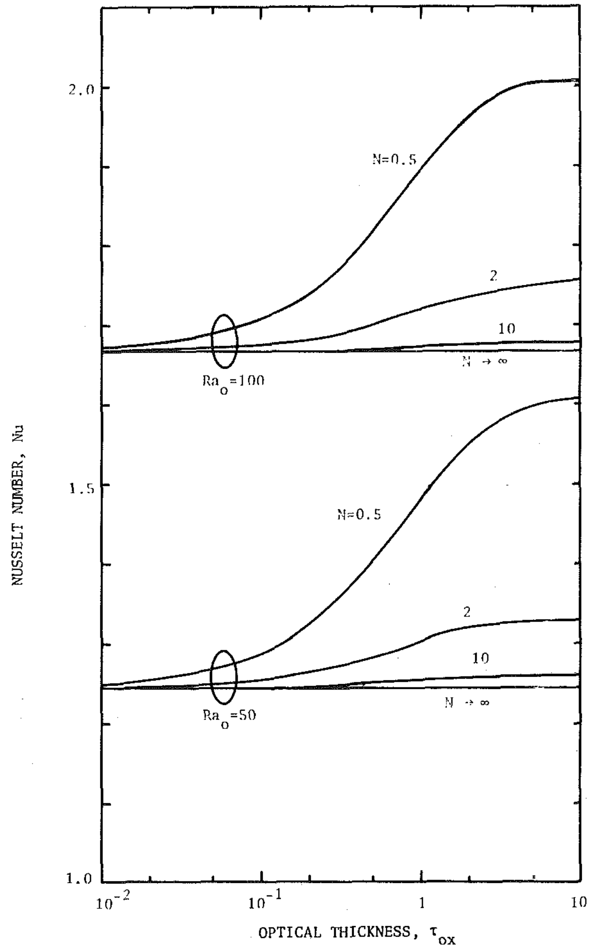

Fig. 2 Nusselt number for simultaneous radiation, convection, and conduction heat transfer with a constant viscosity ($A = 10$, $b = \omega = 0.5$, $\epsilon_h = \epsilon_c = 1$ and $\phi_c = 0.5$)

one-dimensional radiation model, it was necessary to treat ϕ as a function of τ_x only. This was achieved in the numerical computation by taking the arithmetic mean of all the θ's in the y-direction at any given x-position, and calculating ϕ based on the mean θ.

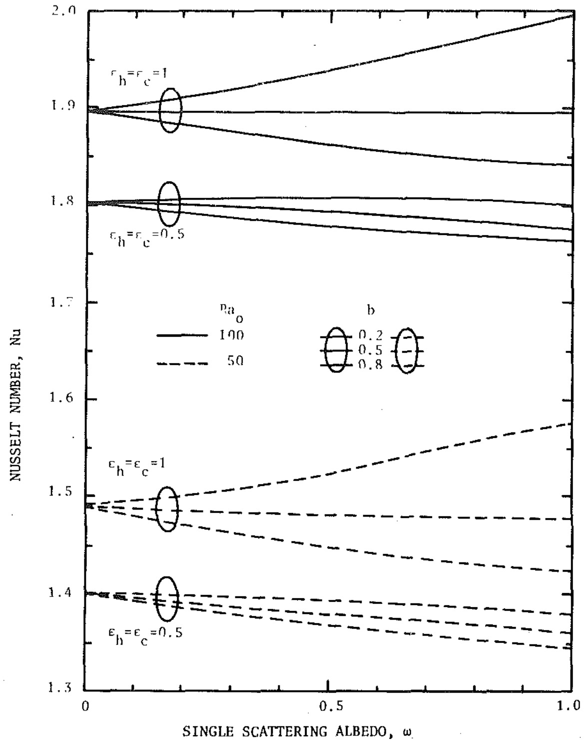

Fig. 3 Influence of ϵ_h, ϵ_c, b and ω on Nu with a constant viscosity ($A = 10$, $N = 0.5$, $\tau_{ox} = 1$ and $\phi_c = 0.5$)

Results and Discussion

Shown in Fig. 1 are some results to illustrate the change in the flow field and temperature distribution due to the influence of thermal radiation. It is seen in Fig. 1(*a*) that the streamlines cease to be centro-symmetrical and change in such a way that the mass flux is decreased along the left wall and increased along the right wall. Thus one might expect that the convective heat flux at the left and right walls would be decreased and increased, respectively. This is indeed affirmed by the fact that the temperature gradient in the horizontal direction has become smaller near the left wall and larger near the right wall as revealed in Fig. 1(*b*).

Figure 2 depicts Nu as a function of τ_{ox} for two different Ra_o and various N. The definition of Nu is

$$\mathrm{Nu} = \left[-\frac{1}{A} \int_o^{\tau_{oy}} \frac{\partial \theta}{\partial \tau_x} d\tau_y + \frac{\tau_{ox}}{N} Q^r \right]_{\tau_x = 0} \quad (13)$$

As $N \to \infty$, Nu is independent of τ_{ox}. This is intuitively expected since τ_{ox} is a radiation parameter and in the limit $N \to \infty$ thermal radiation plays an insignificant role in the total heat transfer. As N decreases, the influence of radiation becomes more important. In the optically thin limit ($\tau_{ox} << 1$), however, the radiation contribution again becomes small. Because a higher Ra_o would cause stronger fluid motion, Nu is higher for $Ra_o = 100$ than for $Ra_o = 50$. It is clear that thermal radiation can be safely neglected only when $N \to \infty$ and/or $\tau_{ox} << 1$.

The results in Fig. 3 demonstrate the effect of changing ϵ_h, ϵ_c, b and ω. A surface with unity emissivity is a perfect emitter and has the highest radiant heat flux among other surfaces with smaller emissivities. This is reflected in Nu where the values for $\epsilon_h = \epsilon_c = 1$ are larger than those for $\epsilon_h = \epsilon_c = 0.5$. The value of Nu is smaller for larger b owing to the fact

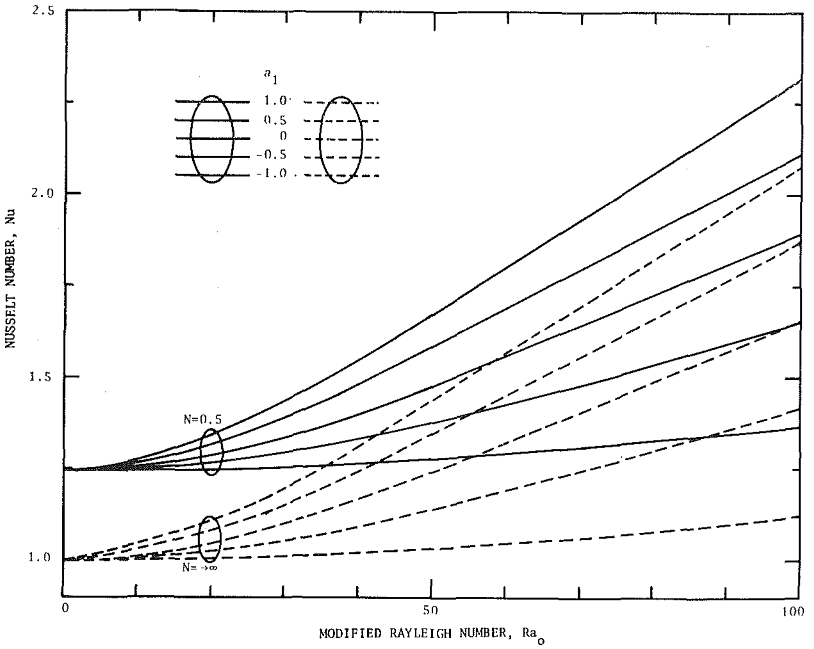

Fig. 4 Simultaneous radiation, convection, and conduction heat transfer with a variable viscosity ($A = 10$, $\tau_{ox} = 1$, $b = \omega = 0.5$, $\epsilon_h = \epsilon_c = 1$, $\phi = 0.5$ and $a_n = 0$ for $n \geq 2$)

that a larger fraction of the scattered radiant energy is directed in the backward direction. The single scattering albedo, ω, has values of zero and one for pure absorbing and pure scattering media, respectively. In general, increasing ω reduces Nu because the radiant heat flux is reduced. But for some cases (e.g., $\epsilon_h = \epsilon_c = 1$ and $b = 0.2$) Nu increases with ω instead. This phenomenon has also been observed by Yuen and Wong [10] in their study of conduction and radiation heat transfer in participating media, and they have provided a detailed explanation which will not be repeated here.

Figure 4 illustrates the general dependence on a temperature dependent viscosity with $a_n = 0$ for $n \geq 2$. A viscosity with a positive a_1 decreases as the temperature increases. With Ra_o defined in terms of the viscosity at the cold wall, such a viscosity allows the fluid to flow more easily as compared to the case of $a_1 = 0$ (constant viscosity). Thus, positive a_1's yield higher Nu. Similar argument would lead to lower Nu for negative a_1's. It is obvious that as $a_1 \rightarrow -\infty$, Nu is independent of Ra_o because the resistance force is too large to allow the fluid to flow. Note that the dash lines for $a_1 > 0$ and the solid line for $a_1 = 0$ cross over at certain Ra_o. The dash and solid lines correspond to $N \rightarrow \infty$ and $N = 0.5$, respectively. As the results for $N \rightarrow \infty$ correspond to those for no radiation, the results in the figure indicate that at Ra_o lower than the cross over point (COP) the error incurred by neglecting thermal radiation is larger than that caused by neglecting the variable viscosity effect and the reverse is true beyond the COP. For example, assume the parameters for a system are as shown in the caption of Fig. 4 and in addition $Ra_o = 40$, $N = 0.5$ and $a_1 = 1$. The correct Nu is 1.55 and the COP is at $Ra_o = 58$. If the variable viscosity effect is neglected, Nu becomes 1.40, and if the variable viscosity effect is considered but the contribution of radiation is neglected, Nu is 1.32. This suggests that below the COP, if one is concerned with the variable viscosity effect, one should also take into consideration the role of thermal radiation. Similarly, a statement with the opposite account can be made when Ra_o is beyond the COP. As $Ra_o \rightarrow 0$, the fluid becomes stagnant and Nu is independent of a_1. Also in this limit, when conduction dominates over thermal radiation ($N \rightarrow \infty$) Nu $\rightarrow$ 1 which is the correct value for pure conduction heat transfer. The trend of larger Nu with increasing Ra_o is consistent with our earlier discussion.

Conclusions

The problem of simultaneous radiation, convection, and conduction heat transfer in vertical enclosure filled with a porous medium has been studied numerically. The analysis considered the effects of emission, and absorption, as well as scattering of thermal radiation by the porous structure. It was found that both thermal radiation and a temperature-dependent viscosity could have appreciable effects on the overall heat transfer process. Their relative importance depends on the values of the independent parameters. When the fluid viscosity decreases with increasing temperature, neglecting thermal radiation causes a larger error than neglecting the variable viscosity effect if Ra_o is below a certain value; this relationship is reversed when Ra_o is above that certain value. The flow pattern ceases to be centro-symmetrical under the influence of thermal radiation, and its contribution to the total heat transfer can be safely neglected only in the limits of $\tau_{ox} << 1$ and/or $N \rightarrow \infty$.

Acknowledgments

This work was supported in part by the National Science Foundation under Grant DME-8105951. Partial support was also provided for the third author (IEE) by the Indonesian Cultural Foundation, Inc., New York.

References

1 Bankvall, C. G., "Natural Convective Heat Transfer in Insulated Structures," Report 38, 1973, Lund Institute of Technology.

2 Burns, P. J., Chow, L. C. and Tien, C. L., "Convection in a Vertical Slot Filled with Porous Insulation," *International Journal of Heat and Mass Transfer*, Vol. 20, 1977, pp. 919-926.

3 Weber, J. E., "The Boundary-Layer Regime for Convection in a Vertical Porous Layer," *International Journal of Heat and Mass Transfer*, Vol. 18, 1975, pp. 569-573.

4 Bejan, A., "A Synthesis of Analytical Results for Natural Convection Heat Transfer across Rectangular Enclosures," *International Journal of Heat and Mass Transfer*, Vol. 23, 1980, pp. 723-726.

5 Blythe, P. A., and Simpkins, P. G., "Convection in a Porous Layer for a

Temperature Dependent Viscosity," *International Journal of Heat and Mass Transfer*, Vol. 24, 1981, pp. 497–506.

6 Özil, E. and Birkebak, R. C., "Effects of Environmental Radiation on the Insulative Properties of a Fibrous Material," *Proceedings of the Sevenths Symposium on Thermophysical Properties*, ASME, New York, 1977, pp. 319–327.

7 Tong, T. W., Yang, Q. S., and Tien, C. L., "Radiative Heat Transfer in Fibrous Insulations. Part II: Experimental Study," to appear in ASME JOURNAL OF HEAT TRANSFER.

8 Whitaker, S., "Radiant Energy Transport in Porous Media," *Industrial and Engineering Chemistry Fundamentals*, Vol. 19, 1980, pp. 210–218.

9 Viskanta, R., "Radiation Transfer and Interaction of Convection with Radiation Heat Transfer," *Advances in Heat Transfer*, Vol. 3, 1966, pp. 175–251.

10 Yuen, W. W., and Wong, L. W., "Heat Transfer by Conduction and Radiation in a One-Dimensional Absorbing, Emitting and Anisotropically-Scattering Medium," ASME JOURNAL OF HEAT TRANSFER, Vol. 102, 1980, pp. 303–307.

Expressions for the Specific Heat Flux to a Cylinder in a Thermal Plasma Crossflow

Xi Chen[1]

Nomenclature

C_p = specific heat at constant pressure
d_o = diameter of cylinder
F = dimensionless stream function
h = specific enthalpy
Pr = Prandtl number
q = local specific heat flux
$\bar{q}$ = average specific heat flux
Re = Reynolds number
S = dimensionless specific enthalpy, $S=(h/h_\infty)-1$
u,v = x- and y-direction components of velocity
x,y = coordinates along surface and normal to it
ϵ,η = dimensionless coordinates defined in equation (8)
κ = thermal conductivity
Λ = "wedge variable" defined in equation (14)
μ = viscosity
ρ = density
γ = angle measured from frontal stagnation point
Ψ = stream function

Subscripts

w = wall
∞ = free flow

Introduction

Although a number of experimental investigations on heat transfer of a cylinder immersed in a thermal plasma crossflow have been reported, few analytical studies can be found in the literature. Analytical expressions of the specific heat flux on the cylinder surface or average over its circumference are of interest in many applications (for example, the use of a cylindrical probe in plasma diagnostics). In a previous paper [1], such analytical expressions were obtained based on a combined analytical/numerical study for an argon plasma. In this note, these results will be extended to include Ar-H_2 (mole ratio of mixture 1:4) plasma and N_2 plasma, and a more realistic boundary condition at the cylinder surface will be employed in the present analysis.

Problem Description

The assumptions employed are: the flow across the cylinder is a steady, two-dimensional and dense plasma with uniform temperature and velocity; the Mach number is small, but the Reynolds number is high so that the boundary layer approximation can be employed; buoyancy force and radiation loss are negligible.

Thus, the governing equations can be written in orthogonal curvilinear (x,y) coordinates as follows

$$\frac{\partial(\rho u)}{\partial x}+\frac{\partial(\rho v)}{\partial y}=0 \qquad (1)$$

$$\rho\left(u\frac{\partial u}{\partial x}+v\frac{\partial u}{\partial y}\right)=\rho_\infty u_1\frac{du_1}{dx}+\frac{\partial}{\partial y}\left(\mu\frac{\partial u}{\partial y}\right) \qquad (2)$$

$$\rho\left(u\frac{\partial h}{\partial x}+v\frac{\partial h}{\partial y}\right)=\frac{\partial}{\partial y}\left(\frac{\kappa}{C_p}\frac{\partial h}{\partial y}\right) \qquad (3)$$

with boundary conditions

$$y=0,\ u=v=0,\ h=h_w \qquad (4)$$

$$y\rightarrow\infty,\ u=u_1,\ h=h_\infty \qquad (5)$$

The velocity component in the x-direction at the outer edge of the boundary layer, u_1, is given by the potential flow relation

$$u_1=2\cdot u_\infty\sin(2x/d_o) \qquad (6)$$

Equations (1–3) with boundary conditions (4) and (5) and relation (6) are used for the computation by a general-purpose program for boundary layer flows.

Analytical Treatment

The following additional assumptions are used in the analysis

$$\rho h=\rho_\infty h_\infty=\text{const.} \qquad (7a)$$

$$\rho\mu=\rho_\infty\mu_\infty=\text{const.} \qquad (7b)$$

$$\rho(\kappa/C_p)=\rho_\infty(\kappa_\infty/C_{p_\infty})=\text{const.}$$
$$\text{or } \mathrm{Pr}=(\mu C_p/\kappa)=\mathrm{Pr}_\infty \qquad (7c)$$

By transforming into the following dimensionless (ξ,η) coordinate system [1, 2]

$$\xi=\int_0^x\left(\frac{u_1}{u_\infty}\right)\frac{dx}{d_o}\quad \eta=\left(\frac{\mathrm{Re}_\infty}{2\xi}\right)^{1/2}\left(\frac{u_1}{u_\infty}\right)\int_0^y\left(\frac{\rho}{\rho_\infty}\right)\frac{dy}{d_o} \qquad (8)$$

and introducing the stream function

$$\Psi(x,y)=u_\infty d_o(2\xi/\mathrm{Re}_\infty)^{1/2}F(\xi,\eta) \qquad (9)$$

the governing equations (1–3) become

$$F'''+FF''+\Lambda[1+S-(F')^2]=2\xi\frac{\partial(F',F)}{\partial(\xi,\eta)} \qquad (10)$$

$$S''+\mathrm{Pr}_\infty FS'=2\xi\mathrm{Pr}_\infty\cdot\frac{\partial(S,F)}{\partial(\xi,\eta)} \qquad (11)$$

with boundary conditions

$$\eta=0,\ F=F'=0,\ S=S_w=(h_w/h_\infty)-1 \qquad (12)$$

$$\eta\rightarrow\infty,\ F'=1,\ S=0 \qquad (13)$$

where the primes denote differentiation with respect to η while $\partial(F',F)/\partial(\xi,\eta)$ and $\partial(S,F)/\partial(\xi,\eta)$ are the Jacobians. Λ is the "wedge variable" defined by

---

[1] Honorary Fellow, Department of Mechanical Engineering, University of Minnesota, Minneapolis, Minn. 55455. Permanent address: Thermophysics Division, Department of Engineering Mechanics, Tsinghua University, Beijing 100084, People's Republic of China.

Contributed by the Heat Transfer Division for publication in the JOURNAL OF HEAT TRANSFER. Manuscript received by the Heat Transfer Division July 5, 1982.

Temperature Dependent Viscosity," *International Journal of Heat and Mass Transfer*, Vol. 24, 1981, pp. 497-506.

6 Özil, E. and Birkebak, R. C., "Effects of Environmental Radiation on the Insulative Properties of a Fibrous Material," *Proceedings of the Sevenths Symposium on Thermophysical Properties*, ASME, New York, 1977, pp. 319-327.

7 Tong, T. W., Yang, Q. S., and Tien, C. L., "Radiative Heat Transfer in Fibrous Insulations. Part II: Experimental Study," to appear in ASME JOURNAL OF HEAT TRANSFER.

8 Whitaker, S., "Radiant Energy Transport in Porous Media," *Industrial and Engineering Chemistry Fundamentals*, Vol. 19, 1980, pp. 210-218.

9 Viskanta, R., "Radiation Transfer and Interaction of Convection with Radiation Heat Transfer," *Advances in Heat Transfer*, Vol. 3, 1966, pp. 175-251.

10 Yuen, W. W., and Wong, L. W., "Heat Transfer by Conduction and Radiation in a One-Dimensional Absorbing, Emitting and Anisotropically-Scattering Medium," ASME JOURNAL OF HEAT TRANSFER, Vol. 102, 1980, pp. 303-307.

Expressions for the Specific Heat Flux to a Cylinder in a Thermal Plasma Crossflow

Xi Chen[1]

Nomenclature

C_p = specific heat at constant pressure
d_o = diameter of cylinder
F = dimensionless stream function
h = specific enthalpy
Pr = Prandtl number
q = local specific heat flux
$\bar{q}$ = average specific heat flux
Re = Reynolds number
S = dimensionless specific enthalpy, $S=(h/h_\infty)-1$
u,v = x- and y-direction components of velocity
x,y = coordinates along surface and normal to it
ϵ,η = dimensionless coordinates defined in equation (8)
κ = thermal conductivity
Λ = "wedge variable" defined in equation (14)
μ = viscosity
ρ = density
γ = angle measured from frontal stagnation point
Ψ = stream function

Subscripts

w = wall
∞ = free flow

Introduction

Although a number of experimental investigations on heat transfer of a cylinder immersed in a thermal plasma crossflow have been reported, few analytical studies can be found in the literature. Analytical expressions of the specific heat flux on the cylinder surface or average over its circumference are of interest in many applications (for example, the use of a cylindrical probe in plasma diagnostics). In a previous paper [1], such analytical expressions were obtained based on a combined analytical/numerical study for an argon plasma. In this note, these results will be extended to include Ar-H_2 (mole ratio of mixture 1:4) plasma and N_2 plasma, and a more realistic boundary condition at the cylinder surface will be employed in the present analysis.

Problem Description

The assumptions employed are: the flow across the cylinder is a steady, two-dimensional and dense plasma with uniform temperature and velocity; the Mach number is small, but the Reynolds number is high so that the boundary layer approximation can be employed; buoyancy force and radiation loss are negligible.

Thus, the governing equations can be written in orthogonal curvilinear (x,y) coordinates as follows

$$\frac{\partial(\rho u)}{\partial x}+\frac{\partial(\rho v)}{\partial y}=0 \tag{1}$$

$$\rho\left(u\frac{\partial u}{\partial x}+v\frac{\partial u}{\partial y}\right)=\rho_\infty u_1\frac{du_1}{dx}+\frac{\partial}{\partial y}\left(\mu\frac{\partial u}{\partial y}\right) \tag{2}$$

$$\rho\left(u\frac{\partial h}{\partial x}+v\frac{\partial h}{\partial y}\right)=\frac{\partial}{\partial y}\left(\frac{\kappa}{C_p}\frac{\partial h}{\partial y}\right) \tag{3}$$

with boundary conditions

$$y=0,\ u=v=0,\ h=h_w \tag{4}$$

$$y\rightarrow\infty,\ u=u_1,\ h=h_\infty \tag{5}$$

The velocity component in the x-direction at the outer edge of the boundary layer, u_1, is given by the potential flow relation

$$u_1=2\cdot u_\infty\sin(2x/d_o) \tag{6}$$

Equations (1-3) with boundary conditions (4) and (5) and relation (6) are used for the computation by a general-purpose program for boundary layer flows.

Analytical Treatment

The following additional assumptions are used in the analysis

$$\rho h=\rho_\infty h_\infty=\text{const.} \tag{7a}$$

$$\rho\mu=\rho_\infty\mu_\infty=\text{const.} \tag{7b}$$

$$\rho(\kappa/C_p)=\rho_\infty(\kappa_\infty/C_{p_\infty})=\text{const.}$$
$$\text{or }\Pr=(\mu C_p/\kappa)=\Pr_\infty \tag{7c}$$

By transforming into the following dimensionless (ξ,η) coordinate system [1, 2]

$$\xi=\int_0^x\left(\frac{u_1}{u_\infty}\right)\frac{dx}{d_o}\quad \eta=\left(\frac{\mathrm{Re}_\infty}{2\xi}\right)^{1/2}\left(\frac{u_1}{u_\infty}\right)\int_0^y\left(\frac{\rho}{\rho_\infty}\right)\frac{dy}{d_o} \tag{8}$$

and introducing the stream function

$$\Psi(x,y)=u_\infty d_o(2\xi/\mathrm{Re}_\infty)^{1/2}F(\xi,\eta) \tag{9}$$

the governing equations (1-3) become

$$F'''+FF''+\Lambda[1+S-(F')^2]=2\xi\frac{\partial(F',F)}{\partial(\xi,\eta)} \tag{10}$$

$$S''+\Pr_\infty FS'=2\xi\Pr_\infty\cdot\frac{\partial(S,F)}{\partial(\xi,\eta)} \tag{11}$$

with boundary conditions

$$\eta=0,\ F=F'=0,\ S=S_w=(h_w/h_\infty)-1 \tag{12}$$

$$\eta\rightarrow\infty,\ F'=1,\ S=0 \tag{13}$$

where the primes denote differentiation with respect to η while $\partial(F',F)/\partial(\xi,\eta)$ and $\partial(S,F)/\partial(\xi,\eta)$ are the Jacobians. Λ is the "wedge variable" defined by

---

[1] Honorary Fellow, Department of Mechanical Engineering, University of Minnesota, Minneapolis, Minn. 55455. Permanent address: Thermophysics Division, Department of Engineering Mechanics, Tsinghua University, Beijing 100084, People's Republic of China.

Contributed by the Heat Transfer Division for publication in the JOURNAL OF HEAT TRANSFER. Manuscript received by the Heat Transfer Division July 5, 1982.

$$\Lambda=\frac{2\xi}{u_1}\frac{du_1}{d\xi}=2\left(\frac{u_\infty}{u_1}\right)^2\cdot\frac{d(u_1/u_\infty)}{d(x/d_o)}\int_o^x\left(\frac{u_1}{u_\infty}\right)\frac{dx}{d_o}\qquad(14)$$

The solutions of equations (10) and (11) can be expressed as [2, 3]

$$F(\xi,\eta)=F_o(\xi,\eta)+2\xi\frac{d\Lambda}{d\xi}F_1(\Lambda,\eta)+\ldots\qquad(15)$$

$$S(\xi,\eta)=S_o(\xi,\eta)+2\xi\frac{d\Lambda}{d\xi}S_1(\Lambda,\eta)+\ldots\qquad(16)$$

Upon substituting (15) and (16) into (10) and (11) and equating coefficients, we obtain the equations for the zero-order terms F_o and S_o as

$$F_o'''+F_oF_o''+\Lambda[1+S_o-(F_o')^2]=0\qquad(17)$$

$$S_o''+\mathrm{Pr}_\infty F_oS_o'=0\qquad(18)$$

with boundary conditions

$$\eta=0,\ F_o=F_o'=0,\ S_o=(h_w/h_\infty)-1\qquad(19)$$

$$\eta\to\infty,\ F_o'=1,\ S_o=0\qquad(20)$$

where the boundary condition for S_o in (19) is in a more general form than that in [1]. We shall limit our discussion to the zero-order terms although the equations and corresponding boundary conditions for higher order terms can be readily obtained by means of a method similar to that used in [3]. Good accuracy may still be obtained for predicting the heat flux, as we shall see later on.

The coupled ordinary differential equations (17) and (18) with boundary conditions (19) and (20) are easily solved by the Runge-Kutta-Gill method. Calculated results may be expressed approximately as

$$(S_o')_w=0.507\,\mathrm{Pr}_\infty^{0.4}\{\Lambda+0.927(1-\Lambda)\cdot[1+0.034(1-\mathrm{Pr}_\infty)]\}\cdot\left[1-\left(\frac{h_w}{h_\infty}\right)^{1.14}\right]\qquad(21)$$

for the following parameter range

$$\mathrm{Pr}_\infty=(0.1-1.0),\ \Lambda=(0.0-1.0),\ (h_w/h_\infty)=(0.0-0.4)$$

If the local specific heat flux due to enthalpy difference is denoted by q, then

$$q=\left(\frac{\kappa}{C_p}\frac{\partial h}{\partial y}\right)_w=\left(\frac{\kappa}{C_p}\right)_\infty\left(\frac{h_\infty}{d_o}\right)\sqrt{\frac{\mathrm{Re}_\infty}{2\xi}}\left(\frac{u_1}{u_\infty}\right)\left(\frac{\partial S}{\partial\eta}\right)_w$$

For a cylinder, we have $\xi=1-\cos\gamma$ from equations (6) and (8). By expressing $(\partial S/\partial\eta)_w\simeq(S_0')_w$ and $(\kappa/C_p)_\infty=\mu_\infty/\mathrm{Pr}_\infty$, we obtain

$$q=1.014h_\infty\left(\frac{u_\infty\rho_\infty\mu_\infty}{d_o}\right)^{0.5}\mathrm{Pr}_\infty^{-0.6}\cos\left(\frac{\gamma}{2}\right)\cdot\{\Lambda+0.927(1-\Lambda)\cdot[1+0.034(1-\mathrm{Pr}_\infty)]\}\cdot\left[1-\left(\frac{h_w}{h_\infty}\right)^{1.14}\right]\qquad(22)$$

Because the boundary layer approximation is not applicable to the separated region along the rear half of a cylinder, the average value of the specific heat flux around the whole cylinder cannot be directly obtained, although the average over its front half may be readily calculated from equation (22). However, considering the experimental fact that approximately 3/4 of the total heat flux entering the cylinder is concentrated at the front half [4], we can express the circumferentially averaged specific heat flux, $\bar{q}$, as

$$\bar{q}=0.60h_\infty\left(\frac{u_\infty\rho_\infty\mu_\infty}{d_o}\right)^{0.5}\mathrm{Pr}_\infty^{-0.6}\left[1-\left(\frac{h_w}{h_\infty}\right)^{1.14}\right]\qquad(23)$$

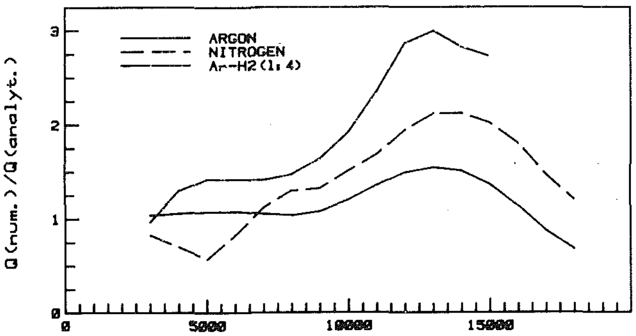

Fig. 1 Correction factors for three types of thermal plasmas as functions of the oncoming plasma temperature

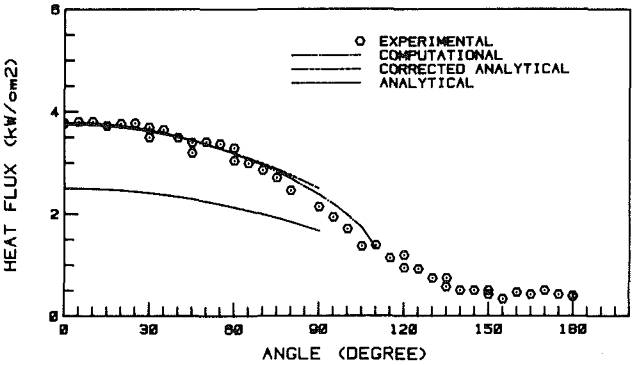

Fig. 2 Comparisons of experimental data [4] with computational, analytical, and corrected analytical results (argon plasma parameters: $T_\infty=1324\mathrm{OK}$, $u_\infty=230$ m/s, $d_o=1.2$ mm)

Comparisons with Computational and Experimental Results

It is seen from equations (22) and (23) that the local specific heat flux and hence its circumferentially averaged value, are proportional to the square root of the oncoming velocity, u_∞, and inversely proportional to the square root of the cylinder diameter. These results are consistent with those by computation including actual plasma properties (same with those used in [5]). Sample computational results were given in [1] for an argon plasma, and similar results are obtained also for Ar-H_2 (mole ratio 1:4) and N_2 plasmas. Thus, the only parameter left in this study is the temperature of the oncoming plasma flow. The simplified analytical solution needs a correction in order to obtain results consistent with computational ones based on actual plasma properties. The computational study shows that we can introduce a correction factor for the expressions of specific heat flux (22) and (23), and that the factor only depends on the oncoming temperature, regardless of the oncoming velocity, the cylinder diameter, or the angular location on the surface of the front part of the cylinder. The temperature-dependent correction factors for three types of thermal plasmas (Ar, Ar-H_2 and N_2) are shown in Fig. 1. These values for the correction factor are obtained by comparisons of the simplified analytical results with corresponding computational data for various combinations of the oncoming plasma temperature, velocity, and cylinder diameter. Equations (22) and (23) should include the correction factor as shown in Fig. 1 for practical applications.

The computational and analytical results for argon plasma are compared with those of an experimental study in Fig. 2. The experimental data are taken from [4]. Specific heat fluxes shown in Fig. 2 are those obtained after subtracting the part due to the current contribution from the experimental heat fluxes [1].

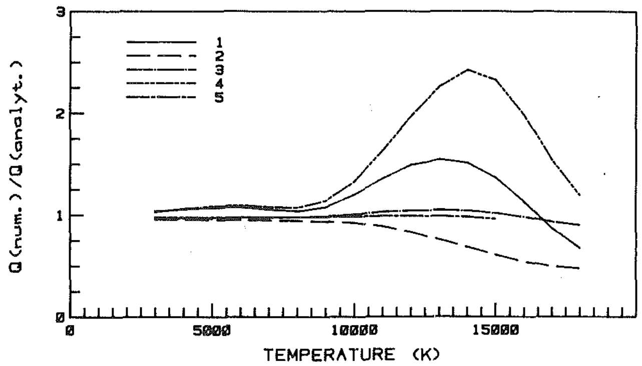

Fig. 3 Ratios of the computational heat flux to that by the analytical solution. All three assumptions (*7a–7c*) are used in the analytical solution. The following properties are used for the computation: 1 – actual properties of argon; 2 – assumptions (*7a*) and (*7c*), actual μ; 3 – assumptions (*7b*) and (*7c*), actual ρ; 4 – assumptions (*7a*) and (*7b*), actual κ/C_p; 5 – assumptions (*7a–7c*).

An examination of Fig. 2 shows that: (*i*) although the analytical solution underestimates the heat fluxes for this particular case, it agrees well with the computational result after a constant correction factor has been included; (*ii*) the computational results are in general agreement with experimental data despite the use of the boundary layer approximation and the potential outer flow relation (6). When one uses Hiemenz's empirical relation (see [2], p. 473) instead of the potential outer flow relation, agreement between the experimental data and computational results gets worse. This is believed to occur because this empirical relation was obtained for a much higher Reynolds number ($\mathrm{Re}_\infty = 1.8 \times 10^4$).

Discussion on the Correction Factor

The main reason for the introduction of the correction factor is that actual properties of a thermal plasma usually do not satisfy perfectly the relations (*7a–7c*) used for the analytical solution. According to assumptions (*7a–7c*), the combinations of properties (ρh), ($\rho\kappa/C_p$), and ($\rho\mu$) should assume constant values everywhere within the boundary layer, but it is not the case. We always underestimate or overestimate their values, more or less, in the analytical solution. The temperature-dependent correction factor is a complicated summation of effects of all the three assumptions. In [1], we discussed the physical significance of the correction factor in this way based on argon plasma properties. A similar discussion can also be performed for the Ar-H_2 plasma or the N_2 plasma, if it is needed.

In order to clarify further the physical implication of the correction factor, some computational results are shown in Fig. 3 for an argon plasma. In this figure, Curve 1 represents the computational heat flux including actual properties to that predicted by the simplified analytical solution. In other words, it shows the correction factor as a function of plasma temperature. Assumptions (*7a*) and (*7c*), (*7b*) and (*7c*), and (*7a*) and (*7b*) were used with the numerical solutions for Curve 2, 3, and 4, respectively, and all three assumptions were used in the analytical solution. Therefore, Curves 2–4 represent the effects only due to assumptions (*7b*), (*7a*), and (*7c*), respectively. An examination of these curves shows that when the temperature is below 9000 K for argon plasma, assumptions (*7a–7c*) are all good enough so that only a few percent error would be introduced by any of them. For a higher temperature, assumption (*7a*) is still good enough, but assumption (*7b*) or (*7c*) would introduce a pronounced error into the analytical solution, although the two assumptions affect in opposite directions. For Curve 5, all three assumptions (*7a–7c*) are used for both computation and analysis. Hence, the ratio of the heat fluxes reflects the error introduced due to using only zero-order terms of the series solutions (15) and (16) in the analytical solution. Curve 5 always assumes a value of approximately 1.0 within the range of the plasma temperature. This fact shows the approximate treatment in the analysis (only using zero-order terms) is not an important source of error.

Acknowledgments

This work was supported in part by the National Science Foundation of the United States under grant NSF/CPE 8008950, and in part by the Ministry of Education, PRC. The author is grateful to Professor E. Pfender for his encouragement, and to Professor S. V. Patankar whose general-purpose computer program for boundary layer flows was used in this study.

References

1 Chen, Xi, "Analysis and Computation of Heat Transfer Around a Cylinder in Argon Plasma Crossflow," 1982 AIAA/ASME 3rd Joint Thermophysics, Fluids, Plasma and Heat Transfer Conference, St. Louis, ASME Paper No. 82-HT-30.

2 Merk, H. J., "Rapid Calculations for Boundary-Layer Transfer Using Wedge Solutions and Asymptotic Expansions," *Journal of Fluid Mechanics*, Vol. 5, 1959, pp. 460–480.

3 Chao, B. T., and Fagbenle, R. O., "On Merk's Method of Calculating Boundary Layer Transfer," *International Journal of Heat and Mass Transfer*, Vol. 17, 1974, pp. 223–240.

4 Kanzawa, A., and Nonouchi, S., "Distribution of Current Density and Heat Flux around a Cylindrical Probe under Atmospheric Pressure," *International Chemical Engineering*, Vol. 16, 1976, pp. 184–189.

5 Chen, Xi, and Pfender, E., "Heat Transfer to a Single Particle Exposed to a Thermal Plasma," *Plasma Chemistry and Plasma Processing*, Vol. 2, 1982, pp. 185–212.

Mixed Convection Over a Horizontal Plate

N. Ramachandran[1], B. F. Armaly[2], and T. S. Chen[2]

Introduction

It is well known that thermal buoyancy forces play a significant role in forced convection heat transfer when the flow velocity is relatively small and the temperature difference between the surface and the free stream is relatively large. Analytical studies of mixed convection in laminar boundary layer flow have been conducted for vertical, horizontal, and inclined flat plates (see, for example, [1–4]). In these studies, various solution methods have been used but the convergence of these solutions becomes increasingly difficult as the buoyancy parameter increases. For that reason, available results are limited to only low values of that parameter. It is clear from previous studies that the available results for horizontal plates are limited to small values of the buoyancy parameter. This fact motivated the present study to provide results for mixed convection over heated horizontal plates for the entire range of the buoyancy parameter from pure forced to pure free convection.

Analysis

The problem of laminar mixed convection flow over a heated isothermal, semi-infinite horizontal flat plate was

---

[1] Department of Mechanical and Aerospace Engineering, University of Missouri-Rolla, Rolla, Mo. 65401.

[2] Department of Mechanical and Aerospace Engineering, University of Missouri-Rolla, Mem. ASME.

Contributed by the Heat Transfer Division for publication in the JOURNAL OF HEAT TRANSFER. Manuscript received by the Heat Transfer Division August 30, 1982.

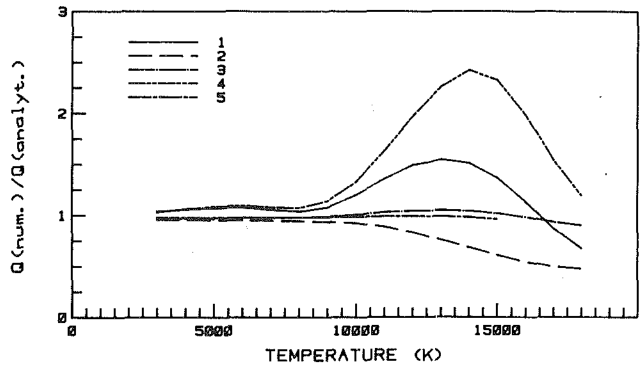

Fig. 3 Ratios of the computational heat flux to that by the analytical solution. All three assumptions (*7a-7c*) are used in the analytical solution. The following properties are used for the computation: 1 – actual properties of argon; 2 – assumptions (*7a*) and (*7c*), actual μ; 3 – assumptions (*7b*) and (*7c*), actual ρ; 4 – assumptions (*7a*) and (*7b*), actual κ/C_p; 5 – assumptions (*7a-7c*).

An examination of Fig. 2 shows that: (*i*) although the analytical solution underestimates the heat fluxes for this particular case, it agrees well with the computational result after a constant correction factor has been included; (*ii*) the computational results are in general agreement with experimental data despite the use of the boundary layer approximation and the potential outer flow relation (6). When one uses Hiemenz's empirical relation (see [2], p. 473) instead of the potential outer flow relation, agreement between the experimental data and computational results gets worse. This is believed to occur because this empirical relation was obtained for a much higher Reynolds number ($\mathrm{Re}_\infty = 1.8 \times 10^4$).

Discussion on the Correction Factor

The main reason for the introduction of the correction factor is that actual properties of a thermal plasma usually do not satisfy perfectly the relations (*7a-7c*) used for the analytical solution. According to assumptions (*7a-7c*), the combinations of properties (ρh), ($\rho\kappa/C_p$), and ($\rho\mu$) should assume constant values everywhere within the boundary layer, but it is not the case. We always underestimate or overestimate their values, more or less, in the analytical solution. The temperature-dependent correction factor is a complicated summation of effects of all the three assumptions. In [1], we discussed the physical significance of the correction factor in this way based on argon plasma properties. A similar discussion can also be performed for the Ar-H_2 plasma or the N_2 plasma, if it is needed.

In order to clarify further the physical implication of the correction factor, some computational results are shown in Fig. 3 for an argon plasma. In this figure, Curve 1 represents the computational heat flux including actual properties to that predicted by the simplified analytical solution. In other words, it shows the correction factor as a function of plasma temperature. Assumptions (*7a*) and (*7c*), (*7b*) and (*7c*), and (*7a*) and (*7b*) were used with the numerical solutions for Curve 2, 3, and 4, respectively, and all three assumptions were used in the analytical solution. Therefore, Curves 2–4 represent the effects only due to assumptions (*7b*), (*7a*), and (*7c*), respectively. An examination of these curves shows that when the temperature is below 9000 K for argon plasma, assumptions (*7a-7c*) are all good enough so that only a few percent error would be introduced by any of them. For a higher temperature, assumption (*7a*) is still good enough, but assumption (*7b*) or (*7c*) would introduce a pronounced error into the analytical solution, although the two assumptions affect in opposite directions. For Curve 5, all three assumptions (*7a-7c*) are used for both computation and analysis. Hence, the ratio of the heat fluxes reflects the error introduced due to using only zero-order terms of the series solutions (15) and (16) in the analytical solution. Curve 5 always assumes a value of approximately 1.0 within the range of the plasma temperature. This fact shows the approximate treatment in the analysis (only using zero-order terms) is not an important source of error.

Acknowledgments

This work was supported in part by the National Science Foundation of the United States under grant NSF/CPE 8008950, and in part by the Ministry of Education, PRC. The author is grateful to Professor E. Pfender for his encouragement, and to Professor S. V. Patankar whose general-purpose computer program for boundary layer flows was used in this study.

References

1 Chen, Xi, "Analysis and Computation of Heat Transfer Around a Cylinder in Argon Plasma Crossflow," 1982 AIAA/ASME 3rd Joint Thermophysics, Fluids, Plasma and Heat Transfer Conference, St. Louis, ASME Paper No. 82-HT-30.

2 Merk, H. J., "Rapid Calculations for Boundary-Layer Transfer Using Wedge Solutions and Asymptotic Expansions," *Journal of Fluid Mechanics*, Vol. 5, 1959, pp. 460–480.

3 Chao, B. T., and Fagbenle, R. O., "On Merk's Method of Calculating Boundary Layer Transfer," *International Journal of Heat and Mass Transfer*, Vol. 17, 1974, pp. 223–240.

4 Kanzawa, A., and Nonouchi, S., "Distribution of Current Density and Heat Flux around a Cylindrical Probe under Atmospheric Pressure," *International Chemical Engineering*, Vol. 16, 1976, pp. 184–189.

5 Chen, Xi, and Pfender, E., "Heat Transfer to a Single Particle Exposed to a Thermal Plasma," *Plasma Chemistry and Plasma Processing*, Vol. 2, 1982, pp. 185–212.

Mixed Convection Over a Horizontal Plate

N. Ramachandran[1], **B. F. Armaly**[2], **and T. S. Chen**[2]

Introduction

It is well known that thermal buoyancy forces play a significant role in forced convection heat transfer when the flow velocity is relatively small and the temperature difference between the surface and the free stream is relatively large. Analytical studies of mixed convection in laminar boundary layer flow have been conducted for vertical, horizontal, and inclined flat plates (see, for example, [1–4]). In these studies, various solution methods have been used but the convergence of these solutions becomes increasingly difficult as the buoyancy parameter increases. For that reason, available results are limited to only low values of that parameter. It is clear from previous studies that the available results for horizontal plates are limited to small values of the buoyancy parameter. This fact motivated the present study to provide results for mixed convection over heated horizontal plates for the entire range of the buoyancy parameter from pure forced to pure free convection.

Analysis

The problem of laminar mixed convection flow over a heated isothermal, semi-infinite horizontal flat plate was

---

[1] Department of Mechanical and Aerospace Engineering, University of Missouri-Rolla, Rolla, Mo. 65401.

[2] Department of Mechanical and Aerospace Engineering, University of Missouri-Rolla, Mem. ASME.

Contributed by the Heat Transfer Division for publication in the JOURNAL OF HEAT TRANSFER. Manuscript received by the Heat Transfer Division August 30, 1982.

recently studied by Chen et al. [2]. In that study the effects of buoyancy force on forced convection were analyzed. The boundary layer equations (given by equations (1-4) in [2]) were transformed from the (x, y) coordinates to the $(\xi(x), \eta(x, y))$ coordinates by introducing

$$\xi = \mathrm{Gr}_x/\mathrm{Re}_x{}^{5/2}, \quad \eta = y\sqrt{u_\infty/\nu x} \qquad (1)$$

along with a reduced stream function $F(\xi, \eta)$ and a dimensionless temperature $\theta(\xi, \eta)$ defined, respectively, as

$$F(\xi,\eta) = \frac{\psi(x,y)}{\sqrt{\nu u_\infty x}}, \quad \theta(\xi,\eta) = \frac{(T-T_\infty)}{(T_w - T_\infty)} \qquad (2)$$

where Re_x and Gr_x are local Reynolds and Grashof numbers respectively, and $\psi(x, y)$ is the stream function. The transformed equations are given by [2].

$$F'''' + \frac{1}{2}(FF''' + F'F'') + \frac{1}{2}\xi\eta\theta' - \frac{1}{2}\xi^2\frac{\partial\theta}{\partial\xi} = \frac{1}{2}\xi\left(F'\frac{\partial F''}{\partial\xi} - F'''\frac{\partial F}{\partial\xi}\right) \qquad (3)$$

$$\frac{1}{\mathrm{Pr}}\theta'' + \frac{1}{2}F\theta' = \frac{1}{2}\xi\left(F'\frac{\partial\theta}{\partial\xi} - \theta'\frac{\partial F}{\partial\xi}\right) \qquad (4)$$

$$F'(\xi,0) = F(\xi,0) = 0, \quad \theta(\xi,0) = 1 \qquad (5a)$$

$$F'''(\xi,0) = -\frac{1}{2}\xi\int_0^\infty \theta d\eta - \frac{1}{2}\xi^2\int_0^\infty \frac{\partial\theta}{\partial\xi}d\eta \qquad (5b)$$

$$F'(\xi,\infty) = 1, \quad \theta(\xi,\infty) = 0 \qquad (5c)$$

In the foregoing equations, the primes denote partial differentiation with respect to η.

The primary physical quantities of interest are the local Nusselt number, Nu_x, the local friction factor, C_f, the velocity distribution $u/u_\infty = F'(\xi,\eta)$, and the temperature distribution $\theta(\xi, \eta)$. The first two quantities can be expressed, respectively, by

$$\mathrm{Nu}_x/\sqrt{\mathrm{Re}_x} = -\theta'(\xi,0), \quad C_f\sqrt{\mathrm{Re}_x} = 2F''(\xi,0) \qquad (6)$$

A finite difference solution scheme, which is a modified version of that developed by Keller and Cebeci [5], was used to solve equations (3-5). The use of this solution scheme, which has been successfully employed in [3, 4], provided a solution over a wide range of buoyancy parameter $0 \leq \xi(x) \leq 10$. The convergence of this solution method becomes somewhat difficult when $\xi > 10$.

To examine the effects of forced flow on free convection, it is convenient to transform the governing equations (equations (1-4) of [2]) from (x, y) coordinates to the $\xi_1(x)$ and $\eta_1(x, y)$ coordinates by introducing

$$\xi_1(x) = \mathrm{Re}_x{}^{5/2}/\mathrm{Gr}_x, \quad \eta_1(x,y) = \frac{y}{x}\left(\frac{\mathrm{Gr}_x}{5}\right)^{1/5} \qquad (7)$$

The parameter, $\xi_1(x)$, is designated as a forced convection parameter, and it is equivalent to the inverse of the buoyancy parameter, $\xi(x)$. The reduced stream function $F_1(\xi_1, \eta_1)$ is defined as

$$F_1(\xi_1,\eta_1) = \frac{\psi_1(x,y)}{5\nu}\left(\frac{\mathrm{Gr}_x}{5}\right)^{-1/5} \qquad (8)$$

wherein $\psi_1(x,y)$ is the stream function. Using these variables along with $\theta_1 = (T-T_\infty)/(T_w - T_\infty)$ the governing equations can be transformed into

$$F_1'''' + 3F_1F_1''' + F_1'F_1'' + \frac{2}{5}\eta_1\theta_1' + \frac{1}{2}\xi_1\frac{\partial\theta}{\partial\xi_1} = \frac{5}{2}\xi_1\left[F_1'''\frac{\partial F_1}{\partial\xi_1} - F_1'\frac{\partial F_1''}{\partial\xi_1}\right] \qquad (9)$$

$$\frac{1}{\mathrm{Pr}}\theta_1'' + 3F_1\theta_1' = \frac{5}{2}\xi_1\left[\theta_1'\frac{\partial F_1}{\partial\xi_1} - F_1'\frac{\partial\theta_1}{\partial\xi_1}\right] \qquad (10)$$

$$F_1'(\xi_1,0) = 0, \quad 3F_1(\xi_1,0) - \frac{5}{2}\xi_1\frac{\partial F_1}{\partial\xi_1}(\xi_1,0) = 0, \quad \theta_1(\xi_1,0) = 1 \qquad (11)$$

$$F_1'(\xi_1,\infty) = \frac{1}{5^{3/5}}\xi_1{}^{2/5}, \quad \theta_1(\xi_1,\infty) = 0 \qquad (12)$$

$$F_1'''(\xi_1,0) = -\frac{2}{5}\int_0^\infty \theta_1 d\eta_1 + \frac{1}{2}\xi_1\int_0^\infty \frac{\partial\theta_1}{\partial\xi_1}d\eta_1 \qquad (13)$$

It should be noted that the forced flow effects come into the problem through the boundary conditions $F_1'(\xi_1,\infty)$. In addition, the finite difference solution scheme which was used to solve equations (3-5) is not suitable for solving the above set of equations, because $\xi_1(x)$ is inversely proportional to the square root of x. For that reason equations (9-13) were solved in this study by the local nonsimilarity and the local similarity methods.

The local wall shear stress and the local Nusselt number for the free convection dominated case have the following expressions.

$$\tau_w = 5(\mu\nu/x^2)(\mathrm{Gr}_x/5)^{3/5}F_1''(\xi_1,0) \qquad (14)$$

$$\mathrm{Nu}_x = -(\mathrm{Gr}_x/5)^{1/5}\theta_1'(\xi_1,0) \qquad (15)$$

The solutions of the two systems of equations, buoyancy effects on forced convection and forced flow effects on free convection as described above, provide results for heat transfer over the entire regime of mixed forced and free convection.

Results and Discussion

Numerical computations were carried out for fluids having Prandtl numbers of 0.01, 0.1, 0.7, 7, 50, and 100 over the entire regime of mixed forced and free convection. The effects of buoyancy force on forced convection was determined by solving equations (3-5), and the effects of forced flow on free convection was determined by solving equations (9-13). Results are summarized in Table 1 and Table 2 and they can be compared on the basis of the following relationships

$$\eta_1 = \left(\frac{\xi}{5}\right)^{1/5}\eta, \quad \xi_1 = \frac{1}{\xi} \qquad (16)$$

$$F_1''(\xi_1,0) = \frac{F''(\xi,0)}{5^{2/5}\xi^{3/5}} \qquad (17)$$

$$\theta_1'(\xi_1,0) = \left(\frac{5}{\xi}\right)^{1/5}\theta'(\xi,0) \qquad (18)$$

The local Nusselt numbers are presented in Fig. 1 as a function of the buoyancy parameter for various Prandtl numbers. The figure contains straight dashed lines and straight solid-dashed lines that represent, respectively, the results for pure forced and pure free convection flows. The solid lines correspond to the mixed forced and free convection results, and they asymptotically approach the pure forced $(\xi = 0)$ and pure free $(\xi_1 = 0)$ convection regimes. For all values of buoyancy parameters, the Nusselt numbers for the mixed forced and free convection regime are higher than what would be in either of the pure forced or pure free convection regime. Significant deviations from the pure forced convection results become apparent at lower values of the buoyancy parameter ξ for fluids having lower Prandtl numbers. On the other hand, significant deviations from the pure free convection results become apparent at higher values of the buoyancy parameter ξ (or lower values of the forced flow parameter ξ_1) for fluids having a larger Prandtl number.

Table 1 Results for $F_1''(\xi_1,0)$ and $-\theta_1'(\xi_1,0)$

	Pr = 0.01		Pr = 0.1		Pr = 0.7		Pr = 7		Pr = 50		Pr = 100	
ξ_1	A_1^*	B_1^*	A_1^*	B_1^*	A_1^*	B_1^*	A_1^*	B_1^*	A_1^*	B_1^*	A_1^*	B_1^*
0.000	2.2964	.1181	1.0659	.2708	.5192	.4892	.2185	.8681	.1028	1.3324	.0787	1.5431
0.005	2.2934	.1189	1.0571	.2724	.5180	.4935	.2227	.8833	.1083	1.3830	.0826	1.5991
0.010	2.2902	.1191	1.0544	.2729	.5181	.4949	.2245	.8891	.1108	1.4026	.0841	1.6174
0.025	2.2826	.1195	1.0501	.2740	.5188	.4978	.2288	.9007	.1147	1.4316	.0867	1.6475
0.050	2.2747	.1199	1.0466	.2757	.5200	.5009	.2337	.9133	.1237	1.4879	.0902	1.6846
0.075	2.2692	.1202	1.0445	.2758	.5209	.5028	.2368	.9206	.1282	1.5132	.0948	1.7276
0.100	2.2666	.1204	1.0422	.2766	.5223	.5050	.2407	.9295	.1337	1.5432	.0975	1.7517

$A_1^* = F_1''(\xi_1,0)$, $B_1^* = -\theta_1'(\xi_1,0)$

Table 2 Results for $F''(\xi,0)$ and $-\theta'(\xi,0)$

	Pr = 0.01		Pr = 0.1		Pr = 0.7		Pr = 7		Pr = 50		Pr = 100	
ξ	A^*	B^*	A^*	B^*	A^*	B^*	A^*	B^*	A^*	B^*	A^*	B^*
0.000	.3321	.0516	.3321	.1450	.3321	.2927	.3321	.6459	.3321	1.2474	.3321	1.5718
0.005	.4023	.0531	.3549	.1418	.3405	.2944	.3344	.6472	.3328	1.2484	.3325	1.5725
0.010	.4646	.0543	.3766	.1435	.3488	.2961	.3368	.6485	.3335	1.2490	.3330	1.5731
0.025	.6244	.0571	.4359	.1477	.3723	.3007	.3437	.6520	.3356	1.2513	.3343	1.5749
0.050	.8417	.0606	.5223	.1534	.4085	.3076	.3549	.6576	.3391	1.2548	.3366	1.5779
0.075	1.0264	.0632	.5987	.1580	.4414	.3134	.3655	.6629	.3425	1.2584	.3388	1.5809
0.100	1.1912	.0653	.6683	.1618	.4725	.3187	.3758	.6679	.3456	1.2615	.3410	1.5839
0.200	1.7289	.0713	.9053	.1738	.5811	.3359	.4141	.6858	.3588	1.2748	.3497	1.5952
0.300	2.1891	.0758	1.1044	.1825	.6747	.3493	.4488	.7012	.3789	1.2870	.3580	1.6060
0.400	2.5860	.0792	1.2808	.1895	.7586	.3603	.4809	.7148	.3831	1.2986	.3661	1.6164
0.500	2.9464	.0821	1.4416	.1954	.8357	.3698	.5099	.7274	.3946	1.3095	.3739	1.6263
0.750	3.7406	.0877	1.7978	.2073	1.0059	.3891	.5744	.7511	.4213	1.3338	.3930	1.6494
1.000	4.4370	.0921	2.1114	.2166	1.1587	.4049	.6414	.7758	.4473	1.3576	.4105	1.6706
2.000	6.7032	.1039	3.1297	.2414	1.6565	.4483	.8476	.8425	.5357	1.4325	.4740	1.7424
3.000	8.2457	.1100	3.9687	.2586	2.0632	.4782	1.0177	.8903	.6114	1.4902	.5297	1.8002
4.000	9.8282	.1162	4.8362	.2673	2.4198	.5014	1.1675	.9282	.6790	1.5382	.5797	1.8493
5.000	11.2598	.1212	5.3588	.2828	2.7433	.5207	1.3031	.9602	.7410	1.5795	.6258	1.8923
6.000	12.5816	.1255	5.9683	.2923	3.0422	.5373	1.4341	.9868	.7984	1.6162	.6690	1.9308
7.000	13.8188	.1292	6.5757	.3014	3.3179	.5582	1.5509	1.0114	.8568	1.6433	.7099	1.9656
8.000	14.9870	.1326	7.0761	.3080	3.5787	.5649	1.6616	1.0336	.9072	1.6735	.7486	1.9977
10.000	17.1776	.1383	7.8987	.3177	4.0417	.5873	1.8683	1.0725	1.0035	1.7259	.8212	2.0551

$A^* = F''(\xi,0)$, $B^* = -\theta'(\xi,0)$

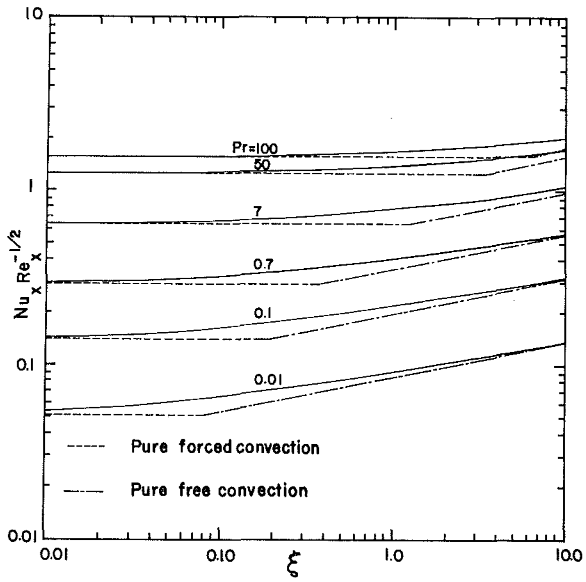

Fig. 1 The effect of buoyancy parameter on local Nusselt number

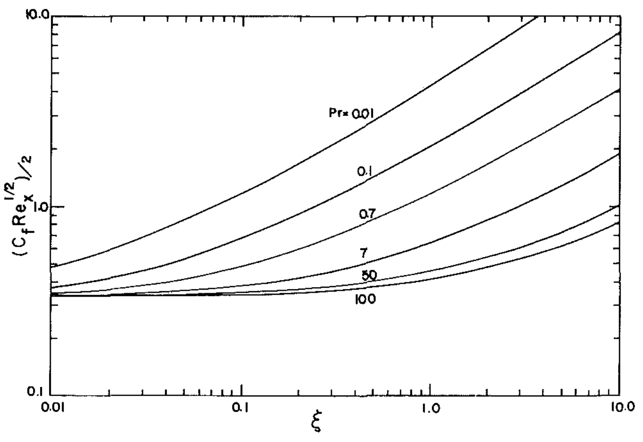

Fig. 2 The effect of buoyancy parameter on local friction coefficient

The local friction factor results are presented as a function of the buoyancy parameter ξ for the various Prandtl numbers in Fig. 2. A higher friction factor is associated with fluids having lower Prandtl numbers, and the friction factor increases as the buoyancy parameter increases. The local friction factor is more sensitive to changes in the buoyancy parameter than is the local Nusselt number, and this sensitivity increases as the Prandtl number decreases. This fact is due to the significant changes that occur in the velocity distribution for fluids with low Prandtl numbers, even for a small increase in the buoyancy parameter.

Representative velocity and temperature distributions are presented in Fig. 3 only for fluids with a Prandtl number, Pr, of 0.7. It is clear from this figure that velocity overshoot, above the free stream velocity, can be quite large. A higher overshoot has been found to be associated with a lower Prandtl number and a higher buoyancy parameter. For example, for fluids with a Prandtl number of 0.1 the overshoot factor is larger than 3 for buoyancy parameter $\xi = 5$, whereas for Pr = 0.7 the overshoot factor is about 1.6 for $\xi = 5$ (Fig. 3). Fluids with Prandtl numbers of 7, 50, and 100 did not

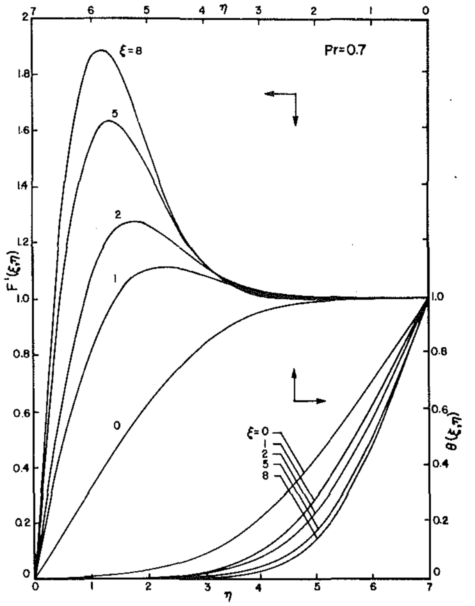

Fig. 3 Velocity and temperature distributions for Pr = 0.70

Table 3 Mixed convection regime

Pr	Region
100	$0.750 \leq \xi \leq 80$
50	$0.503 \leq \xi \leq 40$
7	$0.157 \leq \xi \leq 20$
0.70	$0.049 \leq \xi \leq 9.5$
0.10	$0.045 \leq \xi \leq 2.75$
0.01	$0.010 \leq \xi \leq 2.0$

exhibit an overshoot in velocity for buoyancy parameters smaller than 10 ($\xi < 10$), but they will develop this characteristic at higher values of the buoyancy parameter. The mixed convection regime defined as the region where the Nusselt numbers resulting from mixed convection deviate more than 5 percent from either the pure forced or the pure free convection values, is given in Table 3 for different Prandtl numbers.

Conclusion

From the present results, it has been found that fluids with lower Prandtl numbers are more sensitive to the buoyancy parameter, while fluids with higher Prandtl numbers are more sensitive to the forced convection parameter. Both the Nusselt number and the friction factor are found to increase with increasing buoyancy parameter, and their magnitudes are always higher than the corresponding values for pure forced or pure free convection. The velocity field is more sensitive to the buoyancy effect than the temperature field, and the velocity profiles exhibit a significant overshoot beyond their free stream value.

Acknowledgment

This study was supported in part by a grant from the National Science Foundation (NSF CME 79-19459).

References

1 Lloyd, J. R., and Sparrow, E. M., "Combined Forced and Free Convection Flow on Vertical Surfaces," *International Journal of Heat and Mass Transfer*, Vol. 13, 1970, pp. 434-438.

2 Chen, T. S., Sparrow, E. M., and Mucoglu, A., "Mixed Convection in Boundary Layer Flows on a Horizontal Plate," ASME JOURNAL OF HEAT TRANSFER, Vol. 99, 1977, pp. 66-71.

3 Mucoglu, A., and Chen, T. S., "Mixed Convection on Inclined Surfaces," ASME JOURNAL OF HEAT TRANSFER, Vol. 101, 1979, pp. 422-426.

4 Moutsoglou, A., Tzuoo, S. K. L., and Chen, T. S., "Mixed Convection in Boundary Layer Flows over Inclined Surfaces," Paper No. AIAA-80-1525, AIAA 15th Thermophysics Conference, Snowmass, Colo., July 14-16, 1980.

5 Keller, H. B., and Cebeci, T., "Accurate Numerical Methods for Boundary Layer Flows, Part I: Two-Dimensional Laminar Flows," *Proceedings of 2nd International Conference on Numerical Methods in Fluid Dynamics*, Springer-Verlag, Berlin, 1971.